

Science and Technology of Nuclear Installations

Selected Papers from OECD-NEA PSBT Benchmark

Guest Editors: Maria Avramova, Annalisa Manera,
David Novog, Diana Cuervo, and Alessandro Petruzzi





**Selected Papers from OECD-NEA
PSBT Benchmark**

Science and Technology of Nuclear Installations

**Selected Papers from OECD-NEA
PSBT Benchmark**

Guest Editors: Maria Avramova, Annalisa Manera,
David Novog, Diana Cuervo, and Alessandro Petruzzi



Copyright © 2014 Hindawi Publishing Corporation. All rights reserved.

This is a special issue published in “Science and Technology of Nuclear Installations.” All articles are open access articles distributed under the Creative Commons Attribution License, which permits unrestricted use, distribution, and reproduction in any medium, provided the original work is properly cited.

Editorial Board

Nusret Aksan, Switzerland
Antonio C. M. Alvim, Brazil
Won Pil Baek, Republic of Korea
Stephen M. Bajorek, USA
George Bakos, Greece
Jozsef Banati, Sweden
Ricardo Barros, Brazil
Anis Bousbia Salah, Belgium
Giovanni B. Bruna, France
Nikola avlina, Croatia
Xu Cheng, China
Leon Cizelj, Slovenia
Alejandro Clausse, Argentina
Francesco D' Auria, Italy
Marcos P. de Abreu, Brazil
Giovanni Dell'Orco, France
Juan Carlos Ferreri, Argentina
Nikolay Fil, Russia
Cesare Frepoli, USA
Giorgio Galassi, Italy
Regina Galetti, Brazil

Michel Giot, Belgium
Valerio Giusti, Italy
Horst Glaeser, Germany
Satish Kumar Gupta, India
Ali Hainoun, Syria
Keith E. Holbert, USA
Kostadin Ivanov, USA
Yacine Kadi, Republic of Korea
Ahmed Khedr, Egypt
Tomasz Kozlowski, USA
Tomoaki Kunugi, Japan
Mike Kuznetsov, Germany
Hyeong-Y. Lee, Republic of Korea
Bundit Limmeechokchai, Thailand
Jiri Macek, Czech Republic
Annalisa Manera, USA
Borut Mavko, Slovenia
Oleg Melikhov, Russia
Rafael Mir, Spain
Josef Misak, Czech Republic
Rahim Nabbi, Germany

Manmohan Pandey, India
Yuriy Parfenov, Russia
Yves Pontillon, France
Nik Popov, Canada
Piero Ravetto, Italy
Francesc Reventos, Spain
Enrico Sartori, France
Carlo Sborchia, France
Massimo Sepielli, Italy
Arkady Serikov, Germany
James F. Stubbins, USA
Iztok Tiselj, Slovenia
Rizwan Uddin, USA
Eugenijus Upuras, Lithuania
Richard Wright, Norway
Chao Xu, China
X. George Xu, USA
Yanko Yanev, Bulgaria
Zhiwei Zhou, China
Enrico Zio, Italy
Massimo Zucchetti, Italy

Contents

Selected Papers from OECD-NEA PSBT Benchmark, Maria Avramova, Annalisa Manera, David Novog, Diana Cuervo, and Alessandro Petruzzi
Volume 2014, Article ID 694016, 3 pages

Overview and Discussion of the OECD/NRC Benchmark Based on NUPEC PWR Subchannel and Bundle Tests, M. Avramova, A. Rubin, and H. Utsuno
Volume 2013, Article ID 946173, 20 pages

Comparative Analysis of CTF and Trace Thermal-Hydraulic Codes Using OECD/NRC PSBT Benchmark Void Distribution Database, M. Avramova, A. Velazquez-Lozada, and A. Rubin
Volume 2013, Article ID 725687, 12 pages

Assessment of CTF Boiling Transition and Critical Heat Flux Modeling Capabilities Using the OECD/NRC BFBT and PSBT Benchmark Databases, Maria Avramova and Diana Cuervo
Volume 2013, Article ID 508485, 12 pages

OECD/NRC PSBT Benchmark: Investigating the CATHARE2 Capability to Predict Void Fraction in PWR Fuel Bundle, A. Del Nevo, D. Rozzia, F. Moretti, and F. D'Auria
Volume 2012, Article ID 757356, 10 pages

Evaluation of ASSERT-PV V3R1 against the PSBT Benchmark, Kenneth H. Leung and David R. Novog
Volume 2012, Article ID 863503, 21 pages

Analysis of Void Fraction Distribution and Departure from Nucleate Boiling in Single Subchannel and Bundle Geometries Using Subchannel, System, and Computational Fluid Dynamics Codes, Taewan Kim, Victor Petrov, Annalisa Manera, and Simon Lo
Volume 2012, Article ID 746467, 20 pages

Analysis of the NUPEC PSBT Tests with FLICA-OVAP, Matteo Bucci and Philippe Fillion
Volume 2012, Article ID 436142, 18 pages

CFD Analysis of a Void Distribution Benchmark of the NUPEC PSBT Tests: Model Calibration and Influence of Turbulence Modelling, E. Krepper and R. Rzehak
Volume 2012, Article ID 939561, 10 pages

Numerical Study of the Steady-State Subchannel Test-Case with NEPTUNE.CFD for the OECD/NRC NUPEC PSBT Benchmark, C. Baudry, M. Guingo, A. Douce, J. Laviéville, S. Mimouni, and M. Boucker
Volume 2012, Article ID 524598, 11 pages

Analysis of Subchannel and Rod Bundle PSBT Experiments with CATHARE 3, M. Valette
Volume 2012, Article ID 123426, 10 pages

Validation of the Subchannel Code SUBCHANFLOW Using the NUPEC PWR Tests (PSBT), Uwe Imke and Victor Hugo Sanchez
Volume 2012, Article ID 465059, 12 pages

Accuracy and Uncertainty Analysis of PSBT Benchmark Exercises Using a Subchannel Code MATRA, Dae-Hyun Hwang, Seong-Jin Kim, Kyong-Won Seo, and Hyuk Kwon
Volume 2012, Article ID 603752, 13 pages



Benchmark of Subchannel Code VIPRE-W with PSBT Void and Temperature Test Data, Y. Sung,
R. L. Oelrich Jr., C. C. Lee, N. Ruiz-Esquide, M. Gambetta, and C. M. Mazufri
Volume 2012, Article ID 757498, 11 pages

CFD Modeling of Boiling Flow in PSBT 5×5 Bundle, Simon Lo and Joseph Osman
Volume 2012, Article ID 795935, 8 pages

Editorial

Selected Papers from OECD-NEA PSBT Benchmark

**Maria Avramova,¹ Annalisa Manera,² David Novog,³
Diana Cuervo,⁴ and Alessandro Petruzzi⁵**

¹ *The Pennsylvania State University, 231 Reber Building, University Park, PA 16802, USA*

² *Department of Engineering & Radiological Sciences, University of Michigan, 2355 Bonisteel Boulevard, Ann Arbor, MI 48109-2104, USA*

³ *McMaster University, 1280 Main Street West, Hamilton, ON, Canada L6K 3N3*

⁴ *Universidad Politécnica de Madrid (UPM), Avenida Arco de la Victoria 4, 28040 Madrid, Spain*

⁵ *Nuclear Research Group San Piero a Grado, 1291 Via Livornese, San Piero a Grado, 56100 Pisa, Italy*

Correspondence should be addressed to Annalisa Manera; manera@umich.edu and David Novog; novog@mcmaster.ca

Received 18 April 2013; Accepted 18 April 2013; Published 26 February 2014

Copyright © 2014 Maria Avramova et al. This is an open access article distributed under the Creative Commons Attribution License, which permits unrestricted use, distribution, and reproduction in any medium, provided the original work is properly cited.

Historically, the prediction of safety margins has been based on system level thermal-hydraulic calculations employing suitable empirical formulations for assembly specific geometries and fuel-element grid spacers. These works have assessed response, margins, and consequences for the system based on one-dimensional two-fluid or drift-flux type thermal-hydraulics formulations with fuel-vendor specific hydraulic losses and heat transfer characteristics for various fuel assemblies, including the so-called hot channel. Analysis of the hot channel gives important information on flow rates, fuel element centerline temperature, fuel sheath temperature, and margin to the departure from nucleate boiling. Given the reliance of the above approaches on empirical formulations obtained from complex and often difficult experiments, there is significant interest in obtaining reliable and accurate results from computation tools which employ more fundamental empirical relationships which can be obtained from subsets of the domain or from other scaled experiments.

The need to refine models for best-estimate calculations, based on good-quality experimental data, has been expressed in many recent meetings in the field of nuclear applications. The needs arising in this respect should not be limited to the currently available macroscopic methods but should be extended to next-generation analysis techniques that focus on more microscopic processes. One of the most valuable databases identified for the thermal-hydraulics modeling was

developed by the Nuclear Power Engineering Corporation (NUPEC), Japan, which includes subchannel void fraction and departure from nucleate boiling (DNB) measurements in a representative pressurized water reactor (PWR) fuel assembly. Part of this database is made available for this international benchmark activity entitled as the NUPEC PWR Subchannel and Bundle Tests (PSBT) benchmark. This international project is officially approved by the Japan Ministry of Economy, Trade, and Industry (METI), U.S. Nuclear Regulatory Commission (NRC), and endorsed by the OECD/NEA.

Prediction of local subchannel flows, pressures, temperatures, and other phenomena such as void fraction and critical heat flux (CHF) is becoming increasingly important in the assessment of safety margins for nuclear power plants. In particular the methodologies available for such calculations have seen rapid development over the last ten to fifteen years. These include more mechanistic subchannel analysis codes as well as advanced applications of computational fluid dynamics (CFD). What is interesting is the assessment of the capability of these computational tools to predict the integral effects for experiments performed on whole assemblies under both steady and transient conditions. In this regard, the OECD-NEA has sponsored several international benchmarks pertaining to the thermal-hydraulic phenomena

in boiling water reactors (published elsewhere) and pressurized water reactors which are documented within this special issue.

Of note also is the relative scarcity in the literature of experimental data covering heat transfer, critical heat flux, and local subchannel void fraction distribution for full-scale assemblies under the same thermalhydraulic conditions as a PWR and utilizing water. For this benchmark Japan Atomic Energy Research Institute (JAERI) has released the experimental data including X-ray computer tomography measurements of the local void fraction for a full-scale PWR assembly at reactor pressures and temperatures. The uniqueness of this benchmark is that it provides insight into prediction capabilities across a wide range of conditions for codes that range from 1-dimensional averaged through to CFD. The fine-mesh high-quality subchannel void fraction and departure from nucleate boiling data encourage advancement in understanding and modeling of complex flow behavior in real bundles. Given the uniqueness and high quality of this database, this benchmark program and its subsequent publications have significantly added to the available scientific literature in this field. The published work in this special issue represents examination using a large number of thermalhydraulic tools ranging from macroscopic system type thermalhydraulic codes down to microscopic examinations using two-phase computational fluid dynamics models.

The papers within the special issue span a wide range of simulation methods. A general review and background of the benchmark activities are provided by M. Avramova et al. Of particular interest here are the comparisons of all the benchmark submissions to one another. In another paper, M. Avramova et al. examined the results of the CTF code, a three-fluid modification of the COBRA-TF code, and the US NRC code TRACE for the prediction of the PSBT experiments. This paper also includes a discussion of the time offset of 10 s (developed separately by the CEA in France) which must be applied to the transient portions of the experimental database to account for the heat capacity of the downcomer region in the NUPEC experiment. Further details of the CTF code and the main development issues suggested are included in M. Avramova et al.

The application of the system thermalhydraulic code CATHARE2 to the benchmark is presented by A. Del Nevo et al. Good agreement was found for the 1D results in general; however some overestimation of the central void fraction was observed in the 3D model results at lower void fractions (below 0.6). M. Valette used the CATHARE3 code which has enhancements on the number of fields treated as well as interfacial area transport capabilities. Simulations were also performed with the 1D and 3D capabilities of the code. The 1D predictions captured the average behavior quite well, and the author notes the limitations in applying the 3D module for subchannel analysis given that it was initially designed to simulate 3D flows in downcomers and plenums.

K. H. Leung and D. R. Novog used the ASSERT-PV subchannel code to predict the steady-state and transient NUPEC data and also observed overprediction of the subcooled and low quality void fraction and attributed it to the

range of pressures being different than the normal application range for ASSERT. Despite these differences, the critical channel power was predicted quite well with the ASSERT-PV subchannel code. A further observation of the limitations of the 1995 Groeveneld CHF lookup table at low mass fluxes was also observed. M. Bucci and P. Fillion studied the application of the FLICA-OVAP advanced subchannel code and examined the impact of CHF predictions by using the W3, Shah, and Katto and Ono CHF prediction methods. In these simulations the CHF predictions showed the best agreement with the Shah correlation. The authors also applied a 6 s delay to temperature transients to account for heat capacity effects. The SUBCHANFLOW, a modernized version of the COBRA subchannel code family, was used by M. Imke and V. H. Sanchez and predicted the subchannel and bundle void fractions very well, with similar small overprediction of void fraction in the low elevation and low void fraction region (similar to many other subchannel and CFD studies in this benchmark—further details on this tendency are provided later). The MATRA subchannel code which uses a mixture formulation was used by D. H. Hwang et al. who determined optimum mixing coefficients for their models. Here the uncertainty in void fraction prediction was also on the same order as the experimental error and the DNB was also most accurately predicted using the 1995 Groeneveld table as opposed to the other mechanistic models they tested. Y. Sung et al. used the VIPRE-W subchannel code, a Westinghouse developed version of the EPRI VIPRE-01 code, and also determined the optimal turbulent mixing coefficient for the NUPEC data. The VIPRE-W predicted void fractions using the modified EPRI mixing models were able to capture the void fraction measurements within the experimental uncertainties.

E. Krepper and R. Rezhak present the results obtained with the CFD code ANSYS CFX-12.1 for the void distribution tests of the benchmark. Relevant aspects of the implemented wall boiling model are reviewed highlighting the uncertainties in several model parameters. It is also shown that the measured cross-sectional averaged values can be reproduced well with a single set of calibrated model parameters for different tests case. The multifield NEPTUNE.CFD code was used to study five selected steady-state subchannel test cases by C. Baudry et al. Simulation results for the void fraction using a standard choice for the physical models and a constant, predetermined bubble diameter are compared to experimental data. Also, calculation results with devoted models for the bubble-size distribution are analyzed showing a visible impact on the subcooled run, giving void fraction closer to experiments than those obtained with a fixed bubble size. I. Kim et al. used the subchannel code FLICA4 and the commercial CFD code STAR-CCM+ in addition to the USNRC system code TRACE to analyze the benchmark experiments. The FLICA results show very good agreement with the experimental results with a small bias which is on the same order as the experimental uncertainty. The CFD results show a slightly larger bias, in particular at low void fractions. Additional details of the CFD calculations using STAR-CCM+ were also provided by S. Lo and J. Osman.

While the results show very promising prediction capabilities, there remain some key issues for investigation in the future. In particular not all authors reported the details of their prediction methodology and/or if any specific changes were made to the code or input data in order to match the experimental measurements. On one hand, in this regard a blind benchmark may have shed a more realistic view on the capabilities of both codes and analysts. On the other hand, blind benchmarks must undergo rigorous vetting of the specifications such that the participants do not deviate solely based on unplanned distortions in the input scenario. However, throughout the execution phase of this benchmark there were several discussions and clarifications shared amongst the participants that could only have taken place alongside the experimental results. These were mostly discussions centered on the geometry, conditions, and experimental measurements which helped ensure that the analyses were consistent to the greatest extent practicable. These were especially needed given the long period of time since the measurements were conducted and some discrepancies or lack of information in the original NUPEC documents. Hence, while a blind benchmark may have provided additional information, it would not have been practicable in this case.

Several of the computation results for CFD and subchannel analyses within this benchmark also point to overprediction of void fraction at low total void fraction conditions. One explanation is that the X-ray computed tomography measurements included in the benchmark may not efficiently detect very small amounts of nucleate boiling immediately adjacent to the fuel element surface. However, no additional test data is available which can be used to conclusively define the uncertainty in void fraction measurements under these very low void fraction conditions.

The editors would like to thank Dr. Hideaki Utsuno from Japan Nuclear Energy Safety Organization (JNES), Japan; Mr. Alexander Velazquez-Lozada and Dr. Stephen Bajorek from US NRC; and Dr. Enrico Sartori, Dr. Jim Gulliford, and Dr. Akifumi Yamaji from OECD/NEA, whose support, help, contributions, and encouragement in establishing and carrying out this benchmark are invaluable. This benchmark program is the sum of many efforts including the funding agencies and their staff—the Ministry for Economic Trade and Industry (METI), Japan, US NRC, and the Organization of Economic Co-operation and Development (OECD). Special appreciation goes to Professor Kostadin Ivanov from Pennsylvania State University (PSU) for his input into the program. The editors also wish to express their sincere appreciation for the outstanding support offered by the JNES personnel in providing the test data and discussing the test characteristics. Finally, our thanks go to the many authors and researchers who contributed to the technical success of this benchmark.

*Maria Avramova
Annalisa Manera
David Novog
Diana Cuervo
Alessandro Petruzzi*

Review Article

Overview and Discussion of the OECD/NRC Benchmark Based on NUPEC PWR Subchannel and Bundle Tests

M. Avramova,¹ A. Rubin,¹ and H. Utsuno²

¹ Nuclear Engineering Program, The Pennsylvania State University, University Park, PA 16802, USA

² Japan Nuclear Energy Safety Organization, Kamiyacho MT Building, 4-3-20, Toranomon, Minato, Tokyo 105-0001, Japan

Correspondence should be addressed to M. Avramova; mna109@psu.edu

Received 7 July 2012; Accepted 31 December 2012

Academic Editor: Annalisa Manera

Copyright © 2013 M. Avramova et al. This is an open access article distributed under the Creative Commons Attribution License, which permits unrestricted use, distribution, and reproduction in any medium, provided the original work is properly cited.

The Pennsylvania State University (PSU) under the sponsorship of the US Nuclear Regulatory Commission (NRC) has prepared, organized, conducted, and summarized the Organisation for Economic Co-operation and Development/US Nuclear Regulatory Commission (OECD/NRC) benchmark based on the Nuclear Power Engineering Corporation (NUPEC) pressurized water reactor (PWR) subchannel and bundle tests (PSBTs). The international benchmark activities have been conducted in cooperation with the Nuclear Energy Agency (NEA) of OECD and the Japan Nuclear Energy Safety Organization (JNES), Japan. The OECD/NRC PSBT benchmark was organized to provide a test bed for assessing the capabilities of various thermal-hydraulic subchannel, system, and computational fluid dynamics (CFDs) codes. The benchmark was designed to systematically assess and compare the participants' numerical models for prediction of detailed subchannel void distribution and departure from nucleate boiling (DNB), under steady-state and transient conditions, to full-scale experimental data. This paper provides an overview of the objectives of the benchmark along with a definition of the benchmark phases and exercises. The NUPEC PWR PSBT facility and the specific methods used in the void distribution measurements are discussed followed by a summary of comparative analyses of submitted final results for the exercises of the two benchmark phases.

1. Introduction

The need to refine the models for best-estimate calculations, based on good-quality experimental data, has been expressed in many recent meetings in the field of nuclear engineering. The needs arising in this respect should not be limited to the currently available macroscopic methods but should be extended to next-generation analysis techniques that focus on more microscopic processes. One of the most valuable databases identified for the thermal-hydraulics modeling was developed by the Nuclear Power Engineering Corporation (NUPEC), Japan, which includes subchannel void fraction and departure from nucleate boiling (DNB) measurements in a representative pressurized water reactor (PWR) fuel assembly [1–3]. From 1987 to 1995, NUPEC performed a series of void measurement tests using full-size mock-up tests for both BWRs and PWRs. Void fraction measurements and departure from nucleate boiling (DNB) tests were performed at NUPEC under steady-state and transient pressurized water

reactor (PWR) conditions. Part of this database is made available for an international benchmark activity entitled as the OECD/NRC NUPEC PWR subchannel and bundle tests (PSBT) benchmark [4]. This international project is officially approved by the Japan Ministry of Economy, Trade, and Industry (METI) and US Nuclear Regulatory Commission (NRC) and endorsed by the OECD/NEA. The benchmark team is organized based on the collaboration between Japan and USA.

The fine-mesh high-quality subchannel void fraction and departure from nucleate boiling data encourages the advancement in understanding and modeling complex flow behavior in real rod bundles. Considering that the present theoretical approach is relatively immature, the benchmark specification is designed to systematically assess and compare the participants' analytical models on the prediction of detailed void distributions and DNB. It should be recognized that the purpose of this benchmark is not only the comparison of currently available computational approaches

but, above all, the encouragement to develop novel next-generation approaches that focus on more microscopic processes.

The benchmark consists of two phases with a total of seven exercises, as described below.

- (i) Phase I: void distribution benchmark,
 - (a) exercise 1: steady-state single subchannel benchmark,
 - (b) exercise 2: steady-state bundle benchmark,
 - (c) exercise 3: transient bundle benchmark,
 - (d) exercise 4: Pressure drop benchmark.
- (ii) Phase II: DNB benchmark,
 - (a) exercise 1: steady-state fluid temperature benchmark,
 - (b) exercise 2: steady-state DNB benchmark,
 - (c) exercise 3: transient DNB benchmark.

The exercises in phase I of the benchmark are designed to test the codes' ability to predict void distribution in a single subchannel and a bundle under both steady-state and transient conditions as well as to calculate the pressure drop across a bundle.

The exercises in Phase II of the benchmark are designed to test the codes' ability to predict DNB in a bundle assembly under both steady-state and transient conditions, as well as to predict fluid temperatures under these conditions.

2. Description of PSBT Benchmark

The benchmark exercises were performed at the NUPEC test facility, shown in Figure 1. The facility consists of a high-pressure and high-temperature recirculation loop, a cooling loop, and instrumentation and data recording systems. The recirculation loop consists of a test section, circulation pump, preheater, steam drum (acting as a pressurizer), and a water mixer. The design pressure is 19.2 MPa and the design temperature is 362°C.

Three different test sections were used to perform the benchmark exercises: one for the subchannel void distribution test, one for the rod bundle void distribution test, and one for the bundle DNB measurements.

The transmission method of gamma-ray was used to measure the density and converted to the void fraction of the gas-liquid two-phase flow. In the DNB measurements, thermocouples were used to determine the heat flux axially along the rod bundle. The thermocouples were attached to the inner surface of the heater rods and determine the boiling transition. The bundle power was increased gradually by fine steps (about 30 kW) to the vicinity of DNB power, which was based on preliminary analysis and experience. The occurrence of DNB was confirmed by a rod temperature rise of more than 11°C (20°F) as measured by the thermocouples.

The range of operating conditions for the facility is given in Table 1, and the operating conditions for the four transient scenarios are given in Table 2.

TABLE 1: Range of NUPEC PWR test facility operating conditions.

Quantity	Range
Pressure	4.9–16.6 MPa
Mass velocity	550–4150 kg/m ² s
Inlet coolant temperature	140–345°C

2.1. Subchannel Test Assembly. Four different test assemblies were used to model void distribution in a single subchannel. The subchannels represented by these assemblies are described in Table 3. Figure 2 shows the test section used for the central subchannel void measurement. It simulates one of the subchannel types found in a PWR assembly. Coolant flows in the pressure vessel horizontally through the coolant inlet nozzle located just below the heated section. Similar test sections (Figure 3) were used for the central with thimble, side, and corner subchannel types. The effective heated length is 1555 mm, and the void measurement section begins at 1400 mm from the bottom of the heated section [4].

2.2. Bundle Test Assembly. Three different test assemblies were used to model void distribution in a rod bundle. The bundles represented by these assemblies are described in Table 4. An electrically heated rod bundle was used to simulate a partial section and full length of a PWR fuel assembly. Figure 4 shows the test section used for the rod bundle void measurements. The effective heated length is 3658 mm. The measurements were performed at three axial elevations: upper—3177 mm, middle—2669 mm, and lower—2216 mm, respectively (please note that the measurement elevations are taken from the bottom of heating section). Coolant flows into the pressure vessel horizontally through the coolant inlet nozzle and down through the section between the flow channel and the pressure vessel. The coolant continues into the flow channel, flowing from the bottom of the pressure vessel up through the test assembly, where the bottom of the heated section is located 630 mm above the bottom of the pressure vessel.

Figures 5 and 6 show the two different radial power distributions, named A and B, respectively. All powers shown are relative powers.

Table 5 shows the axial power distribution (based on a cosine shape) that was used in the bundle tests.

The test assemblies used for the DNB measurement benchmark are described in Table 6. The DNB measurements were performed for full-length partial 5 × 5 and 6 × 6 array rod bundles, which simulate 17 × 17 PWR fuel assemblies. Measurements were performed for both steady state and transients. The heater rods used in these bundles are of the same type as those used in the bundles in the void distribution measurements. Three different types of spacer grids were used in these assemblies: simple spacers, nonmixing vane grids, and mixing vane grids [4].

The available experimental data for the steady-state single subchannel benchmark includes CT scanner measurements of the void fraction (subchannel averaged) of four representative subchannel types: typical central, central with a

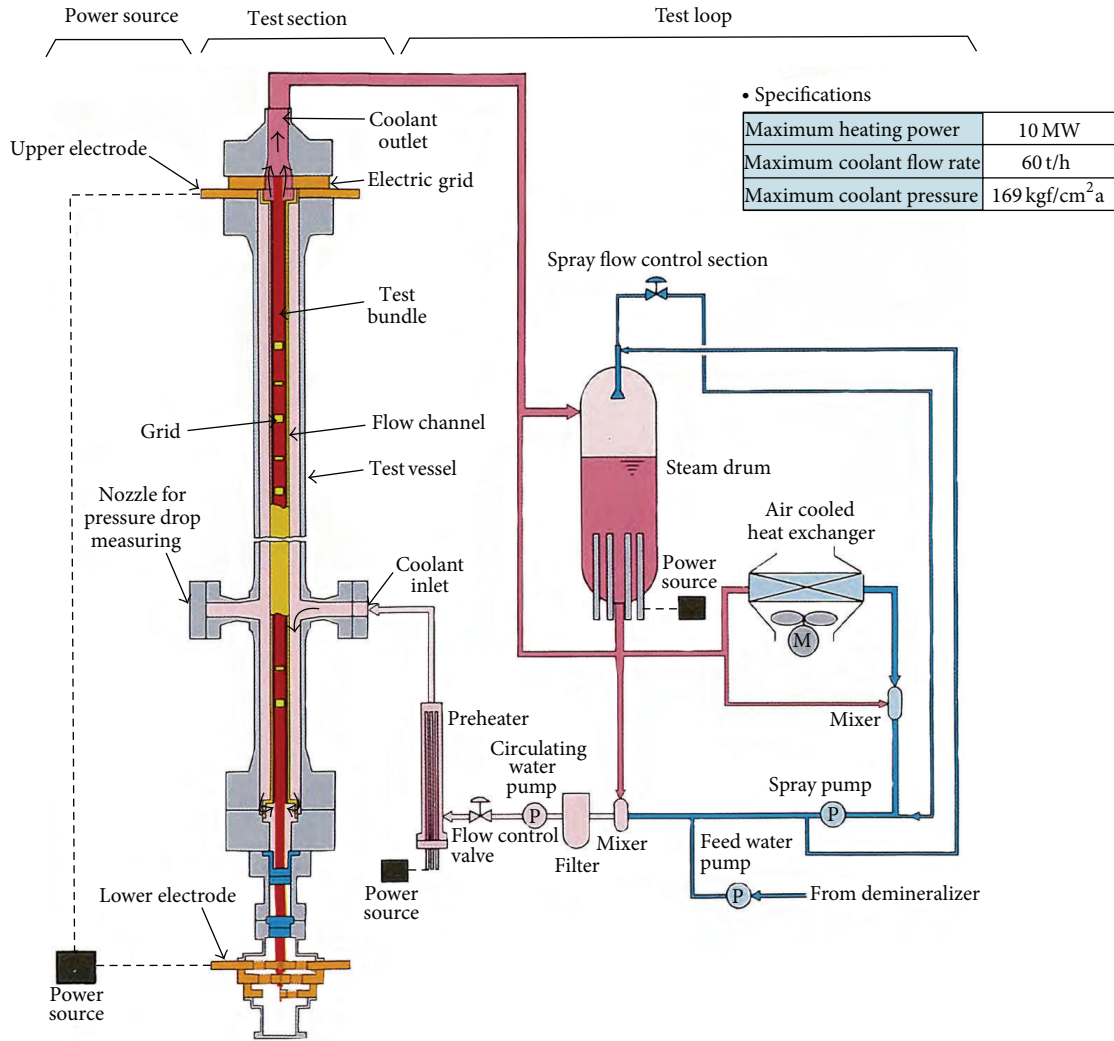


FIGURE 1: System diagram of NUPEC PWR test facility.

TABLE 2: Transient parameters of NUPEC PWR test facility.

Transient scenario	Transient change
Depressurization	-0.03 MPa/s
Temperature increase	1°C/s
Flow reduction	-25%/s
Power increase	15%/s

guide tube, side, and corner subchannels and images of the void distribution within two representative subchannel types: typical central and central with guide tube. The data can be used to assess and improve the current models for void generation (subchannel/system and CFD codes) and void distribution within subchannels (CFD codes).

The steady-state bundle benchmark utilizes experimental data that include X-ray densitometer measurements of void fraction (chordal averaged) at three axial elevations. The averaging is over the four central subchannels. The transient

bundle benchmark is based on data collected for four anticipated transient scenarios: power increase, flow reduction, depressurization, and temperature increase.

The experimental data for the steady-state DNB benchmark include the power at which departure from nucleate boiling occurs and the corresponding location in the bundle. Measured DNB power for four anticipated transient scenarios—power increase, flow reduction, depressurization, and temperature increase—was made available for the transient DNB benchmark. In addition to the void distribution and DNB power measurements, data is available for the subchannel exit fluid temperature.

2.3. Spacer Grid Data. There were three types of spacers instrumented along the axial length: simple spacer (SS), spacer with non-mixing vanes (NMVs), and spacer with mixing vanes (MVs). The simple spacer has only dimples while NMV and MV have dimples and springs. The grids straps are made out of Inconel 600 alloy. Detailed geometrical description of the grids used in the experiment was not

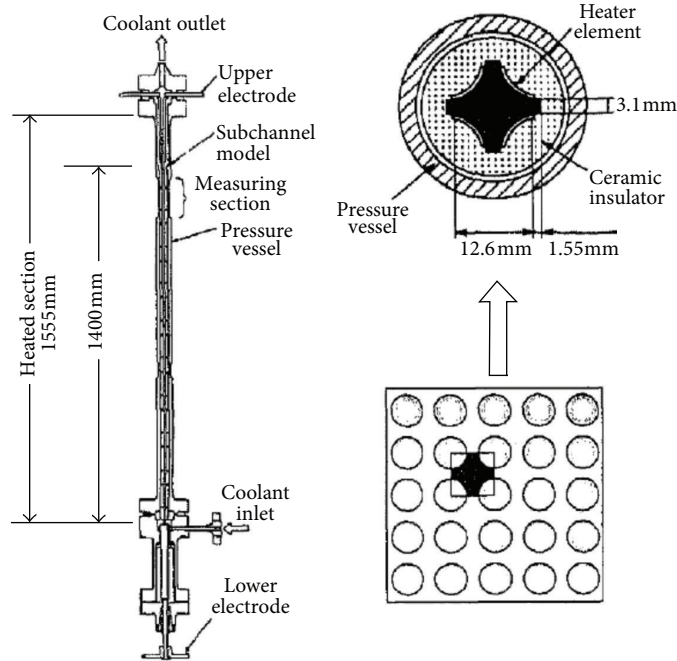


FIGURE 2: Test section for central subchannel void distribution measurement.

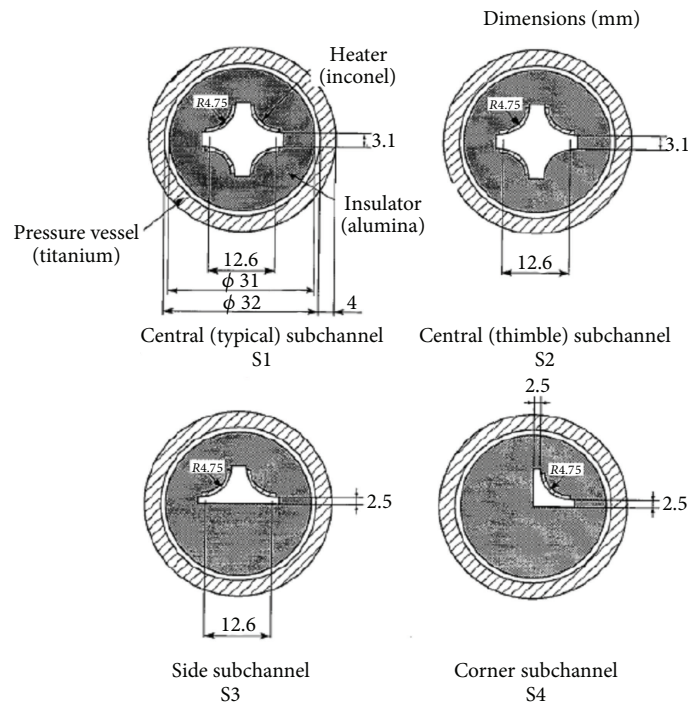


FIGURE 3: Cross-sectional view of subchannel test assembly.

available to the benchmark. As a result, the benchmark team, with the assistance of a benchmark participant, was forced to develop a grid model based on the understanding that the grids used in the experiments were similar to grids for which data was readily available. Table 7 summarizes the grid data that was available as part of the benchmark. Figures 7, 8, and 9 provide three-dimensional views of the simple spacer,

nonmixing vane, and mixing vane grids. The simple spacer has dimples while the mixing vane and nonmixing vane grids have both dimples and springs. These dimples provide a gap (~0.1 mm) around each heating rod, which prevents bowing of these rods when they linearly expand at high temperatures.

Table 7 provides the bundle average spacer pressure loss coefficients for the three types of grids. Depending on the

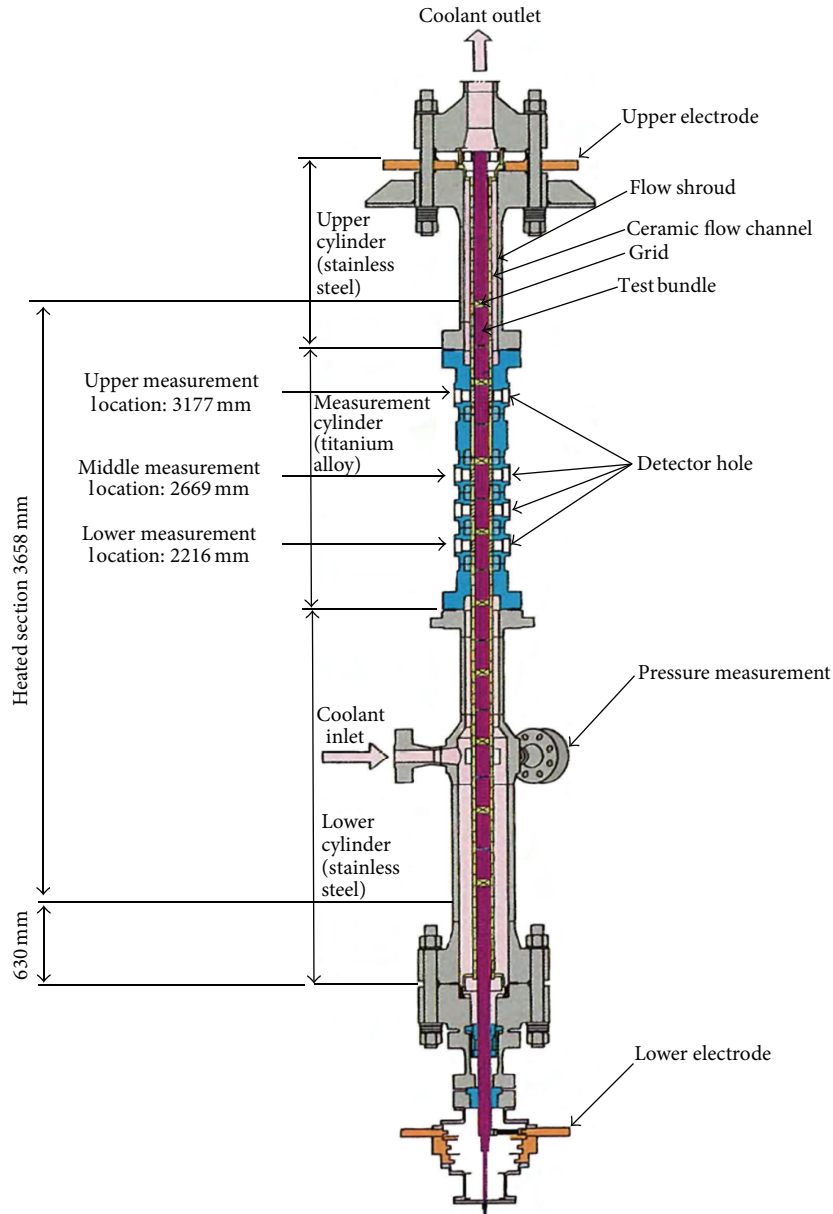


FIGURE 4: Test section for rod bundle void distribution measurement.

participants' computer code and using the provided spacer data, each participant may choose the subchannel grids loss coefficients or other required input values.

2.4. Heater Rod Data. Table 8 summarizes the material and geometrical properties of the heater rods used in the rod bundle tests. Figure 10 provides a cross-sectional view of the heater rods and gives dimensions.

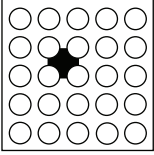
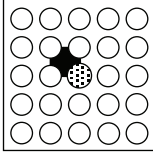
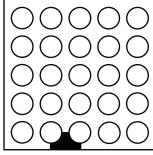
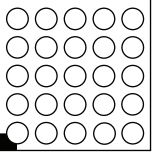
2.5. Measurement Techniques

2.5.1. Void Distribution. A gamma-ray transmission method was used to measure the density of the flow, which was converted to the void fraction of the gas-liquid two-phase

flow. Figure 11 shows the procedure used to perform the void fraction measurements for the entire rod bundle. The top half of the figure shows the procedure used to perform the void fraction measurements for a single subchannel. In the subchannel experiments, a narrow gamma-ray beam CT scanner was used to measure the subchannel averaged void fraction, and a wide gamma-ray beam was used to measure the chordal averaged void fraction. For each subchannel type—corner, side, or center—a relationship between the subchannel averaged and the chordal averaged void fractions was individually derived. These relationships were then used to correct the subchannel averaged void fraction measured with the wide beam in the bundle tests.

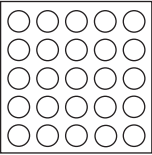
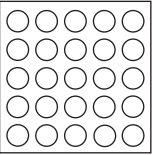
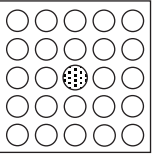
The void measurement systems shown in Figure 11 consist of gamma-ray sources (^{137}Cs), detectors, collimators, and

TABLE 3: Geometry and power shape for subchannel test assemblies for void distribution benchmark.

Item	Data			
Assembly (subjected subchannel)				
	S1	S2	S3	S4
Subchannel type	Center (typical)	Center (thimble)	Side	Corner
Number of heaters	4 × 1/4	3 × 1/4	2 × 1/4	1 × 1/4
Axial heated length (mm)	1555	1555	1555	1555
Axial power shape	Uniform	Uniform	Uniform	Uniform

Black part: subjected subchannel, white circles: heated rod, and circles with dots: thimble rod.

TABLE 4: Geometry and power shape for bundle test assemblies for void distribution benchmark.

Item	Data		
Assembly			
	B5	B6	B7
Rods array	5 × 5	5 × 5	5 × 5
Number of heated rods	25	25	24
Number of thimble rods	0	0	1
Heated rod outer diameter (mm)	9.50	9.50	9.50
Thimble rod outer diameter (mm)	—	—	12.24
Heated rods pitch (mm)	12.60	12.60	12.60
Axial heated length (mm)	3658	3658	3658
Flow channel inner width (mm)	64.9	64.9	64.9
Radial power shape	A	A	B
Axial power shape	Uniform	Cosine	Cosine
Number of MV spacers	7	7	7
Number of NMV spacers	2	2	2
Number of simple spacers	8	8	8
MV spacer location (mm)	471, 925, 1378, 1832, 2285, 2739, 3247		
NMV spacer location (mm)	2.5, 3755		
Simple spacer location (mm)	237, 698, 1151, 1605, 2059, 2512, 2993, 3501		

White circles: heated rod and circles with dots: thimble rod.

MV: mixing vane and NMV: non-mixing vane.

Spacer location is the distance from the bottom of heated length to spacer bottom face.

signal processing units. The attenuation of the gamma-rays, which depends on the void fraction, was detected. The intensity of the gamma-ray source was determined to obtain the count rate of the signal processing (30×10^4 cps). The CT scanner system was used to determine the distribution of density/void fraction over the subchannel at steady-state flow and to define the subchannel averaged void fraction. The system was operated by translate/rotate method. At each translation/rotation location, the intensity of gamma-ray attenuated by the object, the so-called “projection data”, was

detected. An image reconstruction was then performed by a filtered back-projection algorithm to obtain the distribution of the linear attenuation coefficient. A sufficient measuring time was given in order to avoid the effect of the flow motion. Two densitometer systems—in x - and y -directions—were used in the chordal averaged void fraction measurements in the single subchannel tests. Each of them consisted of a gamma source and a detector. They were located at the same tables (the same elevation) as CT, which was fixed during the measurements. A multibeam system was used to

0.85	0.85	0.85	0.85	0.85
0.85	1	1	1	0.85
0.85	1	1	1	0.85
0.85	1	1	1	0.85
0.85	0.85	0.85	0.85	0.85

FIGURE 5: Radial power distribution A.

0.85	0.85	0.85	0.85	0.85
0.85	1	1	1	0.85
0.85	1	0	1	0.85
0.85	1	1	1	0.85
0.85	0.85	0.85	0.85	0.85

FIGURE 6: Radial power distribution B.

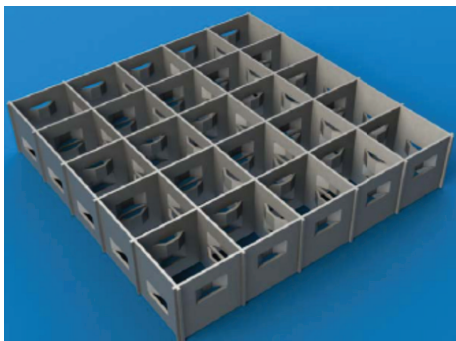


FIGURE 7: View of simple spacer grid.

measure each subchannel void fraction of the rod bundle. Six transmission data of x -direction and six transmission data of y -direction between the rod and rod/channel wall were used to reconstruct the void fraction of the 36 subchannels by an iterative method. These subchannel void fractions corresponded to the chordal measurements of the single subchannel tests. The relationships between the subchannel averaged void fraction and the chordal averaged void fraction obtained in the single subchannel tests were used to determine the

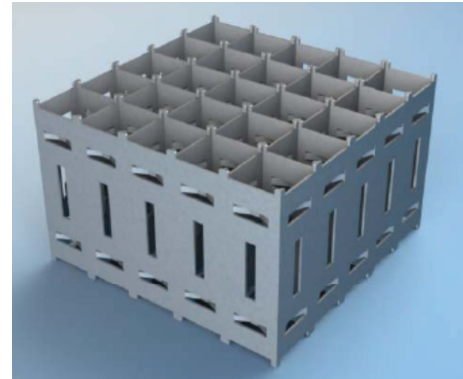


FIGURE 8: View of nonmixing vane spacer grid.

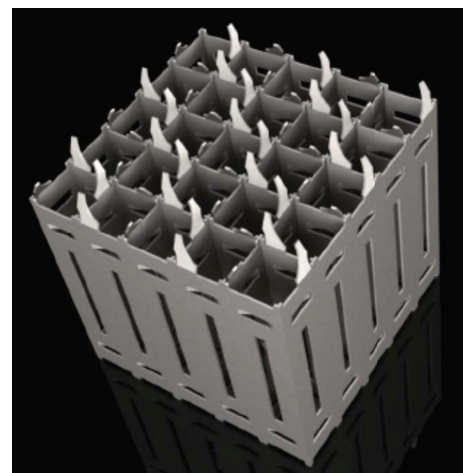


FIGURE 9: View of mixing vane spacer grid.

subchannel averaged void fractions in the rod bundle tests. Such measurements were performed simultaneously at three axial elevations. Table 9 shows the accuracy of the various parameters involved in the experiment. Table 10 summarizes the sources of error in the experiment.

Figure 12 illustrates the relationship between chordal and CT averaged densities as a function of pressure. It was used to determine the uncertainties inherent in the void measurements and to correct the measured values based on the pressure of the test case. The correlation between the chordal and CT averaged values is given by the best-fit curves and was introduced for the high- and low-pressure conditions, respectively. The reference averaged density was 500 kg/m^3 . The uncertainty of the correlation was determined to be less than 18 kg/m^3 , which was regarded as three standard deviations (3σ). Therefore, one standard deviation (1σ) is 6 kg/m^3 . Table 11 shows the number of gamma-ray beams used in the fluid density measurement for both subchannel and rod bundle exercises. Table 12 shows the amount of time required to perform the density measurement.

2.5.2. *Departure from Nucleate Boiling.* The bundle power was gradually increased in fine steps to the expected vicinity

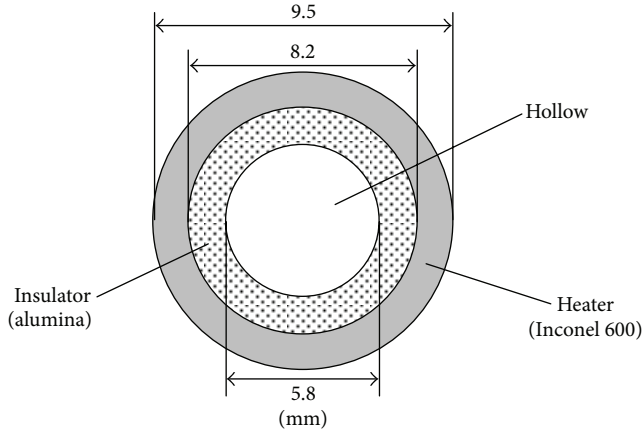


FIGURE 10: Cross-sectional View of Heater Rod.

TABLE 5: Cosine axial power distribution.

Node	Relative power
(Bottom)	
1	0.42
2	0.47
3	0.56
4	0.67
5	0.80
6	0.94
7	1.08
8	1.22
9	1.34
10	1.44
11	1.51
12	1.55
13	1.55
14	1.51
15	1.44
16	1.34
17	1.22
18	1.08
19	0.94
20	0.80
21	0.67
22	0.56
23	0.47
24	0.42
(Top)	

of DNB, which was based on previous analysis operator experience. The onset of DNB was confirmed by a rod temperature rise greater than 11°C (20°F) as measured by the thermocouples seen in Figure 13. The DNB power is defined as the power corresponding to the step immediately preceding the step in which this temperature rise is seen. The

accuracy of the process parameters involved in this process is seen in Table 13. The exit fluid temperatures were measured by the thermocouples shown in Figure 14.

2.6. Experimental Data Analysis. Based on the participants feedback, several studies were performed to determine the validity of the benchmark data. These included (1) study performed on recalculation of the void fraction, (2) study performed on calculation of the quality, (3) study performed on the subchannel CT masking, and (4) study performed on bundle test section downcomer region. In this paper, the studies (1), (2), and (4) performed by the benchmark team are presented.

2.6.1. Recalculation of Void Fraction. At the first PSBT workshop, it was noted by several participants that the “measured” void fractions (which were actually calculated from measured density data) were not consistent with void fractions calculated using the measured densities. As a result, a study was performed to recalculate the void fraction and the quality for each test case in the void distribution benchmark.

Solving the standard equation for mixture density ($\bar{\rho} = \alpha\rho_g + (1 - \alpha)\rho_f$) for the void fraction gives $\alpha = (\bar{\rho} - \rho_f)/(\rho_g - \rho_f)$, where the liquid and vapor densities (ρ_f and ρ_g , resp.) are assumed to be at saturation and the mixture density is taken from the benchmark data. After the recalculation (see Figure 15), it was noted that the measured void fraction was consistently higher than the recalculated void fraction. This recalculation was only performed for the subchannel test cases since those are the only test cases for which fluid density data was available.

2.6.2. Calculation of Quality. Upon completion of the study performed on void distribution, the benchmark team began a study of the calculation of quality based on the experimentally determined densities.

It is recalled that the quality can be expressed using mixture enthalpy as $x = (h_{\text{mix}} - h_f)/(h_g - h_f)$, where h_f and h_g are the liquid and vapor enthalpies, respectively. A number of different expressions were derived to determine the mixture enthalpy in the test sections assuming conservation of energy. After verifying that the axial power distribution was normalized for both the uniform and cosine power shapes, the following equations were obtained.

All four subchannel test sections utilized a uniform axial power distribution. Thus, for all subchannel assemblies, the mixture enthalpy at the measurement section can be given by

$$h_{\text{mix}} = h_{\text{in}} + \left(\frac{1400 \text{ mm}}{1555 \text{ mm}} \right) \times Q [\text{kW}] \times \frac{3600 [\text{s/h}]}{(A [\text{m}^2] G [\text{kg/m}^2\text{h}])}. \quad (1)$$

Figure 16 shows the resulting deviation of the experimental quality from the recalculated quality.

TABLE 6: Test assemblies for DNB measurements.

Assembly	Reference fuel type	Rods array	Type of cell	Power distribution	
				Radial	Axial
A0			Typical cell	A	Uniform
A1		5 × 5	Typical cell	C	Uniform
A2			Typical cell	A	Uniform
A3	17 × 17 M	6 × 6	Typical cell	D	Uniform
A4			Typical cell	A	Cosine
A8		5 × 5	Thimble cell	B	Cosine
A11			Typical cell	A	Cosine
A12			Thimble cell	B	Cosine

TABLE 7: Bundle average spacer pressure loss coefficients.

Spacer type	Loss coefficient
Simple spacer (SS)	0.4
Nonmixing vanes (NMVs) spacer	0.7
Mixing vanes (MVs) spacer	1.0

TABLE 8: Properties of heater rods.

Item	Data
Heater	
Outer diameter (mm)	9.5
Thickness (mm)	0.65
Material	Inconel 600
Heating method	Direct heating
Insulator	
Outer diameter (mm)	8.2
Inner diameter (mm)	5.8
Material	Alumina

Assembly B5 utilized a uniform axial power distribution, so the mixture enthalpies at the three measurement locations can be given as

$$\begin{aligned}
 h_{\text{mix}} &= h_{\text{in}} + \left(\frac{2216 \text{ mm}}{3658 \text{ mm}} \right) \times Q \text{ [kW]} \\
 &\quad \times \frac{3600 \text{ [s/h]}}{(A \text{ [m}^2\text{]} G \text{ [kg/m}^2\text{h]})} \quad (\text{lower elevation}), \\
 h_{\text{mix}} &= h_{\text{in}} + \left(\frac{2669 \text{ mm}}{3658 \text{ mm}} \right) \times Q \text{ [kW]} \\
 &\quad \times \frac{3600 \text{ [s/h]}}{(A \text{ [m}^2\text{]} G \text{ [kg/m}^2\text{h]})} \quad (\text{middle elevation}), \\
 h_{\text{mix}} &= h_{\text{in}} + \left(\frac{3177 \text{ mm}}{3658 \text{ mm}} \right) \times Q \text{ [kW]} \\
 &\quad \times \frac{3600 \text{ [s/h]}}{(A \text{ [m}^2\text{]} G \text{ [kg/m}^2\text{h]})} \quad (\text{upper elevation}).
 \end{aligned} \tag{2}$$

TABLE 9: Accuracy of process parameters in void distribution measurement.

Quantity	Accuracy
Process parameters	
Pressure	1%
Flow	1.5%
Power	1%
Fluid temperature	1 Celsius
Void fraction measurement	
CT measurement	
Gamma-ray beam width	1 mm
Subchannel averaged (steady state)	3% void
Spatial resolution of one pixel	0.5 mm
Chordal measurement	
Gamma-ray beam width (center)	3 mm
Gamma-ray beam width (side)	2 mm
Subchannel averaged (steady state)	4% void
Subchannel averaged (transient)	5% void

Assemblies B6 and B7 utilized a cosine axial power shape. Recalling that the power shape is normalized, it is possible to determine what fraction of the total power has been imparted to the fluid between the flow inlet and the measurement sections. The mixture enthalpies for these two assemblies can be given as

$$\begin{aligned}
 h_{\text{mix}} &= h_{\text{in}} + 0.6598 \times Q \text{ [kW]} \\
 &\quad \times \frac{3600 \text{ [s/h]}}{(A \text{ [m}^2\text{]} G \text{ [kg/m}^2\text{h]})} \quad (\text{Lower Elevation}), \\
 h_{\text{mix}} &= h_{\text{in}} + 0.8172 \times Q \text{ [kW]} \\
 &\quad \times \frac{3600 \text{ [s/h]}}{(A \text{ [m}^2\text{]} G \text{ [kg/m}^2\text{h]})} \quad (\text{Middle Elevation}), \\
 h_{\text{mix}} &= h_{\text{in}} + 0.9353 \times Q \text{ [kW]} \\
 &\quad \times \frac{3600 \text{ [s/h]}}{(A \text{ [m}^2\text{]} G \text{ [kg/m}^2\text{h]})} \quad (\text{Upper Elevation}).
 \end{aligned} \tag{3}$$

TABLE 10: Sources of error for void distribution measurement.

Error source	Chordal averaged		
	Steady state	Transient	CT averaged
γ -ray measurement			
Effect of surrounding condition (magnetic field and temperature) on measurement system	0.1%	0.1%	0.1%
Randomness of γ -ray source decay	0.02%	0.2%	0.1%
Correction error due to background	0.0%	0.0%	0.0%
Correction error due to counting loss	<0.5%	<0.5%	<0.1%
Calibration error	0.1%	0.1%	0.1%
Correction error due to attenuation by surrounding water	0.0%	0.0%	—
Correction error due to scattering from multi- γ -rays	<0.2%	<0.2%	—
Total	<0.55%	<0.6%	<0.2%
Subchannel density			
Transfer to density	<9 kg/m ³	<10 kg/m ³	<15 kg/m ³
Distribution error to subchannel	<5 kg/m ³	<5 kg/m ³	—
Correlation error from chordal averaged to CT averaged	<6 kg/m ³	<6 kg/m ³	—
Subchannel density	<20 kg/m ³	<21 kg/m ³	<15 kg/m ³
Subchannel void*	0.040	0.042	0.030
Uncertainty (1σ)	4%	5%	3%

* Reference averaged density is 500 kg/m³.

TABLE 11: Number of gamma-ray beams.

Test assembly	CT measurement	Chordal measurement
Subchannel	2 (X and Y direction)	2 (X and Y direction)
Rod bundle	—	6 beams \times 2 \times 3 section (total 36 beams)

TABLE 13: Accuracy of process parameters in DNB measurement.

Quantity	Accuracy
Process parameters	
Pressure	1%
Flow	1.5%
Power	1%
Fluid temperature	1 Celsius

TABLE 12: Time required to perform void fraction measurements.

Item	CT measurement	Chordal measurement
Steady state		
Time needed	5 s/step \times ^T 33 \times ^R 17 step (it takes 2 h)	100 s sampling cycle 0.1 s
Measurement	2 times	3 times
Transient		
Time needed	—	200 s
Measurement	—	1 time

After applying these equations and calculating the qualities for each case, the following results were obtained. Figures 17, 18, 19, and 20 show the deviation of experimental quality from recalculated quality for test series 5, 6, 7, and 8 (resp.).

3. Selected Examples of Comparative Analysis of Participant Results

Detailed comparative analysis of submitted participants' results for different exercises of the two phases of the benchmark has been reported in [5, 6]. In this paper, selected examples are shown to illustrate the methodology of comparisons and indicate the observed tendencies.

3.1. Phase I—Void Distribution. There were a total of twenty (20) participants for exercise 1 of phase I—Steady-state single subchannel benchmark [5]. Sixteen (16) of these participants submitted void fraction results, and eight (8) submitted axial void distribution results. Table 14 lists these participants as well as the codes for which results were submitted.

The axial nodalization of the problem varied widely depending on the code type. CFD codes, as expected, had significantly more nodes than the system and subchannel codes: both NEPTUNE [7] and ANSYS (ANSYS) [8] used nodalizations of \sim 100,000–1,000,000 nodes, while both KTH and PSI used about 30 axial nodes for TRACE. CATHARE

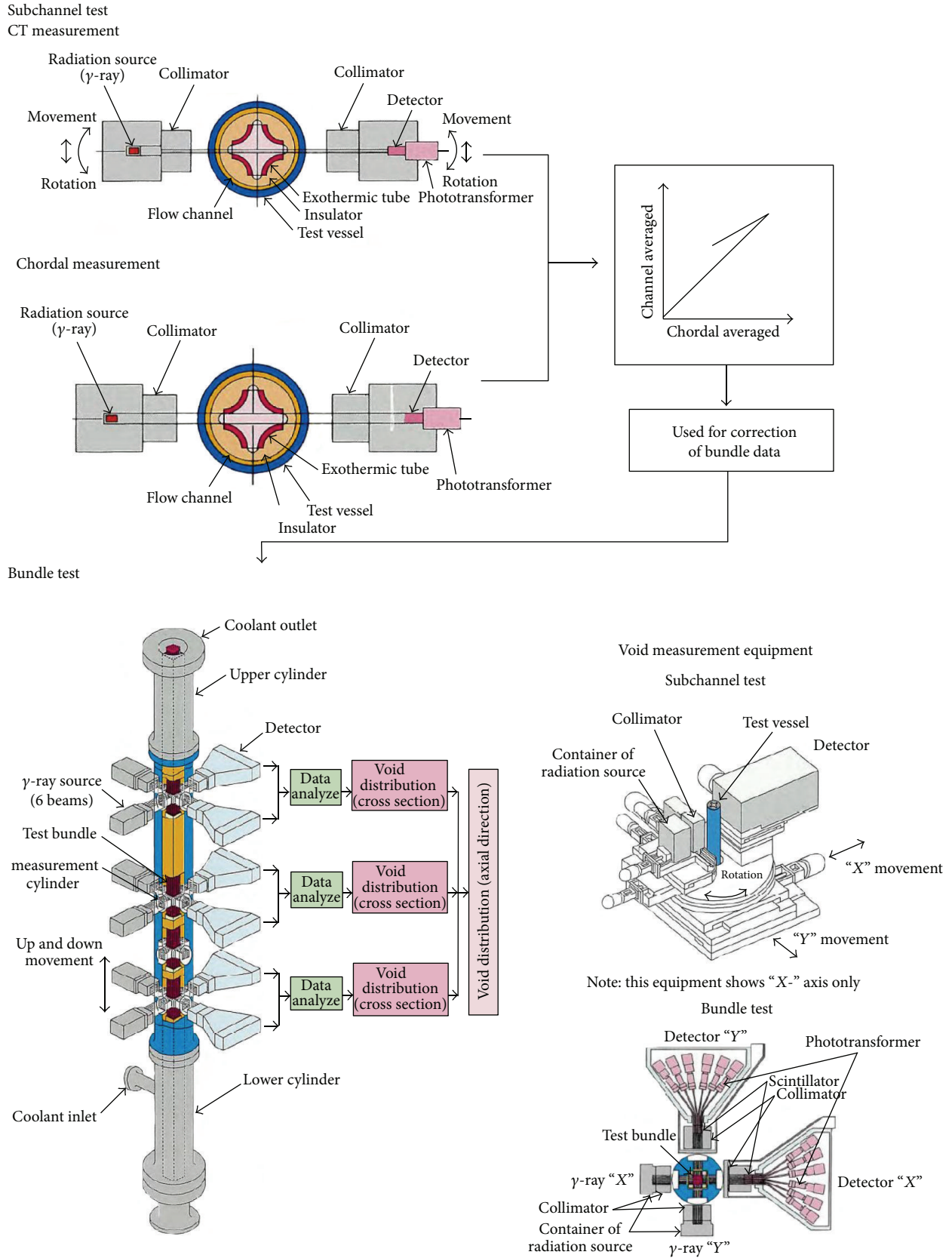


FIGURE 11: Void fraction measurement procedure.

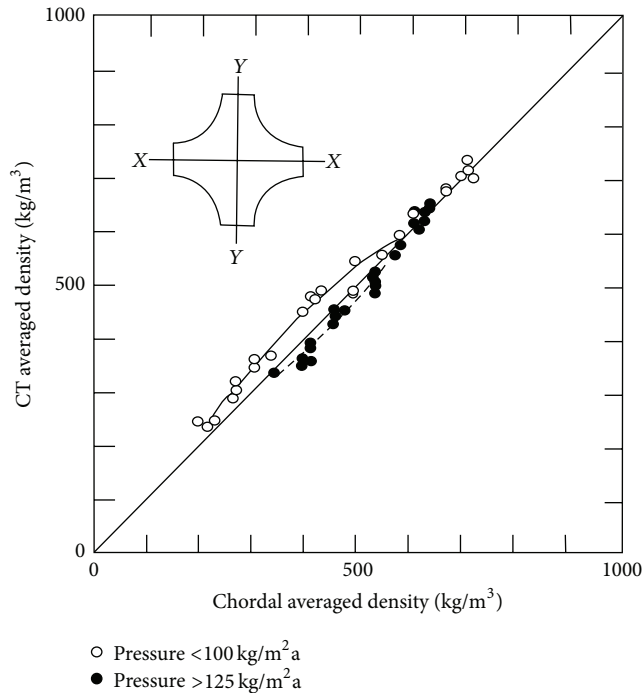


FIGURE 12: Relation Between Chordal and CT Averaged Densities (for S1).

TABLE 14: Phase I, exercise 1 participants and code list.

Participant	Code	Code type
ANL	STAR-CD	CFD
ANSYS	ANSYS	CFD
EDF	NEPTUNE	CFD
GRS	ANSYS-CFX	CFD
HZDR	ANSYS-CFX	CFD
PSI	STAR-CD	CFD
EDF	THYC	Porous media
AREVA	F-COBRA-TF	Subchannel
CEA-Saclay	FLICA-OVAP	Subchannel
CSA	VIPRE	Subchannel
JNES	CHAMP-ITA	Subchannel
KAERI	MATRA	Subchannel
KIT	SUBCHANFLOW	Subchannel
McMaster	ASSERT-PV	Subchannel
PSI	FLICA	Subchannel
CEA-Grenoble	CATHARE 3	System
IRSN	CATHARE 2	System
KTH	TRACE	System
PSI	TRACE	System
UNIPI	CATHARE 2	System

2 (UNIPI) [9] and STAR-CD (PSI) both used approximately 100 axial nodes.

TABLE 15: Phase I, exercise 2 participants and code list.

Participant	Code	Code type
EDF	THYC	Porous media
AREVA	F-COBRA-TF	Subchannel
CEA-Saclay	FLICA-OVAP	Subchannel
CSA	VIPRE	Subchannel
JNES	CHAMP-ITA	Subchannel
KAERI	MATRA	Subchannel
KIT	SUBCHANFLOW	Subchannel
McMaster	ASSERT-PV	Subchannel
NRI	VIPRE	Subchannel
PSI	FLICA	Subchannel
WEC/INVAP	VIPRE	Subchannel
CEA-Grenoble	CATHARE 3	System
Chalmers	RELAP-5	System
KTH	TRACE	System
PSI	TRACE	System
UNIPI	CATHARE 2	System
USNRC	TRACE	System

TABLE 16: Phase II, exercise 2 participants.

Participant	Code	Code type
EDF	THYC	Porous media
CEA-Saclay	FLICA-OVAP	Subchannel
KAERI	MATRA	Subchannel
KIT	SUBCHANFLOW	Subchannel
McMaster	ASSERT-PV	Subchannel
PSI	FLICA	Subchannel
NRI	VIPRE	Subchannel
CEA-Grenoble	CATHARE 3	System
KTH	TRACE	System

TABLE 17: Phase II, exercise 3 participants.

Participant	Code	Code type
EDF	THYC	Porous media
CEA-Saclay	FLICA-OVAP	Subchannel
KAERI	MATRA	Subchannel
KIT	SUBCHANFLOW	Subchannel
McMaster	ASSERT-PV	Subchannel
PSI	FLICA	Subchannel
NRI	VIPRE	Subchannel
KTH	TRACE	System

Finally, a variety of wall drag and heat transfer coefficients were also used. THYC, for example, used Gautier for monophasic and Chen for diphasic heat transfer, while FLICA (PSI) [10] used the Blasius correlation for single-phase friction losses with the Friedel correlation as a two-phase

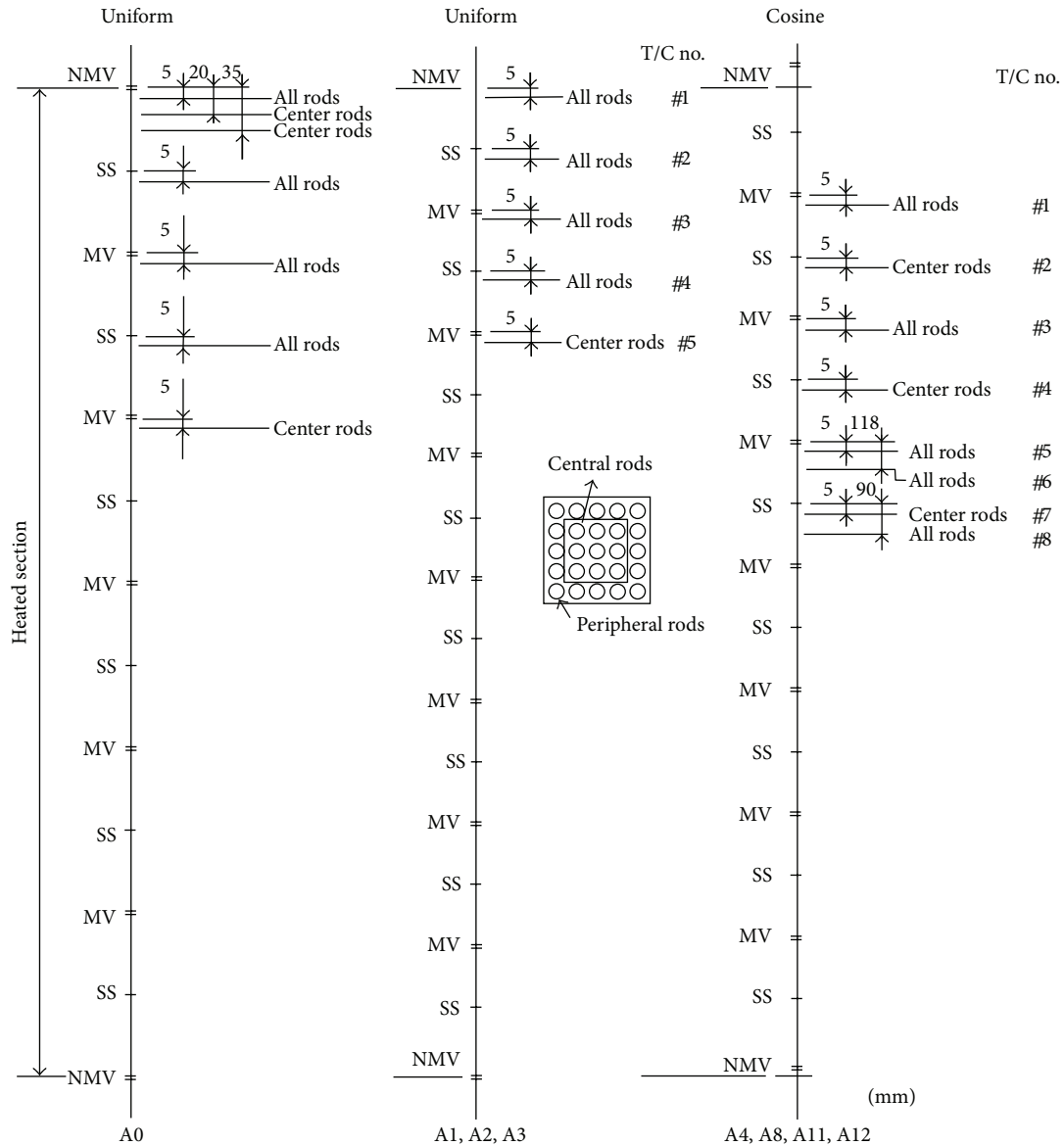


FIGURE 13: Locations of thermocouples for test assemblies.

multiplier. A number of codes used Dittus-Boelter for single-phase heat transfer and a variety of correlations (Jens-Lottes for FLICA (PSI)) were used.

Statistical methodology has been utilized for comparative analysis. Mean error and standard deviation were calculated for each code for each test series. The mean error (where N is the total number of test cases) was represented as $\bar{\alpha} = \sum_{n=1}^N \alpha^n / N$, where the void fraction error for test case “ n ” is represented as $\alpha^n = (\alpha_{code}^n - \alpha_{exp}^n)$.

The standard deviation was given as $\sigma = \pm \sqrt{\sum_{n=1}^N (\alpha^n - \bar{\alpha})^2 / (N - 1)}$.

Figure 21 summarizes the mean error of participant void fraction calculations as compared to measurements, while Figure 22 summarizes the standard deviation of those results.

There was no clear bias in the calculation of void fraction for any of the four subchannels. Although some of the

codes consistently predicted the correct thermal equilibrium quality, there was a tendency to overpredict it at the low elevation and underpredict it at the high elevation.

There were a total of seventeen (17) participants for exercise 2 of phase I—steady-state bundle benchmark [5]. All sixteen submitted void fraction results, while two submitted axial void distribution results. Table 15 lists these participants as well as the codes for which results were submitted.

Some modeling considerations specific to this exercise include increasing the number of axial nodes and modeling spacer grids. A number of the codes (such as THYC) did not model spacer grid effects, while others (CATHARE 3 (CEA-Grenoble) [11]) applied a pressure loss one cell in front of the spacer grid. A number of cross-flow models were also used. THYC used Chexal-Lellouche for drift flux as well as a no-slip condition and Cheng-Todreas for turbulent diffusivity, while CATHARE 3 (CEA-Grenoble) used a turbulent dispersion

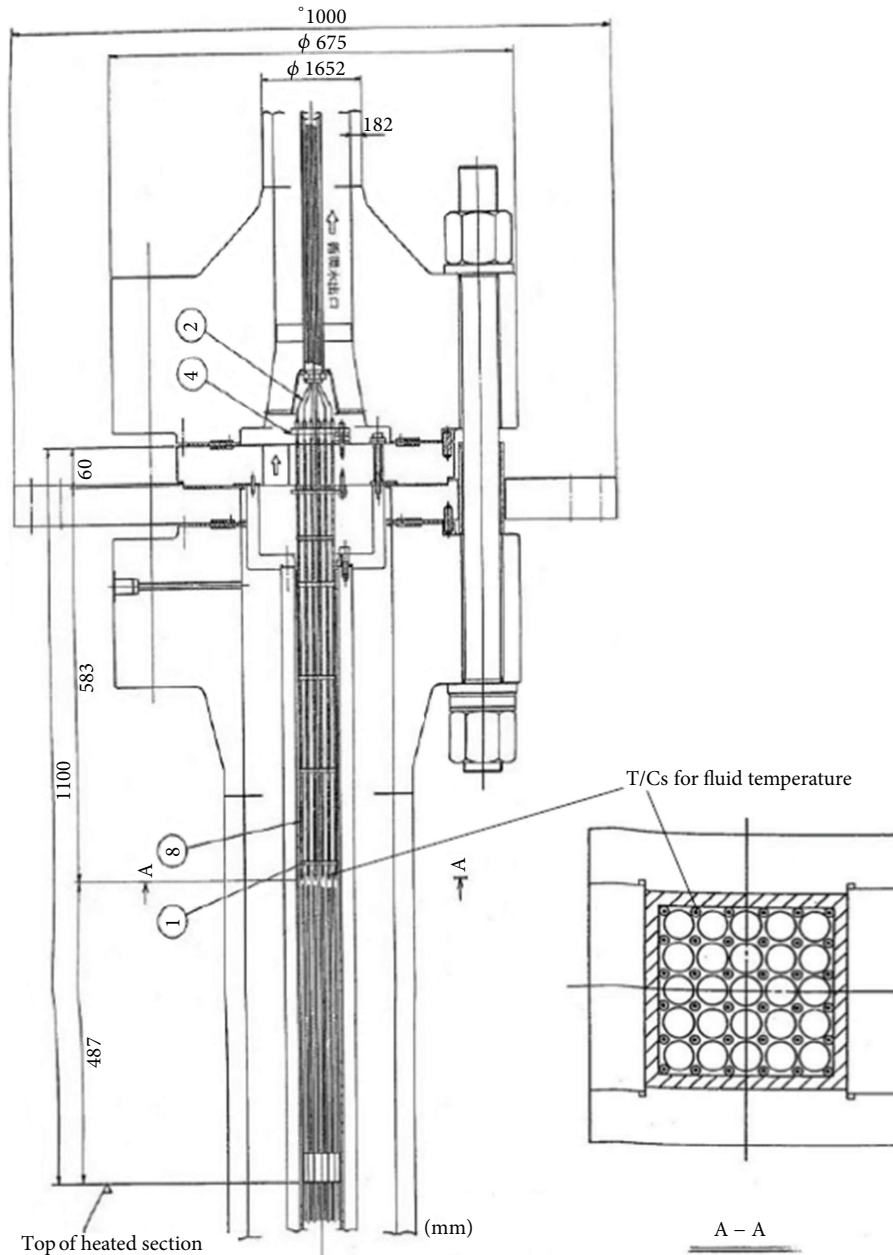


FIGURE 14: Diagram of fluid temperature measurement setup.

term. Yet, other codes did not consider cross-flow effects. Statistical methodology also was utilized to calculate the mean error and standard deviation for each measurement location for each test series. Figures 23, 25, 27, and 29 summarize the error of participants' void fraction predictions, while Figures 24, 26, 28, and 30 summarize the standard deviation of these results.

It was noted that the codes consistently overpredicted the void fraction at the lower elevation in the bundle. However, the results were generally improved at higher elevations, although some underprediction could be seen. Both of these

observations are clearly represented in the plots of mean error for each test series.

The majority of the codes also consistently predicted the correct thermal equilibrium quality at the lower elevations, with the only exceptions being KTH's TRACE and UNIP's CATHARE, which overpredicted the quality. All of the codes tended to underpredict the quality at the upper bundle elevations.

3.2. *Phase II—Departure of Nucleate Boiling.* The list of the participants as well as the codes for which results were

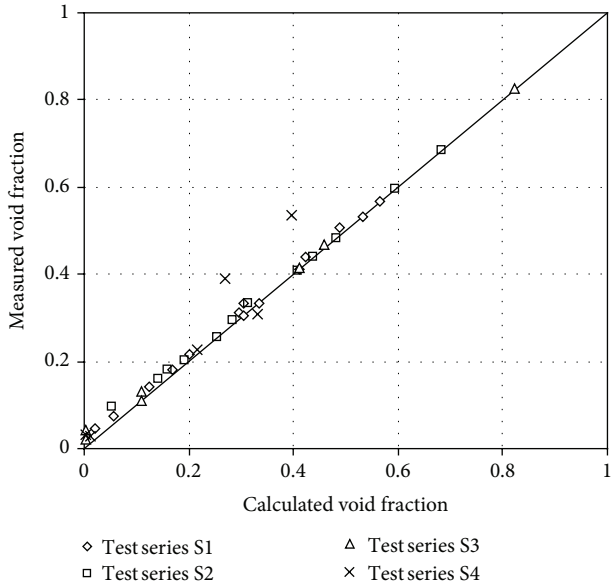


FIGURE 15: Deviation of measured void fraction from recalculated void fraction.

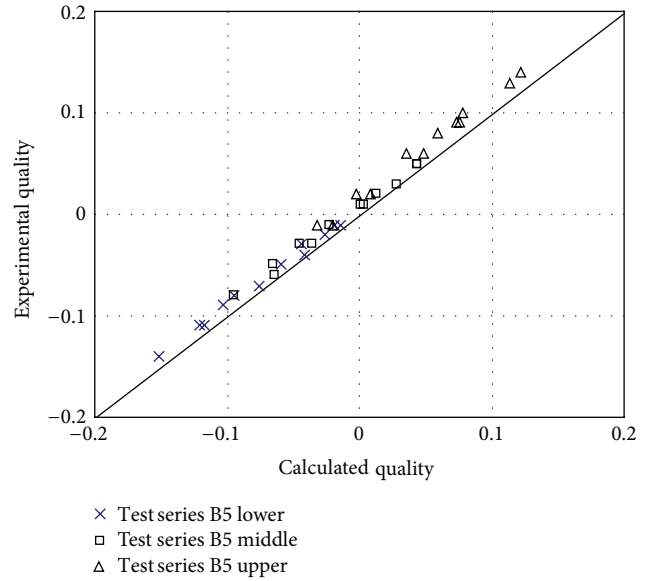


FIGURE 17: Deviation of measured quality from recalculated quality for test series 5.

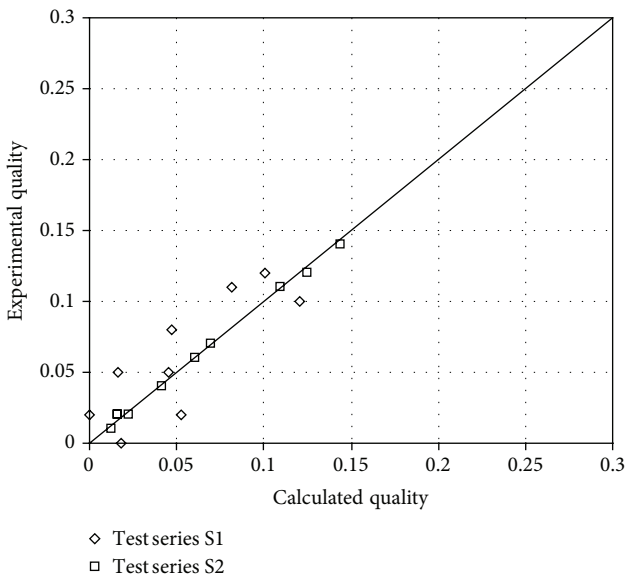


FIGURE 16: Deviation of measured quality from recalculated quality for test series 1 and 2.

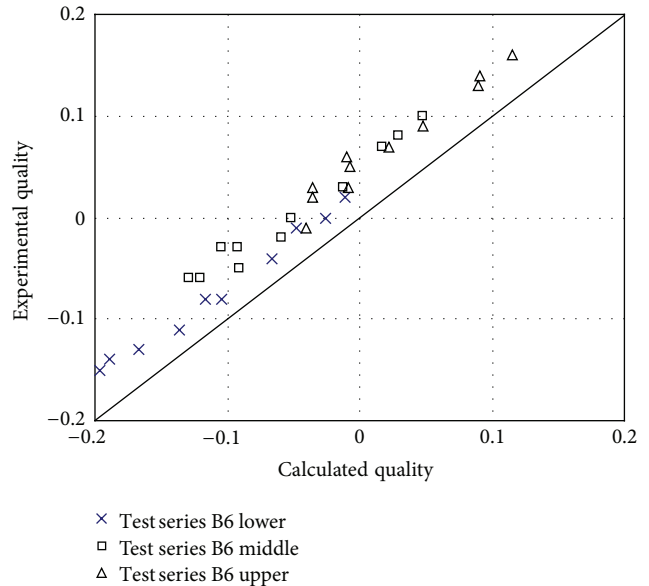


FIGURE 18: Deviation of measured quality from recalculated quality for test series 6.

submitted for exercise 2 of phase II (steady-state DNB) benchmark is shown in Table 16.

The codes used in this exercise varied widely in the DNB modeling approach used. ASSERT-PV, TRACE (KTH), CATHARE 3, and FLICA (PSI) all used Groeneveld lookup tables, while MATRA used the EPRI CHF correlation and FLICA-OVAP [12] used the Shah correlation.

Figure 31 shows the mean error of each code for DNB power for each test series. Figure 32 shows the standard deviation of each code for DNB power for each test series.

The codes were generally able to calculate the DNB power satisfactorily, and there was no observable bias across test series. The DNB power was consistently overpredicted in Test series 0, while it was underpredicted in test series 2, 3, 4, and 13. There was also considerable variation in the predictions of axial elevation of first detected DNB. It should be noted that the measured data represents the first thermocouple at which DNB was detected. Therefore, it is the latest (axially speaking) that the onset of DNB would have occurred and is not an exact value as DNB could have occurred lower on the bundle.

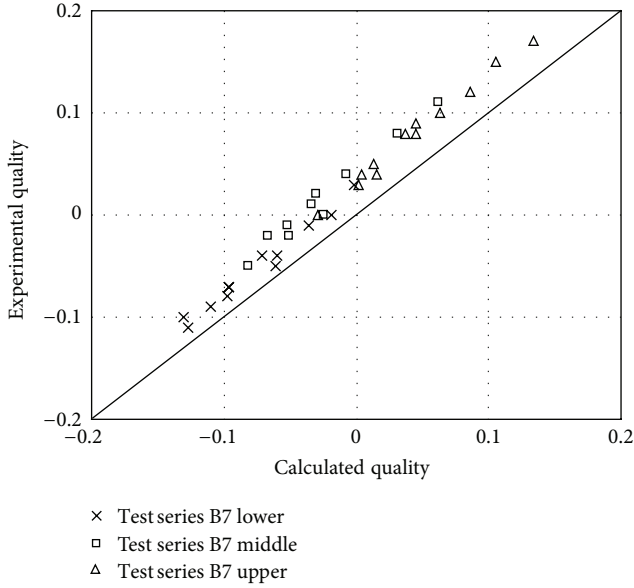


FIGURE 19: Deviation of measured quality from recalculated quality for test series 7.

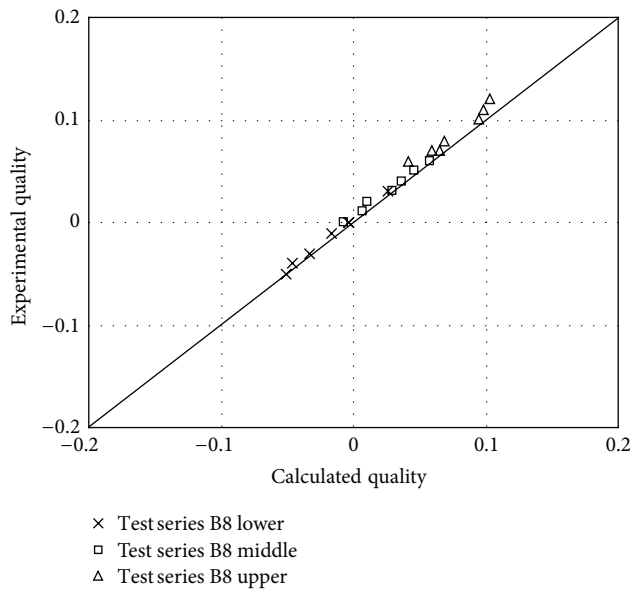


FIGURE 20: Deviation of measured quality from recalculated quality for test series 8.

There were a total of eight (8) participants for exercise 3 of phase II—transient DNB benchmark [6]. Table 17 lists these participants as well as the codes for which results were submitted.

The same statistical methodology was utilized also for these comparisons. The mean error and standard deviation were calculated for each measurement location for each test series. Figure 33 shows the mean error of each code for time of the detected DNB for each test series. Figure 34 shows the mean error of each code for DNB power for each test series.

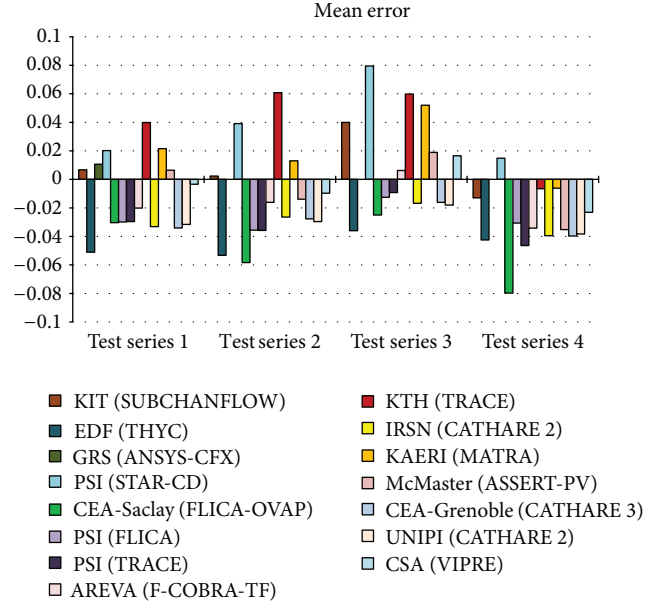


FIGURE 21: Void fraction mean error by test series.

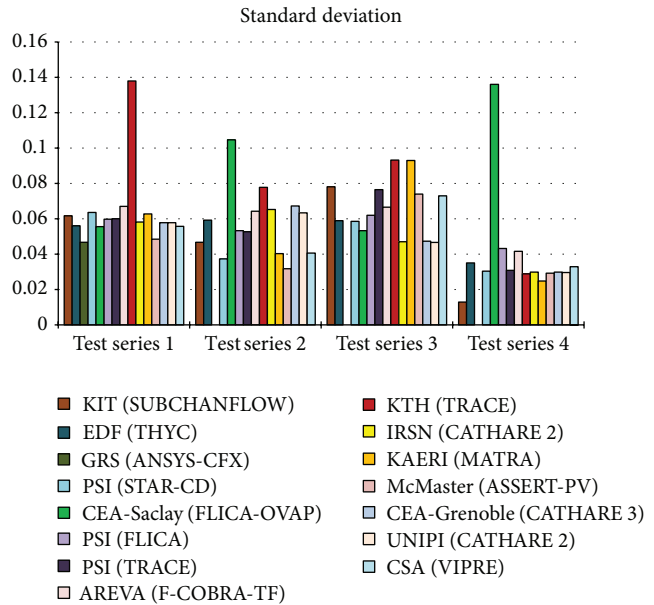


FIGURE 22: Void fraction standard deviation by test series.

In general, codes were not able to predict the time of DNB during the simulated transients. Most of the codes calculate earlier DNB occurrence for both bundle types (with, test series 11, and without, test series 12, thimble rod in the central region). THYC always predicts later DNB. FLICA-OVAP and SUBCHANFLOW [13] predictions show dependence on the radial power shape for both DNB power and DNB time. MATRA [14] seems to give reasonable predictions of the DNB time but significantly overpredicts the DNB power.

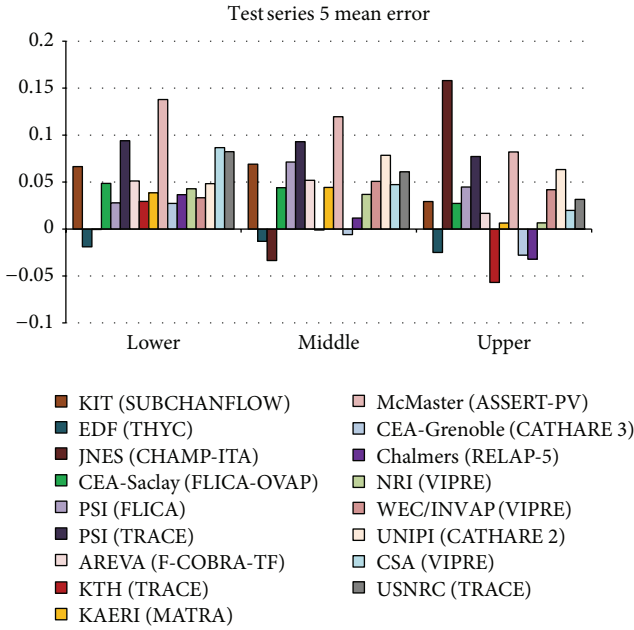


FIGURE 23: Test series 5 void fraction mean error.

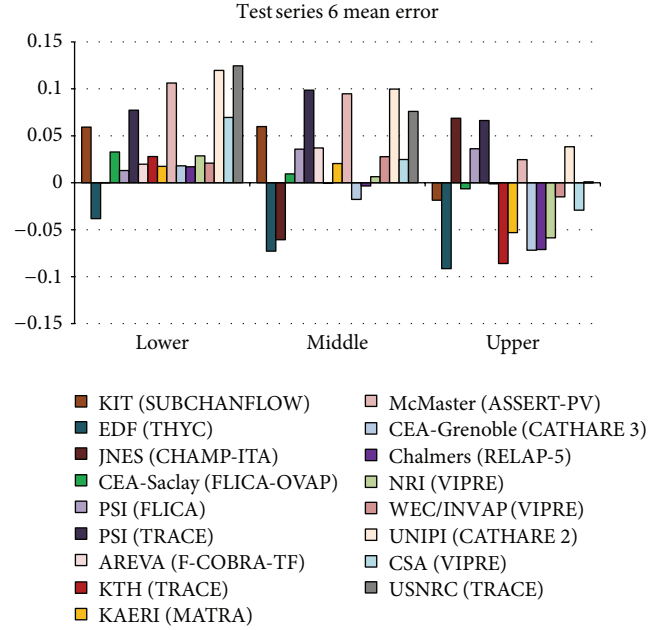


FIGURE 25: Test series 6 void fraction mean error.

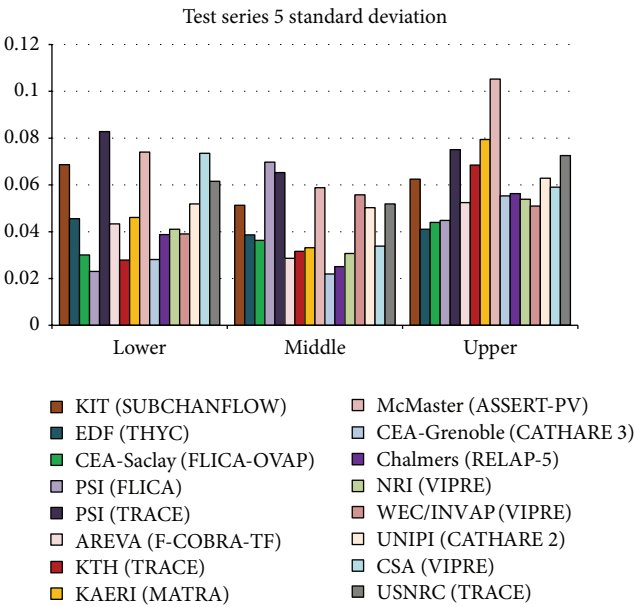


FIGURE 24: Test series 5 void fraction standard deviation.

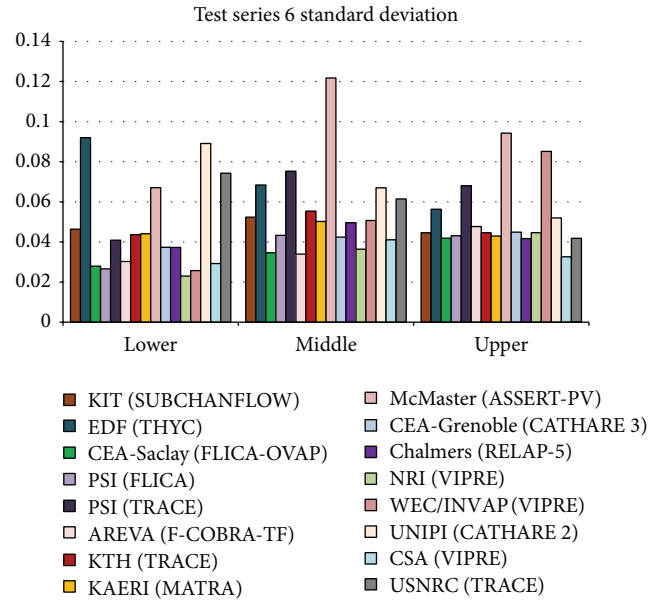


FIGURE 26: Test series 6 void fraction standard deviation.

4. Conclusions

The OECD/NRC PSBT benchmark was designed to provide a set of data for the development and validation of the next generation of thermal-hydraulic codes. It consisted of two phases: a void fraction benchmark and a departure from nucleate boiling benchmark. Data regarding the test sections and conditions was provided to participants for use in calculations. The code results from all participants were then compiled and analyzed. In the development of the benchmark specification, a number of support studies

were performed. The experimental void fraction and quality were recalculated using the experimentally determined fluid density for each of the benchmark test cases, and a deviation between these recalculated values and the measured values was observed. Studies were also conducted to determine the effect of the downcomer region on the fluid temperature and the effect of the CT mask on void fraction at subcooled boiling conditions. The participants' results for each benchmark exercise were analyzed, and conclusions were drawn. In the results for the first phase, it was observed that the codes tended to overpredict the thermal equilibrium quality at

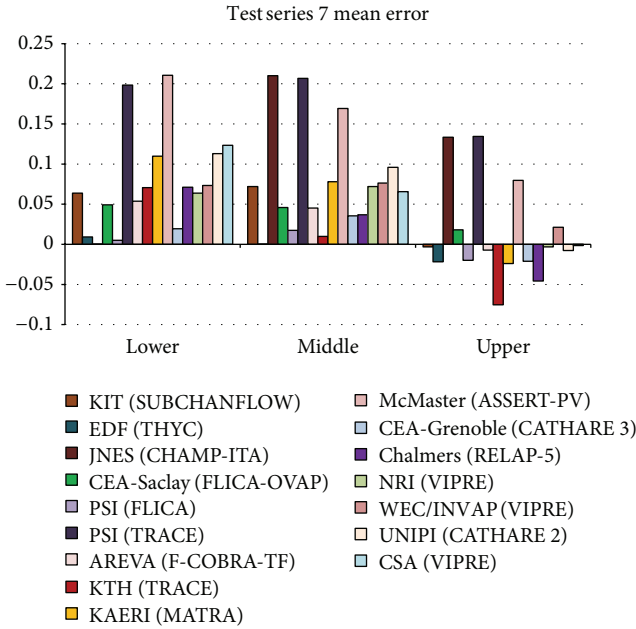


FIGURE 27: Test series 7 void fraction mean error.

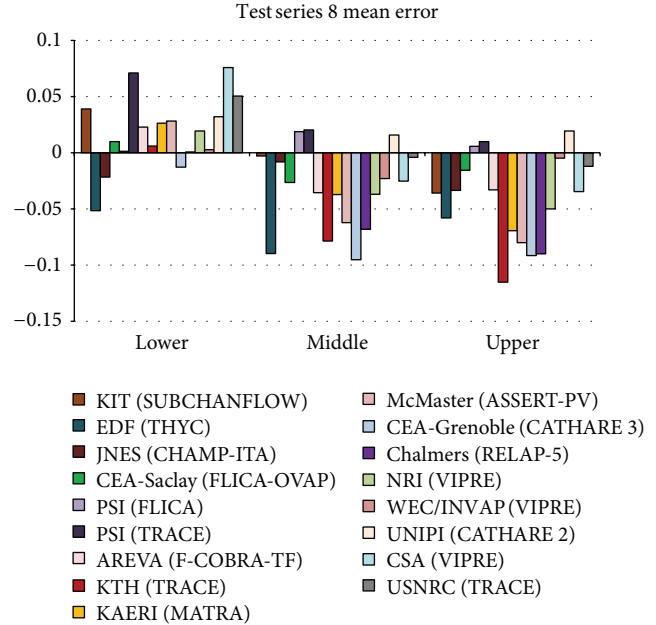


FIGURE 29: Test series 8 void fraction mean error.

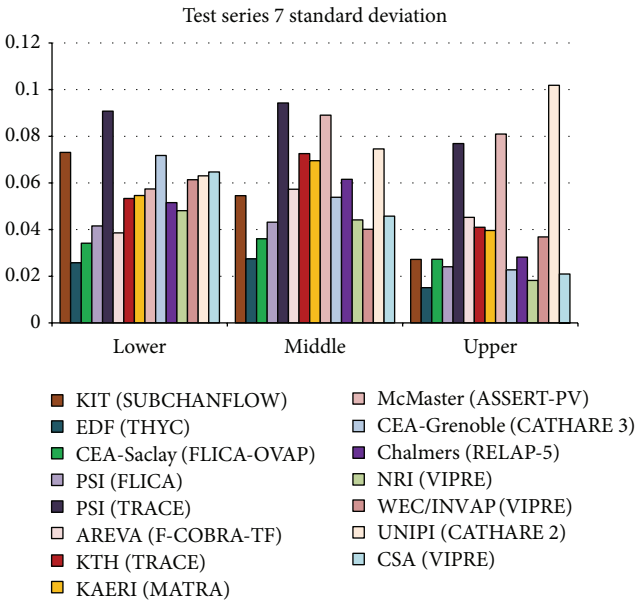


FIGURE 28: Test series 7 void fraction standard deviation.

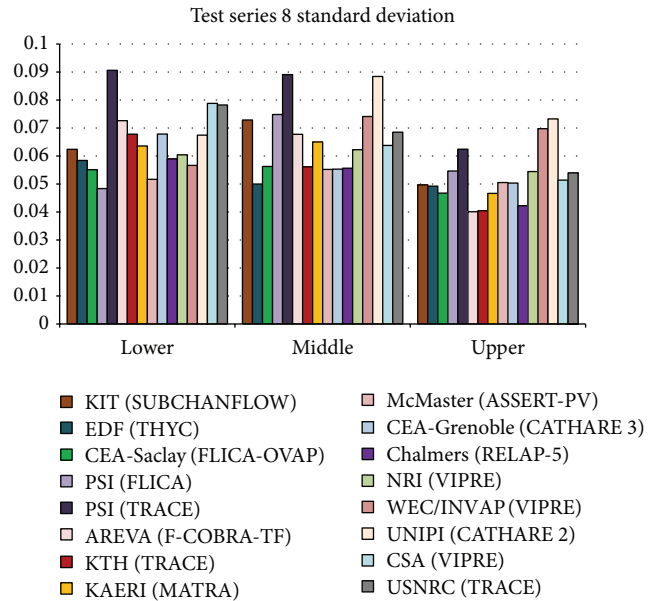


FIGURE 30: Test series 8 void fraction standard deviation.

lower elevations and underpredict it at higher elevations. There was also a tendency to overpredict void fraction at lower elevations and underpredict it at high elevations for the bundle test cases. The overprediction of void fraction at low elevations is likely caused by the X-ray densitometer measurement method used. Under subcooled boiling conditions, the voids accumulate at heated surfaces (and are therefore not seen in the center of the subchannel, where the measurements are being taken), so the experimentally determined void fractions will be lower than the actual void fraction. The underprediction of void fraction at high

elevations is smaller as compared to overprediction at low elevations, and the code results were generally improved at higher elevations. Some of the best results were achieved by codes that used either turbulent mixing or dispersion terms for modeling cross-flow. It was also noted that, for the bundle cases, some of the codes were not correctly calculating the bundle-averaged thermal equilibrium quality, and this may indicate an inability to predict the correct void fraction. A time shift was noted in the void fraction results for the temperature increase transient cases, indicating that the test apparatus may have experienced unexpected heat transfer

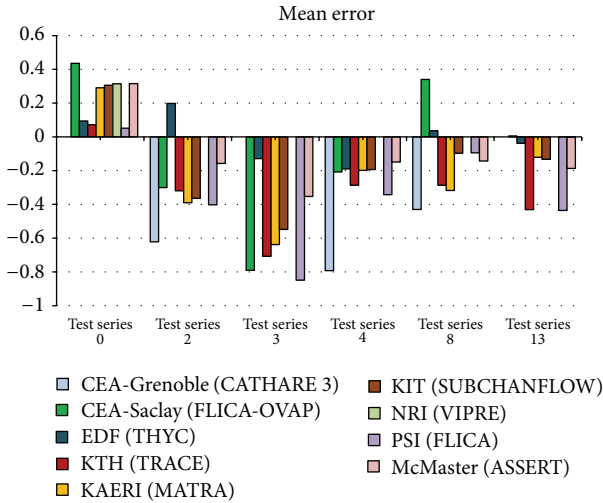


FIGURE 31: Mean error of predicted DNB power.

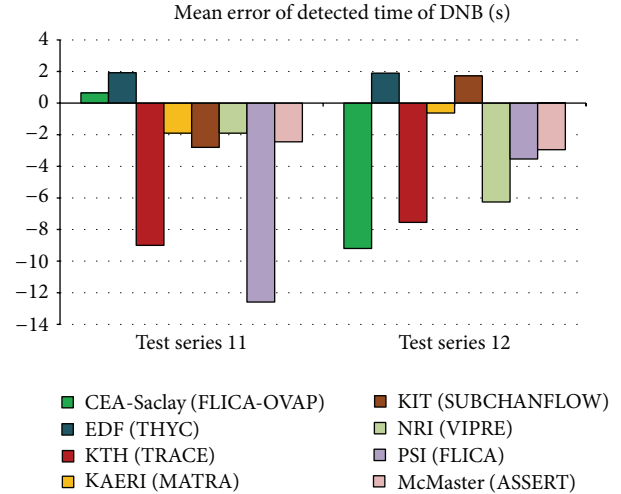


FIGURE 33: Mean error of detected time of DNB.

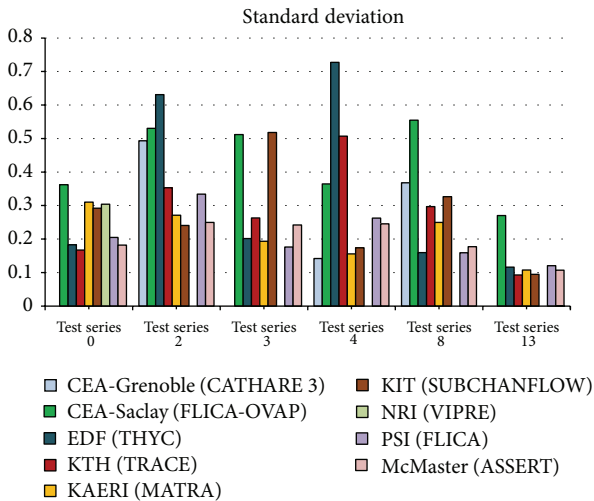


FIGURE 32: Standard deviation of predicted DNB power.

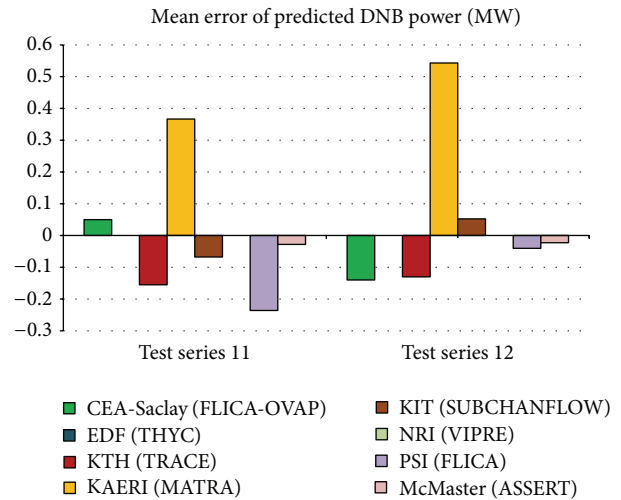


FIGURE 34: Mean error of predicted DNB power.

between the downcomer and test section. This heat transfer is only expected to be of significance in the transient test cases as the steady-state cases allow the system to reach thermal equilibrium.

The participants' results for each benchmark exercise of phase II were analyzed, and conclusions were drawn. Based on the final results for the second phase, a number of conclusions were drawn. The codes were generally able to replicate the results of the mixing test, staying within 5% of the experimental fluid exit temperature. THYC showed the largest errors, while all codes had difficulty with the test case 01-1237. The uncertainty related to the spacer grid orientation in the mixing tests may explain the asymmetries seen in the experimental data, but no sensitivity study was performed to determine the exact effect on the flow, so this uncertainty cannot be quantified. The improvement between FLICA-OVAP and FLICA was noticeable, with the main difference between the two codes being that FLICA-OVAP

implicitly assigned flow regime based on drift flux, while FLICA assumes single phase flows. In exercises 2 and 3, the codes were generally able to predict the DNB power as well as the axial location of the onset of DNB (for the steady-state cases) and the time of DNB (for the transient cases). It was noted that the codes that used the EPRI CHF correlation (such as MATRA and SUBCHANFLOW) had the lowest mean error in exercise 2 for predicted DNB power.

Acknowledgments

The authors would like to acknowledge the help of Alexander Velazquez-Lozada and Stephen Bajorek from the US Nuclear Regulatory Commission. The OECD/NRC PSBT benchmark is financially supported by the US NRC under a cooperative agreement grant.

References

- [1] Proving Test on the Reliability for Nuclear Fuel Assemblies, *Summary Report of Proving Tests on the Reliability for Nuclear Power Plant-1989*, Nuclear Power Engineering Test Center, 1989.
- [2] K. Hori, K. Miyazaki, T. Kurosu, S. Sugiyama, J. Matsumoto, and Y. Akiyama, "In bundle void fraction measurement of PWR fuel assembly," in *Proceedings of the 2nd International Conference on Nuclear Engineering (ICONE-2)*, vol. 1, pp. 69–76, San Francisco, Calif, USA, March 1993.
- [3] Pamphlet of Takasago Engineering Laboratory, Nuclear Power Engineering Center (NUPEC).
- [4] A. Rubin, A. Schoedel, and M. Avramova, "OECD/NRC Benchmark Based on NUPEC PWR Subchannel and Bundle Tests (PSBT). Volume I: Experimental Database and Final Problem Specifications," NEA/NSC/DOC(2010)1, January 2010.
- [5] A. Rubin and M. Avramova, "OECD/NRC Benchmark Based on NUPEC PWR Subchannel and Bundle Tests (PSBT). Volume II: Benchmark Results for the Void Distribution Phase," NEA/NSC/DOC, December 2011.
- [6] A. Rubin and M. Avramova, "OECD/NRC Benchmark Based on NUPEC PWR Subchannel and Bundle Tests (PSBT). Volume III: Benchmark Results for the Departure from Nucleate Boiling Phase," NEA/NSC/DOC, December 2011.
- [7] C. Baudry, M. Guingo, A. Douce et al., "OECD/NEA PSBT benchmark: simulation of the steady-state sub-channel test-case with NEPTUNE CFD," in *Proceedings of the 14th International Topical Meeting on Nuclear Reactor Thermal-Hydraulics (NURETH-14)*, CD-ROM, Ontario, Canada, September 2011.
- [8] T. Frank, F. Reiterer, and C. Lifante, "Investigation of the PWR subchannel void distribution benchmark (OECD/NRC PSBT Benchmark) using ANSYS CFX," in *Proceedings of the 14th International Topical Meeting on Nuclear Reactor Thermal-Hydraulics (NURETH-14)*, CD-ROM, Ontario, Canada, September 2011.
- [9] A. Del Nevo, L. Michelotti, D. Rozzia, F. Moretti, and F. D'Auria, "Void fraction prediction of NUPEC PSBT tests by CATHARE code," in *Proceedings of the 14th International Topical Meeting on Nuclear Reactor Thermal-Hydraulics (NURETH-14)*, CD-ROM, Ontario, Canada, September 2011.
- [10] T. W. Kim and A. Manera, "Prediction of void fraction in a subchannel and bundle geometry with FLICA4 and TRACE," in *Proceedings of the 14th International Topical Meeting on Nuclear Reactor Thermal-Hydraulics (NURETH-14)*, CD-ROM, Ontario, Canada, September 2011.
- [11] M. Valette, "Subchannel and rod bundle PSBT simulation with CATHARE-3," in *Proceedings of the 14th International Topical Meeting on Nuclear Reactor Thermal-hydraulics (NURETH-14)*, CD-ROM, Ontario, Canada, September 2011.
- [12] M. Bucci and P. Fillion, "Analysis of the NUPEC PSBT tests with FLICA-OVAP part 2: DNB benchmark," in *Proceedings of the 14th International Topical Meeting on Nuclear Reactor Thermal-hydraulics (NURETH-14)*, CD-ROM, Ontario, Canada, September 2011.
- [13] A. Berkhan, V. Sánchez, and U. Imke, "Validation of PWR-relevant models of SUBCHANFLOW using the NUPEC PSBT data," in *Proceedings of the 14th International Topical Meeting on Nuclear Reactor Thermal-hydraulics (NURETH-14)*, CD-ROM, Ontario, Canada, September 2011.
- [14] D. H. Hwang, S. J. Kim, and K. W. Seo, "Analysis of PSBT benchmark exercises for void distribution and DNB using a subchannel code MATRA," in *Proceedings of the 14th International Topical Meeting on Nuclear Reactor Thermal-hydraulics (NURETH-14)*, CD-ROM, Ontario, Canada, September 2011.

Research Article

Comparative Analysis of CTF and Trace Thermal-Hydraulic Codes Using OECD/NRC PSBT Benchmark Void Distribution Database

M. Avramova,¹ A. Velazquez-Lozada,² and A. Rubin¹

¹ Department of Mechanical and Nuclear Engineering, The Pennsylvania State University, University Park, PA 16802, USA

² RES/DSA/CDB, US Nuclear Regulatory Commission, Washington, DC 20555-0001, USA

Correspondence should be addressed to M. Avramova; mna109@psu.edu

Received 6 July 2012; Accepted 16 November 2012

Academic Editor: Diana Cuervo

Copyright © 2013 M. Avramova et al. This is an open access article distributed under the Creative Commons Attribution License, which permits unrestricted use, distribution, and reproduction in any medium, provided the original work is properly cited.

The international OECD/NRC PSBT benchmark has been established to provide a test bed for assessing the capabilities of thermal-hydraulic codes and to encourage advancement in the analysis of fluid flow in rod bundles. The benchmark was based on one of the most valuable databases identified for the thermal-hydraulics modeling developed by NUPEC, Japan. The database includes void fraction and departure from nucleate boiling measurements in a representative PWR fuel assembly. On behalf of the benchmark team, PSU in collaboration with US NRC has performed supporting calculations using the PSU in-house advanced thermal-hydraulic subchannel code CTF and the US NRC system code TRACE. CTF is a version of COBRA-TF whose models have been continuously improved and validated by the RDFMG group at PSU. TRACE is a reactor systems code developed by US NRC to analyze transient and steady-state thermal-hydraulic behavior in LWRs and it has been designed to perform best-estimate analyses of LOCA, operational transients, and other accident scenarios in PWRs and BWRs. The paper presents CTF and TRACE models for the PSBT void distribution exercises. Code-to-code and code-to-data comparisons are provided along with a discussion of the void generation and void distribution models available in the two codes.

1. Introduction

In the past few decades, the need of improved nuclear reactor safety analyses has led to a rapid development of advanced methods for multidimensional thermal-hydraulic analyses. These methods have progressively become more complex in order to account for variety of physical phenomena anticipated during steady-state and transient Light Water Reactor (LWR) conditions. The newly developed models must be extensively validated against full-scale high-quality experimental data. The previous publically available void distribution measurements, which include the ISPRA 16-rod tests [1] and the GE 9-rod tests [2], have limited databases. Currently the requirements to the numerical modelling of subchannel void distribution dictate an approach that can be applied to a wide range of geometrical and operating conditions. In the past decade, experimental and computational technologies have tremendously improved the study of

the flow structure. In that sense, the new OECD/NRC PWR Subchannel and Bundle Tests (PSBT) benchmark [3] has provided an excellent opportunity for validation of innovative models for void distribution and departure from nucleate boiling (DNB) prediction under Pressurized Water Reactors (PWRs) conditions. From 1980s to 1990s, NUPEC (Nuclear Power Engineering Corporation) performed a series of void measurement tests using full-size mock-up tests for both Boiling Water Reactors (BWRs) and PWRs. Based on state-of-the-art computer tomography (CT) technology, the void distribution was visualized at the mesh size smaller than the subchannel under actual plant conditions. NUPEC also performed steady state and transient critical power test series based on the equivalent full-size mockups. Considering the reliability not only of the measured data, but also other relevant parameters such as the system pressure, inlet subcooling, and rod surface temperature, these test series supply the first substantial database for the development of truly mechanistic

and consistent models for void distribution and departure from nucleate boiling. The PSBT benchmark was divided into two separate phases, with each consisting of individual exercises. Phase I is Void Distribution Benchmark while Phase II is Departure from Nucleate Boiling Benchmark. The benchmark specification is designed so that it can systematically assess and compare the participants' numerical models for the prediction of detailed subchannel void distributions and departure from nucleate boiling to full scale experimental data on a prototypical PWR rod bundle.

CTF is a version of the COBRA-TF code maintained at the Reactor Dynamics and Fuel Management Group (RDFMG) at Pennsylvania State University (PSU) [4]. The original version of COBRA-TF was developed at the Pacific Northwest Laboratory as a part of the COBRA/TRAC thermal-hydraulic code. Since then, various academic and industrial organizations have adapted, developed, and modified the code in many directions. The code is worldwide used for academic and general research purposes as well. The code version used at PSU originates from a code version modified during the FLECHT SEASET program [5]. Besides the code utilization to teach and train students in the area of nuclear reactor thermal-hydraulic safety analyses, during the last few years at PSU the theoretical models and numerics of COBRA-TF were substantially improved [6]. The code was subjected to an extensive verification and validation program and was applied to variety of LWR steady-state and transient simulations. CTF is a transient code based on a separated flow representation of the two-phase flow. The two-fluid formulation, often used in thermal-hydraulic codes, separates the conservation equations of mass, energy, and momentum to vapor and liquid. CTF extends this treatment to three fields: vapor, continuous liquid, and entrained liquid droplets, which results in a set of nine time-averaged conservation equations. The conservation equations for each of the three fields and for heat transfer from and within the solid structure in contact with the fluid are solved using a semi-implicit, finite-difference numerical technique on an Eulerian mesh, where time intervals are assumed to be long enough to smooth out the random fluctuations in the multiphase flow, but short enough to preserve any gross flow unsteadiness. The code is able to handle both hot wall and normal flow regime maps and it is capable of calculating reverse flow, counter flow, and cross-flow situations. The code is developed for use with either three-dimensional (3D) Cartesian or subchannel coordinates and, therefore, it features extremely flexible nodding for both the thermal-hydraulic and the heat-transfer solutions. This flexibility allows a fully 3D treatment in geometries amenable to description in a Cartesian coordinate system.

TRACE is a multicomponent solver consolidation of four US NRC computer codes: TRAC-P, TRAC-B, RELAP5, and RAMONA. TRACE has been validated and assessed against more than 500 experimental sets of data from separate and integral effect tests, in which comparisons were found to be reasonable in general [7]. TRACE utilizes a finite-volume technique to discretize typical hydraulic components found in a nuclear power plant and calculates the internal energy and equations of motion in each component for two phases.

The energy equation is solved using a semi-implicitly numerical scheme and the equations of fluid motion are solve using the stability-enhancing two-step (SETS) numerical scheme which allows the material Courant limit to be exceeded. This allows very large time steps to be used in slow transients. This set of equations is solved for one and three dimensions in Cartesian and/or cylindrical coordinates. Errors introduced to the solution due to abrupt area changes are corrected by modifying the equations of motion to force Bernoulli flow. For the analysis and results presented in this paper the authors utilized TRACE version-V5.02p2.win32_opt.

The paper presents the CTF and TRACE models for the exercises of the void distribution phase of the OECD/NRC PSBT benchmark. Code-to-code and code-to-data comparisons are provided along with a discussion of the void generation and void distribution models available in the two codes. The following two sections discuss the void generation and distribution models available in CTF and TRACE with a subsequent code-to-code and code-to-data comparisons.

2. CTF Models for Vapor Generation and Distribution

The three-field formulation of the two-phase flow used in CTF is a straightforward extension of the general two-fluid model. Dividing the liquid phase into a continuous liquid field and an entrained liquid drop field allows both fields to have different velocities. The generalized phasic momentum equation is then given as

$$\begin{aligned} \frac{\partial}{\partial t} (\alpha_k \rho_k \underline{U}_k) + \nabla \cdot (\alpha_k \rho_k \underline{U}_k \underline{U}_k) \\ = \alpha_k \rho_k g - \alpha_k \nabla P + \nabla \cdot (\alpha_k \underline{\tau}_{\underline{k}}) \\ + M_k^\Gamma + M_k^d + M_k^T, \end{aligned} \quad (1)$$

where α_k is the average k -phase void fraction; ρ_k is the average k -phase density; \underline{U}_k is the average k -phase velocity vector; g is the acceleration of gravity vector; $\underline{\tau}_{\underline{k}}$ is the average k -phase viscous stress tensor; M_k^Γ is the average supply of momentum to phase k due to mass transfer to phase k ; M_k^d is the average drag force on phase k by the other phases; M_k^T is the average supply of momentum to phase k due to turbulent mixing and void drift.

In the generalized phasic momentum equation the terms representing the momentum exchange at the interface (interfacial momentum terms) are expressed as

$$\underline{M}_{\text{vap}}^d = -\underline{\tau}_{i,\text{vap,liq}}''' - \underline{\tau}_{i,\text{vap,ent}}''' \quad (\text{vapor phase}), \quad (2a)$$

$$\underline{M}_{\text{liq}}^d = \underline{\tau}_{i,\text{vap,liq}}''' \quad (\text{continuous liquid phase}), \quad (2b)$$

$$\underline{M}_{\text{ent}}^d = \underline{\tau}_{i,\text{vap,ent}}''' \quad (\text{entrained liquid phase}), \quad (2c)$$

where $\underline{\tau}_{i,\text{vap,liq}}'''$ is the average drag force per unit volume by the vapor on the continuous liquid and $\underline{\tau}_{i,\text{vap,ent}}'''$ is the average

TABLE 1: CTF modeling of the interfacial drag.

Interfacial drag forces	Between continuous liquid and vapor: $\tau_{I,\text{vap,liq}} = K_{I,\text{vap,liq}} U_{\text{vap,liq}}$ Between entrained liquid and vapor: $\tau_{I,\text{vap,ent}} = K_{I,\text{vap,ent}} U_{\text{vap,ent}}$
	<i>Bubbly flows</i> For small bubbles: $K_{I,\text{vap,liq}} = 0.375 \frac{C_{D\text{bub}}}{r_{\text{bub}}} \alpha_{\text{vap}} \rho_{\text{liq}} U_{\text{vap}} - U_{\text{liq}} $; $C_{D\text{bub}} = \frac{24}{\text{Re}_{\text{bub}}} (1 + 0.1 \text{Re}_{\text{bub}}^{0.75})$
Interfacial drag coefficients	For large bubbles: $K_{I,\text{vap,liq}} = 0.375 \frac{C_{D\text{Lbub}}}{r_{\text{bub}}} \alpha_{\text{vap}} \rho_{\text{liq}} U_{\text{vap}} - U_{\text{liq}} $; $C_{D\text{Lbub}} = \max\left(\frac{24}{\text{Re}_{\text{Lbub}}} (1 + 0.1 \text{Re}_{\text{Lbub}}^{0.75}) \alpha_{\text{liq}}^2, 0.45 \alpha_{\text{liq}}^2\right)$
	<i>Annular flow</i> Between continuous liquid film and vapor core: $K_{I,\text{vap,liq}} = 2 \frac{f_I}{D_{\text{hyd}}} \sqrt{\alpha_{\text{vap}} + \alpha_{\text{ent}}} \rho_{\text{vap}} U_{\text{vap}} - U_{\text{liq}} $; interfacial friction factor f_I by Henstoch and Hanratty
	Between entrained liquid film and vapor core: $K_{I,\text{vap,drop}} = 0.375 \frac{C_{D\text{drop}}}{r_{\text{drop}}} \alpha_{\text{ent}} \rho_{\text{vap}} U_{\text{vap}} - U_{\text{ent}} $; $C_{D\text{drop}} = \frac{24}{\text{Re}_{\text{drop}}} (1 + 0.1 \text{Re}_{\text{drop}}^{0.75})$

drag force per unit volume by the vapor on the entrained liquid.

The momentum exchange due to mass transfer between the three fields can be written as

$$\underline{M}_{\text{vap}}^{\Gamma} = (\Gamma''' \underline{U}) \quad (\text{vapor phase}), \quad (3a)$$

$$\underline{M}_{\text{liq}}^{\Gamma} = -(\Gamma_{\text{liq}}''' \underline{U}) - (S''' \underline{U}) \quad (\text{continuous liquid phase}), \quad (3b)$$

$$\underline{M}_{\text{ent}}^{\Gamma} = -(\Gamma_{\text{ent}}''' \underline{U}) + (S''' \underline{U}) \quad (\text{entrained liquid phase}), \quad (3c)$$

where the Γ''' is the average rate of vapor generation per unit volume and S''' is the average net rate of entrainment per unit volume. Since both liquid fields contribute to the vapor generation, then $\Gamma''' = \Gamma_{\text{liq}}''' + \Gamma_{\text{ent}}'''$.

If η denotes the fraction of the total vapor generation coming from the entrained liquid field, then

$$\Gamma_{\text{vap}}''' = \Gamma''', \quad (4a)$$

$$\Gamma_{\text{ent}}''' = \eta \Gamma''' = -\Gamma_{\text{ent}}''' + S''' = -\eta \Gamma''' + S''', \quad (4b)$$

$$\Gamma_{\text{liq}}''' = (1 - \eta) \Gamma''' = -\Gamma_{\text{liq}}''' - S''' = -(1 - \eta) \Gamma''' - S'''. \quad (4c)$$

The momentum exchange due to turbulent mixing and void drift is neglected in the entrained liquid field in the annular flow regime:

$$M_{\text{ent}}^T = 0 \text{ if } \alpha_{\text{vap}} \geq 0.8. \quad (5)$$

Also, the viscous stress is partitioned into a wall shear and a fluid-fluid shear; the fluid-fluid shear is neglected:

$$\nabla \cdot (\alpha_k \underline{\tau}_{\text{wall},k}) = \underline{\tau}_{\text{wall},k}''', \quad (6)$$

The model for interfacial mass transfer is obtained from the energy jump condition by neglecting the mechanical terms and averaging

$$\Gamma''' = \frac{-q_{I_l}''' - q_{I_v}'''}{h_{fg}}. \quad (7)$$

The interfacial heat transfer, q_I''' , for phase k is given by

$$q_{I_k}''' = h A_I''' (T_s - T_k), \quad (8)$$

where A_I''' is the average interfacial area per unit volume and h is a surface heat transfer coefficient. The vapor generation is divided into four components, two for each phase, depending on whether the phase is superheated or subcooled and the total vapor generation rate is given by the sum of these components. The interfacial area per unit volume, A_I''' , is based on the flow regime, as are the heat transfer coefficients, h . The interfacial drag force per unit volume between any two fields is assumed to be a function of the relative velocity between both fields. The interfacial friction coefficients are flow regime dependent and, therefore, neither void correlation nor two-phase pressure drop correlation has to be applied. Interfacial drag forces are modeled between continuous liquid and disperse vapor in the bubbly flows and between continuous liquid film and vapor core and entrained droplets and vapor core in the annular flow. The treatment of the interfacial drag is described in Table 1.

Turbulent mixing and void drift phenomena are modeled in CTF by the Lahey and Moody approach [8], where the net two-phase mixing (including void drift) is assumed to be proportional to the nonequilibrium void fraction gradient. The void drift is only assumed to occur in bubbly, slug, and churn flow, where liquid is the continuous phase and vapor is the dispersed phase. The single-phase mixing coefficient can be either specified as an input value or calculated using an empirical correlation derived by Rogers and Rosehart [9]. The Beus' model for two-phase turbulent mixing is utilized [10].

TABLE 2: CTF models for turbulent mixing and void drift.

	Mass exchange of the phase k : $\dot{m}_k^{\text{TM}} = -\beta_{\text{TP}} \frac{\bar{G}}{\rho} (\alpha_{k,j} \rho_{k,j} - \alpha_{k,i} \rho_{k,i})$
Turbulent mixing	Momentum exchange of the phase k : $\dot{I}_k^{\text{TM}} = -\beta_{\text{TP}} \frac{\bar{G}}{\rho} \Delta G_k A$
	Energy exchange of the phase k : $\dot{Q}_k^{\text{TM}} = -\beta_{\text{TP}} \frac{\bar{G}}{\rho} \Delta(\alpha_k \rho_k h_k) A$
Single-phase turbulent mixing coefficient	User specified single value based on experimental data or internally calculated using the correlation by Rogers and Rozehart:
	$\beta_{\text{SP}} = \frac{1}{2} 0.0058 \left(\frac{D_{\text{gap}}}{D_{\text{rod}}} \right)^{-1.46} \text{Re}^{-0.1} \left[1 + \left(\frac{D_{\text{hyd},j}}{D_{\text{hyd},i}} \right)^{1.5} \right] \frac{D_{\text{hyd},i}}{D_{\text{rod}}}$
Two-phase turbulent mixing coefficient	Two-phase multiplier by Beus: $\beta_{\text{TP}} = \Theta_{\text{TP}} \beta_{\text{SP}}$;
	$\Theta_{\text{TP}} = 1 + (\Theta_{\text{max}} - 1) \frac{x}{x_{\text{max}}} \text{ if } x \leq x_{\text{max}},$
	$\Theta_{\text{TP}} = 1 + (\Theta_{\text{max}} - 1) \frac{x_{\text{max}} - x_0}{x - x_0} \text{ with } \frac{x_0}{x_{\text{max}}} = 0.57 \text{Re}^{0.0417} \text{ if } x > x_{\text{max}}$
	with $\Theta_{\text{max}} = 5$ and $x_{\text{max}} = \frac{0.4 \sqrt{g \rho_{\text{liq}} (\rho_{\text{liq}} - \rho_{\text{vap}})} d_{\text{hyd}}}{G_{\text{tot}}} + 0.6 / \sqrt{\frac{\rho_{\text{liq}}}{\rho_{\text{vap}}}} + 0.6$
	Mass exchange of the phase k : $\dot{m}_k^{\text{VD}} = \beta \frac{\bar{G}}{\rho} (\alpha_{k,j,\text{EQ}} \rho_{k,j,\text{EQ}} - \alpha_{k,i,\text{EQ}} \rho_{k,i,\text{EQ}}) A$
	Momentum exchange of the phase k : $\dot{I}_k^{\text{VD}} = \beta \frac{\bar{G}}{\rho} (G_{k,j,\text{EQ}} - G_{k,i,\text{EQ}}) A$
Void drift	Energy exchange of the phase k :
	$\dot{Q}_k^{\text{VD}} = \beta \frac{\bar{G}}{\rho} (\alpha_{k,j,\text{EQ}} \rho_{k,j,\text{EQ}} h_{k,j,\text{EQ}} - \alpha_{k,i,\text{EQ}} \rho_{k,i,\text{EQ}} h_{k,i,\text{EQ}}) A,$
	$(\alpha_{k,j,\text{EQ}} \rho_{k,j,\text{EQ}} - \alpha_{k,i,\text{EQ}} \rho_{k,i,\text{EQ}}) = \pm \frac{\bar{\alpha}_{\text{vap}} \bar{\rho}_k}{G_{\text{tot}}} (G_{\text{tot},j,\text{EQ}} - G_{\text{tot},i,\text{EQ}})$

In 1980s, both approaches were representing the state-of-the-art in turbulent mixing and void drift modeling. Nowadays they are still used in the most of the subchannel codes. A detailed description of the current CTF turbulent mixing and void drift models is given in Table 2.

3. TRACE Model Description

The fully conservative forms of the energy and momentum equations are modified in TRACE to provide a set of internal energy and motion equations. This modification reduces the numerical manipulation and computational time of the solution. This modification is also transferred to the conservation of mass equation.

It is assumed that the volume average of a product is equal to the product of volume averages. Only contributions from wall heat fluxes and heat fluxes at phase interfaces within the averaging volume are normally included in the volume average of the divergence of heat flux. Also, only contributions from the stress tensor due to shear at metal surfaces or phase interfaces within the averaging volume are considered. The only portions of the work terms that contribute to change in bulk kinetic energy of motion are retained excluding viscous heating from most of the cases unless a pump component is used in which case the viscous

heating from the pump to the fluid is incorporated by the term of direct heating in the internal energy equation.

These modifications and assumptions yield a set of 6 equations of mass (9) and (10), motion (11) and (12), and internal energy (13) and (14) for gas and gas-liquid mixture. An additional mass equation is added for noncondensable gases but in order to still solving only a single set of motion and energy equations, the nongases are assumed to be in mechanical and thermal equilibrium with the steam.

Mass:

$$\frac{\partial(\alpha \rho_g)}{\partial t} + \nabla \cdot [\alpha \rho_g \vec{V}_g] = \Gamma, \quad (9)$$

$$\frac{\partial((1-\alpha) \rho_l + \alpha \rho_g)}{\partial t} + \nabla \cdot [(1-\alpha) \rho_l \vec{V}_l + \alpha \rho_g \vec{V}_g] = 0. \quad (10)$$

Motion:

$$\frac{\partial \vec{V}_l}{\partial t} + \vec{V}_l \cdot \nabla \vec{V}_l = -\frac{1}{\rho_l} \nabla P + \frac{[f_i - \Gamma(\vec{V}_i - \vec{V}_l) + f_{wl}]}{(1-\alpha) \rho_l} + \vec{g}, \quad (11)$$

TABLE 3: Pre-CHF local drift velocity (v_{gj}) and distribution coefficient (C_O).

	Dispersed bubbly flow ($0 < \alpha < 0.2$)	Transition ($0.2 < \alpha < 0.3$)	Dispersed bubbly flow ($0.3 < \alpha < 0.5$)
Small pipes $Dh < 0.18$	Ishii's Equation (1997)	Interpolation	Kataoka-Ishii's Equation (1987)
Large pipes $Dh > 0.18$	Ishii's Equation (1997)	Interpolation	Kataoka-Ishii's Equation (1987)

$$\frac{\partial \vec{V}_g}{\partial t} + \vec{V}_g \cdot \nabla \vec{V}_g = -\frac{1}{\rho_g} \nabla P + \frac{[f_{wg} - f_i - \Gamma(\vec{V}_g - \vec{V}_l) + f_{wl}]}{(1-\alpha)\rho_g} + \vec{g}. \quad (12)$$

Internal energy:

$$\frac{\partial(\alpha \rho_g e_g)}{\partial t} + \nabla \cdot (\alpha \rho_g e_g \vec{V}_g) = -P \frac{\partial \alpha}{\partial t} - P \nabla \cdot (\alpha \vec{V}_g) + q_{wg} + q_{dg} + q_{ig} + \Gamma h'_v, \quad (13)$$

$$\frac{\partial((1-\alpha)\rho_l e_l + \alpha \rho_g e_g)}{\partial t} + \nabla \cdot ((1-\alpha)\rho_l e_l \vec{V}_l + \alpha \rho_g e_g \vec{V}_g) = -P \nabla \cdot ((1-\alpha)\vec{V}_l + \alpha \vec{V}_g) + q_{wl} + q_{wg} + q_{dl} + q_{dg}. \quad (14)$$

In (9) and (10), the term α is the void fraction; ρ_g and ρ_l are the density of the gas and liquid, respectively; \vec{V}_l and \vec{V}_g the velocity vectors of gas and liquid; and Γ is the interfacial mass-transfer rate (positive from liquid to gas).

In (11) and (12) the additional term P is the fluid or total pressure; f_i is the force per unit volume due to shear at the phase interface; f_{wl} is the wall shear force per unit volume acting on the liquid; f_{wg} is the wall shear force per unit volume acting on the gas; \vec{V}_i is the flow velocity at the phase interface; and \vec{g} is the gravity vector.

The other terms on (13) and (14) are e_g and e_l which are the internal energies of the gas and liquid, respectively. The terms q_{wg} and q_{wl} are the heat transfer rates per unit volume from the wall to gas and from the wall to liquid. The terms q_{dg} and q_{dl} correspond to the power deposited directly to the gas or liquid (without heat-conduction process). The term q_{ig} is the interfacial sensible heat transfer. The term $\Gamma h'_v$ accounts for energy carried with mass transfer at the interface, which is the product of mass transfer rate and appropriate stagnation enthalpy at the interface.

The phase-change rate in the set of equations is calculated using the heat conduction limited model:

$$\Gamma = \frac{-(q_{ig} + q_{il})}{(h'_v - h'_l)}, \quad (15)$$

where

$$q_{ig} = \frac{P}{P} h_{ig} a_i (T_{sv} - T_v), \quad (16)$$

$$q_{il} = h_{il} a_i (T_{sv} - T_l). \quad (17)$$

The term a_i in (16) and (17) is the interfacial area per unit volume, where h_{ih} and h_{il} are the heat transfer coefficients at the liquid/gas interface and T_{sv} the saturation temperature corresponding to the partial pressure P_v .

The interfacial drag force incorporated in the motion equations (11) and (12) is evaluated by (18). The interfacial drag force is evaluated for vertical pipes and for horizontal/inclined pipes. For vertical pipes the set of correlations is calculated for Pre and Postcritical-heat-flux (Pre and Post-CHF) condition and for

$$F_i''' = C_i V_r |V_r|, \quad (18)$$

where C_i is the interfacial drag coefficient and V_r the relative velocity:

$$V_r = V_g - V_L, \quad (19)$$

where V_g is the velocity of the gas phase and V_L is the velocity of the liquid phase.

The velocity of the gas phase is evaluated using the local drift velocity (20), where j is the volumetric flux:

$$v_{gj} = V_g - j. \quad (20)$$

For flow in vertical pipes under Pre-CHF conditions the interfacial drag coefficient is calculated with (21) and the profile factor with (22) subsequently:

$$C_i = \frac{\alpha(1-\alpha)^3 g \Delta \rho}{v_{gj}^2} \cdot P_s, \quad (21)$$

$$P_s = \frac{(((1 - C_0 \langle \alpha \rangle) / (1 - \langle \alpha \rangle)) \bar{V}_g - C_0 \bar{V}_l)^2}{V_r^2}. \quad (22)$$

A drift flux model approach is used to evaluate local drift velocity (v_{gj}) along with the distribution coefficient (C_O). Table 3 summarizes the actual drift flux models used in TRACE for small and large pipes and Bubbly/Slug and the Annular/Mist flow regimes under Pre-CHF condition.

For Post-CHF conditions three principal inverted flow regimes are modeled in TRACE, which are inverted annular, inverted slug, and dispersed flow. These three regimes are defined in terms of void fraction and gas superficial velocity.

The inverted annular regime is used in TRACE for void fractions below 0.6 and the interfacial drag coefficient is calculated using

$$C_{i,IA} = \frac{1}{2} \rho_g f_i A_i'''. \quad (23)$$

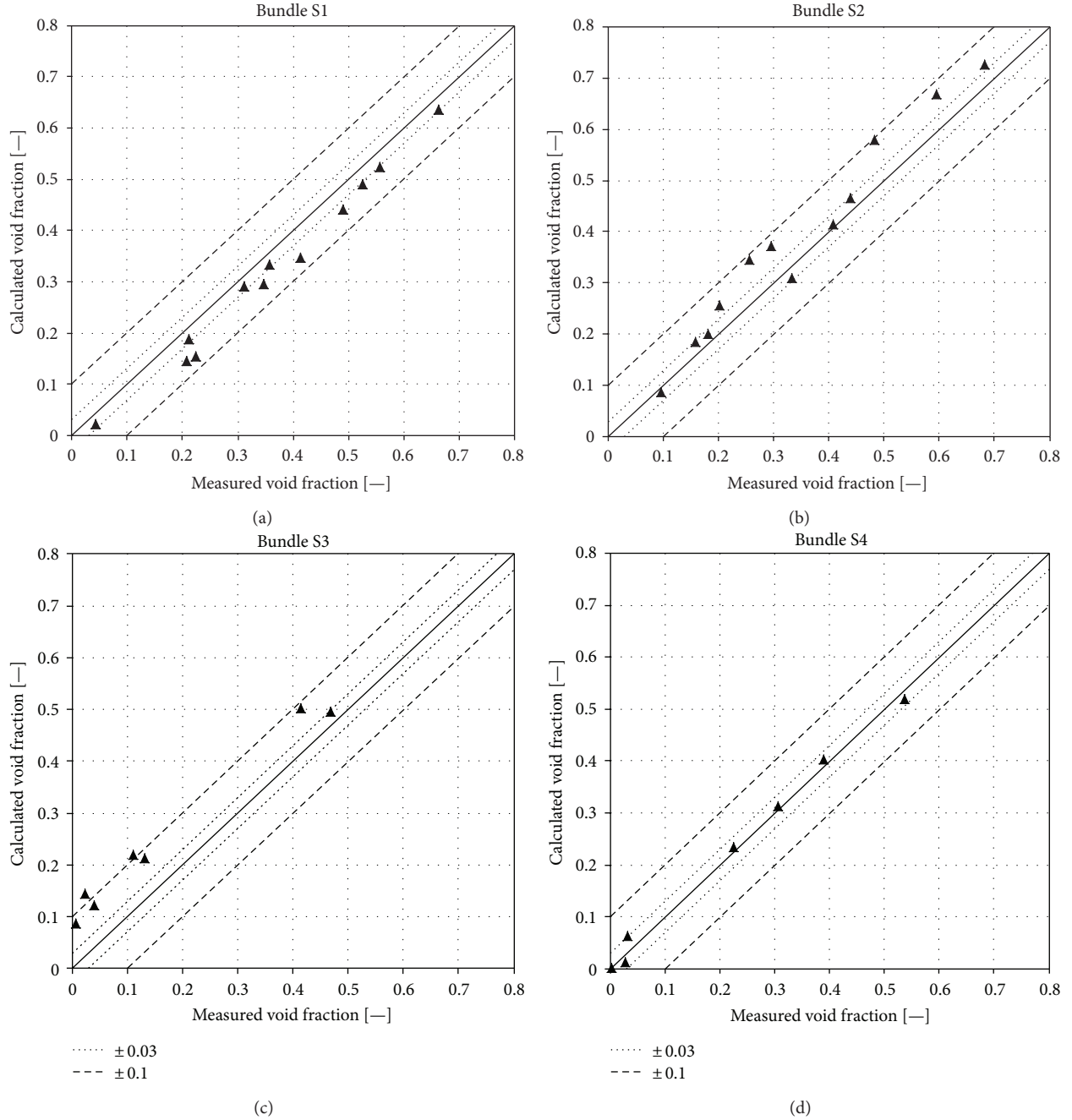


FIGURE 1: CTF predictions of steady-state void fraction in single-subchannel tests.

TABLE 4: Range of NUPEC PWR test facility operating conditions.

Quantity	Range
Pressure	4.9–16.6 MPa
Mass velocity	550–4150 kg/m ² s
Inlet coolant temperature	140–345°C

TABLE 5: Transient parameters of NUPEC PWR test facility.

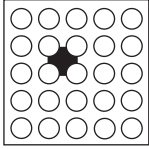
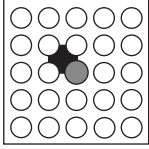
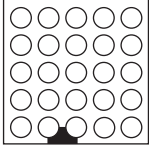
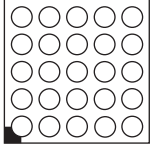
Transient scenario	Transient change
Depressurization	–0.03 MPa/s
Temperature increase	1°C/s
Flow reduction	–25%/s
Power increase	15%/s

Inverted slug regime is used in TRACE for a void fraction between 0.6 and 0.9 and the dispersed flow for a void fraction over 0.9. In both regimes the interfacial drag coefficient is calculated with (24), where $C_{D,MP}$ is the drag coefficient for

multiparticle and A_p''' is the projected area per unit volume. The projected area is calculated differently for each regime:

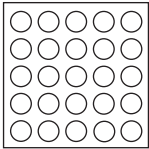
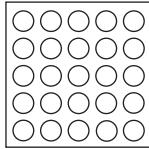
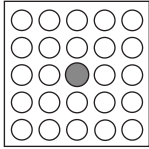
$$C_i = \frac{1}{2} \rho_g C_{D,MP} A_p''' \quad (24)$$

TABLE 6: Assembly data for assemblies S1, S2, S3, and S4.

Item	Data			
Assembly (subjected subchannel)				
	S1	S2	S3	S4
Subchannel type	Center (typical)	Center (thimble)	Side	Corner
Number of heaters	4 × 1/4	3 × 1/4	2 × 1/4	1 × 1/4
Axial heated length (mm)	1555	1555	1555	1555
Axial power shape	Uniform	Uniform	Uniform	Uniform

Dark square: subjected subchannel; White circle: heated rod; Dark circle: thimble rod.

TABLE 7: Assembly data for assemblies B5, B6, and B7.

Item	Data		
Assembly			
	B5	B6	B7
Rods array	5 × 5	5 × 5	5 × 5
Number of heated rods	25	25	24
Number of thimble rods	0	0	1
Heated rod outer diameter (mm)	9.50	9.50	9.50
Thimble rod outer diameter (mm)	—	—	12.24
Heated rods pitch (mm)	12.60	12.60	12.60
Axial heated length (mm)	3658	3658	3658
Flow channel inner width (mm)	64.9	64.9	64.9
Radial power shape	A	A	B
Axial power shape	Uniform	Cosine	Cosine
Number of MV spacers	7	7	7
Number of NMV spacers	2	2	2
Number of simple spacers	8	8	8
MV spacer location (mm)		471, 925, 1378, 1832, 2285, 2739, 3247	
NMV spacer location (mm)		2.5, 3755	
Simple spacer location (mm)		237, 698, 1151, 1605, 2059, 2512, 2993, 3501	

White circle: heated rod; Dark circle: thimble rod; MV: mixing vane; NMV: no mixing vane. Spacer location is distance from bottom of heated length to spacer bottom face.

4. Description of Phase I of the OECD/NRC PSBT Benchmark

The first phase of the PSBT benchmark [3] was intended to provide data for the verification of void distribution models in participants' codes. This phase was composed of four exercises: a steady-state single subchannel benchmark (Exercise I-1), a steady-state rod bundle benchmark (Exercise

I-2), a transient rod bundle benchmark (Exercise I-3), and a pressure drop benchmark (Exercise I-4). The results presented in this paper are for the steady-state single subchannel benchmark, the steady-state rod bundle benchmark, and the transient rod bundle benchmark.

The range of operating conditions for the facility is given in Table 4 and the operating conditions for the four transient scenarios are given in Table 5.

TABLE 8: Test conditions for transient void measurement test series 5T, 6T, and 7T.

Test series	Assembly	Initial conditions				Transients
		Pressure (kg/cm ² a)	Mass flux (10 ⁶ kg/m ² h)	Power (kW)	Inlet temperature (Celsius)	
5T	B5	154.2	11.95	2282.0	300.4	Power increase
		153.8	11.93	2244.0	301.2	Flow reduction
		153.0	11.92	2236.0	300.4	Depressurization
		152.5	11.94	2230.0	301.7	Temperature increase
6T	B6	158.2	11.55	2621.0	288.1	Power increase
		158.4	12.03	2574.0	288.8	Flow reduction
		154.6	12.02	2556.0	288.2	Depressurization
		157.2	11.92	2603.0	288.8	Temperature increase
7T	B7	158.2	12.02	2500.0	291.9	Power increase
		158.1	12.04	2405.0	292.0	Flow reduction
		155.0	11.99	2577.0	291.8	Depressurization
		158.8	11.99	2496.0	290.2	Temperature increase

The properties of each subchannel assembly (Exercise I-1) are given in Table 6.

The properties of the bundle assemblies (Exercise I-2) to be used are given in Table 7.

Four transient scenarios (temperature increase, power increase, depressurization, and flow reduction) were used in Exercise I-3 for each test series, yielding twelve total test cases. The test conditions are summarized in Table 8.

Electrical heaters are used in the PSBT experiments and the heater rod data is specified in the Benchmark Specifications [3] along with radial and axial power distributions to be used for each test simulation.

5. CTF and TRACE Applications to the Void Distribution Phase of the OECD/NRC PSBT Benchmark

The test cases of Exercise I-1 were calculated with CTF for four bundle types—S1, S2, S3, and S4. Only the heated length of the subchannel was modeled in an axial discretization of forty equidistant nodes. Code-to-data comparisons are given in Figure 1. It can be seen that the CTF predictions stay within the error bound of 10% void (the experimental uncertainties for the steady state void fraction CT scanner measurements were specified as 3% void). This is in agreement with a previously observed tendency of CTF to overpredict the vapor generation rate [11], which is due the utilized interfacial drag modeling in CTF.

Eight tests of the steady-state series-5 (5 × 5 bundle B5) were modelled by TRACE and CTF. The heated section of the bundle is modeled in TRACE with a three-dimension component discretized in 23 axial nodes, 2 radial nodes, and 1 azimuthally node assuming that the power distribution is axis symmetrical. As it can be observed in Figure 2, TRACE predicted the void fraction at the upper part of the bundle with an average error of 2% and maximum error of 7%. In the middle part of the bundle TRACE predicted the void fraction with an average error of 8% and a maximum of 13%. On the other hand, for the lower part of the bundle

TRACE overpredicted the void fraction with an average error of 10% and a maximum 16%. The entire B5 bundle was modelled by CTF in a subchannel-by-subchannel basis—no symmetry was used. The heated length was divided axially into seventy equidistant nodes. The pressure losses due to spacer grids were calculated as velocity head losses with a loss coefficient of 1.0. The total cross-flow between two adjacent subchannels was simulated as a sum of the diversion cross-flow due to lateral pressure gradients and the lateral flow due to turbulent mixing and void drift. The steady-state void fraction predictions by CTF show very similar, but slightly better agreement with the measurements as compared to TRACE. The TRACE results obtained from V5.02p2_win32_opt version for this study are similar to the results obtained from other participants in the benchmark and using RELAP5 and TRACE codes [12].

Power increase, flow reduction, depressurization, and temperature increase transients were simulated by NUPEC and selected as benchmark exercise cases. The space-averaged instantaneous axial void fraction profiles during the transients were supplied for code-to-data comparisons. The X-ray densitometer measurements were taken at three intermediate elevations along the heated lengths: 2216 mm, 2669 mm, and 3177 mm. The four transients were simulated with CTF and TRACE for the bundle type B5. Both codes utilised the same configurations used in the steady-state cases. As previously mentioned in TRACE the heated length was divided in 23 axial nodes, where 17 of those nodes upper-faces are located at the same elevation of the spacer grids, in which pressure drops are incorporated into the model with a k factor of 1 as well. CTF and TRACE results are given in Figure 3. The experimental uncertainties were specified as 5% void. As seen in Figures 3, 4, 5, and 6, both codes are capable of reproducing the transient behavior of the bundle average void fraction for the four transient scenarios. The agreement is better at higher axial elevations.

The time shift observed in the temperature increased transient for both codes should be attributed to the heat capacitance effect of the downcomer region. A study was performed by another benchmark participant, CEA-Grenoble

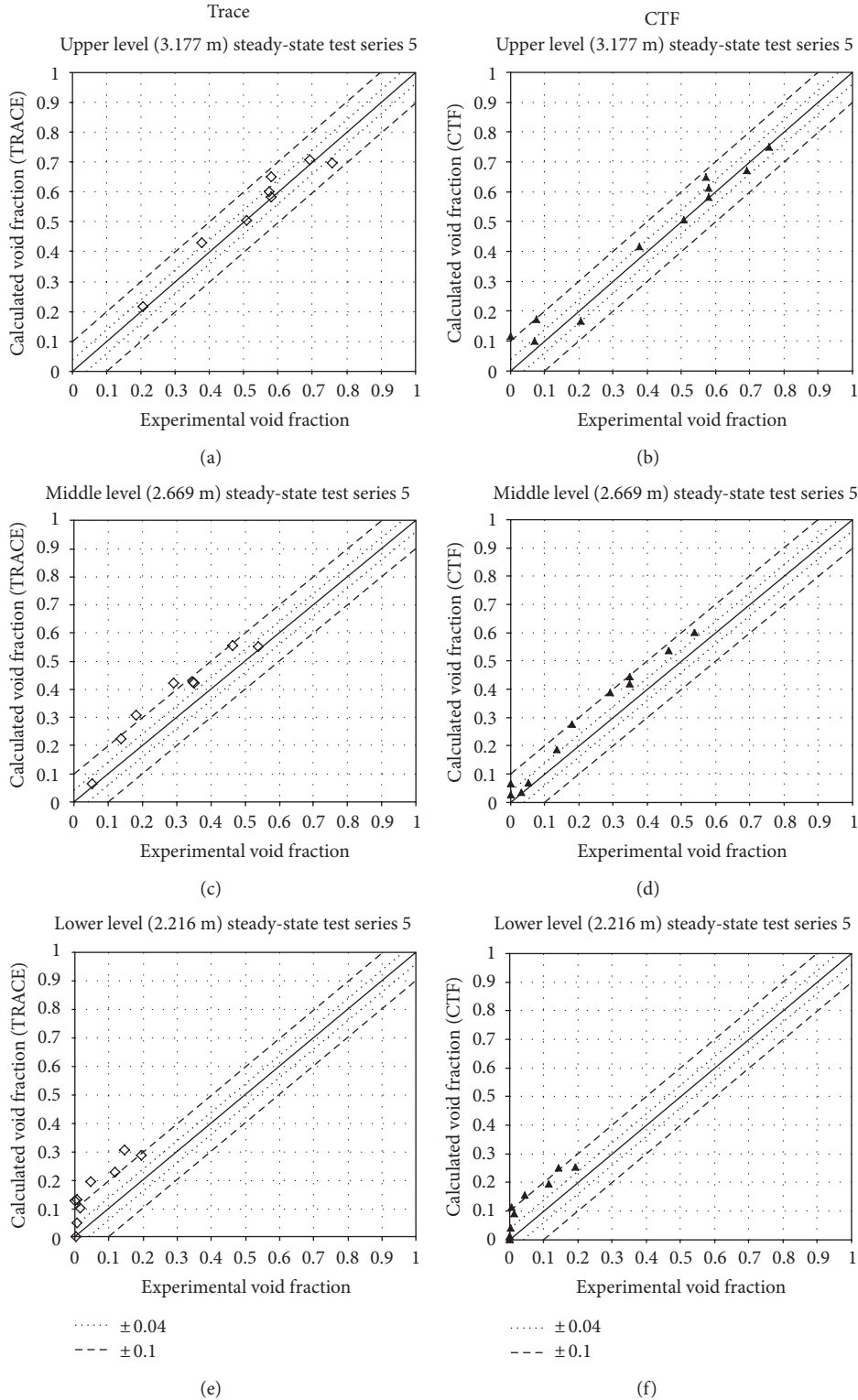


FIGURE 2: TRACE and CTF predictions of steady-state test series 5 of the 5×5 bundle B5.

[13], regarding the heat capacitance effect of the downcomer region in the bundle test section and the location of the fluid temperature measurement. The fluid temperature measurement occurred just before the coolant inlet

nozzle above the downcomer region, so it can be reasonably assumed that there would be some time shift in the flow characteristics due to the time required for the flow to traverse the downcomer. It should be noted that this

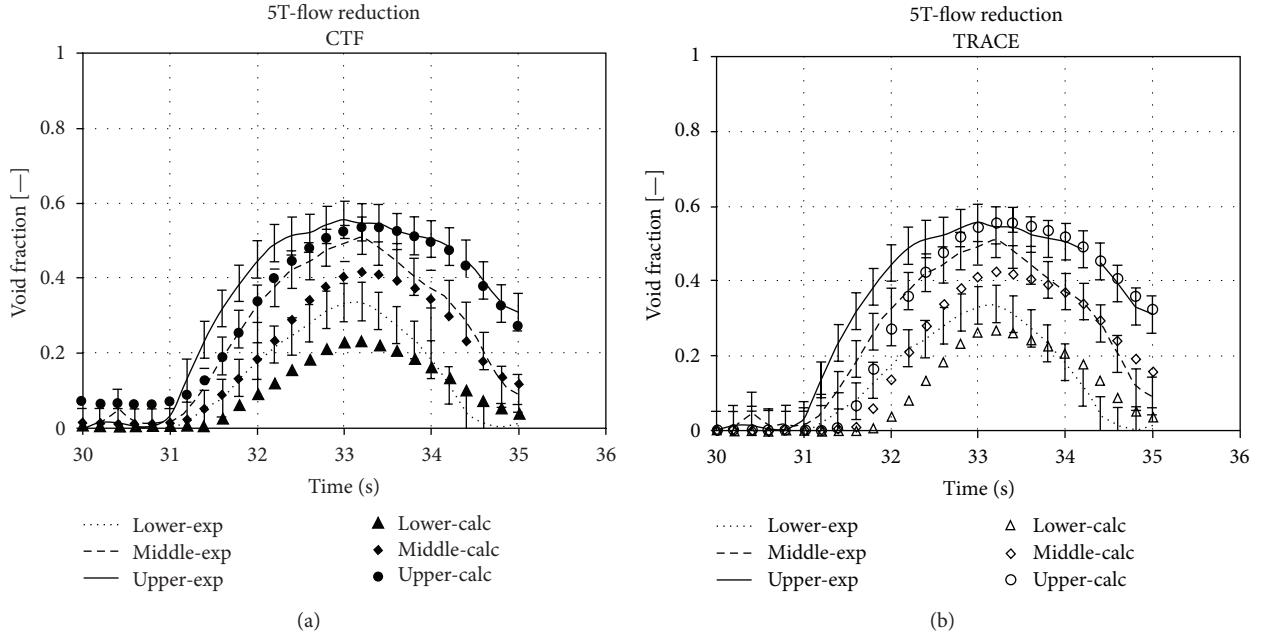


FIGURE 3: CTF (a) and TRACE (b) predictions of void fraction in bundle type B5 during flow reduction transient.

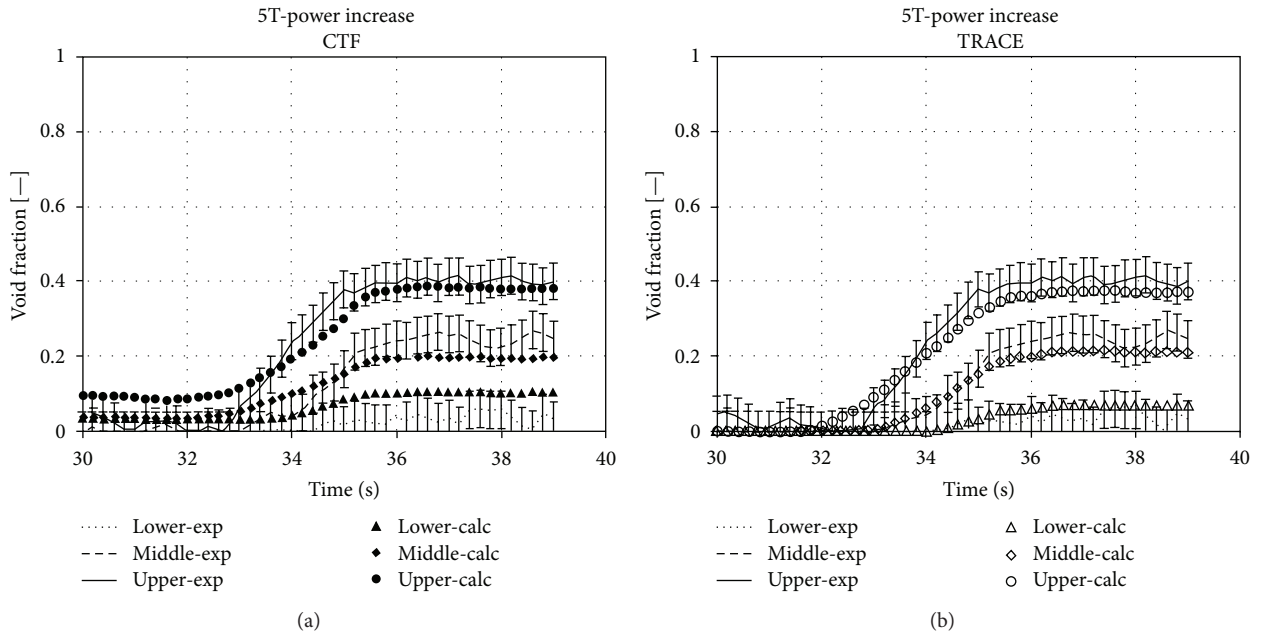


FIGURE 4: CTF (a) and TRACE (b) predictions of void fraction in bundle type B5 during power increase transient.

effect appears to only be significant for the temperature increased transients. The CEA-Grenoble team investigated the effect of the downcomer region and determined that the fluid temperature is reduced and shifted when the downcomer is accounted for. A time shift of 10 seconds for the experimental void fraction data was recommended. In addition, it should be noted that DNB will occur earlier when modeling the downcomer region than the experimental data suggests.

6. Conclusions

On behalf of the OECD/NRC PSBT benchmark team, PSU in collaboration with US NRC has performed supporting calculations of the benchmark exercises using its in-house advanced thermal-hydraulic subchannel code CTF and the US NRC system code TRACE. CTF and TRACE were applied to the steady-state and transient void distribution cases. Both codes were able to reproduce the measured data in a good agreement.

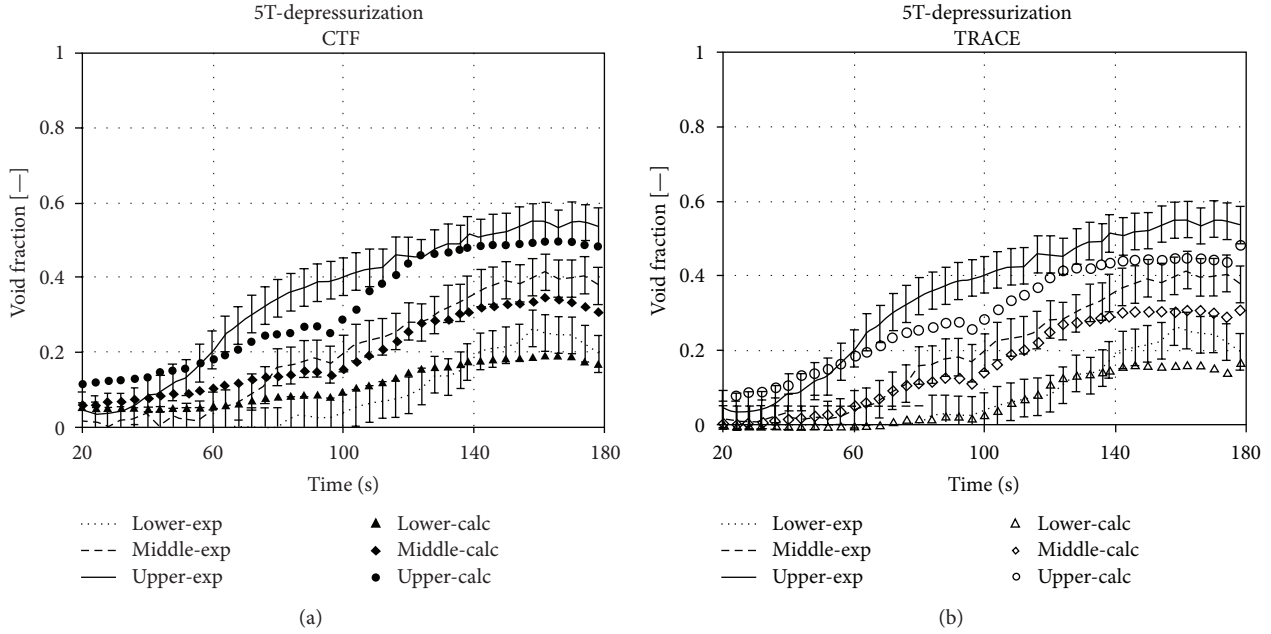


FIGURE 5: CTF (a) and TRACE (b) predictions of void fraction in bundle type B5 during flow depressurization transient.

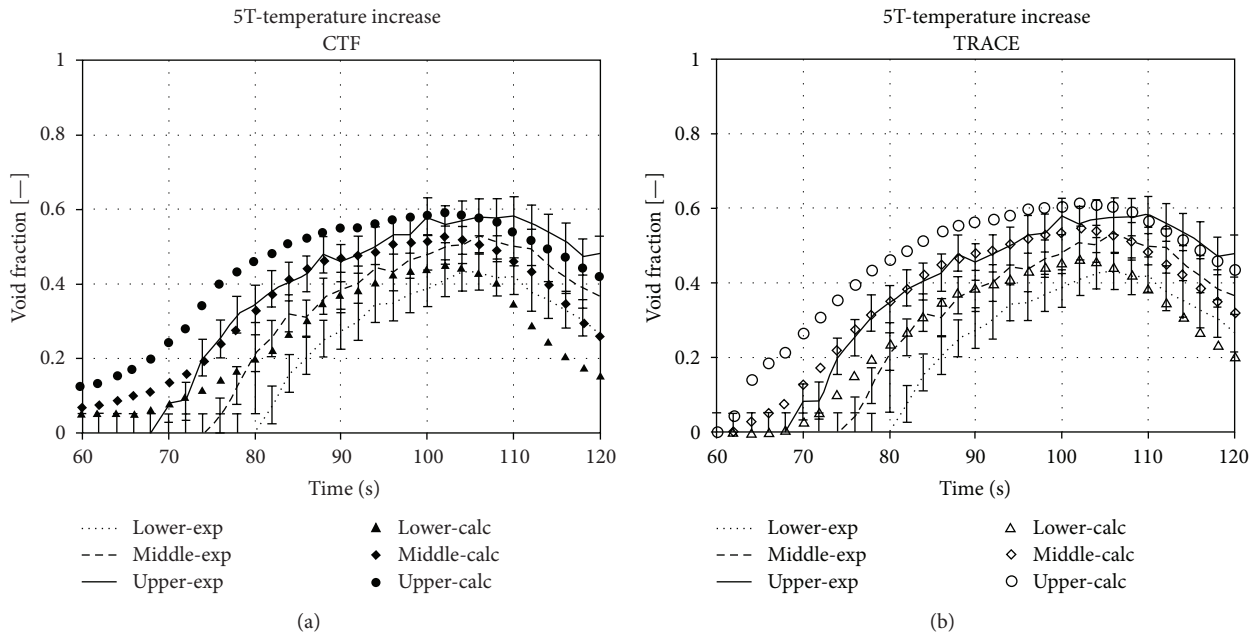


FIGURE 6: CTF (a) and TRACE (b) predictions of void fraction in bundle type B5 during temperature increase transient.

Recently, the need to refine models for best estimate calculations based on good-quality experimental data has arisen for various nuclear applications. One of the most extensive and valuable databases available was developed by the Nuclear Power Engineering Corporation (NUPEC) of Japan, consisting of both void distribution and departure from nucleate boiling (DNB) data for a representative pressurized water reactor (PWR) fuel assembly and these data were assembled in the PSBT benchmark.

The objective of the benchmark was twofold. First, the benchmark aimed to evaluate currently available computational approaches in an effort to understand the strengths and weaknesses of current thermal-hydraulic codes. Second, the benchmark was intended to encourage the development of the next generation of approaches that focus more on microscopic processes.

In the view of the above statements the PSBT data will be incorporated in the Verification and Validation matrices

of both CTF and TRACE codes. The performed comparative analysis in the future will be complemented with uncertainty and sensitivity analysis, which can be used for further improvement of CTF and TRACE models.

References

- [1] H. Herkenrath, W. Hufschmidt, U. Jung, and F. Weckermann, "Experimental investigation of the enthalpy and mass flow distribution in 16-rod clusters with BWR-PWR geometries and conditions," EUR 7575 EN, ISPRA, 1981.
- [2] R. T. Lahey Jr., B. S. Shiralkar, and D. W. Radcliffe, *Two-Phase Flow and Heat Transfer in Multi-Rod Geometries: Subchannel and Pressure Drop Measurements in a Nine-Rod Bundle for Diabatic and Adiabatic Conditions*, 1970, GEAP-13049, GE.
- [3] A. Rubin et al., "OECD/NRC benchmark based on NUPEC PWR subchannel and bundle tests (PSBT). Volume I: experimental database and final problem specifications," NEA/NSC/DOC, 2010.
- [4] "CTF—a thermal-hydraulic subchannel code for LWRs transient analyses. User's manual," Technical Report, RDFMG, The Pennsylvania State University, 2009.
- [5] C. Y. Payk et al., "Analysis of FLECHT SEASET 163-rod blocked bundle data using COBRA-TF," Tech. Rep. NRC/EPRI/Westinghouse-12, 1985.
- [6] M. Avramova, D. Cuervo, K. Ivanov et al., "Improvements and applications of COBRA-TF for stand-alone and coupled LWR safety analyses," in *Proceeding of the International Conference on the Physics of Reactors (PHYSOR '06)*, Vancouver, Canada, September 2006.
- [7] TRACE V5. 0 Theory Manual, "Field Equations, Solution Methods, and Physical Models," USNRC, Washington DC.
- [8] R. T. Lahey and F. J. Moody, *The Thermal Hydraulics of a Boiling Water Nuclear Reactor*, American Nuclear Society (ANS), 1993.
- [9] J. T. Rogers and R. G. Rosehart, "Mixing by turbulent interchange in fuel bundles, correlations and inferences," ASME 72-HT-53, 1972.
- [10] S. G. Beus, "A two-phase turbulent mixing model for flow in rod bundles," Tech. Rep. WAPD-T-2438, Bettis Atomic Power Laboratory, 1970.
- [11] M. Avramova, K. Ivanov, and L. E. Hochreiter, "Analysis of steady state and transient void distribution predictions for phase I of the OECD/NRC BFBT Benchmark using CTF/NEM," in *Proceedings of the 12th International Topical Meeting on Nuclear Reactor Thermal Hydraulics (NURETH-12 '07)*, Pittsburgh, Pa, USA, October 2007.
- [12] M. Avramova, A. Rubin et al., "OECD-NEA/US-NRC/NUPEC PWR Subchannel and bundle test (PSBT) benchmark, Volume II: final results of phase I on void distribution," OECD/NEA Report, 2011.
- [13] M. Valette and C. E. A. -Grenoble, Private Correspondence.

Research Article

Assessment of CTF Boiling Transition and Critical Heat Flux Modeling Capabilities Using the OECD/NRC BFBT and PSBT Benchmark Databases

Maria Avramova¹ and Diana Cuervo²

¹ Department of Mechanical and Nuclear Engineering, The Pennsylvania State University, University Park, PA 16802, USA

² Department of Nuclear Engineering, Technical University of Madrid, 28040 Madrid, Spain

Correspondence should be addressed to Maria Avramova; mna109@psu.edu

Received 6 July 2012; Revised 12 December 2012; Accepted 20 December 2012

Academic Editor: David Novog

Copyright © 2013 M. Avramova and D. Cuervo. This is an open access article distributed under the Creative Commons Attribution License, which permits unrestricted use, distribution, and reproduction in any medium, provided the original work is properly cited.

Over the last few years, the Pennsylvania State University (PSU) under the sponsorship of the US Nuclear Regulatory Commission (NRC) has prepared, organized, conducted, and summarized two international benchmarks based on the NUPEC data—the OECD/NRC Full-Size Fine-Mesh Bundle Test (BFBT) Benchmark and the OECD/NRC PWR Sub-Channel and Bundle Test (PSBT) Benchmark. The benchmarks' activities have been conducted in cooperation with the Nuclear Energy Agency/Organization for Economic Co-operation and Development (NEA/OECD) and the Japan Nuclear Energy Safety (JNES) Organization. This paper presents an application of the joint Penn State University/Technical University of Madrid (UPM) version of the well-known sub-channel code COBRA-TF (Coolant Boiling in Rod Array-Two Fluid), namely, CTF, to the steady state critical power and departure from nucleate boiling (DNB) exercises of the OECD/NRC BFBT and PSBT benchmarks. The goal is two-fold: firstly, to assess these models and to examine their strengths and weaknesses; and secondly, to identify the areas for improvement.

1. Introduction

1.1. Motivation for the Work. The increased use and importance of detailed reactor core descriptions for light water reactor (LWR) safety analysis and coupled local neutronics/thermal-hydraulics evaluations requires the use of advanced two-phase thermal-hydraulic codes. These codes must be extensively validated against full-scale high-quality experimental data. In that sense, the international OECD/NRC Boiling Water Reactor Full-Size-Fine-Mesh Bundle Test Benchmark [1] and the OECD/NRC PWR Sub-Channel and Bundle Tests Benchmark [2] provide an excellent opportunity for validation of models for critical power and departure from nucleate boiling.

The OECD/NRC BFBT and PSBT benchmarks were established to provide test beds for assessing the capabilities of various thermal-hydraulic subchannel, system, and computational fluid dynamics (CFD) codes and to encourage advancements in the analysis of fluid flow in rod bundles. The aim was to improve the reliability of the nuclear reactor

safety margin evaluations. The benchmarks are based on one of the most valuable databases identified for the thermal-hydraulics modelling, which was developed by the Nuclear Power Engineering Corporation in Japan.

This paper presents the results obtained with the thermal-hydraulic code CTF [3] for the Exercise II-1 (steady-state critical power) of the OECD/NRC BFBT benchmark and Exercise II-1 (steady-state departure from nucleate boiling) of the OECD/NRC PSBT benchmark. Transient CHF simulations are not considered in this study. Assessments of the code capabilities for prediction of the steady-state and transient void distribution along with uncertainty and sensitivity analysis were previously performed and published [4–6].

Although CTF was already subjected to an extensive verification and validation program and applied to a variety of LWR steady-state and transient simulations [7, 8], the code assessment to CHF experiments was limited to single-tube geometries. Moreover, the CTF heat transfer package has not been further developed and it is essentially the same as in

the original COBRA-TF code from the early 1980s. A brief description of the CTF flow regimes and heat transfer package is given in the following section.

The goal of the presented work is twofold: firstly, to assess these models and to examine their strengths and weaknesses; and secondly, to identify the areas for improvement.

1.2. Background on the Thermal-Hydraulic Subchannel Code CTF. CTF, a version of the well-known subchannel code COBRA-TF, is being maintained by the Reactor Dynamics and Fuel Management Group (RDFMG) at the Pennsylvania State University (PSU) in cooperation with several partners including the Technical University of Madrid (UPM) in Spain. The original version of COBRA-TF was developed at the Pacific Northwest Laboratory as a part of the COBRA/TRAC thermal-hydraulic code under the sponsorship of US NRC [9]. Since then, various academic and industrial organizations have adapted, developed, and modified the code in many directions. The code is worldwide used for academic and general research purposes. The code version used at PSU originates from the COBRA-TF version modified during the FLECHT SEASET program [10]. In parallel to the code utilization to teach and train students in the area of nuclear reactor thermal-hydraulic safety analyses at PSU and UPM, the theoretical models and numerics of CTF were substantially improved [11, 12].

CTF is a transient code based on a separated flow representation of the two-phase flow. The two-fluid formulation, often used in thermal-hydraulic codes, separates the conservation equations of mass, energy, and momentum to vapor and liquid. CTF extends this treatment to three fields: vapor, continuous liquid, and entrained liquid droplets, which results in a set of nine time-averaged conservation equations. The conservation equations for each of the three fields and for heat transfer from and within the solid structure in contact with the fluid are solved using a semi-implicit, finite-difference numerical technique on an Eulerian mesh, where time intervals are assumed to be long enough to smooth out the random fluctuations in the multiphase flow, but short enough to preserve any gross flow unsteadiness. The code is able to handle both pre- and post-CHF flow regimes and is capable of calculating reverse flow, counter flow, and cross-flow situations. The code is developed for use with either three-dimensional (3D) Cartesian or subchannel coordinates and, therefore, it features extremely flexible nodding for both the thermal-hydraulic and the heat-transfer solution. This flexibility allows a fully 3D treatment in geometries amenable to description in a Cartesian coordinate system.

It is worth mentioning here that CTF is being used at both universities for coupling with different 3D neutron-kinetics codes. At UPM, the code is part of the COBAYA3 [13] system of codes for multiphysics and multiscale core calculations. The code has been coupled with the ANDES nodal scale diffusion code [14] for nodal calculations and with the COBAYA3K pin-by-pin diffusion code [15] for fine-mesh calculations. Both systems of coupled codes are part of a multiscale calculation methodology based on a subdomain decomposition of the core for fast pin-by-pin diffusion

calculations of the whole core [16]. Validation of this system is being carried out [17]. At PSU, a 3D neutron kinetics module was implemented into CTF by a serial integration coupling to the PSU NEM code. The new PSU coupled code system was named CTF/NEM [18].

2. Overview of the CTF Flow Regimes and Heat Transfer Package

2.1. CTF Flow Regime Maps. As in the earlier COBRA-TF versions [9, 10], CTF contains two different types of flow regime maps: “normal wall” map and “hot wall” map. The normal wall map is used when the maximum wall surface temperature in a given computational mesh cell is below the critical heat flux temperature and is, thus, expected to be fully wetted. The hot wall map, on the other hand, is selected when the maximum wall surface temperature exceeds the critical heat flux temperature. The critical heat flux temperature is assumed to be well approximated by a wall superheat of 41.7°C or higher. There is a CHF temperature upper limit of 374.1°C, which corresponds to the critical temperature of water.

The normal wall flow regime map includes the following flow regimes: small bubble; small-to-large bubble (slug); churn/turbulent; and annular/mist. If the maximum wall temperature exceeds the CHF temperature, a whole new range of significantly different flow regimes become possible since the liquid can only partially wet the wall. This occurs in PWRs during accident conditions, like the blowdown phase of a large-break loss of coolant accident (LOCA). The flow regimes recognized in the hot wall map are inverted annular flow; inverted slug flow; dispersed droplet flow; falling flow; and top deluge flow.

A detailed description of the CTF flow regime maps and transition logic can be found in [19]. Since the physical models used in the numerical solution must be defined for each mesh cell, the flow regime must be determined from fluid properties and flow conditions within each cell or in the immediate surrounding cells. Once the flow regime of the mesh cell is correctly identified, the appropriate models can be chosen for calculation of the closure terms such as the interfacial heat transfer, the interfacial drag, and the wall drag.

It has to be mentioned here that the code was developed for vertical two-phase flow in rod bundle geometries and, therefore, horizontal flow regimes were not considered; however, an implementation of a horizontal flow regime map is currently being carried out at PSU [20].

2.2. CTF Heat Transfer Package. The heat transfer models in CTF determine the material heat release rates and the temperature response of the fuel rod and structural components of LWRs during operating and transient conditions. All heat transfer calculations are performed at the beginning of each time step before the hydraulic solution. Heat transfer coefficients based on the liquid conditions in the previous time step are used to advance the material conduction solution. The resultant heat release rates are explicitly coupled to the

hydrodynamic solution as source terms in the fluid energy equations. The CTF heat transfer package consists of a library of heat transfer coefficients and a selection logic. Together these produce a boiling curve that is used to determine the phasic heat fluxes. CTF recognizes the following heat transfer regimes: single-phase liquid convection; single-phase vapor convection; subcooled nucleate boiling; saturated nucleate boiling; transition boiling; inverted annular film boiling; dispersed droplet film boiling; dispersed droplet deposition heat transfer.

CTF selects the appropriate heat transfer regime after evaluating several criteria. If the heated surface temperature is 0.1°C less than the critical heat flux temperature, a pre-CHF heat transfer regime will be selected (i.e., single-phase liquid convection, subcooled nucleate boiling, or saturated nucleate boiling). The single-phase vapor convection regime will be selected if the void fraction is above 0.999, regardless of the heated surface temperature. On the other hand, if the heated surface temperature is greater than or equal to 0.1°C above the critical heat flux temperature, then one of the post-CHF heat transfer regimes will be selected (i.e., transition boiling, inverted annular film boiling, dispersed droplet film boiling, or dispersed droplet deposition heat transfer). A further distinction is made by selecting the transition boiling regime if the heated wall temperature is less than the minimum film boiling temperature and one of the other post-CHF regimes if the heated wall temperature is larger than the minimum film boiling temperature.

Prior to determining the heat transfer regime in the aforementioned manner, it is necessary to first determine the CHF temperature and the minimum film boiling temperature. The CHF temperature is calculated iteratively using the previously calculated CHF. The minimum and maximum boundaries for CHF temperature are 11°C over the liquid saturation temperature (minimum) and the maximum of 111°C over the saturation temperature or the critical temperature of water (maximum). For unheated conductors, the minimum film boiling temperature is set to a constant value of 482°C . For heated structures, the minimum film boiling temperature is set to a minimum value of 482°C for void fractions less than 80% and to a minimum value of 371°C for void fractions equal to or greater than 80%. The minimum film boiling temperature may be much higher, though, and is evaluated using two different methods: first, it is calculated assuming it equals the wall temperature that results in an instantaneous contact temperature equal to the homogeneous nucleation temperature; and second, the Henry's modification of the Berenson correlation is used [19].

If the mesh cell contains a hot wall, CHF is calculated for the annular film dryout region. If the mesh cell does not contain a hot wall, the void fraction is checked because the boiling regime could still be in annular film dryout. If the void fraction is higher than 90%, the annular film dryout CHF is calculated; and if the void fraction is higher than 99%, the annular film dryout CHF is multiplied by a ramping factor to reduce CHF down to 20% of its calculated value as the liquid fraction approaches 0.005. If the void fraction is less than 90%, then CHF is calculated for the forced-convection boiling regime.

The heat transfer regime selection logic and the correlations used in each regime are briefly discussed next.

Single-Phase Vapor. The maximum of the Dittus-Boelter turbulent convection correlation [21]; the FLECHT SEASET 161-rod steam cooling correlation [22]; and a laminar flow Nusselt number is used. For single-phase convection to vapor, all vapor properties are evaluated at the film temperature.

Single-Phase Liquid. Convection to single-phase liquid is computed as the larger of either the Dittus-Boelter turbulent convection correlation or the laminar flow with a limit Nusselt number equal to 7.86 [23].

Nucleate Boiling. When the temperature is greater than saturation but less than the critical heat flux temperature and liquid is present on the wall, the Chen nucleate boiling correlation [24] is used. The Chen correlation applies to both the saturated nucleate boiling region and the two-phase forced convection evaporation region. It automatically makes the transition to single-phase convection at low wall superheat and pool boiling at low flow rate. The Chen correlation assumes a superposition of a forced-convection correlation (Dittus-Boelter type) and a pool boiling equation (Forster-Zuber).

Subcooled Nucleate Boiling. An extension of the Chen nucleate boiling correlation into the subcooled region is used for subcooled nucleate boiling. During the subcooled boiling, vapor generation occurs and a significant void fraction may exist despite the presence of subcooled water. The processes of interest in this regime are forced convection to liquid, vapor generation at the wall, condensation near the wall, and bulk condensation (subcooled liquid core).

Critical Heat Flux and Transition Boiling Regime. Three critical heat flux regimes are considered—pool boiling, forced convection DNB, and annular film dryout. Pool boiling DNB is selected when the mass flux is low (below $30\text{ g/cm}^2\text{-sec}$) and the flow regime is not annular film flow. The pool boiling heat flux is given by Griffith's [25] modification of the Zuber [26] equation. The critical heat flux in this region is chosen as the larger of the Griffith's modification and the forced convection DNB heat flux at a mass flux of $30\text{ g/cm}^2\text{-sec}$. Forced-convection DNB is considered when the mass flux is greater than $30\text{ g/cm}^2\text{-sec}$ and the flow regime is not annular film flow. The critical heat flux is given by the Biasi correlation [27], which consists of two equations: one for low-quality CHF and one for high-quality CHF. The critical heat flux is defined as the maximum of the two equations. If annular flow exists, the departure from nucleate boiling is caused by annular film dryout. In this regime, the critical heat flux is not limited by a correlation, but rather forced convection vaporization exists until the film dries out. Film dryout is a complex function of the film flow rate, the applied heat flux, and the entrainment-deentrainment rate. Film dryout is determined by the solution of the hydrodynamic equations. A value of 41.7°C wall superheat is selected to be a CHF point for annular film dryout and the CHF is set to that given

by the Zuber equation. The critical heat flux temperature is defined using an iterative procedure to determine the wall temperature at which the heat flux from the Chen nucleate boiling correlation is equal to the CHF.

The transition boiling regime is bounded by the CHF point (below which the wall is continuously wetted and nucleate boiling exists) and the minimum stable film boiling point (above which the liquid cannot wet the wall and film boiling exists). It is assumed that the minimum film boiling temperature is the wall temperature that results in an instantaneous contact temperature equal to the homogeneous nucleation temperature. In addition, the minimum film boiling temperature is restricted to varies between 427°C and 649°C.

CTF employs a simple additive scheme for heat transfer beyond the critical heat flux temperature. It is assumed that the transition boiling heat transfer is composed of both liquid contact (wet wall) and film boiling (dry wall).

Heat transfer in the film boiling region is assumed to result either from dispersed flow film boiling or from inverted annular film boiling.

Dispersed Flow Film Boiling. Dispersed flow film boiling is selected if the void fraction is greater than 80%. It is treated by a “two-step” method where the dominant heat transfer mode is forced convection to superheated steam. The steam superheat is determined by the interfacial heat transfer rate to the entrained droplets as part of the hydrodynamic solution. Heat fluxes due to wall-droplet radiation and droplet impingement are superimposed upon the vapor convective heat flux.

Inverted Annular Film Boiling. When the void fraction is less than 60%, inverted annular film boiling is assumed to occur. The heat flux for this regime is computed from the larger of either dispersed film boiling heat flux as defined above or the value from the modified Bromley correlation [28]. At intermediate void fractions (60%–80%), the heat flux is interpolated between the value for inverted annular and dispersed flow film boiling.

3. CTF Application to the Steady-State Critical Power Exercise of the OECD/NRC BWR Full-Size-Fine-Mesh Bundle Test Benchmark

A full-scale bundle, simulating an 8 × 8 high burn-up fuel assembly, was installed in the NUPEC BWR test section for pressure drop, void distribution, and critical power measurements [1]. Three combinations of radial and axial power shapes were tested: (1) beginning of cycle (BOC) radial power pattern/cosine axial power shape; (2) end of cycle (EOC) radial power pattern/cosine axial power shape; and (3) beginning of cycle radial power pattern/inlet peaked axial power shape. The individual radial and axial power distributions for all three combinations are provided in Volume I of the BFBT benchmark specifications [1]. The steady-state test series consisted of three parts: void distribution tests, pressure drop tests, and critical power tests. The pressure drop was measured in both single-phase flow and two-phase flow conditions that cover the normal operational behavior.

CTF has been previously applied to the steady-state and transient void distribution exercises and to the single- and two-phase pressure drop exercises of the BFBT benchmark [4]. These studies have indicated that the code reproduces the qualitative behavior of the steady-state and transient void fraction distributions, but quantitatively overpredicts the vapor content in the BFBT bundles. This coincided with the results of the two-phase pressure drop exercises where the total pressure drop was also slightly overpredicted. The cause of both phenomena is believed to be an overestimation of the interfacial drag forces leading to an overpredicted slip and, subsequently, to an underpredicted vapor velocity yielding a higher void fraction. On the other hand, the code was able to reproduce the radial void distribution, except for the regions next to unheated structures. Regarding the sensitivity to the turbulent mixing coefficient, the code performed better when smaller values were used; larger mixing coefficients resulted in less accurate in-bundle void distribution [4].

In the BFBT tests, the critical power was measured by slowly increasing the bundle power while monitoring the individual heater rod thermocouple signals. The critical power was defined when the peak rod surface temperature became 14°C higher than the steady-state temperature level before dryout occurred. The dryout was observed in the peak power rod located at the peripheral row adjacent to the channel box. The boiling transition was always observed just upstream of spacers. The estimated accuracies of the major process parameters were 1% for the pressure and 1.5% for the power. Figure 1 describes the definition of thermocouple position. Each thermocouple position was identified according to *rod no.*, *axial location*, and *rotational angle*.

In this paper, only results for assembly C2A are shown, because C2A is the bundle used in the above-mentioned assessment of the CTF turbulent mixing model. The supplied measured data includes critical power, axial location of boiling transition, and corresponding boundary conditions (pressure, flow, inlet subcooling, and power shapes). The radial and axial power profiles of assembly type C2A are given in Table 1.

A full C2A bundle model on a subchannel by subchannel resolution (no symmetry) was used in the calculations. The heated length was divided axially into forty (40) equidistant nodes. The number of axial nodes was selected based on the desired aspect ratio and the modelling of the spacer grids. Previous verification studies have shown that the number of axial nodes will not influence the stability of the CTF thermal-hydraulic solution, but will impact the magnitude of the local pressure drop at the spacer locations.

The pressure losses due to spacer grids were calculated as velocity head losses with subchannel loss coefficient as calculated by the Shiralkar’s method [4]. The total cross-flow between two adjacent subchannels is due to diversion cross-flow by lateral pressure gradients and cross-flow by turbulent mixing and void drift. Turbulent mixing and void drift phenomena are modeled in CTF with the Lahey and Moody approach [29], where the net two-phase mixing (including void drift) is assumed to be proportional to the nonequilibrium void fraction gradient. The void drift is only

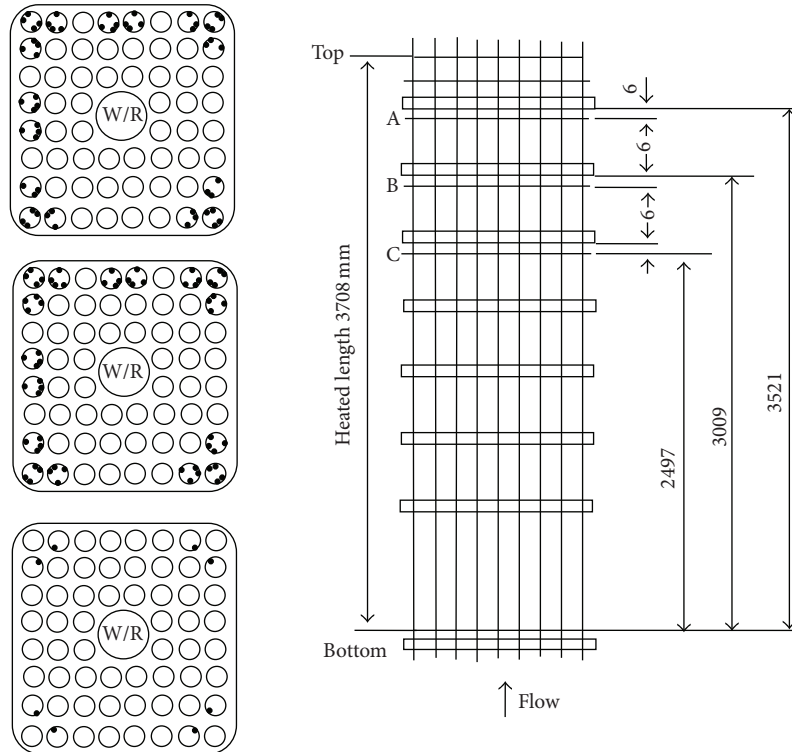


FIGURE 1: Definition of thermocouple position for assembly C2A [1].

assumed to occur in bubbly, slug, and churn flow, where liquid is the continuous phase and vapor is the dispersed phase. The single-phase mixing coefficient is either specified as an input value or calculated using an empirical correlation derived by Rogers and Rosehart [30]. The Beus model for two-phase turbulent mixing is utilized [31].

It is important to mention that the code version used in this study does not consider a multifilm formulation within a subchannel.

Following the experimental procedure, in the code calculations the power was increased gradually until the rod surface temperature became 14°C higher than the temperature at the previous steady-state level; then a dryout occurrence was considered and the critical power was determined. It was found that the criterion of 14°C temperature excursion agrees perfectly with the code prediction of complete film dryout.

Sensitivity studies were performed on the effect of turbulent mixing modeling. The calculations were repeated using three different options: (1) without modelling of turbulent mixing and void drift; (2) Lahey and Moody model with a user-specified single-phase mixing coefficient; and (3) Lahey and Moody model with a single-phase mixing coefficient by Rogers and Rosehart's correlation and Beus' model for two-phase mixing. Results are summarized in Figures 2, 3, 4, 5, and 6 in the form of predicted versus measured (P/M) values. As it can be seen, the best agreement is obtained when turbulent mixing and void drift were not modeled. For this case, the mean relative error in the code predictions was found to be 3.4%. These results should not be misunderstood—it is

a fundamental fact that the lateral exchange of momentum, mass, and heat due to increased turbulence in the flow improve the heat transfer rates. However, for this particular bundle setup, both models available in CTF had an adverse effect on the code accuracy of dryout prediction resulting in an overestimation of the critical power. Stronger was the turbulent mixing, larger was the overprediction (for typical BWR bundles, Rogers and Rosehart's correlation generally gives a single-phase mixing coefficient in the order of $10\text{E}-3$). This is in an agreement with the findings in [4]—stronger mixing, less accurate in-bundle void distribution: larger mixing coefficients led to more homogeneous void distribution pushing the vapor phase away from the peripheral region toward the central channels and resulting in a significant overprediction of the void fraction in the channels next to the water rod. In Table 2, results for a representative test case, SA505500, are given as an example. It can be clearly seen that the current turbulent mixing model gives inaccurate, and in this case less conservative, estimates of the critical power. It should be kept in mind that the axial location of the dryout could be everywhere between thermocouples A and B in Figure 1.

On the other hand, the spacers instrumented along the C2A bundle are ferrule type spacers which are not designed to enhance the flow turbulence and, therefore, any attempt to model enhanced turbulent mixing at the spacer locations (by large coefficients) would be meaningful. Also, in the CTF simulations, the lateral pressure gradient due to spacers was accounted for by applying subchannel-based loss coefficients

TABLE 1: Steady-state critical power measurement conditions for assembly C2A [1].

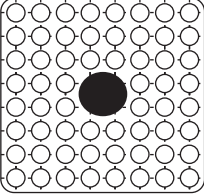
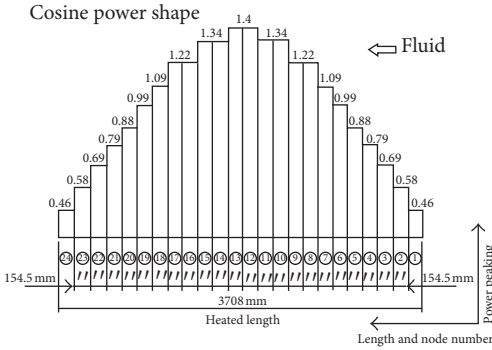
 <p>C2A</p>	 <p>Cosine power shape</p>	<table border="1"> <tr><td>1.15</td><td>1.3</td><td>1.15</td><td>1.3</td><td>1.3</td><td>1.15</td><td>1.3</td><td>1.15</td></tr> <tr><td>1.3</td><td>0.45</td><td>0.89</td><td>0.89</td><td>0.89</td><td>0.45</td><td>1.15</td><td>1.3</td></tr> <tr><td>1.15</td><td>0.89</td><td>0.89</td><td>0.89</td><td>0.89</td><td>0.89</td><td>0.45</td><td>1.15</td></tr> <tr><td>1.3</td><td>0.89</td><td>0.89</td><td></td><td></td><td>0.89</td><td>0.89</td><td>1.15</td></tr> <tr><td>1.3</td><td>0.89</td><td>0.89</td><td></td><td></td><td>0.89</td><td>0.89</td><td>1.15</td></tr> <tr><td>1.15</td><td>0.45</td><td>0.89</td><td>0.89</td><td>0.89</td><td>0.89</td><td>0.45</td><td>1.15</td></tr> <tr><td>1.3</td><td>1.15</td><td>0.45</td><td>0.89</td><td>0.89</td><td>0.45</td><td>1.15</td><td>1.3</td></tr> <tr><td>1.15</td><td>1.3</td><td>1.15</td><td>1.15</td><td>1.15</td><td>1.15</td><td>1.3</td><td>1.15</td></tr> </table>	1.15	1.3	1.15	1.3	1.3	1.15	1.3	1.15	1.3	0.45	0.89	0.89	0.89	0.45	1.15	1.3	1.15	0.89	0.89	0.89	0.89	0.89	0.45	1.15	1.3	0.89	0.89			0.89	0.89	1.15	1.3	0.89	0.89			0.89	0.89	1.15	1.15	0.45	0.89	0.89	0.89	0.89	0.45	1.15	1.3	1.15	0.45	0.89	0.89	0.45	1.15	1.3	1.15	1.3	1.15	1.15	1.15	1.15	1.3	1.15
	1.15		1.3	1.15	1.3	1.3	1.15	1.3	1.15																																																									
1.3	0.45	0.89	0.89	0.89	0.45	1.15	1.3																																																											
1.15	0.89	0.89	0.89	0.89	0.89	0.45	1.15																																																											
1.3	0.89	0.89			0.89	0.89	1.15																																																											
1.3	0.89	0.89			0.89	0.89	1.15																																																											
1.15	0.45	0.89	0.89	0.89	0.89	0.45	1.15																																																											
1.3	1.15	0.45	0.89	0.89	0.45	1.15	1.3																																																											
1.15	1.3	1.15	1.15	1.15	1.15	1.3	1.15																																																											
<p>Axial power profile</p>	<p>Radial power profile</p>																																																																	
Boundary conditions	Pressure (MPa)	5.5, 7.2, 8.6																																																																
	Flow rate (t/h)	10, 20, 30, 45, 55, 60, 65																																																																
	Inlet subcooling (KJ/kg)	25, 50, 84, 104, 126																																																																
No. of cases	Exercise cases	14																																																																

TABLE 2: Results for test case SA505500.

SA505500	Measured data	Without turbulent mixing and void drift	Lahey and Moody model [29]	
			Mixing coefficient of 0.03	Mixing coefficient by Rogers and Rosehart [30]
Critical power	6.13 MW	6.67 MW	8.25 MW	7.59 MW
Radial location	Peripheral rod	Peripheral rod	Central rod next to water channel	Central rod next to water channel
Axial location	3.521 m	3.335 m	3.612 m	3.612 m

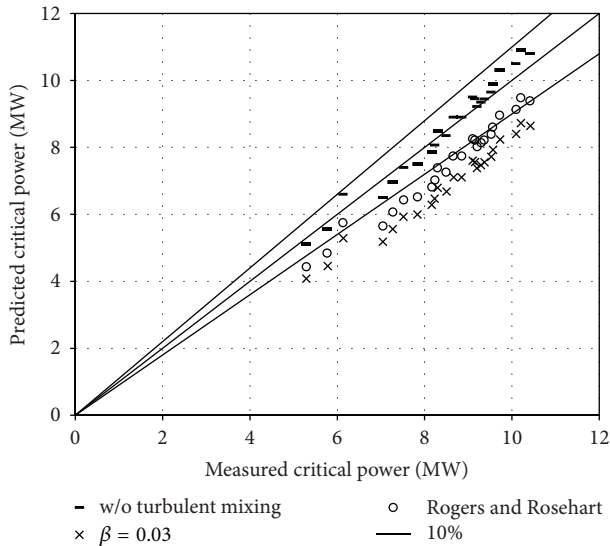


FIGURE 2: Predicted versus measured (P/M) critical power for assembly C2A with different turbulent mixing models.

in both axial and transverse directions. Cross-flow due to coolant temperature and density gradients was handled by the diversion cross-flow models.

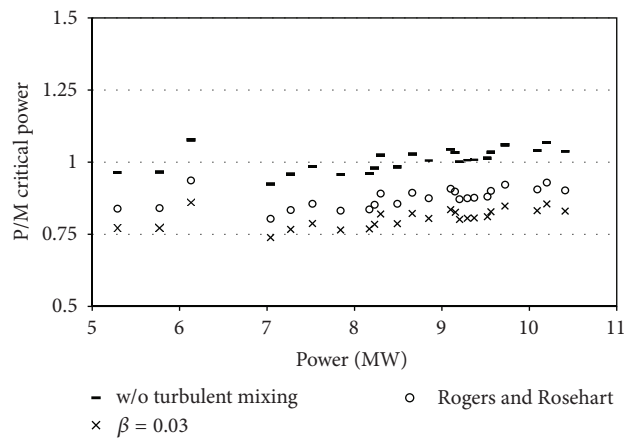


FIGURE 3: P/M Critical Power versus Power for Assembly Type C2A.

Another observation in the code predictions was the bias with the pressure—the code tends to overpredict the critical power at lower pressure (~5.5 MPa) and to underpredict it at higher pressure (~9 MPa). No bias was seen with the flow rate and the inlet subcooling.

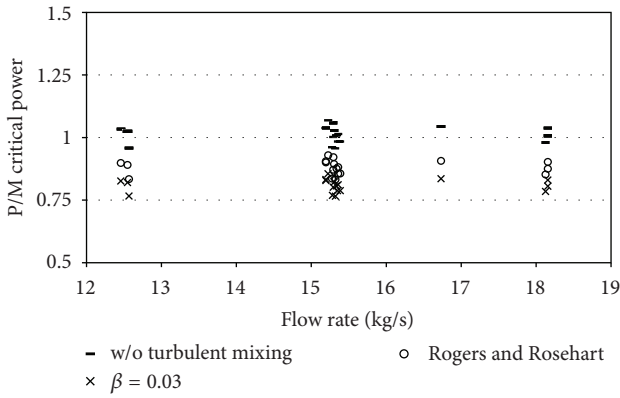


FIGURE 4: P/M critical power versus flow rate for assembly type C2A.

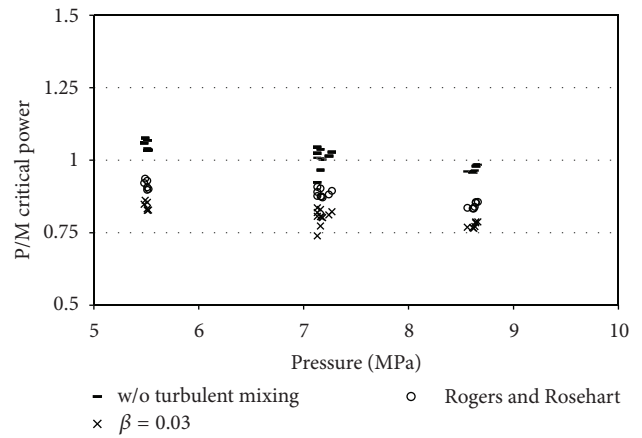


FIGURE 6: P/M critical power versus pressure for assembly type C2A.

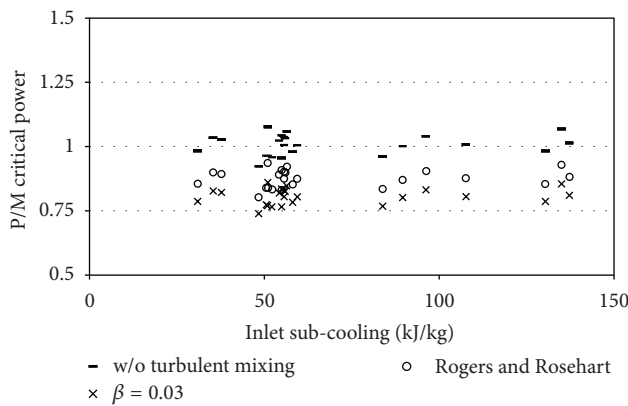
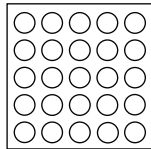


FIGURE 5: P/M critical power versus inlet sub-cooling for assembly type C2A.

4. CTF Application to the Steady-State DNB Exercise of the OECD/NRC PWR Subchannel and Bundle Tests Benchmark

In the NUPEC PWR DNB measurements, the test assembly configuration consisted of twenty-five (25) rods in a 5 × 5 square bundle or thirty-six rods (36) in a 6 × 6 square bundle [2]. The configuration of rods in this geometry approximated a typical 17 × 17 commercial power reactor fuel assembly. Each rod had a heated length of 3.658 m, an outer diameter of 9.5 mm, and a rod pitch of 12.6 mm. Between thirteen (13) and seventeen (17) spacers (both with and without mixing vanes) along the axial length supported the rods in a vertical grid. The rods were cylindrical in shape with a hollow insulator of alumina radially encircled in a heater made from Inconel 600. For the steady-state departure from nucleate boiling cases considered in this paper, a series of experiments were performed in five different configurations [2]. The NUPEC test series (numbered 0, 2, 3, 4, 8, and 13) were conducted at various pressures and temperatures where prior experience demonstrated that departure from nucleate boiling was likely to occur. The thermocouples were attached to the inner surface of the heater rods to determine the boiling

TABLE 3: Geometry and power shape for test assembly A0 [2].

Item	Data
Assembly	
	A0
Rods array	5 × 5
Number of heated rods	25
Number of thimble rods	0
Heated rod outer diameter (mm)	9.50
Thimble rod outer diameter (mm)	—
Heated rods pitch (mm)	12.60
Axial heated length (mm)	3658
Flow channel inner width (mm)	64.9
Radial power shape	A
Axial power shape	Uniform
Number of MV spacers	5
Number of NMV spacers	2
Number of simple spacers	6
MV spacer location (mm)	610, 1219, 1829, 2438, 3048
NMV spacer location (mm)	0, 3658
Simple spacer location (mm)	305, 914, 1524, 2134, 2743, 3353

transition. The bundle power was increased gradually by fine steps to the vicinity of DNB power, which was based on preliminary analysis. The occurrence of DNB was confirmed by a rod temperature rise of more than 11°C as measured by the thermocouples. The DNB power was defined as the power corresponding to the step just before the step where the temperature increased. Figure 7 shows the axial position of the thermocouples for each configuration. The various test

TABLE 4: Geometry and power shape for test assemblies A2 and A3 [2].

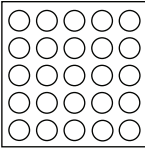
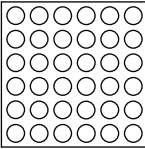
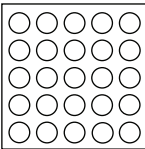
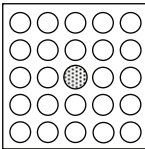
Item	Data	
Assembly		
	A2	A3
Rods array	5 × 5	6 × 6
Number of heated rods	25	36
Number of thimble rods	0	0
Heated rod outer diameter (mm)	9.50	9.50
Thimble rod outer diameter (mm)	—	—
Heated rods pitch (mm)	12.60	12.60
Axial heated length (mm)	3658	3658
Flow channel inner width (mm)	64.9	77.5
Radial power shape	A	D
Axial power shape	Uniform	Uniform
Number of MV spacers	7	7
Number of NMV spacer	2	2
Number of simple spacers	8	8
MV spacer location (mm)	457, 914, 1372, 1829, 2286, 2743, 3200	
NMV spacer location (mm)	0, 3658	
Simple spacer location (mm)	229, 686, 1143, 1600, 2057, 2515, 2972, 3429	

TABLE 5: Geometry and power shape for test assemblies A4 and A8 [2].

Item	Data	
Assembly		
	A4	A8
Rods array	5 × 5	5 × 5
Number of heated rods	25	24
Number of thimble rods	0	1
Heated rod outer diameter (mm)	9.50	9.50
Thimble rod outer diameter (mm)	—	12.24
Heated rods pitch (mm)	12.60	12.60
Axial heated length (mm)	3658	3658
Flow channel inner width (mm)	64.9	64.9
Radial power shape	A	B
Axial power shape	Cosine	Cosine
Number of MV spacers	7	7
Number of NMV spacer	2	2
Number of simple spacers	8	8
MV spacer location (mm)	471, 925, 1378, 1832, 2285, 2739, 3247	
NMV spacer location (mm)	2.5, 3755	
Simple spacer location (mm)	237, 698, 1151, 1605, 2059, 2512, 2993, 3501	

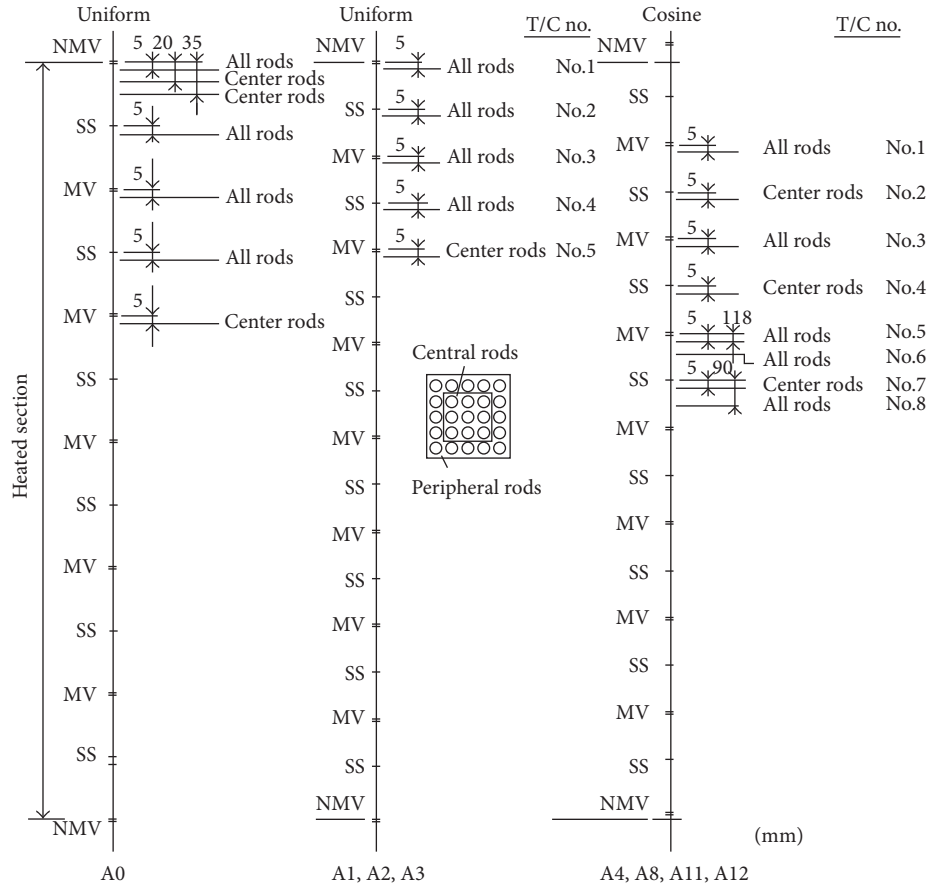


FIGURE 7: Axial thermocouple locations in the PSBT DNB measurements [2].

configurations used several axial and radial power schemes, which provided an ample cross-section of calculation data. Five assemblies were utilized, denoted by A0, A2, A3, A4, and A8 (see Tables 3, 4, and 5). The estimated accuracies of different process parameters for the DNB measurements were 1% for the pressure; 1.5% for the flow; 1°C for the fluid temperature; and 1% for the power.

Approximately, twenty-five (25) tests were chosen from configurations A4 (test series 4 and 13) and A8 (test series 8) as good candidates for the benchmark. Additionally, ten (10) tests were chosen from each of the remaining test series 0, 2, and 3. In total, one hundred (100) tests were modeled with CTF.

Full-bundle models on a subchannel-by-subchannel scale were used in the calculations. The heated length was divided axially into seventy (70) equidistant nodes. The number of axial nodes was selected based on the modelling of the spacer grids. The spacers' pressure losses were calculated with subchannel loss coefficients as specified in [2].

The PSBT bundles were equipped with three (3) different spacer types: single support spacer, nonmixing vane spacers, and mixing vane spacers [2]. While the first two types of spacers mostly affect the pressure drop in the bundle, the third type increases the turbulence and creates strong cross-flows between the subchannels. The code version utilized in

this work does not have the capabilities to simulate transverse flows locally created by the mixing vanes. Instead, a large overall single-phase mixing coefficient of 0.05 was used. The choice of the mixing coefficient value was based on previously performed sensitivity studies on void distribution tests [6].

The default models, described in Section 2, for the flow and heat transfer regimes were utilized in these CTF simulations. The calculations were performed in two sets: (1) without modelling of turbulent mixing and void drift; and (2) turbulent mixing and void drift by Lahey and Moody with a user-specified single-phase mixing coefficient of 0.05 and Beus' model for two-phase mixing enhancement. The simulations without turbulent mixing and void drift were carried out to confirm or disclaim the observations from the C2A BFBT bundle tests, where the model introduces high inaccuracy in the code predictions of void distribution and critical power.

Following the experimental procedure, in the simulations the power was increased gradually until the rod surface temperature became 11°C higher than the temperature at the previous steady-state level; then a dryout occurrence was considered and the critical power was determined.

Code-to-data comparisons are given in Figures 8 and 9. Unlike the C2A BFBT bundle results, the agreement is significantly improved when turbulent mixing and void drift

TABLE 6: Statistical analysis for the BFBT test assembly C2A.

Bundle type	Turbulent mixing: $\beta = 0.03$		Turbulent mixing: Rogers and Rosehart [30]		Without turbulent mixing	
	Mean error	Standard deviation	Mean error	Standard deviation	Mean error	Standard deviation
C2A	-1.63	0.24	-1.03	0.23	0.09	0.32

TABLE 7: Statistical analysis for the PSBT test assemblies A0, A2, A3, A4, and A8.

Bundle type	Turbulent mixing: $\beta = 0.05$ and Beus		Without turbulent mixing	
	Mean error	Standard deviation	Mean error	Standard deviation
A0	0.04	0.18	-0.39	0.12
A2	0.34	0.25	-0.91	0.55
A3	-0.10	0.40	-1.60	0.66
A4 (TS4)	-0.09	0.31	-0.63	0.41
A8	0.09	0.29	-0.35	0.24
A4 (TS13)	-0.08	0.25	-0.67	0.37
Overall	0.01	0.30	-0.62	0.47

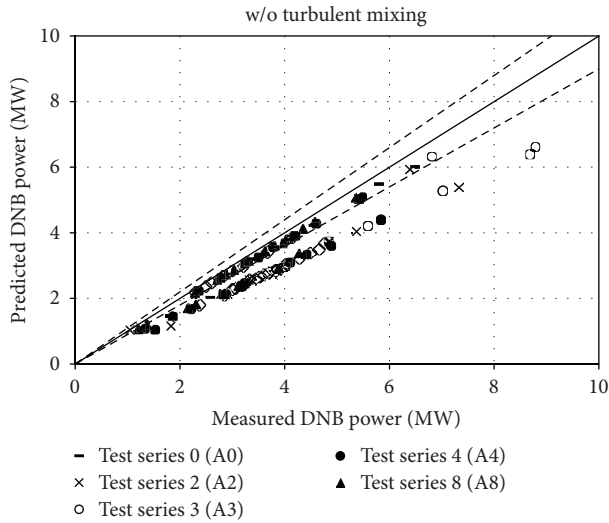


FIGURE 8: Predicted versus Measured DNB without Turbulent Mixing and Void Drift Modeling.

are modelled and a large underprediction on the DNB power is seen if not. No bias with the power, the flow, rate and the subcooling was found (Figures 10, 11, and 12). Similarly to the C2A BFBT critical power calculations, a code bias with the pressure was seen (Figure 13)—the code tends to overpredict the critical power at lower pressure (~ 5 MPa) and to underpredict it at higher pressure (~ 15 MPa).

5. Statistical Analysis

Mean error and standard deviation are calculated for each test series. The mean error is represented as $\overline{CP} = \sum_{n=1}^N CP^n / N$, where the critical power (CP) error for test case “ n ” is given as $CP^n = (CP_{code}^n - CP_{exp}^n)$ and N is the total number of test cases.

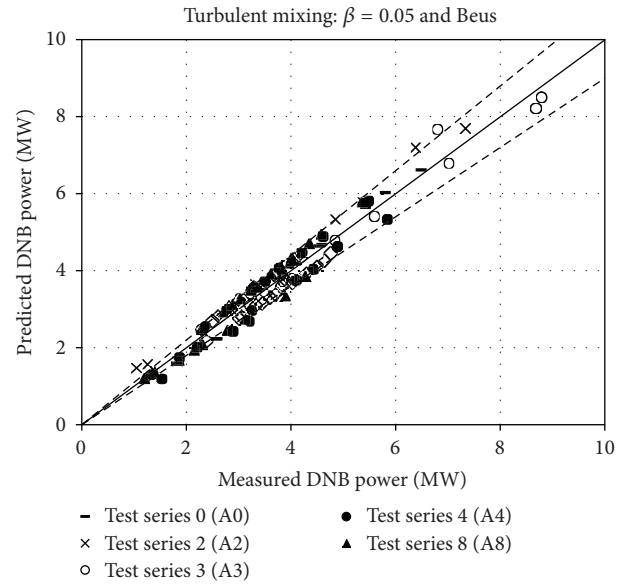


FIGURE 9: Predicted versus measured DNB with turbulent mixing and void drift modeling (single-phase mixing coefficient of 0.05 and two-phase mixing by Beus).

The standard deviation is given as $\sigma = \pm \sqrt{\sum_{n=1}^N (CP^n - \overline{CP})^2 / N - 1}$.

Results are given in Tables 6 and 7, respectively for the BFBT assembly C2A and the PSBT assemblies A0, A2, A3, A4, and A8. As previously discussed, the sensitivity to the turbulent mixing and void drift models showed very inconsistent behavior—the modeling of stronger turbulent mixing worsened the code predictions for critical power in the BWR-type bundle (C2A) and vice-versa improved the code predictions for the departure from nucleate boiling in the PWR-type bundles (A0, A2, A3, A4, and A8).

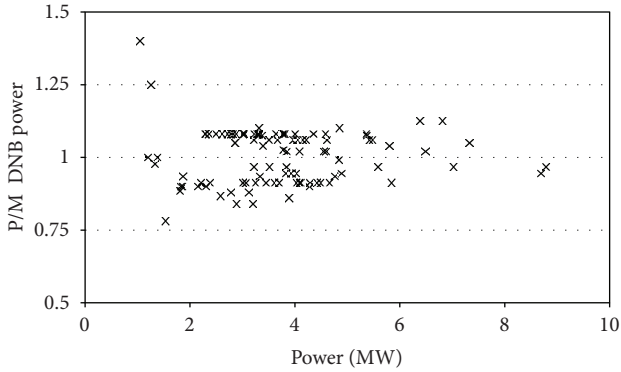


FIGURE 10: P/M DNB power versus power for assembly types A0, A2, A3, A4, and A8.

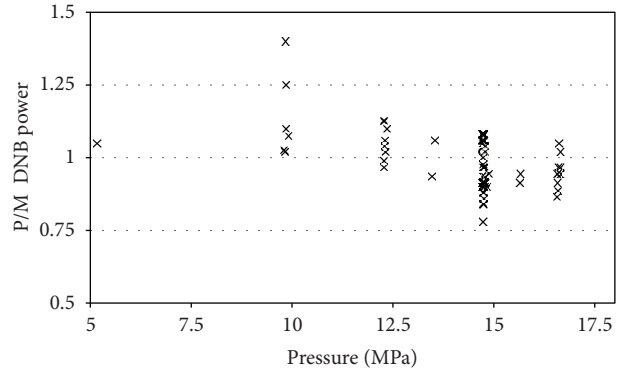


FIGURE 13: P/M DNB power versus pressure for assembly types A0, A2, A3, A4, and A8.

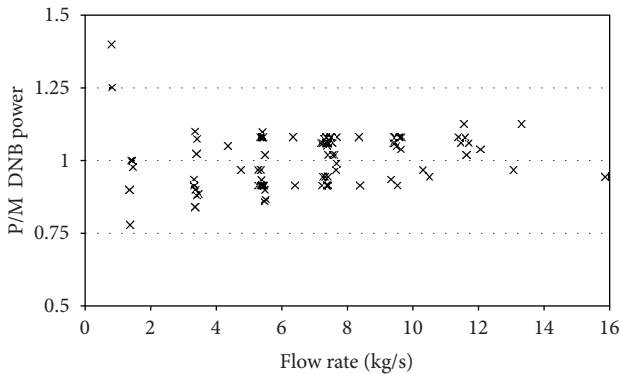


FIGURE 11: P/M DNB power versus flow rate for assembly types A0, A2, A3, A4, and A8.

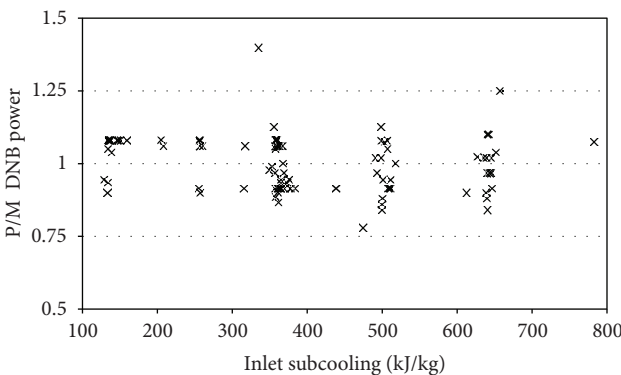


FIGURE 12: P/M DNB power versus subcooling for assembly types A0, A2, A3, A4, and A8.

To recall, no empirical correlations were used to calculate the critical power/critical heat flux. In annular flow regime, the heat flux was not limited by a correlation, but rather forced convection vaporization existed until the film dries out. In CTF, film dryout is a complex function of the film flow rate, the applied heat flux, and the entrainment/de-entrainment rate, and is determined by the solution of the hydrodynamic equations. In these assessments, a rapid

increase of the cladding temperature was used as a criterion for DNB or dryout occurrence.

6. Conclusions

To assess its accuracy of dryout and departure from nucleate boiling prediction, the subchannel thermal-hydraulic code CTF was applied to Exercise II-1 (steady-state critical power) of the OECD/NRC BFBT benchmark and Exercise II-1 (steady-state departure from nucleate boiling) of the OECD/NRC PSBT benchmark. The obtained results showed that the code predicts fairly well the critical power and departure from nucleate boiling power with no specific tendency of over- or underprediction. The boiling crisis location was well captured. However, some areas of potential improvement were identified.

The turbulent mixing and void drift model, including spacer grid effects, has to be enhanced. The current approach of using a larger overall mixing coefficient to capture spacer induced turbulence had proven to be highly inaccurate.

The bias with the pressure indicated possible inconsistencies in the fluid solution and a need of further improvements of flow regime transition logic in CTF.

The code tendency to overpredict the void generation rates and two-phase pressure drop may contribute to an inaccurate boiling crisis prediction and, therefore, the interfacial friction models might need an improvement.

In summary, this work indicated that some code models have to be further improved to address the new trends in nuclear reactor core designs.

References

- [1] B. Neykov, B. Aydogan, F. Hochreiter et al., "OECD-NEA/US-NRC/NUPEC BWR full-size Fine-mesh Bundle Test (BFBT) benchmark," *OECD*, vol. 1, no. 6212, 2006, NEA/NSC/DOC(2005)5.
- [2] A. Rubin et al., "OECD/NRC benchmark based on NUPEC PWR subchannel and bundle tests (PSBT). Volume I: experimental database and final problem specifications," 2010, NEA/NSC/DOC(2010)1.

- [3] CTF, "A Thermal-Hydraulic subchannel code for LWRs transient analyses," User's Manual RDFMG, The Pennsylvania State University, 2004.
- [4] M. Avramova, K. Ivanov, and L. E. Hochreiter, "Analysis of steady state and transient void distribution predictions for phase I of the OECD/NRC BFBT Benchmark using CTF/NEM," in *Proceedings of the 12th International Topical Meeting on Nuclear Reactor Thermal Hydraulics (NURETH-12)*, Pittsburgh, PA, USA, October 2007.
- [5] M. Avramova et al., "Uncertainty analysis of COBRA-TF void distribution predictions for the OECD/NRC BFBT Benchmark," in *Proceedings of the International Conference on Advances in Mathematics, Computational Methods, and Reactor Physics (M&C '09)*, Paper ID 202600, Saratoga Springs, New York, NY, USA, May 2009.
- [6] M. Avramova et al., "Comparative analysis of CTF and TRACE Thermal-Hydraulic codes using OECD/NRC PSBT benchmark void distribution database," in *Proceedings of the 14th International Topical Meeting on Nuclear Reactor Thermal Hydraulics (NURETH-14)*, Toronto, Canada, September 2011.
- [7] M. Avramova, *COBRA-TF development, qualification, and application to LWR analysis [M.S. thesis]*, The Pennsylvania State University, 2003.
- [8] M. Avramova et al., "Improvements and applications of COBRA-TF for stand-alone and coupled LWR safety analyses," in *Proceedings of the American Nuclear Society's Topical Meeting on Reactor Physics (PHYSOR '06)*, Vancouver, Canada, September 2006.
- [9] M. J. Thurgood et al., "COBRA/TRAC a Thermal-Hydraulic code for transient analysis of nuclear reactor vessel and primary coolant systems," 1983, NUREG/CR-3046.
- [10] C. Y. Payk et al., "Analysis of FLECHT SEASET 163-rod blocked bundle data using COBRA-TF," 1985, NRC/EPRI/Westinghouse-12.
- [11] D. Cuervo, M. Avramova, K. Ivanov, and R. Miró, "Evaluation and enhancement of COBRA-TF efficiency for LWR calculations," *Annals of Nuclear Energy*, vol. 33, no. 9, pp. 837–847, 2006.
- [12] M. Avramova, *Development of an innovative spacer grid model utilizing computational fluid dynamics within a subchannel analysis tool [Ph.D. thesis]*, The Pennsylvania State University, 2007.
- [13] J. J. Herrero, J. Jimenez, J. A. Lozano, N. García-Herranz, C. Ahnert, and J. M. Aragonés, *The 3D Cell-Nodal Multi-Scale COBAYA3 Code, NURESIM Deliverable D1. 2. 3*, Department of Nuclear Engineering, Technical University of Madrid (UPM), 2008.
- [14] J. A. Lozano, N. García-Herranz, C. Ahnert, and J. M. Aragonés, "The analytic nodal diffusion solver ANDES in multigroups for 3D rectangular geometry: development and performance analysis," *Annals of Nuclear Energy*, vol. 35, no. 12, pp. 2365–2374, 2008.
- [15] J. J. Herrero, C. Ahnert, and J. M. Aragonés, "3D whole core fine mesh multi-group diffusion calculations by domain decomposition through alternate dissections," in *Proceedings of the Mathematics and Computations and Supercomputing in Nuclear Applications (M&C+SNA '07)*, Monterey, Calif, USA, 2007.
- [16] J. Jiménez, D. Cuervo, and J. M. Aragonés, "A domain decomposition methodology for pin by pin coupled neutronic and Thermal-Hydraulic analyses in COBAYA3," *Nuclear Engineering and Design*, vol. 240, pp. 313–320, 2010.
- [17] J. Jiménez, *Desarrollo e implementación de la descomposición en subdominios mediante disecciones alternadas al acoplamiento neutrónico-termohidráulico en PWR con un sistema de cálculo multiescala [Ph.D. thesis]*, Technical University of Madrid, 2010.
- [18] RDFMG, Nuclear Engineering Program, and PSU, "CTF/NEM a coupled neutronics/Thermal-Hydraulic code for LWRs transient analyses, users manual," 2007, University Park, Pa, USA.
- [19] RDFMG, Nuclear Engineering Program, and PSU, "CTF a Thermal-Hydraulic code for LWRs transient analyses, theory Manual," 2011, University Park, Pa, USA.
- [20] R. K. Salko, M. Avramova, and A. Ohnuki, "Modification of COBRA-TF for improved vessel-wide transient analysis," in *Proceedings of the ANS Winter Meeting*, vol. 103, pp. 977–978, Las Vegas, Nev, USA, November 2010.
- [21] F. W. Dittus and L. M. K. Boelter, *Heat Transfer in Automobile Radiators of Tubular Type*, University of California, Berkeley, Calif, USA, 1930.
- [22] S. Wong and L. E. Hochreiter, "Analysis of the FLECHT SEASET unblocked bundle steam cooling and boil-off tests," 1981, NRC/EPRI/Westinghouse-8.
- [23] E. M. Sparrow, A. L. Loeffler, and H. A. Hubbard, "Heat transfer to longitudinal laminar flow between cylinders," *Journal of Heat Transfer*, vol. 83, no. 4, article 415, 8 pages, 1961.
- [24] J. C. Chen, "A correlation for boiling heat transfer to saturated fluids in convective flow," ASME 63-HT-34, American Society of Mechanical Engineers, 1963.
- [25] P. Griffith et al., *PWR Blowdown Heat Transfer*, vol. 1 of *Thermal and Hydraulic Aspects of Nuclear Reactor Safety*, American Society of Mechanical Engineers, New York, NY, USA, 1977.
- [26] N. Zuber et al., "The hydraulics crisis in pool boiling of saturated and subcooled liquids, part II," in *Proceedings of the International Developments in Heat Transfer Conference*, no. 27, Boulder, Colo, USA, 1961.
- [27] L. Biasi et al., "Studies on burnout, part 3," *Energia Nucleate*, vol. 14, no. 9, pp. 530–536, 1967.
- [28] L. A. Bromley, "Heat transfer in stable film boiling," *Chemical Engineering Progress*, vol. 46, no. 5, pp. 221–226, 1950.
- [29] R. T. Lahey and F. J. Moody, *The Thermal Hydraulics of a Boiling Water Nuclear Reactor*, American Nuclear Society (ANS), 1993.
- [30] J. T. Rogers and R. G. Rosehart, "Mixing by turbulent interchange in fuel bundles. Correlations and influences," ASME, 72-HT-53, 1972.
- [31] S. G. Beus, "A two-phase turbulent mixing model for flow in rod bundles," Bettis Atomic Power Laboratory, WAPD-T-2438, 1970.

Research Article

OECD/NRC PSBT Benchmark: Investigating the CATHARE2 Capability to Predict Void Fraction in PWR Fuel Bundle

A. Del Nevo,¹ D. Rozzia,² F. Moretti,² and F. D'Auria²

¹ENEA UTIS-TCI, CR Brasimone, 40032 Camugnano, Italy

²GRNSPG, University of Pisa, Largo Lucio Lazzarino 2, 56100 Pisa, Italy

Correspondence should be addressed to A. Del Nevo, alessandro.delnevo@enea.it

Received 7 July 2012; Accepted 21 August 2012

Academic Editor: Maria Avramova

Copyright © 2012 A. Del Nevo et al. This is an open access article distributed under the Creative Commons Attribution License, which permits unrestricted use, distribution, and reproduction in any medium, provided the original work is properly cited.

Accurate prediction of steam volume fraction and of the boiling crisis (either DNB or dryout) occurrence is a key safety-relevant issue. Decades of experience have been built up both in experimental investigation and code development and qualification; however, there is still a large margin to improve and refine the modelling approaches. The qualification of the traditional methods (system codes) can be further enhanced by validation against high-quality experimental data (e.g., including measurement of local parameters). One of these databases, related to the void fraction measurements, is the pressurized water reactor subchannel and bundle tests (PSBT) conducted by the Nuclear Power Engineering Corporation (NUPEC) in Japan. Selected experiments belonging to this database are used for the OECD/NRC PSBT benchmark. The activity presented in the paper is connected with the improvement of current approaches by comparing system code predictions with measured data on void production in PWR-type fuel bundles. It is aimed at contributing to the validation of the numerical models of CATHARE 2 code, particularly for the prediction of void fraction distribution both at subchannel and bundle scale, for different test bundle configurations and thermal-hydraulic conditions, both in steady-state and transient conditions.

1. Introductory Remarks

A system code shall demonstrate that it is reliable in simulating and predicting the key phenomena of properly selected scenarios. This is a necessary prerequisite for its applicability in accident analysis aimed at demonstrating that a nuclear system is safe and unlikely to fail. The current generation of thermal-hydraulic system (TH-SYS) codes benefits decades of experience in experimental investigation and code development and qualification. They are considered mature tools to provide best estimate description of phenomena and detailed reactor system representation. However, there is still a large margin to improve and refine the modelling approaches taking advantage of more recent techniques that focus on microscopic mechanisms rather than on macroscopic effects, so that more accurate predictions can be obtained and reduction of uncertainties can be achieved. In this view, the qualification of the traditional methods (system codes) can be further enhanced by validation against high-quality experimental data (e.g., including measurement of local parameters), while in parallel more sophisticated 3D

techniques (such as CFD) are developed and assessed. One of these databases, related to the void fraction measurements, is the pressurized water reactor subchannel and bundle tests (PSBT) conducted by the Nuclear Power Engineering Corporation (NUPEC) in Japan. Selected experiments belonging to this database are used for the OECD/NRC PSBT benchmark.

Prediction of void fraction and DNB in system thermal hydraulics is currently based on empirical approaches. Advancement in understanding and modelling complex flow behaviour in rod bundles would promote the validation of the current approaches and the development of more mechanistic approaches [1].

The aim of the activity is to assess the models of CATHARE2 (six-equation, two-field) code [2, 3] by means of void fraction measurements in subchannel configurations and in full scale bundle of Pressurized Water Reactor (PWR) at wide range of thermal-hydraulic boundary conditions (i.e., pressure, power, inlet temperature, and mass flow rate). In particular, the paper presents the results of four subchannel test sections and the analysis of three bundle configurations in steady-state and transient conditions. Sensitivity

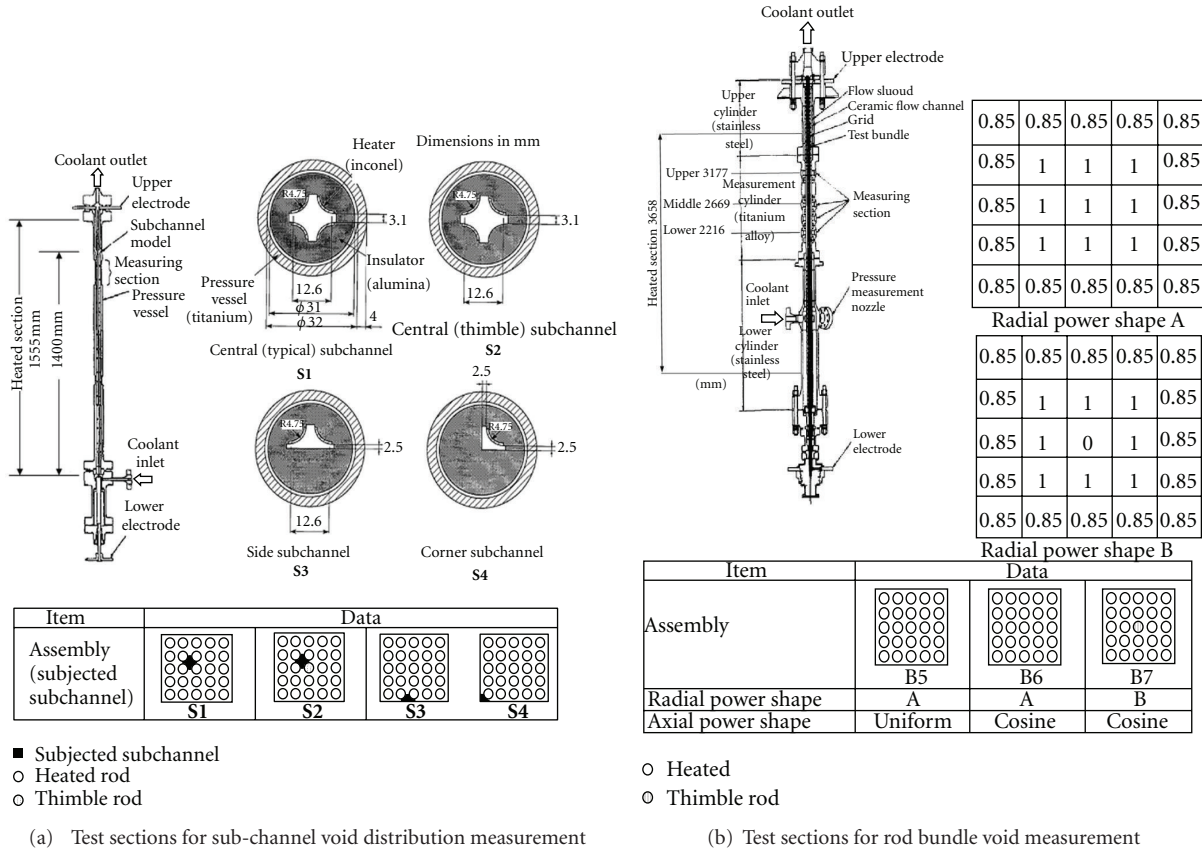


FIGURE 1: Test sections of PWR subchannel and bundle tests.

analyses are carried out addressing nodalization effect and the influence of the initial and boundary conditions of the tests.

2. The OECD/NRC NUPEC PSBT Experimental Database

The pressurized water reactor subchannel and bundle tests were conducted by NUPEC within an extensive experimental campaign aimed at verifying the reliability of fuel assemblies used for commercial nuclear power plants [4]. PSBT is able to simulate the high pressure, high temperature fluid conditions, which are typical of a PWR nuclear power plant (NPP).

The NUPEC test facility (Figure 1) consists of a high pressure and high temperature recirculation loop, a cooling loop, and instrumentation and data recording systems. The recirculation loop consists of a test section, circulation pump, preheater, steam drum (acting as a pressurizer), and a water mixer. The design pressure is 19.2 MPa, and the design temperature is 362°C. The operating conditions of the test facility are shown in Table 1.

The void fraction tests include steady-state subchannel as well as steady-state and transient rod bundle experiments. Four subchannel test assemblies (TS 1, 2, 3, and 4) are used for measuring void fraction, as shown in Figure 1(a). They simulate the subchannel types (central, central with thimble, side, and corner) which are in a PWR assembly. The effective

TABLE 1: Range of NUPEC PWR test facility operating conditions.

Quantity	Range
Pressure	4.9–16.6 MPa
Mass velocity	550–4150 kg/m ² s
Inlet coolant temperature	140–345°C
Surface heat flux	37–186 W/cm ²

heated length is 1555 mm, and the void measurement section begins at 1400 mm from the bottom of the heated section. The overall subchannel database includes 126 tests, under a wide range of test conditions. Among these, 43 are carried out with TS 1, and TS 2 and 20 using TS 3 and TS 4 (see Figure 1(a)). Complete set of details about geometrical data, boundary conditions of the tests, and experimental results is available in [5].

The rod bundle test sections simulate a partial section and full length of a PWR fuel assembly. Figure 1(b) shows the test section used for the rod bundle void measurements. Three different bundles are used to perform the void distribution measurements (test sections B5, B6, and B7). The effective heated length is 3.618 m. Void fraction measures are available at three different elevations 2.216 m, 2.669 m, and 3.177 m, respectively. Steady-state tests were carried out for a wide range of operating conditions. Transient tests were executed increasing the void generation for power increase,

flow rate reduction, depressurization, and coolant temperature increase. In these tests, thermal-hydraulic conditions comparable with typical scenarios were selected ranging from anticipated transients and postulated accidents. Complete set of details about geometrical data, boundary conditions of the tests, and experimental results is available in [5].

3. Thermal-Hydraulic Code Nodalizations

3.1. 1D Models of Subchannel and Bundle Test Sections. Rather simple 1D models were developed for simulating the four subchannel test sections. Here is a summary of the main features of the nodalizations [6, 7]:

- (i) two BCONDIT components for imposing the boundary conditions of the tests (i.e., pressure, mass flow, and inlet temperature);
- (ii) two VOLUME components, which simulate the inlet and the outlet of the test section;
- (iii) one AXIAL component, which models the test section.

The electrical heaters of the subchannel and bundle test sections are modelled with WALL components. The linear power is imposed according to the specifications of the tests. The material properties implemented in the nodalization are provided by means of an external FORTRAN subroutine according to the specification in [5].

3.2. 3D Models of Bundle Test Sections. A nodalization of the bundle test section was also developed that takes advantage of the 3D modelling capabilities of CATHARE2. Here is a summary of the main features of the nodalization:

- (i) two BCONDIT components for imposing the boundary conditions of the tests (i.e., pressure, mass flow, and inlet temperature);
- (ii) two VOLUME components, which model the inlet and the outlet of the test section, and connected to the THREED component by means of two times 36 junctions;
- (iii) a THREED component, having 1296 meshes, which provides a three-dimensional description of the bundle flow. It is discretized according to a Cartesian 6×6 pattern, so that one “cell” corresponds to one subchannel of the bundle and 36 axial nodes;
- (iv) one equivalent heat structure (WALL) is defined for each subchannel;
- (v) spacer grids are accounted for by equivalent pressure loss coefficients;
- (vi) porosity is set at the junctions and at the volumes to account for the presence of the fuel pins and thus the real hydraulic flow areas;
- (vii) turbulence option is activated.

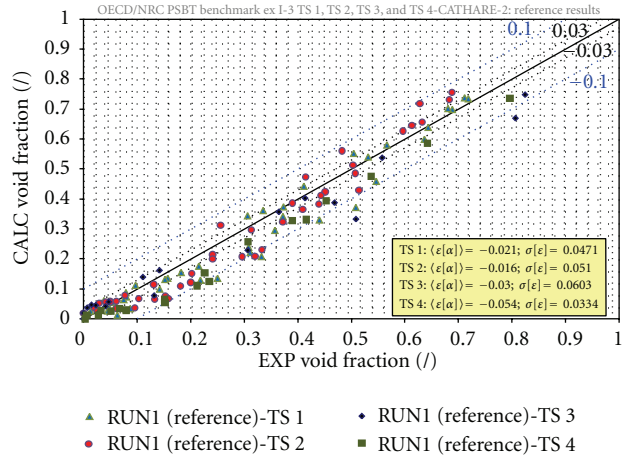


FIGURE 2: Overall subchannels tests (126 tests)—CATHARE2 v2.5.1 code, reference results.

4. Simulating the PSBT Facility Tests by CATHARE2 Code

The results of three different types of experiments [8] are discussed hereafter: (1) steady-state subchannel tests; (2) steady-state bundle tests; (3) transient bundle tests. Details of the boundary conditions of the tests are in [5, 8, 9].

4.1. Posttest Analysis of Steady-State Subchannel Tests. The analysis deals with 126 tests [8] related to the four test sections (see Figure 1(a)). Figure 2 outlines the reference code results (labelled as “RUN1”) in simulating the typical central subchannels (including the case with the thimble) and the other two test sections, referred to the side and corner geometries. Different colours are used to distinguish the four test series. Table 2 provides information about the average absolute errors and the corresponding standard deviations for the various tests, grouped by void fraction ranges and by test series.

The results obtained for the 43 tests with Assembly S1 (TS 1, central subchannel) indicate a systematic underprediction of the void fraction (except at very low and high void fractions). The overall average absolute error on void fraction is -0.021 , while the standard deviation is close to 0.05. The largest errors (about -0.08) are obtained for void fractions between 0.2 and 0.3 and for higher values of inlet coolant temperature and of system pressure (i.e., greater than 10 MPa).

Qualitatively similar results are obtained for Assembly S2 (TS 2, central subchannel with thimble). The same tendency to underprediction of void fraction is shown (except for void fractions below 0.1 and above 0.6). The average error is -0.016 , and the standard deviation is 0.051. Up to void fraction 0.6, the standard deviation increases with the void fraction.

The results obtained for the 40 tests with Assemblies S3 and S4 (TS 3 and 4, side and corner subchannel) show the same tendencies as for the other tests, but with somewhat larger absolute errors (-0.03 and -0.05 , resp.).

TABLE 2: Summary of subchannels results by CATHARE2 code.

Void fraction	TS 1			TS 2			TS 3			TS 4			Overall		
	$\langle \varepsilon[\alpha] \rangle$	$\sigma[\varepsilon]$	Number												
0.0–0.05	0.005	0.0161	6	0.015	0.0092	5	0.013	0.0152	8	-0.004	0.0088	4	0.007	0.0143	23
0.05–0.10	-0.012	0.0244	9	-0.012	0.0264	6	—	—	—	-0.040	0.0132	4	-0.021	0.0251	19
0.10–0.15	-0.042	—	1	-0.040	0.0262	3	-0.002	0.0455	3	—	—	—	-0.028	0.0365	7
0.15–0.20	-0.023	0.0037	3	-0.079	0.0080	4	—	—	—	-0.091	0.0087	2	-0.064	0.0313	9
0.20–0.30	-0.081	0.0384	3	-0.030	0.0533	5	-0.102	—	1	-0.095	0.0200	3	-0.077	0.0485	12
0.30–0.40	-0.038	0.0574	8	-0.057	0.0490	5	-0.043	0.0496	2	-0.056	0.0080	2	-0.048	0.0477	17
0.40–0.60	-0.032	0.0757	7	-0.009	0.0520	10	-0.072	0.0759	4	-0.068	0.0143	3	-0.045	0.0633	24
0.60–0.80	0.007	0.0235	6	0.053	0.0267	5	—	—	—	-0.058	0.0021	2	0.000	0.0446	13
0.80–1.00	—	—	—	—	—	—	-0.107	0.0429	2	—	—	—	-0.107	0.0429	2

The results of the sensitivity calculations (Table 3) are summarized in Table 4 and Figure 3. It appears that the average absolute error can be reduced from the reference results as the boundary conditions varied within the uncertainty of the experimental measurements. In particular, the most accurate prediction is achieved using the minimum mass flow rate as boundary condition. However, the dispersion of the results remains similar to that of the reference calculation and the underestimation of void fraction between 0.2 and 0.6 is only slightly improved.

The sensitivity analysis related to the number of axial meshes (RUNS6 and 7) shows some influence on the axial profile of the void fraction. Mesh convergence is already reached with 38 axial subdivisions, as the void fraction axial profile is very close to the more accurate reference solution (RUN 1). The effect is evidenced in Figure 4, where the void fraction of two tests is plotted as a function of height.

4.2. Posttest Analysis of Steady-State Bundle Tests. The experimental data consists of cross-sectional averages of the void fraction measured at three axial locations (bottom, middle, top) along the tests section height. The average, however, is not performed over the entire cross-section but only over the four central subchannels. This has to be taken into account for a proper comparison between numerical results and experimental data. Therefore, the results from the 3D models (Table 5) are also averaged according to the same procedure for comparison purposes. On the other hand, the results from the 1D models are inherently averaged over the entire cross-section and the comparison with the averaged experimental data would not in principle be appropriate.

The overall database includes 252 steady-state tests, as follows (see Figure 1(b)):

- (i) 73 tests of test series 5—Assembly B5 (no thimble; uniform axial power profile),
- (ii) 74 tests of test series 6—Assembly B6 (no thimble; cosinusoidal axial power profile),
- (iii) 74 tests of test series 7—Assembly B7 (with thimble; cosinusoidal axial power profile),
- (iv) 31 tests of test series 8—Assembly B5 (same as TS 5, i.e., no thimble; uniform axial power profile).

The details of the boundary conditions are reported in Table 1 and [4, 5, 9].

Figure 5 shows a comparison between the results obtained from the 3D model and the measured data, in terms of 4-subchannel cross-sectional averaged void fraction at the three available measurement locations (bottom, centre and top of the test section), for all 73 tests of test series 5 (Assembly B5, with uniform power profile). An annotation in the plot also indicates the absolute accuracy of the experimental data and the absolute error ± 0.1 in terms of void fraction. Such results indicate that the void fraction is generally overpredicted in the 3D simulation. The figure includes the results from the 1D model. The latter are close to the results from 3D model (after averaging over the entire cross-sections), which confirms a consistency between the two models as far as the “integral” performance is concerned. Same qualitative trends, as for TS 5, are observed for the other two test bundles (as described in Figure 1(b)) in Figures 6 and 7 and for the test series 8 using the bundle B5 (Figure 8).

The analysis, based on 252 tests [8], shows generally reasonable (though overestimated) results of the 3D model (Table 5). Limitations are observed in calculating the average void fraction distribution in the central subchannels. According to the results of the test series 5, 6, and 7, the errors are approximately systematic in terms of absolute average void fraction in the range of 0–0.6. In particular, the void fraction is overestimated. For higher values (0.6–0.8), the errors are lower, and, in the case of TS 7, the code void fraction is largely underestimated. These results highlight that the cross flows from the inner towards the outer subchannels of the 3D model are underestimated by the code, until the void fraction is below 0.6.

The test cases with cosine power profile showed higher absolute errors than the uniform axial power profile tests. The code results of TS 8 evidence a good average accuracy. The results are centred across the experimental data and better than those of TS 5. It has to be remarked that TS 5 and TS 8 share the same geometrical configuration, and no difference is reported in the PSBT benchmark specifications. The comparisons with the 1D results highlight that the void fraction, in general, keeps being overestimated in subcooled

TABLE 3: PSBT subchannel tests: list of reference and sensitivity calculations.

Test section	ID	Number of axial nodes	Pressure (1)	Mass flow (1)	Note
Steady-state subchannel	RUN1	100	Nominal	Nominal	Reference
	RUN2	100	Nominal	Minimum	—
	RUN3	100	Nominal	Maximum	—
	RUN4	100	Minimum	Maximum	—
	RUN5	100	Maximum	Nominal	—
	RUN6	38	Nominal	Nominal	—
	RUN7	16	Nominal	Nominal	Effect of pressure drop
	C3	100	Nominal	Nominal	CATHARE3 (2) (same results are RUN1)

(1) Nominal: as specified in [5]. Minimum and maximum: according to the estimated accuracy of the measurement system.

(2) CATHARE3 is the new two-phase thermal-hydraulics system code developed at CEA to expand the capabilities of CATHARE2 (e.g., three field model, and turbulence transport for a continuous field or interfacial area transport for a dispersed field). CATHARE3 was applied against the PSBT data using the standard 6-equation model of CATHARE2. Thus, the task was a verification and a nonregression activity. The results are not reported here for sake of simplicity.

TABLE 4: PSBT subchannel tests, CATHARE2: summary of sensitivity analysis results.

Void fraction	TS 1			TS 2			TS 3			TS 4		
	$\langle \varepsilon[\alpha] \rangle$	$\sigma[\varepsilon]$	Number									
RUN1 (reference)	-0.021	0.0471	43	-0.016	0.0510	43	-0.030	0.0603	20	-0.054	0.0334	20
RUN2	-0.006	0.0489	43	-0.005	0.0493	43	-0.018	0.0617	20	0.044	0.0281	20
RUN3	-0.036	0.0474	43	-0.027	0.0537	43	-0.041	0.0610	20	-0.063	0.0402	20
RUN4	-0.010	0.0434	43	-0.006	0.0472	43	-0.019	0.0577	20	-0.043	0.0279	20
RUN5	-0.032	0.0512	43	-0.029	0.0534	43	-0.040	0.0637	20	-0.063	0.0391	20
RUN6	-0.018	0.0475	43	-0.014	0.0503	43	-0.028	0.0606	20	-0.052	0.0321	20
RUN7	-0.005	0.0500	43	-0.004	0.0488	43	-0.017	0.0622	20	-0.044	0.0276	20

boiling conditions. The activation of the turbulence model improves the accuracy of the results; nevertheless, it should be considered that it has not been developed for such kind of applications [8].

4.3. Posttest Analysis of Transient Bundle Tests. The behaviour of three bundle test sections (i.e., B5, B6, and B7) are simulated in transient conditions (i.e., power increase, pressure decrease, flow decrease, and coolant inlet temperature increase). The analysis deals with 12 transient tests [8] modelled with the 3D and 1D nodalizations (see Section 3). Hereafter the results of three out of twelve tests are reported for sake of simplicity (the overall results are available in [8]). They are (1) a flow reduction test with the bundle B5; (2) the coolant temperature at inlet increase test with the bundle B6; (3) the power increase test with the bundle B7.

The flow reduction test with the bundle B5 is characterized by the following constant boundary conditions: electrical power equal to 2250 kW, system pressure 15.1 MPa, coolant temperature at the inlet 302°C (subcooling 41°C). The experimental and calculated mass flow rate trends are reported in Figures 9(a) and 9(b) that show the time histories of both the calculated and the measured averaged void fractions for the three different measuring locations (as already discussed for the steady-state tests in Section 4.2). During the steady-state period that comes before the flow rate variation (reduction), a noticeable void fraction is predicted by the code at the upper location, while the measured value in the experiment is practically zero. This evidence is consistent with the results

for steady-state tests, which also showed a general tendency to overpredict the void fraction in the central channels. On the other hand, the transient trends are rather well predicted, with a certain tendency to under estimation.

The coolant temperature increase test with the bundle B6 is performed at a system pressure of 15.4 MPa, electrical power equal to 2600 kW, and a constant mass flow rate of 8 kg/s. The coolant temperatures at inlet of the bundle have the trend reported in Figure 10(a), with a subcooling ranging from 49°C to 16°C. Figure 10(b) reports both the calculated and the measured averaged void fractions, for the three different measuring locations. The void fraction predicted at the top and middle locations before the beginning of the temperature rise is above the measured value. The increase in void fraction during the transient is predicted quite in advance and with smoother rates compared to the experiment. This is also connected with the position where the coolant temperature is measured: the thermocouple is upstream the test section. On the contrary, the boundary conditions in the calculation are set just below the fuel bundle. The maximum values of the predicted void fraction are comparable with the measured ones.

The power increase test with the bundle B7 has the following boundary conditions: the system pressure is equal to 15.5 MPa, the coolant temperature inlet is 288°C, corresponding to a subcooling of 57°C, and the mass flow rate is set to 8 kg/s. Figures 11(a) and 11(b) show the time histories of both the calculated and the measured bundle powers and averaged void fractions, for the three different measuring

TABLE 5: PSBT steady-state bundles (TS 5, TS 6, TS 7, TS 8,): summary of reference calculations results by CATHARE2 3D model.

Void fraction	TS 5			TS 6			TS 7			TS 8		
	$\langle \varepsilon[\alpha] \rangle$	$\sigma[\varepsilon]$	Number									
0.0–0.05	0.1003	0.0448	54	0.0931	0.0351	53	0.1031	0.0468	53	0.0469	0.0290	17
0.05–0.10	0.0895	0.0396	21	0.1074	0.0295	21	0.1068	0.0491	21	0.0425	0.0606	3
0.10–0.15	0.1017	0.0644	15	0.1511	0.0785	19	0.1310	0.0718	19	0.0102	0.0514	4
0.15–0.20	0.0801	0.0615	15	0.1408	0.0836	11	0.1323	0.0778	11	0.0392	0.0675	7
0.20–0.30	0.0464	0.0639	26	0.0951	0.0567	21	0.1134	0.0598	21	-0.0333	0.0783	10
0.30–0.40	0.0335	0.0568	27	0.0827	0.0541	33	0.1050	0.0741	33	-0.0344	0.0741	19
0.40–0.60	0.0827	0.0612	48	0.0946	0.0694	47	0.0603	0.0514	47	0.0144	0.0771	25
0.60–0.80	0.0256	0.0388	13	0.0253	0.0555	17	-0.0908	0.0796	17	0.0310	0.0285	8
0.80–1.00	—	—	0	—	—	0	-0.2784	—	0	—	—	0
0.0–1.00 (total)	0.061	0.0599	219	0.091	0.0651	222	0.082	0.0939	222	0.014	0.0675	93

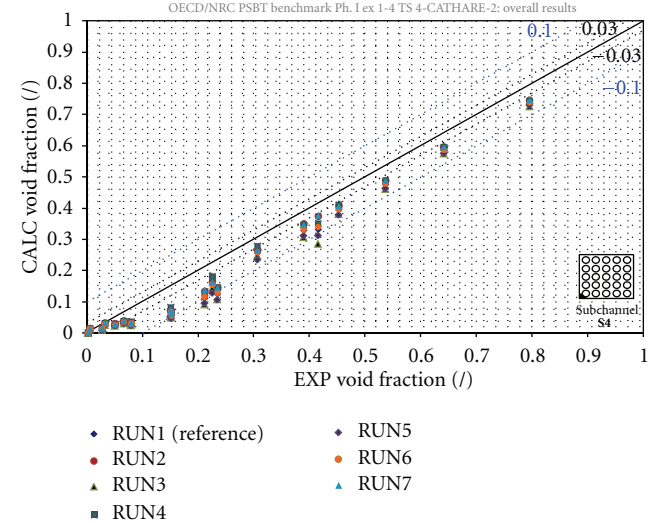
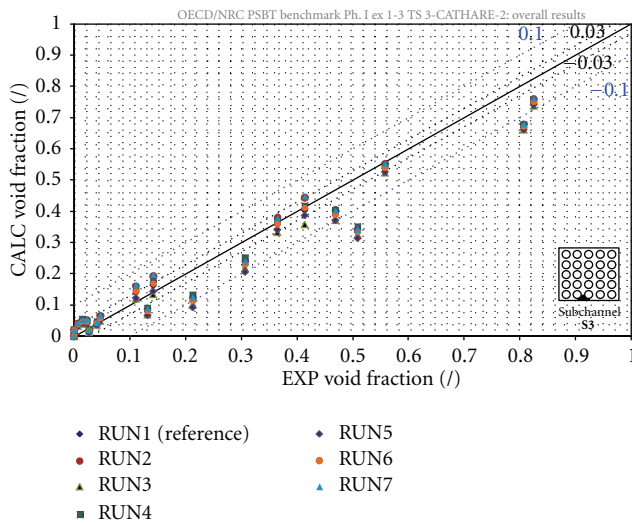
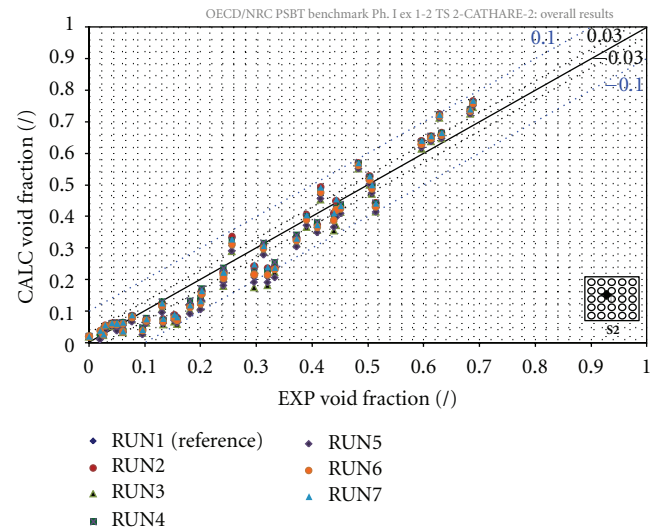
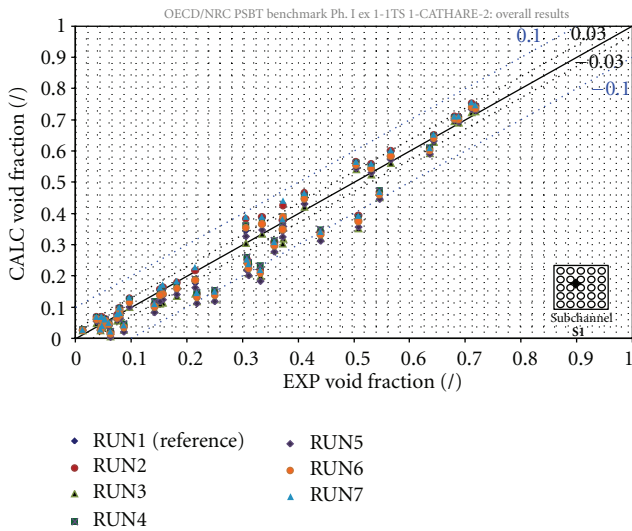
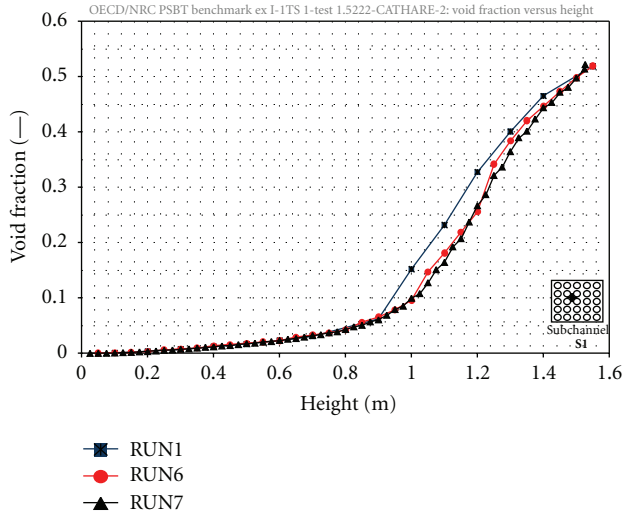
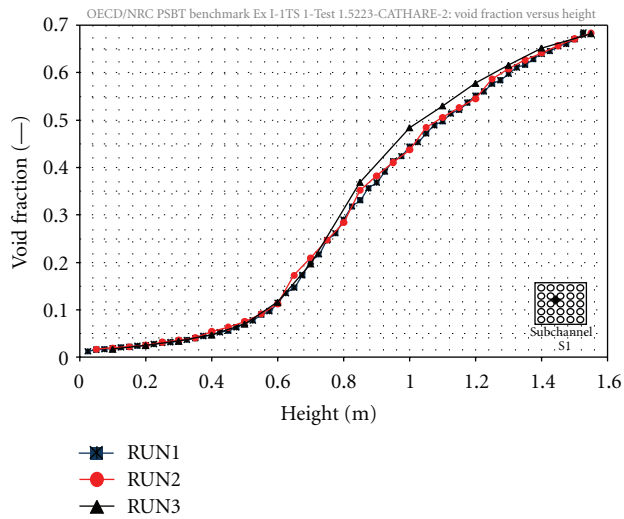


FIGURE 3: Overall subchannels tests (126 tests)—sensitivity calculations.



(a) Test 1.5222



(b) Test 1.5223

FIGURE 4: Test Series 1 (tests 1.5222 and 1.5223)—CATHARE2 code, nodalization effect.

locations. At the top location, the increase in void fraction during the transient is predicted with a certain delay compared to the experiment (except for an earlier “disturbance”); then the calculated void fraction trend stabilizes at the same level as the measured one. On the other hand, the void fraction is noticeably overpredicted at the middle and bottom locations.

In general, the code assessment of CATHARE2 code against the PSBT transient bundle tests demonstrates satisfactory results obtained by the 3D model. In particular,

- (i) a noticeable void fraction is predicted by the code at the upper location (and middle location in the temperature increase test, Figure 10), while the measured value is practically zero. This is consistent with the results observed in the steady-state tests;

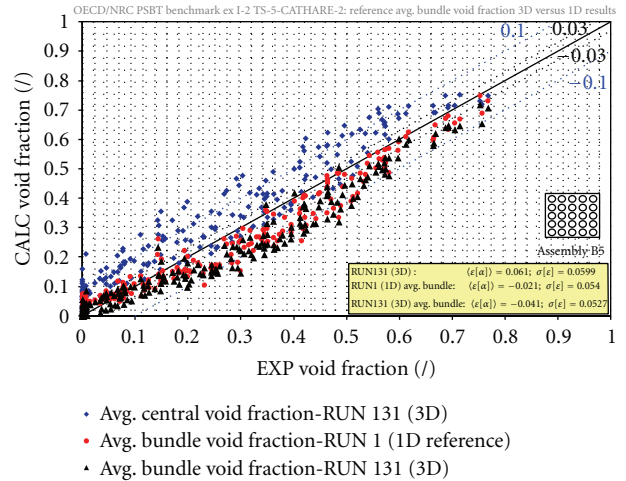


FIGURE 5: PSBT steady-state bundle (TS 5)—CATHARE2 3D and 1D models: central and bundle void fraction exp. versus calc., reference results.

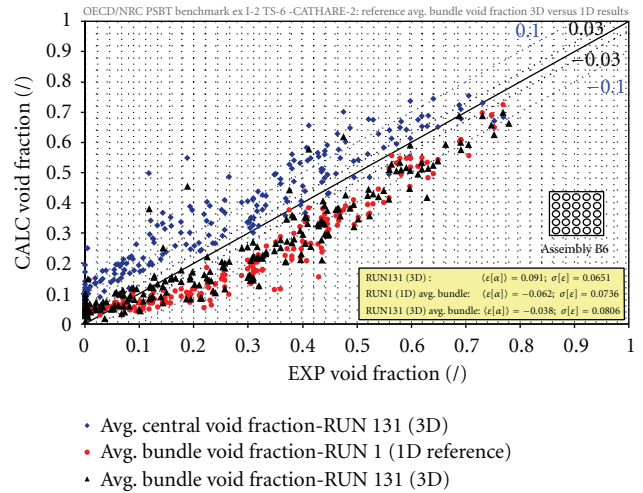


FIGURE 6: PSBT steady-state bundle (TS 6)—CATHARE2 3D and 1D models: central and bundle void fraction exp. versus calc., reference results.

- (ii) good prediction of the maximum void fraction is in general calculated: exceptions are the few disturbances observed at the start of the transients.

5. Conclusive Remarks

This work dealt with the validation of CATHARE2 capabilities in predicting void fraction in convective boiling flows. The validation is performed using the experimental data from NUPEC, also involved in the OECD/NRC PSBT benchmark. Four subchannel and three bundle test sections are simulated in different thermal-hydraulic conditions (i.e., pressure, coolant temperature, mass flow, and power). The overall database includes steady-state and transient tests (i.e., pressure decrease, power increase, coolant inlet temperature increase, and mass flow rate decrease). Sensitivity analyses

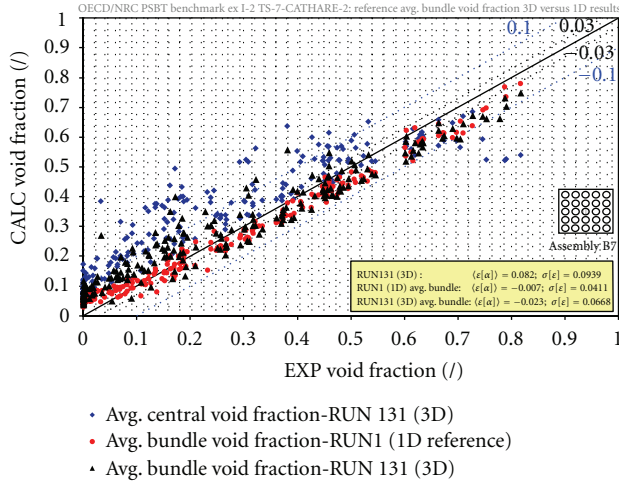


FIGURE 7: PSBT steady-state bundle (TS 7)—CATHARE2 3D and 1D models: central and bundle void fraction exp. versus calc., reference results.

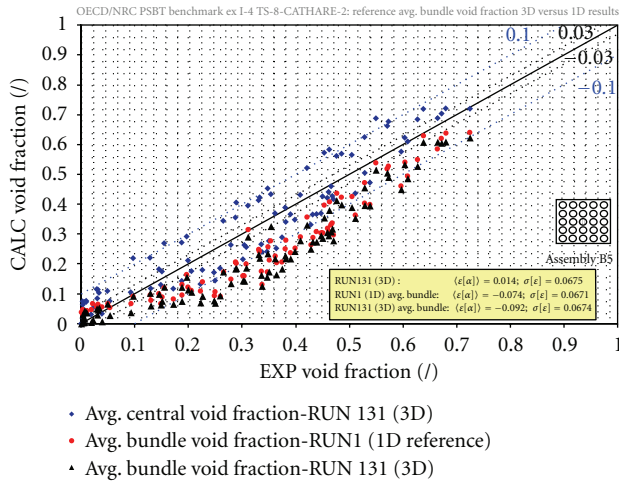
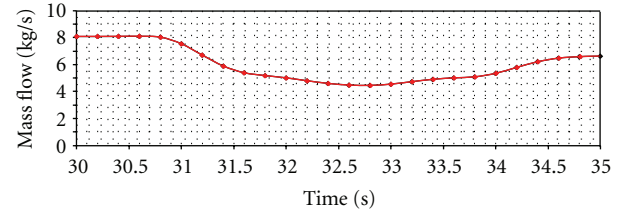


FIGURE 8: PSBT steady-state bundle (TS 8)—CATHARE2 3D and 1D models: central and bundle void fraction exp. versus calc., reference results.

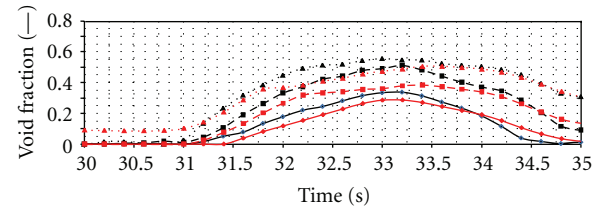
are carried out, which investigate the influence of number of nodes, different code option, initial and boundary conditions of the tests on the code predictions.

The analysis of 126 *steady-state subchannel tests* shows reasonable results for lower values of void fraction; underprediction for intermediate values of void fraction (i.e., 0.2–0.4) and good results for higher values.

- The void fraction is overestimated in subcooled boiling conditions. The opposite is observed in saturated boiling conditions (bubbly, slug, and churn flow regimes).
- The sensitivity analysis demonstrates that the prediction can be improved by varying the boundary conditions of the simulations inside the range of their uncertainty.



(a) mass flow rate versus time



(b) void fraction versus time

FIGURE 9: PSBT transient bundle tests (TS 5)—flow reduction—CATHARE2 3D: calc. versus exp., reference results (RUN131).

- The sensitivities addressing the effect of the number of nodes show the convergence of the mesh for number of nodes larger than 38.

The analysis of 252 *steady-state bundle tests* evidenced conservative (overestimated) results of the 3D model. In particular,

- limitations are observed in calculating the average void fraction distribution in the central subchannels (i.e., void dispersion connected with the cross flow). The errors are approximately systematic in terms of absolute average void fraction in the range of 0–0.6. In particular, the void fraction is overestimated. For higher values (0.6–0.8), the errors are lower, and, in the case of TS 7, the code void fraction is largely underestimated;
- the test cases with cosine power profile showed higher absolute errors than the uniform axial power profile tests;
- the code results of TS 8 evidence a good average accuracy. The results are centred across the experimental data. They are better than those of TS 5, which has the same geometrical configuration;
- the comparisons with the 1D results confirm that the void fraction is, in general, overestimated in subcooled boiling conditions;
- the activation of the turbulence model improves the accuracy results. Nevertheless it should be considered that this option is not developed for such kind of applications.

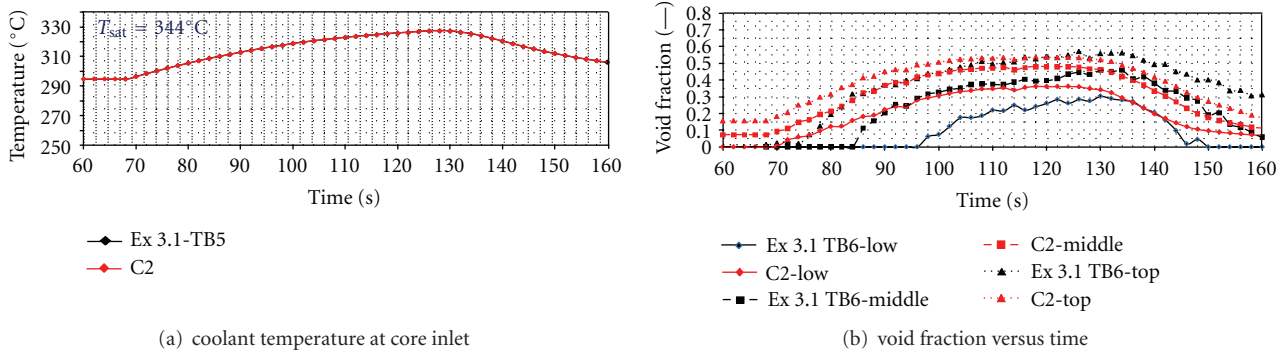


FIGURE 10: PSBT transient bundle tests (TS 6)—temperature increase—CATHARE2 3D: calc. versus exp., reference results (RUN131).

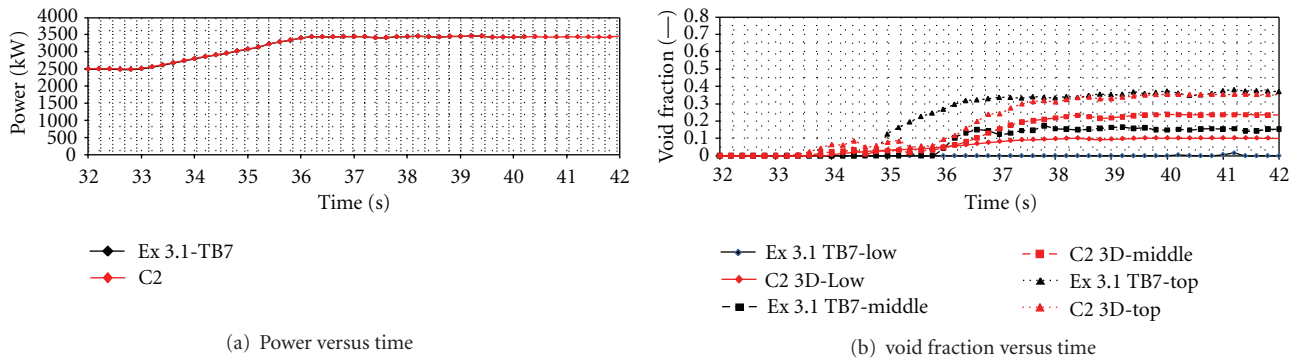


FIGURE 11: PSBT transient bundle tests (TS 7)—power increase—CATHARE2 3D: calc. versus exp., reference results (RUN131).

The analysis of 12 *transient bundle* tests shows satisfactory results of the 3D model. In particular:

- (i) A noticeable void fraction is predicted by the code at the upper location, while the measured value is practically zero. This is consistent with the results observed in the steady-state tests.
- (ii) Good prediction of the maximum void fraction is in general calculated.

Nomenclature

- α : Void fraction
- ε : Average value
- σ : Standard deviation
- 1D: 1 dimensional
- 3D: 3 dimensional
- CATHARE2: Code for analysis of thermal-hydraulics during an accident of reactor and safety evaluation
- CFD: Computational fluid dynamic
- DNB: Departure from nucleate boiling
- ENEA: Agenzia nazionale per le nuove tecnologie, l'energia e lo sviluppo economico sostenibile
- OECD: Organization for Economic Co-operation and Development
- NEA: Nuclear Energy Agency

- NPP: Nuclear power plant
- NRC: Nuclear Regulatory Commission
- NUPEC: Nuclear Power Engineering Corporation
- PSBT: Pressurized water reactor subchannel and bundle tests
- PWR: Pressurized water reactor
- TB: Test bundle
- TS: Test series
- UNIFI: Università di Pisa.

Acknowledgments

The authors would like to acknowledge the OECD Nuclear Energy Agency (NEA) and the NRC that promoted the PSBT benchmark and the CATHARE Team (in particular, M. Vallette and D. Bestion) for the kind and valuable technical support.

References

- [1] B. Niceno, M. Andreani, B. L. Smith et al., “Program of Work for Development and Validation for LOCA,” in *Proceedings of the 7th EURATOM FP, 2008–2012 Collaborative Project: NURISP, SP 2: Thermal Hydraulics, Task D2. 4. 1*, 2009.
- [2] G. Lavalie, *CATHARE2 V2. 5 User Guidelines*, SSTH/LDAS/EM/2004-067, CEA, Grenoble, France, 2005.
- [3] C. Eymard, *CATHARE2 V2. 5 User Manual*, SSTH/LDAS/EM/2004-040, CEA, Grenoble, France, 2005.

- [4] K. Hori, K. Miyazaki, T. Kurosu, S. Sugiyama, J. Matsumoto, and Y. Akiyama, "In bundle void fraction measurement of PWR fuel assembly," in *Proceedings of the 2nd ASME-JSME Nuclear Engineering Joint Conference*, pp. 69–76, March 1993.
- [5] A. Rubin, M. Avramova, and H. Utsuno, "OECD/NRC benchmark based on NUPEC PWR Subchannel and Bundle Tests (PSBT)," in *Proceedings of the International Conference on the Physics of Reactors (PHYSOR '10)*, pp. 2723–2732, May 2010.
- [6] L. Michelotti, A. Del Nevo, D. Rozzia, and F. D'Auria, "Prediction of void fraction in PWR sub-channel by CATHARE 2 Code," in *Proceedings of the International Conference on Acoustics, Speech and Signal Processing (ICAPP '11)*, Nice, France, May 2011, Paper 11396.
- [7] A. Del Nevo, L. Michelotti, D. Rozzia, F. Moretti, and F. D'Auria, "Void fraction prediction of NUPEC PSBT Tests by CATHARE code," in *Proceedings of the NURETH-14*, Ontario, Canada, September 2011, paper 415.
- [8] A. Del Nevo, F. Moretti, D. Rozzia, and F. D'Auria, "Final report on modeling and validation of multi-field models, dynamic interfacial area and turbulence for LOCA conditions," EC FP7 NURISP Project D-2. 4. 2. 10b Rev. 1, 2012.
- [9] JNES, "OECD/NEA Benchmark Based on NUPEC PWR Sub-channel and Bundle Tests (PSBT). Assembly specification and benchmark database (Volume 1)," Japan Nuclear Energy Safety Organization (JNES) SAE-TH08-0019, 2009.

Research Article

Evaluation of ASSERT-PV V3R1 against the PSBT Benchmark

Kenneth H. Leung and David R. Novog

Department of Engineering Physics, McMaster University, 1280 Main Street West, Hamilton, ON, Canada L8S 4L7

Correspondence should be addressed to Kenneth H. Leung, leungk4@mcmaster.ca

Received 7 July 2012; Accepted 18 September 2012

Academic Editor: Alessandro Petruzzi

Copyright © 2012 K. H. Leung and D. R. Novog. This is an open access article distributed under the Creative Commons Attribution License, which permits unrestricted use, distribution, and reproduction in any medium, provided the original work is properly cited.

Void fraction and DNB calculations conducted using ASSERT-PV V3R1 are evaluated against data from the NUPEC database as part of the OECD/NEA Pressurized Water Reactor Subchannel Benchmark Tests (PSBT). Void fraction measurements were well represented in the isolated single subchannel cases, with 77.0% of all predicted values falling within $\pm 2\sigma_{\text{exp}} = 0.06$ of the experimental value. In the B5 type bundle, an average void fraction error of $\bar{\epsilon}_\alpha = -0.0540$ was reported at the lower elevation, while this value was $\bar{\epsilon}_\alpha = -0.0405$ at the upper measurement location. ASSERT was able to predict the steady state DNB power of the bundles to within $\pm 10\%$ of the measured value for a total of 344 times out of 432. Sensitivity studies conducted indicate that the Ahmad correlation with the Groeneveld 1995 CHF lookup table yielded the most accurate results, although some data points fell within the limiting quality region where the accuracy was reduced.

1. Introduction

The prediction of both the void fraction distribution in a rod bundle and the power at which the departure from nucleate boiling (DNB) occurs is an ongoing area of study in the field of thermalhydraulics. To that end, data from tests conducted by the Japanese NUPEC corporation have been released to the international community as part of a benchmark sponsored by the Organization of Economic Cooperation and Development's Nuclear Energy Agency (OECD/NEA). The overarching objective of the Pressurized Water Reactor (PWR) Subchannel Bundle Tests (PSBT) is to assess the current capabilities of both subchannel and Computational Fluid Dynamics (CFD) codes in predicting the void fraction and DNB powers under both steady state and transient conditions [1].

In this study, the Advanced Solution of Subchannel Equations in Reactor Thermalhydraulics (ASSERT) code is evaluated against the benchmark database. ASSERT-PV is a Canadian code developed and maintained by Atomic Energy of Canada Limited (AECL) in support of activities involving fuel design and safety analysis in the Canadian nuclear industry. This code models the behavior of the coolant at the subchannel level and specializes in representing conditions

found in Pressurized Heavy Water Reactors (PHWR). Subchannel codes can represent the fluid conditions at a higher spatial resolution than is typically found in system codes, and utilize empirical relationships developed to model phenomena which occur specifically in rod bundle geometries. However, effects such as inter-subchannel turbulent mixing and DNB are not yet fully understood, and so comparisons of code predictions to datasets are part of an ongoing effort to improve the accuracy of the codes.

2. Facility

The facility used for these experiments was designed to represent conditions which would be found in a typical PWR, and key characteristics are listed in Table 1. Two types of experiments are simulated in this study: isolated single subchannel experiments and rod bundle experiments.

2.1. Subchannel Test Sections. The single subchannel experiments consisted of test sections with cross-sectional shapes identical to what would be found in a bundle. Four geometries were examined corresponding to a typical, thimble, side, and corner subchannel, and these are illustrated in Figure 1. Each test section was 1.4 m in length, and electrically heated

TABLE 1: Summary of facility [1].

Parameter	Range
Pressure (MPa)	4.9–16.6
Mass flux (Mg/m ² s)	0.55–4.15
Inlet temperature (°C)	140.0–345.0

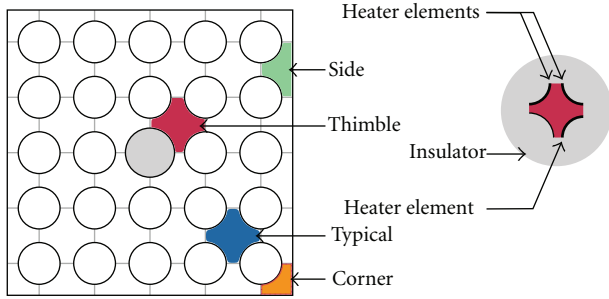


FIGURE 1: Isolated subchannel geometry types (left) and cross-section of the central type test section (right) [1].

along the walls corresponding to where the surface of a rod would be located. The fluid density was measured at the top of test section using gamma densitometry, and the void fraction was deduced from this value.

2.2. Test Bundles. The bundle experiments were conducted using 5×5 and 6×6 arrays of electrically heated rods in several different configurations as listed in Table 2. The bundles are designed to represent a portion of a full height (3658 mm) 17×17 PWR assembly and are supported by mixing vanes and spacer grids. Each rod consisted of an inconel 600 heater surrounding an insulator made of alumina. Gamma densitometry was used to measure the void fraction at three elevations: 2216, 2669, and 3177 mm above the start of the heated section, while the DNB point was determined by monitoring the surface temperature of the rods using thermocouples.

Each of the bundle configurations used different radial and axial power profiles and had a different number of mixing vanes and spacer grids. The void fraction tests were conducted on bundle configurations B5, B6, and B7 while the DNB tests were conducted on bundles A0, A2, A3, A4, A8, A11, and A12. Bundle A1 was used for the subchannel fluid temperature distribution tests. In some cases, the same bundle arrangement was used in both the void fraction and DNB tests, and this is indicated in Table 2 with some configurations having multiple names.

In the void fraction and DNB tests, the rods on the periphery of the bundle were operated at a lower power than those in the central portion of the bundle as illustrated in Figure 2. In several configurations (B7, A8, and A12) the central rod in the bundle was replaced by an unheated thimble rod. In the fluid temperature tests, an asymmetric power distribution was used.

A series of transient tests were also run using these bundles, simulating scenarios involving a power increase, system

depressurization, flow rate reduction, and inlet temperature increase.

3. Code Description

ASSERT is an unequal-velocity unequal-temperature (UVUT) code which solves a set of equations governing the conservation of mass, momentum, and energy. The code utilizes a drift-flux model to represent the relative velocities between the liquid and vapour phases, while a set of closure relationships are used to represent the phenomena such as friction, heat transfer, and turbulent mixing.

3.1. Constitutive Equations. The equations governing the conservation and transport of mass, axial and lateral momentum, and mixture enthalpy are listed in (1), (2), (3), and (4). Although only the equation governing the mixture enthalpy is supplied in (4), the liquid and vapour enthalpies are solved similarly. The drift velocity in the axial direction is supplied in (5), with the relative vapour velocity being defined in a similar manner.

$$A\Delta x \frac{\partial \rho}{\partial t} + A\Delta x \frac{\partial}{\partial x}(\rho u) + \sum_k W_k = 0, \quad (1)$$

$$\begin{aligned} A\Delta x \frac{\partial}{\partial t}(\rho u) + A\Delta x \frac{\partial}{\partial x}(\rho_f u_f u_f + \rho_g u_g u_g) \\ = -A\Delta x \frac{\partial p}{\partial x} - \sum_k [(W_f u_f + W_g u_g)]_k \\ + \sum_k (W'_f \Delta u_f + W'_g \Delta u_g)_k \\ - F_{\text{frict}} + \rho A \Delta x g_x, \end{aligned} \quad (2)$$

$$\begin{aligned} A\Delta x \frac{\partial}{\partial t}(\rho v) + A\Delta x \frac{\partial}{\partial x}(\rho uv) - v A \Delta x \frac{\partial}{\partial x}(\rho u) \\ = -A\Delta x \frac{\partial p}{\partial y} - F_{\text{frict}} \\ + \frac{\partial}{\partial x} \left(A\Delta x \frac{w'_f \Delta u_f + w'_g \Delta u_g}{S \Delta x} \right) \\ + \rho A \Delta x g_y, \end{aligned} \quad (3)$$

$$\begin{aligned} \Delta x A \rho \frac{\partial h}{\partial t} + \Delta x A \frac{(\rho_f u_f h_f + \rho_g u_g h_g)}{\Delta x} \\ - \Delta x A h \left(\frac{\partial \rho_f u_f}{\partial x} + \frac{\partial \rho_g u_g}{\partial x} \right) \\ + \sum_k [(W_f h_f) + (W_g h_g)]_k - h \sum_k (W)_k \\ - \sum_k [(W'_f \Delta h_f + W'_g \Delta h_g)]_k - q = 0, \end{aligned} \quad (4)$$

$$u_r = u_g - u_f,$$

$$u_f = u - \frac{(\alpha \rho)_g}{\rho} u_r, \quad (5)$$

$$u_g = u + \frac{(\alpha \rho)_f}{\rho} u_r.$$

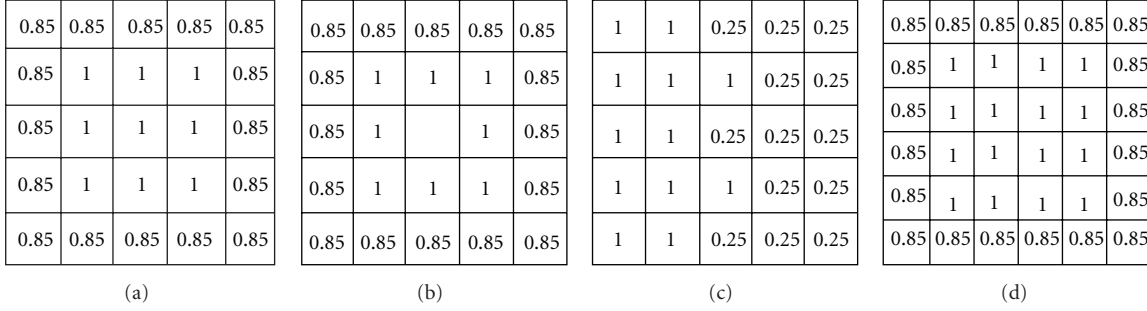


FIGURE 2: Radial power profiles used in the experiments [1].

TABLE 2: Bundle parameters [1].

Parameter	B5, B8, A2	B6, A4, A11	B7, A8, A12	A0	A3	A1
Configuration	5 × 5	5 × 5	5 × 5	5 × 5	6 × 6	5 × 5
Heated rods	25	25	24	25	36	25
Thimble rods	0	0	1	0	0	0
Rod diameter (mm)	9.5	9.5	9.5	9.5	9.5	9.5
Thimble diam (mm)	—	—	12.24	—	—	—
Rod pitch (mm)	12.6	12.6	12.6	12.6	12.6	12.6
Heated length (mm)	3658	3658	3658	3658	3658	3658
Radial power profile	A	A	B	A	D	C
Axial power shape	Uniform	Cosine	Cosine	Uniform	Uniform	Uniform
Number of MVs	7	7	7	5	7	7
Number of NMVs	2	2	2	2	2	2
Number of Ss	8	8	8	6	8	8

3.2. Friction. The turbulent wall friction factor is represented in ASSERT using an implicit approximation to Colebrook-White which is shown in (6). This correlation is valid up until the onset of significant void (OSV), beyond which a two-phase multiplier is applied to represent the additional pressure drop caused by the presence of the vapour. In this study the Friedel correlation (7) was selected for its applicability to the range of conditions being simulated. One has

$$f = \left[-2 \log \left(\frac{\delta d_{\text{hyd}}}{3.7} + \frac{2.51}{\text{Re} \sqrt{f}} \right) \right]^{-2}, \quad (6)$$

$$\Phi_2 = A_1 + \frac{3.24 A_2 A_3}{\text{Fr}^{0.0454} \text{We}^{0.035}},$$

$$A_1 = (1 - X)^2 + X^2 \left(\frac{\rho_f f_{g,\text{only}}}{\rho_g f_{f,\text{only}}} \right), \quad (7)$$

$$A_2 = X^{0.78} (1 - X)^{0.224},$$

$$A_3 = \left(\frac{\rho_f}{\rho_g} \right)^{0.91} \left(\frac{\mu_g}{\mu_l} \right)^{0.19} \left(1 - \frac{\mu_g}{\mu_l} \right)^{0.7}.$$

3.3. Heat Transfer. ASSERT distributes the heat from the rods to either the fluid, vapour, or bubble nucleation. Under single-phase conditions, the heat transfer between the wall

and the fluid is governed by the Dittus-Boelter correlation in (8) for a fluid subjected to heating.

$$H_{\text{Dittus}} = \frac{K_f}{d_{\text{hyd}}} 0.023 \text{Re}^{4/5} \text{Pr}^{2/5}. \quad (8)$$

As the fluid is heated towards its saturation temperature, vapour bubbles will begin to nucleate on the rod walls and ASSERT switches to the Ahmad correlation to represent the two-phase heat transfer. The assumption is that the heat flux from the wall goes either into raising the bulk fluid temperature or creating bubbles [2]. The Ahmad correlation was selected since it covered the widest range of pressures, although it should be noted that the some of the cases in the PSBT database exceed the recommended pressure and mass flux conditions of

$$H_{\text{Ahmad}} = 2.44 \frac{K_f}{d_{\text{hyd}}} \text{Re}^{1/2} \text{Pr}^{1/3} \left(\frac{h_{\text{inlet}}}{h_f} \right)^{1/3} \left(\frac{h_{fg}}{h_f} \right)^{1/3}. \quad (9)$$

This correlation is activated when the bulk fluid temperature in the node is beyond the onset of significant void (OSV) point given by

$$(T_{\text{sat}} - T_f)_{\text{OSV}} = \frac{q''}{H_{\text{Ahmad}}}. \quad (10)$$

3.3.1. Departure from Nucleate Boiling. At the end of each iteration, each node in ASSERT is checked to determine

the margin remaining to the critical heat flux (CHF). The value for the CHF is ascertained by checking the mass flux, pressure, and quality at each node against the 1995 CHF lookup table by Groeneveld et al. [3]. This lookup table was created using data for 8 mm tubes, and so correction factors accounting for the subchannel hydraulic diameter ($F_{CHF,size}$) and the rod to rod gap distance ($F_{CHF,gap}$) are applied. The term K_X in (13) is a quality correction factor built into $F_{CHF,gap}$. One has

$$q''_{CHF,table} = f(G, P, X_{th}), \quad (11)$$

$$q''_{CHF,corrected} = \min(F_{CHF,gap}, F_{CHF,size}) (q''_{CHF,table}), \quad (12)$$

$$F_{CHF,gap} = [1 - 0.25(1 - K_X)] \min\left(1, 0.2 + 9 \frac{S}{d_{rod}}\right), \quad (13)$$

$$F_{CHF,size} = \left(\frac{d_{hyd}}{0.008}\right)^{-1/3}. \quad (14)$$

3.4. Lateral Mixing. Lateral cross-flows are modelled empirically using the method described by Carlucci et al., which splits the mixing into a homogeneous component which is applied to both the liquid and vapour phases, and an incremental component which only affects the vapour [4]. The homogeneous component is based on the mixing rate per unit length relationship reported by Rogers and Tahir and is presented in (15) as a function of the homogeneous viscosity in (16) [4]. The incremental component for each phase was estimated using the least square that fits to experimental data as shown in (17) and (18), where $\Delta w_{l,2\phi}$ and $\Delta w_{g,2\phi}$ are fitting factors as a function of void fraction [4]. Adjustment factors ($F_{mix,obs}$ and $F_{mix,gap}$) are used to account for mixing contributions stemming from obstructions in the flow or changes in the gap size, while $F_{mix,G,p}$ fits the terms as a function of mass flux and pressure [4]. One has

$$w_{hom} = \left[\mu_{hom} a_w \left(\frac{d_{gap}}{d}\right)^{b_w} \left(\frac{G d_{hyd}}{\mu_{hom}}\right)^{0.9} \right]_{hom}, \quad (15)$$

$$\mu_{hom} = \left(\frac{x}{\mu_g} + \frac{1-x}{\mu_l}\right)^{-1}, \quad (16)$$

$$w_l = w_{l,hom} + w_{l,inc},$$

$$w_{l,hom} = F_{mix,obs} (1-x) w_{hom}, \quad (17)$$

$$w_{l,inc} = \frac{F_{mix,G,p} F_{mix,gap}}{F_{mix,obs}} \Delta w_{l,2\phi},$$

$$w_g = w_{g,hom} + w_{g,inc},$$

$$w_{g,hom} = F_{mix,obs} x w_{hom}, \quad (18)$$

$$w_{g,inc} = \frac{F_{mix,G,p} F_{mix,gap}}{F_{mix,obs}} \Delta w_{g,2\phi}.$$

3.5. Nodalization. Each subchannel was represented with 70 nodes in the axial direction. A pressure boundary condition was defined at the inlet while a mass flux boundary was

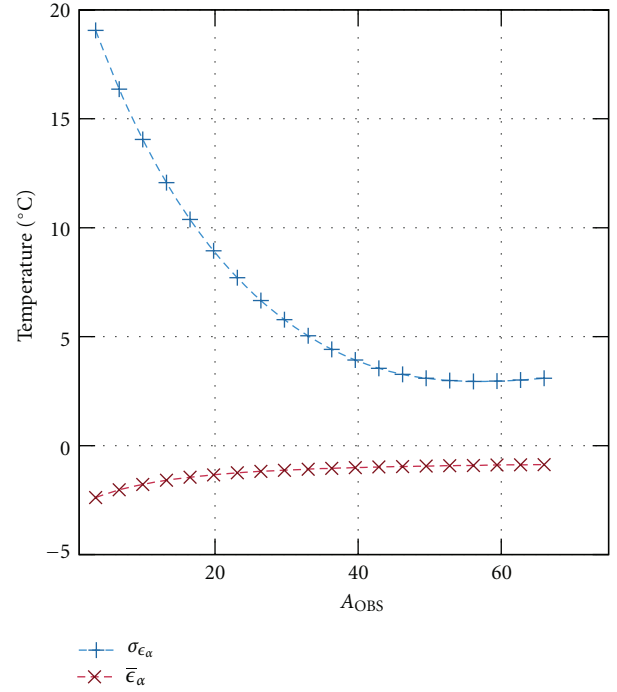


FIGURE 3: Average and standard deviation of the error in fluid temperature as the magnitude of the obstruction mixing coefficient is increased.

imposed at the outlet. Channel walls surrounding the bundle were assumed to be adiabatic. Each of the heated rods was represented by collapsing the thermal conductivity, density, and specific heat capacity of the inconel and alumina into one effective value.

3.6. Mixing Vane Representation. In the Carlucci method, when the flow encounters an obstruction, it is assumed that the mixing rate is enhanced by a factor of $F_{mix,obs}$. The magnitude of the enhancement factor is a product of a fitting coefficient, A_{OBS} ; and the loss or k -factor of the obstruction. As the flow moves downstream from the obstruction (z_{obs}), the magnitude of the multiplier is reduced as a function of the decay coefficient B_{OBS} .

$$F_{mix,obs} = \left(1 + A_{OBS}(k) \left(\exp\left[-B_{OBS} \frac{z_{obs}}{d_{hyd}}\right]\right)\right). \quad (19)$$

The ASSERT code is primarily used to model PHWR fuel channels which, unlike LWRs, do not contain mixing vanes. Since the mixing in the current benchmark is anticipated to be much stronger than in PHWR bundles, the default values for A_{OBS} and B_{OBS} are expected to underrepresent the effects of the vane type obstructions. However the exact geometry of the vane type grids were not released, and so a study on the magnitude of the mixing effects was conducted in order to establish the appropriate values for the lateral momentum source term.

In order to develop a reasonable representation of the lateral flows in the bundle occurring due to obstructions, the mixing vanes and spacer grids were modelled in a manner

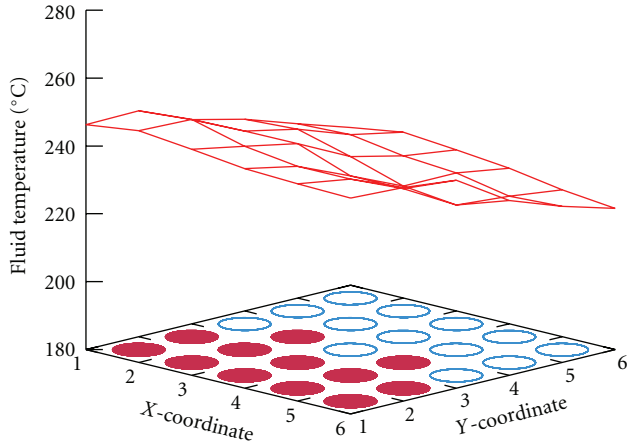
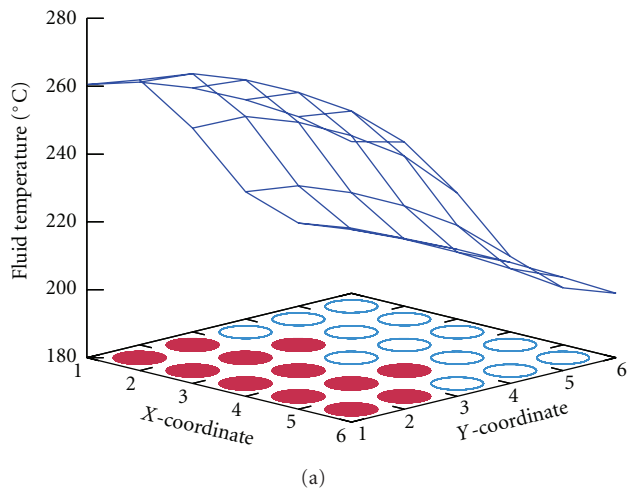
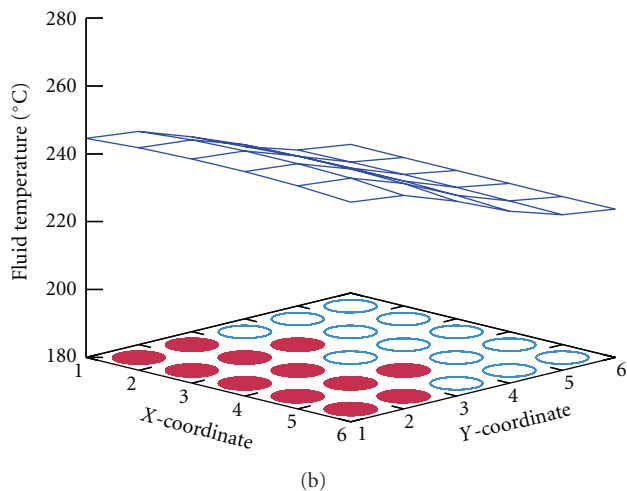


FIGURE 4: Measured outlet fluid temperature for Case 01-3233. Shaded rods operate at 4 times the power of the unshaded rods.



(a)



(b)

FIGURE 5: Predicted outlet fluid temperature for Case 01-3233 with $A_{OBS} = 3.3$ (a) and $A_{OBS} = 49.5$ (b). Shaded rods operate at 4 times the power of the unshaded rods.

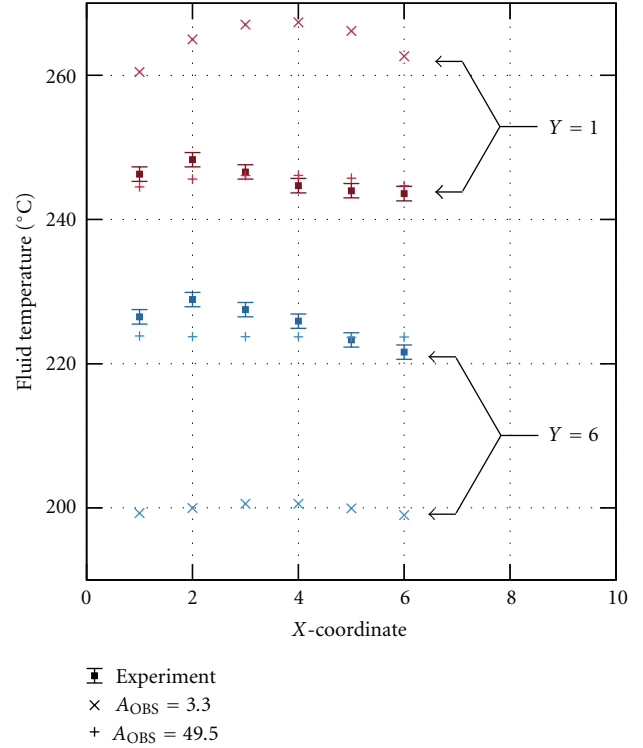


FIGURE 6: Outlet fluid temperatures along the hot side ($Y = 1$) and cold side ($Y = 6$) of the bundle for case 01-3233.

similar to that described by [5]. The method assumes that the k -factor for each obstruction consists of a geometric and a frictional component, with both being functions of the blockage area χ . Each feature of the grid or vane is projected onto a plane perpendicular to the axial flow. Based on these projections, an effective blockage area and effective wetted perimeter were derived for each subchannel in the bundle. Idelchik's formula for losses from a sharp-edged orifice was then used to derive k -factors [6]. The derived values for each subchannel for the mixing vanes and spacer grids are provided in Tables 3 and 4 and are based on the approximate dimensions supplied by [1]. The reported values indicate that while the simple spacer may be regarded as a symmetric object, the mixing vane contains a degree of asymmetry to it.

$$k = k_{\text{geom}} + k_{\text{friction}},$$

$$\chi = \frac{A_{\text{block}}}{A_{\text{up}}},$$

$$k_{\text{geom}} = \left(\frac{\sqrt{0.5\chi + \chi}}{1 - \chi} \right)^2, \quad (20)$$

$$k_{\text{friction}} = \frac{fLP_{\text{up}}}{4A_{\text{up}}} \left[\frac{P_{\text{block}}}{P_{\text{up}}} \left(\frac{1}{\chi} \right)^3 - 1 \right].$$

The value for the decay coefficient B_{OBS} is by default set to $B_{OBS} = 0.013$ which causes the mixing enhancement due to obstructions to be reduced to 50% of the peak value

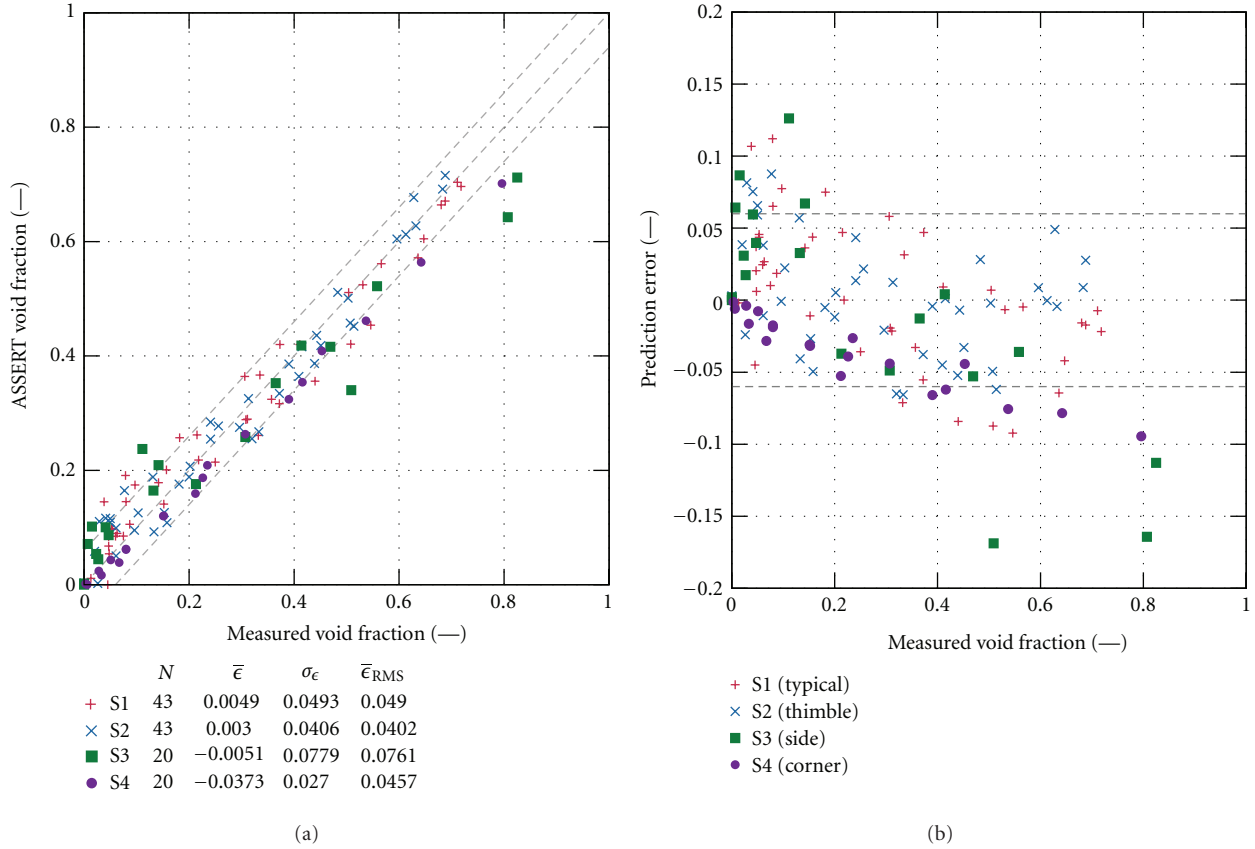


FIGURE 7: Code accuracy in predicting void fraction in a single isolated subchannel. Predicted versus measured results (a) and error versus measured void fraction (b). Error bands displayed correspond to $2\sigma = 0.06$.

TABLE 3: k -factors for the simple spacer.

0.410	0.326	0.326	0.326	0.326	0.410
0.326	0.236	0.236	0.236	0.236	0.326
0.326	0.236	0.236	0.236	0.236	0.326
0.326	0.236	0.236	0.236	0.236	0.326
0.326	0.236	0.236	0.236	0.236	0.326
0.410	0.326	0.326	0.326	0.326	0.410

TABLE 4: k -factors for the mixing vane.

0.534	0.915	0.915	0.915	0.915	1.200
0.915	0.942	0.942	0.942	0.942	0.921
0.915	0.942	0.942	0.942	0.942	0.921
0.915	0.942	0.942	0.942	0.942	0.921
0.915	0.942	0.942	0.942	0.942	0.921
1.200	0.915	0.915	0.915	0.915	0.568

after approximately 9 hydraulic diameters downstream from the blockage. This value is derived for PHWR type fuel channels since the appendages encountered by the flows are typically less disruptive than what would be characteristic of a mixing vane. While the exact geometry of the vanes was not released for proprietary reasons, literature demonstrates

that in experiments with similar split vane type spacers, the mixing enhancement is reduced to 50% of the initial value after travelling about $20 d_{\text{hyd}}$ downstream from the obstruction [7]. The decay coefficient is therefore set to $B_{\text{OBS}} = 0.033$ in order to reflect this PWR type obstruction behaviour.

The derivation of an appropriate value for A_{OBS} comes from the examination of a single case from the fluid temperature distribution tests of series A1. The experimental conditions of this test are summarized in Table 5, and are set so that the fluid is in single phase at the outlet. As illustrated in Figure 1, 12 of the 25 rods are heated with 4 times more power than the others. Using the default value for the mixing magnitude coefficient, $A_{\text{OBS}} = 3.3$, the initial results illustrated in Figures 5 and 6 indicate that the subchannels on the “hot” side of the bundle are at significantly a higher temperature while those on the “cold” side are substantially cooler than what was observed in the experiment. Quantitatively, this is represented by a bundle averaged temperature error of $\bar{\epsilon} = -2.38^\circ\text{C}$ with a standard deviation of $\sigma_{\epsilon} = 19.06^\circ\text{C}$ and is consistent with what would be expected if the lateral momentum source term was underpredicting what was occurring in the experiment.

Increasing the value of A_{OBS} enhances the magnitude of the mixing, and as illustrated in Figure 3, significantly reduces the standard deviation of the error. For the mixing

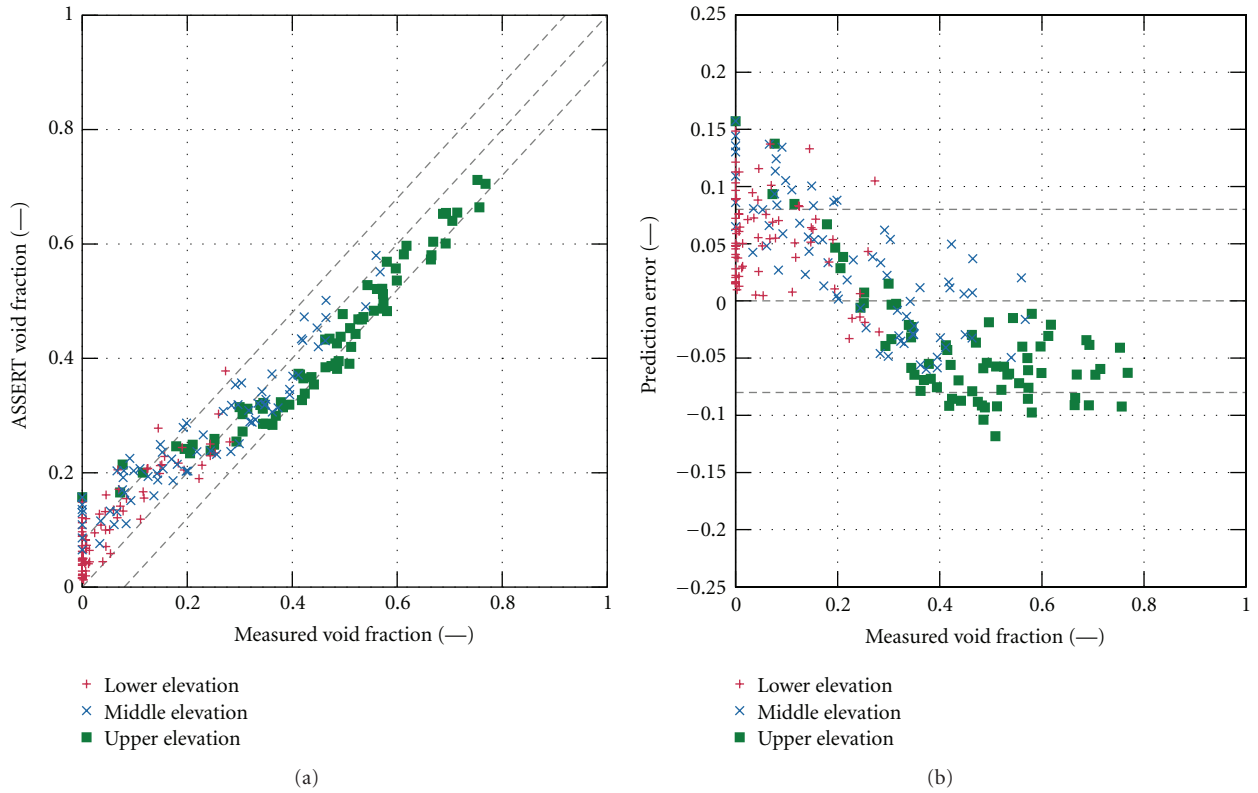


FIGURE 8: Steady state void fraction results for bundle test series B5. Error bands displayed correspond to $2\sigma_{exp} = 0.08$.

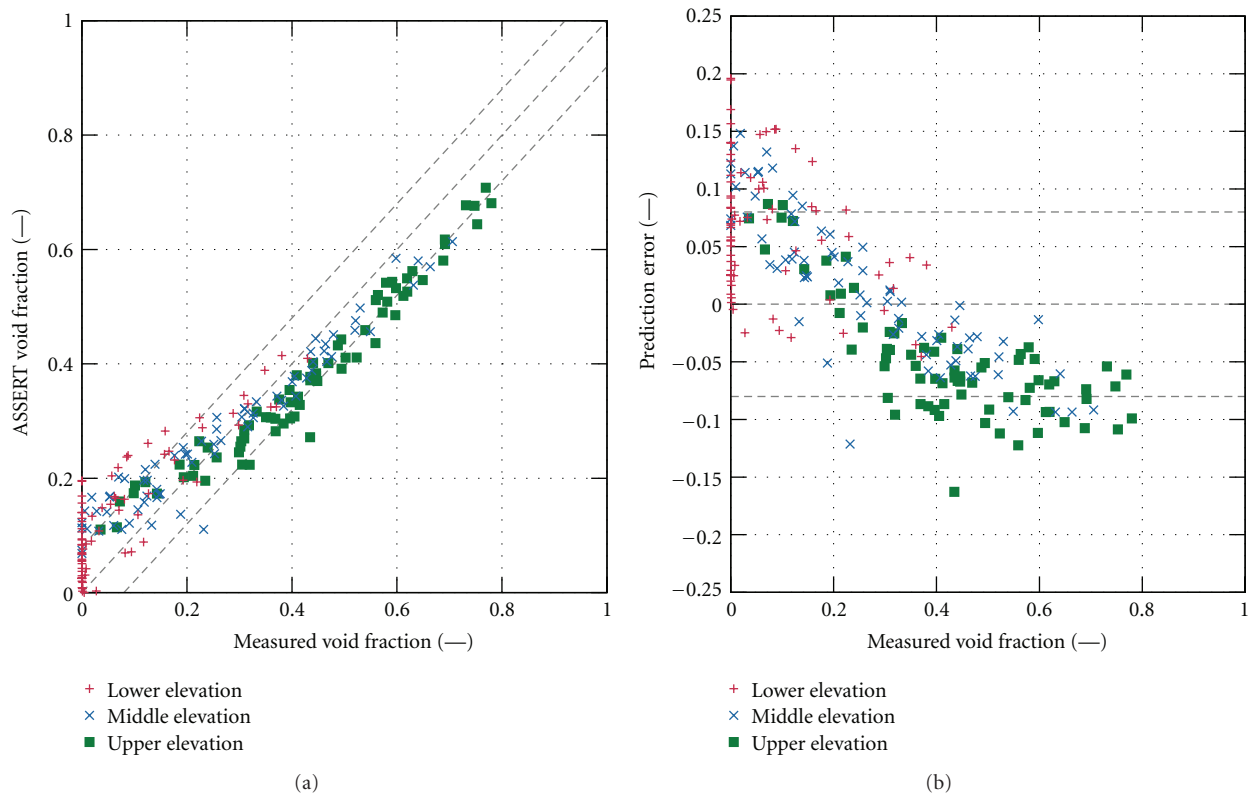


FIGURE 9: Steady state void fraction results for bundle test series B6. Error bands displayed correspond to $2\sigma_{exp} = 0.08$.

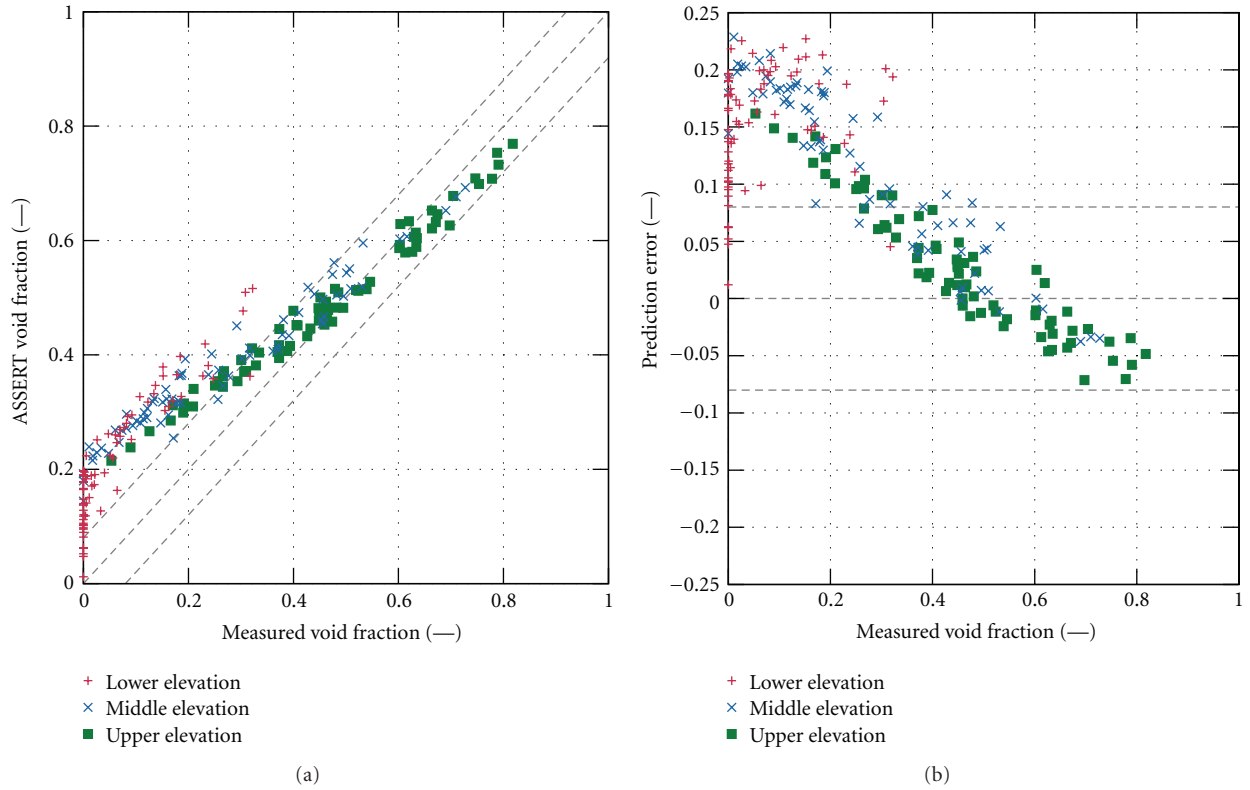


FIGURE 10: Steady state void fraction results for bundle test series B7. Error bands displayed correspond to $2\sigma_{exp} = 0.08$.

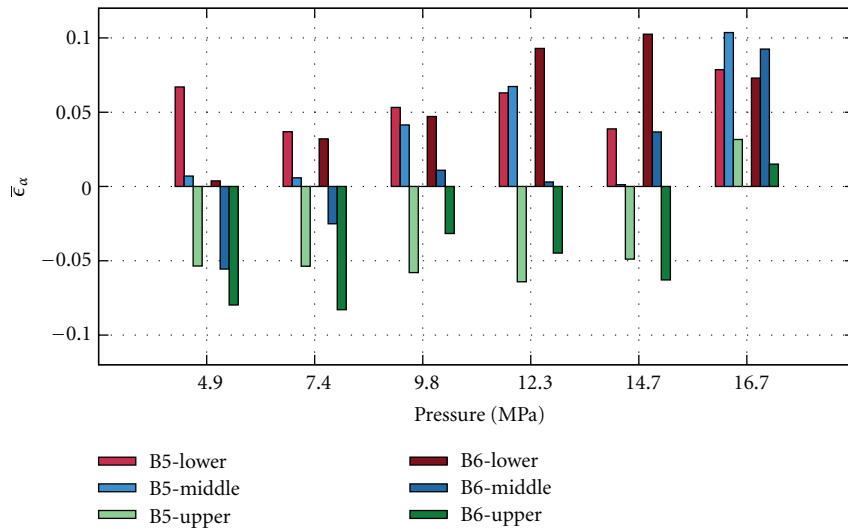


FIGURE 11: Steady state void fraction error for bundles B5 and B6 arranged by system pressure.

vanes used in the current benchmark, σ_ϵ has a minimum value at $A_{OBS} = 49.5$. Figure 5 illustrates the outlet fluid temperature predicted by ASSERT using the increased mixing and shows good qualitative agreement with the experimental results in Figure 4. The minor improvement in the bundle

averaged error is an artifact stemming from fact that the bundle average was taken by summing the temperature of each of the subchannels and dividing by the number of subchannels, rather than weighting each by the mass flow rate. At $A_{OBS} = 49.5$, the bundle averaged error was

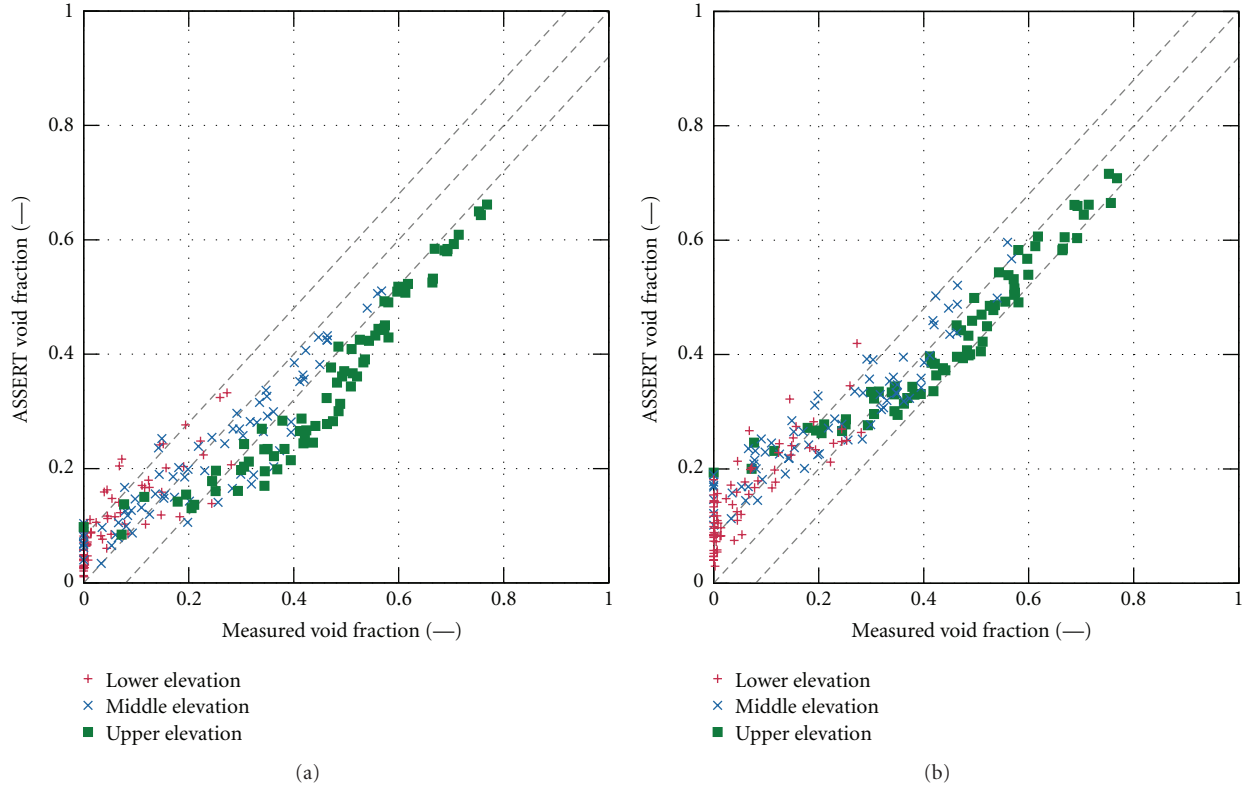


FIGURE 12: Steady state void fraction results for bundle B5 using the Chen (a) and Lahey (b) two-phase heat transfer correlations. Error bands displayed correspond to $2\sigma_{\text{exp}} = 0.08$.

TABLE 5: Test conditions for case 01-3233.

Parameter	Value
Pressure (MPa)	9.81
Mass flux ($\text{Mg}/\text{m}^2\text{s}$)	1.28
Temperature ($^{\circ}\text{C}$)	166.1
Bundle power (MW)	0.98

$\bar{\epsilon} = -0.91^{\circ}\text{C}$ and is within the bounds of the uncertainty of the temperature measurements, which was estimated to be $\pm 1^{\circ}\text{C}$.

4. Results

In this section, a comparison of the ASSERT predictions to the PSBT experimental data is conducted for both the void fraction and the DNB tests. Additionally, sensitivity studies were performed in order to determine the effects of correlation selection.

4.1. Void Fraction. The steady state void fraction portion of the benchmark is divided into two portions: an “isolated subchannel” portion, and a “bundle” portion. In addition, a transient bundle set of data was also run by the participants. The experimental uncertainty in the void fraction has been discussed in depth during the benchmark meetings and is well summarized by [8].

4.1.1. Steady State Single Subchannel. A total of 126 cases using the single subchannel were assessed against experimental data. Table 6 indicates that about 77.0% of all simulated void fractions fell within $\pm 2\sigma_{\text{exp}}$ of the measured value. However the code exhibits a slight tendency to overpredict at low void fractions, while underpredicting at higher values as illustrated in Figure 7. This trend is particularly evident in the S3 and S4 series of tests which represented the side and corner subchannel geometries. Using $\epsilon_{\alpha} = \alpha_{\text{ASSERT}} - \alpha_{\text{exp}}$ as the definition for the code error, the average error ($\bar{\epsilon}_{\alpha}$) for the S3 series of tests was found to be -0.0051 while the root mean square error ($\bar{\epsilon}_{\text{RMS}}$) was 0.0761—which is almost twice that of the other geometries. Several outliers contribute significantly to this at higher void fractions, where in some cases ASSERT underpredicts the measured value by more than 0.15. The ASSERT underprediction for these specific test cases is however consistent with the results reported by other codes and may be an artifact of the measurement process [8, 9].

4.1.2. Steady State Bundle. The steady state bundle results are found in Figures 8, 9, and 10 with a statistical breakdown of the predictions in Table 7. The reported values for both the experimental and simulated void fractions represent the average over the 4 subchannels surrounding the center rod of the bundle. The results for bundles B5 and B6 are similar with the average void error differing by approximately 0.01 at each of the measurement elevations. This is not a surprising

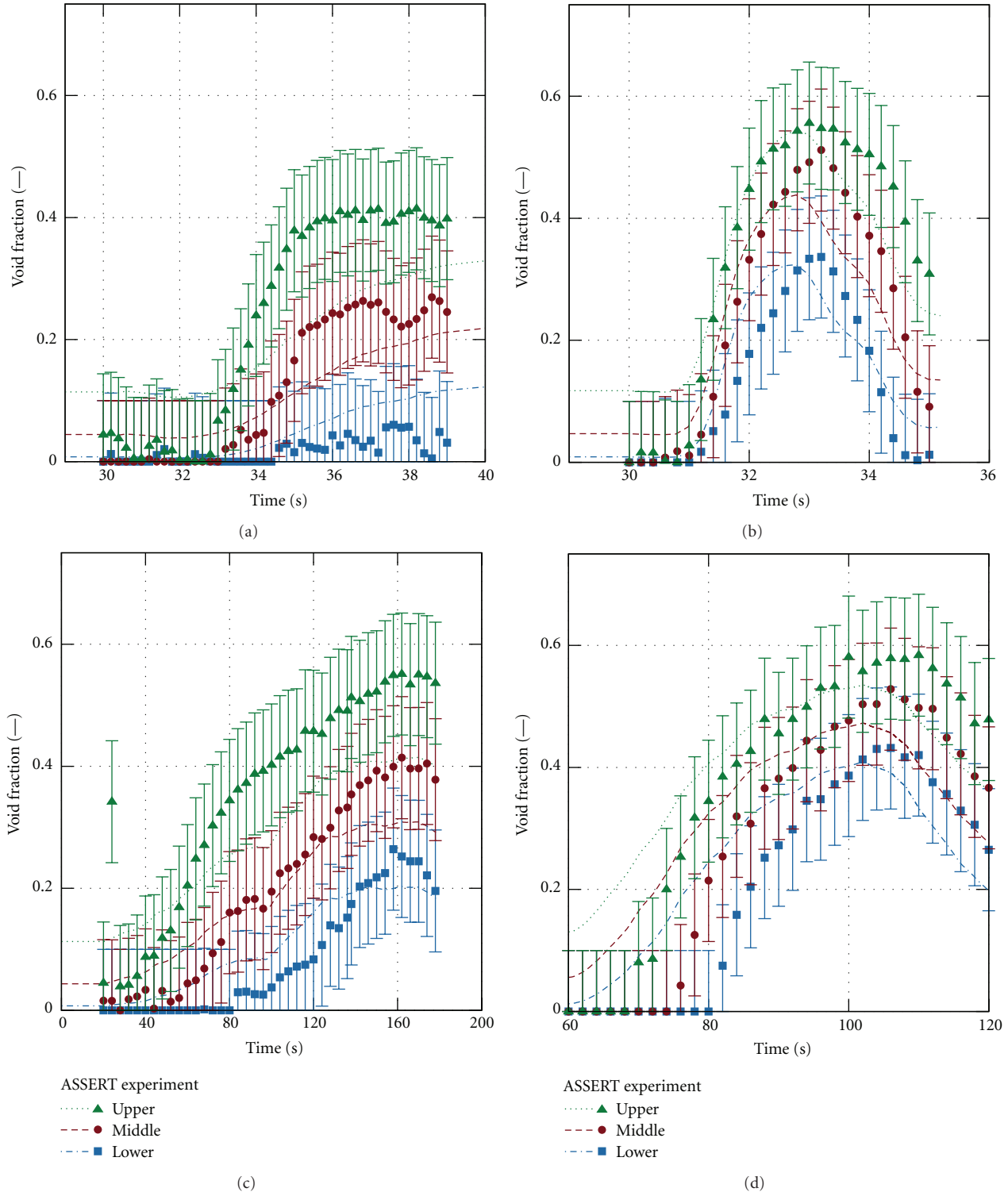


FIGURE 13: Transient void fraction results for bundle test series B5. Power increase (a), flow reduction (b), depressurization (c), and inlet temperature increase (d). Error bands displayed correspond to $2\sigma_{\text{exp}} = 0.10$.

result as the bundles have identical geometries, and only the radial power distribution differs between them. The void predictions for bundle B7 are worse however at low void fractions, with an average overestimation of 0.15 at the

bottom measurement elevation. From this, it is possible to infer that changing the axial power profile—as in the case of B5 and B6—has a minor effect on the accuracy of the void predictions. However, the addition of the unheated thimble

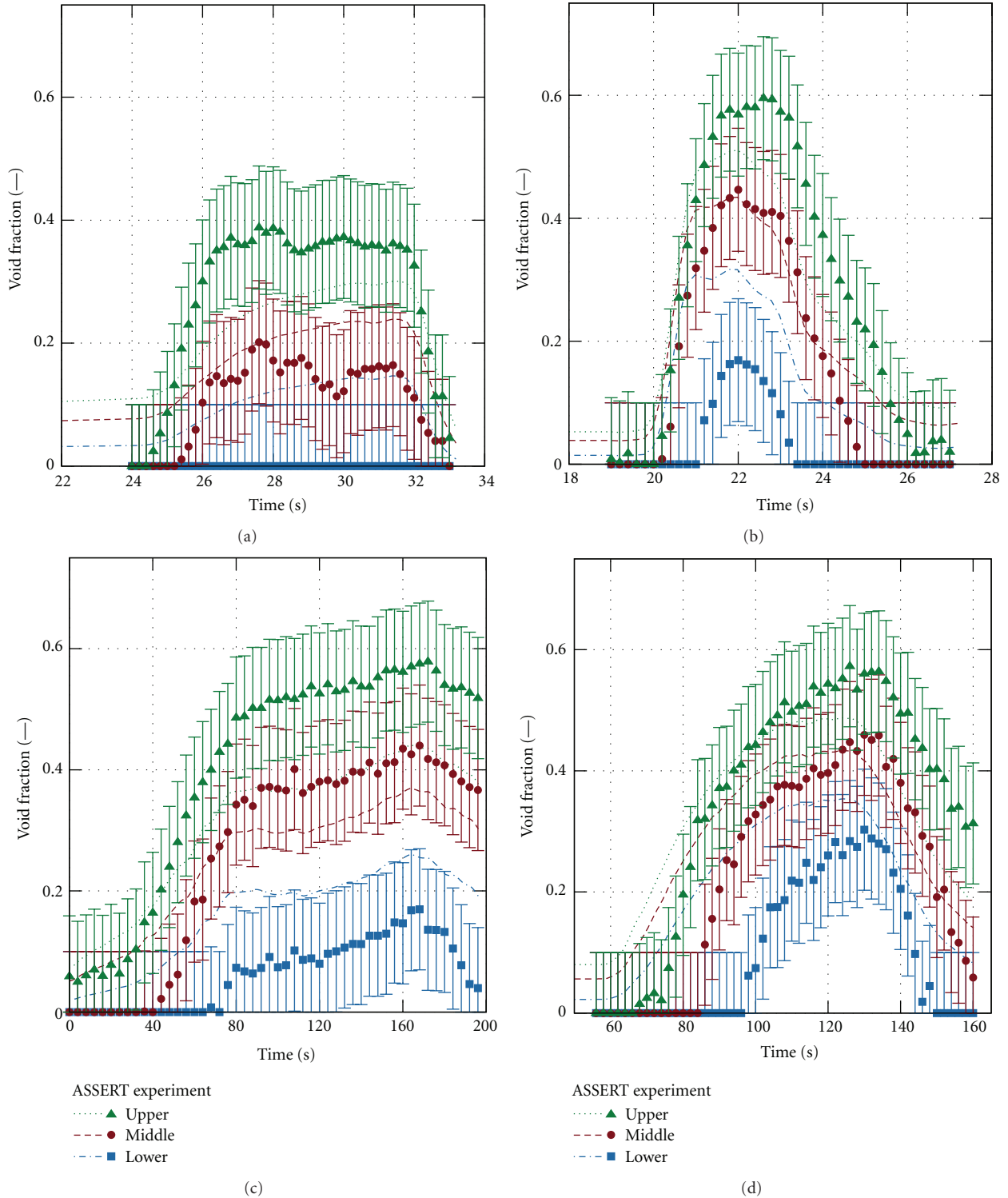


FIGURE 14: Transient void fraction results for bundle test series B6. Power increase (a), flow reduction (b), depressurization, (c) and inlet temperature increase (d). Error bands displayed correspond to $2\sigma_{exp} = 0.10$.

rod in the middle of the bundle plays a more significant role in affecting the overall accuracy of the void predictions, and this is perhaps due to condensation effects which are not explicitly modelled in ASSERT.

The void fraction overprediction in the subcooled region is not entirely unexpected since the two-phase heat transfer correlation was derived from data fitted at lower pressures relative to the current study. In the original work by Ahmad,

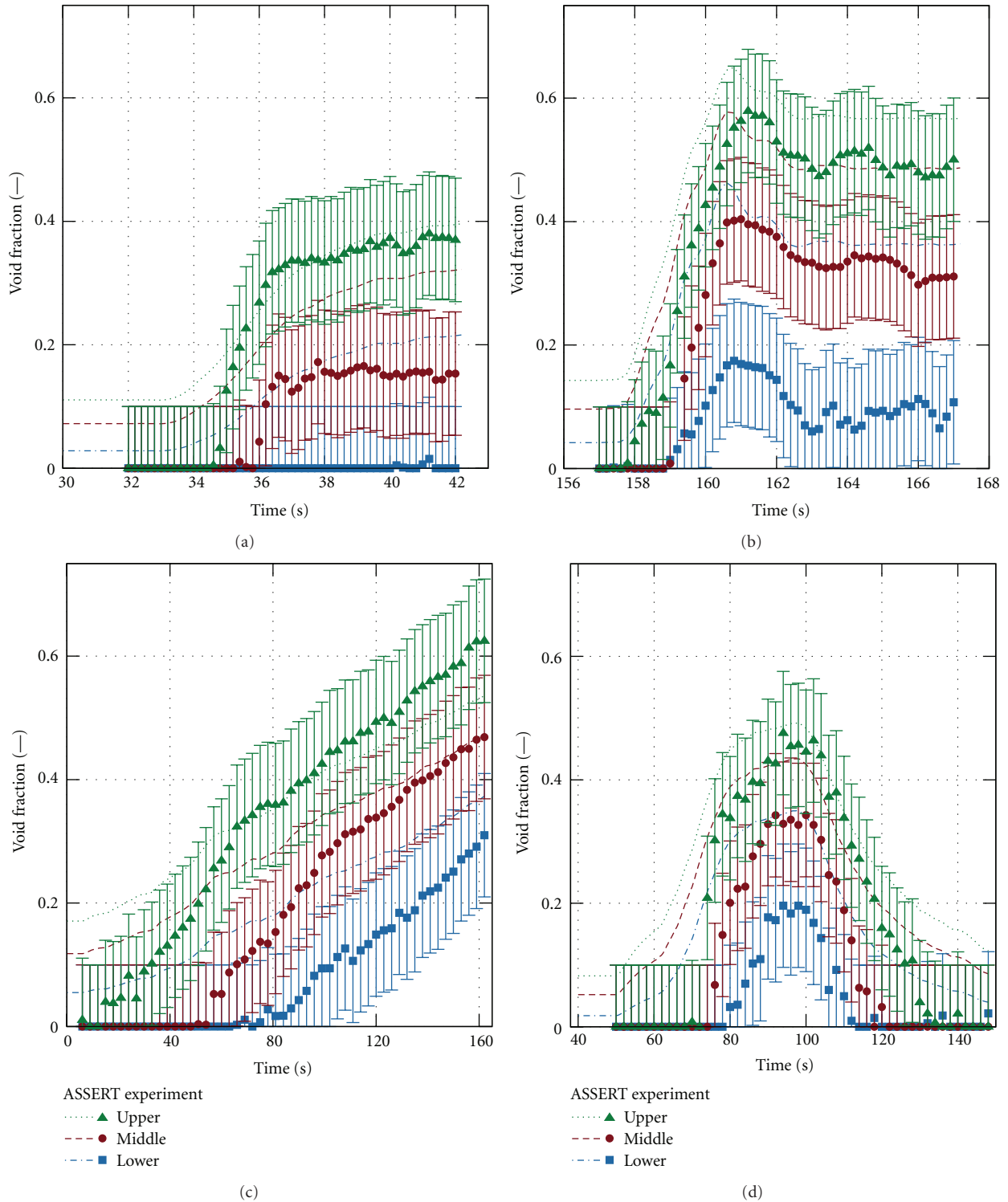


FIGURE 15: Transient void fraction results for bundle test series B7. Power increase (a), flow reduction (b), depressurization (c), and inlet temperature increase (d). Error bands displayed correspond to $2\sigma_{\text{exp}} = 0.10$.

the correlations yielded accurate predictions of the void fraction in a tube under conditions where the pressure was less than 11.03 MPa [2]. However, the paper also compares the derived correlation against the experimental data of

Egen et al. which was taken at 13.79 MPa, and found in several cases that the void fraction would be overpredicted by up to 0.10 near the transition between the subcooled and saturated boiling regimes, which is consistent with the

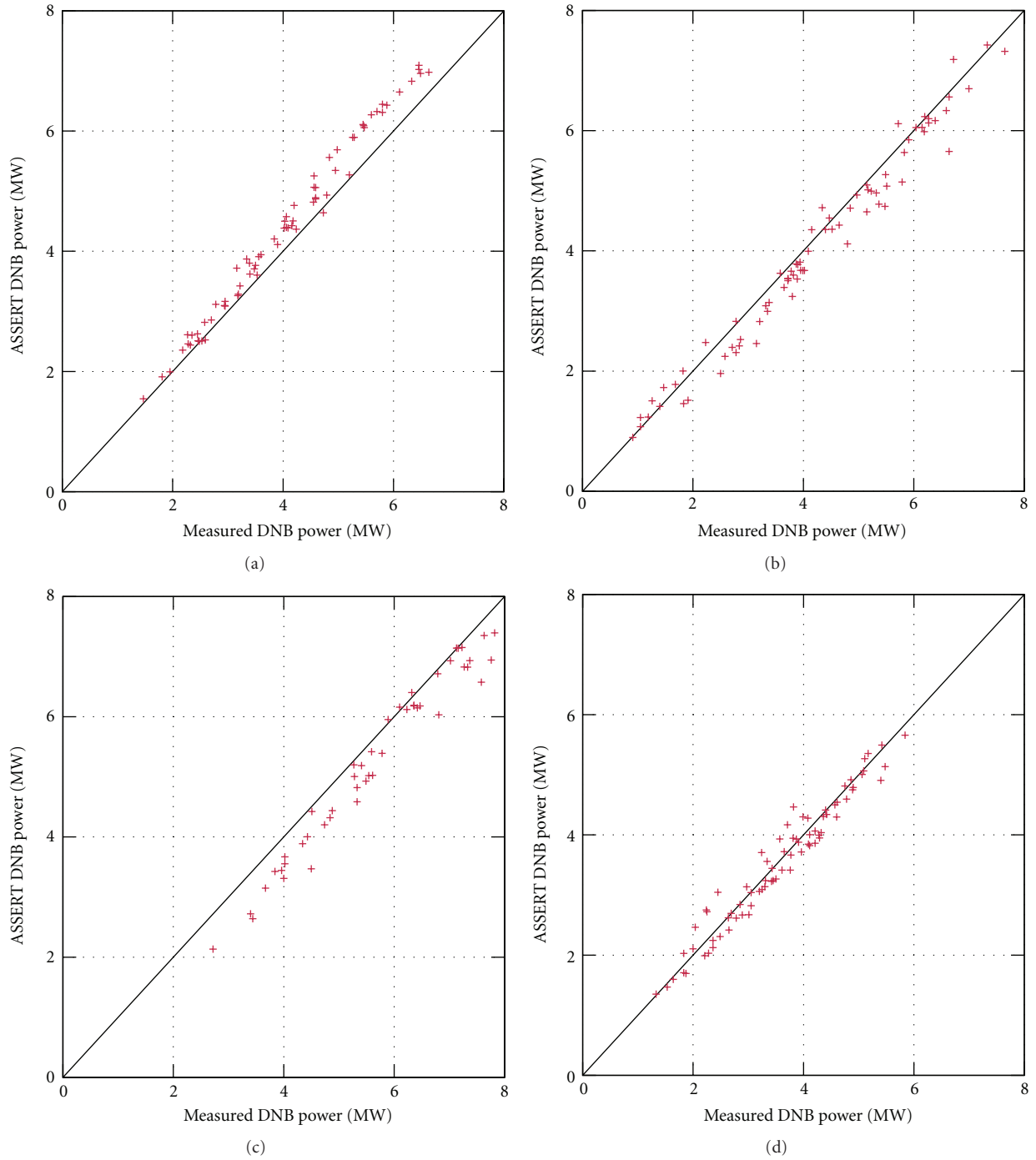


FIGURE 16: Steady state departure from nucleate boiling results for test series A0 (a), A2 (b), A3 (c), and A4 (d). The estimated uncertainty on the power measurements is $2\sigma_{\text{exp}} = 2\%$ and is not illustrated in the figure.

TABLE 6: Accuracy of steady state isolated subchannel void fraction predictions. The value of 1σ is estimated to be ± 0.03 .

Geometry	N_{Points}	Number of points where $ \epsilon_{\alpha} \leq \pm\sigma_{\text{exp}}$ (percent)	Number of points where $ \epsilon_{\alpha} \leq \pm 2\sigma_{\text{exp}}$ (percent)
S1 (typical)	43	19 (44.2%)	33 (76.7%)
S2 (thimble)	43	23 (53.5%)	36 (83.7%)
S3 (side)	20	5 (25.0%)	13 (65.0%)
S4 (corner)	20	9 (45.0%)	15 (75.0%)
Total	126	56 (44.4%)	97 (77.0%)

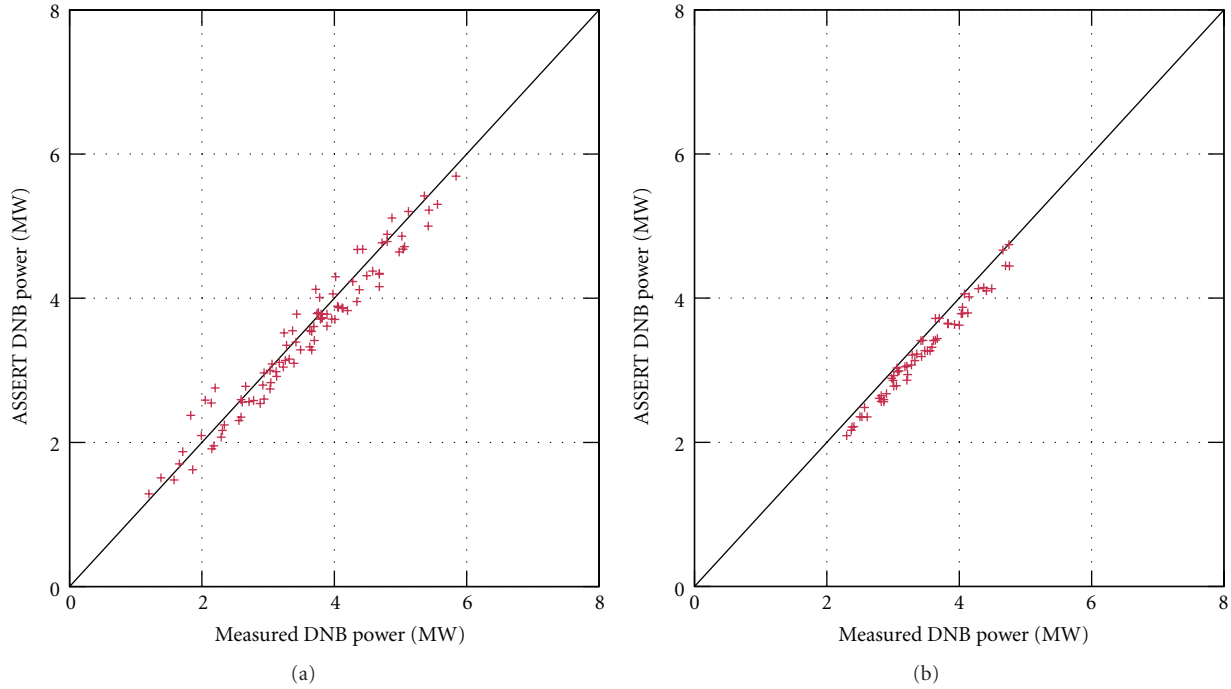


FIGURE 17: Steady state departure from nucleate boiling results for test series A8 (a) and A13 (b). The estimated uncertainty on the power measurements is $2\sigma_{\text{exp}} = 2\%$ and is not illustrated in the figure.

TABLE 7: Accuracy of steady state bundle void fraction predictions in the central 4 channels.

Series	N_{Cases}	Lower ($z = 2216$ mm)			Middle ($z = 2669$ mm)			Upper ($z = 3177$ mm)		
		$\bar{\epsilon}_{\alpha}$	$\sigma_{\epsilon_{\alpha}}$	$\epsilon_{\alpha,\text{RMS}}$	$\bar{\epsilon}_{\alpha}$	$\sigma_{\epsilon_{\alpha}}$	$\epsilon_{\alpha,\text{RMS}}$	$\bar{\epsilon}_{\alpha}$	$\sigma_{\epsilon_{\alpha}}$	$\epsilon_{\alpha,\text{RMS}}$
B5	74	0.0540	0.0395	0.0667	0.0337	0.0578	0.0666	-0.0405	0.0534	0.0667
B6	74	0.0642	0.0575	0.0860	0.0152	0.0650	0.0664	-0.0491	0.0521	0.0714
B7	74	0.1538	0.0497	0.1615	0.1130	0.0749	0.1353	0.0274	0.0581	0.0639

reported ASSERT results [2]. Figure 11 illustrates the average void fraction error at each elevation for the B5 and B6 bundle tests, arranged by the system pressure. The plot suggests that there may be some tendency for the code to overpredict the void fraction as the pressure boundary condition is increased. The data for the B7 bundle is not illustrated as the larger magnitude of the over-prediction makes these trends less obvious.

A sensitivity study on the two-phase heat transfer correlation was also conducted using the cases from the B5 series of tests. Both the results from the Chen correlation, which is based on wall superheat [10], and the Lahey and Moody relationship, which is based on theory [11], are compared against the Ahmad equation. The steady state bundle void fraction predictions using these two relations are presented in Figure 12.

One of the major difficulties in predicting the behaviour of boiling flows is in determining the OSV point, and this is reflected by the variety of different treatments proposed by authors in literature. The Chen correlation postulates that the overall heat transfer coefficient is the sum of a

single phase convective and a nucleate boiling component. Whereas the convective component is simply the Dittus-Boelter relationship from (8), the nucleate boiling portion is a function of many factors including the wall superheat [10]. When extended into the subcooled boiling regime, the Chen correlation is activated by the code as soon as the wall temperature exceeds the local saturation temperature at a computational node. In the PSBT experiments, the inlet subcooling ranged between 15 and 120°C, and so in some of the cases with lower subcooling, the code would predict that the OSV point occurred in the node immediately downstream of the inlet. If the OSV point is prematurely predicted, then the superposition of the two heat transfer mechanisms causes the overall value of the coefficient to be overestimated, which in turn leads to the wall superheat being artificially suppressed. This ultimately means that the void profile with respect to heated length takes on a much gentler slope as compared to the predictions by the Ahmad correlation. The void results using the Chen correlation seem to support this as at the lower ($\bar{\epsilon}_{\alpha} = 0.0453$, $\sigma_{\epsilon_{\alpha}} = 0.0472$) and middle ($\bar{\epsilon}_{\alpha} = -0.0146$, $\sigma_{\epsilon_{\alpha}} = 0.0632$) measurement

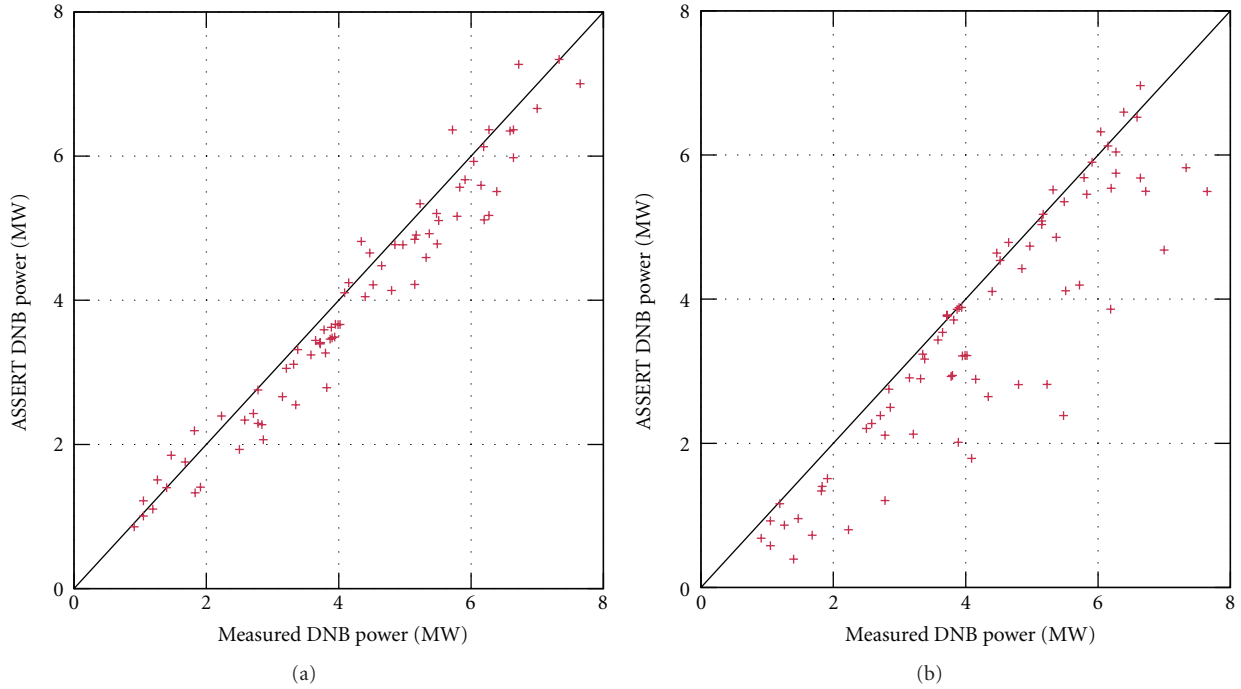


FIGURE 18: Steady state departure from nucleate boiling results for test series A2 using the Biasi correlation (a) and Weisman correlation (b). The estimated uncertainty on the power measurements is $2\sigma_{\text{exp}} = 2\%$ and is not illustrated in the figure.

elevations; they are better on average than what was predicted by the Ahmad correlation. However at the upper measurement elevation, the use of this correlation causes the code to severely underpredict the void ($\bar{\epsilon}_\alpha = -0.1112$, $\sigma_{\epsilon_\alpha} = 0.0538$).

In ASSERT, the Lahey correlation determines the OSV point using the same method as the Ahmad correlation; however, it is fit as a function of the subcooled enthalpy. The results are thus quantitatively similar to those predicted by the Ahmad correlation, although the magnitude varies slightly. At the lower elevation the Lahey correlation predicted the highest average deviation from the measured values ($\bar{\epsilon}_\alpha = 0.0879$, $\sigma_{\epsilon_\alpha} = 0.0455$); however the results are better at the middle ($\bar{\epsilon}_\alpha = 0.0602$, $\sigma_{\epsilon_\alpha} = 0.0647$) and upper ($\bar{\epsilon}_\alpha = -0.0251$, $\sigma_{\epsilon_\alpha} = 0.0598$) measurement points.

4.1.3. Transient Bundle. The transient bundle results are illustrated in Figures 13, 14, and 15. For each of the bundles, a power increase, flow reduction, and inlet temperature increase and depressurization transient was run for a total of 12 tests. General information about the boundary conditions for the tests are provided in Table 8, with a full description of the transient evolution available in [1]. The error trends in the transient portion of the benchmark were consistent with that of the steady state runs as ASSERT tended to overpredict the void fraction in the subcooled boiling region, while under-predicting at saturated conditions. This effect was observed to be more severe in the transients run on the B5 and B6 bundles than the B7 bundle. Additionally in

all 12 of the cases, the code predicted void at each of the measurement elevations, whereas this was not reported in the experimental data.

While the magnitude of the void fraction predicted was incorrect, qualitatively the void development over time followed what was observed in the experiment in all cases except for the coolant temperature increase scenario. Some authors have proposed that the measurement location of the inlet temperature is far enough upstream of the heated section that it causes a 7-second time shift in the temperature profile [12]. Others have attributed this lag effect to the heat capacitance of the experimental apparatus [13]. In both cases, the authors found their predicted results time shifted from what was observed. The temperature shift has not been applied to the results of this study, and the rationale behind that decision is provided in the transient DNB section.

4.2. Departure from Nucleate Boiling

4.2.1. Steady State. The results for the steady state DNB portion of the benchmark are illustrated in Figures 16 and 17 while statistical data is listed in Table 9. The absolute DNB power error in Table 9 is defined as (21) in units of MW, whereas the relative DNB power error is defined as (22), as follows:

$$\epsilon_P = P_{\text{DNB,ASSERT}} - P_{\text{DNB,Exp}}, \quad (21)$$

$$\gamma_P = \frac{P_{\text{DNB,ASSERT}}}{P_{\text{DNB,Exp}}}. \quad (22)$$

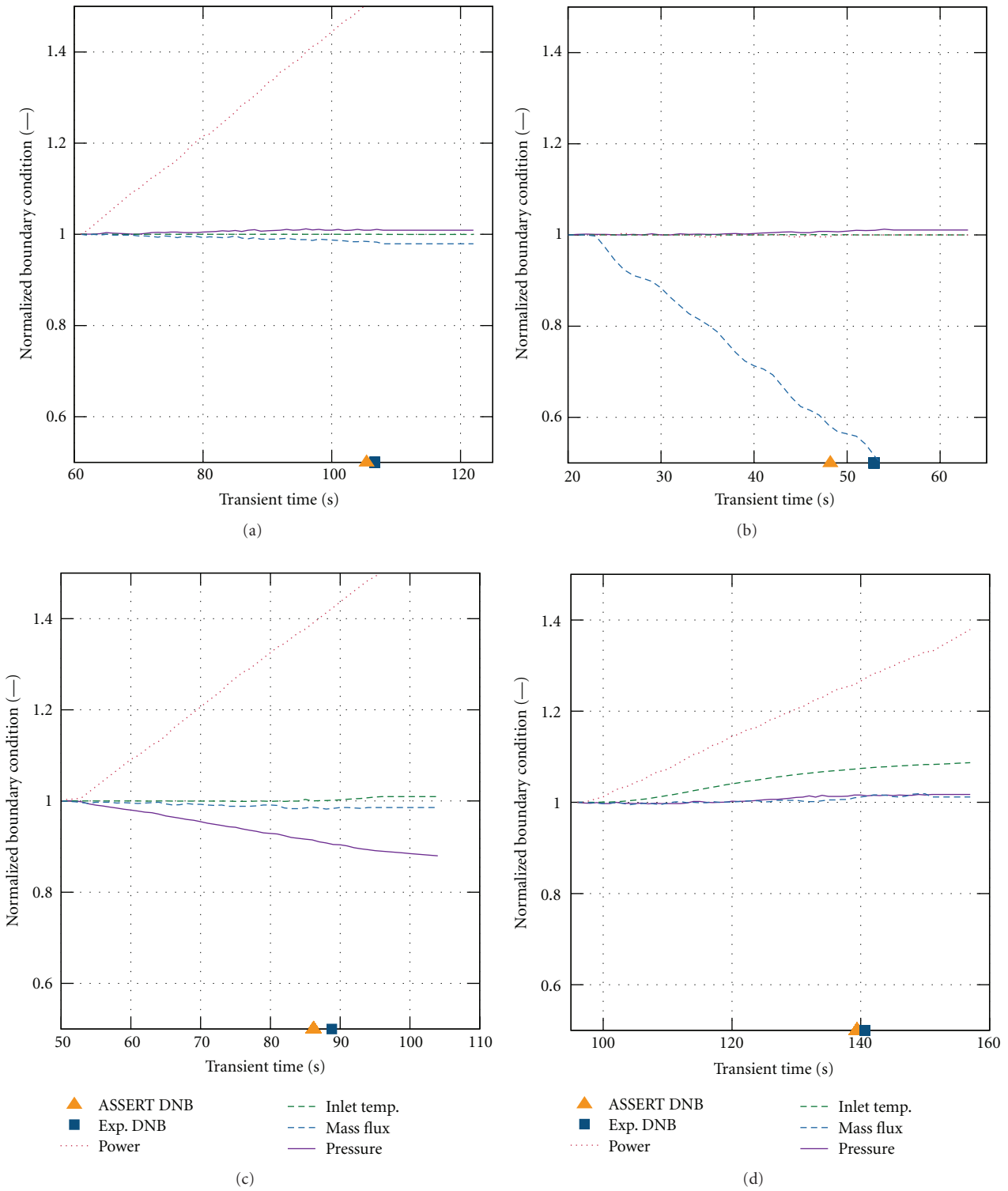


FIGURE 19: Transient departure from nucleate boiling results for test series A11. Power increase (a), flow reduction (b), depressurization (c), and inlet temperature increase (d). Estimated uncertainty on the power measurements is $2\sigma_{exp} = 2\%$.

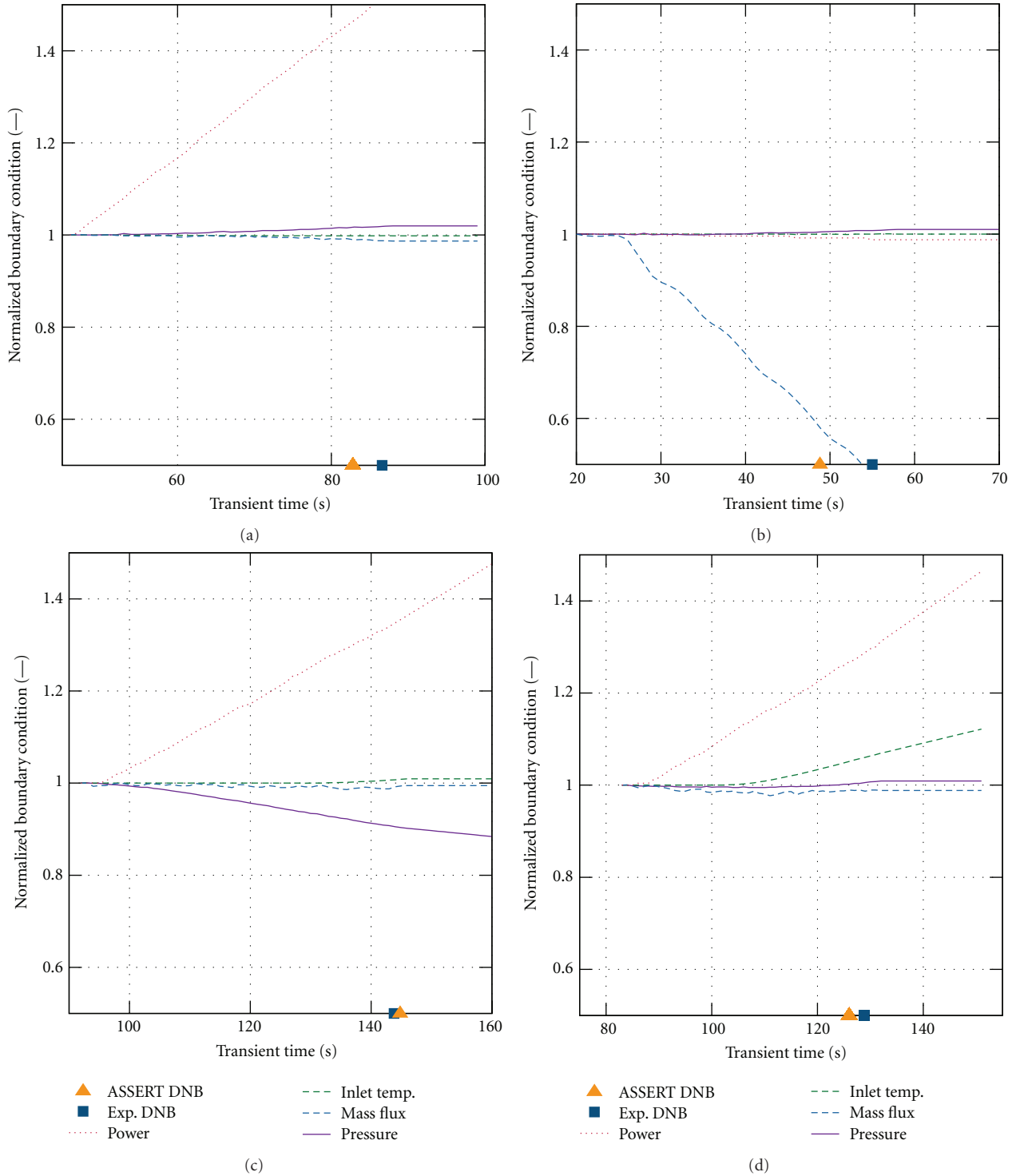


FIGURE 20: Transient departure from nucleate boiling results for test series A12. Power increase (a), flow reduction (b), depressurization (c), and inlet temperature increase (d). Estimated uncertainty on the power measurements is $2\sigma_{\text{exp}} = 2\%$.

Despite the deviation observed in some of the void results, the power at which DNB occurs is predicted very well since the void discrepancy is predominately at low vapour fractions where DNB is not likely to occur. With the exception of the A0 configuration, the code has a slight tendency to underpredict the power at which DNB occurs. This is

most noticeable in the 6×6 bundle or the A3 configuration where the average predicted to measured DNB power was $\bar{y} = 0.930$.

An analysis was conducted on the steady state tests to ascertain the conditions where DNB was least accurately predicted. The 1995 Groeneveld lookup table supplies a

TABLE 8: Initial conditions and maximum rates of change for each of the experiments.

	Pressure (MPa)	Mass flux (Mg/m ² s)	Power (MW)	Inlet temperature (°C)
B5	15.0	3.3	2.3	300.1
B6	15.4	3.3	2.6	288.5
B7	15.5	3.3	2.5	291.5
Max. rate	-0.03 MPa/s	-25%/s	+15%/s	1°C/s

TABLE 9: Accuracy of steady-state DNB bundle predictions.

Test series	N_{Cases}	$\bar{\epsilon}_P$	σ_{ϵ_P}	$\epsilon_{P,\text{RMS}}$	$\bar{\gamma}_P$	σ_{γ_P}
A0	70	0.336	0.216	0.398	1.080	0.043
A2	76	-0.180	0.270	0.325	0.960	0.084
A3	57	-0.370	0.300	0.475	0.930	0.064
A4	76	-0.038	0.242	0.243	0.993	0.080
A8	93	-0.079	0.230	0.320	0.984	0.080
A13	60	-0.184	0.102	0.210	0.945	0.030

value for CHF as a function of the pressure, mass flux, and thermodynamic quality, and based on their analysis 88% of the data will fall within $\pm 10\%$ of the predicted value [3]. Using this as the basis of the current assessment, Tables 10 and 11 list the number of cases in each series of tests which fulfil this criteria and are arranged by mass flux and pressure, respectively.

The results suggest that either the code or the lookup table are less accurate at lower mass fluxes as only 18 of the 32 cases (56.3%) where $G < 1.0 \text{ Mg/m}^2\text{s}$ fell within $\pm 10\%$ of the experimental value—this is compared to the $2.0 \leq G < 3.0$ range where 79 of 92 tests (85.9%) met this criteria. When the cases are split by pressure, it is more difficult to derive conclusions since PSBT tests were run at many different pressures. Most of the cases were run at approximately 15.0 MPa, and the data indicates that 83.6% of the predictions met the accuracy criteria which is close to what would be expected.

During the development of the 1995 Groeneveld CHF look up table, the authors noted that there were several discontinuities in the data which they attributed to experimental uncertainty and second-order effects [3]. At the time, it was understood that there was no physical basis for these discontinuities, and so the data in the table was smoothed with respect to pressure, mass flux, and thermodynamic quality [3]. However in the 2006 version of the lookup table, some of this smoothing was removed since it was determined that the discontinuities were consistent with evidence supporting a sharp drop-off in the CHF with respect to quality under very specific pressure and flow conditions [14]. This drop-off is termed the Limited Quality Region (LQR), and Groeneveld suggests that it may be the transition between entrainment and deposition based dry-out [15].

A closer examination of the 14 PSBT DNB cases in the low mass flux ($G < 1.0 \text{ Mg/m}^2$) region which fell outside

the $\pm 10\%$ bounds found that almost all were over-predicted by between 15 and 30% which is substantially beyond what would be expected given the accuracy of the other cases in the benchmark. These cases were run at mass fluxes of $0.3 < G < 0.6 \text{ Mg/m}^2$ across all benchmark pressures, with DNB being predicted at $X_{\text{th}} > 0.75$. Comparing the boundary conditions used in these outlying cases with the 2006 lookup table shows that every single one of these tests fell either in an area identified as part of the LQR, or in a cell immediately adjacent to it. If the cases falling in the LQR are neglected from the analysis, then the DNB prediction accuracy across all bundles where $G < 1.0 \text{ Mg/m}^2$ improves to 18 of 24 cases falling within $\pm 10\%$ of the experimental value which is more consistent with the results at higher mass fluxes.

While this is only a rudimentary analysis, this seems to suggest that the error may be at least partially attributed to the smoothing in the 1995 version of the lookup table which was used in the code. This result however is contrary to the conclusions of [15], who believes that the LQR phenomena are suppressed in bundles due to the mixing vanes and spacers. This discrepancy suggests that further studies are required in establishing the effects of bundle appendages or spacer grids on the limiting quality phenomena.

A sensitivity study was also conducted in order to assess the different methods of predicting the DNB power, with both the Biasi and the Weisman and Pei correlations being tested against the A2 series of measurements. The results of these tests are illustrated in Figure 18 which shows a tendency for both correlations to underestimate the point at which DNB occurs, with the Biasi correlation having the better overall average of the two ($\bar{\gamma}_{P,\text{Biasi}} = 0.9379$ versus $\bar{\gamma}_{P,\text{Weisman}} = 0.8307$). The Weisman and Pei correlation seemed to have particular difficulty in predicting the cases where the system pressure was below 9.8 MPa, with the average predicted to measured power ratio being $\bar{\gamma}_{P,\text{Weisman},p<9.8\text{MPa}} = 0.6121$ among these cases.

4.2.2. Transient. In this portion of the benchmark, power increase, flow reduction, depressurization, and inlet temperature transients were run with both the A11 and A12 bundle configurations. Initial boundary conditions for these transients are listed in Table 12 while the time at which each bundle reached DNB in the experiment and ASSERT is illustrated in Figures 19 and 20. The power profile and geometry of bundles A11 and A12 are identical to bundles A4 and A8 used in the steady state portion, and since the average prediction error was the smallest in those two series of tests, the transient portion was generally very well predicted. The code predicts the DNB time early in 7 of the 8 tests, which is consistent with the observation that ASSERT has a slight underestimation of the DNB power in the A4 and A8 steady state cases. In the flow reduction transients the DNB time is predicted 4.7 and 6.2 seconds early for the A11 and A12 bundles, respectively, and this represents the largest magnitude of error.

As indicated in Table 12 the error in the DNB time predicted in the inlet temperature increase scenario is consistent with the results obtained by the other transients.

TABLE 10: Number of cases where ASSERT steady state DNB predictions fell within $\pm 10\%$ of measured value, arranged by mass flux.

Mass flux (Mg/m ² s)	A0	A2	A3	A4	A8	A13	Total
$G < 1$	—	7/12	—	5/10	6/10	—	18/32
$1 \leq G < 2$	8/10	7/12	5/10	16/21	17/22	4/4	57/79
$2 \leq G < 3$	6/9	8/10	9/15	6/6	16/16	34/36	79/92
$3 \leq G < 4$	28/41	26/33	18/24	31/32	34/38	20/20	157/188
$4 \leq G$	6/10	7/9	6/8	7/7	7/7	—	33/41
Total	48/70	55/76	38/57	65/76	80/93	58/60	344/432

TABLE 11: Number of cases where ASSERT steady state DNB predictions fell within $\pm 10\%$ of measured value, arranged by pressure.

Pressure (MPa)	A0	A2	A3	A4	A8	A13	Total
$4.7 \leq p < 5.2$	—	12/14	—	0/4	6/8	—	18/26
$7.3 \leq p < 7.8$	—	4/6	—	5/9	5/9	—	14/24
$9.7 \leq p < 10.2$	12/15	9/16	9/12	14/15	16/18	—	60/76
$12.1 \leq p < 12.6$	11/14	5/7	6/11	12/13	15/16	4/4	53/65
$13.1 \leq p < 13.6$	—	—	—	—	—	4/4	4/4
$14.6 \leq p < 15.1$	18/26	17/23	14/21	21/21	21/24	42/44	133/159
$15.3 \leq p < 15.8$	2/2	3/3	1/1	2/2	4/4	4/4	16/16
$16.3 \leq p < 16.8$	5/13	5/7	8/12	11/12	13/14	4/4	46/62
Total	48/70	55/76	38/57	65/76	80/93	58/60	344/432

This is something which was not expected since there has been much discussion on applying a time shift on the results of the void inlet temperature increase transients. If inlet temperature measurements were “lagged”, it would mean that any change in the temperature reported would not propagate to the heated section until after a 6- or 7-second delay has elapsed. This implies that true inlet temperature at the reported DNB time is lower and should be roughly the value which was recorded 7 seconds earlier. In the A11 transient this corresponds to about a -2.5°C discrepancy, whereas it is approximately -6.1°C in the A12 case—which is significant. It would also mean that if ASSERT is reporting that DNB occurs at approximately the same time as the experiment, then the result represents a much larger under-prediction than what was observed in the other transients of the series which all have very similar initial conditions.

On average while the A4 and A8 steady state DNB powers were predicted to within 2% of the measured power, there is a scatter of $\sigma_{\gamma_p} = 0.08$, meaning that in the ASSERT transient results presented, it is possible that the temperature lag does exist; however its effect may be obscured by the natural scatter of the code. Ultimately, the exact nature of the time delay is inconclusive, which is why in this study, the reported results for both the void fraction and DNB inlet temperature increase transients have been left unshifted.

5. Conclusions

Predictions from ASSERT-PV V3R1 were compared against data from the OECD/NEA PSBT benchmark. Although the single subchannel void tests were predicted well, in the bundle tests the lateral momentum induced by the mixing vanes and spacer grids exceeds the default values of the

Carlucci mixing correlation which were derived for PHWR designs, and so some adjustments to the mixing coefficients were required. Specifically, the coefficients for the magnitude of the mixing enhancement due to a flow obstruction and the decay length were adjusted based on an estimation of loss coefficient or “ k -factor” at each subchannel, a set of fluid temperature measurements, and results reported in literature.

A comparison of the simulated values against the experimental data showed good agreement under nucleate boiling conditions, although the code demonstrated a tendency to over-predict the void in the subcooled regime. Changing the two-phase heat transfer correlation used did affect the steady state results; however it was determined that the default correlation of Ahmad was the most accurate—despite being used outside its recommended range. The error in the transient results was qualitatively similar to the steady state cases, with void overpredictions occurring in the subcooled regions.

Good agreement was obtained in the steady state DNB portion of the benchmark, albeit the code was observed to slightly under-predict the power. A decline in the accuracy of the predictions was also observed under boundary conditions with lower mass fluxes and pressures. This was attributed to the boundary conditions falling within the limiting quality region which is not represented in the CHF lookup table used in the code. In the transient tests, the code predicted DNB occurring within 3 seconds of the experimental result, except during the flow reduction tests. The Biasi and Weisman DNB correlations were also tested against the Groeveneld lookup table and did not yield results which were more accurate. The Biasi correlation in particular had difficulty predicting the DNB power at lower pressures.

TABLE 12: Transient initial conditions, predicted and measured DNB times.

Bundle	Transient	Power (MW)	Mass flux (Mg/m ² s)	Pressure (MPa)	Inlet temperature (°C)	$t_{\text{DNB,exp}}$ (s)	$t_{\text{DNB,sim}}$ (s)
A11	Power increase	2.50	3.11	15.32	291.0	106.7	105.4
	Flow reduction	2.50	3.11	15.31	293.1	52.9	48.2
	Depressurization	2.52	3.13	15.33	291.7	88.8	86.2
	Temp. increase	2.48	3.07	15.16	291.6	140.6	139.4
A12	Power increase	2.51	3.17	15.31	291.3	86.6	82.8
	Flow reduction	2.51	3.25	15.33	292.5	55.0	48.8
	Depressurization	2.50	3.17	15.32	290.6	143.8	144.8
	Temp. increase	2.50	3.16	15.28	291.2	128.8	126.0

Nomenclature

A : Subchannel cross-sectional area
 d_{hyd} : Hydraulic diameter
 d_{rod} : Rod diameter
 f : Friction factor
 g : Gravitational acceleration
 G : Mass flux
 h_f : Liquid enthalpy
 h_{fg} : Latent heat of vaporization
 h_g : Vapour enthalpy
 H : Heat transfer coefficient
 k : Pressure loss coefficient
 K_f : Bulk fluid thermal conductivity
 P : Power
 p : Pressure
 q'' : Heat flux
 S : Gap width
 t : Time
 \vec{u} : Axial velocity
 \vec{v} : Lateral velocity
 W_k : Lateral mass flow rate to subchannel k
 W' : Intersubchannel turbulent mixing rate
 Δx : Axial node spacing
 X : Mass quality
 X_{th} : Thermodynamic quality.

Greek Symbols

α : Void fraction
 δ : Roughness height
 ϵ_P : Absolute error
 γ_P : Relative error
 μ : Viscosity
 Φ_2 : Two-phase multiplier
 ρ_f : Fluid density
 ρ_g : Vapour density
 σ_{exp} : Experimental uncertainty.

Dimensionless Numbers

Fr : Froude number
 Re : Reynolds number
 Pr : Prandtl number
 We : Weber number.

Acknowledgments

The authors would like to thank Dr. Yanfei Rao (AECL Chalk River Labs) for his support and advice on the ASSERT code, as well Mr. Adam Rubin and Dr. Maria Avramova (Penn State University) for their tireless efforts in organizing and coordinating the PSBT benchmark activities. The authors also would like to acknowledge AECL for the use of the code, and the financial support of NSERC and UNENE.

References

- [1] A. Rubin, A. Schoedel, M. Avramova, H. Utsuno, S. Bajorek, and A. Valazquez-Lozada, "OECD/NRC benchmark based on NUPEC PWR subchannel and bundle tests (PSBT)," Tech. Rep., OECD/NEA, 2010.
- [2] S. Y. Ahmad, "Axial distribution of bulk temperature and void fraction in a heated channel with inlet subcooling," *Journal of Heat Transfer*, vol. 92, no. 4, pp. 595–609, 1970.
- [3] D. C. Groeneveld, L. K. H. Leung, P. L. Kirillov et al., "The 1995 look-up table for critical heat flux in tubes," *Nuclear Engineering and Design*, vol. 163, no. 1-2, pp. 1–23, 1996.
- [4] L. N. Carlucci, N. Hammouda, and D. S. Rowe, "Two-phase turbulent mixing and buoyancy drift in rod bundles," *Nuclear Engineering and Design*, vol. 227, no. 1, pp. 65–84, 2004.
- [5] M. Glück, "Validation of the sub-channel code F-COBRA-TF. Part I. Recalculation of single-phase and two-phase pressure loss measurements," *Nuclear Engineering and Design*, vol. 238, no. 9, pp. 2308–2316, 2008.
- [6] I. E. Idelchik, *Handbook of Hydraulic Resistance*, Hemisphere Publishing Corporation, 2nd edition, 1976.
- [7] H. L. McClusky, M. V. Holloway, D. E. Beasley, and M. E. Conner, "Development of swirling flow in a rod bundle subchannel," *Journal of Fluids Engineering*, vol. 124, no. 3, pp. 747–755, 2002.
- [8] H. Gabriel and M. Glück, "Prediction of void fraction for PWR and BWR conditions with the subchannel code F-COBRA-TF," *Nuclear Engineering and Design*, vol. 241, no. 9, pp. 3952–3966, 2011.
- [9] M. Valette, "Subchannel and rod bundle PSBT simulations with cathare 3," in *Proceedings of the International Topical Meeting on Nuclear Reactor Thermalhydraulics (NURETH'11)*, 2011.
- [10] J. G. Collier and J. R. Thome, *Convective Boiling and Condensation*, Oxford University Press, New York, NY, USA, 3rd edition, 1994.

- [11] R. T. Lahey Jr. and F. J. Moody, *The Thermal Hydraulics of a Boiling Water Nuclear Reactor*, American Nuclear Society, 2nd edition, 1993.
- [12] T. W. Kim and A. Manera, “Prediction of void fraction in a subchannel and bundle geometry with FLICA4 and TRACE,” in *Proceedings of the International Topical Meeting on Nuclear Reactor Thermalhydraulics (NURETH '11)*, 2011.
- [13] M. Avramova, A. Velazquez-Lozada, and A. Rubin, “Comparative analysis of CTF and TRACE thermalhydraulics codes using OECD/NEA PSBT benchmark void distribution database,” in *Proceedings of the International Topical Meeting on Nuclear Reactor Thermalhydraulics (NURETH '11)*, 2011.
- [14] D. C. Groeneveld, J. Q. Shan, A. Z. Vasić et al., “The 2006 CHF look-up table,” *Nuclear Engineering and Design*, vol. 237, no. 15–17, pp. 1909–1922, 2007.
- [15] D. C. Groeneveld, “Anomalies and other concerns related to the critical heat flux,” *Nuclear Engineering and Design*, vol. 241, no. 11, pp. 4604–4611, 2011.

Research Article

Analysis of Void Fraction Distribution and Departure from Nucleate Boiling in Single Subchannel and Bundle Geometries Using Subchannel, System, and Computational Fluid Dynamics Codes

Taewan Kim,^{1,2} Victor Petrov,³ Annalisa Manera,³ and Simon Lo⁴

¹ Nuclear Energy and Safety Research Department, Paul Scherrer Institute, 5232 Villigen, Switzerland

² Department of NPP Engineering, KEPCO International Nuclear Graduate School, Ulsan 689-882, Republic of Korea

³ Department of Nuclear Engineering and Radiological Sciences, University of Michigan, Ann Arbor, MI 48109, USA

⁴ CD-adapco, Trident House, Basil Hill Road, Didcot OX11 7HJ, UK

Correspondence should be addressed to Taewan Kim, taewan.kim@kings.ac.kr

Received 30 April 2012; Accepted 20 July 2012

Academic Editor: David Novog

Copyright © 2012 Taewan Kim et al. This is an open access article distributed under the Creative Commons Attribution License, which permits unrestricted use, distribution, and reproduction in any medium, provided the original work is properly cited.

In order to assess the accuracy and validity of subchannel, system, and computational fluid dynamics codes, the Paul Scherrer Institut has participated in the OECD/NRC PSBT benchmark with the thermal-hydraulic system code TRACE5.0 developed by US NRC, the subchannel code FLICA4 developed by CEA, and the computational fluid dynamic code STAR-CD developed by CD-adapco. The PSBT benchmark consists of a series of void distribution exercises and departure from nucleate boiling exercises. The results reveal that the prediction by the subchannel code FLICA4 agrees with the experimental data reasonably well in both steady-state and transient conditions. The analyses of single-subchannel experiments by means of the computational fluid dynamic code STAR-CD with the CD-adapco boiling model indicate that the prediction of the void fraction has no significant discrepancy from the experiments. The analyses with TRACE point out the necessity to perform additional assessment of the subcooled boiling model and bulk condensation model of TRACE.

1. Introduction

An international benchmark program, namely, the OECD/NRC NUPEC BWR Full-Size Bundle Test (BFBT) Benchmark [1], was organized by OECD/NEA and US NRC to encourage advancement in subchannel analysis methods. About 30 organizations from 15 countries had participated in the benchmark and an extensive validation of subchannel, computational fluid dynamic (CFD), and thermal hydraulic system codes had been carried out. Building on the success of the BFBT benchmark, OECD/NEA and US NRC have organized an additional international benchmark program for pressurized water reactor (PWR) conditions [2]. The benchmark, namely the OECD/NRC NUPEC PWR subchannel and bundle tests (PSBT) Benchmark, aims at assessing the capabilities of system codes, subchannel codes, and CFD

codes to predict detailed void distributions and departure from nucleate boiling (DNB) in subchannels on the basis of experimental data measured at a full-scale prototypical PWR rod bundle in NUPEC test facility.

Meanwhile, the Paul Scherrer Institute (PSI) is engaged in strengthening its subchannel analysis capability for light water reactors in Switzerland. Following the experience from the European Union NURESIM and NURISP projects, PSI has opted for the subchannel analysis code FLICA4 developed at CEA in France [3]. Besides, the application of CFD for subchannel analysis is also considered as the new frontier of the state-of-the-art methodologies. In this context, PSI decided to participate in the PSBT benchmark with FLICA4 and a commercial CFD code, namely, STAR-CD [4]. In addition, analyses using the system code TRACE (TRAC/RELAP Advanced Computational Engine) [5] of the

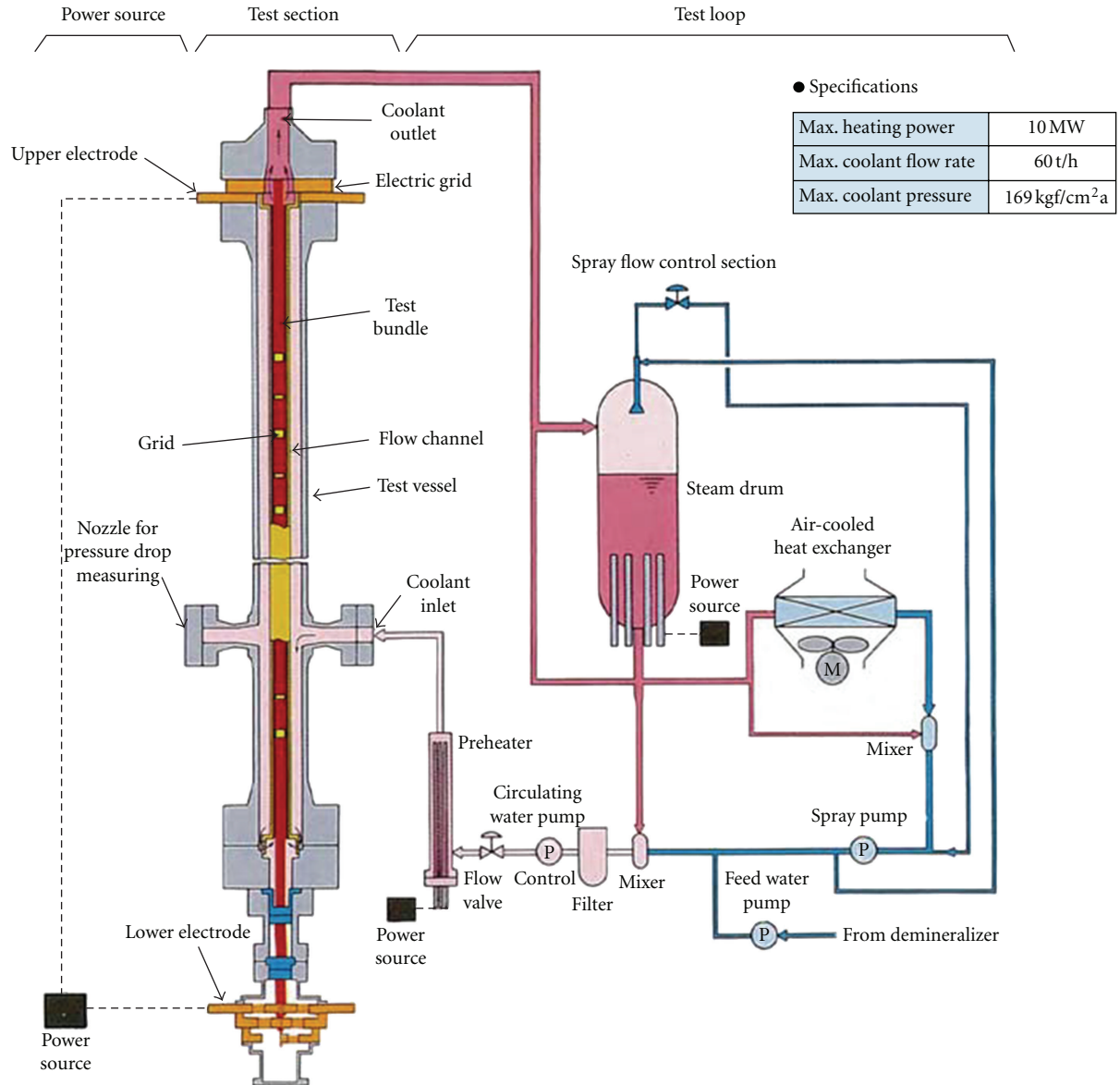


FIGURE 1: NUPEC test facility [2].

NUPEC experiments have been carried out in parallel to evaluate the applicability of TRACE for subchannel analysis.

This paper reviews the different analyses of the PSBT Benchmark that were conducted at PSI, and discusses and compares the results obtained with the different thermal hydraulic codes.

2. Benchmark Description

The OECD/NRC PSBT benchmark aims at encouraging advancement in subchannel analysis of fluid flow in rod bundles under the conditions typical for PWRs. The benchmark is aimed at assessing the capabilities of system-codes, subchannel codes, and CFD codes to predict void distributions, including DNB, in PWR rod bundle geometry on the basis of experimental data measured at the NUPEC

test facility [2]. The NUPEC test facility depicted in Figure 1 consists of a high pressure and high temperature recirculation loop, a cooling loop, and instrumentation and data acquisition systems. The recirculation loop consists of a test section, circulation pump, preheater, steam drum (acting as a pressurizer), and a water mixer. Different test sections were constructed to represent a single subchannel and a complete rod bundle, respectively. The design pressure is 19.2 MPa and the design temperature is 362°C.

The benchmark consists of two phases: phase I for void distribution benchmark and phase II for DNB benchmark. Benchmark phase I includes four exercises: steady-state single subchannel exercise, steady-state and transient bundle exercises, and pressure drop exercise. Phase II consists of three exercises, which are steady-state fluid temperature exercise and steady-state and transient DNB exercises for bundle geometries.

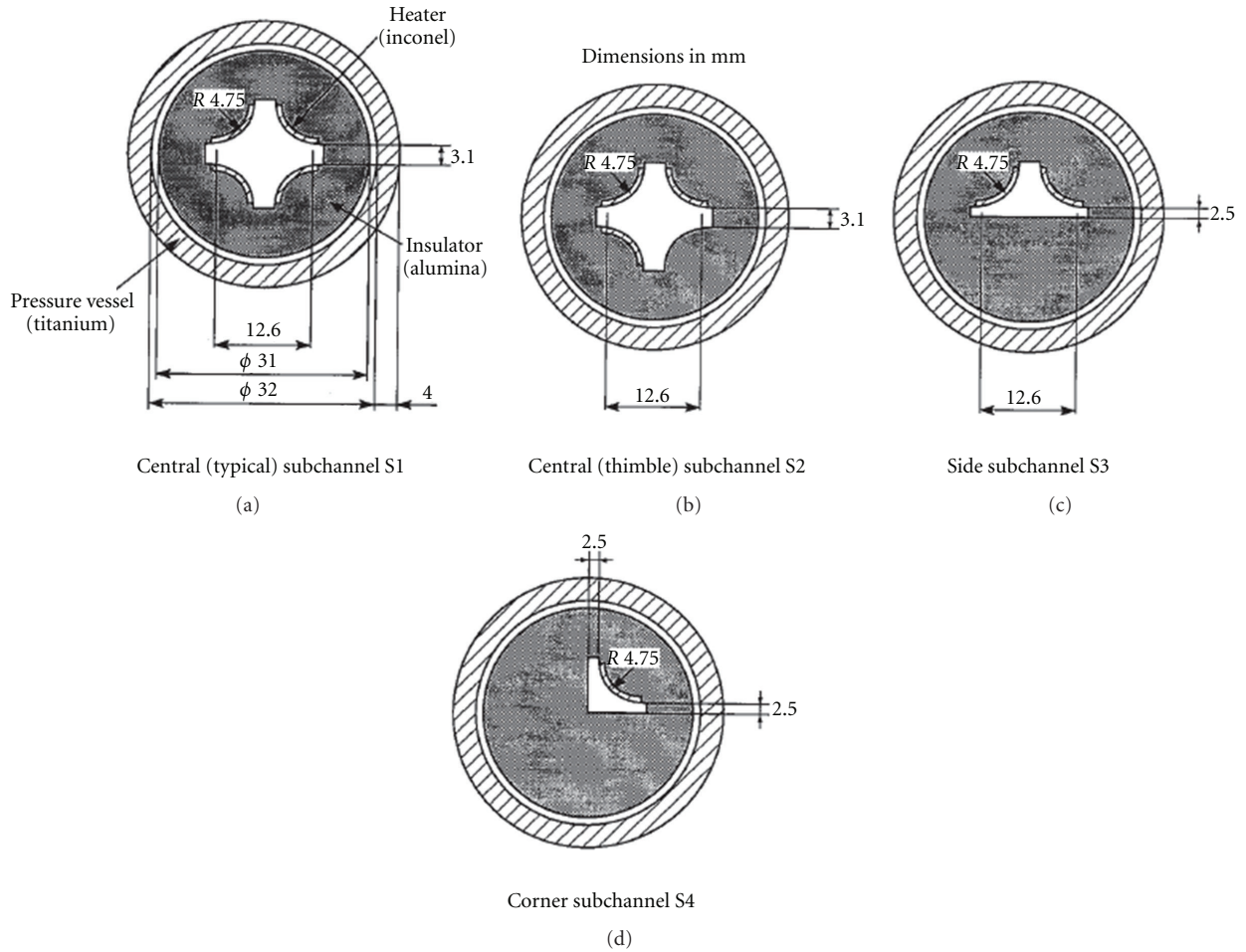


FIGURE 2: Cross-sectional view of subchannel test assembly [2].

TABLE 1: Geometry and power shape for single-channel tests [2].

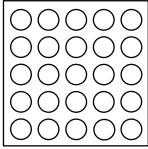
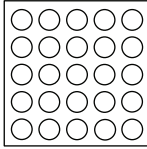
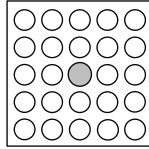
Item	Data			
Assembly (subjected subchannel)				
	S1	S2	S3	S4
Subchannel type	Center (typical)	Center (thimble)	side	corner
Number of heaters	4 × 1/4	3 × 1/4	2 × 1/4	1 × 1/4
Axial heated length (mm)	1555	1555	1555	1555
Axial power shape	Uniform	Uniform	Uniform	Uniform

■: subjected subchannel, white circle : heated rod, gray circle : thimble rod.

TABLE 2: Geometrical parameters of each subchannel [2].

	Subchannel type			
	Typical (S1)	Thimble (S2)	Side (S3)	Corner (S4)
Flow area, mm ²	107.098	107.098	68.464	42.592
Heated perimeter, mm	29.845	22.384	14.923	7.461
Wetted perimeter, mm	54.645	54.645	44.923	33.161

TABLE 3: Geometry and power shape for each bundle [2].

Item	Data		
Assembly			
	B5	B6	B7
Rods array	5 × 5	5 × 5	5 × 5
Number of heated rods	25	25	24
Number of thimble rods	0	0	1
Heated rod outer diameter (mm)	9.50	9.50	9.50
Thimble rod outer diameter (mm)	—	—	12.24
Heated rods pitch (mm)	12.60	12.60	12.60
Axial heated length (mm)	3658	3658	3658
Flow channel inner width (mm)	64.9	64.9	64.9
Radial power shape	A	A	B
Axial power shape	Uniform	Cosine	Cosine
Number of MV spacers	7	7	7
Number of NMV spacers	2	2	2
Number of simple spacers	8	8	8
MV spacer location (mm)	471, 925, 1378, 1832, 2285, 2739, 3247		
NMV spacer location (mm)	2.5, 3755		
Simple spacer location (mm)	237, 698, 1151, 1605, 2059, 2512, 2993, 3501		

White circle : heated rod, gray circle : thimble rod.

MV: mixing vane. NMV: no mixing vane.

Spacer location is distance from bottom of heated length to spacer bottom face.

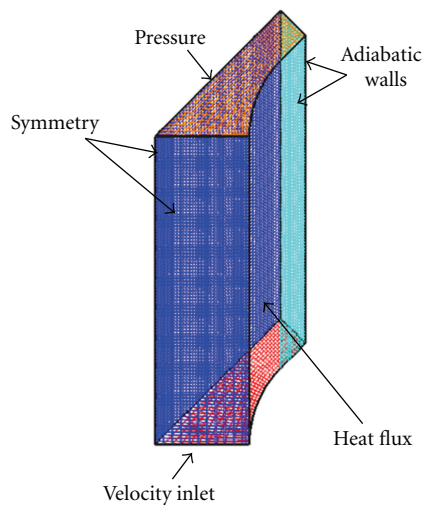


FIGURE 3: CFD model.

3. Thermal Hydraulic Codes

Three different codes have been employed for the PSBT benchmark: the subchannel analysis code FLICA4 v1.10.8, the system code TRACE v5.0 Patch 2, and the CFD code STAR-CD v4.14.

3.1. FLICA4. FLICA4 is a three-dimensional (3D) two-phase flow analysis code developed for subchannel analysis by CEA in France. The two-phase flow model in FLICA4 is based on a 4-equation model, combined with a drift flux model to describe the relative velocity between phases. The drift-flux model developed by Chexal et al. [6] has been selected for the benchmark, based on a sensitivity analysis with cases randomly selected out of the benchmark database [7]. The Dittus-Boelter [8] and Jens-Lottes [9] correlations were employed to model the single-phase and two-phase heat transfer, respectively. The F3 correlation was employed to model the mass transfer between phases and proportional coefficient, KV_0 , in the correlation was decided by a sensitivity analysis [7] (note that the F3 model/correlation refers to the model/correlation used in FLICA3-M [10]). The friction coefficient in FLICA4 is calculated as a product of the single-phase friction factor, two-phase multiplier, and heated wall corrector. The single-phase friction factor was calculated by using the default F3 model, which employs the Blasius model [11], while the Friedel model [12] was used as the two-phase multiplier. The F3 model, which requires four user-defined coefficients, was employed for the heated wall corrector. The turbulence model based on a mixing length approach was applied in the calculation. This model includes four empirical coefficients in the correlations for turbulent viscosity and conductivity. The required coefficients were

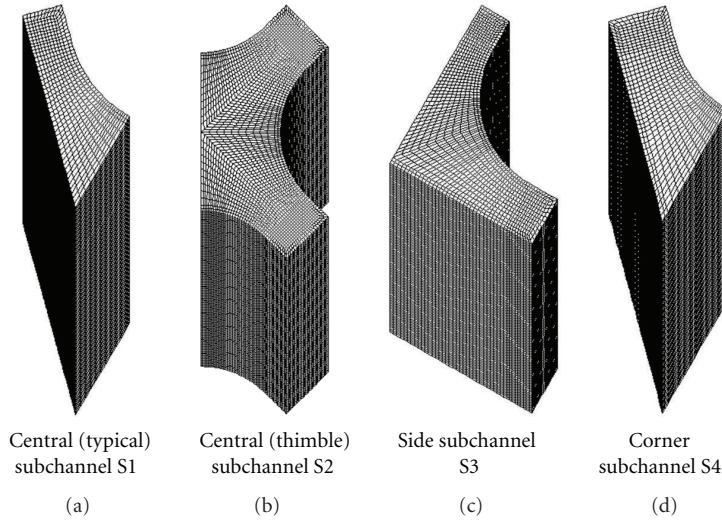


FIGURE 4: Hexahedral computational mesh.

derived from a sensitivity analysis for several cases selected randomly from the benchmark database.

3.2. *TRACE*. TRACE is the latest best-estimate thermal-hydraulic system code developed by US NRC for analyzing steady-state and transient neutronic/thermal-hydraulic behavior of light water reactors. In TRACE, a two-fluid 6-equation model of the steam-water flow is employed. The Gnielinski correlation [13] is used as a single-phase heat transfer coefficient and two-phase multipliers by Aggour et al. [14] and Rezkallah and Sims [15] are employed for bubbly/slug regime. The subcooled boiling heat transfer is modeled by means of the Lahey’s mechanistic model [16]. As for wall friction, the Churchill formula [17] and a void-fraction-based two-phase multiplier [5] are employed for single-phase and two-phase conditions, respectively. The interfacial heat transfer in bubbly flow regime is modeled by means of the Ranz-Marshall correlation [18], with the interfacial area concentration by Ishii and Mishima [19]. For the cap bubble/slug flow regime, the Ranz-Marshall correlation with consideration of small bubbles is implemented. The interfacial heat transfer under subcooled boiling condition is modeled by using the Lahey and Moody model [20].

3.3. *STAR-CD*. STAR-CD is a CFD code developed by CD-adapco. The governing transport equations solved are the conservation laws of mass, momentum, and energy for each of the two phases. These equations are solved in 3 dimensions. The numerical algorithm used for this benchmark is IPSA (Interphase Slip Algorithm) [21–23]. It is fully implicit, using the pressure-correction-based method extended to multiphase flows. No flow regime map is used. Bubbly flow is assumed anywhere where the gaseous phase is present. Interfacial momentum transfer includes models for drag force, turbulent drag force, virtual mass, force and momentum transfer due to mass transfer. Interfacial mass transfer is due to evaporation or condensation as computed

TABLE 4: Cosine power profile [2].

Node	Relative Power
	Cosine
(Bottom)	
1	0.42
2	0.47
3	0.56
4	0.67
5	0.80
6	0.94
7	1.08
8	1.22
9	1.34
10	1.44
11	1.51
12	1.55
13	1.55
14	1.51
15	1.44
16	1.34
17	1.22
18	1.08
19	0.94
20	0.80
21	0.67
22	0.56
23	0.47
24	0.42
(Top)	

by the boiling model. Interfacial energy transfer is due to temperature difference between the two phases and the saturation temperature. Wall drag is calculated by standard

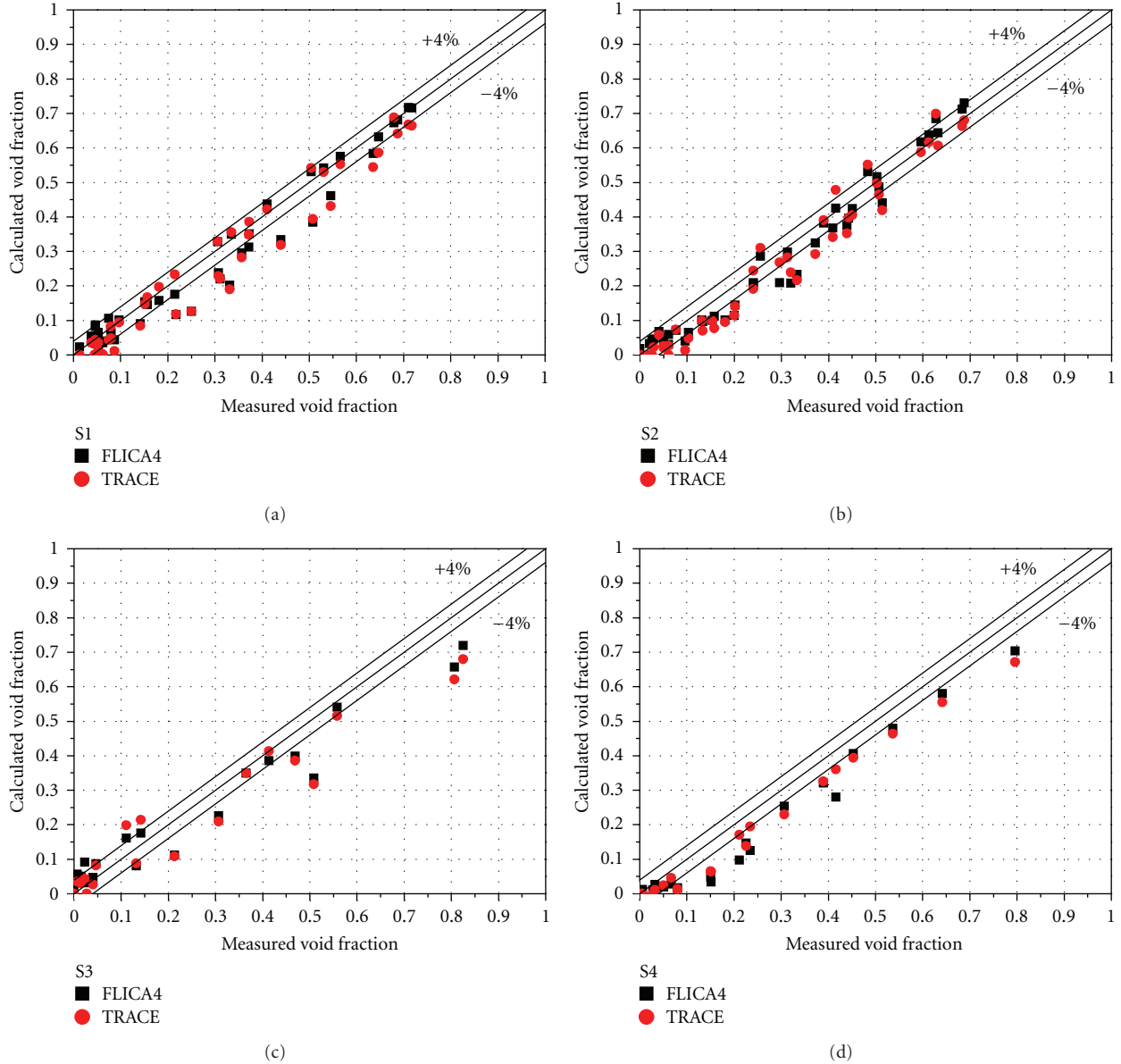


FIGURE 5: Void fraction predictions for single-channel exercise.

TABLE 5: Bundle average spacer pressure loss coefficients [2].

Spacer type	Loss Coefficient
Simple spacer (SS)	0.4
Nonmixing vanes spacer (NMV)	0.7
Mixing vanes spacer (MV)	1.0

wall function used in CFD codes. Wall boiling heat transfer is calculated by the “wall heat partitioning” model of Kurul and Podowski [24]. The lift force acting on the bubbles in radial direction was neglected. All the calculations were performed applying the liquid properties as a function of temperature and pressure.

Total wall heat flux is made up of three components, as follows:

$$\dot{q}_T'' = \dot{q}_C'' + \dot{q}_q'' + \dot{q}_e'' \quad (1)$$

where \dot{q}_C'' : convective heating, \dot{q}_q'' : quenching, and \dot{q}_e'' : evaporation.

For the nucleation site density, the Hibiki and Ishii model [25] with the following application range was used:

- (i) pressure: 0.101–19.8 MPa;
- (ii) mass flux: 0–886 kg/m²sec;
- (iii) contact angle: 5°–90°;
- (iv) Number density: 1.0E+04–1.51E+10 sites/m².

The bubble departure diameters were calculated using Kocamustafaogullari’s correlation [26], which is based on

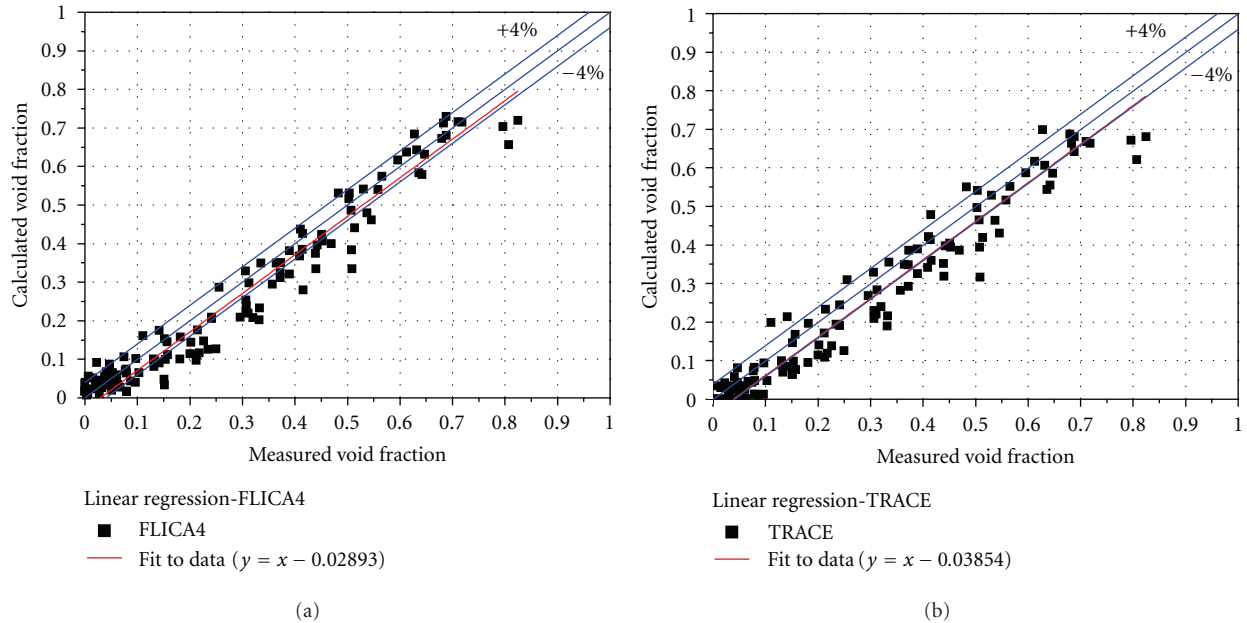


FIGURE 6: Results from linear regression analyses.

TABLE 6: Mean absolute error of void fraction.

Code	Lower	Middle	Upper	Overall
FLICA4				
Averaged error (%)	1.18	3.54	1.59	2.10
Mean absolute error (%)	2.95	5.29	4.04	4.09
TRACE				
Averaged error (%)	9.54	7.45	3.35	6.78
Mean absolute error (%)	10.1	9.49	6.49	8.71

TABLE 7: Initial conditions for transient bundle tests [2].

Test series	Assembly	Pressure (kg/cm ² a)	Initial conditions			Transients
			Mass flux (10 ⁶ kg/m ² h)	power (kW)	Inlet temperature (Celsius)	
5T	B5	154.2	11.95	2282.0	300.4	Power increase
		153.8	11.93	2244.0	301.2	Flow reduction
		153.0	11.92	2236.0	300.4	Depressurization
		152.5	11.94	2230.0	301.7	Temperature increase
6T	B6	158.2	11.55	2621.0	288.1	Power increase
		158.4	12.03	2574.0	288.8	Flow reduction
		154.6	12.02	2556.0	288.2	Depressurization
		157.2	11.92	2603.0	288.8	Temperature increase
7T	B7	158.2	12.02	2500.0	291.9	Power increase
		158.1	12.04	2405.0	292.0	Flow reduction
		155.0	11.99	2577.0	291.8	Depressurization
		158.8	11.99	2496.0	290.2	Temperature increase

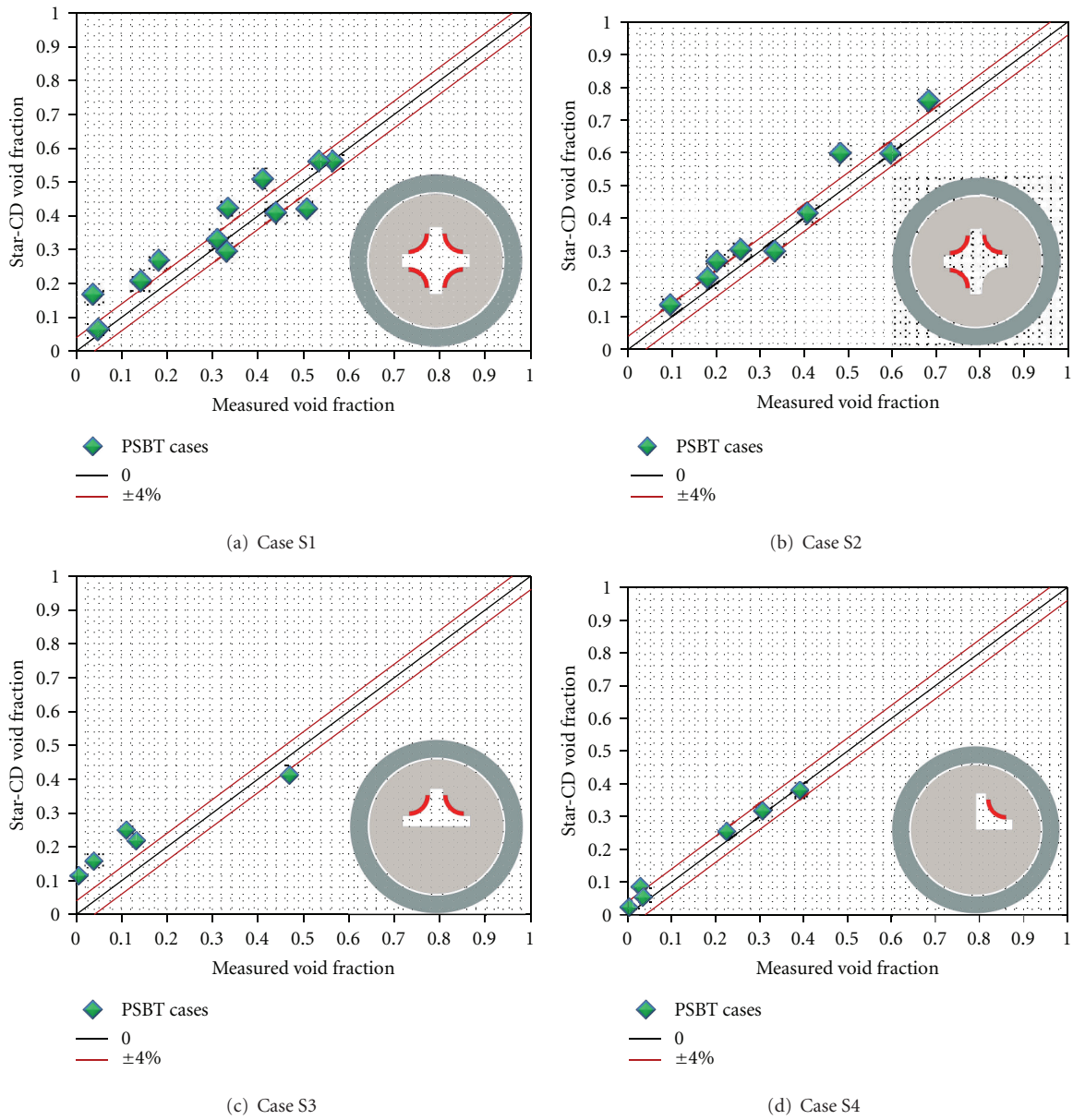


FIGURE 7: Section average void fraction results.

TABLE 8: Test assemblies for phase II [2].

Assembly	Reference fuel type	Rods array	Type of cell	Power distribution	
				Radial	Axial
A0	17 × 17 M	5 × 5	Typical cell	A	Uniform
A1			Typical cell	C	Uniform
A2			Typical cell	A	Uniform
A3		6 × 6	Typical cell	D	Uniform
A4			Typical cell	A	Cosine
A8		5 × 5	Thimble cell	B	Cosine
A11			Typical cell	A	Cosine
A12			Thimble cell	B	Cosine

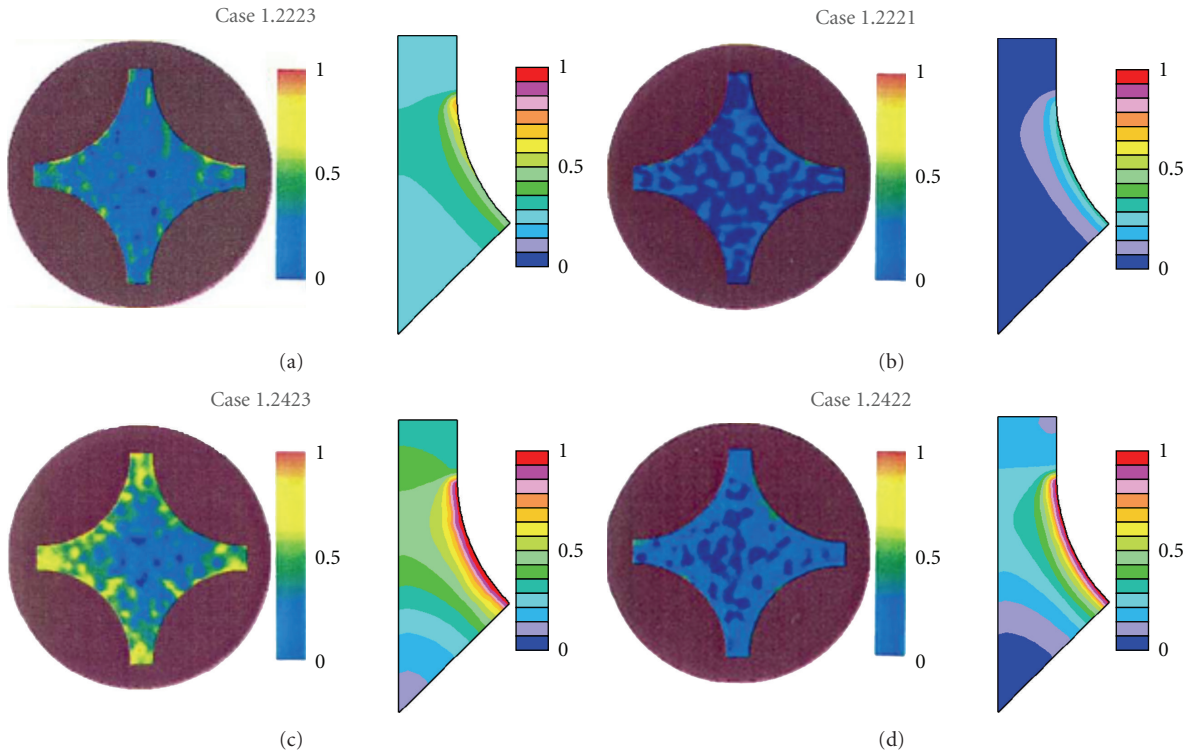


FIGURE 8: Void fraction distribution in a measuring section (CFD versus experimental data).

TABLE 9: Test series for exercise 2 of PSBT benchmark phase II [2].

Test series	Test section	Assembly	Test mode		DNB	Measurement Fluid temperature
			Steady state	Transient		
0		A0	Y		Y	
1	5 × 5	A1	Y			Y
2		A2	Y		Y	
3	6 × 6	A3	Y		Y	
4		A4	Y		Y	
8		A8	Y		Y	
11T	5 × 5	A11		Y	Y	
12T		A12		Y	Y	
13		A4	Y		Y	

TABLE 10: Test series for transient DNB exercise [2].

Test series	Assembly	Initial conditions				Transients
		Power (MW)	Mass flux (10 ⁶ kg/m ² h)	Pressure (kg/cm ² a)	Inlet temperature (°C)	
1 1T	A4	2.50	11.18	156.2	291.0	Power increase
		2.50	11.19	156.1	293.1	Flow reduction
		2.52	11.28	156.3	291.7	Depressurization
		2.48	11.04	154.6	291.6	Temperature increase
12T	A8	2.51	11.40	156.1	291.3	Power increase
		2.51	11.71	156.3	292.5	Flow reduction
		2.50	11.42	156.2	290.6	Depressurization
		2.50	11.38	155.8	291.2	Temperature increase

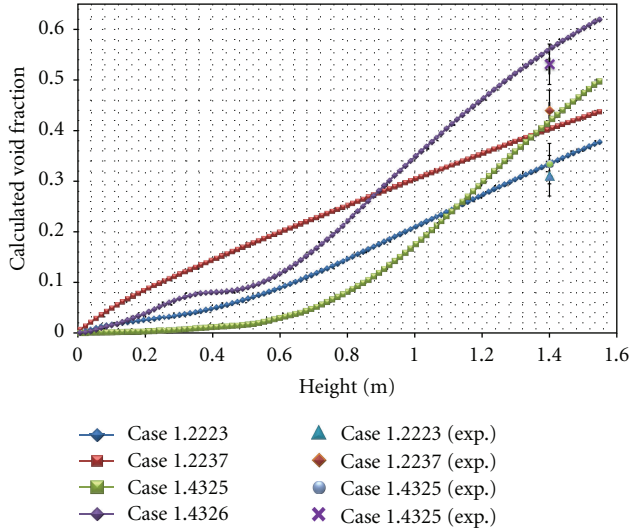


FIGURE 9: Axial void profile for 4 runs with S1 type of geometry.

water experimental data at pressures from 0.0067 to 14.187 MPa. The computed bubble diameters in the flow were obtained from the Kurul and Podowski formulation using linear interpolation between two bubble diameters at a specified liquid subcooling [24].

The numerical algorithm and its parameters (i.e., relaxation factors, difference scheme, etc.) were kept the same for all geometries of the benchmark exercise and were not adjusted from run to run.

4. PSBT Benchmark Phase I: Void Distribution Benchmark

4.1. Single Subchannel Experiments

4.1.1. Description of Experiments. A series of steady-state experiments were performed to measure the void distribution in a single subchannel. The test section consists of four different geometries, which simulate various subchannels in a bundle as described in Table 1. The length of the heated section is 1.555 m and the void fraction was measured at 1.4 m from the bottom of the heated section. The cross-sectional view and the geometrical parameters of each subchannel test assembly are depicted in Figure 2 and listed in Table 2, respectively. The ranges of boundary conditions were as follows:

- (i) pressure: 4.90–16.6 (MPa),
- (ii) mass Flux: $4.94\text{E} + 02$ – $4.14\text{E} + 03$ ($\text{kg}/\text{m}^2\text{-sec}$),
- (iii) power: 12.5–90.0 (kW),
- (iv) inlet temperature: 164.1–345.0 ($^{\circ}\text{C}$).

4.1.2. Thermal Hydraulic Model

(1) *FLICA4 and TRACE.* Identical nodalizations were used for the single-channel analyses carried out with FLICA4 and TRACE. The single-channel test section was nodalized by

means of a one-dimensional pipe divided into 32 axial nodes. Four different geometries were prepared, to take into account the difference in cross-section and hydraulic diameter of each case. The Chexal-Lellouche drift-flux model was employed for the FLICA4 calculations. Multipliers for the turbulent diffusivity and viscosity, K_t and M_t , were set to 0.01 based on a sensitivity analysis. A value of $1.0\text{E} - 4$ was assigned to the recondensation coefficient, $KV0$. As for the TRACE model, the single channel was modeled with a PIPE (one-dimensional) component. Inlet mass flux and temperature and outlet pressure were imposed as boundary conditions.

(2) *STAR-CD.* In order to reduce the needs in computational resources, all subchannel geometries were modeled utilizing subchannel symmetry. 1/8 symmetry could be employed for the central subchannel, while the half symmetry could be exploited for the central (thimble) side and corner subchannels. Heated rods were not modeled explicitly, instead heat fluxes were applied as boundary conditions on the channel side walls. The height of the computational model is the same as the heated length of the experimental test section (1555 mm). A flat velocity profile was used for the inlet boundary condition, since no additional data about the inlet manifold geometry was made available to the benchmark participants. A summary of the boundary conditions applied to the CFD model is shown in Figure 3 (uniform velocity profile at the inlet; pressure outlet; constant heat flux at heated wall; adiabatic wall for unheated section; symmetry planes). Boundary values were specified according to the benchmark specifications [2].

Computational cells distribution and mesh size were kept the same for each run in the test series. The CFD meshes used are shown in Figure 4:

- (i) 53600 hexahedral cells for S1;
- (ii) 214400 hexahedral cells for S2;
- (iii) 114800 hexahedral cells for S3;
- (iv) 62200 hexahedral cells for S4.

The number of axial cell layers was set to 100 for each subchannel geometry. Mesh sensitivity studies performed on the 1/8 symmetry sector model of the type S1 geometry showed that there is no significant effect on the section averaged void fraction value after reaching 250 cells per axial cell layer.

4.1.3. Results

(1) *FLICA4 and TRACE.* The results of the void fraction for S1 to S4 are depicted in Figure 5. Generally, both FLICA4 and TRACE could predict the experimental results well. However, both codes underpredicted the void fraction, taking into account a measurement accuracy of 4.0% (absolute void fraction), especially for the corner subchannel type (S4).

The bias of the calculation results from FLICA4 and TRACE has been assessed by using the linear regression method. Figure 6 shows the results from the linear regression for the void fraction calculated by FLICA4 and TRACE. Each

0.85	0.85	0.85	0.85	0.85
0.85	1.00	1.00	1.00	0.85
0.85	1.00	1.00	1.00	0.85
0.85	1.00	1.00	1.00	0.85
0.85	0.85	0.85	0.85	0.85

(a) Type A

0.85	0.85	0.85	0.85	0.85
0.85	1.00	1.00	1.00	0.85
0.85	1.00	0.00	1.00	0.85
0.85	1.00	1.00	1.00	0.85
0.85	0.85	0.85	0.85	0.85

(b) Type B

FIGURE 10: Radial power distribution [2].

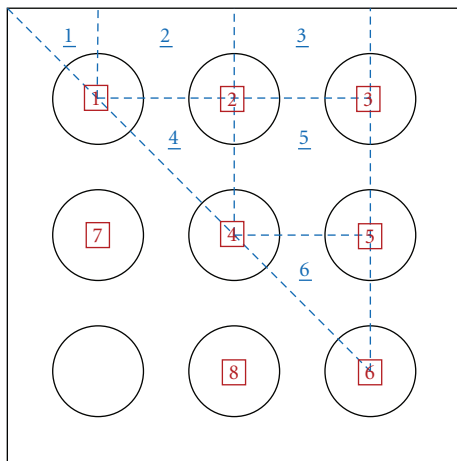


FIGURE 11: 1/8 symmetrical model for FLICA4.

result is fitted by a linear function with a high correlation coefficient (adjusted R^2) of 0.95. The linear regression analyses indicate that the void fraction results from FLICA4 and TRACE are biased from the experiments by 2.89% and 3.85% on average, respectively. The mean absolute errors of the FLICA4 and TRACE calculations are found to be 4.46% and 4.95%, respectively, which are slightly higher than the measurement error, assessed at 4.0% absolute void fraction. Both codes therefore reproduce the experimental data reasonably well.

(2) *STAR-CD*. Figure 7 shows the comparison between experimental and calculated cross-section averaged void fraction for different subchannel geometries ((a) S1, (b) S2, (c) S3, and (d) S4).

The red lines indicate error bars of $\pm 4\%$. Figure 8 shows the radial void fraction distribution in the measuring cross-section for selected cases; quantitative comparisons were not performed since only graphical data were available for the radial void fraction distributions. Figure 9 shows the computed axial void distribution profiles for selected cases. In general, for all geometries no significant discrepancy was

found between computed and experimental cross-section averaged void fractions. However, a slight overprediction of the void fraction has been observed especially for cases with low void fractions. Further verification of the boiling model aimed at assessing the prediction of radial void fraction distributions is required; however, suitable experimental data was unfortunately not available within the PSBT benchmark.

4.2. Steady-State Bundle Experiments

4.2.1. *Description of Experiments*. A series of steady-state experiments were performed to measure the void distribution in bundle geometry. The void fraction from the experiment is the one averaged over the four central subchannels. The three different 5×5 bundles as given in Table 3 were employed for the experiments. Bundles B5 and B6 have the same geometry but different axial power profiles: uniform and cosine shapes. Bundle B7 has a thimble rod at the center of the test section and cosine axial power shape. Two radial power distributions as depicted in Figure 10 were used for the experiments: type A and B, respectively. The two radial profiles are basically identical except for the non-heated thimble rod in type B. The cosine axial power profile applied in this experiment is given in Table 4. The bundles were equipped with three different grid spacers: spacer with mixing vane (MV), spacer without mixing vane (NMV), and simple spacer (SS), respectively. The number and location of each spacer are also listed in Table 3 and the bundle average pressure loss coefficients for the three types of spacers are provided in Table 5.

4.2.2. *Thermal Hydraulic Model*. Analyses of the steady-state bundle experiments have been conducted by means of FLICA4 and TRACE only.

(1) *FLICA4*. Since the geometry and the radial power distribution adopted for the bundle tests are fully symmetric, the symmetric boundary condition was employed so that each test assembly was described by means of a 1/8 symmetrical model as depicted in Figure 11. The symmetrical model consists of six subchannels subdivided in 100 axial nodes. A

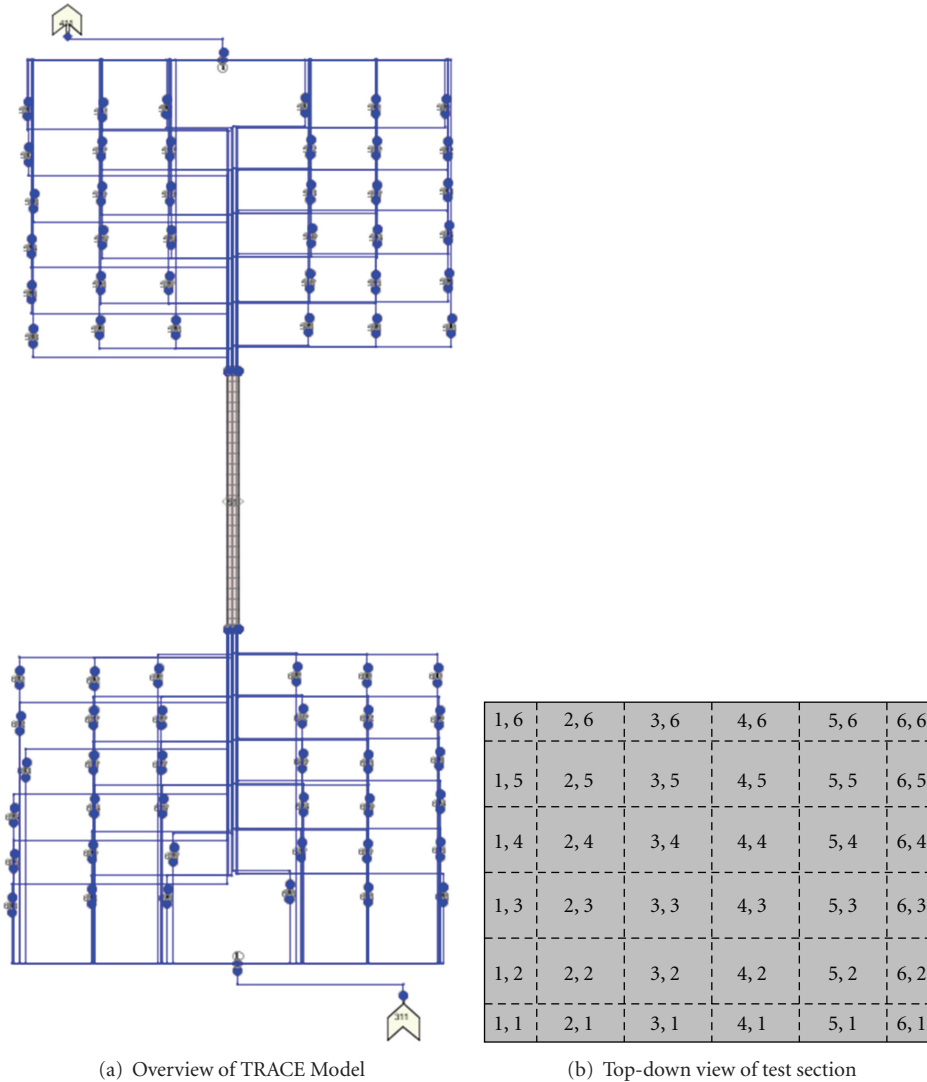


FIGURE 12: Nodalization for TRACE.

sensitivity study on the axial nodalization has shown negligible difference between 25 and 100 axial nodes. However, for better resolution, 100 axial nodes were employed in all the calculations.

The Chexal-Lellouche drift-flux model was employed and a value of $7.5E - 4$ was adopted for the recondensation coefficient, KV_0 , based on a sensitivity results with cases randomly selected out of the benchmark database. For all the bundle cases, except for assembly B7, coefficients for turbulent diffusivity and viscosity, K_t and M_t , were set to 0.01 based on a sensitivity analysis. For assembly B7 that has a guide thimble at the center, K_t and M_t were set to 0.05 also based on a sensitivity analysis. The pressure drop due to the spacers was taken into account by means of the singular pressure drop model in FLICA4.

(2) *TRACE*. The bundles are described by using a 3D rectangular VESSEL component of TRACE as depicted in

Figure 12. This includes 100 heat structures, each representing a quarter of a single heater rod. The VESSEL component was nodalized with 25 axial levels and the K-factors were prescribed at the relevant elevation in order to model the pressure drop introduced by spacers. No local K-factor was used on the crossflow connections. Since the 3D VESSEL component cannot be connected directly to the FILL component (which provides the inlet boundary conditions) and the BREAK component (which provides the outlet boundary conditions), PIPE components were introduced at the inlet and outlet of the VESSEL components.

4.2.3. Results. The void fraction was measured at three different elevations: 2216 mm (lower), 2669 mm (middle), and 3177 mm (top) from the bottom of the test section. The calculated void fractions at the four central subchannels were averaged and compared with the experimental data. The results of both codes presented in Figure 13 indicate

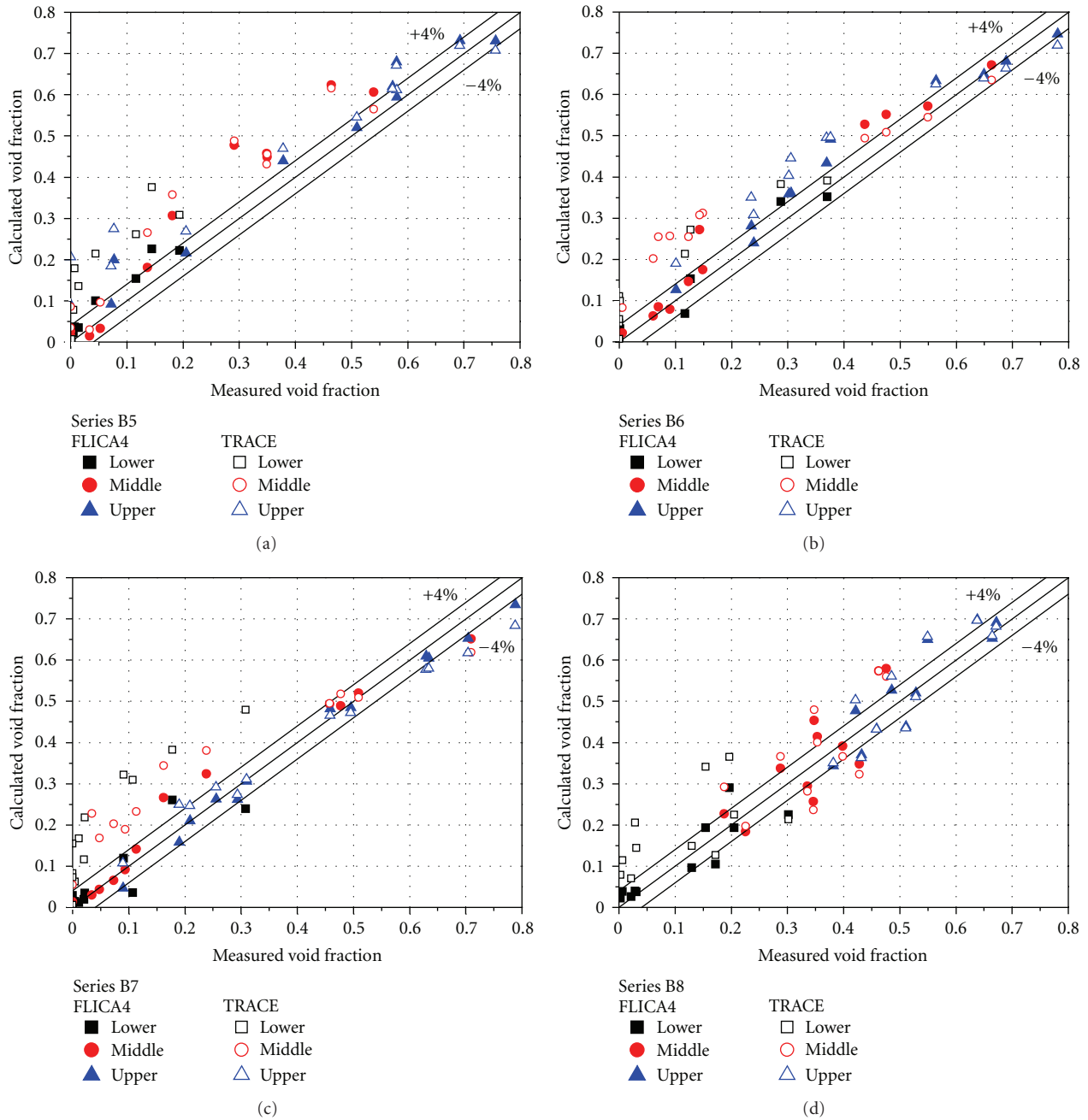


FIGURE 13: Void fraction of bundle exercise.

that, in general, both codes overpredicted the void fractions with respect to the experiments. In particular, TRACE overpredicted the void fraction in the lower and middle regions considerably. The linear regression method was applied to estimate the bias of each calculation quantitatively. As shown in Figure 14, the results from FLICA4 and TRACE are biased by +2.10% and +6.78% on average, respectively. The accuracies of the calculation represented by the mean absolute error are 4.09% and 8.71% for FLICA4 and TRACE, respectively. Considering the measurement error of 4.0% void fraction, the difference between the experiments and

the TRACE results is relatively high. As confirmed by the mean absolute error of each region listed in Table 6, the discrepancy between TRACE and experimental data is mainly encountered for the lower and middle regions, where smaller void fraction is expected. TRACE tends to overpredict the void fraction especially for values below 40%. In Figure 15, the axial void fraction profile of a case from test series B5 is presented together with experimental data. The void fraction predicted by TRACE starts to rapidly increase at an elevation of about 1.8 m. This result points out the necessity to further investigate and validate the subcooled

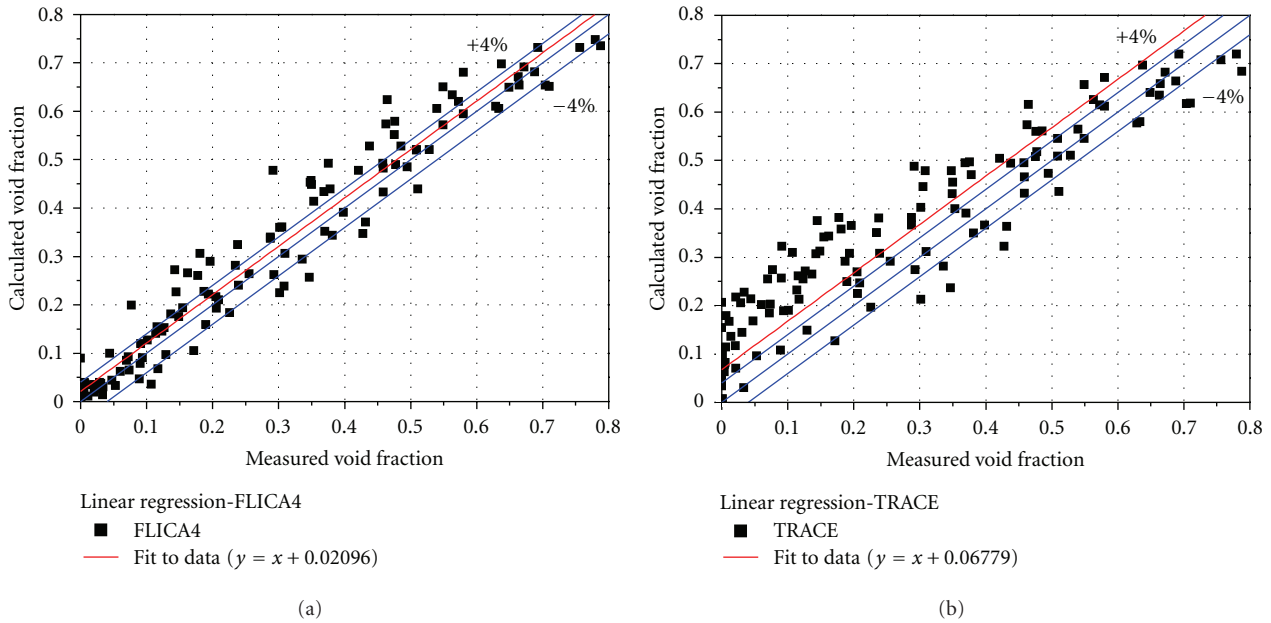


FIGURE 14: Results from linear regression analysis.

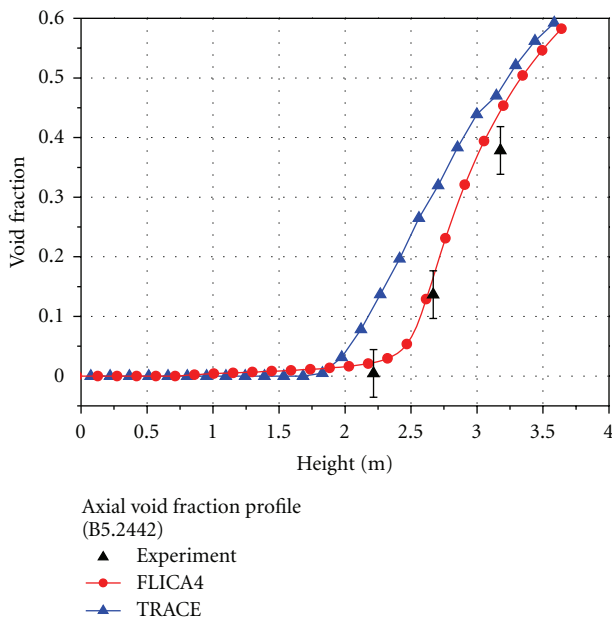


FIGURE 15: Axial void fraction profile of case B5.2442.

boiling model and bulk condensation model in TRACE. FLICA instead reproduces the experimental data reasonably well.

4.3. Transient Bundle Experiments

4.3.1. Description of Experiments and Thermal Hydraulic Model. The transient experiments were conducted with assemblies B5, B6, and B7. Four different transient experiments were performed for each assembly: a power increase, a flow

reduction, a depressurization, and a temperature increase. The initial conditions for each transient test are summarized in Table 7.

The transient experiments were analyzed by means of FLICA4 only. The FLICA4 models for the transient experiments are the same as the ones used for the steady-state analyses. As for the steady-state cases, since the void fraction is averaged over the four central subchannels in the experiment, the void fraction of the subchannel 6 in the FLICA4 model can be considered as the averaged void fraction.

4.3.2. Results. The analysis has been carried out for all transient cases specified as part of the benchmark. As an example, the calculation results from transient exercise 5T are reported in Figure 16 together with the experimental data. In general, FLICA4 is found to reproduce the experimental data reasonably well even in fast transients such as power increase and flow reduction. However, a large discrepancy was observed for the temperature increase case. It is presumed that the discrepancy is originated from a delay in the experimental inlet temperature variation. In fact, since the inlet temperature measurement was located between the preheater and the inlet nozzle of the test vessel, the actual temperature increase at the inlet of the test section would happen with some delays with respect to the temperature variation at the measuring point. Because the distance between measuring point and the test section inlet is unknown, it is not possible to estimate the delay in inlet temperature variation appropriately. Nevertheless, when shifting the FLICA4 results for test case 5T by 6.0 sec with respect to the original simulation time (see Figure 17), very good agreement with the experimental data is obtained. The time shift by 6.2 sec due to the mass flow rate difference

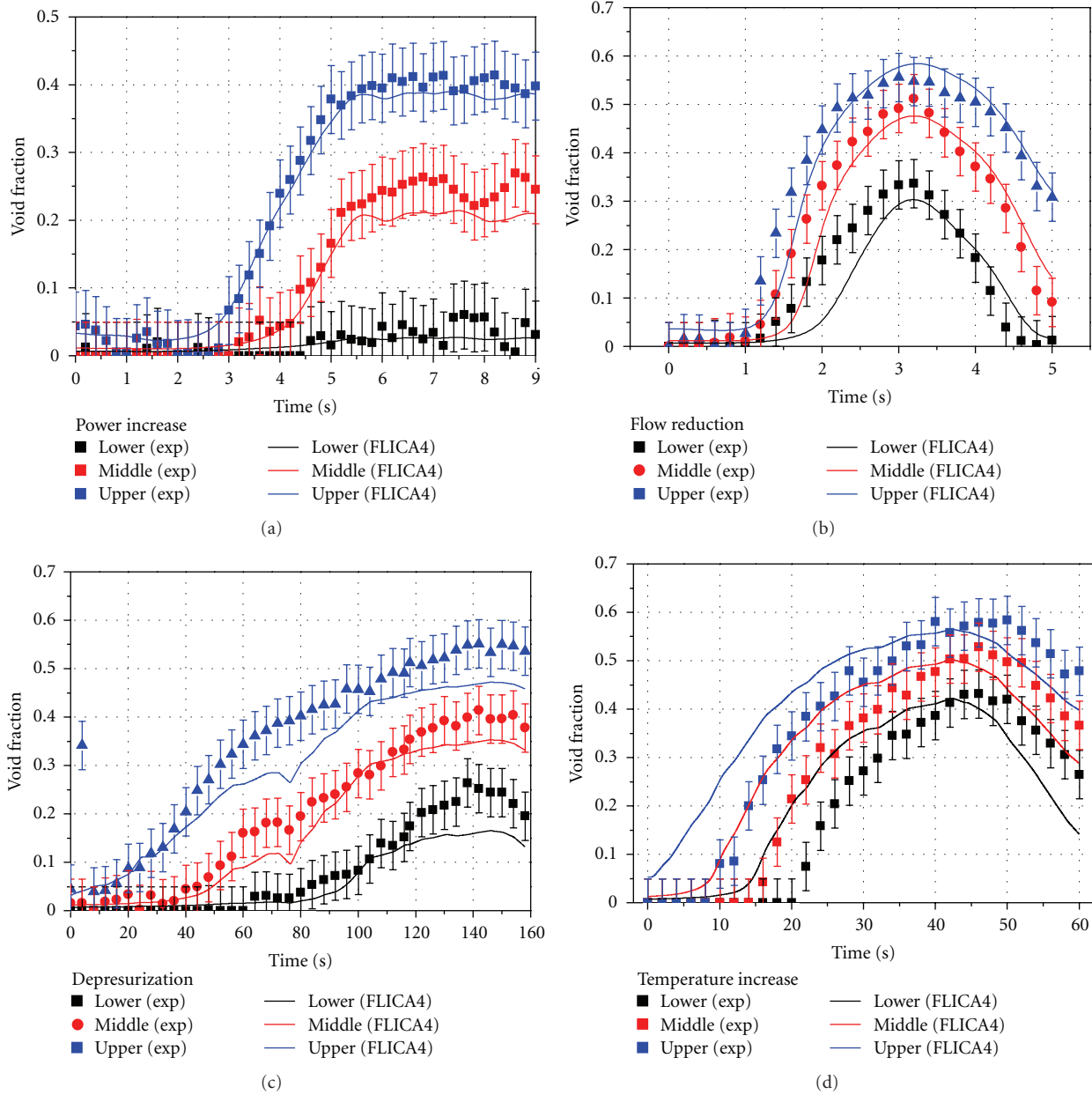


FIGURE 16: Axial void fraction of transient exercise 5T.

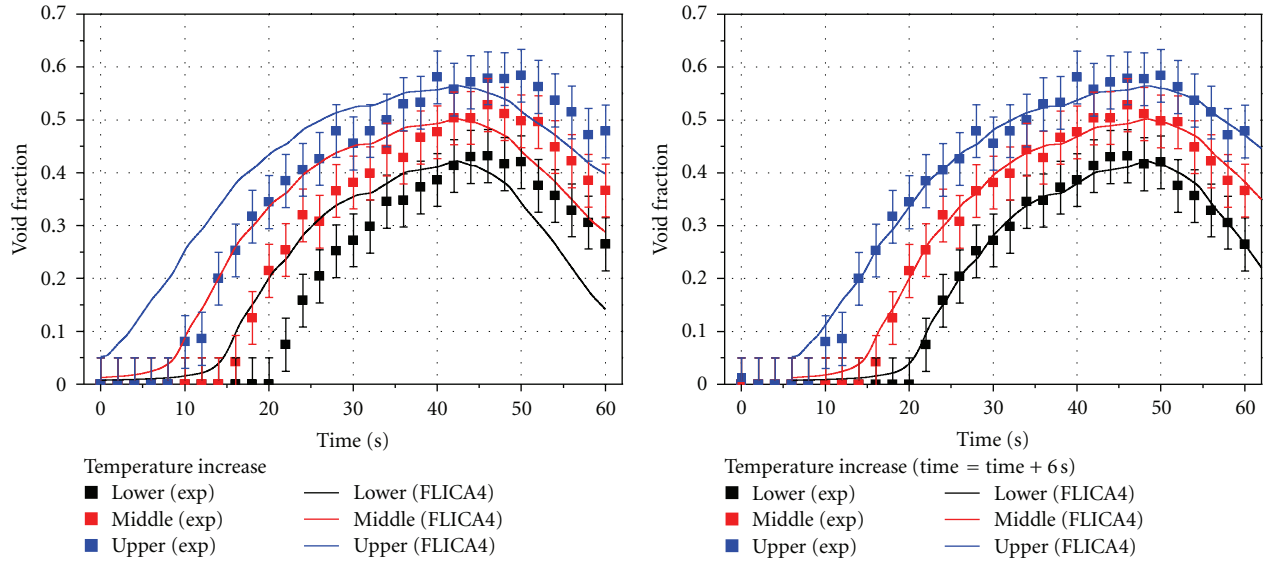
from case 5T produces consistent results for test cases 6T and 7T. Therefore, it can be reasonably concluded that the transient exercise was well predicted by FLICA4.

5. PSBT Benchmark Phase II: DNB Benchmark

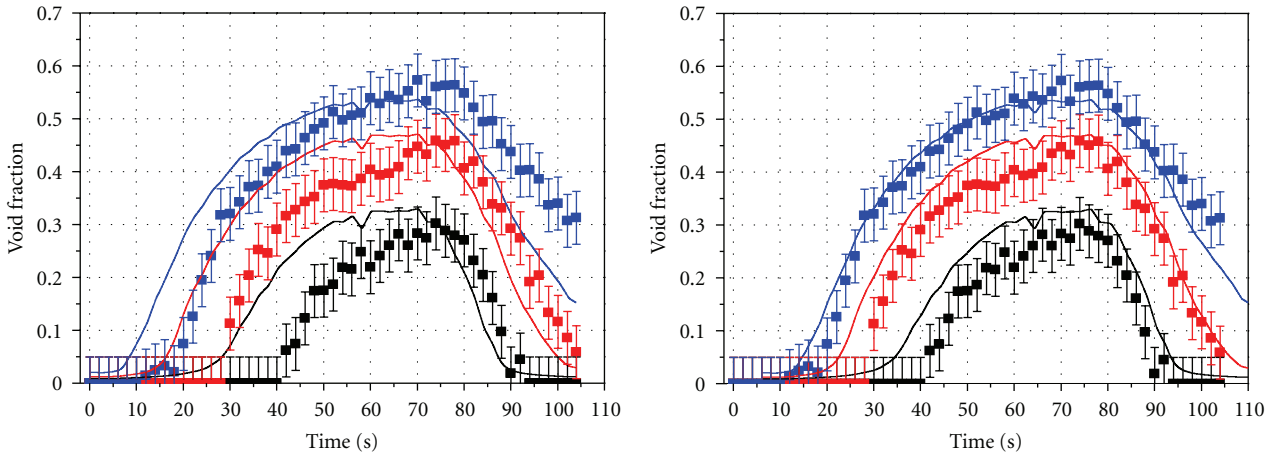
5.1. Description of Experiments. PSBT benchmark phase II aims at developing and assessing mechanistic models for DNB prediction. Both steady-state and transient DNB exercises are included in phase II and all the tests were carried out with bundles. In the experiments, the occurrence of DNB was detected by a sudden increase of the surface temperature measured by thermocouples attached to the

heater rods. The heating power was increased in fine steps to the vicinity of DNB power estimated by preliminary analysis and experience. In the experiment, a sudden surface temperature increase of more than 11°C confirmed the occurrence of DNB and the corresponding DNB power was defined as the power just before the sudden temperature increase.

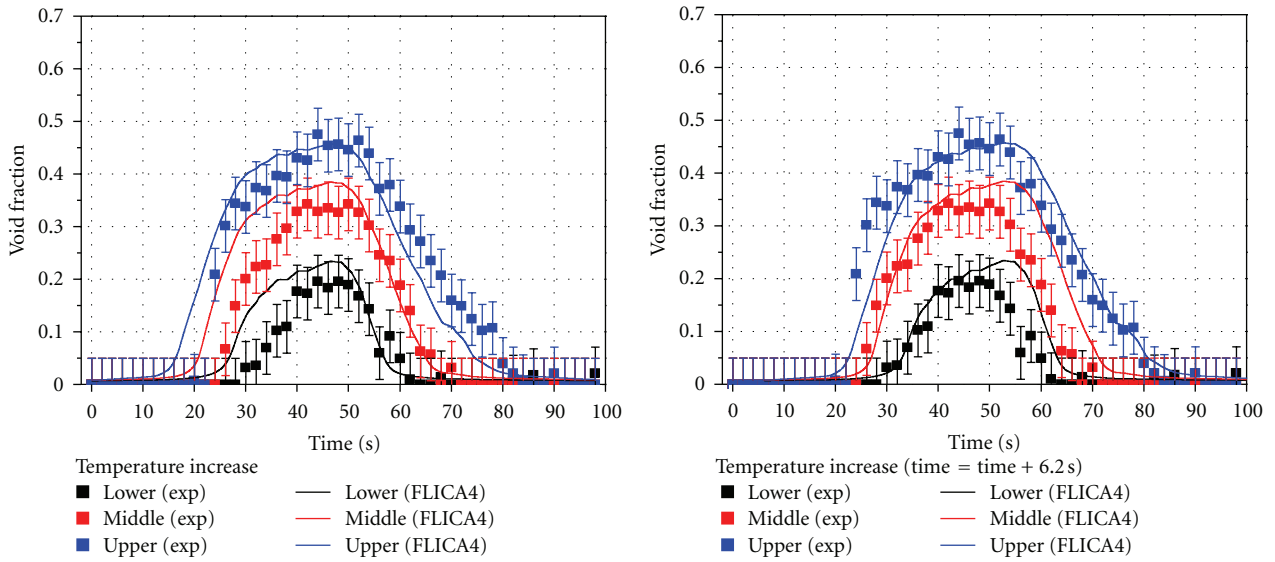
As listed in Table 8, eight different assemblies are employed for phase II. All assemblies consist of a 5 × 5 subset of a typical 17 × 17 fuel assembly type, except for assembly A3 which is 6 × 6. As for the assemblies A8 and A12, a thimble rod is located in the center of each assembly. Three different types of spacer are included in the test assembly and the loss coefficient for each spacer is the same as the one used



(a) 5T—temperature increase



(b) 6T—temperature increase



(c) 7T—temperature increase

FIGURE 17: Axial void fraction with original and modified time.

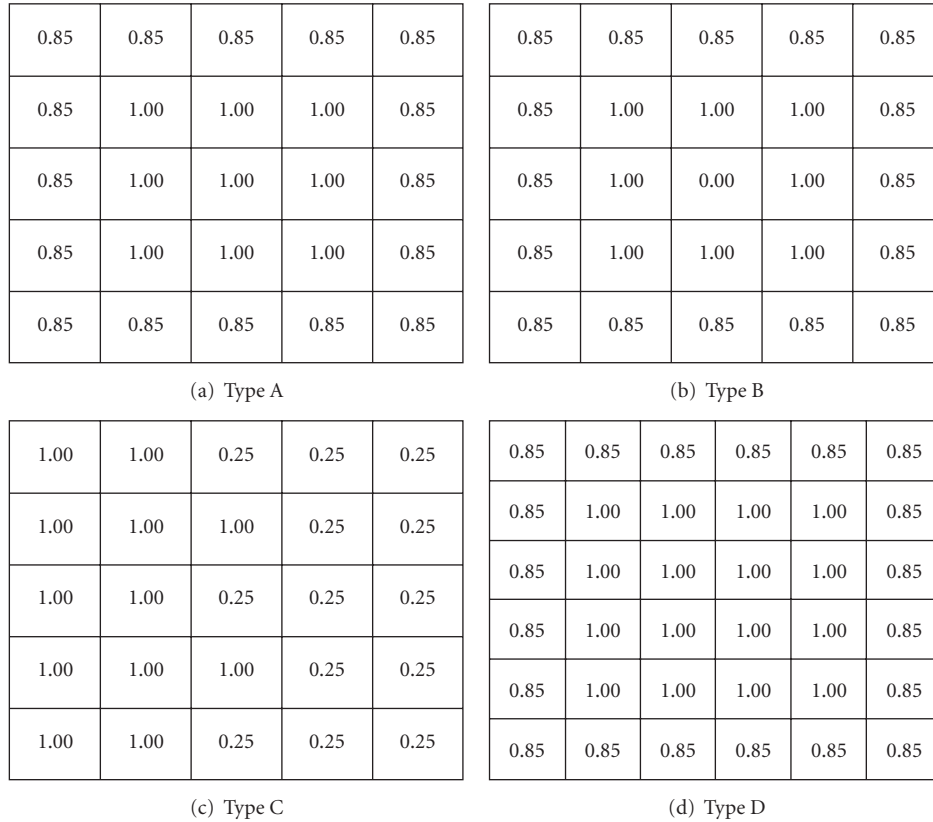


FIGURE 18: Radial power distribution [2].

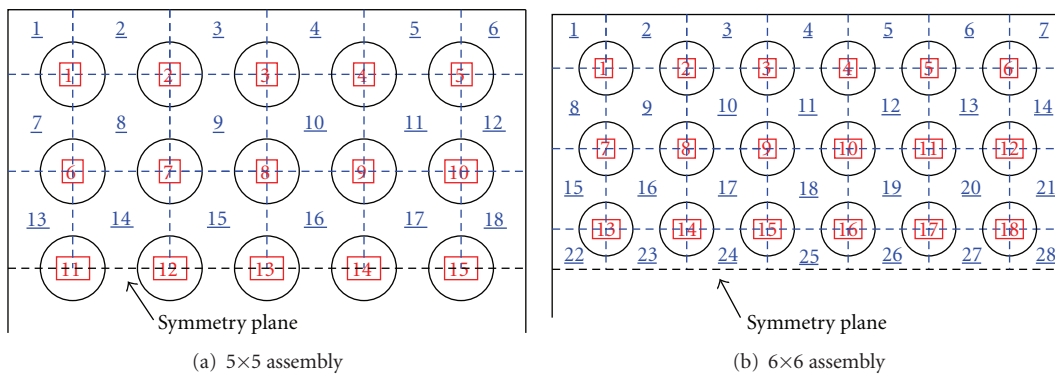


FIGURE 19: 1/2 symmetry model.

in phase I of the benchmark. Two axial power profiles are considered in this benchmark: uniform and cosine shapes, respectively. The cosine axial power profile used in phase II is the same as the one used in phase I. In total four radial power distributions are employed in this exercise, as depicted in Figure 18.

5.2. *Thermal Hydraulic Model.* FLICA4 is employed for the analyses of PSBT benchmark phase II. Thermal hydraulic models for the FLICA4 calculations are generated on the basis of information on the geometry and the power distribution. Unlike in phase I, it was not always possible

to adopt 1/8 symmetry in the models for phase II due to the radial power distribution C, which allows implementing 1/2 symmetry only. Therefore, for consistency, all models have been generated by using a 1/2 symmetry, as depicted in Figure 19. The models were nodalized axially with 100 nodes.

The Chexal-Lellouche drift-flux model was employed and a value of $7.5E - 4$ was imposed for the reconcondensation coefficient, $KV0$. The multipliers for turbulent diffusivity and viscosity, K_t and M_t , were set to 0.01 based on the results from phase I. The pressure drop by the spacers was considered by means of the singular pressure drop model in FLICA4. In the FLICA4 analysis, the parameter used as

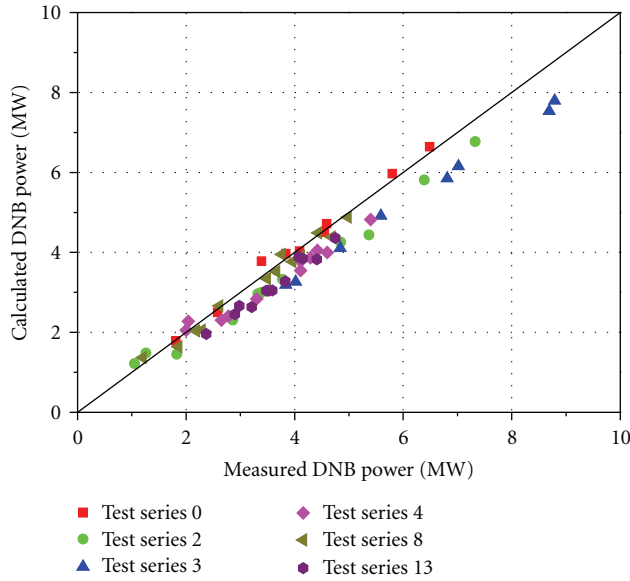


FIGURE 20: Results of steady-state DNB exercises.

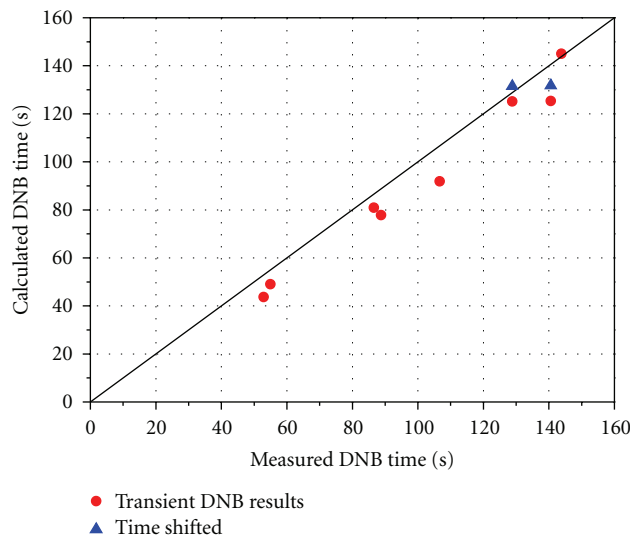


FIGURE 21: Results of transient DNB exercise.

indicator for the occurrence of DNB was the minimum DNB ratio (MDNBR), defined as the ratio of the critical heat flux (CHF) predicted by a given correlation to the heat flux at each axial node of each heater rod. DNB is confirmed when the MDNBR is less than unity. For the CHF prediction, the W3 correlation [27] and the Groeneveld look-up table [28] with a correction factor for the diameter as given in (2) were employed,

$$\dot{q}_{\text{CHF}}'' = f(P, G, X) \cdot \sqrt{\frac{D_{8\text{mm}}}{D_{\text{ch}}}}, \quad (2)$$

However, due to limitation in the application ranges, the W3 correlation could not be used for all the cases in phase II. Sensitivity studies carried out with both correlations, which will be discussed in more detail in Section 5.5, indicate that

the DNB power predicted by the Groeneveld look-up table is slightly lower than the one from the W3 correlation. However, no significant discrepancy was observed. Considering robustness and conservatism in the analysis, it was decided to retain the Groeneveld look-up table for the phase II DNB analysis.

5.3. Results for Steady-State DNB Tests. Selected cases from the test series highlighted in Table 9 are analyzed for benchmark purpose. The results from all the calculations are plotted in Figure 20. In general, FLICA4 predicts lower DNB powers with respect to experimental data, that is, the results are conservative. The same trend was observed from most of the other participating organizations [29]. The mean absolute error of the DNB power prediction by FLICA4 is 10.1%. Consequently, a comparison with the results obtained by other participants indicates that FLICA4 predicts the DNB power slightly more conservatively but not less accurately than other state-of-the-art subchannel analysis codes.

5.4. Results for Transient DNB Tests. The transient DNB benchmark was conducted for test series 11T and 12T, which include four transient scenarios in each test as indicated in Table 10, a power increase, a flow reduction, a depressurization, and a temperature increase, respectively. The parameter of interest in this benchmark exercise is the time of DNB occurrence.

Results from the transient DNB benchmark exercise are depicted in Figure 21. The plot includes the calculated times of DNB which were shifted by 6.5 sec and 6.3 sec for the temperature increase transients of test series 11T and 12T, respectively, in order to take into account the location of the inlet temperature measurement and the mass flow rate of each test series, as done for the transient void fraction benchmark. The results indicate that FLICA4 predicts DNB earlier than in the experiment. This is consistent with the results from the steady-state DNB benchmark where lower DNB power is predicted. A comparison with the preliminary results by other participants [30] where the same earlier DNB occurrence was predicted indicates that FLICA4 produces acceptable results also for transient DNB calculations.

5.5. Assessment of CHF Models in FLICA4. FLICA4 includes three models to predict the CHF: the W3 correlation, the Groeneveld look-up table, and the SUDO correlation [31]. However, since the SUDO correlation was developed for rectangular channel, an assessment of this correlation is not conducted in this analysis.

The W3 correlation is one of the most widely used correlations for evaluation of DNB in PWRs and it is applicable to circular, rectangular, and rod bundle geometries. The correlation has been developed for axially uniform heat flux, with a correction factor for nonuniform flux distribution. In addition, local spacer effects can be taken into account by specific correction factors [32].

The Groeneveld look-up table was developed jointly by AECL (Canada) and IPPE (Russia) and has a very wide range of applications. Compared against the combined AECL-IPPE

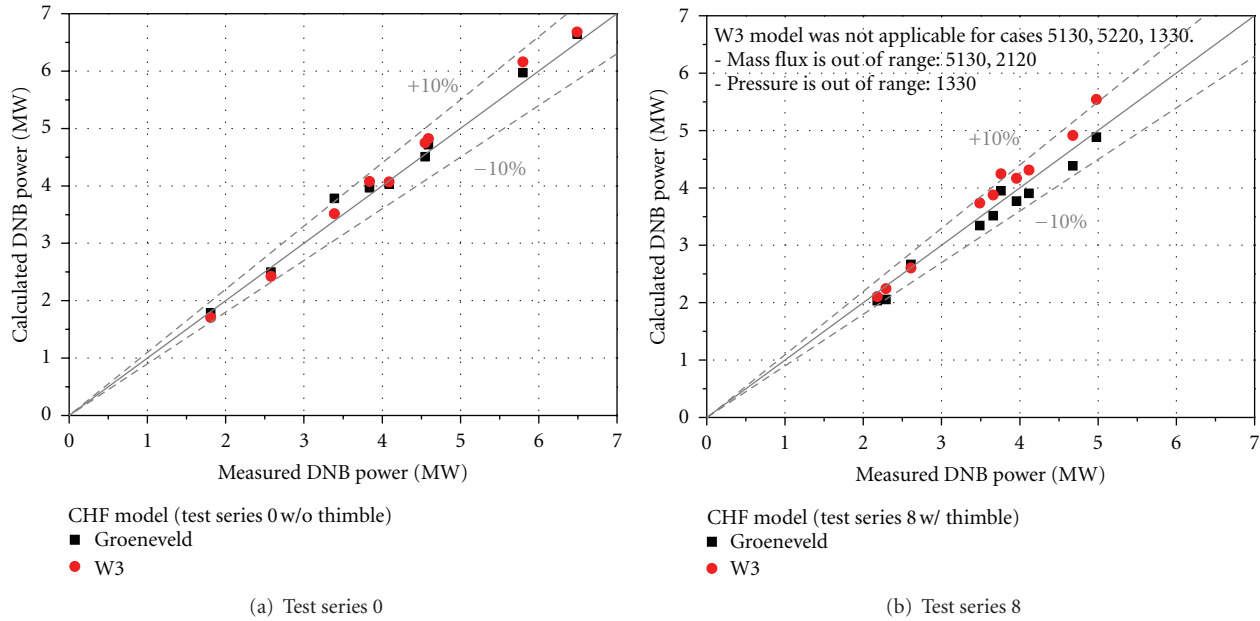


FIGURE 22: DNB Results with different CHF models.

CHF database, it is known that the Groeneveld look-up table can predict the CHF data with an overall root-mean-square (RMS) error of 7.82%.

Selected cases from test series 0 and 8 of the benchmark are employed to assess the two CHF models. Each test series represents tests with or without a guide thimble at the center. The calculation results presented in Figure 22 indicate that, in general, the W3 correlation predicts slightly higher DNB power than the Groeneveld look-up table, that is the Groeneveld correlation produces more conservative results than the W3 correlation. The RMS errors are 5.2% and 6.1% for analyses with the Groeneveld look-up table and the W3 correlation, respectively. In addition, due to the limitations in the range of applicability, 3 out of 13 cases in test series 8 could not be analyzed with the W3 correlation. Therefore, considering all together the accuracy, the conservatism, and the range of applicability, the Groeneveld look-up table was deemed the most appropriate to estimate the CHF for this benchmark.

6. Conclusion

In order to assess the range of validity and the accuracy of the subchannel analysis code FLICA4 and the commercial CFD code STAR-CD including a boiling model recently developed by CD-adapco, PSI has participated in an international benchmark based on the NUPEC PWR subchannel and bundle tests (PSBT) organized by OECD/NEA and US NRC. The tests have been analyzed by employing the US NRC code TRACE as well, in order to assess the applicability of TRACE to a subchannel analysis.

The results from the void distribution benchmark indicate that a reasonable agreement with the experimental data is obtained with FLICA4. The void fraction prediction by

STAR-CD shows no significant discrepancy for the single Subchannel experiments. It is worthwhile mentioning that all the benchmark cases were calculated without any tuning of the boiling model and numerical algorithms. This fact demonstrates that the boiling model used in STAR-CD is able to predict void fractions over a wide range of void fraction values with acceptable accuracy. TRACE instead tends to overpredict the void fraction, especially for values lower than 40%. The analysis of the axial void fraction profile reveals that overprediction by TRACE is caused by an earlier increase of the void fraction along the axis of the channel, pointing out the necessity of additional assessments for the subcooled boiling model and bulk condensation model currently implemented in the TRACE code.

The DNB benchmark exercises have been analyzed with FLICA4 only. The steady-state benchmark exercise results indicate that FLICA4 slightly underpredict the DNB power. However, considering the accuracy of Groeneveld look-up table and the uncertainties in the experimental data, it can be concluded that the prediction of the DNB power by FLICA4 is acceptable and furthermore conservative. The transient DNB prediction reveals that FLICA4 predicts DNB earlier than in the experiments, which is consistent with the result from the steady-state DNB benchmark. In addition, an assessment of the CHF models of FLICA4 has been carried out by using the benchmark data. It is found that the Groeneveld look-up table predicts more conservative DNB powers with higher accuracy than the W3 correlation.

Acknowledgments

The authors would like to thank the benchmark organizers and colleagues participating in the PSBT benchmark for the cooperation and meaningful discussion. This

work has been performed within the STARS project (<http://stars.web.psi.ch/>) of Paul Scherrer Institute and was partially funded by the Swiss Federal Nuclear Safety Inspectorate (ENSI).

References

- [1] B. Neykov, A. Aydogan, L. Hochreiter et al., “NUPEC BWR full-size fine-mesh bundle test (BFBT) Benchmark, volume I: specifications,” NEA/NSC/DOC(2005)5, 2006.
- [2] A. Rubin, A. Schoedel, M. Avramova, H. Utsuno, S. Bajorek, and A. Velazquez-Lozada, “OECD/NRC benchmark based on NUPEC PWR subchannel and bundle tests (PSBT), volume I: experimental database and final problem specifications,” NEA/NSC/DOC(2010)1, 2010.
- [3] I. Toumi, A. Bergeron, D. Gallo, E. Royer, and D. Caruge, “FLICA-4: a three-dimensional two-phase flow computer code with advanced numerical methods for nuclear applications,” *Nuclear Engineering and Design*, vol. 200, no. 1, pp. 139–155, 2000.
- [4] CD-adapco, *CCM User Guide: STAR-CD Version 4.06*, 2008.
- [5] US NRC, *TRACE V5.0 Theory Manual: Field Equations, Solution Methods, and Physical Models*, U.S. Nuclear Regulatory Commission, Washington, DC, USA, 2009.
- [6] B. Chexal, G. Lellouche, J. Horowitz, and J. Healzer, “A void fraction correlation for generalized applications,” *Progress in Nuclear Energy*, vol. 27, no. 4, pp. 255–295, 1992.
- [7] T. Kim, “Collaboration with CEA saclay for OECD-NEA PSBT benchmark—single channel benchmark with FLICA4,” PSI Memorandum SB-RND-ACT-003-10.002, 2010.
- [8] F. W. Dittus and L. M. K. Boelter, “Heat transfer in automobile radiators of the tubular type,” *University of California Publications in Engineering*, vol. 2, no. 13, pp. 443–461, 1930, Reprinted in *International Communications in Heat and Mass Transfer*, vol. 12, pp. 3–22, 1985.
- [9] CEA, *FLICA4 User Guide – Reference Manual of Modules and Procedures*, 2009.
- [10] P. Raymond, B. Spindler, and R. Lenain, “Pressurized water reactor thermal-hydraulic core analysis with the FLICA computer code,” *Nuclear Engineering and Design*, vol. 124, no. 3, pp. 299–313, 1990.
- [11] F. P. Incropera and D. P. Dewitt, *Introduction to Heat Transfer*, John Wiley & Sons, New York, NY, USA, 3rd edition, 1996.
- [12] L. Friedel, “Improved friction pressure drop correlations for horizontal and vertical two phase pipe flow,” in *Proceedings of the European Two Phase Flow Group Meeting*, Ispra, Italy, June 1979.
- [13] V. Gnielinski, “New equations flow regime heat and mass transfer in turbulent pipe and channel flow,” *International Chemical Engineering*, vol. 16, pp. 359–368, 1976.
- [14] M. A. Aggour, M. M. Vijay, and G. E. Sims, “A correlation of mean heat transfer coefficients for two-phase two-component flow in a vertical tube,” in *Proceedings of the 7th International Heat Transfer Conference*, vol. 5, pp. 367–372, 1982.
- [15] K. S. Rezkallah and G. E. Sims, “An examination of correlations of mean heat transfer coefficients in two-phase two-component flow in vertical tubes,” *AIChE Symposium Series*, vol. 83, no. 257, pp. 109–114, 1987.
- [16] R. T. Lahey, “A mechanistic subcooled boiling model,” in *Proceedings of the 6th International Heat Transfer Conference*, vol. 1, pp. 293–297, Toronto, Canada, 1978.
- [17] S. W. Churchill, “Friction factor equations spans all fluid-flow regimes,” *Chemical Engineering*, vol. 84, no. 24, pp. 91–92, 1977.
- [18] E. Ranz and W. R. Marshall, “Evaporation from Droplets: part I and II,” *Chemical Engineering Progress*, vol. 48, pp. 141–180, 1952.
- [19] M. Ishii and K. Mishima, “Study of two-fluid model and interfacial area,” Argonne National Laboratory Report ANL-80-111 (NUREG/CR-1873), 1980.
- [20] R. T. Lahey and F. J. Moody, *The Thermal-Hydraulics of a Boiling Water Nuclear Reactor*, ANS Monograph, 1977.
- [21] D. B. Spalding, “The calculation of free-convection phenomena in gas—liquid mixtures,” in *Heat Transfer and Turbulent Buoyant Convection Studies and Applications for Natural Environment, Buildings and Engineering Systems*, D. B. Spalding and N. Afgan, Eds., vol. 2, pp. 569–586, Hemisphere, New York, NY, USA, 1976.
- [22] D. B. Spalding, “Numerical computation of multi-phase fluid flow and heat transfer,” in *Recent Advances in Numerical Methods in Fluids*, C. Taylor and K. Morgan, Eds., vol. 1, pp. 139–168, Pineridge Press, Swansea, UK, 1980.
- [23] D. B. Spalding, “Developments in the IPSA procedure for numerical computation of multi-phase flow phenomena with interphase slip, unequal temperatures, etc,” in *Numerical Methodologies in Heat Transfer*, T. M. Shih, Ed., Proceedings of the Second National Symposium, pp. 421–436, Hemisphere, New York, NY, USA, 1983.
- [24] N. Kurul and M. Z. Podowski, “Multi-dimensional effects in subcooled boiling,” in *Proceedings of the 9th Heat Transfer Conference*, Jerusalem, Israel, 1990.
- [25] T. Hibiki and M. Ishii, “One-dimensional drift-flux model for two-phase flow in a large diameter pipe,” *International Journal of Heat and Mass Transfer*, vol. 46, no. 10, pp. 1773–1790, 2003.
- [26] G. Kocamustafaogullari, “Pressure dependence of bubble departure diameter for water,” *International Communications in Heat and Mass Transfer*, vol. 10, no. 6, pp. 501–509, 1983.
- [27] L. S. Tong, “Heat transfer in water-cooled nuclear reactors,” *Nuclear Engineering and Design*, vol. 6, no. 4, pp. 301–324, 1967.
- [28] D. C. Groeneveld, L. K. H. Leung, P. L. Kirillov et al., “The 1995 look-up table for critical heat flux in tubes,” *Nuclear Engineering and Design*, vol. 163, no. 1–2, pp. 1–23, 1996.
- [29] A. Rubin, “Comparative analysis of submitted participants’ preliminary results for exercise II-2,” in *Proceedings of the 2nd PSBT Workshop*, Stockholm, Sweden, April 2011.
- [30] A. Rubin, “Comparative analysis of submitted participants’ preliminary results for exercise II-3,” in *Proceedings of the 2nd PSBT Workshop*, Stockholm, Sweden, April 2011.
- [31] Y. Sudo, K. Miyata, H. Ikawa, M. Kaminaga, and M. Ohkawara, “Experimental study of differences in DNB heat flux between upflow and downflow in vertical rectangular channel,” *Journal of Nuclear Science and Technology*, vol. 22, no. 8, pp. 604–618, 1985.
- [32] N. E. Todreas and M. S. Kazimi, *Nuclear Systems: Vol. 1, Thermal Hydraulic Fundamentals*, Hemisphere, New York, NY, USA, 1990.

Research Article

Analysis of the NUPEC PSBT Tests with FLICA-OVAP

Matteo Bucci and Philippe Fillion

CEA, DEN, DM2S/STMF, 91191 Gif-sur-Yvette, France

Correspondence should be addressed to Philippe Fillion, philippe.fillion@cea.fr

Received 2 May 2012; Accepted 2 July 2012

Academic Editor: Alessandro Petrucci

Copyright © 2012 M. Bucci and P. Fillion. This is an open access article distributed under the Creative Commons Attribution License, which permits unrestricted use, distribution, and reproduction in any medium, provided the original work is properly cited.

This paper discusses the results of a computational activity devoted to the prediction of two-phase flows in subchannels and in rod bundles. The capabilities of the FLICA-OVAP code have been tested against an extensive experimental database made available by the Japanese Nuclear Power Energy Corporation (NUPEC) in the frame of the PWR subchannel and bundle tests (PSBT) international benchmark promoted by OECD and NRC. The experimental tests herein addressed involve void fraction distributions and boiling crisis phenomena in rod bundles with uniform and nonuniform heat flux conditions. Both steady-state and transient scenarios have been addressed, including power increase, flow reduction, temperature increase, and depressurization, representative of PWR thermal-hydraulics conditions. After a brief description of the main features of FLICA-OVAP, the relevant physical models available within the code are detailed. Results obtained in the different tests included in the PSBT void distribution and DNB benchmarks are therefore reported. The relevant role of selected physical models is discussed.

1. Introduction

Based on NUPEC PWR subchannel and bundle tests (PSBT), an international benchmark has been promoted by OECD and NRC and has been coordinated by Penn State University [1]. The aim of this benchmark is to encourage advancement and assessment of numerical models in subchannel analysis of fluid flow in rod bundles, which has very important relevance for the nuclear reactor safety margin evaluation. An important database of void fraction and critical heat flux measurements in steady-state and transient conditions has been carried out by NUPEC on a prototypical PWR rod bundle. Different types of subchannel or rod bundle geometries and a wide range of flow conditions at high pressure have been investigated (see Table 1) allowing the assessment of the key models and correlations in these conditions.

The Service de Thermohydraulique et de Mécanique des fluides (STMF) at the Commissariat à l'Énergie Atomique et aux Énergies Alternatives (CEA), France, has been involved in the PSBT benchmark performing calculations with the FLICA-OVAP code [2]. FLICA-OVAP is an advanced two-phase flow thermal-hydraulics code based on a full 3D subchannel approach. It is designed to analyze flows in light

water reactors cores such as PWRs, BWRs, and experimental reactors. To provide a relevant answer to different core concepts and multiple industrial applications, several models coexist in the FLICA-OVAP platform: the homogeneous equilibrium model, the four equations drift flux model, the two-fluid model, and finally, a general multifield model, with a variable number of fields for both vapor and liquid phases. For each model, an adapted set of closure laws is proposed concerning heat and mass transfer, interfacial and wall forces, and turbulence.

2. The FLICA-OVAP Code

A detailed description of the FLICA-OVAP code can be found in [3]. In this section we give a summary description of the four-equation drift flux model and the relevant closure laws adopted in this analysis. Details of the models adopted to predict boiling crisis in the PSBT benchmark will be also presented extensively.

2.1. The Four-Equation Drift Flux Model. The four balance equations describing two-phase flows in the drift flux model are, respectively, the mixture mass balance equation, the

TABLE 1: Operating conditions of the NUPEC PWR test facility.

Quantity	Range
Pressure	4.9–16.6 MPa
Mass flux	550–4150 kg/m ² /s
Inlet coolant temperature	140–345 °C
Wall heat flux	0.37–1.86 MW/m ²

mixture momentum balance equation, the mixture energy balance equation, and the steam mass balance equation (porosities are omitted for the sake of simplicity):

(i) *mixture mass conservation*

$$\frac{\partial}{\partial t} \left(\sum_{k=v,l} \alpha_k \rho_k \right) + \nabla \cdot \left(\sum_{k=v,l} \alpha_k \rho_k \mathbf{u}_k \right) = 0, \quad (1)$$

where α_k , ρ_k , \mathbf{u}_k are the volume fraction, the density, and the velocity for the phase k .

(ii) *mixture momentum balance*

$$\begin{aligned} \frac{\partial}{\partial t} \left(\sum_{k=v,l} \alpha_k \rho_k \mathbf{u}_k \right) + \nabla \cdot \left(\sum_{k=v,l} \alpha_k \rho_k \mathbf{u}_k \otimes \mathbf{u}_k \right) \\ + \nabla P - \nabla \cdot \left(\sum_{k=v,l} \alpha_k \underline{\tau}_k \right) = \rho \mathbf{g} + \mathbf{F}_w, \end{aligned} \quad (2)$$

where P is the pressure, \mathbf{g} , the gravity, and \mathbf{F}_w , the friction forces. The tensor $\underline{\tau}_k$ represents the viscous and the Reynolds stress terms for the phase k . The mixture density ρ is defined as

$$\rho = \sum_{k=v,l} \alpha_k \rho_k. \quad (3)$$

(iii) *mixture energy balance*

$$\begin{aligned} \frac{\partial}{\partial t} \left(\sum_{k=v,l} \alpha_k \rho_k E_k \right) + \nabla \cdot \left(\sum_{k=v,l} \alpha_k \rho_k H_k \mathbf{u}_k \right) \\ - \nabla \cdot \left(\sum_{k=v,l} \alpha_k \mathbf{q}_k \right) = q_w + \rho \mathbf{g} \cdot \mathbf{u}, \end{aligned} \quad (4)$$

where E_k and H_k are the total energy and the total enthalpy of the phase k , \mathbf{q}_k includes molecular and turbulent heat fluxes, and q_w is the volumetric source term of thermal power.

(iv) *steam mass*

$$\frac{\partial}{\partial t} (\alpha_v \rho_v) + \nabla \cdot (\alpha_v \rho_v \mathbf{u}_v) - \nabla \cdot (K_c \nabla c) = \Gamma_v, \quad (5)$$

The model is closed by a drift flux correlation and a general equation of state with the assumption that, in presence of liquid, the vapor is in saturation conditions.

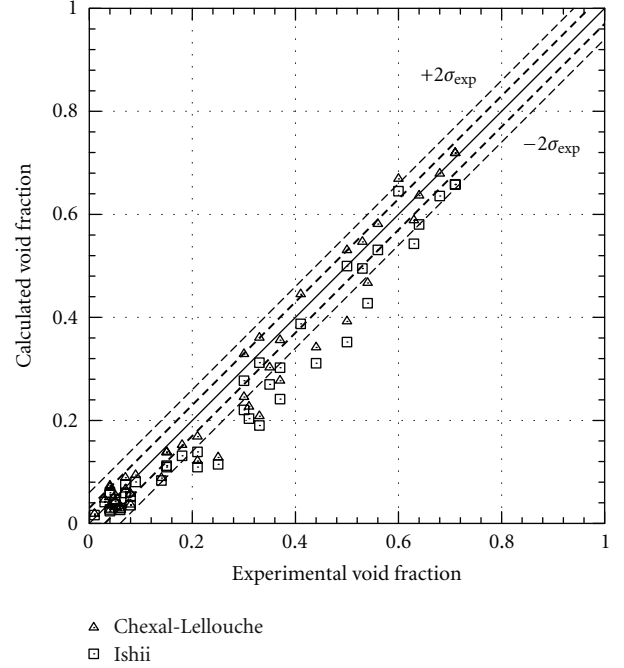


FIGURE 1: Comparison of void fractions predicted by the Chexal-Lellouche and the Ishii drift correlations against experimental data (subchannel S1 series).

2.2. *The Drift Flux Correlation.* FLICA-OVAP includes several Zuber-Findlay type correlations in order to estimate the relative velocity \mathbf{u}_r between the vapor velocity \mathbf{u}_v and the liquid velocity \mathbf{u}_l . The general form of these correlations is:

$$\mathbf{u}_v = C_0 \langle \mathbf{j} \rangle + \langle \langle \mathbf{v}_{g,j} \rangle \rangle = C_0 \langle \mathbf{j} \rangle + \langle \mathbf{V}_{g,j} \rangle, \quad (6)$$

where C_0 is the distribution parameter, $\langle \mathbf{j} \rangle = \alpha \mathbf{u}_v + (1-\alpha) \mathbf{u}_l$ is the area-averaged total volumetric flux, and $\mathbf{V}_{g,j}$ is the void-weighted area-averaged drift velocity. The Chexal-Lellouche correlation [4] and a correlation derived from Ishii [5] are implemented in the code. The Chexal-Lellouche correlation covers a large range of pressure, diameters, flows whereas the Ishii correlation, firstly established for bubbly, slug, and churn turbulent flow in adiabatic conditions, allows taking into account nucleate boiling on heated walls.

2.3. *Pressure Drop.* Friction forces \mathbf{F}_w are given by the sum of distributed \mathbf{F}_{fric} and singular pressure drops \mathbf{F}_{sing}

$$\mathbf{F}_w = \mathbf{F}_{\text{sing}} + \mathbf{F}_{\text{fric}}. \quad (7)$$

Singular friction due to spacer or mixing grids or other pressure drops are given by

$$\mathbf{F}_{\text{sing}} = -\frac{1}{2} \rho \underline{\mathbf{K}}_{\text{sing}} \|\mathbf{u}\| \mathbf{u}, \quad (8)$$

where $\underline{\mathbf{K}}_{\text{sing}}$ is an antisymmetric tensor. Distributed friction at walls is instead accounted for by

$$\mathbf{F}_{\text{fric}} = -\frac{1}{2D_h} \rho \begin{pmatrix} f_w^X & & \\ & f_w^Y & \\ & & f_w^Z \end{pmatrix}, \quad (9)$$

TABLE 2: Range of parameters for the Shah model covered by the NUPEC tests.

	D [m]	z/D	G (max/min)	x_i (max/min)	x_{crit} (max/min)
Series 0	0.009711	376.67	4944.4/1408.3	-0.062/-0.96	0.49/-0.20
Series 2	0.009711	376.67	4769.4/316.7	-0.053/-0.97	1.00/-0.06
Series 3	0.009989	366.21	4702.8/1361.1	-0.045/-0.87	0.58/-0.05
Series 4	0.009711	376.67	4725.0/566.7	-0.058/-0.98	1.00/0.06
Series 13	0.009711	376.67	3861.1/1361.1	-0.057/-0.50	0.50/0.20
Series 8	0.008867	412.55	4816.7/575.0	-0.058/-0.97	1.00/0.11

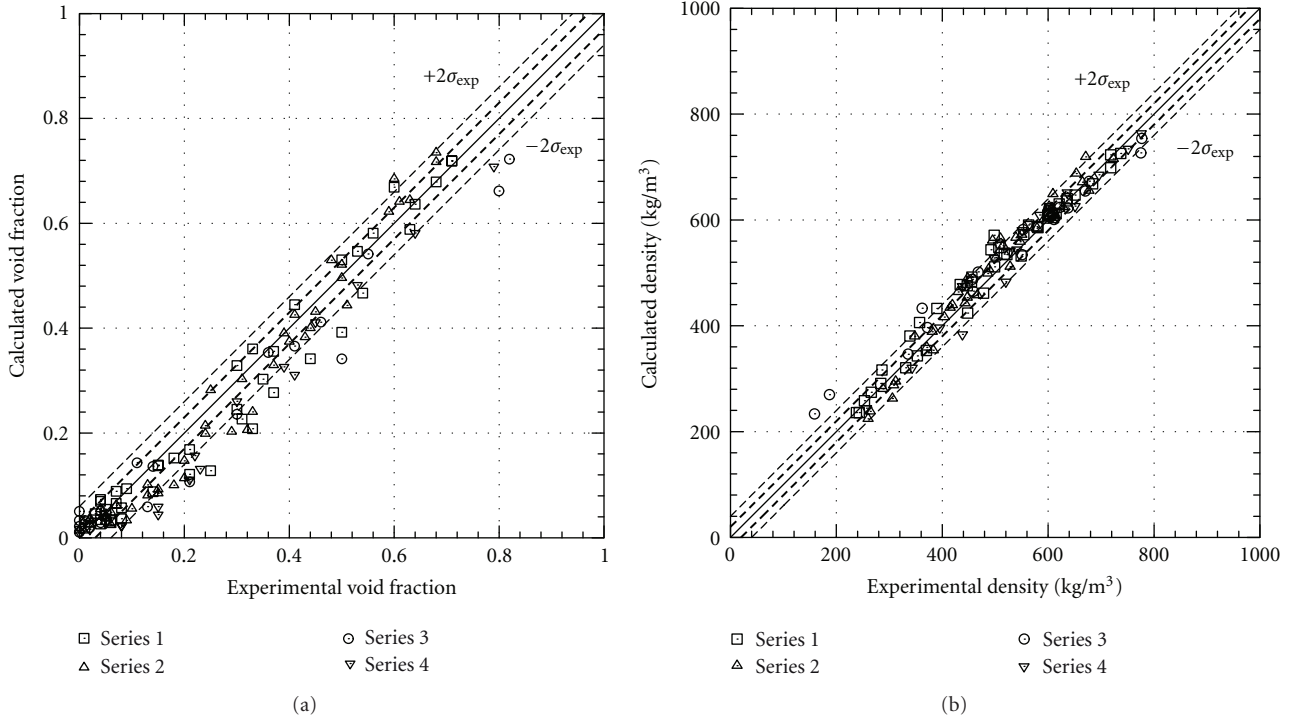


FIGURE 2: Calculated void fractions (a) and densities (b) versus experimental data for subchannel series 1 to 4 with the Chexal-Lellouche drift correlation.

where the different friction terms f_w are given by the product of the isothermal friction factor f_{iso} , the heating wall correction f_{heat} , and the two-phase flow multiplier $f_{2\phi}$. The isothermal friction factor in turbulent flows is given by

$$f_{iso} = 0.194Re^{-0.2}, \quad (10)$$

whereas the heating wall correction was estimated by an in-house model already used in the FLICA-4 code [6]. In this analysis the Chisholm correlation [7] was used for $f_{2\phi}$, given by

$$f_{2\phi} = 1 + (\phi_{10}^2 - 1) \left(1 + \frac{D_{heat}}{D_h} C_\phi q'' \right), \quad (11)$$

where ϕ_{10}^2 is the adiabatic two-phase frictional pressure drop multiplier, C_ϕ , a parameter accounting for heat flux, D_{heat} is the heated diameter, and q'' , the wall heat flux. In the runs of the PSBT benchmark C_ϕ was set equal to 0 and thus $f_{2\phi} = \phi_{10}^2$.

2.4. *Diffusion Effects.* To account for viscous and turbulent diffusion effects, the tensor $\underline{\tau}_k$ is introduced in the momentum equation, given by

$$\tau_k^{ij} = \mu_k \left(1 + M_{t,k}^{ij} \right) \left(\frac{\partial u_k^i}{\partial x_j} + \frac{\partial u_k^j}{\partial x_i} - \frac{2}{3} \sum_{l=x,y,z} \frac{\partial u_k^l}{\partial x_l} \delta_{ij} \right), \quad (12)$$

where $\mu_k M_{t,k}^{ij}$ is the turbulent viscosity, which is limited to the liquid phase. An anisotropic formulation is used for turbulent viscosity

$$M_{t,l}^{ij} = M_{t0}^{ij} (Re - Re_t)^{b_M} f_M(f_{2\phi}), \quad (13)$$

where $Re = GD_h/\mu_l$ is the Reynolds number, M_{t0}^{ij} , b_M , Re_t are parameters, and $f_M(f_{2\phi})$ is a function of the two-phase flow multiplier.

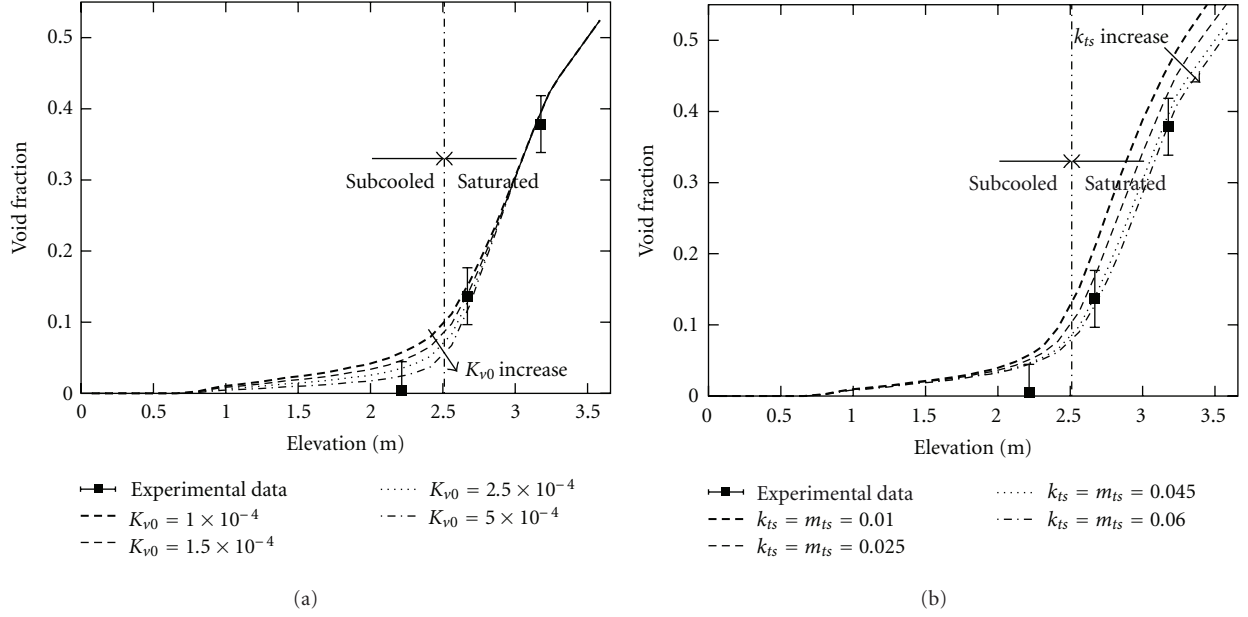


FIGURE 3: PSBT run 5.2442. Sensitivity analysis for K_{v0} (a), k_{ts} and m_{ts} (b) on the void fraction profile in the central subchannel.

TABLE 3: Choice of X and K for the Katto and Ohno model.

$R' < 0.15$	$R' > 0.15$
$X_1 < X_2 \quad X = X_1$	$X_1 < X_5 \quad X = X_1$
$\left. \begin{array}{l} X_1 > X_2 \\ X_2 < X_3 \end{array} \right\} X = X_2$	$\left. \begin{array}{l} X_1 > X_5 \\ X_5 > X_4 \end{array} \right\} X = X_5$
$\left. \begin{array}{l} X_1 > X_2 \\ X_2 > X_3 \end{array} \right\} X = X_3$	$\left. \begin{array}{l} X_1 > X_5 \\ X_5 < X_4 \end{array} \right\} X = X_4$
$K_1 > K_2 \quad K = K_1$	$K_1 > K_2 \quad K = K_1$
$K_1 < K_2 \quad K = K_2$	$\left. \begin{array}{l} K_1 < K_2 \\ K_2 < K_3 \end{array} \right\} K = K_2$
	$\left. \begin{array}{l} K_1 < K_2 \\ K_2 > K_3 \end{array} \right\} K = K_3$

Similarly, molecular and turbulent heat fluxes are given by

$$\sum_{k=v,l} \alpha_k \mathbf{q}_k = \frac{\lambda_l}{C_{Pl}} (\mathbf{1} + \mathbf{K}_{t,l}) \nabla h_x, \quad (14)$$

where $h_x = xh_v + (1-x)h_l$ is the flow enthalpy based on the flow quality x . The turbulent conductivity is given by

$$K_{t,l}^{ij} = K_{t0}^{ij} (\text{Re} - \text{Re}_t)^{b_K} f_K(f_{2\varphi}), \quad (15)$$

where K_{t0}^{ij} , b_K , Re_t are parameters and $f_K(f_{2\varphi})$ is a function of the two-phase flow multiplier. In this analysis, the value

of M_{t0}^{ij} and K_{t0}^{ij} was varied as a function of the axial position. Two different values have been adopted for each parameter depending whether the considered axial position was downward a mixing or a spacer grid.

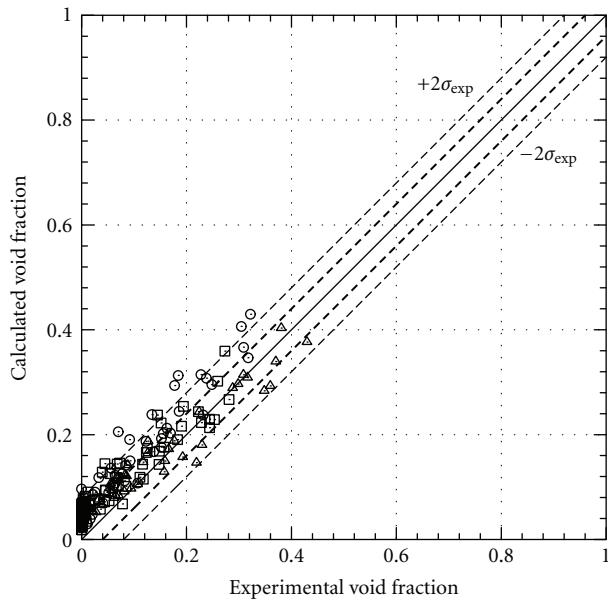
2.5. Wall Temperature. Wall temperatures are estimated on the basis of the bulk temperature and the heat transfer coefficient as

$$T_w = T_b + \frac{q''}{h} = T_b + \frac{q''}{\text{Nu} \lambda / D_h}. \quad (16)$$

The Nusselt number and the bulk temperature depend on the heat transfer regime. Four different regimes can be distinguished: single-phase convection heat transfer, subcooled nucleate boiling (SNB), saturated nucleate boiling (SANB) and post-critical-heat-flux (post-CHF) heat transfer. In single-phase heat transfer and SNB, the bulk temperature is equal to the liquid phase temperature, whereas in SANB it is equal to the saturation temperature. In forced convection conditions, the single-phase heat transfer coefficient is estimated by the Dittus-Boelter correlation. The onset of significant void (OSV), which is the transition between single-phase heat transfer and SNB can be predicted with the Forster and Grief correlation in low-pressure conditions or the Jens and Lottes correlation in high pressure conditions. In the present analysis, the Jens and Lottes correlation was used [8], which allows estimating the minimum wall superheat ΔT_{sat} demanded to achieve net vapor generation

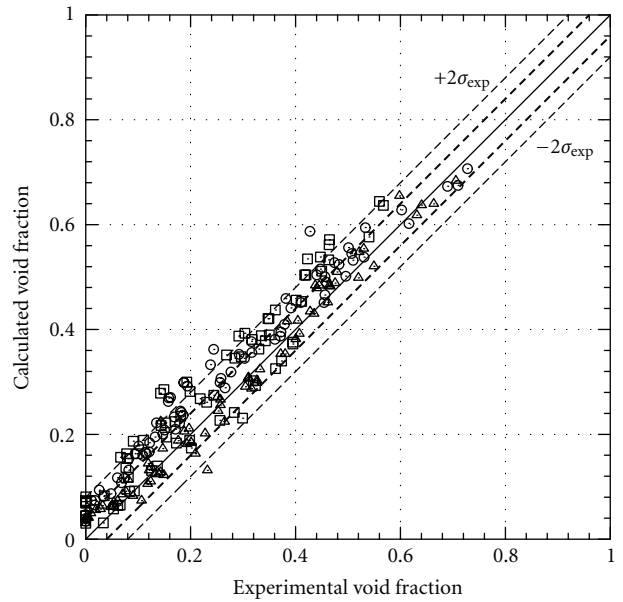
$$\Delta T_{\text{sat}} = 7.91 \left(\frac{q''}{10^4} \right)^{0.25} \exp \left(\frac{-P}{62 \cdot 10^5} \right). \quad (17)$$

Vapor generation starts when wall temperature estimated with Dittus-Boelter correlation exceeds this value. Finally, in post-CHF conditions, the choice of correlation depends



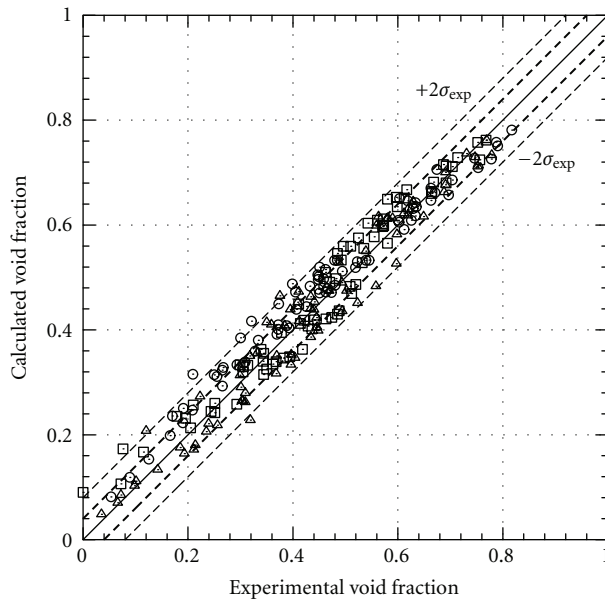
- Series 5
- △ Series 6
- Series 7

(a)



- Series 5
- △ Series 6
- Series 7

(b)



- Series 5
- △ Series 6
- Series 7

(c)

FIGURE 4: Steady-state rod bundle exercises. Comparison of calculated void fraction profiles in the central subchannel against experimental data: lower (a), medium (b), and upper (c) elevations.

TABLE 4: Range of parameters for the Katto and Ohno model covered by the NUPEC tests.

	Z [m]	D [m]	Z'	R' (max/min)	W' (max/min)
Series 0	3.658	0.009711	376.67	0.159185/0.070185	$1.28 \times 10^{-6}/3.97 \times 10^{-8}$
Series 2	3.658	0.009711	376.67	0.158337/0.030672	$5.04 \times 10^{-5}/4.13 \times 10^{-8}$
Series 3	3.658	0.009989	366.21	0.156657/0.070549	$1.33 \times 10^{-6}/4.28 \times 10^{-8}$
Series 4	3.658	0.009711	376.67	0.156156/0.031256	$1.35 \times 10^{-5}/4.17 \times 10^{-8}$
Series 13	3.658	0.009711	376.67	0.156156/0.096048	$6.76 \times 10^{-7}/8.28 \times 10^{-8}$
Series 8	3.658	0.008867	412.55	0.156323/0.031191	$1.48 \times 10^{-5}/3.99 \times 10^{-8}$

TABLE 5: Geometry and power shape of rod bundle test assembly (from [1]).

Item	Data			
	S1	S2	S3	S4
Assembly (subjected subchannel)				
Subchannel type	Center (typical)	Center (thimble)	Side	Corner
Number of heaters	4 × 1/4	3 × 1/4	2 × 1/4	1 × 1/4
Axial-heated length (mm)	1555	1555	1555	1555
Axial power shape	Uniform	Uniform	Uniform	Uniform
Number of runs	43	43	20	20

on the boiling characteristics, whether it is IAFB (inverted annular film boiling) or DFFB (dispersed flow film boiling).

2.6. *The Mass Transfer Term Γ_v .* The mass transfer term Γ_v appearing in the steam mass balance equation is given by the sum of two contributions: the vapor generation on walls Γ_{wv} and the mass transfer between the liquid and the vapor phase Γ_{vl} . In subcooled nucleate boiling, only a portion χ_v of the heat flux transferred from the wall to the mixture is used to vaporize the liquid phase, whereas the remaining part is used to heat the liquid phase up.

The vapor generation at walls is thus given by

$$\Gamma_{wv} = \frac{\chi_v q''}{h_{lv}} \frac{4}{D_{\text{heat}}}, \quad (18)$$

where χ_v is a function of the saturation temperature, the liquid phase temperature, and the wall superheat demanded to have subcooled nucleate boiling, given by

$$\chi_v = \frac{T_{w,lc} - T_{\text{sat}} - \Delta T_{\text{sat}}}{T_{w,lc} - T_l - \Delta T_{\text{sat}}}. \quad (19)$$

If the mixture is in saturation conditions, it is $\chi_v = 1$.

The mass transfer between the two phases Γ_{vl} is instead given by

$$\Gamma_{vl} = \frac{q_{vl}}{h_v - h_l}, \quad (20)$$

where h_v and h_l are vapor and liquid enthalpy and q_{vl} is the heat transferred between the two phases, given by

$$q_{vl} = K_{v0} \frac{G^2}{\log(1 + \text{Re}/\text{Re}_0)} f(P, \rho, \mu_l, \mathbf{u}, \mathbf{u}_r) \frac{\rho c(c^* - c)}{1 - c}, \quad (21)$$

where K_{v0} is a mass transfer parameter, G is the mass flux, $\text{Re} = GD_h/\mu_l$ is the Reynolds number, c^* , the equilibrium quality based on the mixture enthalpy $h = ch_v + (1 - c)h_l$, $f(P, \rho, \mu_l, \mathbf{u}, \mathbf{u}_r)$, a function depending on local conditions, D_h , the hydraulic diameter, and μ_l , the liquid viscosity. Re_0 is a parameter of the model.

3. Prediction of the Boiling Crisis

To predict boiling crisis conditions, several models are currently available within FLICA-OVAP. The W3 correlation [9] is appropriate to predict departure from nucleate boiling (DNB) phenomena of interest for pressurized water reactors. However, boiling crisis experienced in NUPEC tests can be close to dryout conditions. Two models have been therefore implemented in the code: the model of Shah [10] and the model of Katto and Ohno [11]. Both models can predict critical heat flux values for both DNB and dryout conditions. An accurate description of them is given in the following sections.

3.1. *The Shah Model.* The Shah model [10] consists of two separate correlations to determine the boiling number Bo , defined as

$$\text{Bo} = \frac{q''_{\text{CHF}}}{Gh_{lv}}. \quad (22)$$

The first correlation covers conditions where the critical heat flux depends on the upstream conditions, named UCC (upstream conditions correlation). The second, named LCC (local conditions correlation), depends only on local quantities.

TABLE 6: Geometry and power shape of rod bundle test assembly.

Item	Data										
	B5	B6	B7								
Assembly											
Rods array	5 × 5	5 × 5	5 × 5								
Number of heated rods	25	25	24								
Number of thimble rods	0	0	1								
Heated rod outer diameter (mm)	9.50	9.50	9.50								
Thimble rod outer diameter (mm)	—	—	12.24								
Heated rod pitch (mm)	12.60	12.60	12.60								
Axial-heated length (mm)	3658	3658	3658								
Flow channel inner width (mm)	64.9	64.9	64.9								
Radial power shape	Pattern A					Pattern B					
	0.85	0.85	0.85	0.85	0.85	0.85	0.85	0.85	0.85	0.85	
	0.85	1.00	1.00	1.00	0.85	0.85	1.00	1.00	1.00	0.85	
	0.85	1.00	1.00	1.00	0.85	0.85	1.00	0.00	1.00	0.85	
	0.85	1.00	1.00	1.00	0.85	0.85	1.00	1.00	1.00	0.85	
	0.85	0.85	0.85	0.85	0.85	0.85	0.85	0.85	0.85	0.85	
	Axial power shape	Uniform					Cosine				
	Number of mixing vane spacers	7					7				
	Number of no mixing vane spacers	2					2				
	Number of simple spacers	8					8				
Mixing vane spacer location (mm) (Loss coefficient 1.0 [1])	471, 925, 1378, 1832, 2285, 2739, 3247 from the beginning of the test section										
No mixing vane spacer location (mm) (Loss coefficient 0.7 [1])	2.5, 3755 from the beginning of the test section										
Simple spacer location (mm) (Loss coefficient 0.4 [1])	237, 698, 1151, 1605, 2059, 2512, 2993, 3501 from the beginning of the heated section										

TABLE 7: Test series for void fraction measurements.

Test series	Assembly	Test mode	
		Steady-state	Transient
5	B5	74 runs	4 runs
5T			
6	B6	74 runs	4 runs
6T			
7	B7	74 runs	4 runs
7T			
8	B5	31 runs	

TABLE 8: Average absolute errors in steady-state DNB tests (%).

	1D Shah	1D Katto and Ohno	3D Shah	3D Katto and Ohno
Series 0	15.5	10.9	13.7	5.6
Series 2	13.5	16.0	12.3	18.3
Series 3	8.5	10.9	10.0	15.0
Series 4	14.8	14.6	13.7	19.1
Series 8	11.5	15.6	14.3	12.9
Series 13	4.8	16.4	4.6	19.6

3.1.1. *The UCC Correlation.* The UCC correlation is

$$Bo = 0.124 \left(\frac{D}{z_{\text{eff}}} \right)^{0.89} \left(\frac{10^4}{Y} \right)^n (1 - x_{i,\text{eff}}), \quad (23)$$

with

$$Y = \left[\frac{GDC_{p_f}}{\lambda_f} \right] \left[\frac{G^2}{\rho_f^2 g D} \right]^{0.4} \left[\frac{\mu_f}{\mu_g} \right]^{0.6}. \quad (24)$$

In the previous equations, z_{eff} is the effective tube length and $x_{i,\text{eff}}$ is the effective inlet quality, defined as

$$\begin{aligned} x_{i,\text{eff}} &= x_i, & z_{\text{eff}} &= z_{\text{crit}}, & \text{for } x_i < 0, \\ x_{i,\text{eff}} &= 0, & z_{\text{eff}} &= z_{\text{sat}}, & \text{for } x_i > 0, \end{aligned} \quad (25)$$

where z_{crit} is the distance from the inlet section and the location of the boiling crisis, where the critical heat flux is

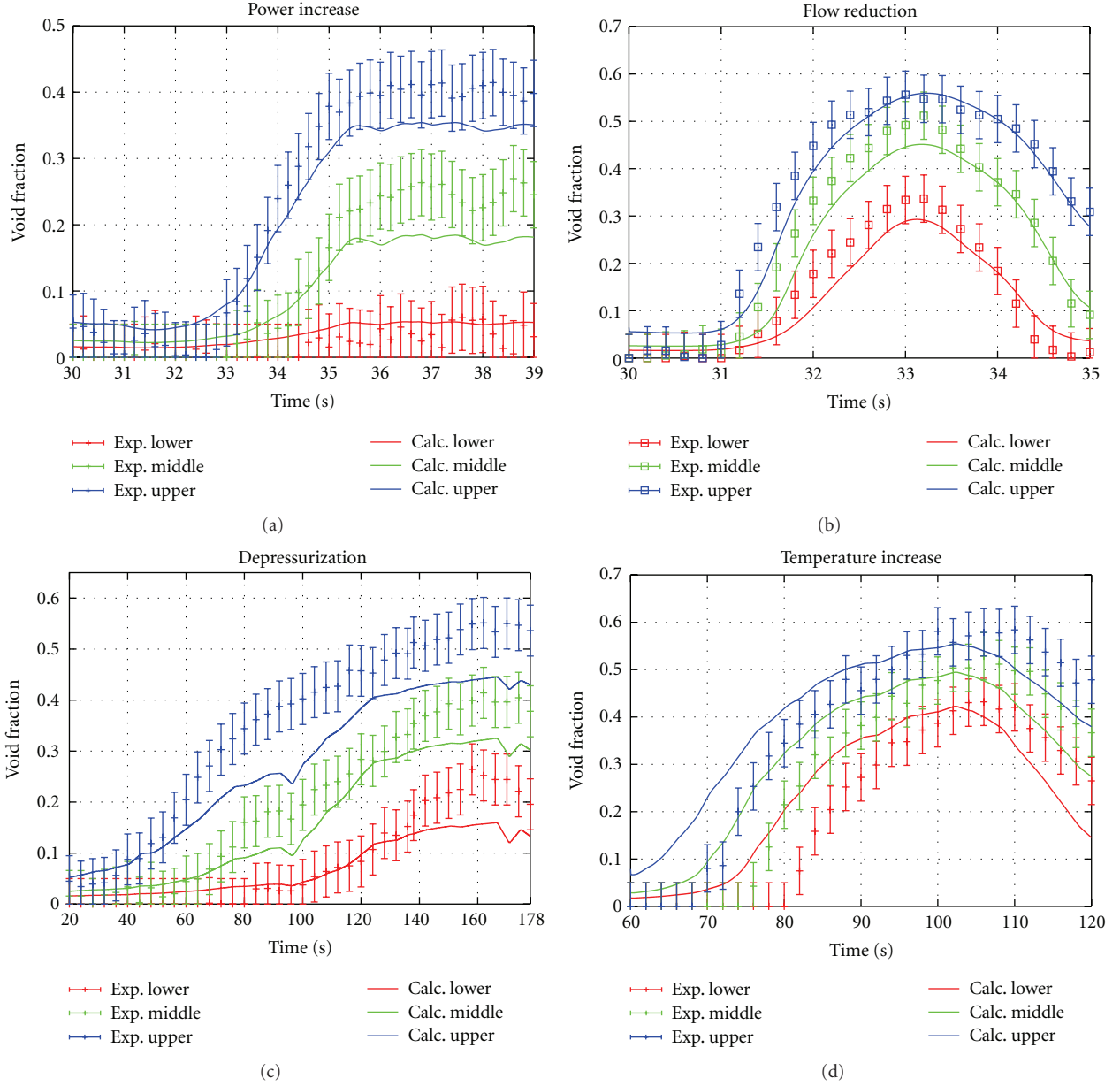


FIGURE 5: Transient T5: comparison between calculated and measured void fractions.

calculated, and z_{sat} is the boiling length, which for uniformly heated tubes is given by

$$\frac{z_{\text{sat}}}{D} = \frac{z_{\text{crit}}}{D} + \frac{x_i}{4\text{Bo}}. \quad (26)$$

For water flows, when $Y \leq 10^4$, $n = 0$, otherwise it is given by

$$n = \left(\frac{D}{z_{\text{eff}}} \right)^{0.54} \quad \text{for } Y \leq 10^6, \quad (27)$$

$$n = \frac{0.12}{(1 - X_{i,\text{eff}})^{0.5}} \quad \text{for } Y > 10^6.$$

3.1.2. *The LCC Correlation.* The LCC correlation is expressed by

$$\text{Bo} = F_E F_X \text{Bo}_0. \quad (28)$$

The entrance factor F_E is given by

$$F_E = 1.54 - 0.032 \left(\frac{z_{\text{crit}}}{D} \right). \quad (29)$$

When the previous correlation gives $F_E < 1$, it is used $F_E = 1$.

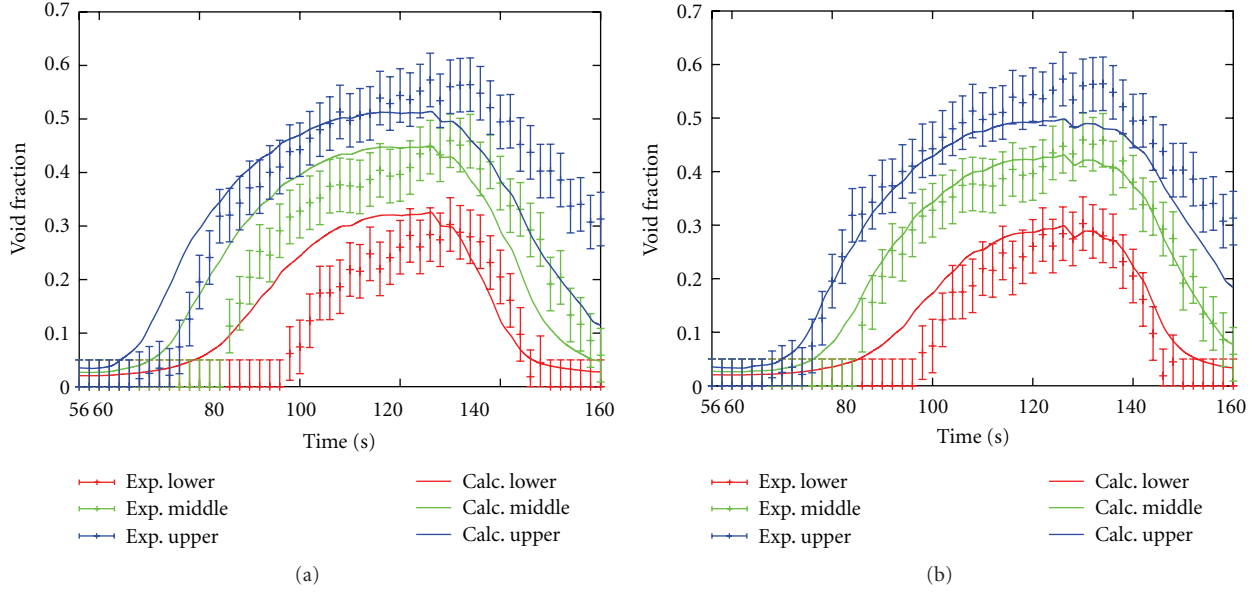


FIGURE 6: Temperature increase transient T6: original (a) and delayed (b) inlet temperature boundary conditions.

Bo_0 is defined as the boiling number at $x_{crit} = 0$, given by the maximum value obtained by the following equations

$$\begin{aligned} Bo_0 &= 15Y^{-0.612}, \\ Bo_0 &= 0.082Y^{-0.3}(1 + 1.45P_r^{4.03}), \\ Bo_0 &= 0.0024Y^{-0.105}(1 + 1.15P_r^{3.39}), \end{aligned} \quad (30)$$

where P_r is the reduced pressure given by $P_r = P/P_c$ where P_c is the critical pressure, that is 22.064 MPa for water. The value of F_X depends on the quality at the location of the boiling crisis x_{crit} . When $x_{crit} > 0$, the following equation is used

$$F_X = F_3 \left[1 + \frac{(F_3^{-0.29} - 1)(P_r - 0.6)}{0.35} \right]^c. \quad (31)$$

When $P_r > 0.6$, $c = 1$, otherwise $c = 0$. F_3 is instead given by

$$F_3 = \left(\frac{1.25 \times 10^5}{Y} \right)^{0.833x_{crit}}. \quad (32)$$

When $x_{crit} < 0$, F_X is given by

$$F_X = F_1 \left[1 - \frac{(1 - F_2)(P_r - 0.6)}{0.35} \right]^b. \quad (33)$$

As in the previous case, when $P_r > 0.6$, $b = 1$, otherwise $b = 0$. F_1 is given by

$$\begin{aligned} F_1 &= 1 + 0.0052(-x_{crit}^{0.88})Y^{0.41} \quad \text{for } Y \leq 1.4 \times 10^7, \\ F_1 &= 1 + 0.0052(-x_{crit}^{0.88})(1.4 \times 10^7)^{0.41} \quad \text{for } Y > 1.4 \times 10^7. \end{aligned} \quad (34)$$

Finally, F_2 is given by

$$\begin{aligned} F_2 &= F_1^{-0.42} \quad \text{for } F_1 \leq 4, \\ F_2 &= 0.55 \quad \text{for } F_1 > 4. \end{aligned} \quad (35)$$

3.1.3. Choice between UCC and LCC Correlation. For water, the UCC correlation is used when $Y \leq 10^6$. When $Y > 10^6$, the correlation giving the lower value of the boiling number Bo is used, with exception of cases where $z_{eff} > 160/P_r^{1.14}$, for which the UCC formulation is always adopted. In this analysis, the UCC correlation was used in all calculations.

3.1.4. Range Covered by the Shah Correlation. The Shah correlation was tested against 62 experimental databases with 23 different fluids, covering the following operating conditions:

- (i) $0.315 \times 10^{-3} < D < 37.5 \times 10^{-3} \text{ m}$,
- (ii) $1.3 < z/D < 940$,
- (iii) $4 < G < 29051 \text{ kg/m}^2/\text{s}$,
- (iv) $-4 < x_i < 0.85$,
- (v) $-2.6 < x_{crit} < 1$.

Only 15 tests over the whole database are not included in the range covered by the Shah correlation. In Table 2 the values of experimental quantities relevant for the Shah model are reported.

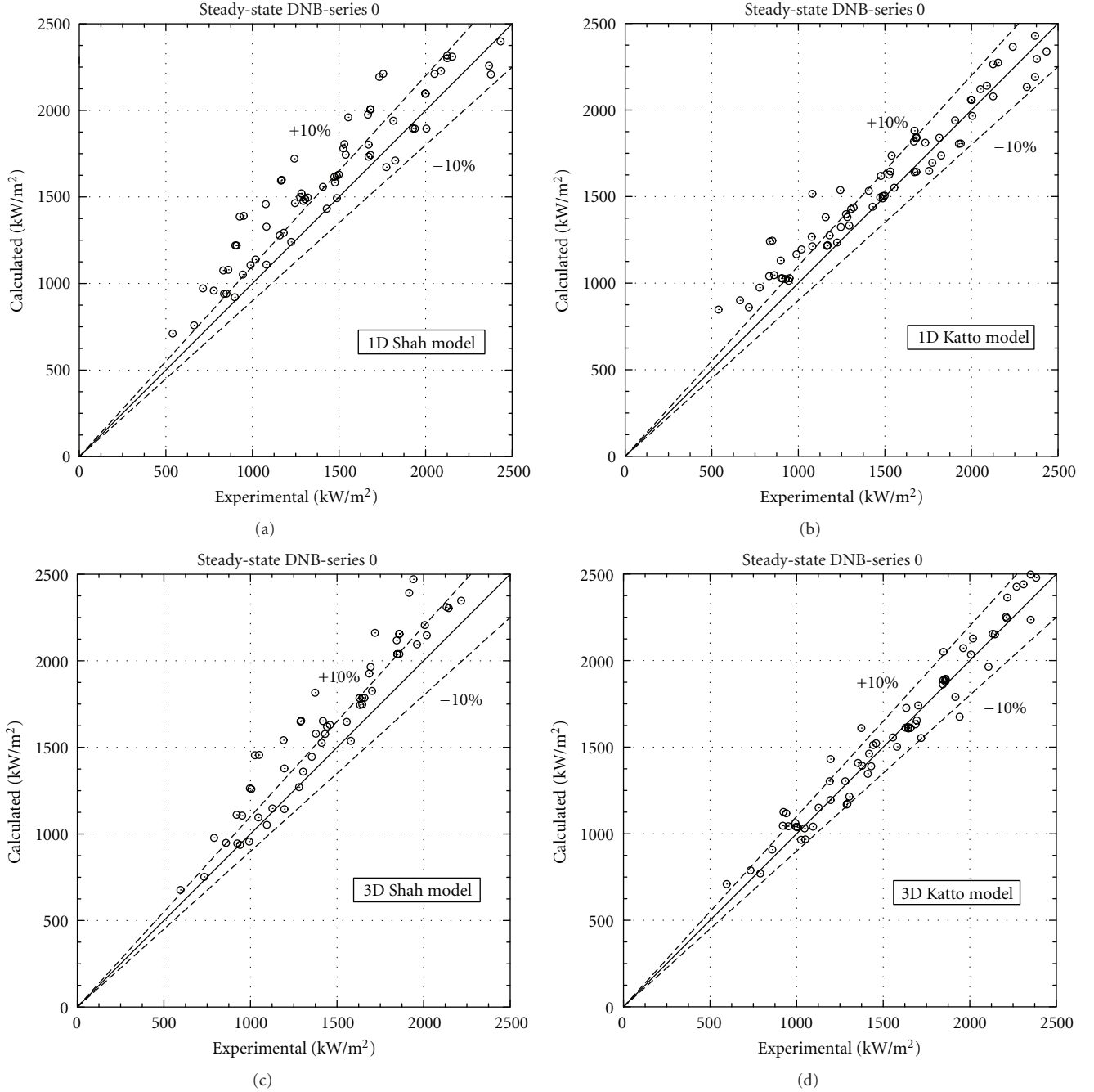


FIGURE 7: Computed versus experimental critical heat fluxes (Series 0).

3.2. *The Katto and Ohno Model.* The correlation of Katto and Ohno [11] provides the value of the critical heat flux as

$$q''_{\text{CHF}} = XG(h_{lv} + K\Delta h_{\text{sub},i}), \quad (36)$$

where $\Delta h_{\text{sub},i}$ is the subcooling inlet enthalpy. The terms X and K are functions of three-dimensionless terms:

$$\begin{aligned} Z' &= \frac{z}{D}, \\ R' &= \frac{\rho_g}{\rho_f}, \\ W' &= \frac{\sigma \rho_f}{(G^2 z)}. \end{aligned} \quad (37)$$

Five different values of X must be determined

$$\begin{aligned} X_1 &= \frac{CW'^{0.043}}{Z'}, \\ X_2 &= \frac{0.1R'^{0.133}W'^{0.333}}{1 + 0.0031Z'}, \\ X_3 &= \frac{0.098R'^{0.133}W'^{0.433}Z'^{0.27}}{1 + 0.0031Z'}, \\ X_4 &= \frac{0.0384R'^{0.6}W'^{0.173}}{1 + 0.28W'^{0.233}Z'}, \\ X_5 &= \frac{0.234R'^{0.513}W'^{0.433}Z'^{0.27}}{1 + 0.0031Z'}. \end{aligned} \quad (38)$$

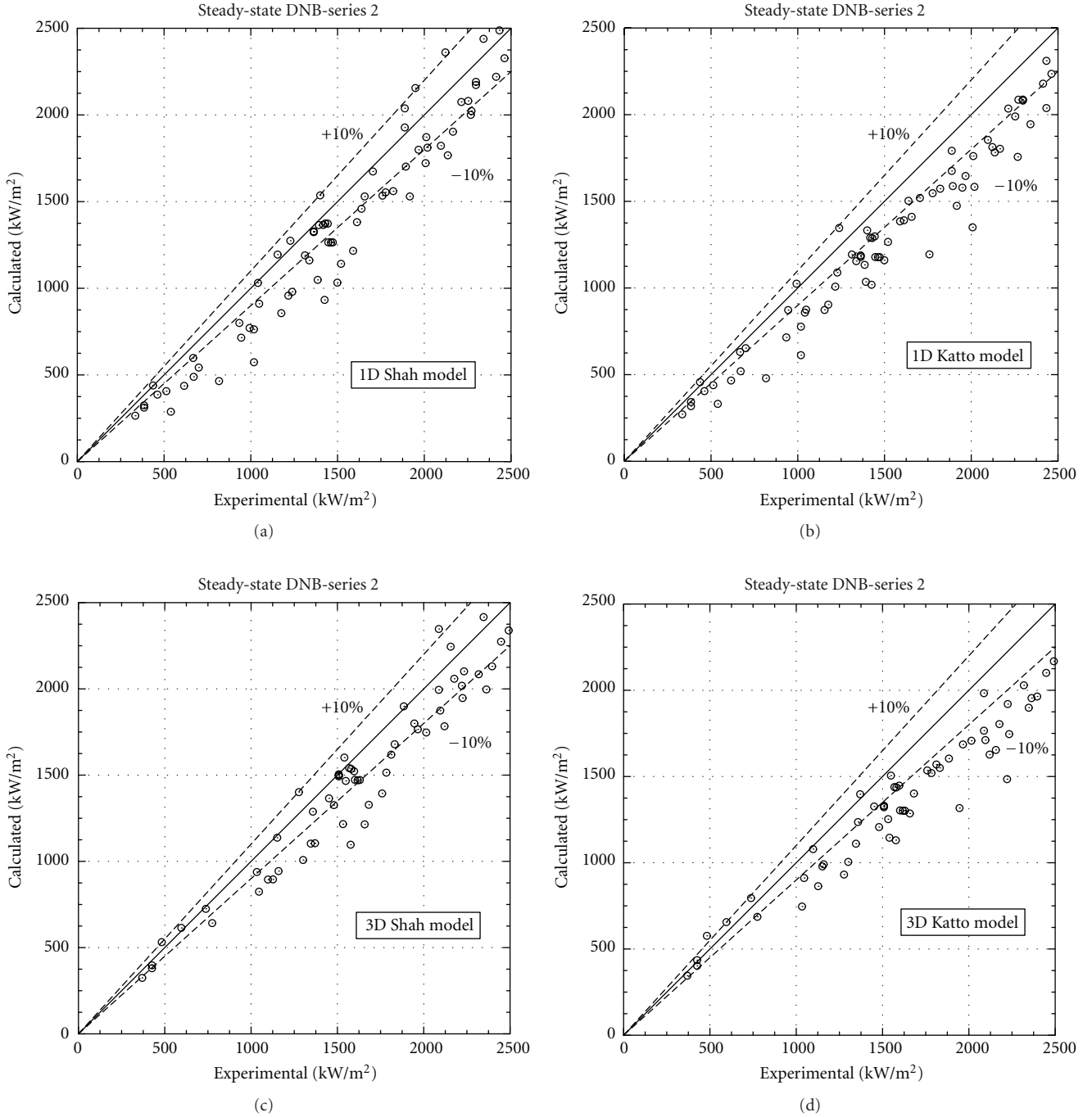


FIGURE 8: Computed versus experimental critical heat fluxes (Series 2).

The value of C in the relationship of X_1 is given by

$$\begin{aligned}
 C &= 0.25 \quad \text{for } Z' < 50, \\
 C &= 0.25 + 0.0009(Z' - 50) \quad \text{for } 50 < Z' < 150, \\
 C &= 0.34 \quad \text{for } Z' > 150.
 \end{aligned} \tag{39}$$

Three values of K must be determined

$$K_1 = \frac{0.261}{CW^{0.043}}, \tag{40}$$

$$K_2 = \frac{0.833[0.0124 + (1/Z')]}{R^{0.133}W^{0.333}}, \tag{41}$$

$$K_3 = \frac{1.12[1.52W^{0.233} + (1/Z')]}{R^{0.6}W^{0.173}}. \tag{42}$$

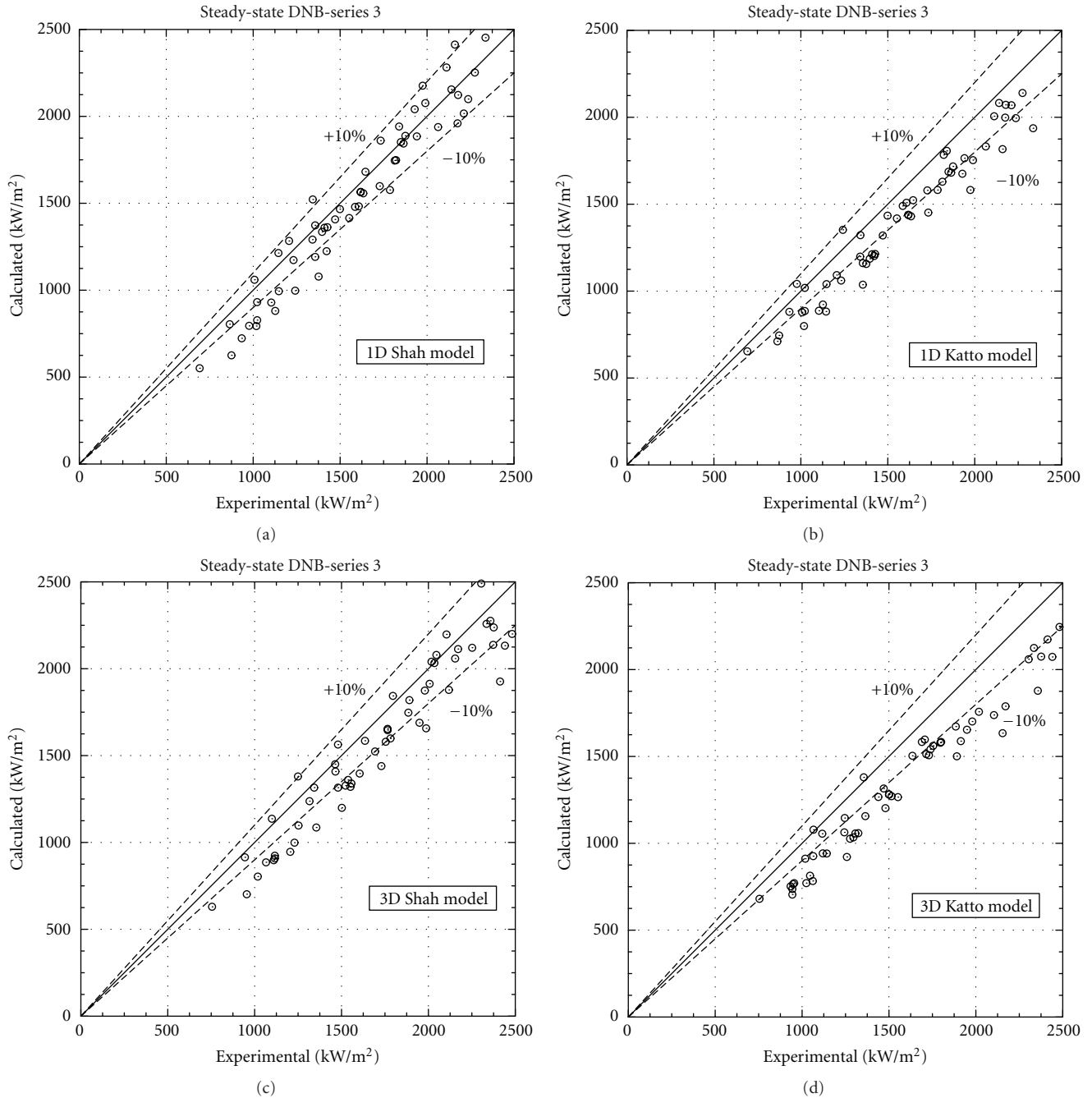


FIGURE 9: Computed versus experimental critical heat fluxes (Series 3).

The appropriate values of X and K must be determined according to Table 3.

3.2.1. Range Covered by the Katto and Ohno Correlation. The Katto and Ohno correlation covers the following operating conditions:

- (i) $0.01 < z < 8.8$ m,
- (ii) $0.001 < D < 0.038$ m,
- (iii) $5 < Z' < 880$,

(iv) $0.0003 < R' < 0.41$,

(v) $3 \times 10^{-9} < W' < 2 \times 10^{-2}$.

All experimental tests are included in the range covered by the Katto and Ohno correlation (see Table 4).

4. Void Distribution Results

4.1. Subchannel Exercises. Four series of measurements of void fraction were performed in sections representative of subchannel types in a PWR assembly. Table 5 gives the

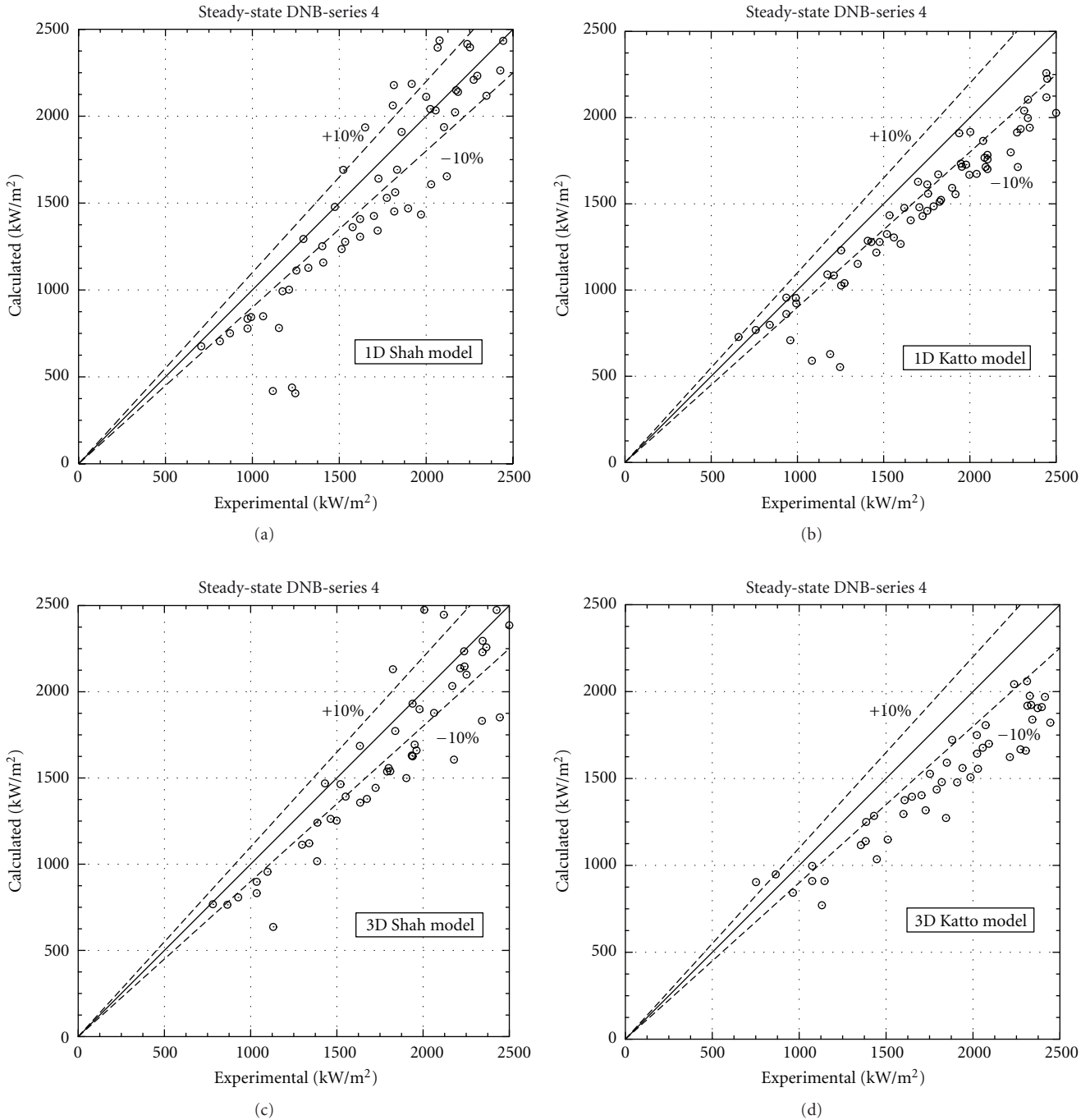


FIGURE 10: Computed versus experimental critical heat fluxes (Series 4).

geometry (center, typical, and thimble subchannels, side and corner subchannels) and power shape for these series. The heated length is 1555 mm, and the void measurement section is located at 1400 mm from the bottom of the heated section.

According to the given test matrix (power value and boundary conditions), the flow is saturated at the location where the void fraction is measured for the most runs. This situation allows only partial assessment of the subcooled boiling models. In contrast, drift flux model plays a major role to obtain good agreement with experimental data.

Chexal-Lellouche and Ishii correlations have been compared for series 1 (Figure 1). It is shown that the Ishii correlation tends to underpredict the void fraction more than the Chexal-Lellouche one. Even if it is not obvious to extend this conclusion to other configurations, the Chexal-Lellouche correlation has been thus adopted for other subchannel and bundle calculations.

Calculated densities and void fractions are compared against the experimental data in Figure 2. Experimental densities measured by CT scan are declared to be affected

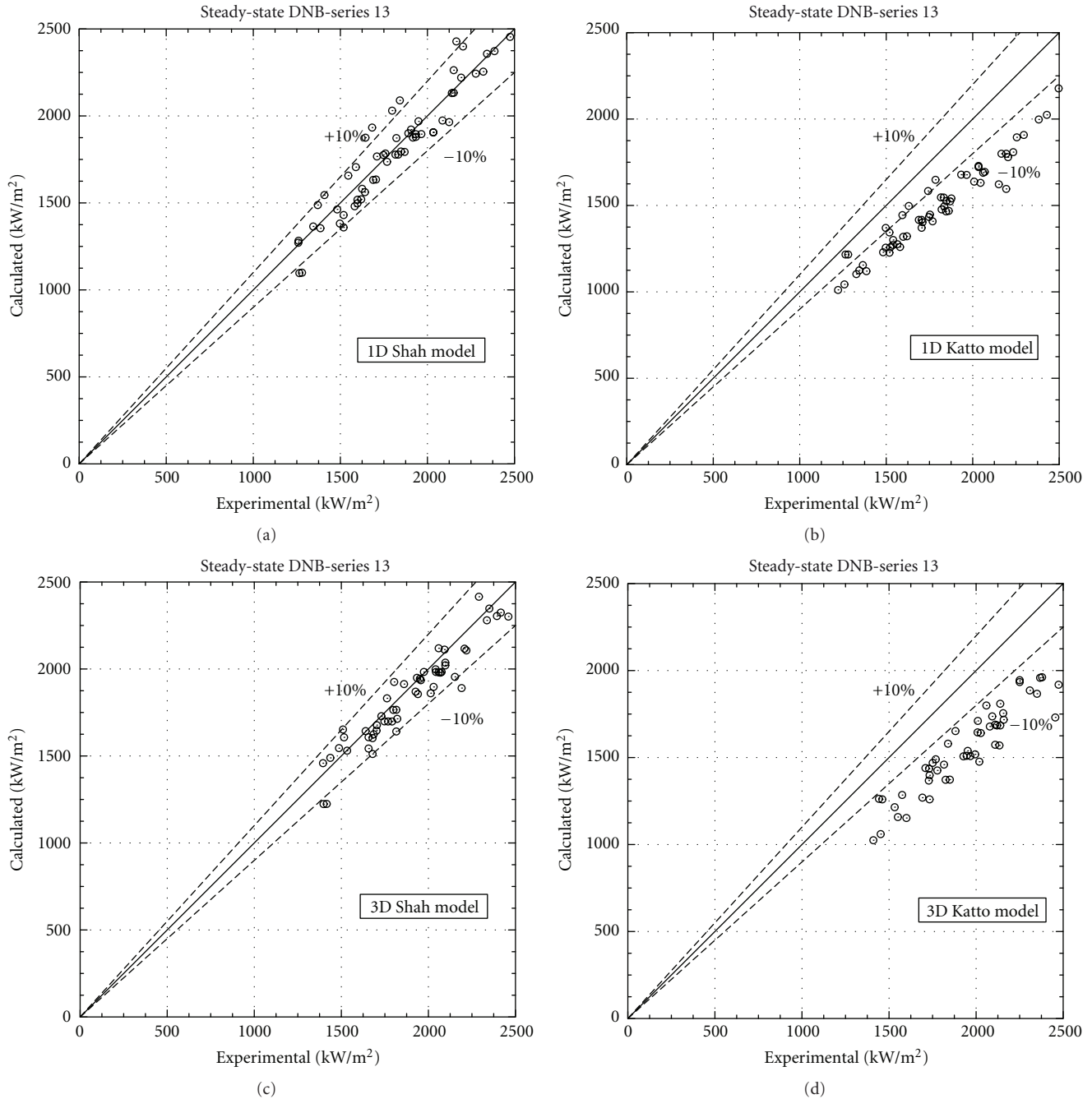


FIGURE 11: Computed versus experimental critical heat fluxes (Series 13).

by an uncertainty of 15 kg/m^3 ($\sigma_{\text{exp}} = 15 \text{ kg/m}^3$ in Figure 2(b)) [12]. Experimental void fraction resumed basing on measured densities are presumed to be affected by an uncertainty of 3% of void fraction ($\sigma_{\text{exp}} = 3\%$ in Figure 2(a)) [12]. It happens that densities obtained by the code match well the experimental ones, whereas void fractions are slightly underestimated for the lowest value of this quantity. Indeed, physical properties and correlations adopted to convert density to void fraction could be the cause for this discrepancy.

4.2. Subchannel Exercises. A partial section of the full length 17×17 type PWR fuel assemblies was considered. The rod bundle test is a 5×5 square array. The heated section is 3658 mm high, and density measurements are set at 2216 mm (Lower), 2669 mm (Middle), and 3177 mm (Upper). In Table 6 are shown the geometry and power shape of the rod bundle test assemblies considered. Three assembly configurations were considered: B5, B6, and B7. The main difference between these three configurations is in the power distribution. Assembly B5 has a uniform axial

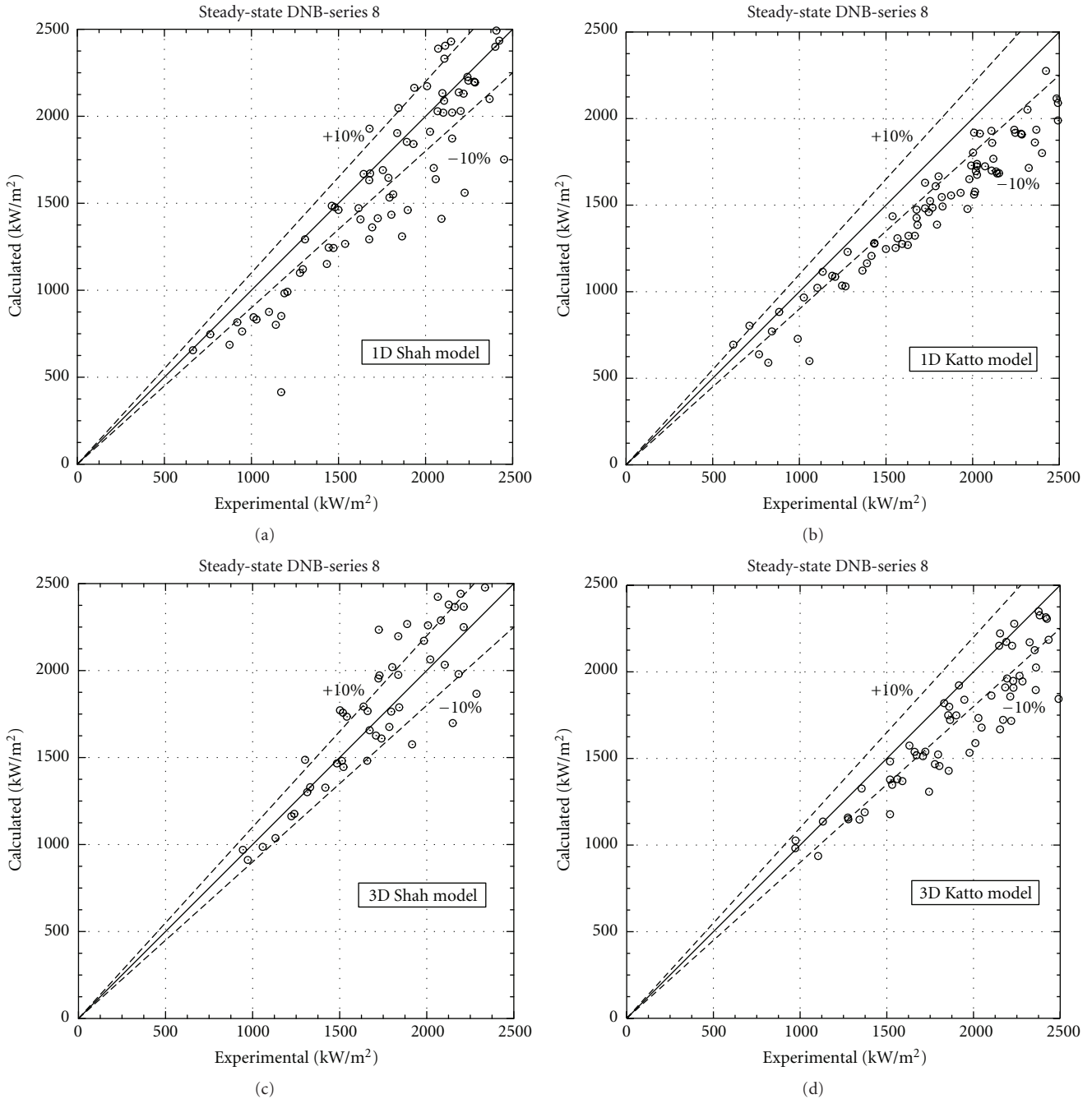


FIGURE 12: Computed versus experimental critical heat fluxes (Series 8).

power distribution and pattern A radial power distribution. Assembly B6 has the same radial power distribution of assembly B5 but cosine axial power distribution. Assembly B7 has a cosine axial power distribution and pattern B radial power distribution. For this radial power distribution, the central rod is a thimble rod (i.e., no power is generated inside this rod) of larger diameter with respect to the fuel rods. The gamma-ray transmission method (chordal averaged) was adopted in the tests performed to measure the density and then converted to the void fraction of the gas-liquid two-phase flow. The declared uncertainties are 4% of void

fraction ($\sigma_{\text{exp}} = 4\%$ in Figures 3 and 4) for steady-state bundle tests and 5% of void fraction ($\sigma_{\text{exp}} = 5\%$ in Figures 5 and 6) for transient bundle tests. In Table 7 are shown the test series for void fraction measurements.

4.2.1. *Steady-State Exercises.* For the results at the lower and middle elevations, subcooled nucleate boiling models (condensation and wall heat transfer) play a major role for the prediction of void fraction. At the upper elevation, the fluid is generally saturated, and the drift model becomes important. Moreover, diffusion terms play also a major

TABLE 9: Comparison between calculated and experimental boiling crisis detection time.

Boiling crisis detection time (s)	Series 11		Series 12	
	EXP	CALC	EXP	CALC
Power increase	106.7	108.7	86.6	72.2
Flow reduction	52.9	48.8	55.0	42.9
Depressurization	88.8	90.8	143.8	140.9
Temperature decrease	140.6	143.3	128.8	121.4

role, and turbulent diffusion promoted by the presence of mixing grid spacers must be taken into account. Standard parameters $K_{t0}^{ij}(z) = k_{tb}$ and $M_{t0}^{ij}(z) = m_{tb}$ (the turbulent Prandtl number is assumed equal to 1) adopted for bare bundles (without any spacer) have to be increased in the region upstream mixing grid spacers in order to reproduce the enhancement of turbulent mixing. In (15) and (13), K_{t0}^{ij} and M_{t0}^{ij} have been therefore adapted for the PSBT assemblies by means of piecewise functions: it was assumed that $K_{t0}^{ij}(z) = k_{ts}$ and $M_{t0}^{ij}(z) = m_{ts}$ downstream a mixing grid spacer, instead of taking the standard values k_{tb} and m_{tb} . Despite the values of k_{tb} and m_{tb} are reliably assessed to be around 0.010 for PWR type bundles [6], the appropriate values to be adopted for k_{ts} and m_{ts} are not known for these particular mixing grid spacers and thus, to better identify reasonable values for these coefficients, a sensitivity analysis has been performed. A sensitivity analysis for the coefficient K_{v0} in the condensation model was also conducted. A sample result is shown in Figure 3, where combined effects of these parameters are reported for run 5.2442. In the subcooled and at the beginning of the saturated region, void fraction is strongly reduced as K_{v0} increases, but this parameter does not affect results at the end of the bundle, where the flow is fully saturated. On the other hand, the effect of the turbulent diffusion coefficients k_{ts} and m_{ts} is significant when the void fraction increases, since it determines the flatness of the void distribution profile in the bundle. Detailed experimental density maps would have been useful to assess a reliable value for the turbulent diffusion coefficients, but these maps are not readily exploitable. As far as we could deduce basing on the void fraction profile in the central subchannel, a value for k_{ts} and m_{ts} was chosen equal to 0.045. The value of K_{v0} was instead taken equal to 1.5×10^{-4} , which is in the standard range of values adopted in thermal-hydraulic analysis performed with this model. Figure 4 shows the calculated void fraction against the experimental values for series 5, 6, and 7, with the following parameters: $K_{v0} = 1.5 \times 10^{-4}$, $k_{ts} = m_{ts} = 0.045$, $k_{tb} = m_{tb} = 0.01$.

4.2.2. Transient Exercises. For the transient simulations, three different configurations were taken into account as shown in Table 7. Test series 5T considers the same assembly conditions used for steady-state series 5, with a uniform axial power distribution, and pattern A of radial power distribution.

For transient test series 6T the same assembly conditions used for steady-state series 6 were applied, which means a

cosine axial power distribution, and pattern A radial power distribution. Test series 7T considers the same assembly conditions used for steady-state test series 7, which are cosine axial power distribution, and pattern B radial power distribution.

For each transient analysis, four different scenarios were considered: power increase, flow reduction, depressurization, and temperature increase. Boundary conditions were provided for each scenario, using table where the dependent variables (i.e., power, pressure, mass flux, and inlet temperature resp.,) were specified as function of the simulation time. Same parameters and models as for steady-state bundle computations were used.

Figure 5 shows complete results for transients 5T, also representative of the other transient series 6T and 7T. FLICA-OVAP presents an overall agreement against the experimental void fraction for the transients, although discrepancies with experimental data can be observed, in particular for the temperature increase transient. For the power increase transient, the evolution of the void fraction follows the data, but the void fraction is underestimated at the middle and upper locations. The results concerning the depressurization have more discrepancy as time increases, but are consistent with the experimental evolution.

For the temperature increase transient, a shift of calculated void fractions profiles with respect to experimental values can be noticed. This discrepancy has been noticed by several participants to the first PSBT/OECD workshop in Pisa. Fluid temperature probe is located in a pipe between the preheater and the inlet nozzle of the test section [12]. It is therefore reasonable to guess that a delay of several seconds occurs between the measurement point and the inlet of the heated section. This point has been investigated by JNES [12] but the distance from the measurement location to the inlet of the heated section (where the temperature boundary condition has to be applied in thermal-hydraulics codes) was not clarified. As far as we can say basing on the result obtained by FLICA-OVAP, if a delay of 6 s is assumed for the inlet temperature with respect to other boundary conditions (i.e., the initial temperature is maintained during 6 s and then the temperature variation is applied), the agreement between calculated and experimental void fraction profiles is improved. It can clearly be seen in Figure 6, where these profiles are compared for the calculations with and without the time delay of 6 seconds.

5. DNB Results

The two models adopted in this work, the Shah and the Katto and Ohno models, have been developed and tested mostly in single-channel uniform heat flux conditions.

In this work, the applicability of them to bundle geometries with nonuniform heat flux profile has been investigated. Each experimental series of the NUPEC database has been calculated by the two models, adopting a twofold approach.

In a first step, homogenized one-dimensional calculations have been performed, adopting a bundle-averaged description.

In a second step, three-dimensional calculations have been performed, adopting a subchannel description. In this case, the two boiling crisis models are applied at the subchannels scale. The fundamental difference with the first approach consists in having different hydraulic diameters depending on whether the selected subchannel is a central, a side or a corner subchannel. However, some special approach has to be taken for side and corner subchannels, since CHF models tend to underestimate their critical heat flux. Moreover, as observed by Tong and Tang [13, Section 5.4.5.2, Figure 5.54], for a given inlet enthalpy, critical heat fluxes in the presence of cold walls are even higher than for internal subchannels. For the sake of simplicity, the possibility to have boiling crisis in side and corner subchannels was thus excluded.

In the following paragraphs, for each series, results obtained via the bundle-averaged and the subchannel approach will be shown for the two models. The performances of the different models are also summarized in Table 8.

5.1. Steady-State Series

5.1.1. Series 0, Series 2, and Series 3. Series 0, Series 2 investigate boiling crisis in rod bundle (rods array: 5×5) and uniform heat flux. The two series differ only for the position of mixing and spacer grids. In Series 3, the bundle is also modified, adopting an array of 36 rods (6×6). The axial power shape is uniform for all series, but peripheral rods have a slightly lower power with respect to central rods: the radial power distribution factor is 0.85 for peripheral rods and 1.0 for central rods.

In Figures 7, 8, and 9, calculated and experimental critical heat fluxes are compared, respectively, for Series 1, Series 2, and Series 3. It is ascertained that the Shah model tends to predict higher critical heat flux values than the Katto and Ohno model, for both the bundle-averaged and the subchannel approach. Moreover, in this particular configuration with uniform heat flux and a moderate radial offset, 1D or 3D calculations give very similar results.

5.1.2. Series 4 and Series 13. Series 4 and Series 13 introduce the effect of nonuniform axial profile. A cosine shape was adopted on the same bundle geometry used for Series 2. To deal with nonuniform heat flux, a correction factor was adopted, as proposed by Tong and Tang [13]. In Figures 10 and 11 calculated and experimental critical heat fluxes are compared, respectively, for Series 4, Series 13. As for previous tests, the Shah model predicts higher critical heat flux values than the Katto and Ohno model, providing a better agreement with experimental values. Minor differences are experienced between the homogenized and the subchannel description.

5.1.3. Series 8. Series 8 includes the presence of a central thimble rod, representing guide tube for control rods. Contrarily to the previous series, the results of the homogenized and the subchannel approaches are different (see Figure 12). As expected, in the presence of a radial heterogeneous power shape, a better description is achieved with the subchannel

approach. In general the Shah model gives a better estimate of critical heat fluxes.

5.2. Transient Series. Two experimental campaigns have been consecrated to detect boiling crisis in transient conditions. Different transient conditions have been investigated by NUPEC, including power increase, inlet temperature decrease, flow reduction, and depressurization. Two series of data have been proposed, Series 11 and Series 12, involving different bundle configurations. Series 11 is based on the bundle configuration adopted for Series 4 (cosine axial power shape, rods array 5×5), whereas Series 12 involves a central thimble rod. In the following tables, results obtained by the Shah model with the subchannel approach are listed. Boiling crisis is relatively well predicted for Series 11, whereas a larger discrepancy is ascertained for Series 12 (see Table 9).

6. Conclusions and Perspectives

This paper has presented the current capabilities of the FLICA-OVAP code in predicting void distribution and boiling crisis phenomena. The NUPEC database released in the frame of the OECD/PSBT international benchmark has been addressed.

Void fraction measurements in the subchannel configurations are of major interest for the validation of mass transfer model and the OSV criterion. In this analysis, the attention was focused on the mass transfer model, but further improvement of this work could include the analysis of other OSV criteria. Results obtained by FLICA-OVAP with a set of standard coefficients for the different models show a good agreement of the calculated densities and a slight underestimation of the void fraction at the measurement location, mainly located in the saturated regime for the considered runs.

For the steady-state bundle tests, the K_{v0} coefficient and diffusion coefficients k_t and m_t are the key parameters to fit the void fraction. In particular, mixing grid spacers play a major role, since they enhance the turbulence in the downstream flow. It was found that a reasonably good agreement between calculated and experimental void fraction profiles is achieved when the turbulent diffusion associated to mixing grid is taken equal to $k_{ts} = m_{ts} = 0.045$. Adopting the same set of parameters, a reasonably good agreement between calculated and experimental void fraction was also ascertained for transient tests, even if a systematic underestimation of void fraction at the middle and upper measurement locations has been found.

Discrepancies noticed on temperature increase transients were corrected by applying a delay of 6 s of the original inlet temperature boundary conditions, in order to simulate the residence time of the fluid between the temperature probe where the boundary conditions are given and the inlet of the test section.

Results obtained from the subcooled region suggest possible directions to be pursued in order to improve the current modeling: further developments and validation will involve the OSV criterion and the modeling of heat flux and heat flux partitioning in subcooled nucleate boiling, but

also the modeling of inter-phase mass transfer and turbulent diffusion terms.

To predict boiling crisis, two different models have been tested: the Shah and the Katto and Ohno model. Both a bundle-averaged and subchannel approaches have been investigated. The Shah model, as implemented in the FLICA-OVAP code allows achieving a better prediction of critical heat fluxes in the different investigated configurations. Nevertheless, when the details of the radial power shape become important, better agreement was obtained with the subchannel approach permitting a local description of bundle thermal-hydraulics. Encouraging results were also obtained from the analysis of transient tests aimed at predicting the onset of boiling crisis. Future activities are also planned for future developments of the code, including the implementation of Groeneveld's look-up table [14] and other models based on local approaches.

References

- [1] A. Rubin, A. Schoedel, M. Avramova, H. Utsuno, H. Bajorek, and S. Velasquez-Lozada, "OECD/NRC benchmark based on NUPEC PWR subchannel and bundle tests (PSBT). Volume I: Experimental Database and Final Problem Specifications," Tech. Rep. NEA/NSC/DOC(2010)1, NEA/NSC, November 2010.
- [2] P. Fillion, A. Chanoine, S. Dellacherie, and A. Kumbaro, "FLICA-OVAP: a new platform for core thermal-hydraulic studies," *Nuclear Engineering and Design*, vol. 241, no. 11, pp. 4348–4358, 2011.
- [3] M. Bucci, A. Charmeau, and P. Fillion, "FLICA-OVAP: elements of validation for LWRs thermal-hydraulics studies," in *Proceedings of the International Congress on Advances in Nuclear Power Plants (ICAPP '11)*, Nice, France, May 2011.
- [4] B. Chexal, G. Lellouche, J. Horowitz, and J. Heizer, "A void fraction correlation for generalized applications," *Progress in Nuclear Energy*, vol. 27, no. 4, pp. 255–295, 1992.
- [5] M. Ishii, "One dimensional drift-flux model and constitutive equations for relative motion between phases in various two-phase flow," Tech. Rep. ANL-77-27, ANL, 1977.
- [6] E. Royer, S. Aniel, A. Bergeron et al., "FLICA4: Status of numerical and physical models and overview of applications," in *Proceedings of the 11th International Topical Meeting on Nuclear Reactor Thermal-Hydraulics (NURETH-11)*, Avignon, France, October 2005.
- [7] D. Chisholm, "Friction during the flow of two-phase mixtures in smooth tubes and channels," Tech. Rep. NEL-529, National Engineering Laboratory, Department of Trade and Industry, 1972.
- [8] W. Jens and P. Lottes, "Analysis of heat transfer burnout, pressure drop and density data for high pressure water," Tech. Rep. ANL-4627, Argonne National Laboratory (ANL), 1951.
- [9] N. E. Todreas and M. S. Kazimi, *Nuclear Systems I*, Taylor & Francis, 1993.
- [10] M. M. Shah, "Improved general correlation for critical heat flux during upflow in uniformly heated vertical tubes," *International Journal of Heat and Fluid Flow*, vol. 8, no. 4, pp. 326–335, 1987.
- [11] Y. Katto and H. Ohno, "An improved version of the generalized correlation of critical heat flux for the forced convective boiling in uniformly heated vertical tubes," *International Journal of Heat and Mass Transfer*, vol. 27, no. 9, pp. 1641–1648, 1984.
- [12] H. Utsuno, "OECD/NRC benchmark based on NUPEC PWR subchannel and bundle tests (PSBT). Assembly specification and Benchmark Database. Volume I Addendum," Tech. Rep. JNES/SAE-TH08-0019, JNES, 2010, (Addendum).
- [13] L. S. Tong and Y. S. Tang, *Boiling Heat Transfer and Two-Phase Flow*, Taylor & Francis, 2nd edition, 1997.
- [14] D. C. Groeneveld, J. Q. Shan, A. Z. Vasić et al., "The 2006 CHF look-up table," *Nuclear Engineering and Design*, vol. 237, no. 15-17, pp. 1909–1922, 2007.

Research Article

CFD Analysis of a Void Distribution Benchmark of the NUPEC PSBT Tests: Model Calibration and Influence of Turbulence Modelling

E. Krepper and R. Rzehak

Institute of Fluid Dynamics, Helmholtz-Zentrum Dresden-Rossendorf, P.O. Box 510119, 01314 Dresden, Germany

Correspondence should be addressed to E. Krepper, e.krepper@hzdr.de

Received 26 March 2012; Accepted 27 July 2012

Academic Editor: Diana Cuervo

Copyright © 2012 E. Krepper and R. Rzehak. This is an open access article distributed under the Creative Commons Attribution License, which permits unrestricted use, distribution, and reproduction in any medium, provided the original work is properly cited.

The paper presents CFD calculations of the void distribution tests of the PSBT benchmark using ANSYS CFX-12.1. First, relevant aspects of the implemented wall boiling model are reviewed highlighting the uncertainties in several model parameters. It is then shown that the measured cross-sectionally averaged values can be reproduced well with a single set of calibrated model parameters for different test cases. For the reproduction of patterns of void distribution cross-sections, attention has to be focussed on the modelling of turbulence in the narrow channel. Only a turbulence model with the capability to resolve turbulent secondary flows is able to reproduce at least qualitatively the observed void distribution patterns.

1. Introduction

Based on NUPEC PWR Subchannel and Bundle Tests (PSBT), an international benchmark has been promoted by OECD and NRC and coordinated by Penn State University (PSU). The benchmark includes void distribution and departure from nucleate boiling exercises. In the first exercises the void fraction distribution was investigated in a steady state subchannel grade benchmark. In the present paper some of the single-channel steady state void fraction measurements are analysed to investigate the capabilities of present CFD modelling of wall boiling.

For engineering calculations, currently the most widely used CFD approach to model two-phase flows with significant volume fractions of both phases is the Eulerian two-fluid framework of interpenetrating continua (see, e.g., [1–3]). In this approach, balance equations for mass, momentum, and energy are written for each phase, that is, gas and liquid, separately and weighted by the so-called volume fraction which represents the ensemble averaged probability of occurrence for each phase at a certain point in time and space. Exchange terms between the phases appear as source/sink terms in the balance equations. These exchange terms consist of analytical

or empirical correlations, expressing the interfacial forces, as well as the heat and mass fluxes, as functions of the average flow parameters. Since most of these correlations are highly problem-specific, their range of validity has to be carefully considered and the entire model has to be validated against experiments.

For the case of boiling flows, where heat is transferred into the fluid from a heated wall at such high rates that vapour is generated, additional source terms describing the physics of these processes at the heated wall have to be included. A CFD wall boiling model implemented in CFX following the lines of Kurul and Podowski [4, 5] was calibrated and validated by several authors, for example, Krepper et al. [6] against experimental results of Bartolomej and Chanturiya [7]. In these tests, subcooled flow boiling of water at high pressure flowing upwards in a vertical pipe heated from the outside was investigated and measurements of the axial development of void fraction, wall temperature and cross sectionally averaged liquid temperature were provided.

The aim of this work is to investigate the applicability of the CFX models to the PSBT tests. In Section 1 the PSBT tests for the void fraction distribution and the parameters of the selected tests are described briefly. In Section 2 the

most important model details used for the simulations are described and critically reviewed. In Section 3 the sensitivity of the different parts of the models is investigated in view of the knowledge discussed in Section 2. The parameters are calibrated to only a single test. In the following Section 4 these calibrated models are applied to additional tests without any further change of model parameters. The cross sectionally averaged values of the selected tests are summarized for comparison to the calculations of other participants in the benchmark. In Section 5 the influence of the turbulence model on the void fraction distribution is investigated.

2. The OECD Benchmark Test

The PWR Subchannel and Bundle Tests (PSBT) were conducted by NUPEC (1987–1993) within an extensive experimental campaign aimed at verifying the reliability of fuel assemblies used for commercial nuclear power plants [8, 9]. Void fraction measurements and departure from nucleate boiling (DNB) tests were performed under PWR thermal-hydraulic conditions including steady states and transients such as power increase, flow reduction, depressurization, and temperature increase. The void fraction in each experiment was measured by gamma-ray transmission. These tests form the basis of an OECD benchmark for CFD and subchannel codes [10].

The subchannel test section, as shown in Figure 1, simulates a single subchannel of a PWR fuel assembly. The effective heated length is 1500 mm where the void measurement section is located near close to the top end at 1400 mm from the bottom of the heated section.

For the analysis different tests in different pressure regions were selected (see Table 1).

3. The Models

3.1. Modelling of Boiling at a Heated Wall: The General Model Structure. In boiling, heat is transported from the hot wall to the fluid by several different mechanisms. On parts of the wall, where no bubbles reside, heat flows directly to the subcooled liquid in the same way as in single-phase flow. On parts of the wall where bubbles grow, heat is consumed by the generation of vapour which occurs at the so-called nucleation sites. Moreover, there is a liquid mixing mechanism due to the bubbles which leave the wall. As a consequence of the recirculation around the detaching bubbles, cold liquid from the bulk of the flow is brought into contact with the hot wall which leads to additional cooling. This mechanism is termed quenching. The total supplied heat flux is accordingly expressed as the sum of three contributions as

$$Q_{\text{tot}} = Q_C + Q_Q + Q_E, \quad (1)$$

where Q_C , Q_Q , and Q_E denote the heat flux components due to single-phase turbulent convection, quenching, and evaporation, respectively. The individual components in this heat flux partitioning are then modelled as functions of the

wall temperature and other local flow parameters. Once this is accomplished, (1) can be solved iteratively for the local wall temperature T_W , which satisfies the wall heat flux balance. Denoting the fraction of area influenced by the bubbles as A_W , the heat flux components are expressed as discussed in the following.

The turbulent convection heat flux is calculated in the CFX model version in much the same way as for a pure liquid flow without boiling, but multiplied by the fraction of area unaffected by the bubbles, that is,

$$Q_C = (1 - A_W)h_C(T_W - T_L). \quad (2)$$

Here, h_C is the heat transfer coefficient which is written using the temperature wall function $T^+(y^+)$ known from Kader [11] as

$$h_C = \frac{\rho C_P u_\tau}{T^+}, \quad (3)$$

where nondimensional variables (indicated by superscript “+”) and the friction velocity u_τ are defined as usual. Note that (2) and (3) may be evaluated at any location y , provided it is used consistently whenever a variable depends on position. Q_Q is represented in terms of the quenching heat transfer coefficient h_Q :

$$Q_Q = A_W h_Q (T_W - T_L). \quad (4)$$

A grid-independent solution for Q_Q is obtained by evaluating the non-dimensional temperature profile at a fixed value of y^+ . The evaporation heat flux Q_E is obtained via the evaporation mass flux at the wall:

$$Q_E = \dot{m}_W H_{LG}, \quad (5)$$

where the generated vapour mass \dot{m}_W is expressed in terms of the bubble diameter at detachment d_W , bubble generation frequency f , and nucleation site density N as

$$\dot{m}_W = \rho_G \frac{\pi}{6} d_W^3 f N. \quad (6)$$

In terms of bubble detachment diameter and nucleation site density, the wall area fraction A_W influenced by vapour bubbles is given by

$$A_W = \pi \left(a \frac{d_W}{2} \right)^2 N. \quad (7)$$

Here, a is the so-called bubble influence factor, for which a value of 2 is commonly used [4, 5]. Since $A_W = 1$ corresponds to the case where the whole surface is under the influence of bubbles, A_W as calculated by (7) has to be limited to values smaller than one. Moreover, it should be kept in mind that already as A_W approaches 1 the assumptions of the model are not really satisfied anymore.

Correlations for the yet undetermined quantities used in the CFX wall boiling model are discussed in the following.

3.2. Bubble Size at Detachment. The bubble size at detachment depends on the liquid subcooling. Also the liquid properties which depend on the system pressure, the flow rate, and the heat flux have an influence.

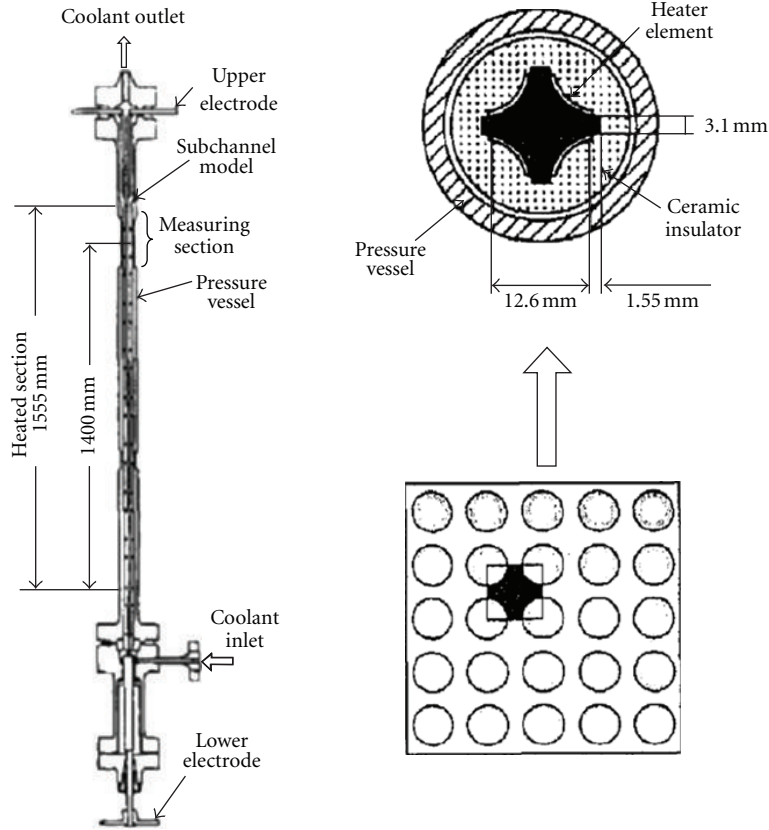


FIGURE 1: Test section for the subchannel void measurement [10].

TABLE 1: Selected tests.

Run	Pressure [MPa]	Mass flux [$10^6 \text{ kg m}^{-2} \text{ h}^{-1}$]	Inlet temperature [$^{\circ}\text{C}$]	Power [kW]	Outlet quality
1.2211	15	11	295.4	90	-0.04
1.2223	15	11	319.6	70	0.04
1.2237	15	11	329.6	60	0.08
1.2422	15	5	284.1	60	0.02
1.2423	15	5	299.3	60	0.10
1.4324	10	5	238.9	60	0.00
1.4325	10	5	253.8	60	0.05
1.4326	10	5	268.8	60	0.11
1.4411	10	2	253.7	20	0.00
1.6222	5	5	204.2	50	0.02

An investigation of the bubble size at detachment was performed by Tolubinsky and Kostanchuk [12] for water at different pressures and subcoolings. The observed dependence on the liquid subcooling at atmospheric pressure can be fitted to a correlation:

$$d_W = d_{\text{ref}} e^{-((T_{\text{sat}} - T_L)/(\Delta T_{\text{ref}d}))}. \quad (8)$$

A least squares fit gives parameter values are $d_{\text{ref}} = 0.0013 \text{ m}$ and $\Delta T_{\text{ref}d} = 53 \text{ K}$ under these conditions.

To match the tests of Bartolomej and Chanturiya [7] which were conducted at much higher pressures relevant for typical nuclear energy applications the values of d_{ref} and

$\Delta T_{\text{ref}d}$ had to be adjusted to $d_{\text{ref}} = 0.6 \text{ mm}$ and $T_{\text{ref}d} = 45 \text{ K}$ (e.g., [6]).

3.3. Nucleation Site Density. The situation concerning data on nucleation site density is much less clear. Most of the time, correlations are expressed in the form of power laws depending on the wall superheat as

$$N = N_{\text{ref}} \left(\frac{T_W - T_{\text{sat}}}{\Delta T_{\text{ref}N}} \right)^p. \quad (9)$$

However, a recent compilation [13] shows that vastly different parameter values are required to match different data

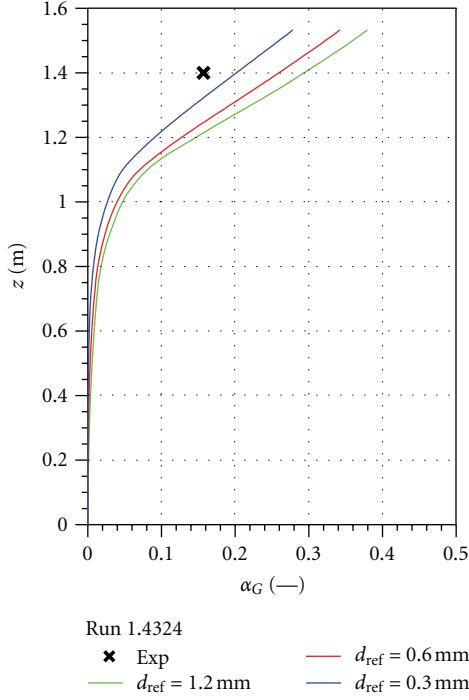


FIGURE 2: Cross-sectionally averaged gas fraction for different values d_{ref} (8).

sets. A likely reason for this fact is that nucleation site density is highly dependent on the microscale topography of the boiling surface, which in turn depends strongly on the processes that were used to finish the surface. These processes are very diverse and in most boiling experiments not specifically controlled or characterized.

For the tests of Bartolomej and Chanturiya [7] $N_{\text{ref}} = 0.8 \times 10^6 \text{ m}^{-2}$ and $\Delta T_{\text{ref}N} = 10 \text{ K}$ were found to yield the best results in the model framework.

3.4. Further Model Aspects. The bubble detachment frequency f is given according to Cole [14] as a function of the detachment size d_w . The quenching heat transfer coefficient is calculated as suggested by Mikic and Rohsenow [15].

In the bulk, vapour is assumed to be at saturation condition. Where the liquid is subcooled, that is, $T_L < T_{\text{sat}}$, vapour is condensing and calculated with the transfer rate:

$$\dot{m} = \frac{h_{LG}(T_{\text{sat}} - T_L)A_I}{H_{LG}}. \quad (10)$$

Here, h_{LG} is the interfacial heat transfer coefficient, calculated according to Ranz and Marshall [16] and A_I is the interfacial area. To close the phase transition model in the bulk bubbly flow with a mean bubble diameter d_B , Kurul and Podowski [4] and also Anglart et al. [17] proposed to calculate the bubble diameter d_B locally as a linear function of liquid subcooling T_{sub} :

$$d_B = \frac{d_{B,1}(T_{\text{sub}} - T_{\text{sub},2}) + d_{B,2}(T_{\text{sub}} - T_{\text{sub},1})}{T_{\text{sub},2} - T_{\text{sub},1}}. \quad (11)$$

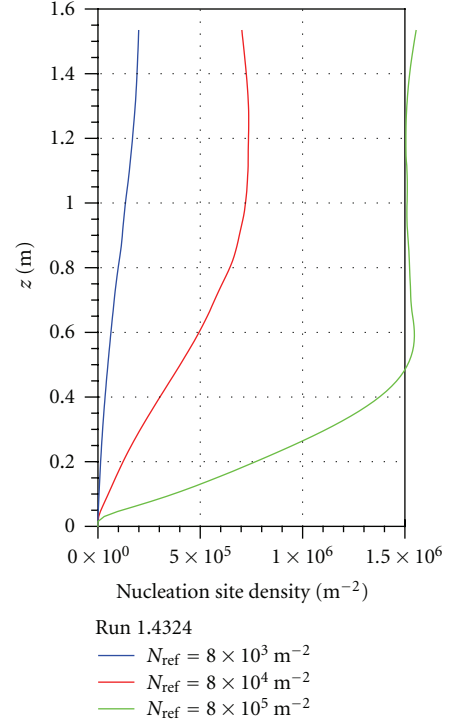


FIGURE 3: Nucleation site density N (9).

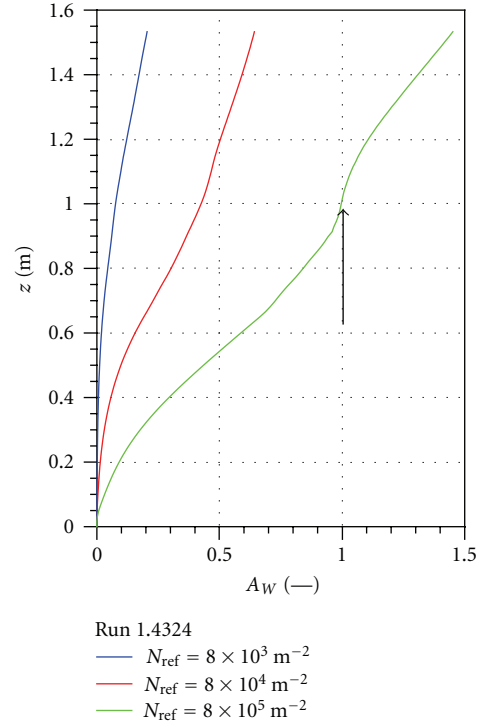


FIGURE 4: Bubble influence area A_W (7).

Reference subcooling conditions for typical nuclear energy applications have been given as $d_{B,1} = 0.1 \text{ mm}$ at $T_{\text{sub},1} = -13.5 \text{ K}$ and $d_{B,2} = 2 \text{ mm}$ at $T_{\text{sub},2} = 5 \text{ K}$ in [17].

In a two-phase turbulent flow gaseous bubbles have an influence on the liquid turbulence. This effect is described by increasing the turbulent viscosity according to Sato et al.

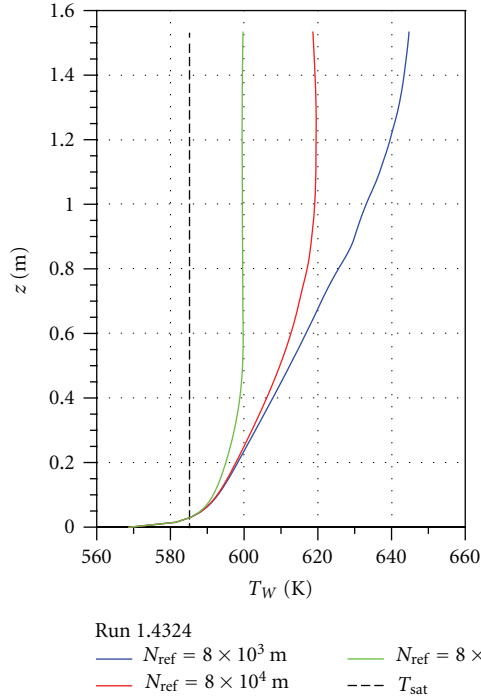


FIGURE 5: Wall temperature.

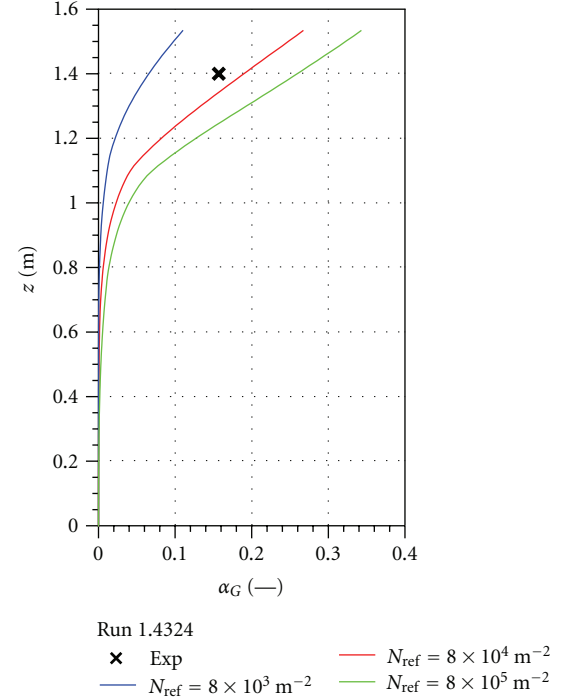


FIGURE 6: Cross sectionally averaged gas fraction.

[18]. Conversely the liquid turbulence flow structures influence the gas distribution, which is described by a turbulent dispersion force according to Burns et al. [19].

For momentum exchange between the phases, finally, the Ishii and Zuber [20] drag law was used. Furthermore, a lift force according to Tomiyama et al. [21], a turbulent dispersion force according to Burns et al. [19], and a wall force according to Antal et al. [22] were included.

3.5. *Evaluated Quantities.* Quantities requested for the benchmark have been evaluated as follows. The mixed density ρ_{MIX} was calculated according to

$$\rho_{\text{MIX}} = \alpha_L \rho_L + \alpha_G \rho_G, \quad (12)$$

and the mixed enthalpy H_{MIX} according to

$$H_{\text{MIX}} = \frac{\alpha_L \rho_L H_L + \alpha_G \rho_G H_G}{\rho_{\text{MIX}}} \quad (13)$$

with the temperature-dependent static enthalpies for liquid H_L and gas H_G . The quality X was then calculated according to

$$X = \frac{H_{\text{MIX}} - H_{L\text{Sat}}}{H_{G\text{Sat}} - H_{L\text{Sat}}} \quad (14)$$

with the enthalpies at saturation for liquid $H_{L\text{Sat}}$ and gas $H_{G\text{Sat}}$.

4. Model Setup

4.1. *General Setup.* For most of the tests calculations were done for only 1/8 of the channel making use of the geometric

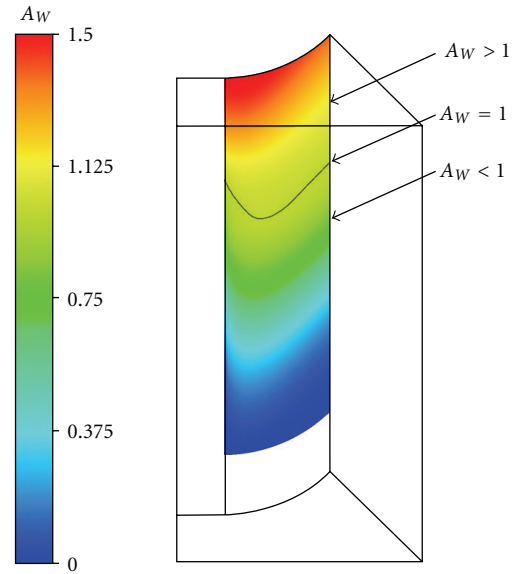


FIGURE 7: Distribution of the area fraction occupied by gas A_w (7) on the heated wall for $N_{\text{ref}} = 8 \times 10^5 \text{ m}^{-2}$ (compare Figure 4). Only 1/8 of the channel is simulated considering the geometric symmetries.

symmetries. The mesh consisted of 720000 nodes; 1000 axial subdivisions were considered. To check the validity of this simplification for some tests furthermore 1/4 of the channel (850000 nodes) or the whole (1400000 nodes) were simulated with the same results. An inlet condition was set at the bottom. Upstream of the heated length an

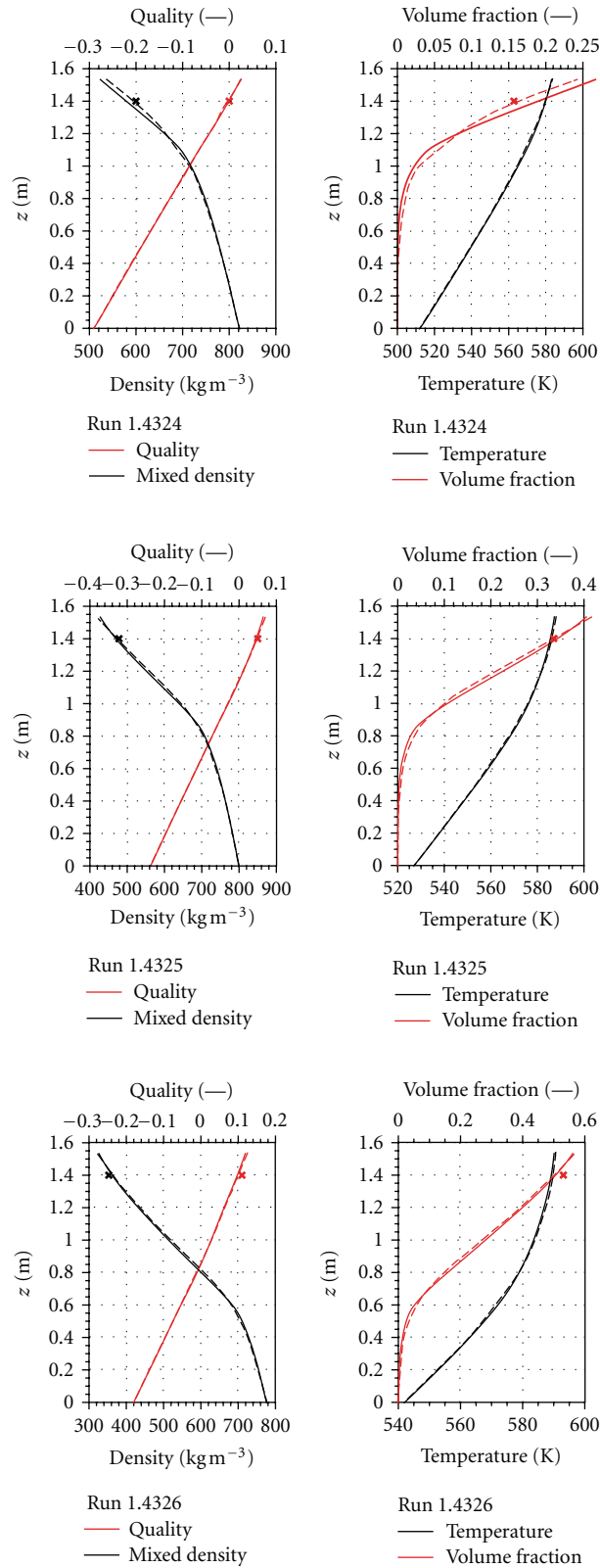


FIGURE 8: Cross sectionally averaged values for runs 1.4324, 1.4325, and 1.4326; solid lines: Shear Stress Turbulence model (SST), dotted lines: Reynolds Stress Turbulence model (BSL).

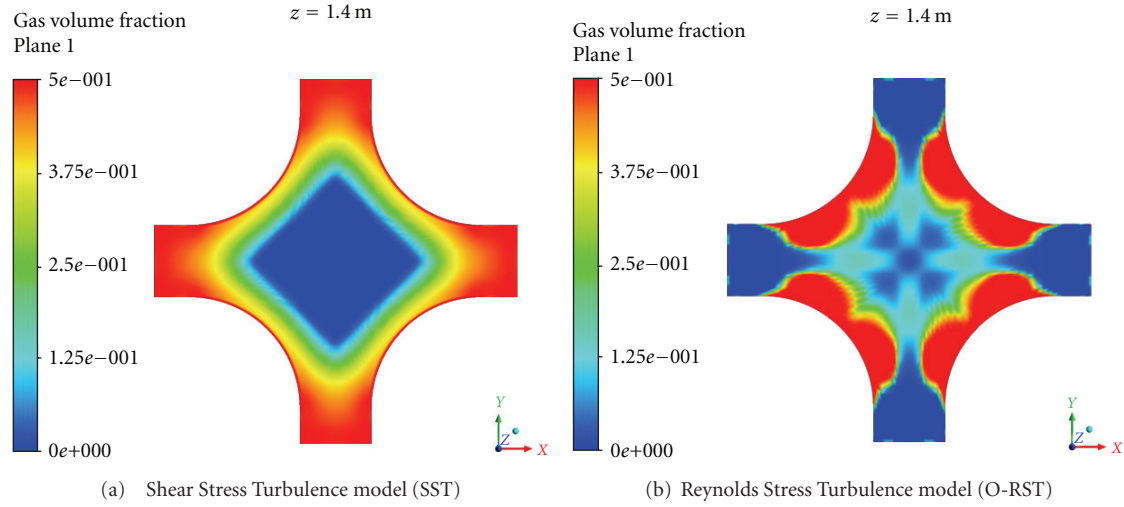


FIGURE 9: Cross sectionally averaged gas fraction at an axial distance of 1.4 m for run 1.2422.

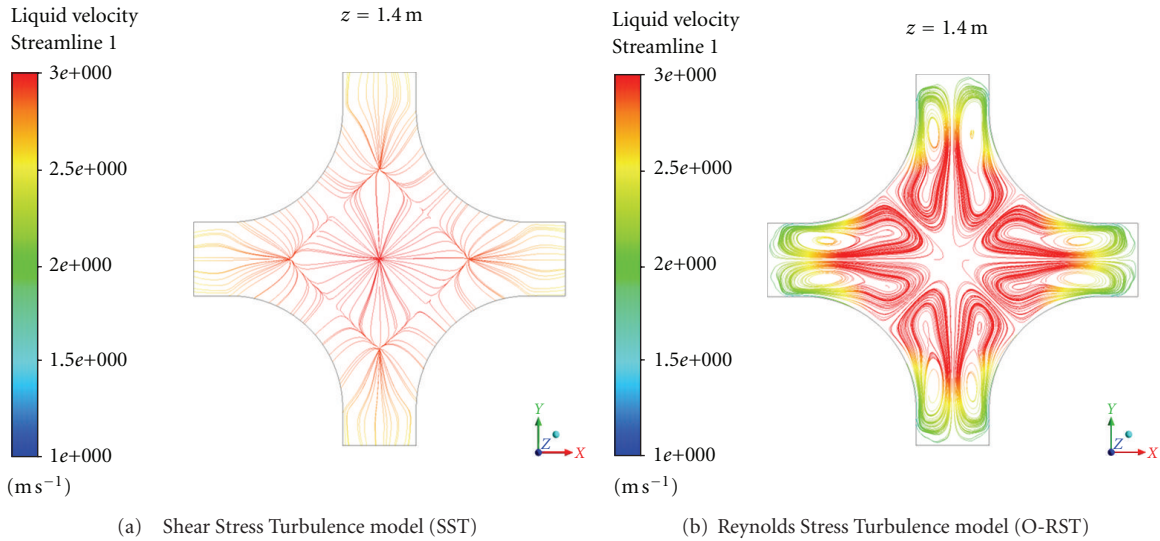


FIGURE 10: Velocity stream lines projected in a plane at an axial height of 1.4 m for run 1.2422.

unheated part of 0.5 m length was simulated to model flow development. For the liquid and gas properties the water steam tables according to IAPWS IF97 were applied. In Section 3 the turbulence of the liquid phase was modelled by a Shear Stress Transport (SST) model [23]. In Section 4 two different Reynolds Stress Turbulence models were applied for comparison. The influence of the turbulence model is investigated in Section 5.

4.2. Calibration of Boiling Model Parameters

4.2.1. Bubble Size at Detachment. Earlier investigations [24] have shown that the bubble size at detachment has a sensitive influence on the calculated gas fraction since it determines the part of heat transferred by evaporation. To demonstrate the influence of this parameter different values d_{ref} (8) were investigated and the resulting cross sectionally

averaged gas fraction for the test case 1.4324 is shown in Figure 2. Nevertheless, because of similar conditions as in the Bartolomej and Chanturiya [7] test cases, $d_{ref} = 0.6$ mm was assumed for the further simulations.

4.2.2. Nucleation Site Density. The nucleation site density has almost no influence on the liquid temperature, a small influence on the gas void fraction but a strong influence on the wall superheating $T_W - T_{sat}$. The common lack of information on the nucleation site density can be compensated by adjusting N_{ref} to match the measured wall temperature. Unfortunately, the wall temperatures are not available in the PSBT data. For the test case 1.4324 different values of the reference nucleation site density N_{ref} (9) were assumed to calculate the circumferentially averaged nucleation site density N (see Figure 3), bubble influence area A_W (see Figure 4), wall temperature T_W (see Figure 5), and the

TABLE 2: Results.

Run	Pressure [MPa]	Turbulence model	Mixed density [kg m^{-3}]	Void fraction [-]	Quality	ΔP [Pa m^{-1}]
1.2211	15	Exp	610	0.038	-0.040	
		BSL-RSM	588.6	0.090	-0.043	17481.9
		SST	572.9	0.117	-0.037	17805.2
1.2223	15	Exp	456	0.311	0.040	
		O-RSM	471.2	0.266	0.073	13685.8
		SST	494.5	0.212	0.059	15403.9
1.2237	15	Exp	390	0.440	0.080	
		O-RSM	431.9	0.327	0.110	12175.5
		SST	447.2	0.291	0.101	15725.2
1.2422	15	Exp	522	0.182	0.020	
		BSL-RSM	520.8	0.187	0.015	8865.2
		O-RSM	513.2	0.202	0.017	9363.2
1.2423	15	Exp	507.3	0.215	0.017	9468.4
		O-RSM	357	0.508	0.100	
		SST	424.3	0.346	0.095	8927.7
1.4324	10	Exp	438	0.325	0.082	9401.9
		BSL-RSM	600	0.157	0.000	
		SST	593.8	0.166	-0.002	5751.6
1.4325	10	Exp	578.9	0.190	0.000	6604.5
		BSL-RSM	478	0.335	0.050	
		SST	473	0.336	0.048	9796.8
1.4326	10	Exp	470	0.343	0.046	10279.4
		BSL-RSM	353	0.531	0.110	
		SST	363.3	0.503	0.099	9700
1.4411	10	Exp	361.9	0.506	0.098	10503.2
		BSL-RSM	599	0.152	0.000	
		O-RSM	614.6	0.124	0.000	7506.5
1.6222	5	Exp	616.1	0.121	0.000	7541.9
		O-RSM	617.1	0.122	-0.004	7691
		O-RSM	549	0.306	0.020	
		O-RSM	578.9	0.263	0.016	7224.8

Exp: experiment.

BSL-RSM: Baseline Reynolds Stress.

O-RSM: Omega Reynolds Stress.

SST: Shear Stress Transport.

cross sectionally averaged gas volume fraction (see Figure 6). Figure 7 shows furthermore for $N_{\text{ref}} = 8 \times 10^5 \text{ m}^{-2}$ the distribution of the area fraction occupied by gas A_W on the heated wall. For axial heights $> 1 \text{ m}$ (Figure 4) and for different areas (Figure 7) $A_W > 1$ is found which does not seem reasonable. Therefore, N_{ref} was set to a smaller value of $8 \times 10^4 \text{ m}^{-2}$ for all simulated cases. For all simulated cases compliance with the condition $A_W < 1$ was checked.

5. Results

The calculations for the cross-sectional averages listed in Table 2 were performed applying a Shear Stress Transport (SST) model for the liquid phase turbulence. This model blends a $k-\epsilon$ model in the bulk and a $k-\omega$ model in the near wall region [23]. Furthermore, the corresponding Reynolds Stress model, the Baseline Reynolds Stress model (BSL-RSM)

were investigated. This model has the same model structure as the SST model. In some cases the convergence of the BSL-RSM runs was questionable. The $k-\omega$ Reynolds Stress model (O-RSM) proved to be numerically more stable. The details of these approaches to turbulence modeling can be found in the ANSYS solver manual.

Calculating the cross sectionally averaged values, no significant differences between the different turbulence models could be discerned (examples for selected tests see Figure 8). In Section 5, however, a strong influence of turbulence modelling on the gas fraction distribution is shown.

The experiments do not provide values on bubble sizes or on temperatures of the heated wall. Exploiting this information gap for calibration of the correlations for the bubble size at detachment and the nucleation site density, at least cross-sectionally averaged values for the mixed density

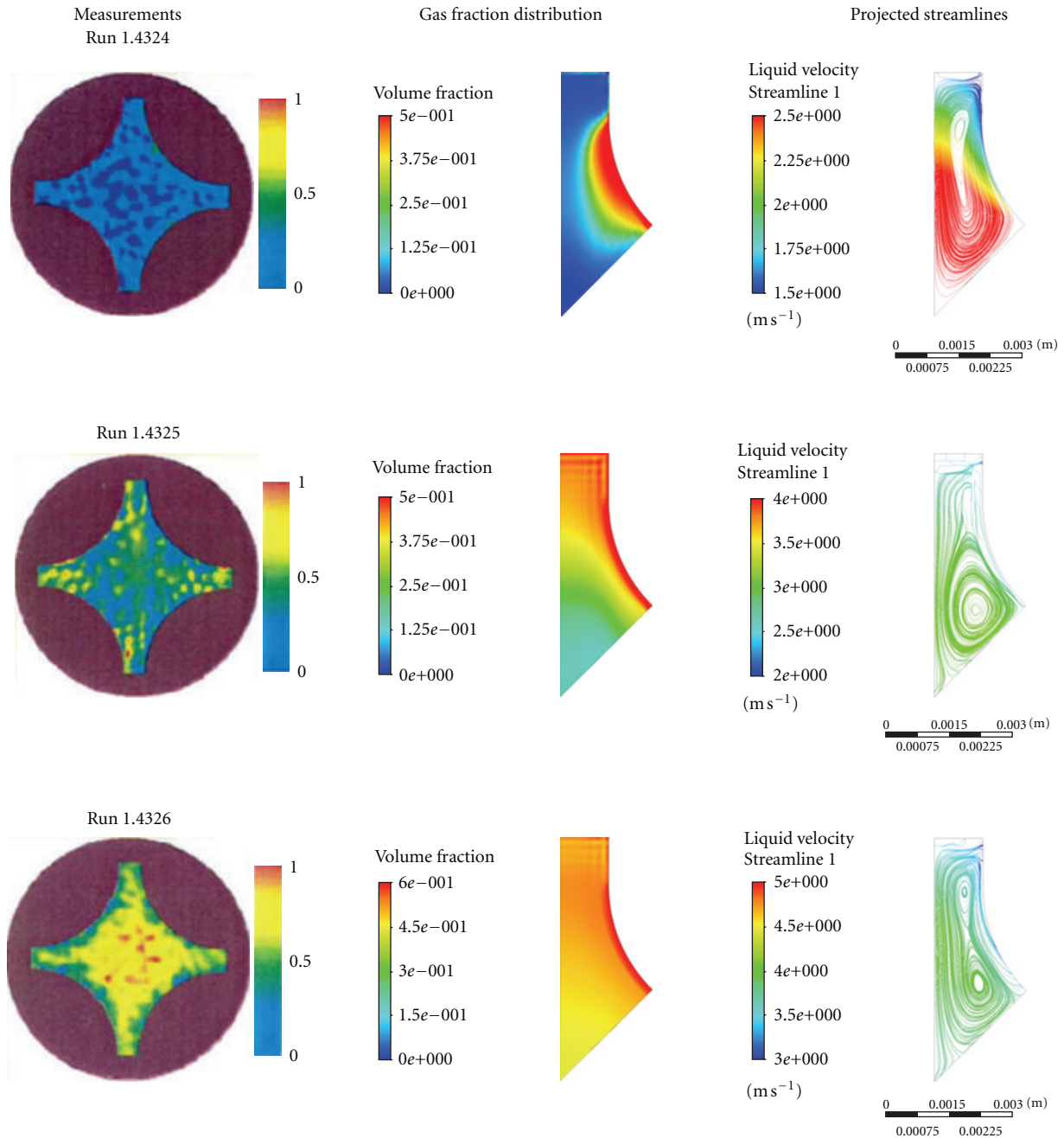


FIGURE 11: Tendencies of gas fraction distribution for the runs 1.4324, 1.4325, and 1.4326.

and gas fractions can be calculated with good agreement to experimental data.

6. Influence of the Turbulence Model on the Gas Fraction Distribution

Considering the cross-sectional distribution of the gas fraction, remarkable differences between the calculations using different turbulence models were found. Applying a turbulence model with a scalar turbulent viscosity, like the SST-model, the maximum of the gas was found near the heated

wall in all cases. Figure 9(a) shows the calculated distribution for run 1.2422. In contrast, the measured gas distributions published in the benchmark specifications show significant amounts of gas also in the core of the channel. This is more similar to the results obtained by a Reynolds Stress model (see Figure 9(b)). The reason for these different patterns is probably that the SST model is not able to capture the secondary flows (see Figure 10).

Figure 11 shows the comparison of different runs with increasing inlet temperature (compare Table 1). With increasing inlet temperature the maximum gas fraction is

shifted from the corner zones towards the core regions of the channel. The figure clearly shows the influence of the liquid flow field on the gas distribution similar to the measurements.

7. Conclusion

Current CFD implementations of a wall boiling model are able to calculate the gas fractions in good agreement with measurements. The model review in Section 3 has shown which information is necessary to perform meaningful calculations. With suitably calibrated correlations for the bubble size at detachment and the nucleation site density, at least cross sectionally averaged values for the mixed density and gas fractions can be calculated with good agreement to experimental data. In the corresponding experiments besides the measurement of gas fraction the determination of the temperature at the heated wall is urgent necessarily. Further research to reduce the number of model parameters that have to be determined by model calibration would be highly desirable. The distribution of gas within a cross section has been shown to depend strongly on the modelling of turbulence. Indication has been given that common two-equation models are too simplified for subchannel geometries while anisotropic Reynolds Stress models show a better potential. In order to make a stringent qualification of models, however, much more detailed CFD-grade data are urgently needed. While all of our calculations were performed for steady-state conditions, numerical convergence was a subject requiring special attention which could indicate that the real solution might contain transient elements.

Acknowledgment

The work was funded by the German Federal Ministry of Education and Research under the contract no. 02NUK010A.

References

- [1] D. A. Drew and S. L. Passman, *Theory of Multicomponent Fluids*, Springer, New York, NY, USA, 1998.
- [2] G. H. Yeoh and J. Y. Tu, *Computational Techniques for Multiphase Flows—Basics and Applications*, Butterworth-Heinemann, Elsevier Science and Technology, 2010.
- [3] M. Ishii and T. Hibiki, *Thermo-Fluid Dynamics of Two-Phase Flow*, Springer, New York, NY, USA, 2nd edition, 2011.
- [4] N. Kuru and M. Z. Podowski, “Multidimensional effects in forced convection subcooled boiling,” in *Proceedings of the 9th International Heat Transfer Conference*, Jerusalem, Israel, 1990.
- [5] N. Kuru and M. Podowski, “On the modeling of multidimensional effects in boiling channels ANS,” in *Proceedings of 27th National Heat Transfer Conference*, Minneapolis, Minn, USA, 1991.
- [6] E. Krepper, B. Končar, and Y. Egorov, “CFD modelling of subcooled boiling—concept, validation and application to fuel assembly design,” *Nuclear Engineering and Design*, vol. 237, no. 7, pp. 716–731, 2007.
- [7] G. G. Bartolomej and V. M. Chanturiya, “Experimental study of true void fraction when boiling subcooled water in vertical tubes,” *Thermal Engineering*, vol. 14, pp. 123–128, 1967, translated from *Teploenergetika*, vol. 14, no. 2, pp. 80–83, 1967.
- [8] K. Hori, Y. Akiyama, K. Miyazaki, and etal, “In bundle void fraction measurement of PWR fuel assembly,” in *Proceedings of ICONE 2*, vol. 1, pp. 69–76, San Francisco, Calif, USA, March 1993.
- [9] K. Hori, Y. Akiyama, K. Miyazaki, T. Kurosu, and S. Sugiyama, “Void fraction in a single channel simulating one subchannel of a PWR fuel assembly,” in *Two-Phase Flow Modeling and Experimentation*, pp. 1013–1027, 1995.
- [10] JNES, “OECD/NEA Benchmark based on NUPEC PWR subchannel and bundle tests (PSBT),” Assembly Specification and Benchmark Database (Volume 1), JNES/SAE-TH08-0019, April 2009.
- [11] B. A. Kader, “Temperature and concentration profiles in fully turbulent boundary layers,” *International Journal of Heat and Mass Transfer*, vol. 24, no. 9, pp. 1541–1544, 1981.
- [12] V. I. Tolubinsky and D. M. Kostanchuk, “Vapour bubbles growth rate and heat transfer intensity at subcooled water boiling heat transfer,” in *Proceedings of the 4th International Heat Transfer Conference*, vol. 5, Paris, France, 1970, paper no. B-2.8.
- [13] N. I. Kolev, “Uniqueness of the elementary physics driving heterogeneous nucleate boiling and flashing,” *Nuclear Engineering and Technology*, vol. 38, no. 1, pp. 33–42, 2006.
- [14] R. Cole, “A photographic study of pool boiling in the region of the critical heat flux,” *AIChE Journal*, vol. 6, no. 4, pp. 533–542, 1960.
- [15] B. B. Mikic and W. M. Rohsenow, “A new correlation of pool-boiling data including the fact of heating surface characteristics,” *ASME Journal of Heat Transfer*, vol. 91, no. 2, pp. 245–250, 1969.
- [16] W. E. Ranz and W. R. Marshall, “Evaporation from drops,” *Chemical Engineering Progress*, vol. 48, no. 3, pp. 141–146, 1952.
- [17] H. Anglart, O. Nylund, N. Kuru, and M. Z. Podowski, “CFD prediction of flow and phase distribution in fuel assemblies with spacers,” *Nuclear Engineering and Design*, vol. 177, no. 1–3, pp. 215–228, 1997.
- [18] Y. Sato, M. Sadatomi, and K. Sekoguchi, “Momentum and heat transfer in two-phase bubble flow-I. Theory,” *International Journal of Multiphase Flow*, vol. 7, no. 2, pp. 167–177, 1981.
- [19] A. D. Burns, T. Frank, I. Hamill, and J. M. Shi, “The favre averaged drag model for turbulence dispersion in Eulerian multiphase flows,” in *Proceedings of the 5th International Conference on Multiphase Flow (ICMF’04)*, Yokohama, Japan, 2004.
- [20] M. Ishii and N. Zuber, “Drag coefficient and relative velocity in bubbly, droplet or particulate flows,” *AIChE Journal*, vol. 25, no. 5, pp. 843–855, 1979.
- [21] A. Tomiyama, H. Tamai, I. Zun, and S. Hosokawa, “Transverse migration of single bubbles in simple shear flows,” *Chemical Engineering Science*, vol. 57, no. 11, pp. 1849–1858, 2002.
- [22] S. P. Antal, R. T. Lahey, and J. E. Flaherty, “Analysis of phase distribution in fully developed laminar bubbly two-phase flow,” *International Journal of Multiphase Flow*, vol. 17, no. 5, pp. 635–652, 1991.
- [23] F. R. Menter, “Two-equation eddy-viscosity turbulence models for engineering applications,” *AIAA Journal*, vol. 32, no. 8, pp. 1598–1605, 1994.
- [24] E. Krepper and R. Rzehak, “CFD for subcooled flow boiling: simulation of DEBORA experiments,” *Nuclear Engineering and Design*, vol. 241, no. 9, pp. 3851–3866, 2011.

Research Article

Numerical Study of the Steady-State Subchannel Test-Case with NEPTUNE_CFD for the OECD/NRC NUPEC PSBT Benchmark

C. Baudry, M. Guingo, A. Douce, J. Laviéville, S. Mimouni, and M. Boucker

EDF R&D, Fluid Dynamics, Power Generation and Environment Department-6, Quai Watier 78401 Chatou, France

Correspondence should be addressed to M. Guingo, mathieu.guingo@edf.fr

Received 30 March 2012; Accepted 27 July 2012

Academic Editor: Diana Cuervo

Copyright © 2012 C. Baudry et al. This is an open access article distributed under the Creative Commons Attribution License, which permits unrestricted use, distribution, and reproduction in any medium, provided the original work is properly cited.

The multifield computational fluid dynamics (CFD) code NEPTUNE_CFD is applied to carry out a numerical study of the steady-state subchannel test-case of the OECD/NRC NUPEC PWR subchannel and bundle tests (PSBTs) international benchmark, focusing on the simulation of a subset of five selected experimental runs of the centered subchannel configuration. First, using a standard choice for the physical models and a constant, predetermined bubble diameter, the calculated void fraction is compared to experimental data. Besides, the mesh sensitivity of the calculated void fraction is investigated by performing simulations of three grid levels, and the propagation of the experimental uncertainties on the input parameters of the simulations is also studied. Last, calculation results with devoted models for the bubble-size distribution are analyzed. Their impact is visible on the subcooled run, giving void fraction closer to experiments than those obtained with a fixed bubble-size. Void-fraction distribution with bubble-size models is also shown to come closer to experiment for another run with a higher equilibrium quality.

1. Introduction

The OECD/NRC PWR subchannel and bundle Tests (PSBT) benchmark was an international project endorsed by the OECD/NEA (Organisation for Economic Co-operation and Development/Nuclear Energy Agency) and supported by US NRC (United States National Regulatory Commission) and METI (Japanese Ministry of Economy, Trade and Industry), in which a large experimental database of void-fraction measurements performed at NUPEC (Nuclear Power Engineering Corporation) under PWR (Pressurized Water Reactor) thermal-hydraulic conditions in different geometric configurations (different types of isolated subchannels or rod bundle) has been made available to the participants for numerical simulation. One of the purposes of this benchmark is to provide experimental data that can be used for the validation of numerical models of void-fraction distribution over a wide range of operating conditions, and for the development of novel approaches. PSBT was not a blind benchmark, in the sense of the experimental value of the variables of interest were provided to the participants. The benchmark was organized in two phases; the first focusing on a void-distribution benchmark while

the topic of the second was the departure from nucleate boiling (DNB) phenomenon. More details on the benchmark organization can be found at [1]. Each phase encompassed several exercises: the current paper focuses on the simulation of the steady-state subchannel exercise of phase I (i.e., Exercise I-1). For each simulated run of this exercise, three main results were asked from the participants.

- (i) A numerical calculation of the cross-section void fraction at a given elevation, to be compared to experimental data.
- (ii) A 2D view of the void-fraction distribution in this section. Ideally, this result could also be compared to an experimental view obtained by chromotomography. However, this comparison was proven difficult due in particular to the fairly low resolution of the experimental view. Therefore, in the following, only one of these experimental views will be used for comparison with numerical simulations.
- (iii) The evolution of the cross-section averaged void fraction with respect to the elevation. No experimental data was available for this result. However, it seemed interesting to analyze how the different

codes predicted, for instance, the transition to fully-developed subcooled boiling for some of the runs.

This paper aims at presenting and analyzing simulations carried out with the multifield computational fluid dynamics (CFD) code NEPTUNE_CFD [2] for Exercise I-1. Following the NEA/CSNI best practice guidelines [3], a mesh sensitivity analysis is performed on three grid refinements, and the influence of the experimental uncertainties on the numerical results is assessed. As a first step, the standard set of parameters of the code is applied, with in particular the use of a second-order (Reynolds stress) turbulence model, as well as a constant, predetermined bubble diameter. In the last part of the paper, the impact of more detailed descriptions of the bubble-size distribution is presented.

2. Experimental Configuration of the Steady-State Subchannel Exercise

The test facility of the steady-state subchannel exercise represents one of the subchannel types found in a PWR assembly. The effective heated length is 1.555 m, while the measurement of the void fraction takes place at 1.4 m from the bottom of the heated section. The external diameter of the rod is 9.5 mm; the rod pitch and the rod gap measure, respectively, 12.6 mm and 3.1 mm. The heating power is uniformly distributed. Additional details about the experimental apparatus may be found in [4]. The void fraction is measured by using the chromotomography (CT) technique, which also gives the local distribution of the time-averaged void fraction at the measuring section [5]. The initial set of experimental runs of Exercise I-1 counted approximately 40 runs, taking place in different subchannel types (center, center with a guide tube, side and corner). However, after discussion between participants and PSBT organizers, five runs have been selected to be more precisely analyzed:

- (i) the run whose operating conditions are the closest to PWR normal conditions (reference 1.2211),
- (ii) two runs with a higher inlet temperature and a relatively low wall heat flux (references 1.2223 and 1.2237),
- (iii) two runs differing only by the value of the inlet temperature (references 1.4325 and 1.4326), with a lower heat flux and a lower pressure than run 1.2211. Run 1.4325 was also chosen due to its particular void-fraction distribution at the measuring section, mainly located in the non-heated corners of the domain.

The value of the controlling parameters of the runs and the cross-section averaged void-fraction measurements are summarized in Table 1. Furthermore, the estimated uncertainties on the flow parameters and on the void-fraction measurement provided by the experimentalists are given in Table 2. It can be observed that run 1.2211 is the only selected run in subcooled conditions in the whole subchannel (with a negative thermal equilibrium quality at the measuring section).

TABLE 1: Characteristics of the five selected test-cases. In bold font, the run whose condition are the closest to PWR normal conditions.

	1.2211	1.2223	1.2237	1.4325	1.4326
Outlet pressure (bar)	147.2	147.2	147.4	98.4	98.2
Inlet temperature (K)	295.4	319.6	329.6	253.6	268.8
Inlet mass flow rate (kg·m ⁻² ·s ⁻¹)	3030.6	3030.6	3036.1	1397.2	1394.4
Wall heat flux (kW)	90	69.8	60	59.8	59.8
Equilibrium quality	-0.04	0.04	0.08	0.05	0.11
Averaged void fraction	0.04	0.31	0.44	0.34	0.53
Averaged fluid density (kg·m ⁻³)	610	456	390	478	353

TABLE 2: Given experimental uncertainties on the controlling parameters of the test-case and on the void-fraction measurements.

	Estimated exp. uncertainties (1 σ)
Pressure	1%
Inlet temperature	1 K
Mass flow rate	1.5%
Wall heat flux	1%
Averaged void fraction	0.03

3. The NEPTUNE_CFD Code

3.1. Main Features of the Code. NEPTUNE_CFD is a 3D, multifield CFD code developed in the framework of the NEPTUNE project, financially supported by CEA (Commissariat à l'Énergie Atomique et aux Énergies Alternatives), EDF, IRSN (Institut de Radioprotection et de Sécurité Nucléaire) and AREVA-NP. It is mainly devoted to the study and the simulation of nuclear reactor applications involving multiphase flows, such as two-phase pressurized thermal shock (PTS) and departure from nucleate boiling (DNB) applications. The need to simulate PTS applications have led in particular to the development and the numerical implementation of specific methods of interface detection for free surface flows [6]. The code follows the classical multifield one-pressure formulation [7]. For each phase k , the basic set of resolved conservation equations (mass, momentum and total enthalpy denoted H_k) is the following:

$$\begin{aligned}
 & \frac{\partial \alpha_k \rho_k}{\partial t} + \text{div}(\alpha_k \rho_k \mathbf{U}_k) = \Gamma_k, \\
 & \frac{\partial \alpha_k \rho_k \mathbf{U}_k}{\partial t} + \text{div}(\mathbf{U}_k \otimes \alpha_k \rho_k \mathbf{U}_k) \\
 & = \text{div}(\alpha_k \boldsymbol{\tau}_k + \boldsymbol{\Sigma}_k) - \alpha_k \nabla P + \mathbf{I}'_k + \Gamma_k \mathbf{U}_k + \alpha_k \rho_k \mathbf{g} + \alpha_k \mathbf{S}_k, \\
 & \frac{\partial \alpha_k \rho_k H_k}{\partial t} + \text{div}(\alpha_k \rho_k \mathbf{U}_k H_k) \\
 & = \text{div}(\alpha_k \lambda_k \nabla T_k) + \text{div}((\alpha_k \boldsymbol{\tau}_k + \boldsymbol{\Sigma}_k) \mathbf{U}_k) \\
 & + \alpha_k \frac{\partial P}{\partial t} + \mathbf{U}_k \cdot \mathbf{I}'_k + \alpha_k \rho_k \mathbf{g} \cdot \mathbf{U}_k + \Gamma_k H_k + \Pi'_k.
 \end{aligned} \tag{1}$$

Additionally, the following relation on volume fractions holds:

$$\sum \alpha_k = 1. \quad (2)$$

In these equations, α_k is the volume fraction, ρ_k is the density, \mathbf{U}_k is the velocity, τ_k and Σ_k are, respectively, the laminar and the turbulent stress tensor; Γ_k is the interfacial mass transfer, \mathbf{I}'_k represents the momentum transfer from all the other phases to phase k , Π_k represents the heat transfer between phases, P is the pressure, T_k is the temperature, and λ_k is the conductivity. Additional jump relations are supplied for the interfacial transfers.

The spatial discretization is a full unstructured finite-volume approach with a collocated arrangement of all-variables. The numerical algorithm used is a semi-implicit, pressure-based method where the system of equations is solved in two major fractional steps: first, a prediction of the velocities based on the momentum equations; then, the coupling between phase fraction, pressure, and energy through mass and energy equations and a simplified form of momentum equations [8].

3.2. Physical Modeling for the Current Study. The turbulence of the liquid phase is modeled using a second-order, RANS (Reynolds-Averaged Navier-Stokes) model [9] including bubble-induced turbulence effects, whereas a turbulent dispersion model is applied on the gas phase [10]. The interfacial transfer of momentum is considered as the sum of different contributions, namely, the drag force (modeled by using the correlation developed by Ishii and Zuber [11]), the added mass force (by using the expression of Zuber [12]) and the formulation of the lift force proposed by Tomiyama et al. [13]. As a general feature of the NEPTUNE-CFD code, no flow-regime map is used, as the flow is regarded as bubbly.

At the heating wall, the heat transfer model is an extension of the approach of Kurul and Podowski [14], which is often referred to as the RPI (rensselaer polytechnic institute) model and which consists in splitting the heat flux into three terms: one heating the liquid phase in contact with the wall, one responsible for the bubble generation, and the last one arising from the arrival of liquid water at the wall, caused by bubble departure (the so-called “quenching” flux). When the void fraction in the boundary cells is sufficiently high, a fourth flux is introduced to take into account the convective heat transfer transmitted to the vapor. In the bulk, the recondensation model is based on the Ranz-Marshall correlation.

For the first series of calculations, a constant, pre-determined diameter for the bubbles has been taken equal to 0.3 mm, based on previous experimental observations carried out in PWR conditions [15]. It can be thus expected for this modeling choice to behave more satisfactorily for runs with a relatively low void fraction (i.e., where coalescence and fragmentation phenomena can be neglected). As a second step, the influence of a more refined description of the bubble-size distribution has been studied by performing simulations using the interfacial area models of Yao and

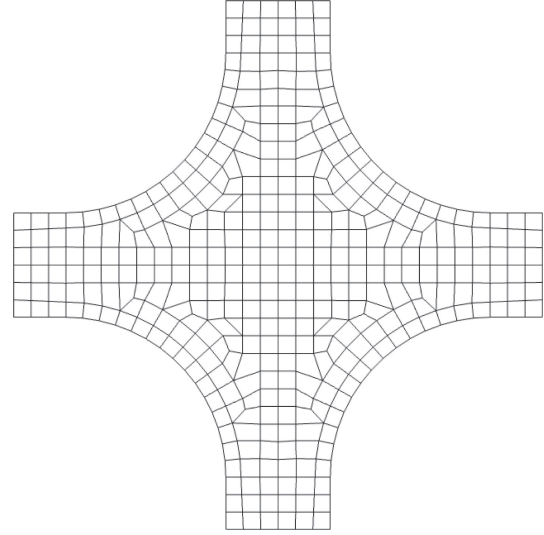


FIGURE 1: Cross-section view of grid level 1.

TABLE 3: Characteristics of the grids used in the simulations.

	Grid level 1	Grid level 2	Grid level 3
Total number of cells	154,812	602,040	1,561,152
Number of cells in the axial direction	400	520	520
Number of cells in a cross-section	388	1160	3008
Cell size in the axial direction	4 mm	3 mm	3 mm
Distance-to-wall of the boundary-cell centers	0.25 mm	0.15 mm	0.1 mm

Morel [16] and Ruyer and co-workers [17], which have been validated in PWR conditions in a vertical duct geometry.

4. Computational Strategy

4.1. Time Convergence. In order to reach the steady state, a transient algorithm is used in NEPTUNE-CFD. The time step chosen is time-dependent, with a maximal CFL number set to 1 for stability reasons and convergence of the iterative numerical algorithm.

4.2. Characteristics of the Grids. Following the NEA/CSNI (Committee on the Safety of Nuclear Installations) best practice guidelines, three grids with different refinements have been used for this study. Their main features are recapitulated in Table 3; cross-section views of the grids are proposed in Figures 1, 2, and 3. The normalized wall-normal distance of the boundary-cells centers ranges from approximately 75 (run 1.4326, grid level 3) to approximately 320 (run 1.2211, grid level 1), supporting the use of a high-Reynolds formulation of a second-order RANS turbulence model. It can be seen that the refinement factor from grid level 1 to grid level 3 is approximately equal to 3 following two perpendiculars belonging to a cross-section, and 1.3 in the axial direction.

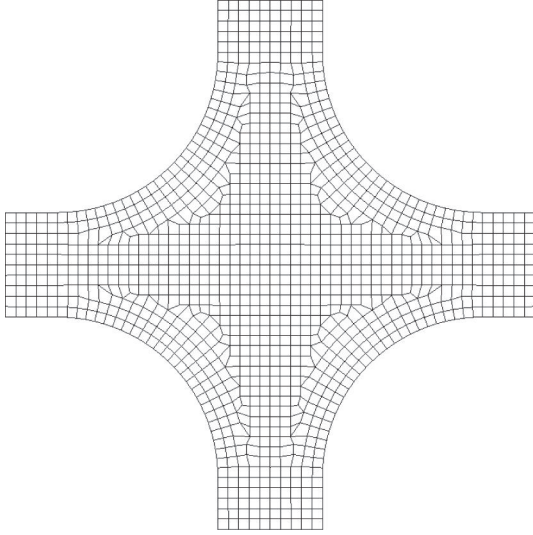


FIGURE 2: Cross-section view of grid level 2.

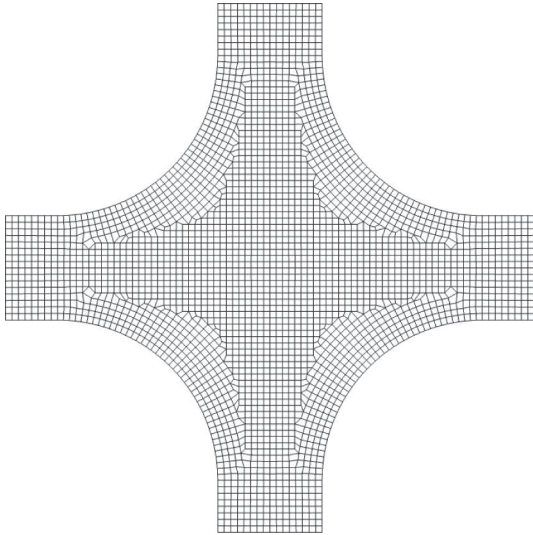


FIGURE 3: Cross-section view of grid level 3.

4.3. *Boundary and Initial Conditions.* The profiles of the inlet velocities and turbulent variables (Reynolds stresses and mean dissipation) have been calculated before-hand through devoted calculations, so as to get developed flow profiles. The procedure followed for these calculations amounts to calculating a case without thermal power in an infinite channel of the same cross section; and then selecting the profiles of the variables where they do not vary anymore. The initial conditions for velocities, temperature and turbulent variables are taken equal to the inlet conditions.

5. Results Obtained with a Constant, Predetermined Bubble Diameter

5.1. *Void Fraction at the Measuring Section.* The calculations have been carried out on 36 to 144 cores on the EDF R&D

TABLE 4: Cross-section averaged void fraction obtained on the three grid levels.

	1.2211	1.2223	1.2237	1.4325	1.4326
Exp. values	0.04	0.31	0.44	0.34	0.53
Grid level 1	0.06	0.25	0.36	0.44	0.63
Grid level 2	0.07	0.25	0.36	0.44	0.63
Grid level 3	0.07	0.25	0.36	0.44	0.63

Ivanhoe cluster (Westmere 2.93 GHz Infiniband). The time to reach the steady state represents approximately 2 to 4 seconds of “physical” time. First, calculations were run under nominal conditions on the three grid levels to investigate the grid sensitivity of the results. The values of the cross-section averaged void fraction at the 1.40-meter section are summarized in Table 4. It can be observed that simulations performed on grid level 1 give void-fraction values very close to those obtained on grid level 3 (the discrepancy is of order of ± 0.01).

Concerning the comparison with the experimental values for the cross-section averaged void fraction:

- (i) for run 1.2211 (subcooled), the simulations overestimate the void fraction by 0.03; thus, reaching the upper bound of the 1σ -uncertainty on the void-fraction measurement.
- (ii) for runs 1.2223 and 1.2237 (high inlet temperature and low wall heat flux), the simulations underestimate the experimental void fraction by 0.06 to 0.08;
- (iii) for runs 1.4325 and 1.4326 (low pressure), the void fraction is overestimated by 0.1.

On average, the deviation between numerical results and experimental data is then of the order of 0.06 void-fraction units; and consequently more visible on the subcooled run (1.2211).

5.2. *Axial Evolution of the Flow.* The axial evolution of the cross-section averaged void fraction for the five runs are presented from Figures 5, 6, 7, 8, and 9, as well as the axial evolution of the wall temperature at a given location of a heating wall (see Figure 4).

It can be seen that for almost every run (except for the subcooled run 1.2211), vapor is generated right from the start of the heated section. Furthermore, concerning runs 1.2223, 1.2237, and 1.4325, a change of the slope in the evolution of the mean void fraction is visible, respectively, for an elevation approximately equal to 0.9 m, 0.6 m, and 0.9 m. This change occurs at the same elevation as an increase of the wall temperature, indicating the beginning of the fully-developed subcooled boiling (FDB) [18]. Runs 1.4325 and 1.4326 exhibit approximately the same behavior. For instance, for run 1.4325, different regimes are observed:

- (i) from the bottom of the subchannel to approximately 0.7 m, the mean void fraction is rising slowly, corresponding to the partial subcooled boiling regime;
- (ii) from 0.7 m up, the void fraction rises more rapidly, corresponding to the FDB regime.

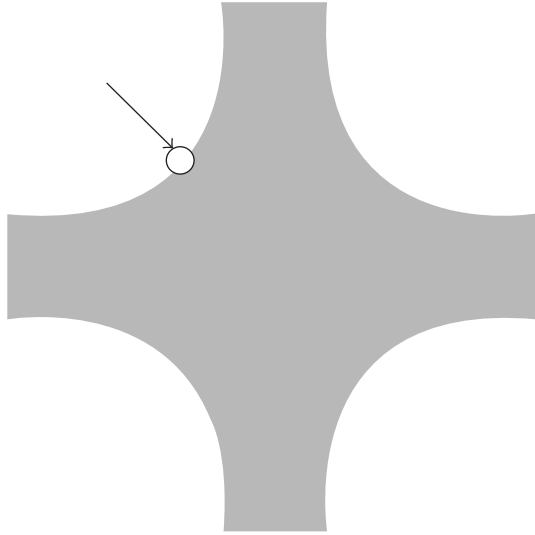


FIGURE 4: Position of the probe monitoring the axial evolution of the wall temperature.

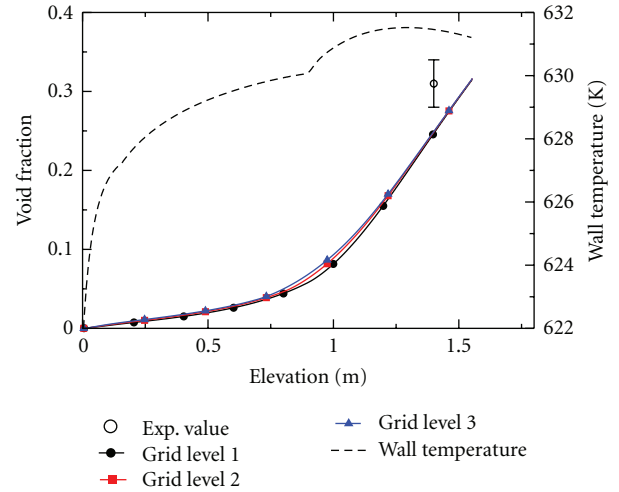


FIGURE 6: Run 1.2223. Axial evolution of the cross-section averaged void fraction for the 3 grid levels.

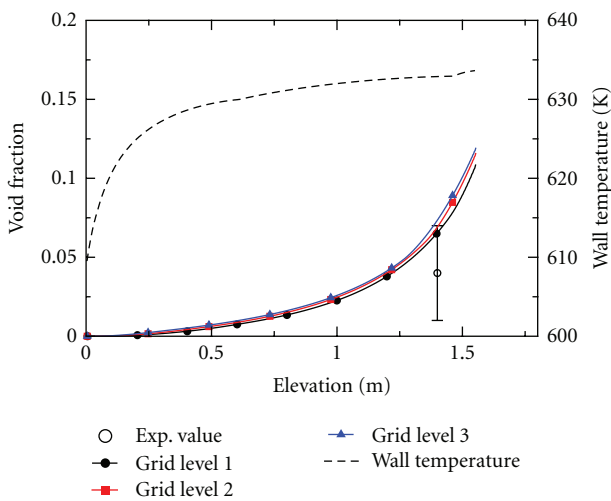


FIGURE 5: Run 1.2211. Axial evolution of the cross-section averaged void fraction for the 3 grid levels.

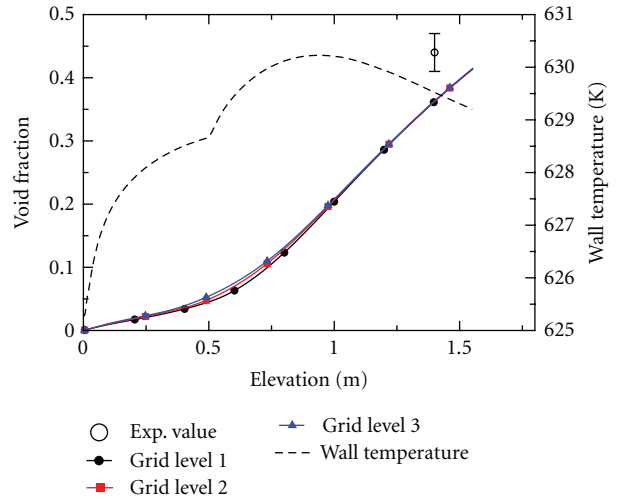


FIGURE 7: Run 1.2237. Axial evolution of the cross-section averaged void fraction for the 3 grid levels.

(iii) finally, towards the end of the domain, the wall temperature jumps from 605 K to several thousands Kelvin (not represented): in this region, the calculated near-wall void fraction exceeds 0.8, which is the threshold value used in the code to switch continuously from the nucleate boiling to a pseudo-film boiling. In this model, the totality of the imposed heat flux is transferred to the vapor (rising its temperature above saturation), therefore, bringing about a drop of the heat transfer coefficient. Let us note that this model is not yet considered as validated.

Furthermore, Figure 10 represents the evolution of the average liquid temperature and of the saturation temperature for run 1.4325. At the end of the domain, the two temperatures

are almost equal, corresponding to the saturated boiling regime.

5.3. *Propagation of the Experimental Uncertainties.* As the estimated uncertainties on the controlling parameters of the flow are provided (see Table 2), it is interesting to analyze the effects of these uncertainties on the simulations. For this purpose, a series of calculations has been performed in which one of the controlling parameters is taken equal to its nominal values plus or minus the value of the relative uncertainties, the other parameters remaining fixed to the nominal values. This procedure makes it possible to study the effect of one uncertainty independently from the others. In order to keep a reasonable time-to-result, the coarsest grid has been used (grid level 1). The results obtained for the void fraction are recapitulated in Table 5.

TABLE 5: Effect of the experimental uncertainties on the calculated void fraction.

	1.2211	1.2223	1.2237	1.4325	1.4326
Exp. values	0.04	0.31	0.44	0.34	0.53
Nominal Calc. values (α_{nom})	0.07	0.25	0.36	0.44	0.64
Pressure $\pm 1\%$	$\alpha_{\text{nom}} \pm 0.02$	$\alpha_{\text{nom}} \pm 0.02$	$\alpha_{\text{nom}} \pm 0.02$	$\alpha_{\text{nom}} \pm 0.01$	$\alpha_{\text{nom}} \pm 0.01$
Inlet Temp. $\pm 1\text{ K}$	$\alpha_{\text{nom}} \pm 0.02$	$\alpha_{\text{nom}} \pm 0.02$	$\alpha_{\text{nom}} \pm 0.02$	$\alpha_{\text{nom}} \pm 0.01$	$\alpha_{\text{nom}} \pm 0.01$
Mass flow rate $\pm 1.5\%$	$\alpha_{\text{nom}} \pm 0.01$				
Wall heat flux $\pm 1\%$	$\alpha_{\text{nom}} \pm 0.01$				

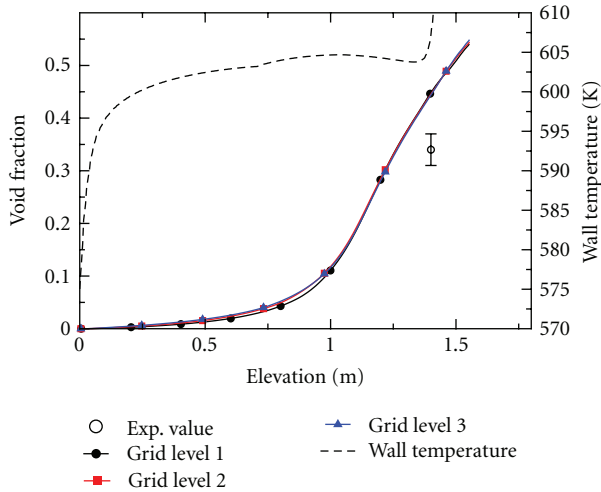


FIGURE 8: Run 1.4325. Axial evolution of the cross-section averaged void fraction for the 3 grid levels.

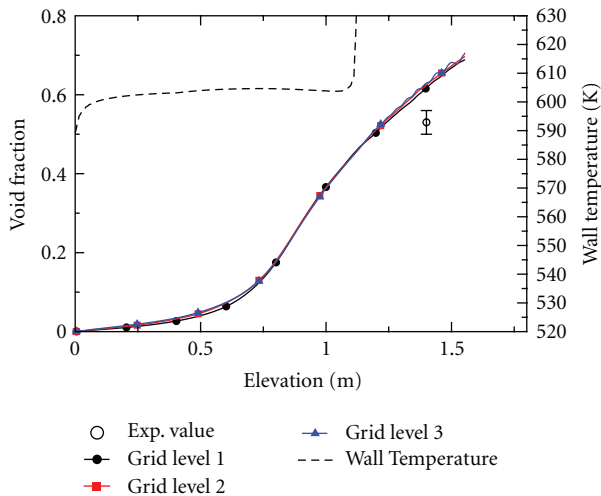


FIGURE 9: Run 1.4326. Axial evolution of the cross-section averaged void fraction for the 3 grid levels.

These series of calculations show that for a relatively small variation of any parameter, the result on the averaged void fraction is modified by approximately 0.01, whatever its absolute value. Consequently, the relative impact on the void-fraction value of a single parameter variation is

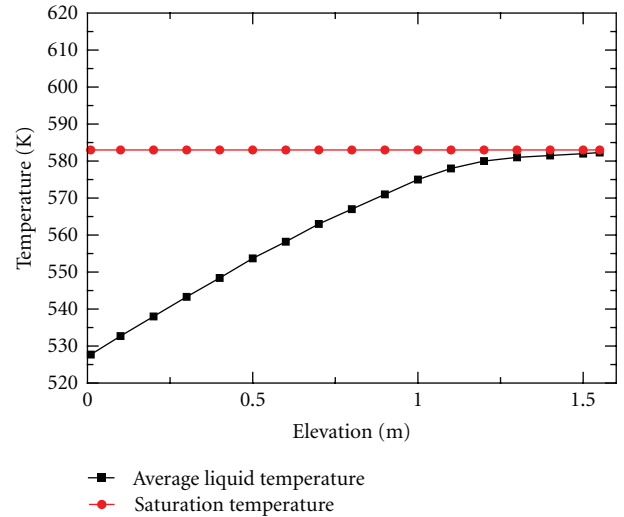


FIGURE 10: Run 1.4325: Longitudinal evolution of the average liquid temperature and of the saturation temperature.

more visible on the subcooled case, that is, the run that shows the lowest void-fraction value. Furthermore, it can be seen that within the bounds provided for the experimental uncertainties, no input parameter seems to have a foremost importance with respect to the others on the calculated void fraction.

As a second step, two additional series of calculations have been carried out: for each series, the set of parameters expected to give the highest or the lowest value of the averaged void fraction has been chosen. The results obtained are reported in Table 6. These simulations show that taking the two “opposite” sets of parameters give numerical results that may span on a range quite wide: for instance, for run 1.4325, the void-fraction value varies on a 0.08-wide interval, representing approximately 15% of the nominal value. The impact is more visible for run 1.2211, where a calculated 0.03-wide variation represents nearly 50% of the nominal value.

6. Effect of More Refined Descriptions of Bubble-Size Distribution

The calculations presented so far have been obtained by using a constant and uniform predetermined bubble diameter equal to 0.3 mm. In order to further investigate the five runs, simulations have been run by using dedicated models for

TABLE 6: Calculated void-fraction values with two “opposite” sets of parameters.

	1.2211	1.2223	1.2237	1.4325	1.4326
Exp. Values	0.04	0.31	0.44	0.34	0.53
Nominal Calc. values (α_{nom})	0.07	0.25	0.36	0.44	0.64
Pressure – 1%					
Inlet Temp. + 1 K					
Mass flow rate – 1.5%	0.08	0.28	0.39	0.48	0.65
Wall heat flux + 1%					
Pressure + 1%					
Inlet Temp. – 1 K					
Mass flow rate + 1.5%	0.05	0.21	0.32	0.40	0.58
Wall heat flux – 1%					

the bubble-size distribution, namely, the model proposed by Yao and Morel [16], further referred to as the Yao-Morel model, and the model developed by Ruyer and co-workers [17, 19], further referred to as the Ruyer-Seiler model. The Yao-Morel model follows the so-called “single-size” approach for bubbly flows [20]. This approach considers that the bubbles have locally the same size, often represented by the Sauter mean diameter, which is directly connected to the local void fraction and to the interfacial area, the latter being obtained by the resolution of an additional transport equation. This equation takes into account bubble-size variation caused by gas compressibility, and contains terms standing for bubble coalescence and fragmentation that need to be modeled.

The Ruyer-Seiler model can be regarded as more refined since it follows the “moment-density” approach, which consists of assuming a certain form for the bubble diameter distribution function, and then solving equations on the moments defining this distribution. The Ruyer-Seiler model assumes a quadratic form for the bubble-diameter distribution whose graph extends from the origin and is consequently defined by only one parameter. Another possibility of postulated form for the bubble-diameter distribution is a log-normal law, as proposed for instance by Kamp and co-workers [21, 22].

In this section, we specifically focus on two runs: run 1.2211, whose conditions are the closest to PWR normal conditions, and run 1.4325, which exhibits an interesting void fraction distribution according to the experimental 2D view obtained by chromo-tomography.

6.1. Mesh Sensitivity Analysis. First, the two interfacial-area models have been applied on the three grid levels and for the five runs, to analyze the sensitivity of the results to the grid levels. The averaged void fractions obtained are summarized in Table 7, where it is shown that the discrepancy is of the order of 0.01 void-fraction units from grid level 1 to grid level 3, as it was the case for the computations with a fixed bubble diameter. Figures 11, 12 represent the longitudinal distribution of the averaged void fraction for the three grid levels for run 1.2211, and show that the mesh influence remains in the 0.01-limit in the whole domain.

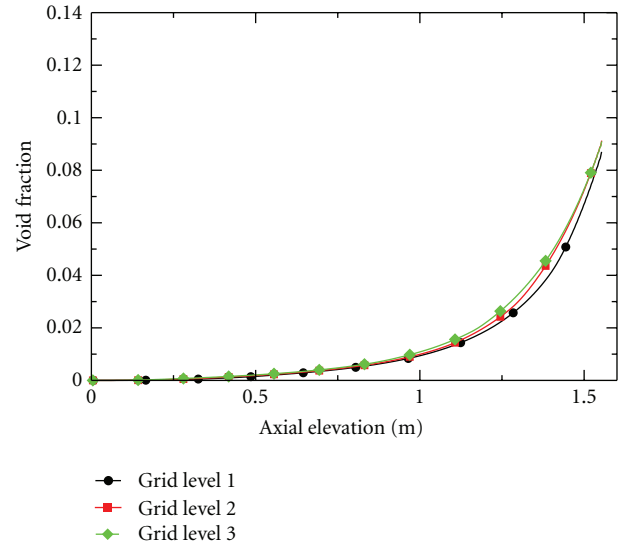


FIGURE 11: Yao-Morel model: Grid influence on the void-fraction axial evolution for run 1.2211.

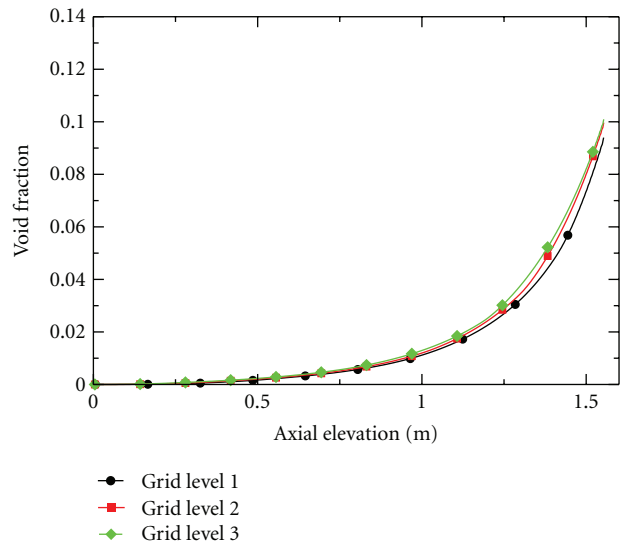


FIGURE 12: Ruyer-Seiler model: Grid influence on the void-fraction evolution for run 1.2211.

6.2. Analysis of Run 1.2211 with Interfacial-Area Models. As shown in Figure 13, the behavior of the two bubble-size models is quite similar concerning the averaged void fraction: From the whole heated length, they predict a void fraction lower than the one obtained with a fixed bubble size. Besides, at the measuring section, the void fraction predicted by the models is closer to the experimental value.

This underprediction with respect to the previous calculations can be connected to the size of the bubbles calculated by the models at the measuring section. The calculated average, minimum, and maximum size of the bubbles at the measuring section are summarized in Table 8. It can be observed that the mean bubble size calculated by the devoted models is smaller than the initial choice of 0.3 mm

TABLE 7: Cross-section averaged void fraction obtained on the three grid levels for the two interfacial-area models used. Y-M stands for the Yao-Morel model; R-S stands for the Ruyer Seiler model.

	1.2211		1.2223		1.2237		1.4325		1.4326	
Exp. values	0.04		0.31		0.44		0.34		0.53	
Bubble-size model	Y-M	R-S								
Grid level 1	0.04	0.05	0.24	0.24	0.36	0.36	0.44	0.45	0.61	0.61
Grid level 2	0.05	0.05	0.24	0.24	0.36	0.36	0.44	0.45	0.61	0.61
Grid level 3	0.05	0.05	0.24	0.25	0.36	0.36	0.44	0.45	0.61	0.61

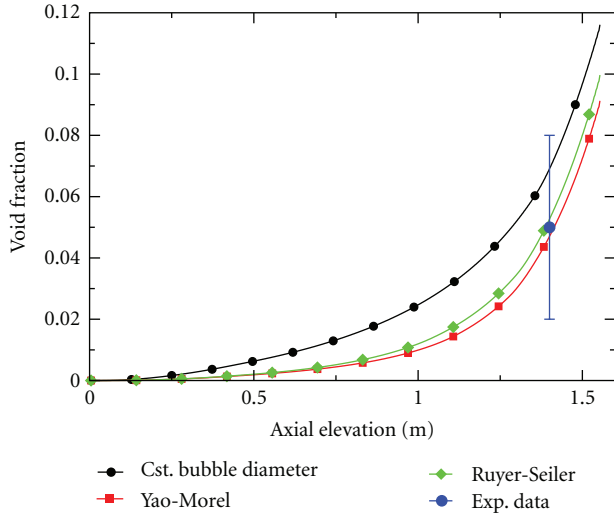


FIGURE 13: Comparison of calculated axial distribution of the mean void fraction for the bubble-size models.

TABLE 8: Run 1.2211. Characteristics of the bubble-diameter at the measuring section with different modeling choices.

	Average	Minimum	Maximum
Fixed bubble diameter	0.3 mm	0.3 mm	0.3 mm
Yao-Morel model	0.09 mm	0.005 mm	0.15 mm
Ruyer-Seiler model	0.15 mm	0.05 mm	0.2 mm

used for the first calculation. This smaller size brings about an increase of the core-flow recondensation phenomenon (due to the higher interfacial area of smaller bubbles), and consequently a decrease of the void fraction.

Cross-section views of the bubble-diameter distributions at the measuring section are proposed in Figures 14, 15, showing quite a similar behavior; with the biggest bubbles (0.2 mm-diameter for the Ruyer-Seiler model, 0.15 mm for the Yao-Morel model) found above the heated walls, whereas the smallest are located in the center and the corners of the domain. To provide a detailed representation, the color scaling has been chosen as the most adapted for each case and is consequently not the same on the two figures.

6.3. Analysis of Run 1.4325 with Interfacial-Area Models. As can be seen in Table 7, the averaged void fraction for run 1.4325 obtained by using interfacial-area models is

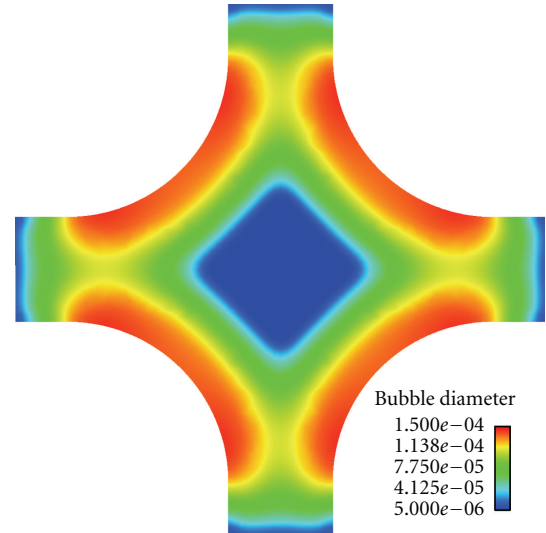


FIGURE 14: Bubble-diameter distribution at the measuring section for run 1.2211 by using the Yao-Morel model.

very similar to the one obtained with a fixed bubble-size diameter (of the order of 0.45). However, the void fraction distribution predicted by the three calculations present notable discrepancies, as presented by Figures 16, 17, and 18 (with a color scaling adapted to the case).

With a fixed bubble diameter set to 0.3 mm, the void fraction is mostly concentrated in a thin layer adjacent to the heated wall, reaching locally peak values of approximately 0.85 and thus triggering the activation of the model of pseudo-film boiling, as described in Section 5.2. With dedicated bubble-size models, on the opposite, consider the following.

- (i) The peak value of the void fraction predicted by applying the bubble-size models is quite lower (0.65 for the Yao-Morel model; 0.55 for the Ruyer-Seiler model). Lower void-fraction peak values calculated by the bubble-size models cause the flow to remain in the nucleate boiling remain for the whole elevation, as presented in Figure 19.
- (ii) Besides, for these calculations (and especially with the Ruyer-Seiler model), high void-fraction values are found near the nonheated corners of the domain, phenomenon that can be seen on the experimental view. The effect of the lift force, which depends on

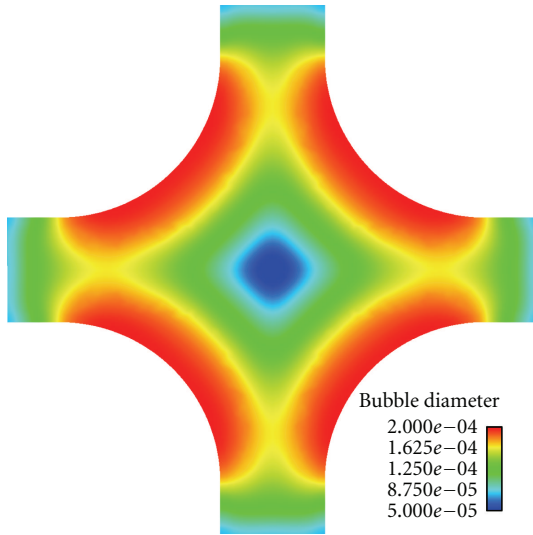


FIGURE 15: Bubble-diameter distribution at the measuring section for run 1.2211 by using the Ruyer-Seiler model.

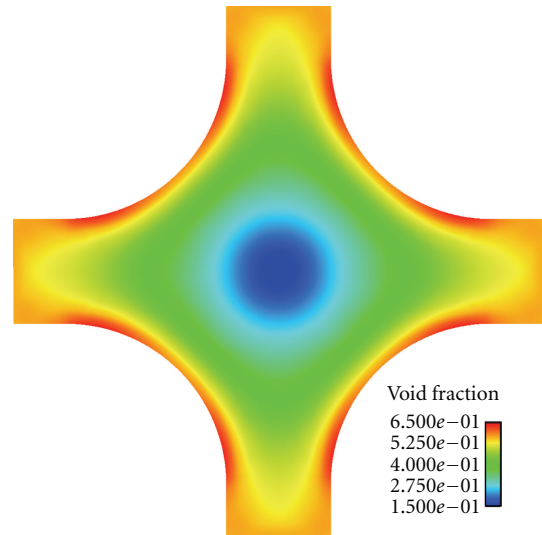


FIGURE 17: Void-fraction distribution at the measuring section for run 1.4325 by using the Yao-Morel model.

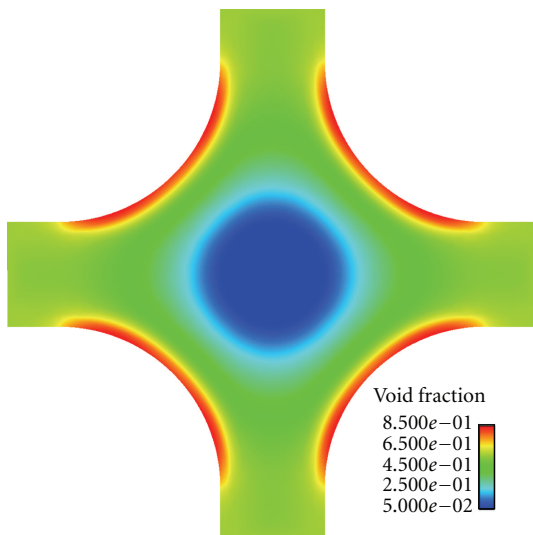


FIGURE 16: Void-fraction distribution at the measuring section for run 1.4325 with a fixed bubble diameter set to 0.3 mm.

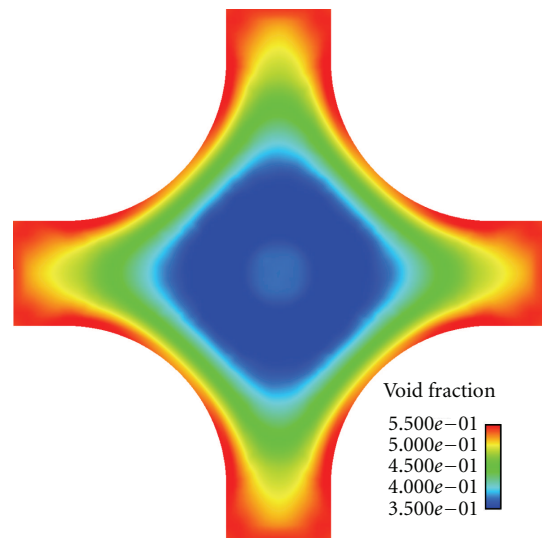


FIGURE 18: Void-fraction distribution at the measuring section for run 1.4325 by using the Ruyer-Seiler model.

the bubble size, may account for this phenomenon, as the average bubble-size predicted by the Ruyer-Seiler model at the measuring section is approximately equal to 1 mm, thus, very different from the calculations with a fixed bubble size. It should be noted that, even if the mean bubble diameter is different, the averaged void fraction is only slightly impacted since recondensation is very small in this case.

7. Conclusion

In this paper, we reported simulations with the multifield CFD code NEPTUNE_CFD in the framework of the first exercise of the OECD/NRC PSBT benchmark, which were

carried out on a centered, isolated subchannel geometry and were compared to experimental data. A standard set of physical models was used, as well as a fixed bubble diameter. In nominal conditions, the discrepancy between calculated and experimental mean void fraction at the measurement section is on average of the order of ± 0.06 void-fraction units. Following the NEA/CSNI best practice guidelines, the impact of the grid on the axial evolution of the mean void fraction has been investigated by using three grid levels, and shown to be of the order of 0.01 void-fraction units. Furthermore, a study of the numerical propagation of the experimental uncertainties has been carried out, providing an envelope of calculated void-fraction varying from 0.05 to 0.1 around the mean value. This sensitivity analysis could be

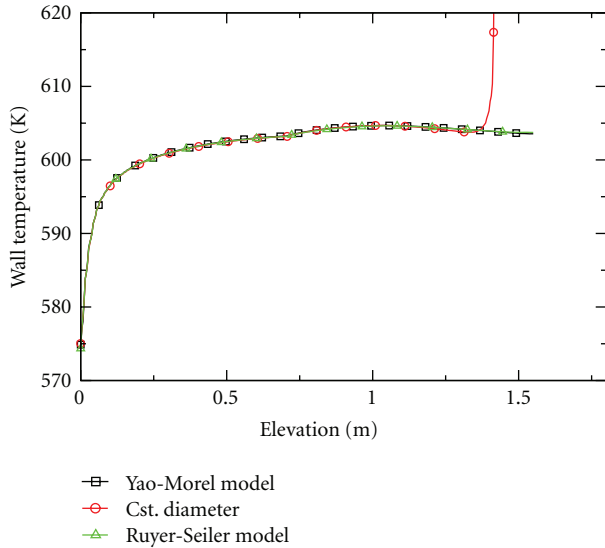


FIGURE 19: Evolution of the wall temperature at the probe position for different bubble-size models.

deepened by sampling all input parameters together, in order to study the coupling between these parameters.

As a second step, models allowing to simulate the dispersion in size of the bubbles have been applied. The use of these models impacted only slightly the axial evolution of the mean void fraction (of the order of 0.01 to 0.02 void-fraction units compared to the fixed-diameter calculation), and was more clearly seen on the subcooled run, with reduced difference between calculated and experimental averaged void fraction. Furthermore, for another run with a higher equilibrium quality, void-fraction distribution with bubble-size models is also shown to come closer to experiment. To further investigate the behavior of the different bubble-size models, as a future work, it would be relevant to study the difference between the break-up and coalescence terms in the two models. On a longer term, to improve the quality of the simulations of saturated (high void fraction) cases, novel methods are being developed in the NEPTUNE project which consider the simulation of large bubbles with interface locating technics, while keeping a statistical treatment for the smaller ones [23].

Acknowledgments

This work has been achieved in the framework of the NEPTUNE project, financially supported by CEA (Commissariat à l'Énergie Atomique et aux Énergies Alternatives), EDF, IRSN (Institut de Radioprotection et de Sécurité Nucléaire), and AREVA-NP.

References

[1] PSBT page on the OECD website. July 2012, <http://www.oecd-nea.org/science/wprs/egrsltb/PSBT>.
 [2] A. Guelfi, D. Bestion, M. Boucker et al., "NEPTUNE: a new software platform for advanced nuclear thermal hydraulics,"

Nuclear Science and Engineering, vol. 156, no. 3, pp. 281–324, 2007.

- [3] Nuclear Energy Agency—Committee on the Safety of Nuclear Installations, "Best practice guidelines for the use of CFD in nuclear reactor safety applications," Technical Report NEA/CSNI, 2007.
- [4] K. Hori, Y. Akiyama, K. Miyazaki, T. Kurosu, and S. Sugiyama, "Void Fraction in a single channel simulating one subchannel of a PWR fuel assembly," in *Two-Phase Flow Modelling and Experimentation*, G. P. Celata and R. K. Shah, Eds., vol. 1, ETS edition, 1995.
- [5] K. Hori, K. Miyazaki, T. Kurosu, S. Sugiyama, J. Matsumoto, and Y. Akiyama, "In bundle void fraction measurement of PWR fuel assembly," in *Proceedings of the 2nd ASME/JSME Nuclear Engineering Joint Conference*, F. Peterson, Ed., vol. 1, March 1993.
- [6] P. Coste, J. Pouvreau, C. Morel, J. Laviéville, M. Boucker, and A. Martin, "Modeling turbulence and friction around a large interface in a three-dimension two-velocity eulerian code," in *Proceedings of the 12th International Topical Meeting on Nuclear Reactor Thermal Hydraulics (NURETH '12)*, Pittsburgh, Pa, USA, October 2007.
- [7] M. Ishii, *Thermo-Fluid Dynamic, Theory of Two-Phase*, Eyrolles, 1975.
- [8] N. Méchitoua, M. Boucker, J. Laviéville, J. M. Hérard, S. Pigny, and G. Serre, "An unstructured finite volume solver for two phase water/vapour flows based on an elliptic oriented fractional step method," in *Proceedings of the 10th International Topical Meeting Nuclear Reactor Thermal Hydraulics (NURETH '10)*, Seoul, Republic of Korea, 2003.
- [9] S. Mimouni, F. Archambeau, M. Boucker, J. Laviéville, and C. Morel, "A second order turbulence model based on a Reynolds stress approach for two-phase boiling flow. Part I: Application to the ASU-annular channel case," *Nuclear Engineering and Design*, vol. 240, no. 9, pp. 2233–2243, 2010.
- [10] M. Lance and M. L. de Bertodano, "Phase distribution phenomena and wall effects in bubbly two-phase flows," *Multiphase Science and Technology*, vol. 8, pp. 69–123, 1994.
- [11] M. Ishii and N. Zuber, "Drag coefficient and relative velocity in bubbly, droplet or particulate flows," *AIChE Journal*, vol. 25, no. 5, pp. 843–855, 1979.
- [12] N. Zuber, "On the dispersed two-phase flow in the laminar flow regime," *Chemical Engineering Science*, vol. 19, no. 11, pp. 897–917, 1964.
- [13] A. Tomiyama, H. Tamai, I. Zun, and S. Hosokawa, "Transverse migration of single bubbles in simple shear flows," *Chemical Engineering Science*, vol. 57, no. 11, pp. 1849–1858, 2002.
- [14] N. Kurul and M. Podowski, "Multidimensional effects in forced convection subcooled boiling," in *Proceedings of the 9th International Heat Transfer Conference*, vol. 1, p. 21, Jerusalem, Israel, 1990.
- [15] S. Mimouni, F. Archambeau, M. Boucker, J. Laviéville, and C. Morel, "A second order turbulence model based on a Reynolds stress approach for two-phase boiling flow and application to fuel assembly analysis," *Nuclear Engineering and Design*, vol. 240, no. 9, pp. 2225–2232, 2010.
- [16] W. Yao and C. Morel, "Volumetric interfacial area prediction in upward bubbly two-phase flow," *International Journal of Heat and Mass Transfer*, vol. 47, no. 2, pp. 307–328, 2004.
- [17] P. Ruyer, N. Seiler, M. Weiss, and F. P. Weiss, "A bubble size distribution model for the simulation of bubbly flows," in *Proceedings of the 6th International Conference on Multiphase Flows*, Leipzig, Germany, 2007.

- [18] J. G. Collier and J. R. Thome, *Convective Boiling and Condensation*, Oxford Science, 3rd edition, 1994.
- [19] N. Seiler and P. Ruyer, "Advanced model for polydispersion in size in boiling flows," in *190ème Session Du Comité Scientifique Et Technique De La Société HydroTechnique De France : Modélisation Des Écoulements Diphasiques bouillants*, 2008.
- [20] T. Hibiki and M. Ishii, "One-group interfacial area transport of bubbly flows in vertical round tubes," *International Journal of Heat and Mass Transfer*, vol. 43, no. 15, pp. 2711–2726, 2000.
- [21] A. M. Kamp, *Écoulements turbulents à bulles dans une conduite en micropesanteur [Ph.D. thesis]*, Institut National Polytechnique de Toulouse, 1996.
- [22] A. M. Kamp, A. K. Chesters, C. Colin, and J. Fabre, "Bubble coalescence in turbulent flows: a mechanistic model for turbulence-induced coalescence applied to microgravity bubbly pipe flow," *International Journal of Multiphase Flow*, vol. 27, no. 8, pp. 1363–1396, 2001.
- [23] R. Denèfle, S. Mimouni, J. P. Caltagirone, and S. Vincent, "Multifield hybrid approach from bubble to slug flow transition modelling," in *Advances in Fluid Mechanics IX*, M. Rahman and C. A. Brebbia, Eds., WIT, 2012.

Research Article

Analysis of Subchannel and Rod Bundle PSBT Experiments with CATHARE 3

M. Valette

CEA Grenoble, Commissariat à l'Énergie Atomique et aux Énergies Alternatives, DEN, DM2S/SMTH, 38054 Grenoble, France

Correspondence should be addressed to M. Valette, michel.valette@cea.fr

Received 28 March 2012; Accepted 1 July 2012

Academic Editor: Maria Avramova

Copyright © 2012 M. Valette. This is an open access article distributed under the Creative Commons Attribution License, which permits unrestricted use, distribution, and reproduction in any medium, provided the original work is properly cited.

This paper presents the assessment of CATHARE 3 against PWR subchannel and rod bundle tests of the PSBT benchmark. Noticeable measurements were the following: void fraction in single subchannel and rod bundle, multiple liquid temperatures at subchannel exit in rod bundle, and DNB power and location in rod bundle. All these results were obtained both in steady and transient conditions. Void fraction values are satisfactory predicted by CATHARE 3 in single subchannels with the pipe module. More dispersed predictions of void values are obtained in rod bundles with the CATHARE 3 3D module at subchannel scale. Single-phase liquid mixing tests and DNB tests in rod bundle are also analyzed. After calibrating the mixing in liquid single phase with specific tests, DNB tests using void mixing give mitigated results, perhaps linked to inappropriate use of CHF lookup tables in such rod bundles with many spacers.

1. Introduction

CATHARE 3 is a new two-phase thermalhydraulics system code developed at CEA Grenoble [1]. It has been designed to expand the capabilities of CATHARE 2 and to improve the simulation accuracy of light water reactor accidents. New features include additional field, like a droplet field or a bubble field, and coupled equations of turbulence transport for a continuous field or interfacial area transport for a dispersed field. Beside the unchanged choices for numerical schemes for time and space discretization, a numerical solver gathering the different modules of a circuit has been rewritten and improved compared to CATHARE 2 in order to allow new capabilities of coupling with external codes, for example, for neutronics, or detailed CFD. A preliminary version V1 needs a wide validation program. This paper deals with the 1D and 3D module validation of the code against various boiling experiments at subchannel scale.

Following the BWR Full-size Fine-Mesh Bundle tests (BFBT) benchmark, the PWR subchannel and bundle tests (PSBT) benchmark [2] is proposed by OECD/NRC. Both are based upon a NUPEC database obtained in full-scale subchannels and rod bundles and include detailed

measurements of fluid temperature, void fraction, and critical power or DNB power in steady and transient conditions. These experiments are useful to check and validate the code closure laws in rod bundles, especially the turbulence dispersion coefficients for heat in single-phase flow and void in two-phase flow, the wall and interfacial friction coefficients, and the wall-to-fluid heat transfer models. The PSBT phase I exercises are devoted to the void fraction measurements, performed in single subchannels and in 5×5 rod bundles in steady and transient conditions. In the first exercise, phase II features liquid temperature measurements in all subchannels of a heterogeneously heated rod bundle in steady conditions, and, in the following exercises, DNB measurements taken in various rod bundles in steady and transient conditions, that is, power value and location of first detected DNB.

Single subchannel experiments are simulated by the CATHARE 3 pipe 1D module while rod bundle cases are simulated with the CATHARE 3 3D module meshed at a subchannel scale, that is, one cell per subchannel in a horizontal cross cut. The 3D module for the rod bundle has been coupled with a 1D module in order to improve the inlet flow simulation along the downcomer.

Useful balance equations and closure laws are briefly presented in the following Section 2. Then, results of comparisons between simulations and measurements of void fraction for Phase I exercises are presented in Section 3. In Section 4 are presented the results of temperature and DNB simulations of Phase II exercises.

2. CATHARE 3 Balance Equations and Closure Laws

Both 1D and 3D modules of CATHARE 3 solve the same set of balance equations, except that the energy balances are written using enthalpy in the 3D module and internal energy in the pipe module. The closure laws remain identical as far as possible. A first-order donor cell scheme is used in both modules as far as space discretization is concerned. For time discretization, the pipe module calls a fully implicit scheme, while the 3D module uses a semi-implicit scheme.

Contrary to the preceding BFBT simulations [3], featuring high void two phase flow, most of the PSBT benchmark database remain in the low- or medium-void range and hence, simulations do not need an additional droplet field beside the standard 6-equation model because the boiling flow regime never changes towards an annular dispersed flow.

For a given generation of steam along a single heated channel, the local void fraction is governed by wall and interfacial friction. In a 3D flow inside a rod bundle, cross-flows between adjacent subchannels lead to void dispersion. Also turbulent dispersion or diffusion may affect the temperature map in the single phase region. The void dispersion phenomena can be modelled by a mixing term in the momentum balance equations. The temperature dispersion (caused by nonrandom flow from one subchannel to a neighbour) and diffusion (caused by random fluctuations of flow between adjacent subchannels) are modelled by a single term in the liquid energy balance equation. The velocity diffusion is presently neglected in the momentum equation; its implementation had no effect on results of several tests, either in single phase or two phase flow in bundles.

2.1. Momentum Balance. Consider the following equation:

$$\begin{aligned} \alpha_k \rho_k \left[\frac{\partial}{\partial t} V_k + V_k \cdot \nabla V_k \right] \\ = -\alpha_k \nabla P + p_i \nabla \alpha_k + (-1)^k \tau_i + \tau_{pk} + \alpha_k \rho_k g. \end{aligned} \quad (1)$$

Wall frictions τ_p of both phases are calculated using the Blasius friction coefficient f_k multiplied by a phase-dependent multiplier c_k

$$\begin{aligned} \tau_{pk} = \chi c_k f_k \rho_k \frac{|V_k| V_k}{2}, \\ \text{with } c_g = \alpha^{1.25}, \quad c_l = \frac{(1-\alpha) \rho_l}{(1-\alpha) \rho_l + \alpha \rho_g}. \end{aligned} \quad (2)$$

Interfacial friction in bubbly, slug, and churn vertical flow is given by

$$\tau_i = \frac{K_l \rho_l + K_g \rho_g}{L} \alpha (1-\alpha)^{3.6} [V_g - V_l]^2. \quad (3)$$

L is the maximum bubble size, limited by the Laplace length ℓ and the hydraulic diameter $K_g = 29$

$$\begin{aligned} K_l = (F_\mu)^{0.25} f_l \\ \text{with } F_\mu = \frac{\mu_l}{\sqrt{\rho_l \sigma \ell}}, \quad f_l = 2.81 + 34 \left(\frac{L}{D_h} \right)^5 \left(6 - \frac{5L}{D_h} \right). \end{aligned} \quad (4)$$

τ_i and τ_p are unchanged compared to CATHARE 2 6-equation model.

The mixing term p_i is calculated from an assessment of the turbulent kinetic energy.

For a single-phase flow in a tube or a subchannel (far from a spacer grid), the turbulent kinetic energy k_l can be assessed by

$$k_l = 0.0367 V_l^2 \text{Re}^{-1/6} \quad (5)$$

(see [4]). The associated turbulent viscosity can be assessed as

$$\nu_t = 0.5 D_H \sqrt{k_l} \quad (6)$$

and the dispersion term p_i :

$$p_i = 0.4 \mu_t \frac{V_l}{D_H}. \quad (7)$$

The coefficient 0.4 comes from an order of magnitude for the velocity gradients between subchannels; the velocity difference is evaluated at 40% of the axial velocity, which is close to the velocity module.

At the end, it comes

$$p_i = 0.038 \rho_l V_l^2 \text{Re}^{-1/12}. \quad (8)$$

The coefficient 0.5 in the ν_t formula has been adjusted so as to better match the void fraction measurements in the PSBT Phase I tests, and the temperature measurements in the Phase II, given a Pr_t equal to 1 (see (9) below). This coefficient appears to be several orders of magnitude above the figure calculated using simple turbulence [4, 5]; the void dispersion due to cross flows (and not only diffusion) seems to be the main driving phenomena (see [6]).

2.2. Continuous Liquid Energy Balance. It is written using internal energy e_l for the 3D module as follows:

$$\begin{aligned} \frac{\partial}{\partial t} (\alpha_l \rho_l e_l) + \nabla \cdot (\alpha_l \rho_l e_l V_l) \\ = q_{li} + \chi c q_{pl} - \Gamma H_{lc} - P \left[\frac{\partial \alpha_l}{\partial t} + \nabla \cdot (\alpha_l V_l) \right] \\ + \nabla \cdot \left[\alpha_k \left(\lambda_l T_l + \frac{\rho_l \nu_{tl}}{\text{Pr}_t} \nabla e_l \right) \right]. \end{aligned} \quad (9)$$

The molecular diffusion is neglected compared to the turbulent diffusion term.

To summarize, the turbulence is modelled here by two different algebraic terms: one described just above in the energy balance and the $p_i \text{ grad } \alpha$ in the momentum equations. No additional transport equation of turbulence quantity was solved in this study.

The Departure from Nucleate Boiling appears on a hot wall when the heat flux towards the fluid exceeds the so-called ‘‘Critical Heat Flux,’’ which is assessed in six-equation model of CATHARE 2 and CATHARE 3 using home-made polynomials interpolating CHF lookup tables, given the local values of mass flux, pressure, and steam quality. The tables are based on the 1995 Groeneveld tables [7], using a simple rod bundle coefficient but no effect of the spacer grids.

3. Overview of the PSBT Benchmark

The PWR Subchannel and Bundle Tests (PSBT) benchmark is proposed by OECD/NRC. Pennsylvania State University (PSU) under the sponsorship of U.S. Nuclear Regulatory Commission (NRC) prepared the specification and organized the benchmark with the Japan Nuclear Energy Safety (JNES) Organization. The Nuclear Power Engineering Corporation (NUPEC) released a database including various single subchannel and full-scale rod bundle tests in boiling conditions, with detailed void distribution and DNB measurements. Both system codes and CFD codes can match their results against the averaged (macroscopic data at subchannel scale) or fine experimental results.

Two phases are proposed:

The first one is devoted to the void distribution and includes four exercises.

- Exercise 1—steady-state single subchannel benchmark,
- Exercise 2—steady-state bundle benchmark,
- Exercise 3—transient bundle benchmark,
- Exercise 4—pressure drop benchmark.

The second is devoted to DNB prediction and includes three exercises.

- Exercise 1—steady-state fluid temperature benchmark,
- Exercise 2—steady-state DNB benchmark,
- Exercise 3—transient DNB benchmark.

This benchmark, especially through its accurate measurements, is a very good opportunity to assess the capabilities of system codes such as CATHARE 3 to simulate boiling flows in PWR core geometry.

4. Void Fraction in PSBT Phase I Exercises

4.1. Exercise I.1 Steady State in Single Subchannels. Four different geometries of single subchannels, for central, side, and corner locations (side and corner are relative to a rod

bundle in a square box) have been tested, resulting in void fraction measurements at 1400 mm level inside a 1555 mm long heated subchannel (Figure 1). They fit to standard PWR rod bundle subchannel geometry (except the heated length shorter than a real reactor core), with an additional test section corresponding to a central subchannel heated by 3 and not 4 contributing rods, one rod being replaced by a thimble. The axial power distribution is uniform. The CT scanner gives for every steady run a detailed void fraction array through the measuring section. Results can be compared with CFD simulations or averaged over the cross section for comparisons with 1D module simulation by system codes.

A set of 39 tests is proposed in the benchmark among a large database of 126 tests. The range of flow pressure is from 50 to 170 Bars and the range of mass flux is 500 to 4200 kg m⁻² s⁻¹. We calculated the whole database and compared the simulation results versus the measurement data.

Calculations were performed using a quasiuniform 31 cell meshing.

The void fraction has been measured by a γ -ray attenuation CT scanner measurement in 1 mm wide beams, giving an array of values throughout the cross section. These values can be integrated in the whole cross section, giving a single void fraction figure associated to an experimental error bar of $\pm 3\%$.

The results are gathered in Figure 2. One can see a good coherence, but yet a slight bias, negative in any series, and a medium dispersion of the predicted values. Some rare points are outside the range $\pm 10\%$. The result statistics is presented in Table 1, given in % of void for the difference ‘‘predicted minus measured fraction.’’

Some examples of void axial profiles simulated by CATHARE 3 in various flow conditions in the standard central subchannel are shown on Figure 3, as well as the measured value at 1.4 m elevation.

4.2. Exercise I.2 Steady State in Rod Bundles. Several types of rod bundles were tested, most of them including a 5×5 matrix of rods settled with 17 spacer grids of 3 different types, with uniform or cosine power profile and with or without a central thimble instead of a heated rod. The heated length was 3658 mm; the rod diameter and pitch were 9.5 and 12.6 mm (Figure 4).

The heated part of the rod bundle was modelled by a 3D grid, with 6×6 cells in the x - y directions at the subchannel scale, and 66 cells in the z direction, taking one axial short cell for every 17 spacer grid, with 3 axial cells between two adjacent spacers. The 3 different kinds of spacer grids (Mixing Vane spacer, NonMixing Vane spacer, simple spacer) are described by their porosities, hydraulic diameter, and pressure loss coefficient in every subchannel.

An array of void fraction values in the different subchannels was measured at 3 different levels along the upper part of the heated length, reconstructed by 6 chordal averaged values in x and 6 in y directions. Here on Figure 5 is shown an example of the sensitivity of the void fraction distribution to the $p_i \text{ grad } \alpha$ term.

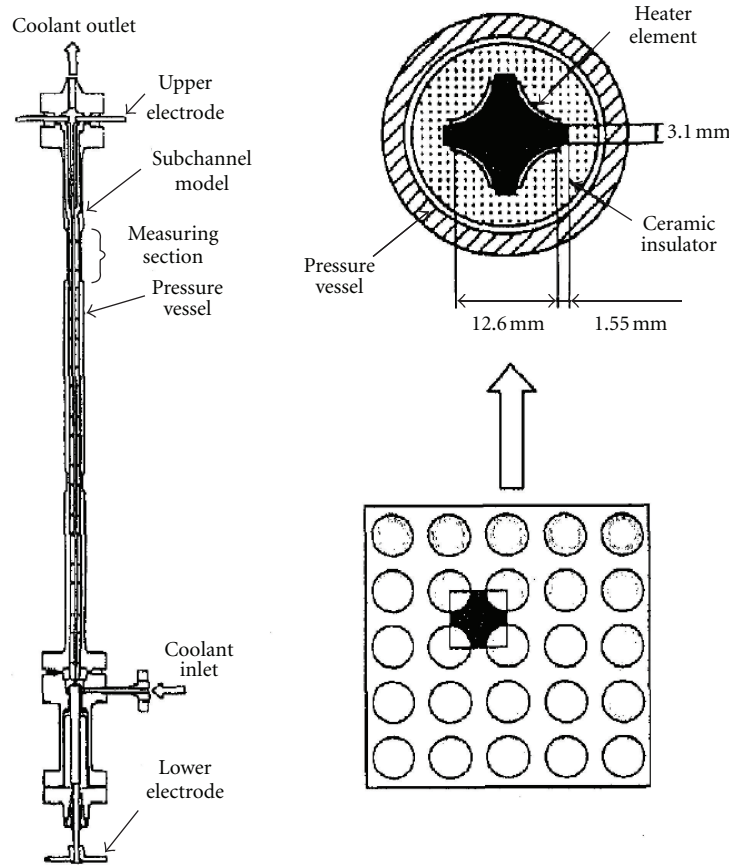


FIGURE 1: Test section for void measurement in a central subchannel.

TABLE 1: Distribution of deviations: “calculated minus measured void fraction” in the different series of single subchannel PSBT tests.

	Test number	Average	Standard dev.
Series 1: standard central subchannel	43	-2.3%	4.8%
Series 2: central subchannel close to a thimble	43	-1.8%	5.3%
Series 3: lateral subchannel	20	-3.0%	6.0%
Series 4: corner subchannel	20	-5.4%	3.2%
All series	126	-2.7%	5.0%

Only the averaged value of the 4 central subchannel void fractions was available in the benchmark database, and this is the compared data versus the void calculated by CATHARE 3 hereafter on Figure 6 for all the tests of the benchmark.

The points are more dispersed than for the single subchannel tests. The statistics of the results (difference: computed minus measured void fraction given in absolute %) is presented in Table 2.

The series number correspond to 3 different bundles; the series 8 is tested with the same bundle as series 5 as repeated cases, which appear to be less satisfying.

4.3. Exercise I.3 Transient in Rod Bundles for Void Fraction Prediction. A set of 12 transient tests is proposed in the benchmark, including power increase (PI), flow reduction, temperature increase (TI), and depressurization in each of the 3 same tested bundles as in the steady tests of

the exercise 2. The void fraction was also measured at the same 3 elevations during the transient.

The flow parameters (pressure, flow rate, and inlet temperature) were measured outside of the main vessel, near the inlet nozzle (referred as Coolant Inlet on Figure 7) and should be imposed as boundary conditions in the simulation. As the inlet conditions remain in quasi-incompressible liquid subcooled conditions, pressure and flow values remain more or less uniform all along the inlet pipes and devices, and the parameter variations are not delayed between the inlet nozzle and the bottom of the heated length in the bundle.

Hence, except for the “Temperature Increase” transients, as the inlet temperature remains quasicontant during the transient, the same computational domain was considered as in the previous steady tests, that is, the heated length in the rod bundle only and the requested inlet conditions were applied at the bottom of the heated length.

TABLE 2: PSBT rod bundle comparison statistics for void fraction tests.

Series	5	6	7	8	All gathered
Power profile	Uniform	Cosine	Cosine	Uniform	
Central thimble	No	No	Yes	No	
Average	-0.22%	-2.39%	1.13%	-6.65%	-1.96%
Standard deviation	4.27%	5.43%	5.64%	6.73%	6.32%

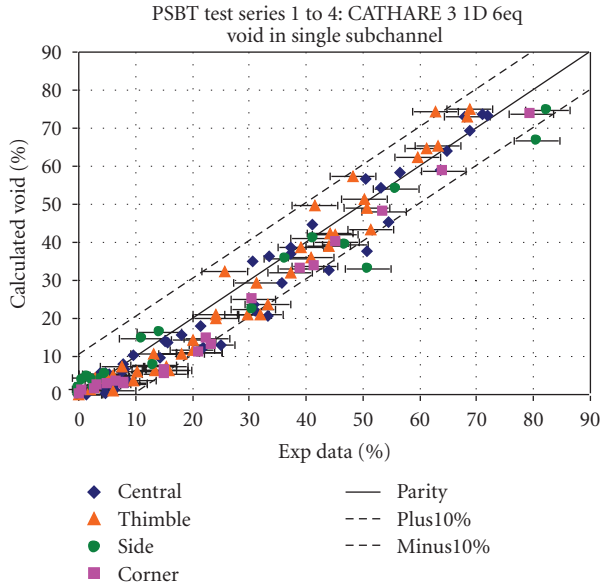


FIGURE 2: PSBT single subchannel test comparison (thimble means a central subchannel close to an unheated thimble).

An example of comparison is given below (Figure 8) for the test 7TPI, in the bundle B7 (with a central thimble and a cosine power profile) and given a linear increase of power, keeping constant the flow rate, pressure, and inlet temperature. The void fraction is slightly underpredicted at the upper location but is satisfactory in front of the 2 lower void measurement elevations. The other tests show less satisfactory results, the upper and medium level void often remaining underpredicted. This behaviour is consistent with the conclusions of the preceding exercise for steady tests, where the higher void fractions are underpredicted while the lower void fractions are more satisfactory.

For this 7TPI test, the location of the inlet temperature measurement is not sensitive because the temperature remains more or less constant during the transient. However, for Temperature Increase tests, this location must be at the boundary of the computational domain. Otherwise, a temperature delay would induce a bias in the simulation. Hence, for these TI transients, another domain has been set up, adding the downcomer as an axial module upstream the 3D module simulating the whole rod bundle.

An example of simulation is presented on Figure 9.

The comparison is less satisfying than for the other test 7TPI. All maximum void fractions are underpredicted and while the time of void take off is well predicted, the time of maximum void is delayed and the void curves seem to be

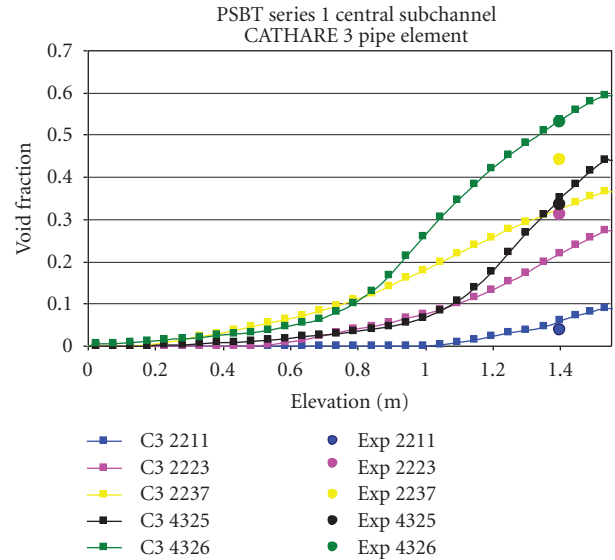


FIGURE 3: PSBT single subchannel test comparison: axial void profiles of 5 tests in a standard central subchannel.

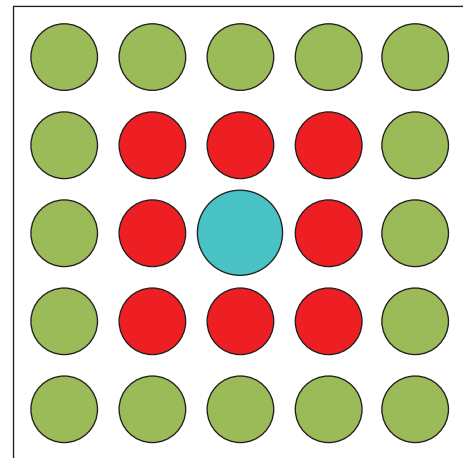


FIGURE 4: Power distribution in the bundle B7: red: 100%, green: 85%, blue: unheated thimble.

widened. This seems to be the consequence of a too large axial diffusion of void and perhaps also of the temperature step in the inlet part of the domain.

4.4. Exercise I.4 Pressure Drop in Rod Bundle. No data is available for code-to-data comparison for this exercise, except a single value given at the beginning of one transient test

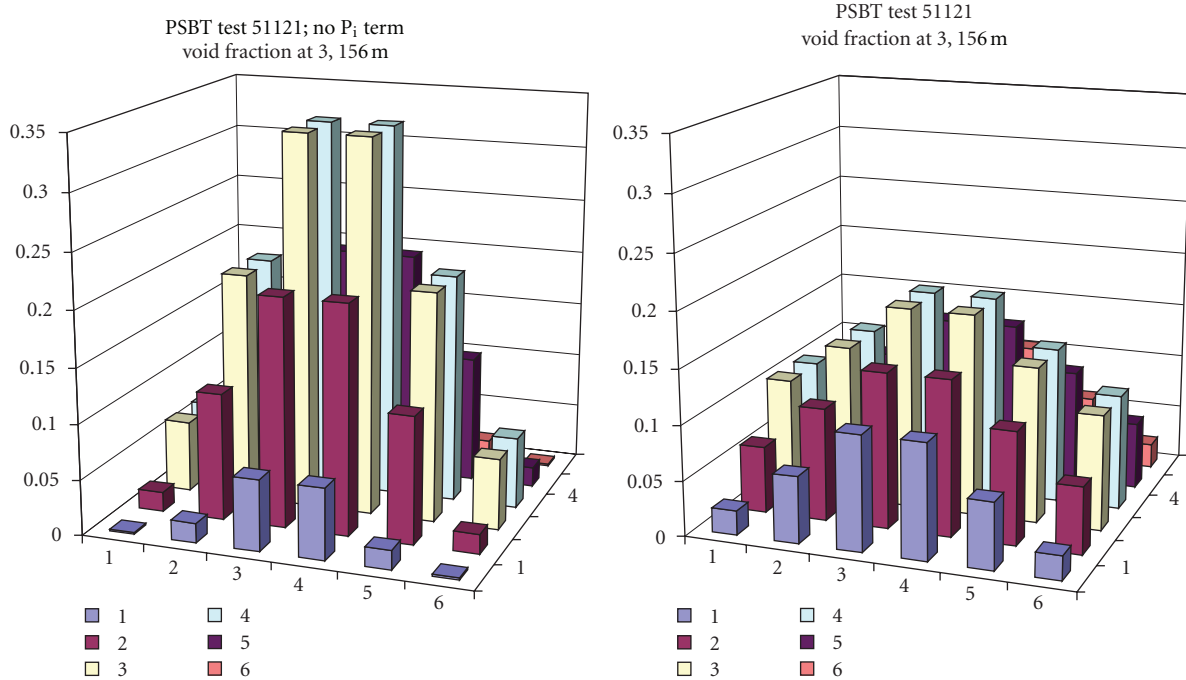


FIGURE 5: Sensitivity to the void diffusion term.

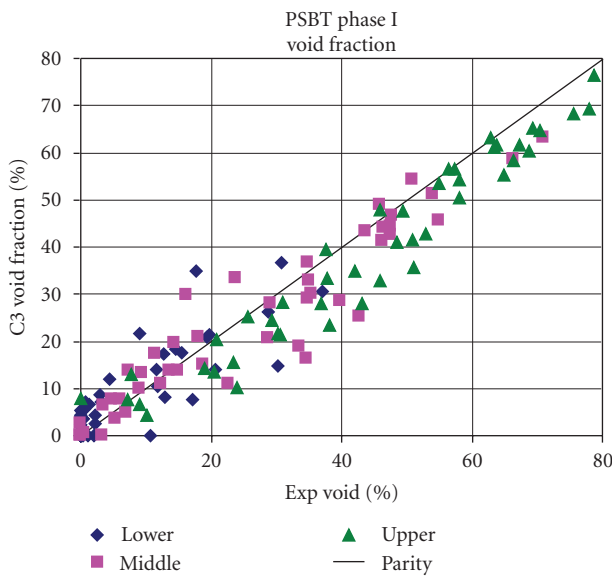


FIGURE 6: PSBT rod bundle test comparison of predicted and measured void fraction in central region at 3 different elevations along the heated length; lower: 2216 mm; medium: 2669 mm; upper: 3177 mm.

(7TPI) in nonboiling steady-state condition. The benchmark specifications recommended the pressure loss coefficients to be used for every type of spacer grid. Using these values, CATHARE 3 predicted the overall bundle pressure drop at 1.85 kg cm^{-2} , while the measured pressure drop is

1.6 kg cm^{-2} . This can be considered as a satisfying bias, considering the constant pressure loss coefficient with no dependency on the flow Reynolds number.

5. Departure from Nucleate Boiling in PSBT Phase II Exercises

5.1. Exercise II.1 Steady-State Fluid Temperature in Rod Bundles. This exercise is particularly useful to assess the code capabilities for turbulent dispersion and diffusion in single-phase flow.

In a 5×5 rod bundle featuring a heterogeneous power distribution (Figure 10), a set of 36 thermocouples measure fluid temperature in every subchannel 50 cm above the top of the heated length.

Nine tests at high pressure (from 50 to 170 bars) are proposed for simulations in a wide range of mass fluxes (between 500 and $4700 \text{ kg/m}^2\text{s}$). In Figure 11 are presented the compared W/E profiles of temperatures, averaged in the N/S direction. The x -axis numbers correspond to the subchannel columns 1 to 6. The shown temperature gradient is due to the power distribution and is governed by the diffusion and dispersion across the subchannels. The actual profile is more complex due to mixing vanes, which tend to swirl the flow but this effect is not modeled by CATHARE 3.

A first step of analysis allowed us to calibrate the turbulent viscosity used in the liquid energy balance (also in the void mixing term which is not useful in this exercise). Figure 11 shows the sensitivity of the turbulent viscosity value.

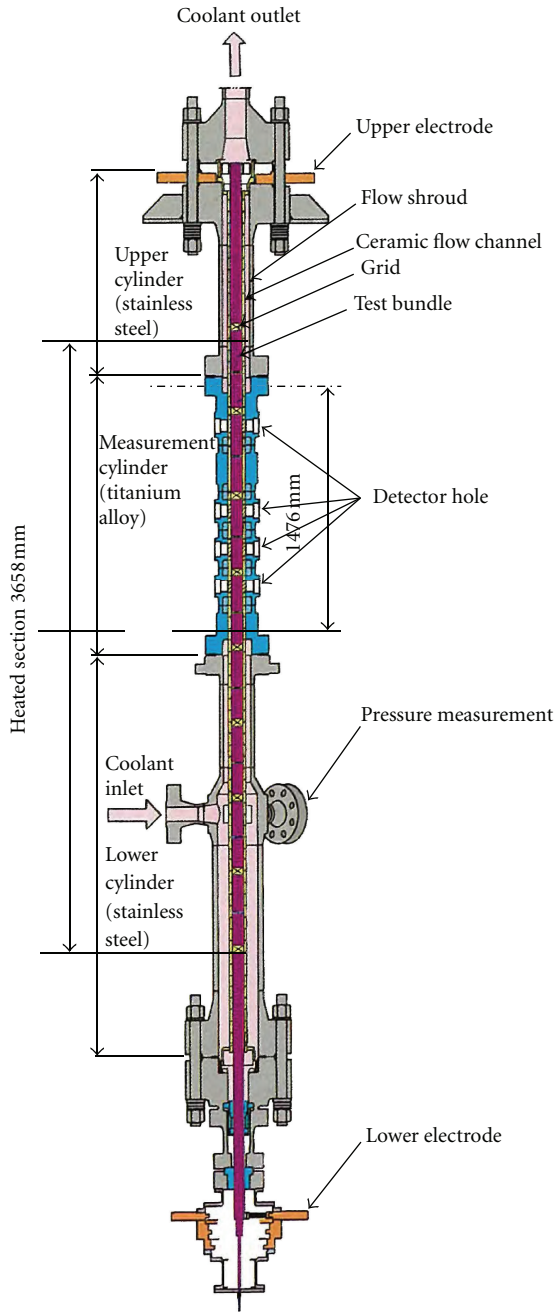


FIGURE 7: PSBT test vessel and flow channel structures.

The profiles of half of the proposed tests are correctly predicted. The other tests show unbalanced measured temperatures at the outlet compared to inlet flow parameters and bundle power and hence, comparisons are not significant.

In the Table 3, one can see that the parameters of the two correct tests presented on Figure 12 are very close except the inlet temperature (which obviously may have a slight effect on the Reynolds number). However, the temperature profiles show unexplained different behaviours, which are not predicted by CATHARE 3.

Using the available correct tests, a satisfying value of the temperature dispersion parameter has been selected, and

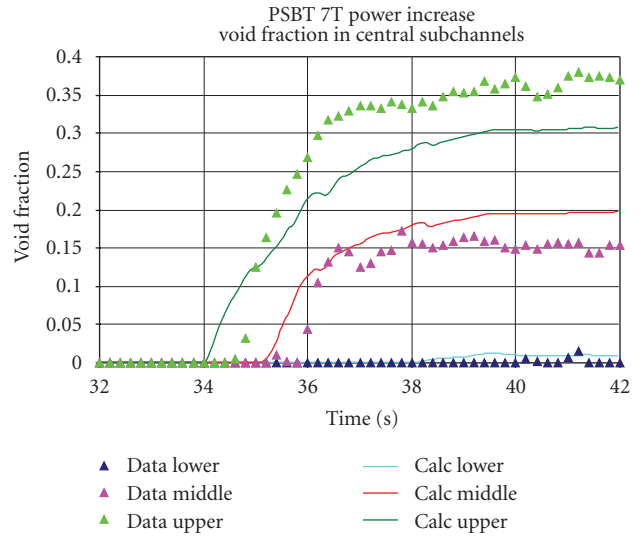


FIGURE 8: Comparison of void fraction transient predicted by CATHARE 3 and measured in PSBT 7TPI test.

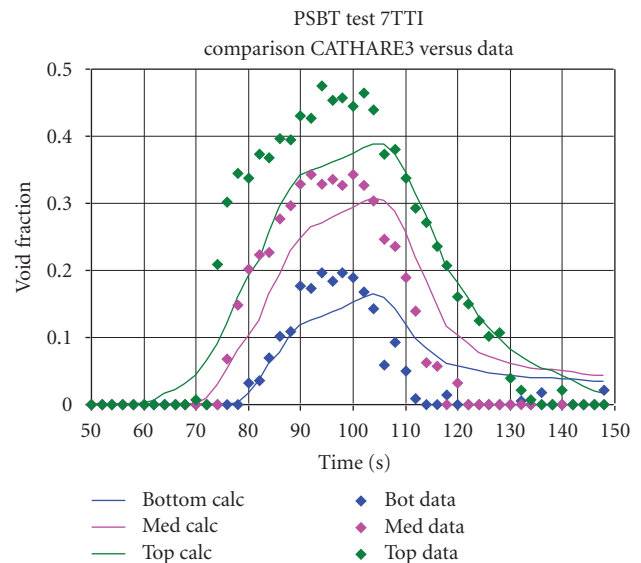


FIGURE 9: Comparison of void fraction transient predicted by CATHARE 3 and measured in PSBT 7TTI test.

implemented in CATHARE 3 for the other void and DNB simulations.

5.2. Exercise II.2 Steady State DNB in Rod Bundles. As for the void fraction tests proposed in phase I, different bundles were tested. The DNB is detected both in experiments and simulation by a significant rise of the wall temperature (more than 11°C) when the bundle power is slowly increased.

We calculated 6 test series in 5 different bundles corresponding to several geometries and power profiles, as shown in Table 4. The DNB location is given only in the A4 and A8 bundles. All calculated tests of bundles 4 and 8 were run at the same pressure of 150 bars, while the range in series 0,2,3 spreads from 50 to 170 bars.

TABLE 3: Test parameters for temperature measurements.

Test number	Pressure (kg/cm ² a)	Mass flux (10 ⁶ kg/m ² hr)	Inlet temperature (°C)	Power (MW)
01-6232	169.1	2.10	251.5	0.42
01-5252	150.0	1.95	113.9	0.41

TABLE 4: Results of 6 series of DNB simulations in rod bundles.

Bundle	Rods	Spacers	Radial power	Axial power	Calculated tests	Predicted power	Std dev	Small flow rate tests
A0	5 × 5	13	A	Uniform	9	96.80%	6.24%	0
A2	5 × 5	17	A	Uniform	11	87.70%	17.04%	2, overpredicted
A3	6 × 6	17	D	Uniform	8	79.46%	3.90%	0
A4	5 × 5	17	A	<i>Cosine</i>	20	78.44%	3.07%	2, over 5 std dev
A4	5 × 5	17	A	<i>Cosine</i>	27	78.50%	3.72%	0
A8	5 × 5	17	B (thimble)	<i>Cosine</i>	24	81.79%	8.70%	2, overpredicted

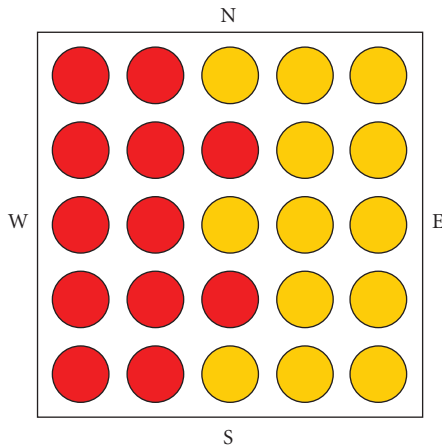


FIGURE 10: Rod power distribution in fluid temperature measurement tests; red rod power 100%, yellow 25%.

Some statistics of the simulation results (relative power: computed over data in % of experimental data) are given in Table 4.

One can see that the result for bundle A0 is satisfying results while the others show a significant bias.

The A3 bundle, featuring a 6 × 6 rod array, is not better than the A2 bundle, while the side effects are weaker.

The results in the bundle A2 are weakened by two tests at very low flow rate (330 kg m⁻² s⁻¹), which are overpredicted contrary to the 9 other tests; this enlightens the large value of the standard deviation for this bundle. A similar behaviour exists in series 4 and series 8 where the 2 tests at very low flow rate show significant differences (larger DNB power) compared to the other tests. Generally speaking, the location of the first detected DNB matches better in the series 4 than in the series 8.

The general underprediction of the DNB power in rod bundles may be linked to the use of lookup tables in a 3D analysis; such tables can predict CHF or DNB given 3 parameters: mass flux, pressure, and steam quality. These tables were built using 1D analysis of numerous tests. But in a 3D analysis, the steam quality and the mass flux

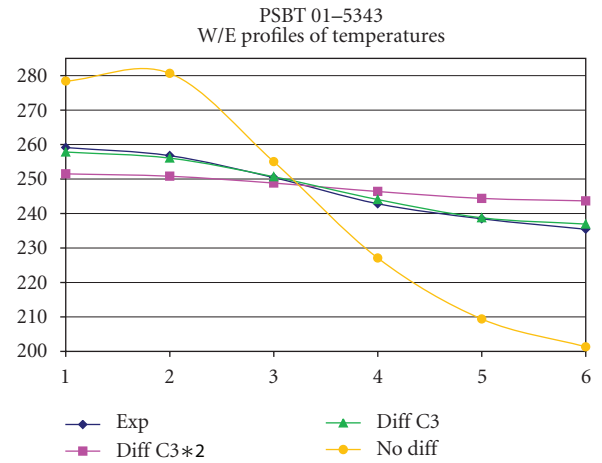


FIGURE 11: Sensitivity of the temperature profile to the turbulent diffusion term.

must obey a local definition with local void fraction and velocities and may display wrong values. As a consequence, the code computation of the local CHF may deviate from the recommended value. Better results can be expected when this point is improved.

Moreover, the better results for the A0 bundle seem point out that the CHF is better predicted with 13 spacers than with 17. The number of 13 is closer to the usual number of spacers in industrial bundles and CHF experiments used to build up the lookup tables. So, the DNB predictions would depend strongly on the spacer number, either through the CHF calculated with the lookup tables, or through the mixing effects simulated in the 3D computation. From this point of view, CATHARE 3 is not able now to predict the DNB power at subchannel scale with accuracy better than 20% in a new bundle.

Given the underprediction of the high-void fraction noticed in the preceding sections, the predicted DNB power should have been overpredicted because the local CHF increases when the local void fraction decreases. This also shows that these lookup tables are not convenient for

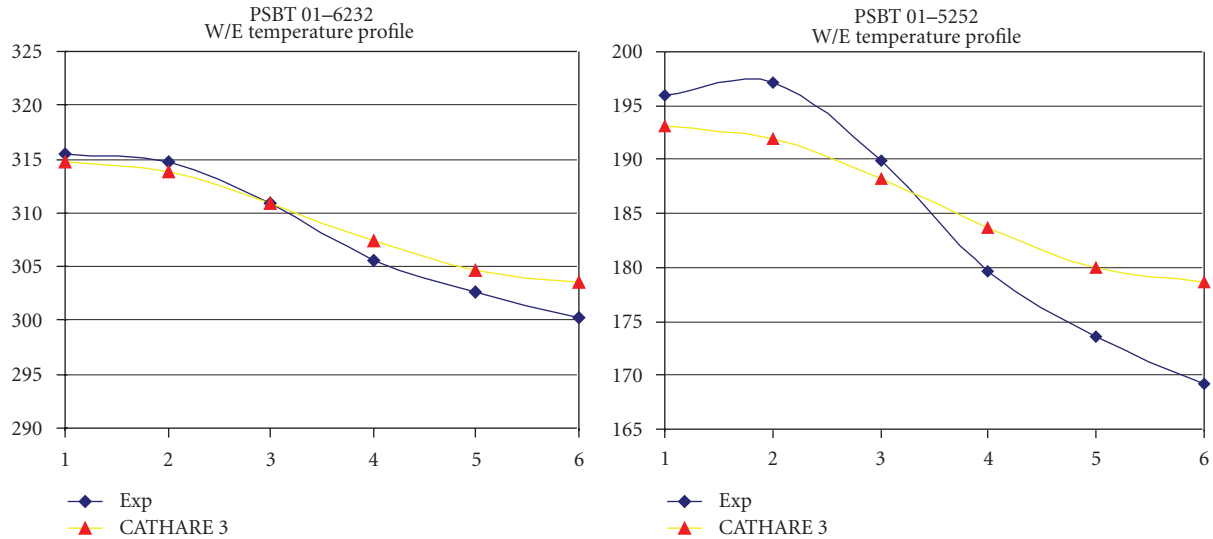


FIGURE 12: Temperature profiles in 2 fluid temperature measurement tests.

the analysis of the PSBT tests. It has to be noted that the original purpose of the 3D module of CATHARE2 and 3 was an improvement of the code behaviour in very large volumes within the reactor vessel such as the downcomer and the lower plenum. Applying this module in core subassemblies at subchannel scale is beyond the usual scope of the module, and the BFBT and PSBT benchmarks were just opportunities to check the module capabilities.

5.3. Exercise II.3 Transient DNB in Rod Bundles. Several tests were proposed in the benchmark specification report, in the rod bundles A4 and A8 (see Table 4 for details). As an example, the Temperature Increase transients prescribed a linear increase of the inlet temperature while the three other flow parameters (flow rate, pressure, and power) remained unchanged. The simulation results show the same behaviour as in the steady tests: the DNB power occurred at 86% of the experimental value. This behaviour is also seen in other transients: Flow Reduction, Power Increase, and Depressurization.

6. Conclusion

The 1D and 3D modules of the CATHARE 3 system code were used for the simulations of PSBT benchmark tests. Results of void fraction in phase I and temperature measurements and DNB power measurements in phase II have been compared to calculation results. The void comparisons show that our models of wall and interfacial friction, coupled with void dispersion, lead to satisfactory results, with a slight bias towards void underprediction, for both single subchannels and full rod bundles.

The exercise 1 of phase II, devoted to single-phase mixing and cross flows in liquid phase, shows good results as far as the experimental heat balance of the tests remains satisfactory.

In the exercise 2 of benchmark phase II, steady DNB simulations in 5 different rod bundles show significant underprediction of the critical power in the whole bundle (20% bias). The main reason should be a poor local CHF assessment, more than a rough mixing model. The analysis of transient tests for exercise 3 confirmed this behaviour. The CHF lookup tables in CATHARE 3 underpredict the CHF values in the PSBT rod bundles, which have 17 spacer grids. Improving these features would require improving the modelling of the interaction between spacer grids, turbulence, and local CHF or using CHF correlations designed for specific bundles.

Nomenclature

Roman Letters

- c : Wall friction phase multiplier
- e : Internal energy
- f : Wall friction coefficient
- g : Gravity
- H : Enthalpy
- k : Turbulent kinetic energy
- K : Interfacial friction coefficient
- ℓ : Laplace length
- P : Pressure
- p_i : Void dispersion coefficient
- Pr : Prandtl number
- q : Heat flux
- t : Time
- T : Temperature
- V : Velocity

Greek Letters

- α : Phase volume fraction
- Γ : Boiling/condensation rate
- χ : Friction area (or heated area) over control volume

λ : Molecular heat conductivity
 μ : Dynamic viscosity
 ν : Kinematic viscosity
 ρ : Phase density
 σ : Surface tension
 τ_i : Interfacial stress
 τ_p : Wall stress

Indexes

i: Interface
k: Any phase
l: Liquid phase
p: Wall
t: Turbulent.

Acknowledgments

This work was made in the frame of the development of the NEPTUNE project, which is jointly developed by the Commissariat à l'Énergie Atomique et aux énergies alternatives (CEA, France) and Electricité de France (EDF) and also supported by the Institut de Radioprotection et de Sécurité Nucléaire (IRSN, France) and AREVA-NP.

References

- [1] P. Emonot, A. Souyri, J. L. Gandrille, and F. Barré, "CATHARE-3: a new system code for thermal-hydraulics in the context of the NEPTUNE project," *Nuclear Engineering and Design*, vol. 241, no. 11, pp. 4476–4481, 2011.
- [2] A. Rubin, A. Schoedel, M. Avramova, H. Utsuno, S. Bajorek, and A. Velazquez-Lozada, "OECD/NRC benchmark based on NUPEC PWR subchannel and bundle tests (PSBT)," Volume I: Experimental Database and Final Problem Specifications NEA/NSC/DOC (2010)1, November 2010.
- [3] M. Valette, "Analysis of boiling two phase flow in rod bundle for NUPEC BFBT benchmark with 3-field neptune system code," in *Proceedings of the 12th International Topical Meeting on Nuclear Reactor Thermal Hydraulics (NURETH '07)*, Pittsburgh, Pa, USA, September-October 2007.
- [4] M. Chandesris, G. Serre, and P. Sagaut, "A macroscopic turbulence model for flow in porous media suited for channel, pipe and rod bundle flows," *International Journal of Heat and Mass Transfer*, vol. 49, no. 15-16, pp. 2739–2750, 2006.
- [5] M. Chandesris and D. Jamet, "Derivation of jump conditions for the turbulence $k - \epsilon$ model at a fluid/porous interface," *International Journal of Heat and Fluid Flow*, vol. 30, no. 2, pp. 306–318, 2009.
- [6] M. Drouin, O. Grégoire, O. Simonin, and A. Chanoine, "Macroscopic modeling of thermal dispersion for turbulent flows in channels," *International Journal of Heat and Mass Transfer*, vol. 53, no. 9-10, pp. 2206–2217, 2010.
- [7] D. C. Groeneveld, L. K. H. Leung, P. L. Kirillov et al., "The 1995 look-up table for critical heat flux in tubes," *Nuclear Engineering and Design*, vol. 163, no. 1-2, pp. 1–23, 1996.

Research Article

Validation of the Subchannel Code SUBCHANFLOW Using the NUPEC PWR Tests (PSBT)

Uwe Imke and Victor Hugo Sanchez

*Institute for Neutron Physics and Reactor Technology (INR), Karlsruhe Institute of Technology (KIT),
Hermann-von-Helmholtz-Platz 1, 76344 Eggenstein-Leopoldshafen, Germany*

Correspondence should be addressed to Uwe Imke, uwe.imke@kit.edu

Received 19 March 2012; Accepted 5 June 2012

Academic Editor: David Novog

Copyright © 2012 U. Imke and V. H. Sanchez. This is an open access article distributed under the Creative Commons Attribution License, which permits unrestricted use, distribution, and reproduction in any medium, provided the original work is properly cited.

SUBCHANFLOW is a computer code to analyze thermal-hydraulic phenomena in the core of pressurized water reactors, boiling water reactors, and innovative reactors operated with gas or liquid metal as coolant. As part of the ongoing assessment efforts, the code has been validated by using experimental data from the NUPEC PWR Subchannel and Bundle Tests (PSBT). The database includes single-phase flow bundle outlet temperature distributions, steady state and transient void distributions and critical power measurements. The performed validation work has demonstrated that the two-phase flow empirical knowledge base implemented in SUBCHANFLOW is appropriate to describe key mechanisms of the experimental investigations with acceptable accuracy.

1. Introduction

The requirements for computational resources of high-resolution computational fluid dynamics (CFD) are still large, so the thermal-hydraulic analysis of nuclear reactor cores is frequently performed using subchannel computer codes. The current development of subchannel codes concentrates on refined modeling of two-phase flow. The two-fluid formulation separates the conservation equations of mass, energy, and momentum to vapor and liquid. The COBRA-TF family of subchannel codes [1, 2] extends this treatment to a different description of continuous liquid and entrained liquid droplets, which results in a set of nine conservation equations. This kind of refinement needs additional constitutive relations which have to be derived from single-effect experiments. For example, the behavior of droplets colliding with grid spacers and the entrainment of droplets in the vapor flow has to be described by physical models, which are validated using such experimental data [3]. In addition, the computational requirements are growing strongly along with the number of equations to be solved.

For the design and safety assessment of nuclear power plants, the coupled multiphysics description of the core

behavior becomes more and more important [4]. Fast running and extensively validated numerical tools are needed for industrial, regulatory and research purposes. Therefore a good performance of the thermal-hydraulic calculation is essential, if it is combined with numerical simulation of neutron physics or fuel pin mechanics.

An alternative to the simulation of the processes on a microscale level is to use empirical correlations related to pressure drop, heat transfer, void generation, and so forth collected over the last decades. These correlations are combined with liquid-vapor mixture equations for the conservation of mass, momentum, and energy as used by legacy codes. After a critical review of various legacy subchannel codes freely available, it was decided to develop SUBCHANFLOW as a modern and modular subchannel code starting from the COBRA-family [5, 17, 18] using the above-mentioned three-equation approach for the mixture of liquid and vapor. The experimental data from the NUPEC PWR Subchannel and Bundle Tests (PSBT) [16] are used to show the quality of results which can be reached by a simple approach based on validated correlations.

The present paper starts with an overview about the main features of the new code. Subsequently, the validation

procedure for PWR conditions is described starting from single-channel simulations. The mixing parameter to be used in the PWR-related investigations is deduced from steady-state single-phase flow bundle experiments. The boiling models are validated against void fraction distribution measurements for bundle steady-state and transient flow tests. Finally, the critical heat flux phenomenon is investigated and the SUBCHANFLOW predictions are compared to measurement data. All results are obtained with the current version SUBCHANFLOW 2.1.

2. Main Features of SUBCHANFLOW

2.1. Programming Features. SUBCHANFLOW is a fast running and flexible simulation tool, which is easy to maintain by keeping the code structures as simple as possible. The bases for the source code are the legacy subchannel programs COBRA-IV-I [18] and COBRA-EN [5]. The old methods of data management like Fortran EQUIVALENCE and swapping to hard disk are removed. The Fortran COMMON structure is replaced by a global data structure centralized in one single Fortran module complemented by a description of each global variable name. The thermophysical properties of the coolants and solid materials are summarized in separate modules. All arrays are dynamically allocated depending on the problem-specific input data. The code is prepared to be used as a library called by another simulation tool. There is an error management control that will shut down the code in case of difficulties closing all files and deallocating the memory. The portability of the code is assured by avoiding functions that depend on operating systems. Consequently, SUBCHANFLOW can be compiled under WINDOWS, LINUX, or other UNIX systems using a standard Fortran 95 compiler. The input deck is designed as a text-based “User Interface” with comprehensive keywords and simple tables. Long tables can be fed in by external files named in the input deck. A manifold output is created to be used with different postprocessing tools for example to generate simple curves or more extensive three-dimensional diagrams.

2.2. Modeling Features. SUBCHANFLOW can handle both rectangular and hexagonal fuel bundles and core geometries built from these. As boundary conditions, the total flow rate or a channel-dependent flow rate can be selected. It is possible to distribute the flow automatically to the parallel channels depending on the friction at the bundle inlet. In addition, a pure top-bottom pressure difference boundary can be applied for steady-state calculations. Fluid temperature at the inlet and pressure at the outlet always have to be prescribed as boundary conditions [19].

In opposite to the majority of subchannel codes, SUBCHANFLOW uses rigorously SI units internally in all modules [20]. Modern coolant properties and state functions are implemented for water using the IAPWS-97 formulation (The International Association for the Properties of Water and Steam). In addition, property functions for liquid metals (sodium and lead) and gases (helium and air) are available too. An iterative steady-state numerical procedure is available

to determine the power at which critical heat flux conditions appear during the simulation.

In SUBCHANFLOW, profit is taken from the many valuable empirical correlations for pressure drop, heat transfer coefficients, void generation, etc., collected over the last decades. Consequently, it does not follow the general trend to describe two-phase flow by simulating the processes on a microscale basis (e.g., separate conservation equations for liquid droplets, films or vapor bubbles). In SUBCHANFLOW, a three-equation two-phase flow model that is a mixture equation for mass, momentum, and energy balance is implemented. The constitutive relations are expressed as mixture equations for wall friction and wall heat flux as well as a slip velocity relation. In addition, user defined empirical correlations can be implemented. In the present paper, only the correlations used for the actual PSBT validation campaign are mentioned.

2.3. Basic Conservation Equations. In subchannel codes, a channel consists of a finite fraction of the total cross-sectional area of the nuclear reactor core region. The smallest possible channel would be the size of a subchannel surrounded by the fuel rods (see Figures in Table 3). For the numerical simulation, a subchannel is divided into several axial mesh volumes. Transport of mass, momentum, and energy is possible along the axial direction and between the neighboring channels through the gap formed by the fuel rods (lateral direction, cross-flow). The basic transport equations are based on the Euler approach including friction at solid surfaces. In the lateral momentum equation, the convective transport of lateral momentum is neglected because the friction term dominates the cross-flow. In the energy equation, the heat flux from the rod surfaces is the main source term. For transient conditions, a slip between vapor and liquid is taken into account in the enthalpy time derivative. Turbulent transport of momentum and energy between neighboring channels is described by a simple empirical mixing model. For an axial mesh volume (j) in channel (i) surrounded by volumes of neighboring channels (n) through a gap (k), the basic conservation equations in finite difference form are the following.

Mass conservation:

$$A_{i,j} \frac{\Delta X_j}{\Delta t} (\rho_{i,j} - \rho_{i,j}^{\text{old}}) + (m_{i,j} - m_{i,j-1}) + \Delta X_j \sum_k w_{k,j} = 0. \quad (1)$$

Energy conservation:

$$\begin{aligned} & \frac{A_{i,j}}{\Delta t} \left[\rho''_{i,j} (h_{i,j} - h_{i,j}^{\text{old}}) + h_{i,j} (\rho_{i,j} - \rho_{i,j}^{\text{old}}) \right] \\ & + \frac{1}{\Delta X_j} (m_{i,j} h_{i,j} - m_{i,j-1} h_{i,j-1}) + \sum_k w_{k,j} h_{k,j} \\ & = Q_{i,j} - \sum_k w'_{k,j} (h_{i,j} - h_{n(k),j}). \end{aligned} \quad (2)$$

Axial momentum:

$$\begin{aligned} & \frac{\Delta X_j}{\Delta t} (m_{i,j} - m_{i,j}^{\text{old}}) + m_{i,j} U'_{i,j} + \Delta X_j \sum_k w_{k,j} U'_{k,j} \\ & = -A_{i,j} (p_{i,j} - p_{i,j-1}) - g A_{i,j} \Delta X_j \rho_{i,j} \\ & \quad - \frac{1}{2} \left(\frac{\Delta X f \Phi^2}{D_h \rho_{\text{liq}}} + K v' \right) \Big|_{i,j} \frac{m_{i,j}}{A_{i,j}} \\ & \quad - \Delta X_j \sum_k w'_{k,j} (U'_{i,j} - U'_{n(k),j}). \end{aligned} \quad (3)$$

Lateral momentum:

$$\begin{aligned} & \frac{\Delta X_j}{\Delta t} (w_{k,j} - w_{k,j}^{\text{old}}) + (\bar{U}'_{k,j} w_{k,j} - \bar{U}'_{k,j-1} w_{k,j-1}) \\ & = \frac{s_k}{l_k} \Delta X_j \Delta p_{k,j-1} - \left(K_G \frac{\Delta X v'_k}{s_k l_k} \right) \Big|_{j} w_{k,j} \Big| w_{k,j}. \end{aligned} \quad (4)$$

Slip correction for enthalpy derivative based on the two-phase flow basic energy equation (Tong's function) [21]:

$$\begin{aligned} \rho'' & = \left(\rho^{\text{old}} - h_{\text{fg}} \frac{\partial \psi}{\partial h} \right) \\ \psi & = \rho_{\text{liq}} x (1 - \alpha) - \rho_{\text{vap}} \alpha (1 - x). \end{aligned} \quad (5)$$

Effective specific volume

$$\begin{aligned} v' & = \frac{x^2}{\alpha \rho_{\text{vap}}} + \frac{(1-x)^2}{(1-\alpha) \rho_{\text{liq}}} \\ U' & = \frac{m}{A} v'. \end{aligned} \quad (6)$$

2.4. Numerical Solution Procedure. The conservation equations along with the constitutive equations, for example, to calculate the void fraction, represent the system of equations of the mixture two-phase flow model. The basic flow variables such as the axial and lateral flow rates, the pressure, the enthalpies, and the void fractions are calculated in each time step axially layer by layer. For each axial layer, the coolant enthalpies are calculated first from the energy conservation equations. The axial pressure gradients are calculated from the combined axial and transverse momentum equation. The mass flow rates in the lateral directions are calculated from the transverse momentum equation, knowing the axial pressure gradients. The axial mass flow rates are deduced from the mass continuity equation. From the enthalpy of each computational cell, the steam quality and then, through the quality/void correlation, the steam volume fraction and hence the coolant density are computed. This procedure is repeated several times during each time step resulting in a fully implicit scheme. For steady-state calculations, the time step is set to a very large value. The sketched solution algorithm is limited to cases with axial flow rates which always keep positive (upflow). The linear equation system built up by the energy equations in each layer is solved by the SOR (successive overrelaxation) method. The equation system for

TABLE 1: Boundary conditions for single channel tests.

Pressure range (MPa)	5–17
Flow rates (kg/s)	0.053–0.44
Power range (kW)	12.5–90
Inlet subcooling range (°C)	5–100

TABLE 2: Closure correlations.

Physical phenomenon	Correlation	Reference
Single-phase friction	Blasius	[5, 6]
Two-phase friction	Armand	[5, 7]
Single-phase heat transfer	Dittus-Boelter	[8]
Boiling heat transfer	COBRA-IV-I boiling curve	[9]
Subcooled boiling	Bowring	[10, 11]
Steam slip	Chexal-Lellouche	[12]

the pressure gradients can be solved by a direct scheme or by the SOR method which needs much less computer storage. The fuel rod or heater rod temperatures are calculated in each iteration step depending on power release and cladding to coolant heat transfer. For each axial layer, the rod is divided into a number of radial rings to solve the heat conduction equation in radial direction by a finite volume method. Axial heat conduction can be accounted for in transient simulations, if necessary.

3. Validation Using PSBT Benchmark Data

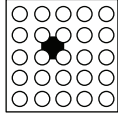
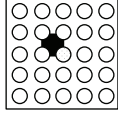
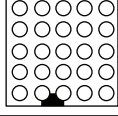
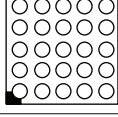
The validation of SUBCHANFLOW started with earlier versions [19, 20, 22] and it was continuously repeated with each new major release. Here, the validation work performed with the latest version will be presented and discussed. A detailed description of the PSBT benchmark as well as of the experimental data is given in [16].

3.1. Flow in a Single Subchannel. A typical NUPEC test assembly consists of four different geometrical types of subchannels: the center channels surrounded by four rods, the center channels surrounded by 3 fuel rods and a guide tube, the side channels surrounded by two rods and a part of the assembly wall and the corner channel surrounded by one rod and two wall parts (see Table 3). A basic test for a subchannel code is to simulate boiling in these kinds of heated single channels. Then, the predicted void fraction can be compared to the one measured in the PSBT tests. The single subchannel test section is uniformly heated along 1555 mm and the void measurement was made at 1400 mm from the bottom of the heated section. Tests are done with different pressure, coolant flow rate, power, and inlet temperature as given in Table 1.

The closure correlations used in SUBCHANFLOW are summarized in Table 2 while in Table 3 the geometrical configuration and the global result expressed by the standard deviation (see Equation (7)) between experimental values and simulation results are shown:

$$\sigma = \sqrt{\frac{1}{N-1} \sum_{i=1}^N (T_{\text{exp},i}^2 - T_{\text{sim},i}^2)}. \quad (7)$$

TABLE 3: Global result for different subchannel types.

Case name	Configuration	Void fraction standard deviation
S1		0.05
S2		0.04
S3		0.08
S4		0.03

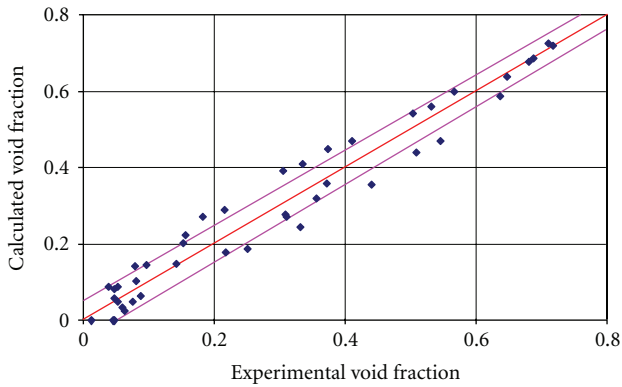


FIGURE 1: Comparison between calculated and measured void fraction for subchannel type S1.

In Figures 1, 2, 3, and 4 the comparison of the measured and calculated void fraction in the different types of single subchannels is exhibited. The ± 0.05 absolute void fraction envelope of the exact agreement is given by the pink straight lines. The standard deviation for the difference of measured and calculated values is given in Table 3. The estimated accuracy for the void measurements is 0.03 (absolute void fraction) [16].

The majority of the points lie within the 0.05 void fraction error band. Only for the case S3 SUBCHANFLOW considerably overpredicts the void fraction as long as it is below 0.2. There is also a large under prediction of one single point for a void fraction of around 0.5 (see Figure 3). There is no clear and systematic explanation for this behavior. Outliers in the measurement procedure are supposed.

3.2. Determination of Cross-Flow Mixing Coefficient. Under single-phase flow conditions, the cross-flow between neighboring subchannels is divided into two categories: turbulent mixing and diversion cross-flow. The turbulent mixing is an inter-subchannel mixing due to turbulence of the fluid flow.

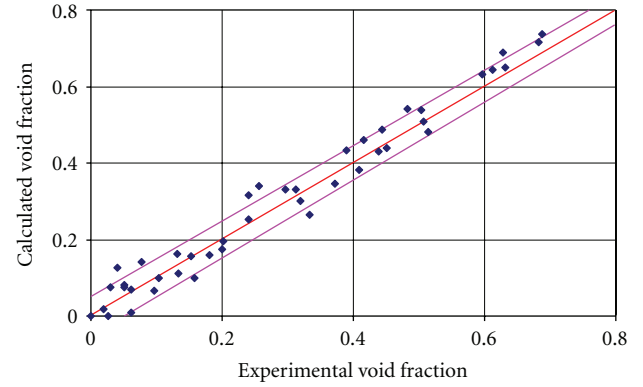


FIGURE 2: Comparison between calculated and measured void fraction for subchannel type S2.

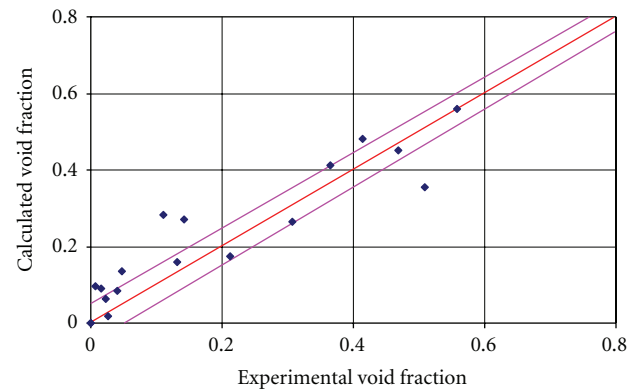


FIGURE 3: Comparison between calculated and measured void fraction for subchannel type S3.

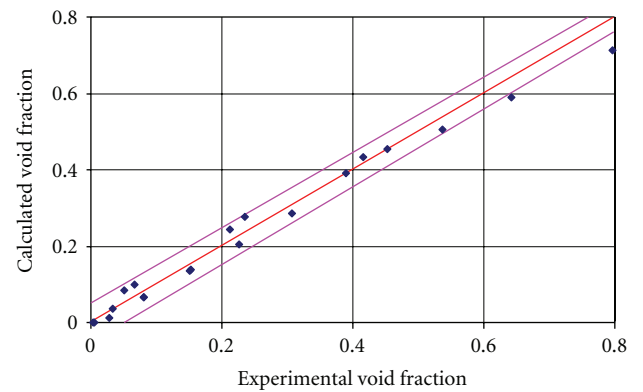


FIGURE 4: Comparison between calculated and measured void fraction for subchannel type S4.

By this mixing, momentum and energy transfer between subchannels take place, but no net mass transfer. A void drift model leading to turbulent exchange of vapor volume between neighboring channels is implemented in SUBCHANFLOW in addition. In the present benchmark, it does not give better results than the standard energy transfer model and is not used. The diversion cross-flow occurs due to lateral pressure gradients, which may be introduced by

differences of subchannel geometry or obstructions such as spacers.

In most subchannel codes, the turbulent cross-flow between channel i and channel j through gap k is defined by

$$w'_{i,j} = \beta_{i,j} s_k 0.5 (G_i + G_j), \quad (8)$$

$$w'_{i,j} = -w'_{j,i}.$$

The subchannel analysis of bundles is very sensitive to the mixing coefficient β . Several correlations are published to model the influence of Reynolds number and channel geometry [23, 24]. In case of assemblies containing mixing vane spacers, a simple method is to use a constant value, which may be determined by single-phase flow experiments measuring the exit subchannel temperature [13]. There is a steady-state fluid temperature experiment in the PSBT test series that uses a special lateral power distribution for a 5 by 5 rod array containing 7 mixing vane spacers (see Table 4). These data are used to find a mixing coefficient valid for the assembly under consideration. Figure 5 shows the comparison between calculated and measured temperatures at the outlet of each subchannel for several typical flow conditions. An optimum mixing coefficient of 0.06 was found with a standard deviation of about 5°C.

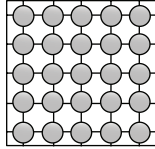
3.3. Steady-State Bundle Void Fraction Distribution. Table 5 gives an overview about all test bundle geometries used in the present paper for void fraction and DNB (departure from nucleate boiling) simulations.

The main measurement data for bundle experiments provided by PSBT are X-ray densitometer measurements of void fraction at three axial elevations (2.2 m, 2.7 m, and 3.2 m related to a heated length of 3.7 m). The resulting void is an average over the four central subchannels of the bundle. Four steady-state bundle tests are investigated (referenced here as cases B5, B6, B7, B8). The basic rod configuration is the same as for the steady-state single-phase outlet temperature test. B5 has a uniform axial power profile. B6 and B7 have a cosine profile. In the case of B7, the central rod is replaced by a guide tube with a diameter of 12.24 mm. The radial power profile is described by 9 central rods having a relative power of 1.0, whereas the boundary rods are heated with a relative power of 0.85. B8 is a repetition case of B5. In Table 6, the range of boundary conditions is given for all tests performed to measure steady-state bundle void fraction distributions.

In addition to the correlations used for the simulation of the single-channel experiments, SUBCHANFLOW uses the closure laws summarized in Table 7.

In Figures 6, 7, and 8 the comparison of the calculations with the measured void fractions at the three axial levels is shown for case B5. Again the 0.05 void envelope is indicated. Generally, the majority of the SUBCHANFLOW predictions are in acceptable agreement with the data. But there is a tendency of SUBCHANFLOW to overpredict the void fraction at the lower and middle parts of the bundle for void fractions below 0.4, while SUBCHANFLOW tends to underpredict the void fraction at the upper level of the bundle when the void fraction is between 0.3 and 0.55.

TABLE 4: Steady-state mixing experiment conditions.

Configuration					
Lateral power distribution	1	1	0.25	0.25	0.25
	1	1	1	0.25	0.25
	1	1	0.25	0.25	0.25
	1	1	1	0.25	0.25
	1	1	0.25	0.25	0.25
Rod outer diameter (mm)	9.5				
Rod pitch (mm)	12.6				
Axial heated length (mm)	3658				
Assembly inner width (mm)	64.9				
Axial power shape	Uniform				
Simulation cross-flow mixing coefficient	0.06				
Standard deviation (°C)	4.8				

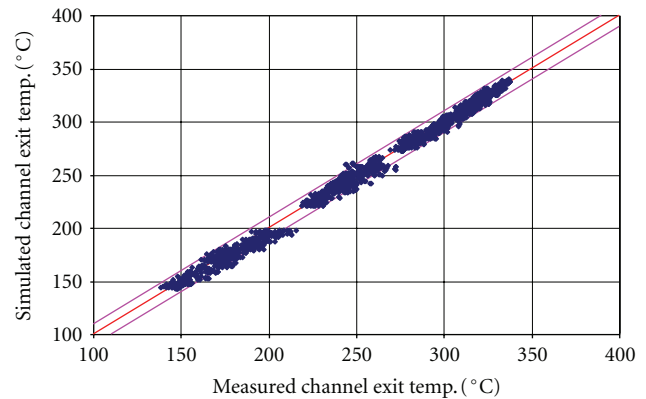

 FIGURE 5: Comparison of calculated and measured channel outlet temperatures for a mixing coefficient of 0.06 (envelope: $\pm 10^\circ\text{C}$).

Table 8 summarizes the results of all 4 test cases. The accuracy of the experimental data is about 0.04 (absolute void fraction) [16]. Depending on case and level, the standard deviation is varying between 0.04 and 0.08.

3.4. Transient Bundle Void Fraction Distribution. Transient void tests were performed with three different bundle types (B5, B6 and B7) representing PWR-relevant scenarios: power increase (PI), flow reduction (FR), depressurization (DP), and inlet temperature increase (TI). In the present paper, only the test cases for bundle type B7 are presented and discussed. All four scenarios have nearly the same initial conditions as documented in Table 9. The transient boundary conditions can be found in Figures 9–12. All transients lead to an increase of void fraction at the bundle exit. The void measurement technique was the same as that used for the steady-state tests and the void fraction data were taken again at the three axial elevations (lower, middle, upper). They are

TABLE 5: Geometry of test bundles for void and DNB measurements.

Case name	B5	B6	B7	A0	A2	A3	A4, A11, A13	A8, A12
Number of rods	25	25	25	25	25	36	25	25
Guide tubes	0	0	1	0	0	0	0	1
Rod pitch (mm)	12.6	12.6	12.6	12.6	12.6	12.6	12.6	12.6
Rod dia. (mm)	9.5	9.5	9.5	9.5	9.5	9.5	9.5	9.5
Guide tube dia. (mm)			12.24					12.24
Heated length (mm)	3658	3658	3658	3658	3658	3658	3658	3658
Assembly inner width (mm)	64.9	64.9	64.9	64.9	64.9	77.5	64.9	64.9
Power shape	Uniform	Cosine	Cosine	Uniform	Uniform	Uniform	Cosine	Cosine
Mixing vane spacers	7	7	7	5	7	7	7	7
Nonmixing vane spacers	2	2	2	2	2	2	2	2
Simple spacers	8	8	8	6	8	8	8	8

TABLE 6: Boundary conditions for steady state bundle void fraction tests.

Pressure range (MPa)	4.8–16.6
Mass flux ($\text{kg}/(\text{m}^2\text{s})$)	550–4170
Power (MW)	0.97–4.0
Inlet temperature ($^{\circ}\text{C}$)	143–322

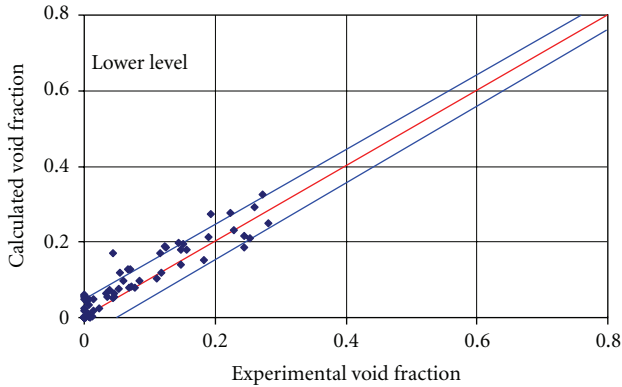


FIGURE 6: Comparison of calculated and measured void fraction for case B5 at the lower axial level.

again averaged over the four central subchannels of the 5×5 test bundle.

The calculated time-dependent void profiles are very similar to the measured values as can be observed in Figures 13, 14, 15, and 16. Based on the comparison of predictions and data, it can be stated that the void fractions predicted at the lower axial position are overestimated. On the other hand, the comparison of the predicted void fraction at the upper level is slightly underpredicted. In general, most of the predictions are qualitatively following the evolution of the measured data during the transient test phase.

The considerable overprediction of the void fraction by SUBCHANFLOW at the lower bundle part for the overpower (Figure 13) and mass flow reduction (Figure 14) transients indicates that the subcooled boiling model may need further review. The comparison of the SUBCHANFLOW predictions

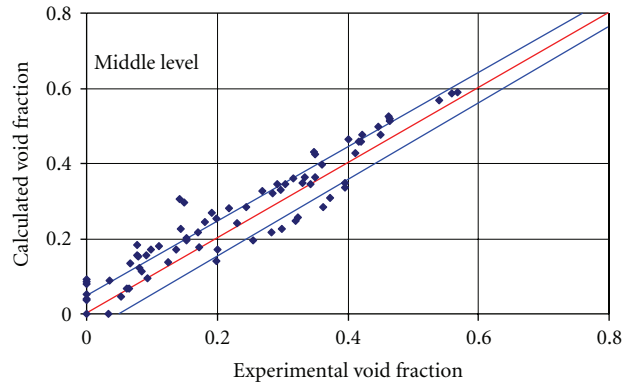


FIGURE 7: Comparison of calculated and measured void fraction for case B5 at the middle axial level.

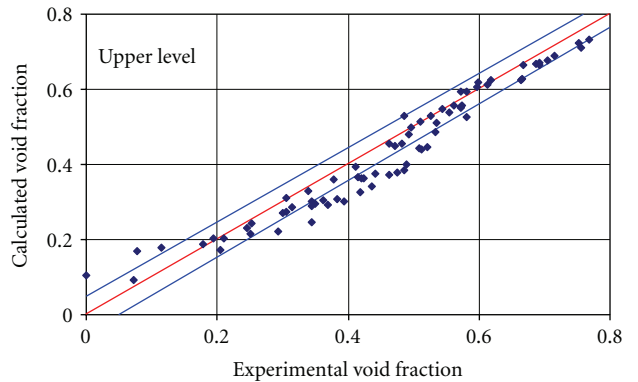


FIGURE 8: Comparison of calculated and measured void fraction for case B5 at the upper axial level.

with the measured void for the temperature transient is quite reasonable for all three levels (see Figure 16).

3.5. Steady-State Critical Heat Flux. There are several hundreds of critical heat flux (CHF) correlations for tubes, annular space, and other simple geometries in the open literature, which can be used to calculate the occurrence of

TABLE 7: Empirical correlations used for the bundle tests.

Process	Correlation	Reference
Single-phase lateral mixing	Constant coefficient 0.06	[13]
Two-phase lateral mixing	No mass transport, Beus multiplier	[14, 15]
Pressure-driven lateral flow	Constant resistance pressure loss coefficient 0.5	[5]
	Constant axial flow pressure loss coefficient	
Effect of spacers	Mixing vane: 1.0	[16]
	Nonmixing vane 0.7	
	Simple: 0.4	

TABLE 8: Void fraction standard deviations for all steady state test cases.

Test	Level	Standard deviation
B5	Lower	0.035
	Middle	0.059
	Upper	0.050
B6	Lower	0.045
	Middle	0.043
	Upper	0.080
B7	Lower	0.061
	Middle	0.057
	Upper	0.035
B8	Lower	0.041
	Middle	0.083
	Upper	0.082

TABLE 9: Initial conditions for B7 transients.

Pressure (MPa)	15.5
Mass flux (kg/(m ² s))	3300
Power (kW)	2500
Inlet temperature (°C)	291

critical boiling conditions. For fuel assemblies, a more accurate method is to use a specific CHF correlation or lookup tables especially fitted for the specific geometry and spacer grid type. The geometry and the grid spacers have a considerable influence on the CHF phenomenon. For the same thermohydraulic local conditions, the CHF may strongly vary. The well-known EPRI correlation [25] is a generalized bundle correlation that is used in COBRA-EN [5]. It covers PWR and BWR normal operating conditions as well as loss of coolant accident boundary conditions. This correlation is implemented in SUBCHANFLOW together with an iterative method to determine steady-state critical heat flux without simulating a transient. It is used in the present subchannel mode simulations instead of simple-geometry-based correlations with correction factors because typical bundle properties are implicitly included. The DNB benchmark data provide the power at which the critical heat flux condition is met for various bundle geometries (Table 5). In addition, the axial power profile and the radial power distribution changed in the different experiments. The radial power distribution has the same scheme for all DNB tests. The rods at the edge

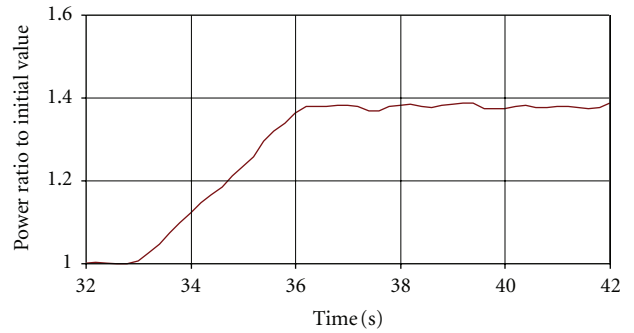


FIGURE 9: Transient power during the PI test.

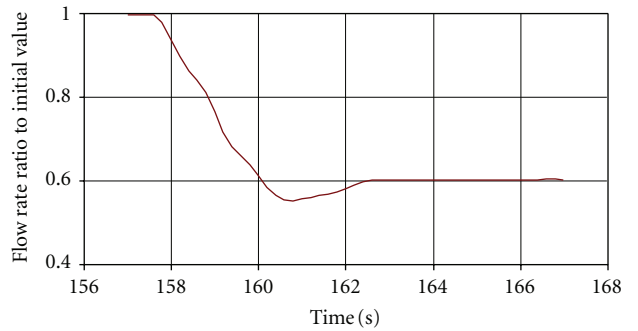


FIGURE 10: Transient flow rate behavior in the FR test.

of the assembly have a relative power of 0.85, as all inner rods have a relative power of 1.0.

The occurrence of DNB during the tests is detected by a rod temperature rise of 11°C measured by the thermocouples. The corresponding power is defined as critical power. The temperature is measured with an accuracy of 1°C, whereas the power has a measurement error of 1% [16].

The SUBCHANFLOW predictions for many tests are compared to the measured critical power in Figure 17 to Figure 22. An error band of ±10% is indicated in the graphs.

The predictions of the critical power for the tests of bundle type A0 have a standard deviation of 8 % but with a tendency to an overprediction (Figure 17). On the contrary, the critical power predictions for the bundle type A2 are generally underpredicted and several predictions are outside the error band of ±10%. The only difference between the bundle types A0 and A2 is the number of spacer of the mixing

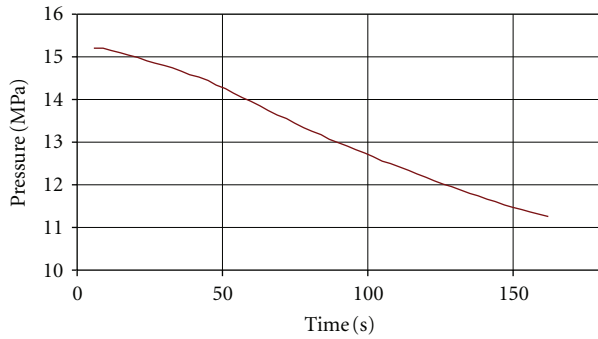


FIGURE 11: Pressure decrease in the DP test.

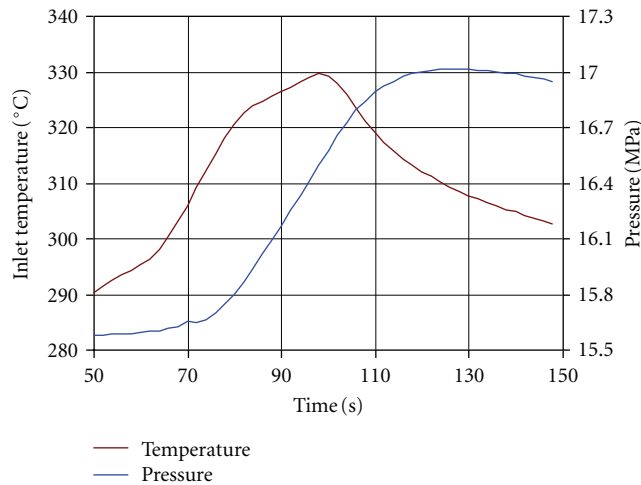


FIGURE 12: Inlet temperature and pressure during the TI test.

vanes type: 5 instead of 7. This may be a reason for the under prediction.

If one compare the results obtained for A2 and A3 (Figures 18 and 19), they are similar in the sense that there is a tendency for an under prediction. But the predictions for the bundle type A3 (Figure 19) are better than the ones for bundle type A2. The only difference between A2 and A3 is the number of rods: 25 and 36, respectively.

The axial power profile for bundle types A0, A2, and A3 is uniform which is not really representative for reactor conditions. The following test series with bundle type-A4, A8, A11, A12, and A13 were performed with cosine shaped axial power profile and hence are more close to real reactor conditions. Bundle types A4, A11, and A13 are repetition tests and they do not contain guide tubes, while A8 and A12 consist of 24 simulator rods and one guide tube.

The comparison of the SUBCHANFLOW predictions with the CHF data for these bundle types is good, especially for the test series A13 which is a repetition of the test series A4 (Figures 20 and 22). But also for the most realistic test configuration (A8) the comparison of predictions and data is quite acceptable (Figure 21).

In summary, the following statement can be made: the best simulation result is achieved for cases A0, A4, A8, and A13 with standard deviations of 8%, 9%, 8%, and 5%. A4

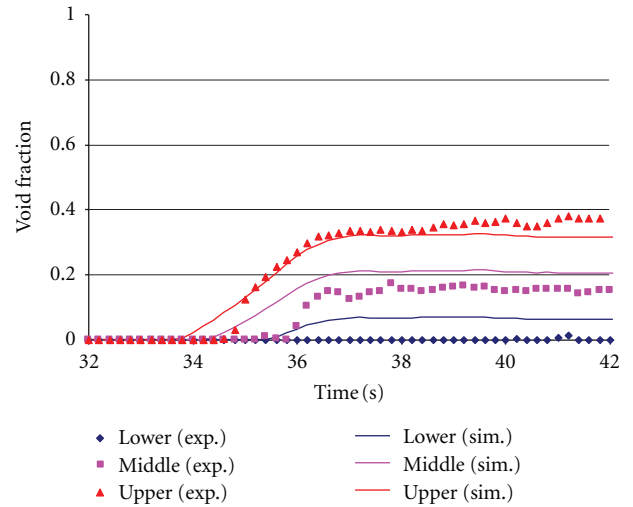


FIGURE 13: Void fraction comparison for power increase transient.

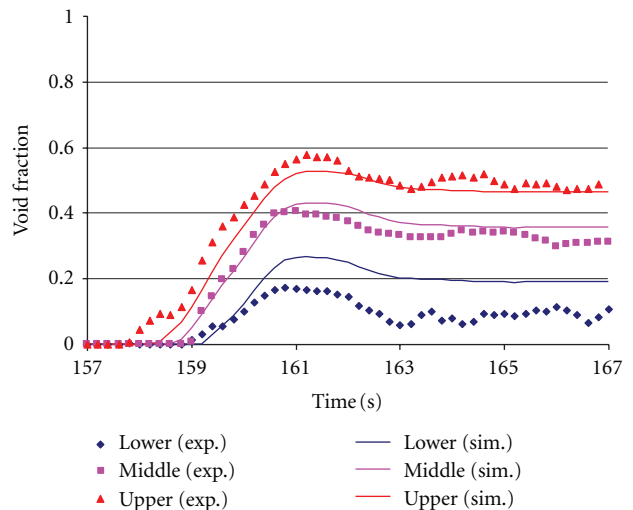


FIGURE 14: Void fraction comparison for flow reduction transient.

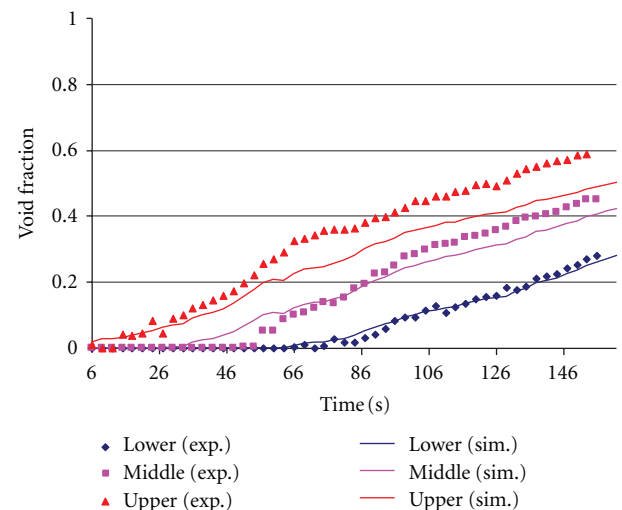


FIGURE 15: Void fraction comparison for power depressurization transient.

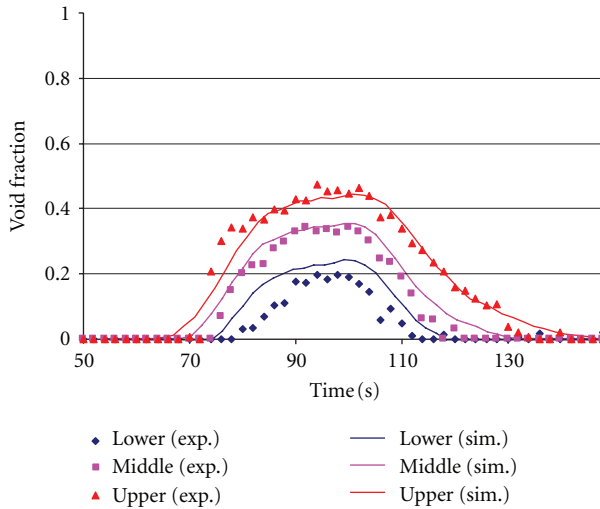


FIGURE 16: Void fraction comparison for inlet temperature increase transient.

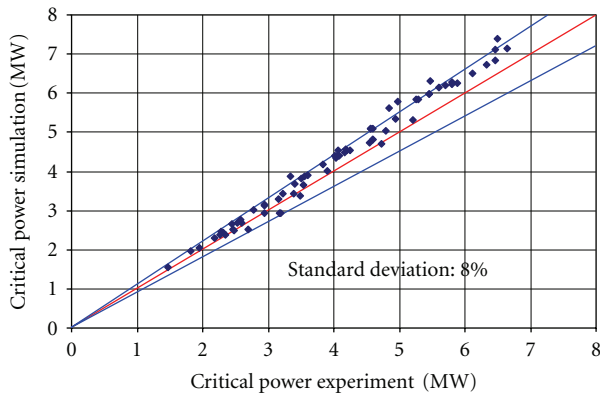


FIGURE 17: Measured and simulated critical power values for assembly A0.

and A13 have the same geometry and a cosine axial power shape. A0 and A8 are different in number of spacers, power profile and A8 contains a guide tube. In case of A2 and A3, the simulations underestimate the critical power on average by 10% and 8%. A3 is the only case with a 6 by 6 rod array. A2 has the same geometry as A4, but uses a uniform power shape instead of a cosine shape. Compared to A0, A2 has a different number of spacers, but the power profile is the same. We do not find a clear correlation of the quality of the results by comparing the geometry and power shapes. Finally, the EPRI correlation gives good results for 4 test cases and underestimates the results for two cases, which is conservative in the sense of reactor safety.

For several test runs, the axial and radial location of the occurrence of DNB is documented in the PSBT benchmark. SUBCHANFLOW detects first occurrence of DNB always at the 3×3 -center rods. For 27% of the documented cases, DNB was experimentally found at peripheral rods. For the axial location the average simulation result is 0.05 m above the average measured value at 2.64 m of the heated length

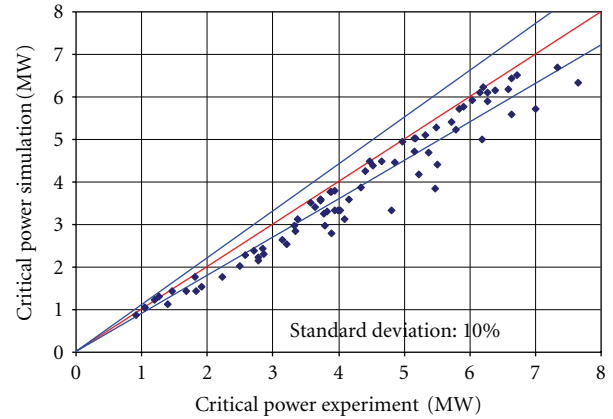


FIGURE 18: Measured and simulated critical power values for assembly A2.

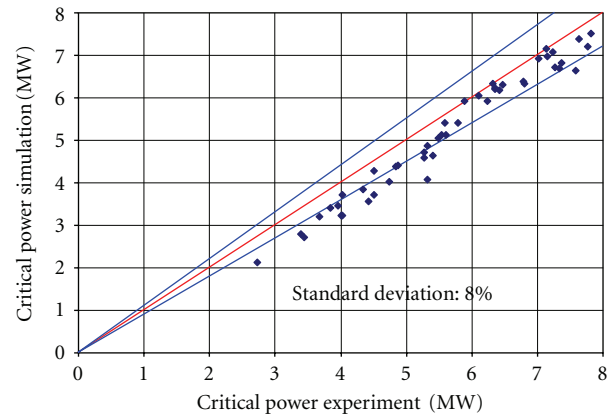


FIGURE 19: Measured and simulated critical power values for assembly A3.

(3.66 m). There is a strong scattering of the simulation results compared to the measurements expressed by a standard deviation of 0.44 m.

3.6. Transient Tests under Critical Heat Flux Conditions. For the investigation of the DNB phenomena, four PWR relevant transient scenarios were carried out at the NUPEC PSBT facility: power increase (PI), flow reduction (FR), depressurization (DP), and temperature increase (TI). Assemblies A4 and A8 are used with an initial inlet temperature of about 291°C and a system pressure of 15.6 MPa. The mass flux at steady-state is about 3100 kg/(sm²). The steady-state power is 2.5 MW. The details of the transient behavior of important parameters are found in [16]. Table 10 shows the comparison of the transient time for the incidence of a critical heat flux condition and the corresponding critical power of the predictions (sim.) and the experiments (exp.).

The maximum deviation between measured and predicted critical power is about 5%. The transient tests were conducted using bundle geometries which give good accordance between simulation and experiment for steady-state, too. So the results are consistent regarding the bundle type

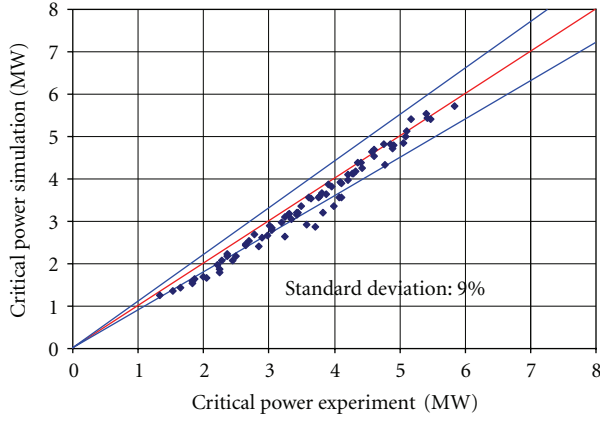


FIGURE 20: Measured and simulated critical power values for assembly A4.

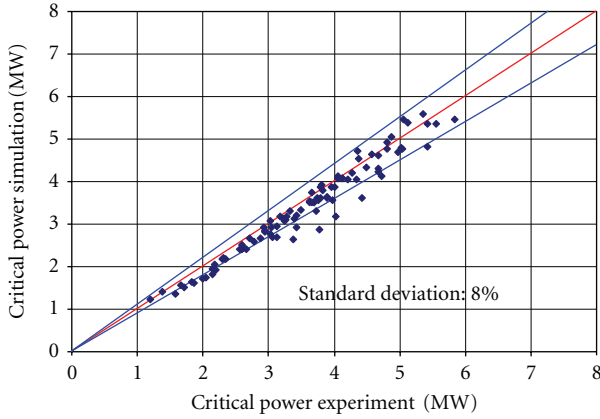


FIGURE 21: Measured and simulated critical power values for assembly A8.

used. There is only one case (A8 PI) in which the simulated critical power is significantly larger than the measured one.

4. Summary and Outlook

The main features and validation effort for SUBCHANFLOW regarding PWR relevant phenomena were presented and discussed. A subchannel code based on the experience and empirical formulations of the last decades has been developed and validated using the PSBT benchmark data for typical bundle configurations used in pressurized light water reactors. In a first step, boiling in single subchannels was investigated to validate the basic empirical correlations used for boiling forced flow conditions. Furthermore, the single-phase flow turbulent mixing coefficient was derived from code predictions in comparison to outlet temperatures of a radial nonuniform heated bundle. The predicted void fractions at three axial levels for different bundle configurations and flow boundary conditions agree well with the steady-state and transient void measurements. DNB data for test bundles with uniform and cosine power shape were evaluated by adopting the EPRI critical heat flux model

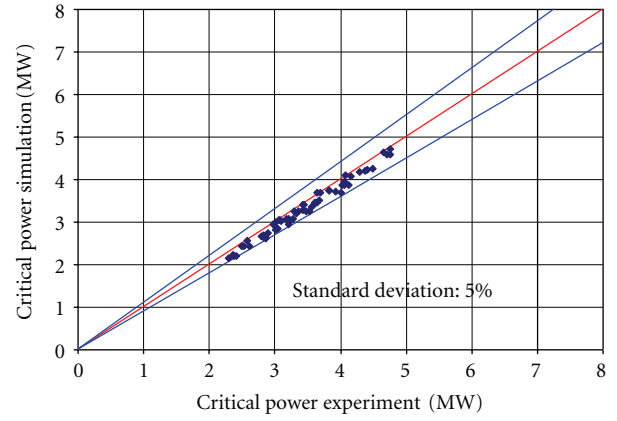


FIGURE 22: Measured and simulated critical power values for assembly A13.

TABLE 10: Occurrence of critical heat flux conditions in transient tests.

Case	Exp. DNB time (s)	Sim. DNB time (s)	Exp. critical power (MW)	Sim. critical power (MW)
A4 PI	106.7	101.9	3.81	3.66
A4 FR	52.9	52.5	2.50	2.50
A4 DP	88.8	82.6	3.59	3.40
A4 TI	140.6	140.8	3.16	3.15
A8 PI	86.6	90.0	3.81	3.89
A8 FR	55.0	52.3	2.48	2.49
A8 DP	143.8	144.0	3.37	3.37
A8 TI	128.8	134.8	3.22	3.27

correlation. The standard deviation from the exact accordance of simulation and experiment at in maximum about 10%. For some cases, an underestimation of critical power is observed, which is conservative regarding reactor safety.

The performed investigations clearly demonstrate the prediction capability of SUBCHANFLOW which is an important pillar of the multiphysical and multiscale developments at KIT [26–28]. The validation of SUBCHANFLOW related to BWR and innovative reactor phenomena is underway. The integration of this code in the NURESIM platform and the coupling to the reactor dynamic code COBAYA for both square and hexagonal geometries is also advanced [26].

Nomenclature

- A : Subchannel flow area (m^2)
- D_h : Hydraulic diameter (m)
- f : Single-phase friction coefficient (empirical correlation)
- g : Gravity (m/s^2)
- G : Mass flux ($kg/(m^2s)$)
- h : Specific mixture enthalpy (J/kg)
- h_{fg} : Evaporation enthalpy (J/kg)

K : Axial pressure loss coefficient (e.g.,) of spacers
 K_G : Lateral gap pressure loss coefficient (empirical constant)
 l : Distance of neighboring subchannels midpoints (m)
 m : Mass flow rate at axial cell boundary (kg/s)
 N : Number of measurements
 p : Pressure at axial cell boundary (Pa)
 Δp : Pressure difference between neighboring channels (Pa)
 Q : Linear power released to subchannel (W/m)
 s : Gap width between two neighboring rods (m)
 T_{exp} : Measured temperature ($^{\circ}\text{C}$)
 T_{sim} : Calculated temperature ($^{\circ}\text{C}$)
 Δt : Time step (s)
 w : Linear mass flow rate through the gap (kg/(ms))
 w' : Turbulent cross-flow (kg/(ms))
 ΔX : Length of axial cell (m)
 x : Steam quality
 α : Void fraction (empirical correlation, calculated from steam quality)
 β : Mixing coefficient (empirical constant)
 ρ : Density (kg/m³)
 σ : Standard deviation
 Φ^2 : Two-phase friction multiplier (empirical correlation)
 Old: Value at previous time step
 Liq: Liquid
 Vap: Vapor
 i : Channel i
 j : Axial cell j
 k : Gap k
 $n(k)$: Channel neighbor belonging to gap k .

References

- [1] M. J. Thurgood et al., "COBRA/TRAC—A Thermal-Hydraulic Code for Transient Analysis of Nuclear Reactor Vessel and Primary Coolant Systems," NUREG/CR-3046, 1983.
- [2] C. Y. Payk et al., "Analysis of FLECHT SEASET 163-Rod Blocked Bundle Data using COBRA-TF," NRC/EPRI/Westinghouse-12, 1985.
- [3] M. Avramova, *Development of an innovative spacer grid model utilizing computational fluid dynamics within a subchannel analysis tool [Ph.D. thesis]*, Penn State University, 2007.
- [4] K. Ivanov and M. Avramova, "Challenges in coupled thermal-hydraulics and neutronics simulations for LWR safety analysis," *Annals of Nuclear Energy*, vol. 34, no. 6, pp. 501–513, 2007.
- [5] D. Basile, R. Chierici, M. Beghi, E. Salina, and E. Brega, "COBRA-EN, an Updated Version of the COBRA-3C/MIT Code for Thermal-Hydraulic Transient Analysis of Light Water Reactor Fuel Assemblies and Cores," Report 1010/1 (revised 1.9.99), ENEL-CRTN Compartimento di Milano.
- [6] H. Blasius, "Das Ähnlichkeitsgesetz bei Reibungsvorgängen in Flüssigkeiten," *Forschungs-Arbeit des Ingenieur-Wesens* 131, 1913 (in German).
- [7] A. A. Armand, *The Resistance During the Movement of a Two-Phase System in Horizontal Pipes*, vol. 828 of *AERE-Lib/Trans*, Izvestiya Vsesojuznogo Teplotekhnicheskogo Instituta, 1946.
- [8] P. W. Dittus and L. M. K. Boelter, "Heat transfer in automobile radiators of the tubular type," *University of California Publications in Engineering*, vol. 2, no. 13, pp. 443–461, 1930, reprinted in *International Communications in Heat and Mass Transfer*, vol. 12, pp. 3–22, 1985.
- [9] C. L. Wheeler et al., "COBRA-IV-I: an Interim Version of COBRA for Thermal-Hydraulic Analysis of Rod Bundles Nuclear Fuel Elements and Cores," BNWL-1962, Battelle, Pacific Northwest Laboratory, Richland, Washington, DC, USA, 1976.
- [10] R. W. Bowring, "Physical model based on bubble detachment and calculation of steam voidage in the subcooled region of a heated channel," Tech. Rep. HPK-10, Institutt for Atomenergi, Halden, Norway, 1962.
- [11] H. Dorra, S. C. Lee, and S. G. Bankoff, "A Critical Review of Predictive Models For The Onset of Significant Void in Forced-Convection Subcooled Boiling," WSRC-TR-93-404, Westinghouse Savannah River Corporation, 1993.
- [12] B. Chexal, G. Lellouche, J. Horowitz, and J. Healzer, "A void fraction correlation for generalized applications," *Progress in Nuclear Energy*, vol. 27, no. 4, pp. 255–295, 1992.
- [13] S.-H. Ahn and G.-D. Jeun, "Effect of spacer grids on CHF at PWR operating conditions," *Journal of the Korean Nuclear Society*, vol. 33, no. 3, pp. 283–297, 2001.
- [14] S. G. Beus, "A Two-Phase Turbulent Mixing Model for Flow in Rod Bundles," Bettis Atomic Power Laboratory, WAPD-T-2438, 1970.
- [15] M. Glück, "Validation of the sub-channel code F-COBRA-TF. Part II. Recalculation of void measurements," *Nuclear Engineering and Design*, vol. 238, no. 9, pp. 2317–2327, 2008.
- [16] A. Rubin, A. Schoedel, M. Avramova, H. Utsuno, S. Bajorek, and A. Velazquez-Lozada, "OECD/NRC Benchmark Based on NUPEC PWR Subchannel and Bundle Tests (PSBT), Volume I: Experimental Database and Final Problem Specifications," US NRC OECD Nuclear Energy Agency, 2010.
- [17] D. S. Rowe, "COBRA IIIC: A Digital Computer Program for Steady-State and Transient Thermal Analysis of Rod Cundle Nuclear Fuel Elements," BNWL-1695, Pacific Northwest Laboratory, 1973.
- [18] C. L. Wheeler et al., "COBRA-IV-I: An Interim Version of COBRA for Thermal Hydraulic Analysis of Rod Bundle Nuclear Fuel Elements and Cores," BNWL-1962, Pacific Northwest Laboratory, 1976.
- [19] U. Imke, V. Sanchez, and R. Gomez, "SUBCHANFLOW: an empirical knowledge based subchannel code," in *Proceedings of the Annual Meeting on Nuclear Technology*, pp. 4–6, Berlin, Germany, May 2010.
- [20] V. Sánchez, U. Imke, and R. Gomez, "SUBCHANFLOW: a thermal-hydraulic sub-channel program to analyse fuel rod bundles and reactor cores," in *Proceedings of the 17th Pacific Basin Nuclear Conference*, pp. 24–30, Cancún, México, October 2010.
- [21] L. S. Tong, *Boiling Heat Transfer and Two-Phase Flow*, John Wiley & Sons, 1965.
- [22] A. Berkhan, V. Sánchez, and U. Imke, "Validation of PWR relevant models of SUBCHANFLOW using the NUPEC PSBT Data," in *Proceedings of the 14th International Topical Meeting on Nuclear Reactor Thermal Hydraulics (NURETH-14)*, pp. 25–29, Toronto, Canada, September 2011.
- [23] J. T. Rogers and R. G. Rosehart, "Mixing by turbulent interchange in fuel bundles. Correlations and interfaces," in: ASME, 72-HT-53, 1972.

- [24] J. T. Rogers and A. E. E. Tahir, "Turbulent interchange mixing in rod bundles and the role of secondary flows," in *ASME, Heat Transfer Conference*, San Francisco, Calif, USA, 1975.
- [25] D. G. Reddy and C. F. Fighetti, "Parametric Study of CHF Data Volume 2, A generalized subchannel CHF correlation for PWR and BWR fuel assemblies," EPRI-NP-2609, 1983.
- [26] M. Calleja, V. Sanchez, and U. Imke, "Implementation of SUBCHANFLOW in the SALOME Platform and Coupling with the Reactor Dynamic Code COBAYA3," Jahrestagung Kerntechnik, Berlin, Germany, 17.19. Mai, 2011.
- [27] A. Gomez, V. Sanchez, U. Imke, and R. Macian, "DYNSUB: A Best Estimate Coupled System for the Evaluation of Local Safety Parameter," Jahrestagung Kerntechnik, Berlin, Germany, 17.19. Mai, 2011.
- [28] Ivanov, V. Sanchez, and U. Imke, "Application of a coupled code system NCNP-SUBCHANFLOW to study conventional and innovative PWR fuel assembly types," Jahrestagung Kerntechnik, Berlin, Germany, 17.19. Mai, 2011.

Research Article

Accuracy and Uncertainty Analysis of PSBT Benchmark Exercises Using a Subchannel Code MATRA

Dae-Hyun Hwang, Seong-Jin Kim, Kyong-Won Seo, and Hyuk Kwon

Advanced Reactor Development Division, Core Design Department, Korea Atomic Energy Research Institute, 1045 Daedeok-daero, Yuseong-gu, Daejeon 305-353, Republic of Korea

Correspondence should be addressed to Dae-Hyun Hwang, dhhwang@kaeri.re.kr

Received 19 April 2012; Accepted 30 June 2012

Academic Editor: Alessandro Petruzzi

Copyright © 2012 Dae-Hyun Hwang et al. This is an open access article distributed under the Creative Commons Attribution License, which permits unrestricted use, distribution, and reproduction in any medium, provided the original work is properly cited.

In the framework of the OECD/NRC PSBT benchmark, the subchannel grade void distribution data and DNB data were assessed by a subchannel code, MATRA. The prediction accuracy and uncertainty of the zone-averaged void fraction at the central region of the 5×5 test bundle were evaluated for the steady-state and transient benchmark data. Optimum values of the turbulent mixing parameter were evaluated for the subchannel exit temperature distribution benchmark. The influence of the mixing vanes on the subchannel flow distribution was investigated through a CFD analysis. In addition, a regionwise turbulent mixing model was examined to account for the nonhomogeneous mixing characteristics caused by the vane effect. The steady-state DNB benchmark data with uniform and nonuniform axial power shapes were evaluated by employing various DNB prediction models: EPRI bundle CHF correlation, AECL-IPPE 1995 CHF lookup table, and representative mechanistic DNB models such as a sublayer dryout model and a bubble crowding model. The DNBR prediction uncertainties for various DNB models were evaluated from a Monte-Carlo simulation for a selected steady-state condition.

1. Introduction

The critical heat flux (CHF) is a parameter of great importance, which constrains the thermal power capability of a light water nuclear reactor (LWR). It is usually predicted by a local parameter CHF correlation accompanied with an appropriate thermal-hydraulic field analysis code to obtain the local subchannel grade conditions in the fuel assembly. For this purpose, the subchannel approach has been widely adopted in the design calculation of an LWR core since it provides reasonably accurate results on the flow and enthalpy distributions in rod bundles with a pertinent computing time.

The OECD/NRC PWR Subchannel and Bundle Tests (PSBT) benchmark was organized on the basis of the NUPEC database. The purposes of the benchmark are the encouragement to develop a theoretically based microscopic approach as well as a comparison of currently available computational approaches. The benchmark consists of two separate phases: a void distribution benchmark and DNB benchmark.

Subchannel-grade void distribution data was employed for validation of a subchannel analysis code under steady-state and transient conditions. The DNB benchmark provided subchannel fluid temperature data, which can be used to determine the turbulent mixing parameter for a subchannel code. The steady-state and transient DNB data can be used to evaluate and improve the currently available DNB prediction models in PWR bundles. The NUPEC PWR test facility consists of a high-pressure and high-temperature recirculation loop, a cooling loop, and a data recording system [1]. The void fraction was measured by two different methods: A gamma-ray beam CT scanner system was used to determine the distribution of density/void fraction over the subchannel at a steady-state flow and to define the subchannel averaged void fraction with an accuracy of $\pm 3\%$. A multibeam system was also used to measure chordal averaged subchannel void fraction in a rod bundle with accuracies of $\pm 4\%$ and $\pm 5\%$ for steady and transient states, respectively.

The purposes of this study are to evaluate the accuracy and uncertainty of the MATRA code for the PSBT

benchmark exercises of the subchannel void distribution under steady-state and transient conditions, as well as to provide the analysis results for the subchannel temperature distribution and DNB benchmark problems. The prediction accuracy, which is the closeness of agreement between the predicted value and the true value, was evaluated by comparing the code predictions with the measured data. On the other hand, the prediction uncertainty was evaluated by considering the propagation of uncertainties for the boundary operating conditions and code modelling parameters.

2. MATRA Code Models for PSBT Benchmark Analysis

2.1. Subchannel Analysis Code MATRA. MATRA is a subchannel analysis code, which adopts mixture transport equations for the two-phase flow conditions [2]. The governing equations for the subchannel geometry were derived from the integral balances on an arbitrary fixed control volume. It was assumed that the flow is a transient, single component, and a two-phase mixture of liquid and vapor in a thermodynamic equilibrium state. The continuity, energy, and axial/lateral momentum equations for a vertical subchannel i are expressed as follows.

Continuity:

$$A_i \frac{\partial \rho_{m,i}}{\partial t} + \frac{\partial \dot{m}_i}{\partial z} + \sum_j w_{ij} + \sum_j w'_{i \rightarrow j} = 0. \quad (1)$$

Energy:

$$A_i \frac{\partial}{\partial t} \rho_{m,i} h_{m,i} + \frac{\partial}{\partial z} (\dot{m}_i h_i) + \sum_j w_{ij} h^* + \sum_j w'_{ij} (h_i - h_j) = Q. \quad (2)$$

Axial momentum:

$$\begin{aligned} \frac{\partial \dot{m}_i}{\partial t} + \frac{\partial}{\partial z} \left(\frac{\dot{m}_i^2 v'}{A_i} \right) + \sum_j w_{ij} u^* + f_T \sum_j w'_{ij} (u_i - u_j) \\ = -A_i \frac{\partial P}{\partial z} - F_z. \end{aligned} \quad (3)$$

Lateral momentum:

$$\begin{aligned} \frac{\partial w_{ij}}{\partial t} + \frac{\partial}{\partial z} (w_{ij} u_i) + \frac{1}{l} \sum_j w_{ij} v_i \\ = \frac{s_{ij}}{l} (P_i - P_j) - \frac{1}{2} K_{ij} \frac{w_{ij} |w_{ij}|}{\rho^* s_{ij} l}. \end{aligned} \quad (4)$$

The source terms in the above equations are expressed as

$$\begin{aligned} Q &= \frac{\partial}{\partial z} \left(k_i \frac{\partial T_i}{\partial z} A_i \right) - \sum_j \frac{k_j s_{ij}}{l} (T_i - T_j) + \sum_n \xi_n \langle q_n'' \rangle, \\ F_z &= \frac{1}{2} \left\{ \frac{f \phi^2}{d_{hy} \rho_m} + \frac{K v'}{\Delta x} \right\} \frac{\dot{m}_i^2}{A_i} + A_i \rho_{m,i} g. \end{aligned} \quad (5)$$

The major unknowns of the governing equations are the coolant density (ρ), axial flow rate (\dot{m}), cross flow (w_{ij}), pressure (P), and enthalpy (h). Subscript “ m ” means the two-phase mixture property, and superscript “ $*$ ” means the donor-channel property. The last term of the left-hand side of conservation equations (1), (2), and (3) represents the net exchange of mass, energy, and axial momentum due to a turbulent mixing between subchannel i and its surrounding subchannels. By introducing a turbulent mixing parameter, β , which is defined as a ratio of the lateral fluctuating mass flux to the axial mass flux of the fluid in the subchannel, the turbulent mixing flow rate per unit length from subchannel i to j is expressed as

$$w'_{ij} = \beta \cdot s_{ij} \cdot G_{\text{avg}}. \quad (6)$$

The turbulent mixing parameter is normally determined from a thermal mixing test under single-phase conditions. Two different models for the interchannel turbulent mixing phenomenon are available in the MATRA code: the equal-mass-exchange (EM) model and the equal-volume-exchange and void-drift (EVVD) model. The net fluctuating mass velocity from channel i to channel j for the EVVD model is expressed as

$$\begin{aligned} w'_{i \rightarrow j} \\ \equiv w'_{ij} - w'_{ji} \\ = (w'_{ij})_{SP} \cdot \theta \cdot \left[(\alpha_j - \alpha_i) - K_{VD} \frac{(G_j - G_i)}{G_{\text{avg}}} \right], \end{aligned} \quad (7)$$

where $(w'_{ij})_{SP}$ is the turbulent mixing flow rate per unit length under single-phase conditions and θ is a two-phase multiplier for the turbulent mixing rate. A detailed description of the correlation parameters is given in [3]. The net fluctuating mass velocity ($w'_{i \rightarrow j}$) becomes zero when the EM model is employed for the analysis. Important models of the MATRA code for an analysis of the PSBT benchmark are summarized in Table 1.

2.2. PSBT Benchmark Test Bundles. Geometry information for the PSBT benchmark test bundles is summarized in Table 2. The benchmark data provided the steady-state void fraction averaged over the four central subchannels (CNTR) as shown in Figure 1. The region averaged void fraction was evaluated from the void fractions of subchannels 15, 16, 21, and 22 calculated by the MATRA code.

3. Analysis of Void Distribution Benchmark Problems

3.1. Single-Channel Void Distribution Benchmark. A single subchannel void distribution benchmark provides cross-sectional averaged void fraction at the exit of four different subchannel types found in a PWR assembly: central typical, central thimble, side, and corner subchannel types, which correspond to channel types I, II, III, and IV as shown in Figure 1. The homogeneous equilibrium bulk boiling model

TABLE 1: MATRA models for an analysis of PSBT benchmark exercises.

Parameters	Values
(i) Two-phase flow models	
Field equations	Homogeneous mixture
Subcooled boiling void fraction	Levy model
Bulk boiling void fraction	Modified Armand model
Two-phase friction multiplier	Armand model
(ii) Subchannel interaction models	
Crossflow resistance factor	0.5
Turbulent mixing parameter for single-phase	0.04
Two-phase turbulent mixing model	EM model
(iii) Hydraulic Resistance Models	
Bundle friction factor	$0.184 \text{ Re}^{-0.2}$
Spacer grid loss factor (MV/NMV/SS) ^(*)	1.0/0.7/0.4 [1]

(*) MV: Mixing Vaned, NMV: Nonmixing Vaned, SS: Simple Support.

TABLE 2: Geometry of test bundles for PSBT benchmark exercises.

Item	Data							
	B5/B6	B7	A0	A1	A2	A3	A4	A8
Test bundle	B5/B6	B7	A0	A1	A2	A3	A4	A8
Type of experiment	Void	Void	DNB	Mix	DNB	DNB	DNB	DNB
Rod array	5 × 5	5 × 5	5 × 5	5 × 5	5 × 5	6 × 6	5 × 5	5 × 5
Number of heated rods	25	24	25	25	25	36	25	24
Number of thimble rods	0	1	0	0	0	0	0	1
Heated rod O.D.	9.50	9.50	9.50	9.50	9.50	9.50	9.50	9.50
Thimble rod O.D.	—	12.24	—	—	—	—	—	12.24
Heated rod pitch	12.60	12.60	12.60	12.60	12.60	12.60	12.60	12.60
Axial heated length	3658	3658	3658	3658	3658	3658	3658	3658
Flow channel inner width	64.9	64.9	64.9	64.9	64.9	77.5	64.9	64.9
Axial power shape	Uni/Cos	Cos	Uni	Uni	Uni	Uni	Cos	Cos
Number of MV spacers	7	7	5	7	7	7	7	7
Number of NMV spacers	2	2	2	2	2	2	2	2
Number of SS spacers	8	8	6	8	8	8	8	8
TS Cross-section (Figure 1)	(a)	(b)	(a)	(a)	(a)	—	(a)	(b)

Length: [mm].

tends to overpredict the void fraction in comparison with the modified Armand model, while the low-void fraction was not adequately predicted if a subcooled boiling model was not employed. As the result, this model revealed relatively large scatterings against the void fraction measurement error ($2\sigma = \pm 6\%$) [1] as shown in Figure 2(a). On the other hand, the effects of subcooled boiling models in the MATRA code were examined for the single-channel void distribution benchmark exercises. The subcooled and bulk boiling models described in Table 1 revealed a slightly overprediction of the channel exit void fraction for central typical and side subchannels, as shown in Figure 2(b).

3.2. Steady-State Bundle Void Distribution Benchmark. The experimental data include a chordal averaged void fraction at three axial elevations, 2216 mm, 2669 mm, and 3177 mm, from the bottom of the heated length. The void prediction error, which represent the difference between the predicted

and measured void fractions, are plotted in Figure 3 at the lower and upper axial levels. As the axial elevation increases, the error of mean ($P-M$) decreases from 5.1% to -3.4% , while the standard deviation remains within $6.0\% \sim 6.9\%$ for all axial levels. The maximum error of mean ($P-M$) was calculated as 11% at the lower elevation of B7, which has a central unheated rod and cosine axial power shape. The statistics of the void prediction error are summarized in Table 3.

An uncertainty of the predicted void fraction may be caused by various parameters involved in the calculations, such as the hydraulic and thermal input variables, dimensions of the bundle components, and modelling parameters used in the code. A prediction uncertainty of the void fraction was evaluated for a case selected from the benchmark exercises. The pressure, inlet temperature, mass flux, and bundle power for the selected case (Run no. 7.6322) were 4.87 MPa, 168.6°C, 2239 kg/m²s, and 3536 kW, respectively. The selected parameters for this uncertainty analysis are

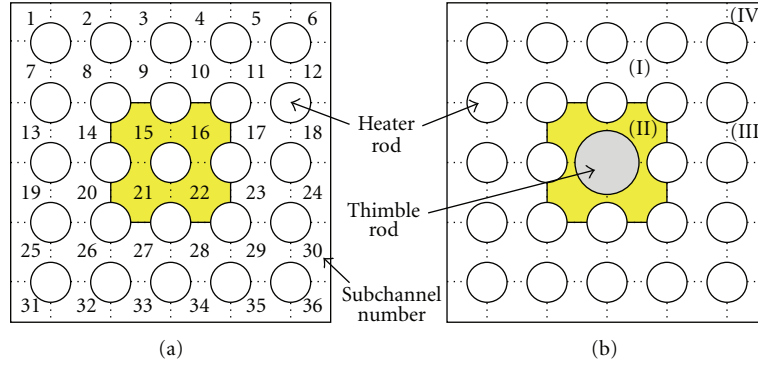


FIGURE 1: Cross-sectional view of PSBT 5 × 5 test bundles.

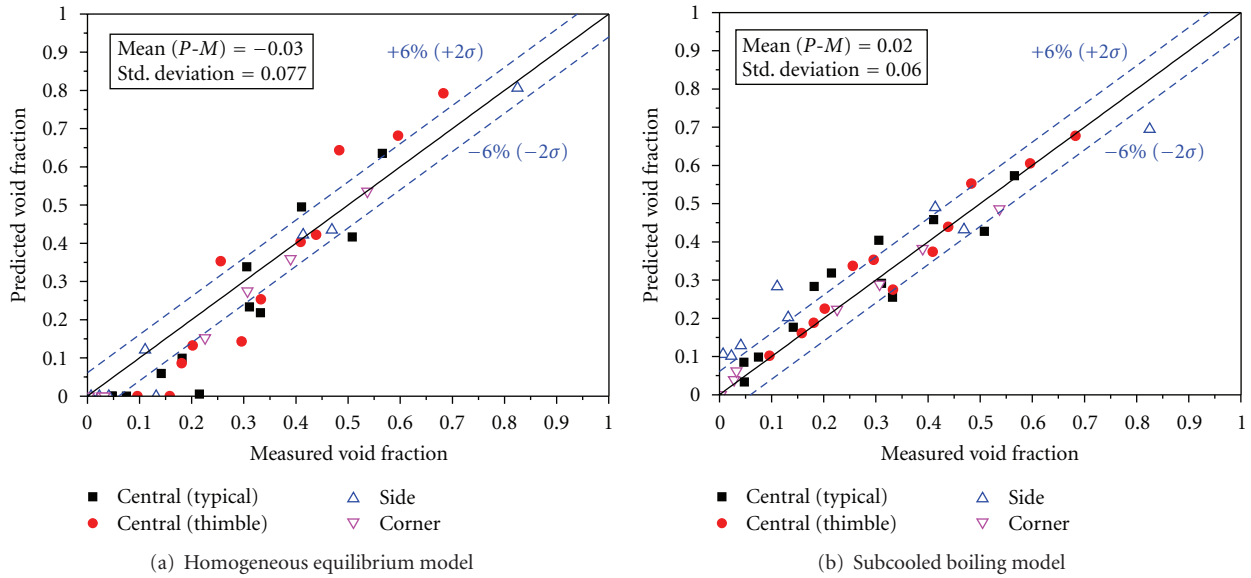


FIGURE 2: Prediction of single-channel void fraction using different void models.

described in Table 4. The accuracy and probability distribution function for the operating parameters were determined from the benchmark specifications [1]. In this table, the accuracy ranges represented one standard deviation for the normal distribution, or the boundary values for the flat distribution. The uncertainty data for the modelling parameters, which includes the bundle pressure loss factors and the turbulent mixing parameter, were approximately determined from the design information for a typical PWR [4]. The uncertainties of the selected parameters were propagated to the uncertainty of the void fraction through the physical models of two-phase flows employed in the MATRA code.

The uncertainty of a void fraction was evaluated from a Monte-Carlo simulation with the MATRA code by employing a simple random sampling technique for the selected parameters. The frequency distributions of the void fractions calculated by the MATRA code at lower and upper elevations are plotted in Figure 4 from 2,000 samplings combining each parameter. As shown in the figure, it was revealed that the uncertainty of the calculated void fraction tends to reduce as the axial elevation increases.

The two-sided tolerance limits ($= \bar{x} \pm ks$) with 95% probability and a 95% confidence level were evaluated for estimating the magnitude of uncertainty for this selected case, where \bar{x} and s are the sample mean and sample standard deviation of the predicted void fraction, respectively. A nonparametric method [5] was applied to determine the tolerance limits, since it was revealed that the data was not drawn from a normally distributed population at a 5% significance level. As a result, the interval of tolerance limits ($= ks$) for the region averaged void fraction at the axial levels of 2216 mm, 2669 mm, and 3177 mm were calculated as 4.6%, 2.3%, and 1.5%, respectively.

3.3. Transient Bundle Void Distribution Benchmark. A transient bundle void distribution benchmark provided sub-channel averaged void fraction at 3 different axial levels of the CNTR region under four transient conditions: power increase (PI), flow reduction (FR), depressurization (DP), and temperature rise (TI). These data are important for a benchmark of the subchannel analysis codes in terms of

TABLE 3: Statistics of void prediction error for steady-state void distribution exercises.

Test bundle	Series no.	Axial elevation		
		2216 mm	2669 mm	3177 mm
B5	5	3.9/4.6(*)	4.4/3.3	0.6/8.0
B6	6	2.0/4.3	2.2/5.0	-5.1/4.3
B7	7	11.0/5.5	7.9/7.0	-2.3/4.0
B5	8	2.8/6.5	-3.6/6.6	-6.9/4.7
Total		5.1/6.3	2.9/6.9	-3.4/6.0

(*) Mean/standard deviation of ($P-M$), in %.

TABLE 4: Uncertainty parameters.

Parameter	Accuracy	pdf
Operating parameters;		
(i) Pressure	$\pm 1\%$	Normal
(ii) Channel flow rate	$\pm 1.5\%$	Normal
(iii) Bundle power	$\pm 1\%$	Normal
(iv) Channel inlet temperature	$\pm 1^\circ\text{C}$	Flat
Modeling parameters;		
(i) Bundle friction factor	$\pm 10\%$	Flat
(ii) Spacer grid loss factor	$\pm 10\%$	Flat
(iii) Turbulent mixing parameter	$\pm 10\%$	Normal

predicting a CHF for a reactor transient or accident conditions. The implicit scheme employed in the MATRA code allowed no restrictions in the time step size for the transient calculations. The analysis results revealed the maximum deviation between the predicted and measured values of the averaged void fraction for the four different transients of PI, FR, DP, and TI as 0.247, 0.216, 0.209, and 0.285, respectively. For the FR transient, the maximum/minimum values of ($P-M$) of the void fraction at CNTR region were calculated as 0.076/-0.126 for B5 and 0.216/-0.077 for B7, respectively. Similar to the steady-state bundle void distribution benchmark, the maximum deviation between the benchmark data and the MATRA prediction was found at the lower elevation of the B7 bundle for this transient problem.

An uncertainty analysis for a transient bundle void distribution benchmark was conducted for the parameters described in Table 4. The FR transients for test bundles B5 and B7 were selected for the uncertainty analysis. From a Monte-Carlo simulation with the MATRA code, the range of the predicted void fraction at each time step was plotted as the grey region in Figure 5. The maximum deviations of the void fraction between the maximum and minimum predicted values (i.e., the width of grey region) at each time step were calculated as 11% for B5 and 12%~13% for B7 at different axial levels during the FR transients.

4. Analysis of Mixing and DNB Benchmark Problems

4.1. Subchannel Exit Temperature Distribution Benchmark. The accuracy of a subchannel analysis code is fairly dependent on the modeling of interchannel exchanges between

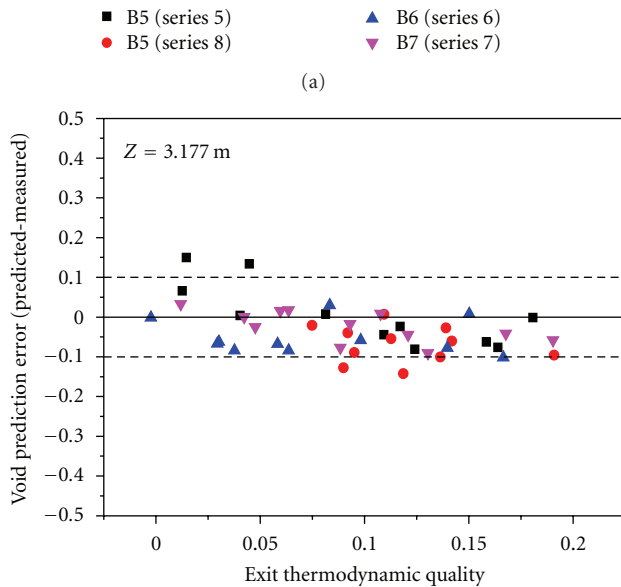
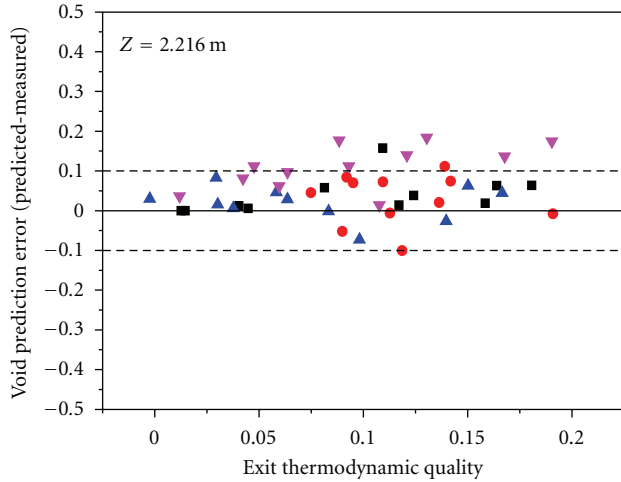
adjacent subchannels, such as a diversion cross flow and turbulent mixing [6]. The diversion cross flow caused by a lateral pressure difference between subchannels is calculated from the lateral momentum equation. The turbulent mixing term is considered in the subchannel equations by (6), which implies a turbulent mixing parameter defined as

$$\beta \equiv \frac{\varepsilon_{ij}}{z_{ij}} \times \frac{\rho}{G} = \frac{v'_{ij}}{G/\rho}, \quad (8)$$

where ε_{ij} , z_{ij} , and v'_{ij} are the mean turbulent eddy diffusivity of the heat, the mixing distance, and the fluctuating velocity between subchannels i and j , respectively. Traditionally, a constant value of β has been applied to the whole subchannel analysis region.

In the PSBT subchannel exit temperature distribution benchmark, the subchannel exit temperatures were measured at the exit of a 5×5 mixing test bundle (A1), which has a large gradient of radial power distribution. The average power in the hot region is 4-times higher than that in the cold region. The optimum value of β is determined at the condition when the rms error of the subchannel exit temperatures between the predicted and measured values becomes minimum for various values of β . An increase of β in the MATRA code will reduce the predicted difference of the temperature rise between the hot and the cold regions. Figure 6 shows a comparison of the subchannel exit temperature distributions between the MATRA results and PSBT data. If there is a temperature gradient in each region due to additional mixing effect, it may reduce the exit temperature differences between the two regions, and finally increase the optimum β in comparison with the case of no temperature gradient in each region. As shown in the Figure 6, a temperature gradient between HH-HC, as well as CH-CC, was observed in the experimental data which did not appear in the MATRA results. This discrepancy results in a significantly higher value of the optimum β , as shown in Table 5. For various operating conditions, the mean value of β was calculated as 0.08 as summarized in Table 5.

It was thought that the temperature gradient appearing in the experimental data was attributed to the thermal mixing in the diagonal direction of the test bundle, which may be caused by the alignment of mixing vanes mounted in the spacer grids. A numerical analysis using a CFD code (ANSYS, version 12.1) was conducted for a selected case (Test number 01-5237) to investigate the influence of spacer grids with mixing vanes on the subchannel temperature gradient



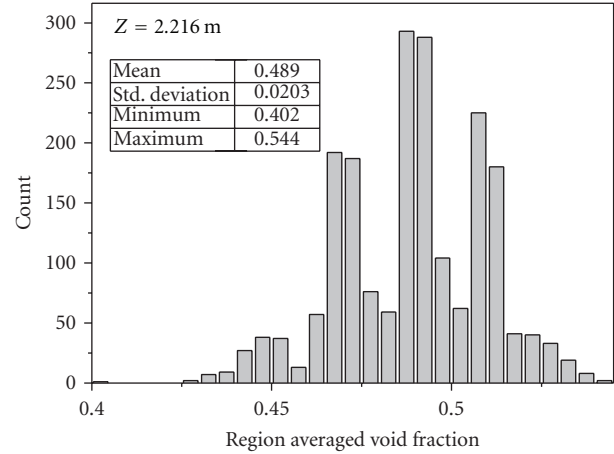
(a)

(b)

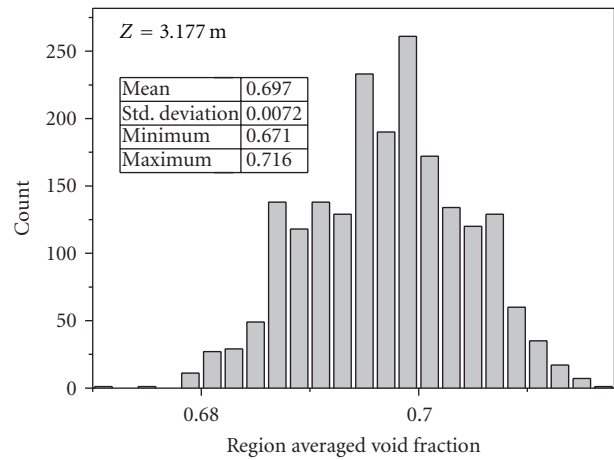
FIGURE 3: Prediction accuracy of subchannel void fraction at various elevations.

in test bundle A1. A simplified grid model was adopted for the analysis which focused on the effect of the mixing vanes. The computational meshes for the upper and lower parts of the mixing vanes were generated by applying a hexagonal sweep method, while tetrahedron meshes were applied to the mixing vane region. The standard $k-\epsilon$ turbulence model and the convergence criterion of the 10^{-6} RMS residual were used for the analysis of the flow characteristics. The geometry of the mixing vanes remarkably affects the flow distribution, as shown in Figure 7.

Figure 7 shows the streamline from the inlet. To investigate the mixing between each region, the start surface and expressed colour of the streamline were divided into two surfaces and colours. The blue and red colours indicate the streamline starting at the HC and HH regions, respectively.



(a)



(b)

FIGURE 4: Uncertainty of predicted void fraction at various elevations for Run no. 7.6322.

The cross-sectional view is configured from the end of the first mixing vane. It was noted that the flow direction is drastically changed after going through the mixing vane, and the cross flow is formed as shown in this Figure 7. Moreover, the cross flow generated by the mixing vane induces vigorous mixing in the diagonal direction between the HC and CH regions.

The diagonal mixing effects caused by the mixing vanes cannot be reflected adequately by a single optimum β in the subchannel analysis code. From the experimental result, it was inferred that the thermal mixing inside the HC region may occur more vigorously than the region HH as shown in Figure 6. A regionwise β model was introduced into the MATRA code to examine the local mixing effect. For the selected case of 01-5237, the regionwise β values were empirically fitted from the subchannel-wise exit temperature distribution data, which results 0.015, 0.4, 0.2, and 0.03 for the HH, CH, HC, and CC regions, respectively. As shown in Figure 8, the regionwise mixing model may improve the accuracy of the subchannel exit temperatures, specifically for

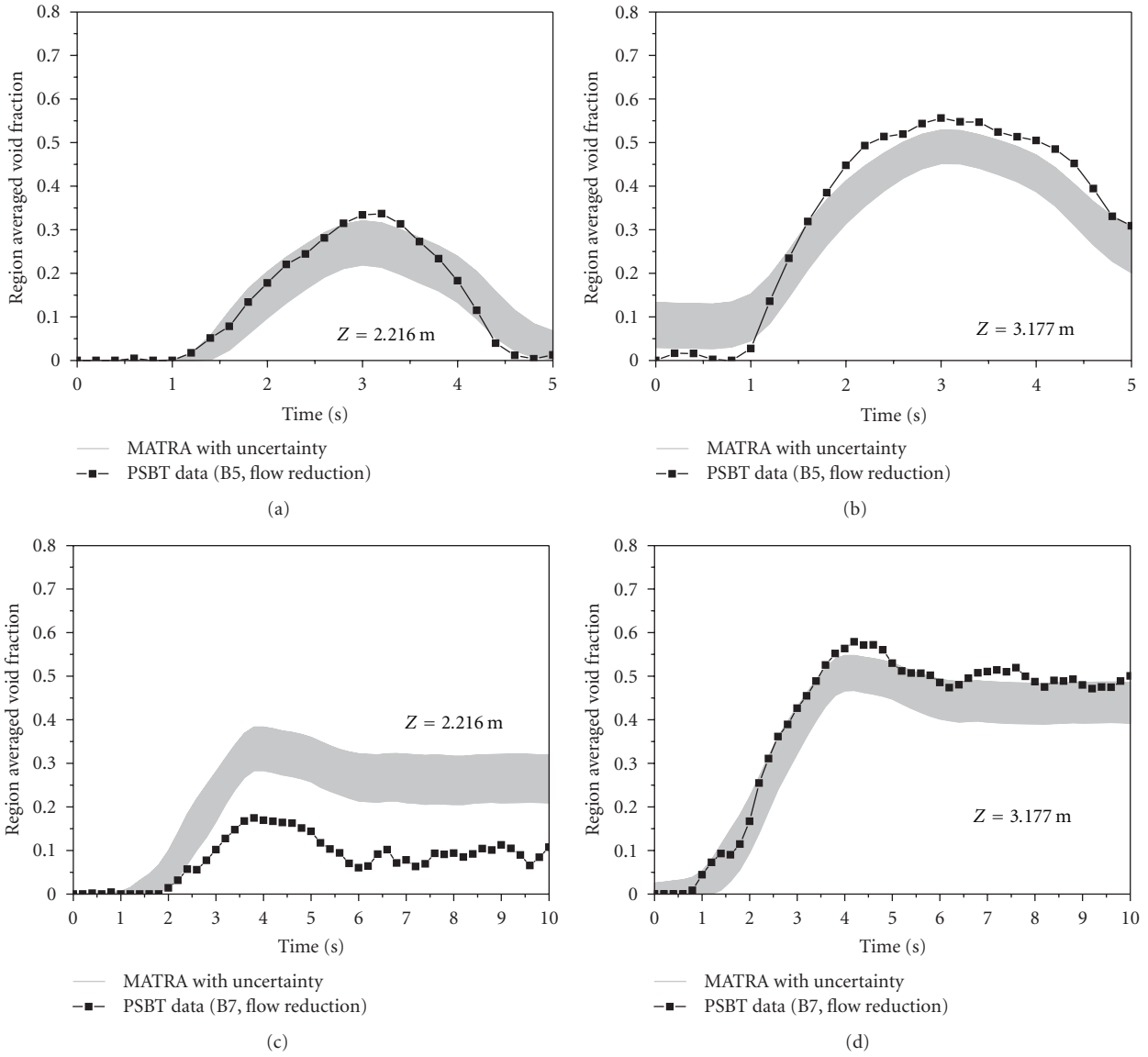


FIGURE 5: Uncertainty of subchannel void prediction for flow reduction transients.

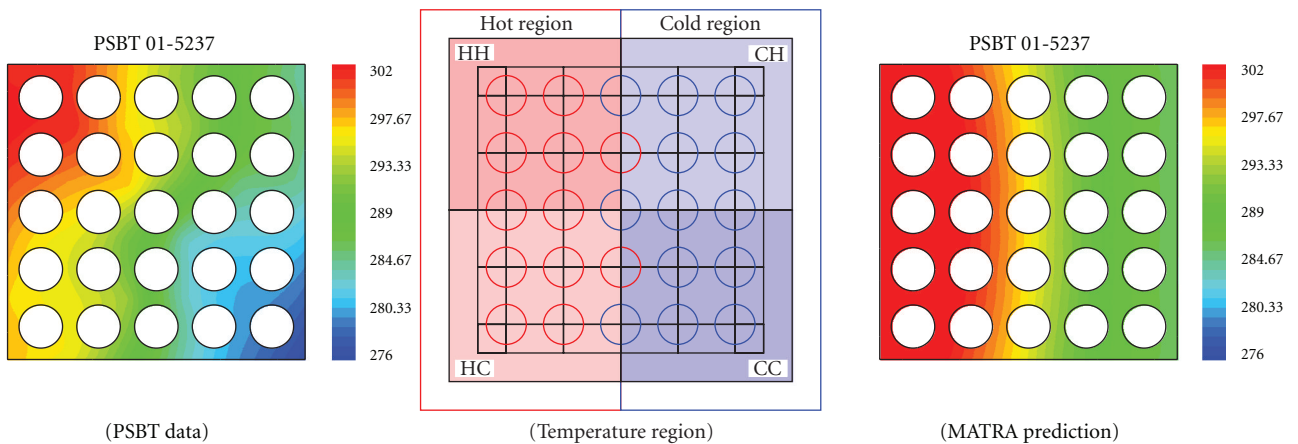


FIGURE 6: Comparison of fluid temperature distribution in a 5×5 test bundle.

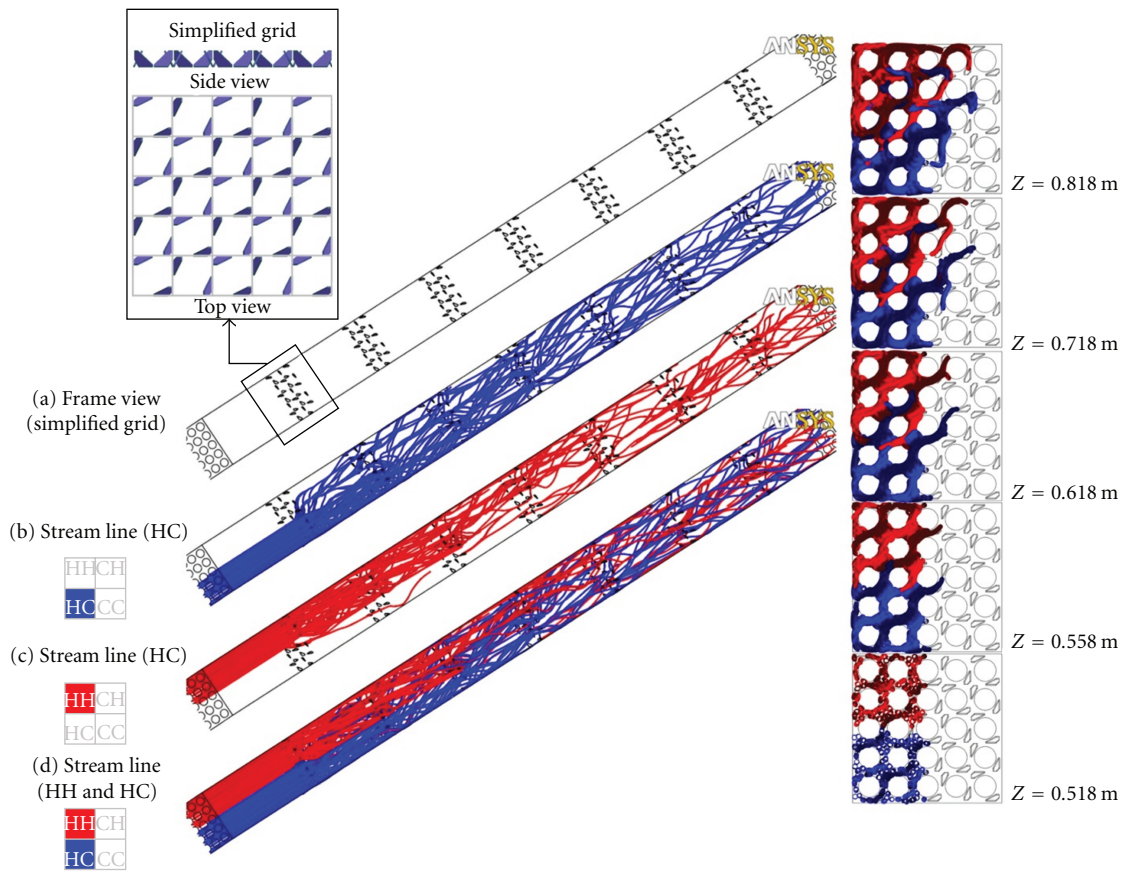


FIGURE 7: Modelling and results of CFD analysis for Test number 01-5237.

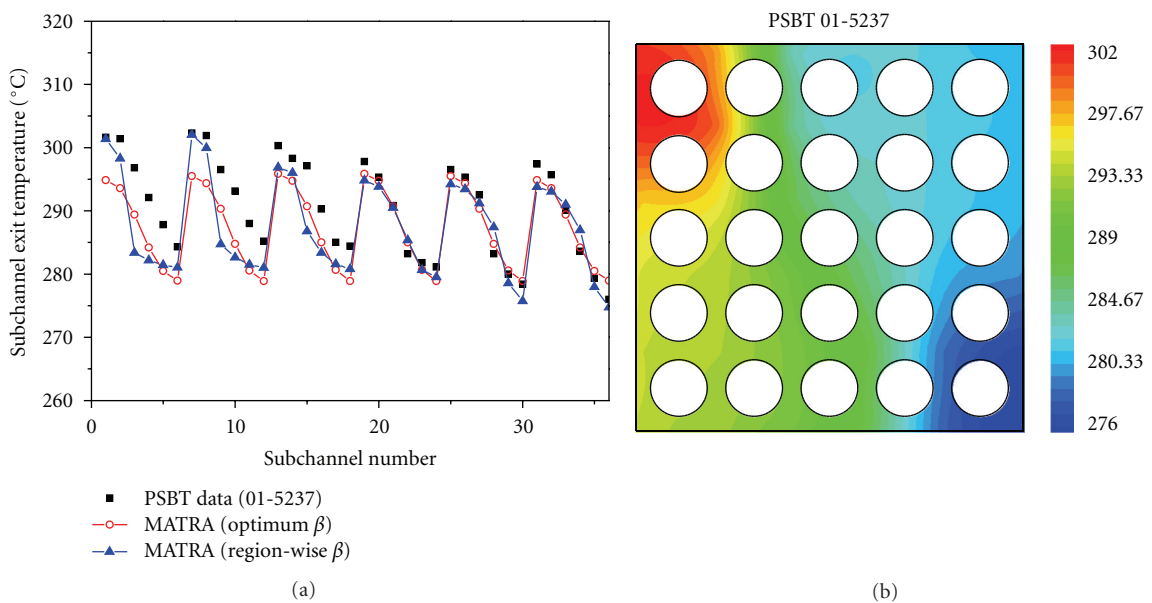


FIGURE 8: Effects of regionwise turbulent mixing parameters in the MATRA code.

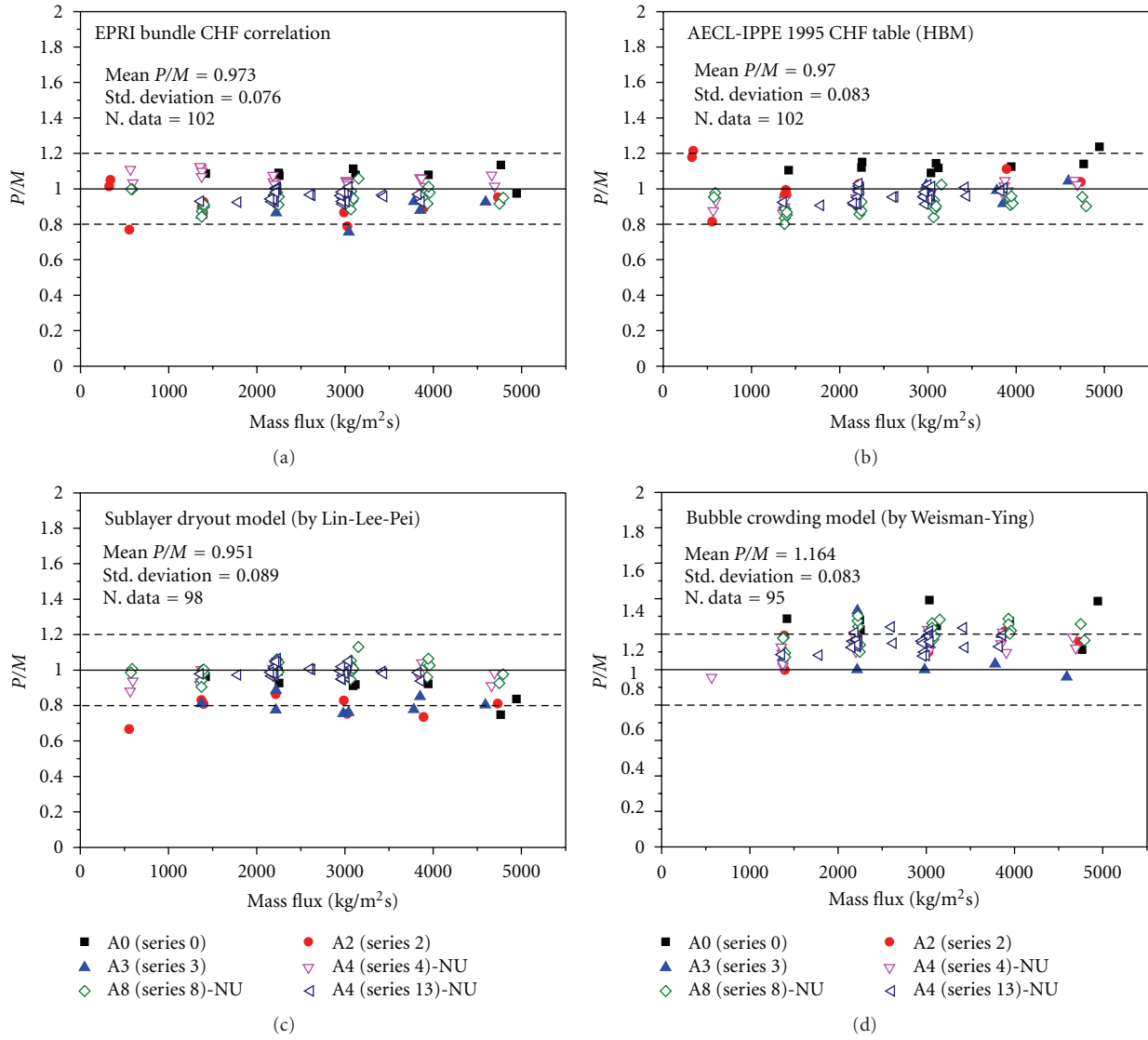


FIGURE 9: Accuracy of various CHF prediction models with MATRA for steady-state DNB benchmark.

TABLE 5: Optimum value of β at various operating conditions.

Test number	P (MPa)	G (kg/m ² s)	T_{in} (°C)	Measured exit temperature (°C)				Optimum β
				HH	HC	CH	CC	
01-1237	4.9	4722	86.0	174.6	170.0	155.8	147.7	0.072
01-5125	14.7	3038	289.2	330.3	327.5	322.7	319.3	0.081
01-5215	14.7	3041	282.9	335.6	334.5	328.0	322.4	0.084
01-5237	14.7	4708	229.4	299.6	294.6	287.8	280.7	0.089
01-5252	14.7	541	113.9	194.6	194.2	175.9	172.4	0.053
01-5342	14.7	533	164.5	260.1	256.9	244.7	239.8	0.080
01-5343	14.7	1397	165.3	257.9	252.9	242.4	235.5	0.093
01-6232	16.6	583	251.5	315.3	312.1	304.8	300.9	0.083
01-6233	16.6	1361	254.0	322.7	318.2	311.5	305.1	0.089

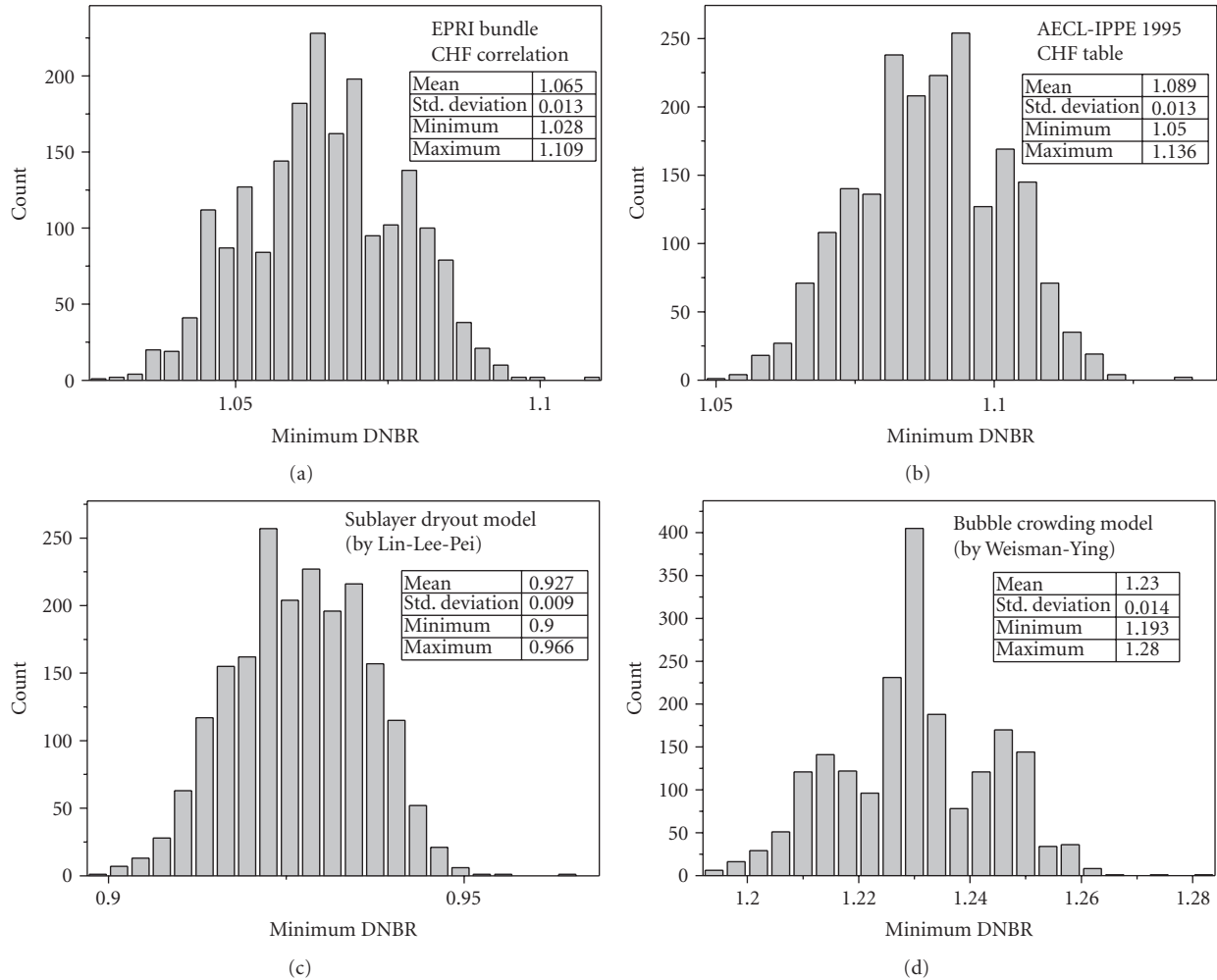


FIGURE 10: Uncertainty of predicted DNBR for a selected case (test bundle A0, Run 5350).

the rod bundles with nonhomogeneous mixing characteristics due to mixing vanes. However, it is necessary to develop an appropriate algorithm for determining nonhomogeneous turbulent mixing parameters from the experimental data and/or CFD analysis results.

4.2. Steady-State DNB Benchmark. The steady-state DNB benchmark data provided the power at which DNB occurred and the corresponding location in the bundle. The prediction accuracy of the MATRA code was evaluated for uniform and nonuniform axial power shapes by employing various DNB prediction models: a generalized bundle CHF correlation, a generalized tube CHF correlation, and two kinds of mechanistic DNB models.

The EPRI correlation [7] is a generalized bundle CHF correlation that has been developed on the basis of the local fluid conditions obtained with a subchannel code. The applicable range of the correlation covers normal operating conditions of PWR and BWR as well as hypothetical LOCA conditions.

A CHF lookup table method [8] was adopted as a generalized tube CHF correlation. It provides CHF values

for water-cooled tubes at discrete values of pressure, mass velocity, and critical quality. Linear interpolation between table values gives the CHF for a specific condition, and several correction factors were introduced to extend the CHF table to various shapes of the boiling channel. The applicability of the CHF lookup table method has been assessed for rod bundle CHF data with a subchannel analysis code [9].

Two mechanistic models for DNB were selected: a sublayer dryout model and a bubble crowding model. A sublayer dryout model was developed on the basis of dryout mechanisms of a thin liquid sublayer underneath a vapor blanket (microlayer) resulting from the Helmholtz instability at the microlayer-vapor interface. Lin and his coworkers [10] suggested an improved model for low quality flows. Key parameters associated with this model are sublayer thickness, blanket velocity, and blanket length. The sublayer thickness was determined by a force balance on the vapor blanket in the radial direction between the evaporation thrust and the lift force. The velocity of vapor blanket was determined by a balance between the buoyancy force and drag force. The mean length of a vapor blanket was assumed to be equal to

TABLE 6: P/M statistics for steady-state DNB benchmark exercises.

TS (series)	APS	EPRI Bundle correlation [7]	AECL-IPPE 1995 CHF Table [8]	Sublayer dryout model [10]	Bubble crowding model [12]
A0 (0)	Uniform	+0.073/0.046(*)	+0.136/0.042	-0.089/0.077	+0.272/0.084
A2 (2)	Uniform	-0.097/0.084	+0.021/0.113	-0.210/0.061	+0.137/0.069
A3 (3)	Uniform	-0.115/0.062	-0.034/0.054	-0.198/0.046	+0.091/0.126
A4 (4)	Cosine	+0.054/0.038	-0.043/0.054	-0.024/0.043	+0.125/0.068
A8 (7)	Cosine	-0.055/0.049	-0.094/0.051	+0.003/0.049	+0.207/0.067
A4 (13)	Cosine	-0.039/0.028	-0.036/0.037	-0.004/0.033	+0.152/0.044
All data		-0.027/0.076	-0.030/0.083	-0.049/0.089	+0.164/0.083

(*) mean relative bias error/standard deviation of P/M .

the critical Helmholtz wavelength at the vapor-liquid interface. They examined the model for selected rod bundle data with the COBRA-IIIC/MIT-1 code [11].

The near-wall bubble crowding model postulated that CHF at low qualities occurs when the bubbles near the heated wall coalesce into a vapor film. The bubble layer near the wall was assumed to become so thick that it inhibits enthalpy transport between the fluid in the core region and the liquid near the wall. Weisman and his coworkers suggested that CHF occurs when the void fraction in the bubbly layer just exceeds the critical value of 0.82. During the modelling of a turbulent interchange between the bubbly layer and the core regions, two empirically determined parameters have been adopted. Weisman and Ying [12] suggested an extended version of the bubble crowding model to high quality and low velocity conditions. They evaluated the model for rod bundle data under PWR conditions using the COBRA-IV-I code [13].

It is known that two different methodologies can be used for the prediction of CHF by a local parameter CHF correlation: the direct substitution method (DSM) and the heat balance method (HBM) [14]. For a calculation of CHF in rod bundles by HBM, it was assumed that (1) the local mass velocity distribution within a test bundle remained unchanged at different power levels, and (2) the enthalpy rise in the subchannel was proportional to the bundle power. The EPRI correlation was applied with DSM, while the other three CHF prediction models were applied with HBM. At a given experimental condition, the CHF values were calculated in all subchannels with the local thermal hydraulic parameters calculated by the MATRA code to find out the minimum DNBR location in the test bundle.

For the test bundles with nonuniform axial power shapes, the predicted CHF value was determined at the location where the critical bundle power becomes minimum. An iterative calculation was required for the HBM, until the predicted critical bundle power coincided with the bundle power, which was used for a determination of the local thermal hydraulic conditions. During this iterative calculation, it was assumed that the ratio of the hot-subchannel enthalpy rise to the bundle-averaged enthalpy rise remains constant for various bundle powers. Pertinent correction factors for a nonuniform axial power shape were employed for the EPRI correlation and CHF lookup table method, while an

additional correction factor was not required for the mechanistic DNB models.

The statistics of predicted-to-measured CHF ratio (P/M) for the steady-state DNB benchmark exercises are summarized in Table 6. The mean relative bias error ($\bar{\delta}$) is defined as follows:

$$\bar{\delta} \equiv \frac{1}{N} \sum_{n=1}^N \left\{ \left(\frac{P}{M} \right)_n - 1 \right\}. \quad (9)$$

The parametric behaviours of P/M with respect to the bundle average mass flux are shown in Figure 9 for different DNB models. As a result, it was found that the EPRI correlation and CHF lookup table revealed similar prediction accuracy. The sublayer dryout model underpredicted the CHF by 4.9%, while the bubble crowding model overpredicted it by 16.4%. The standard deviation for all of the benchmark data was calculated to be within 7.6%~8.9% for the four different DNB prediction models.

The uncertainty of predicted DNBR was evaluated by considering the uncertainty parameters described in Table 4. The frequency distributions of DNBR at a selected condition (test bundle A0, Run 5350) from a Monte-Carlo simulation with 2,000 samplings are shown in Figure 10 for various DNB models. As a result, it was appeared that the DNBR frequency distribution for a bubble crowding model was somewhat different from those for the empirical DNB models as shown in the Figure 10. It may be attributed to the uncertainty of void fraction which propagated to the uncertainty of mechanistic DNB model through the modelling parameters, such as the effective quality or the turbulent transport velocity between core and bubbly layer. The relative standard deviations of DNBR for the four different DNB prediction models lay in 1.0%~1.2%, while the relative standard deviation of the local void fraction was calculated as 5.5%.

5. Conclusions

The PSBT benchmark data for the void fraction and DNB exercises were evaluated by a subchannel analysis code, MATRA. The prediction accuracy of the MATRA code for the steady-state bundle void distribution exercises revealed a mean ($P-M$) error of 2.9%~5.1%. The MATRA code tended

to over-predict the void fraction at lower elevations under the steady and transient conditions.

The uncertainty of the MATRA code under steady-state and transient conditions was evaluated by considering the uncertainties of selected operating and modelling parameters with a Monte-Carlo simulation method. For Run no. 7.6322 of the steady-state bundle void distribution benchmark, the interval of tolerance limits for the region averaged void fraction at the axial levels of 2216 mm, 2669 mm, and 3177 mm were calculated as 4.6%, 2.3%, and 1.5%, respectively. For the flow reduction transient, the maximum/minimum values of (P-M) of the void fraction at CNTR region were calculated as 0.076/−0.126 for B5 and 0.216/−0.077 for B7, respectively.

For the fluid temperature benchmark data, the best estimated value of the turbulent mixing parameter (β) was calculated as 0.08 with a standard deviation of 0.011. As a result of the CFD analysis, the temperature gradients inside the hot and cold regions were possibly explained by the mixing vane effect. A regionwise β model was examined to reflect the diagonal mixing effects caused by mixing vanes. It was revealed that the temperature gradients in the hot and cold regions could be predicted approximately by using the regionwise β model.

DNB data for test bundles with uniform and cosine axial power shape was evaluated by employing various CHF prediction models. The mean error and standard deviation of P/M for the two different mechanistic DNB models, that is, a sublayer dryout model and a near wall bubble crowding model, were calculated as −4.9%~+16.4% and 8.3%~8.9%, respectively. The AECL-IPPE 1995 CHF lookup table with HBM and EPRI CHF correlation revealed the mean error to be −3.0% and −2.7%, respectively. As a result of DNBR uncertainty analysis for a selected case (test bundle A0, Run 5350), the relative standard deviations were calculated as 1.0%~1.2% with various DNB models.

Further research works for improving the subcooled boiling models in rod bundles, or for an accurate modeling of the spacer grid effects on the thermal-hydraulic interactions between subchannels in connection with a CFD analysis would contribute to enhance the accuracy of the subchannel codes.

Nomenclature

A :	Channel flow area (m^2)
d_{hy} :	Channel hydraulic diameter (m)
f :	Single-phase friction factor
f_T :	Turbulent momentum factor
g :	Gravity acceleration (m/sec^2)
G :	Mass flux ($kg/m^2\text{-sec}$)
h :	Flow enthalpy (kJ/kg)
h_m :	Mixture enthalpy (kJ/kg)
k :	Thermal conductivity of fluid ($kW/m\text{-}^\circ C$)
k :	Two-sided tolerance factor
K :	Form loss factor
K_{ij} :	Crossflow resistance factor
K_{VD} :	Void drift coefficient
l :	Centroid distance between adjacent channels (m)
\dot{m} :	Mass flow rate (kg/sec)

P :	Pressure ($kg/m\text{-}sec^2$)
q'' :	Surface heat flux (kW/m^2)
s :	Sample standard deviation
s_{ij} :	Gap between channel i and j (m)
T :	Fluid temperature ($^\circ C$)
u :	Axial flow velocity (m/sec)
v :	Lateral flow velocity (m/sec)
v' :	Effective specific volume (m^3/kg)
w_{ij} :	Crossflow from channel i to j ($kg/m\text{-}sec$)
w'_{ij} :	Turbulent mixing flow rate per unit axial length ($kg/m\text{-}sec$)
\bar{x} :	Sample mean
α :	Void fraction
β :	Turbulent mixing parameter
$\bar{\delta}$:	Mean relative bias error
ϕ^2 :	Two-phase friction multiplier
ρ_m :	Two-phase mixture density (kg/m^3)
σ :	Standard deviation
ξ :	Heated perimeter (m).

Subscript

avg:	Averaged for channel i and j
i, j :	Channel index
n :	Rod index.

Superscript

*: Donor channel property.

Acknowledgments

The authors thank Dr. Utsuno at NUPEC, Professor Avramova at Pennsylvania State University and Dr. Choi at OECD for their efforts pertaining to the benchmark program. This work has been carried out under the R&D program supported by the Ministry of Education, Science and Technology of the Republic of Korea.

References

- [1] A. Rubin et al., "OECD/NRC benchmark based on NUPEC PWR subchannel and bundle tests (PSBT) volume I: experimental database and final problem specifications," NEA/NSC/DOC (2010)1, 2010.
- [2] Y. J. Yoo, D. H. Hwang, and D. S. Sohn, "Development of a subchannel analysis code MATRA applicable to PWRs and ALWRs," *Nuclear Engineering & Technology*, vol. 31, no. 3, pp. 314–327, 1999.
- [3] D. H. Hwang, Y. J. Yoo, W. K. In, and S. Q. Zee, "Assessment of the interchannel mixing model with a subchannel analysis code for BWR and PWR conditions," *Nuclear Engineering & Design*, vol. 199, no. 3, pp. 257–272, 2000.
- [4] Westinghouse, *AP1000 Design Control Document*, Chapter 4.4, 2004.
- [5] R. E. Walpole and R. H. Myers, *Probability and Statistics for Engineers and Scientists*, Macmillan, New York, NY, USA, 1978.
- [6] J. T. Rogers and R. G. Rosehart, "Mixing by turbulent interchange in fuel bundles: correlations and inferences," ASME, 72-HT-53, 1972.

- [7] D. G. Reddy and C. F. Fighetti, "Parametric study of CHF sata volume 2. A generalized subchannel CHF correlation for PWR and BWR fuel assemblies," EPRI-NP-2609, 1983.
- [8] D. C. Groeneveld, L. K. H. Leunga, P. L. Kirillov et al., "The 1995 look-up table for critical heat flux in tubes," *Nuclear Engineering & Design*, vol. 163, no. 1-2, pp. 1-23, 1996.
- [9] D. H. Hwang et al., "A comprehensive assessment of round tube CHF prediction models for square-latticed rod bundles," in *Proceedings of the 12th International Heat Transfer*, vol. 4, p. 309, Grenoble, France, 2002.
- [10] W. S. Lin, C. H. Lee, and B. S. Pei, "Improved theoretical critical heat flux model for low-quality flow," *Nuclear Technology*, vol. 88, no. 3, pp. 294-306, 1989.
- [11] R. Bowering and P. Moreno, "COBRA IIIC/MIT computer code manual," MIT, Department of Nuclear Engineering, 1976.
- [12] J. Weisman and S. H. Ying, "A theoretically based critical heat flux prediction for rod bundles at PWR conditions," *Nuclear Engineering & Design*, vol. 85, no. 2, pp. 239-250, 1985.
- [13] C. L. Wheeler et al., "COBRA-IV-I: an interim version of COBRA for thermal-hydraulic analysis of rod bundle nuclear fuel elements and core," BNWL- 1962, Battelle Northwest Lab, 1976.
- [14] F. Inasaka and H. Nariai, "Evaluation of subcooled critical heat flux correlations for tubes with and without internal twisted tapes," *Nuclear Engineering & Design*, vol. 163, no. 1-2, pp. 225-239, 1996.

Research Article

Benchmark of Subchannel Code VIPRE-W with PSBT Void and Temperature Test Data

Y. Sung,¹ R. L. Oelrich Jr.,¹ C. C. Lee,¹ N. Ruiz-Esquide,² M. Gambetta,² and C. M. Mazufri²

¹ Westinghouse Nuclear Fuel Business Unit, 1000 Westinghouse Drive, Suite 452, Cranberry Township, PA 16066, USA

² INVAP Nuclear Engineering Department, Avenida Comandante Luis Piedrabuena 4950 San Carlos de Bariloche, R8403CPV Rio Negro, Argentina

Correspondence should be addressed to Y. Sung, sungy@westinghouse.com

Received 23 March 2012; Accepted 1 July 2012

Academic Editor: Maria Avramova

Copyright © 2012 Y. Sung et al. This is an open access article distributed under the Creative Commons Attribution License, which permits unrestricted use, distribution, and reproduction in any medium, provided the original work is properly cited.

This paper summarizes comparisons of VIPRE-W thermal-hydraulic subchannel code predictions with measurements of fluid temperature and void from pressurized water reactor subchannel and bundle tests. Using an existing turbulent mixing model, the empirical coefficient derived from code predictions in comparison to the fluid temperature measurement is similar to those from previous mixing tests of similar bundle configurations. The predicted steady-state axial void distributions and time-dependent void profiles based on the Lellouche and Zolotar model generally agree well with the test data. The void model tends to predict lower void at the upper elevation under bulk boiling. The void predictions are in closer agreement with the measurements from the power increase, temperature increase, and flow reduction transients than the depressurization transient. Additional model sensitivity studies showed no significant improvement in the code predictions as compared to the published test data.

1. Introduction

VIPRE-W (VIPREW or VIPRE) is Westinghouse version of the VIPRE-01 (VIPRE-01 is owned by the Electric Power Research Institute, Palo Alto, CA, USA) thermal-hydraulic subchannel code developed for light water reactor core design applications. The Penn State University (PSU), in cooperation with the Japan Nuclear Energy Safety Organization (JNES), under the sponsorship of the Organization for Economic Co-Operation and Development (OECD) and the United States Nuclear Regulatory Commission (USNRC), has developed benchmark exercises based on the Nuclear Power Engineering Corporation (NUPEC) pressurized water reactor (PWR) subchannel and bundle tests (PSBTs) [1]. The benchmark exercises include Phase I/Exercise 2 for the steady-state void distributions, Phase I/Exercise 3 for the transient void distributions, and Phase II/Exercise 1 for the steady-state fluid temperature distributions in the 5×5 rod bundles under PWR design conditions. This paper summarizes comparisons of VIPRE-W code predictions with the PSBT fluid temperature and void data, as well as sensitivity studies on the VIPRE-W modeling options.

2. Test Description

The PSBT problem specifications [1] provide a description of the NUPEC test facility and rod bundle designs. The test bundles were in 5×5 configurations for the void and exit temperature measurements, simulating a PWR 17×17 fuel assembly design with a fuel rod outside diameter (OD) of 9.5 mm containing simple support and mixing vane (MV) grid spacers. The test section for the rod bundle void distribution measurement and an axial diagram indicating locations of grid spacers and pressure taps are shown in Figure 1. The effective heated length is 3658 mm. Similar to rod bundle tests performed at the former Heat Transfer Research Facility (HTRF) in New York [2]; the test rods were heated electrically using different wall thicknesses in order to create uniform or cosine axial power profiles. For example, the heater rods for the uniform axial power profile were made of Inconel 600 tubes with a wall thickness of 0.65 mm. The tube inside was fit with an insulator tube made of alumina having an OD of 8.2 mm and an inside diameter (ID) of 5.8 mm. Table 1 describes different test bundles used for the void and exit temperature measurements. For the void

TABLE 1: Description of PSBT void and mixing tests.

Parameter	B5	B6	B7	A1
Number of heated rods	25	25	24	25
Heated rod (OD) (mm)	9.50	9.50	9.50	9.50
Thimble rod OD (mm)	—	—	12.24	—
Rod-to-rod pitch (mm)	12.60	12.60	12.60	12.60
Test section inner width (mm)	64.9	64.9	64.9	64.9
Axial power profile	Uniform	Cosine	Cosine	Uniform
Hot/cold rod power ratio	1.00/0.85	1.00/0.85	1.00/0.85	1.00/0.25
Grid spacers and axial elevations (mm)		7 mixing vane grid spacers: 471, 925, 1378, 1832, 2285, 2739, 3247 2 nonmixing vane grid spacers: 2.5, 3755 8 simple support grid spacers: 237, 698, 1151, 1605, 2059, 2512, 2993, 3501		
Test description	Steady-state and transient void	Steady-state and transient void	Steady-state and transient void	Steady-state mixing

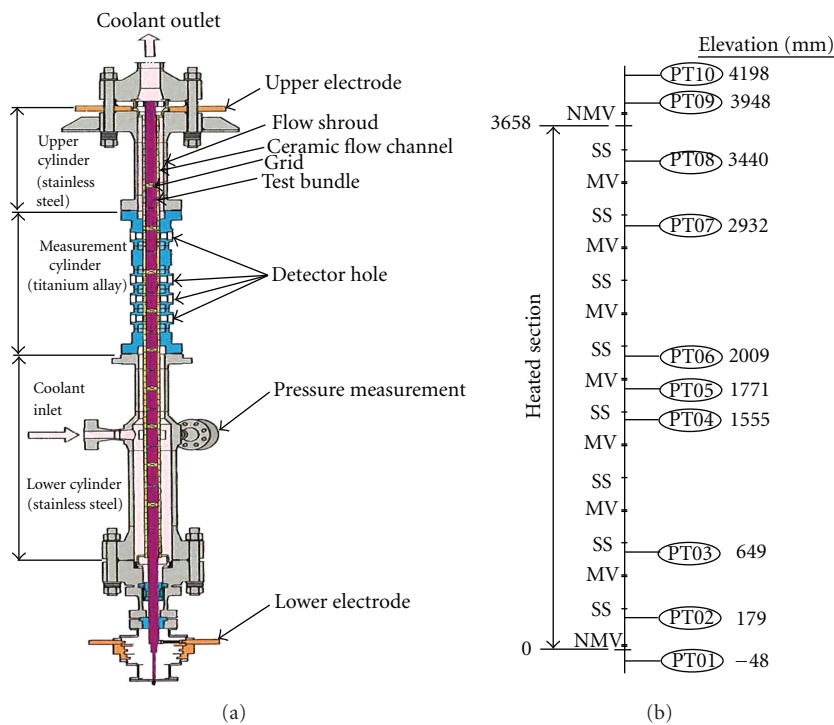


FIGURE 1: PSBT test section and axial diagram of test bundles [1].

tests, the inner rods of a test bundle with the higher power were designated as “hot” rods, while the peripheral rods at lower power were “cold” rods. For the mixing test, the cold and hot rods were arranged in two columns on each side of the 5×5 test bundle, with three cold rods and two hot rods arranged alternatively in the central column. The test data were provided as part of the USNRC/OECD benchmark specifications [1].

2.1. *Mixing Test.* A fluid temperature test is often referred to as a mixing test, since it was designed to measure turbulent mixing effect in the bundle with a relatively large power gradient between hot and cold rods. In the PSBT mixing test (A1), thirty-six thermocouples were placed at the exit of each subchannel of the 5×5 test bundle for measuring fluid temperature. A total of 59 experimental data was taken from the test in the range shown in Table 2.

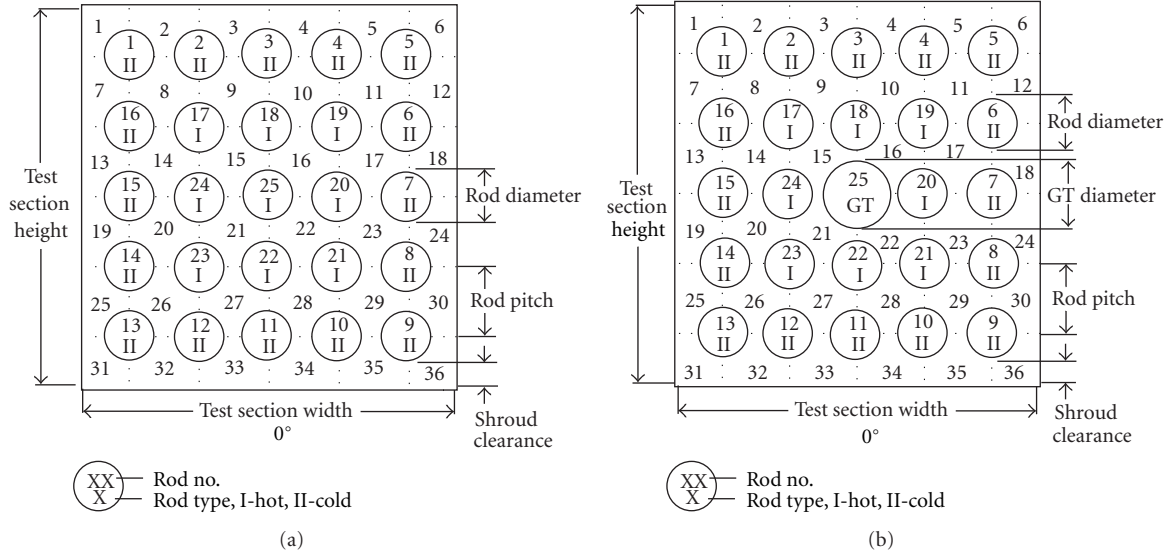


FIGURE 2: VIPRE-W modeling of PSBT rod bundles.

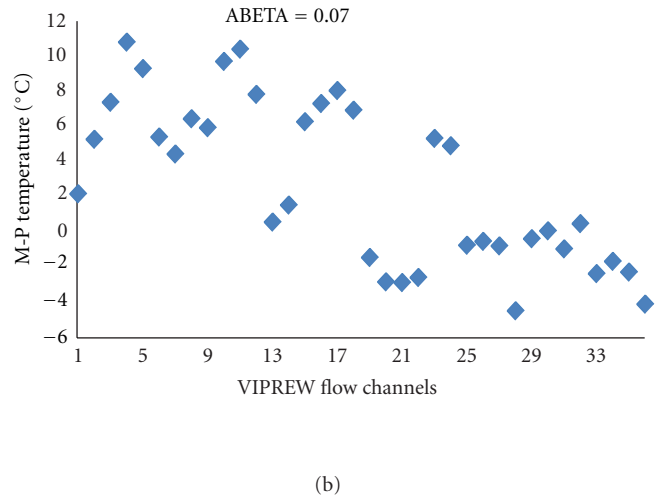
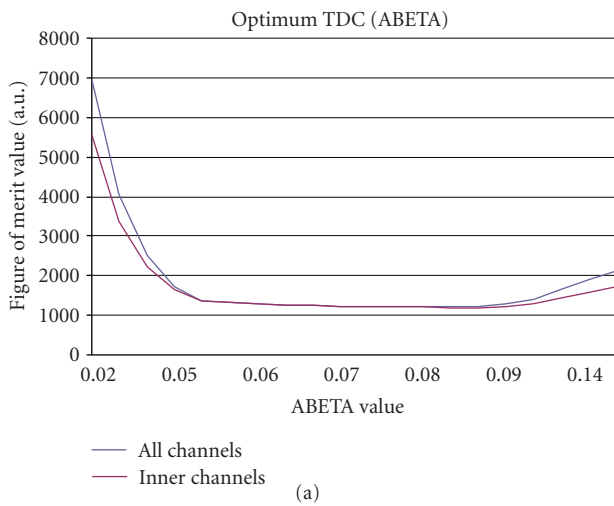


FIGURE 3: (a) ABETA sensitivity study. (b) Temperature difference versus channels.

TABLE 2: Data range of PSBT mixing test.

Parameters of mixing test	Range
Pressure (bar)	49–166
Mass flux (10^6 kg/m ² h)	0.44–17.08
Inlet temperature (°C)	84.5–289.2
Bundle power (MW)	0.11–3.44

TABLE 3: Data range of PSBT void tests.

Parameters of void tests	Range
Pressure (bar)	48.0–166
Mass flux (10^6 kg/m ² h)	2.0–15.0
Inlet temperature (°C)	143–322
Bundle power (MW)	0.97–4.0
Void fraction	0.0–0.80

The mixing test was conducted mainly under the single-phase flow conditions.

2.2. *Steady-State Void Tests.* The steady-state void tests were performed with three different bundles, B5, B6, and B7, as described in Table 1. Seventy-four void distribution

measurements were collected from each bundle in the range shown in Table 3.

A gamma-ray transmission method was used for measuring density of the flow, which was then converted to the void fraction of the vapor-liquid two-phase flow [1]. The measurements were taken at three elevations, 2216 mm (lower), 2669 mm (middle), and 3658 mm (upper). The measured

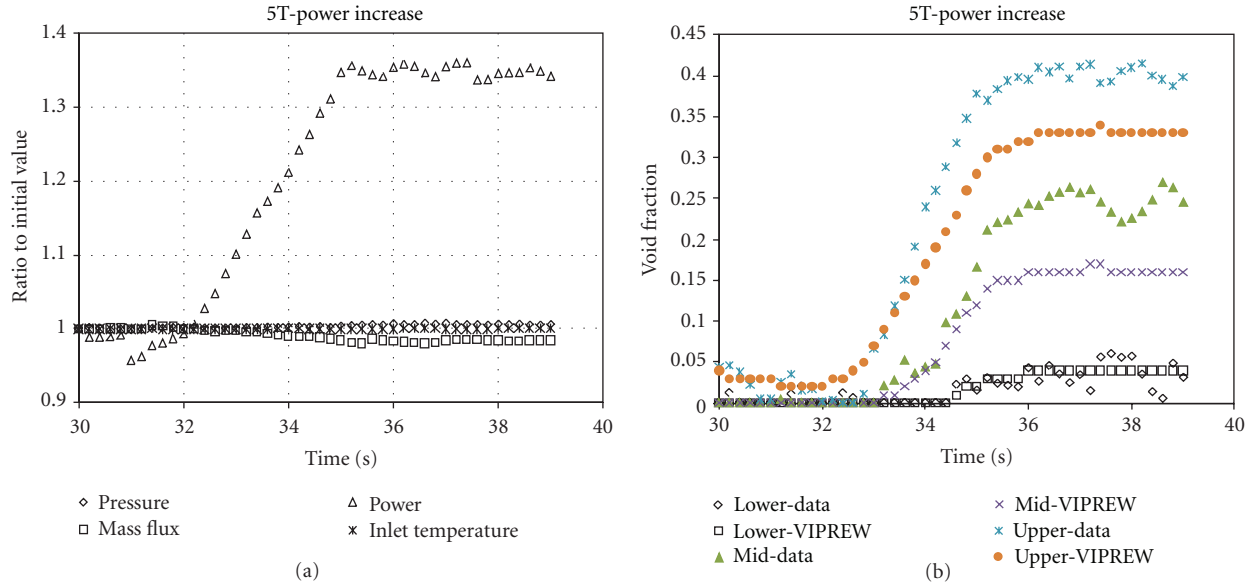


FIGURE 4: (a) B5T power increase (PI) transient. (b) B5T PI void comparison.

TABLE 4: Average differences between matched data pairs.

Parameter ($N = 31$)	Measured data			Testing conditions			
	Δ Void (lower)	Δ Void (middle)	Δ Void (upper)	Δ Pressure (bar)	Δ Flow (10^6 kg/m ² h)	Δ Temperature ($^{\circ}$ C)	Δ Power (MW)
Mean	0.011	0.062	0.022	0.516	0.035	-0.528	0.007
Standard deviation	0.030	0.049	0.026	0.629	0.071	0.367	0.014

data were averaged over the four central subchannels of the 5×5 test bundles.

A repeatability test was performed with another bundle, B8, similar to B5, with the uniform axial power profile and heated rods only (no guide thimble tube). A total of 31 matched pairs having similar test conditions of pressure, flow, inlet temperature and power were identified. The average differences (B8 – B5) in the test conditions and void measurements are given in Table 4. The matched pairs can be used for evaluating repeatability of the PSBT void test results. There appeared to be larger variations in the void measurements at the middle elevation of the rod bundle than data obtained from either the lower or the upper elevations.

2.3. Transient Void Tests. Transient void tests were performed also with the three bundles, B5, B6, and B7, for four scenarios: power increase, flow reduction, depressurization, and inlet temperature increase. The initial conditions of the transient tests were set to be representative of PWR design conditions shown in Table 5. The void measurement technique was the same as that used for the steady-state tests. Again, measurements were taken at three elevations, 2216 mm (lower), 2669 mm (middle), and 3658 mm (upper). The measured data were averaged over the four central subchannels of the 5×5 test bundles.

3. VIPRE-W Code and Modeling

VIPRE-W is an enhanced version of the VIPRE-01 sub-channel code. VIPRE-01 was developed based on several versions of the COBRA code by the Battelle Pacific Northwest Laboratories for the Electric Power Research Institute (EPRI). It solves the finite difference equations for mass, energy, axial, and lateral momentum conservation for an interconnected array of channels, assuming incompressible and thermally expandable homogeneous flow. Although the formulation is homogeneous, empirical models are incorporated into the code to account for subcooled boiling and vapor/liquid slip in two-phase flow. Additional features of the VIPRE-W code include models for post-CHF fuel temperature calculations and fuel boiling duty evaluation at highly subcooled boiling conditions [3] and linkage to software libraries containing proprietary correlations and models. The new features enhance the code capability for PWR core design and licensing applications, but they do not alter the fundamental solution scheme of the VIPRE-01 code.

The VIPRE-W modeling of the test bundles is consistent with the benchmark specifications [1]. The radial geometric models are shown in Figure 2. The axial nodal length was set to be about 45.4 mm (1.8 inch). The two-phase flow model for comparison with the void data consisted of a profile fit

TABLE 5: Initial condition of transient void tests.

Test bundle	Initial conditions				Transients
	Pressure (bar)	Mass flux (10^6 kg/m ² h)	Power (kW)	Inlet temperature ($^{\circ}$ C)	
B5	151.2	11.95	2282	300.4	Power
	150.8	11.93	2244	301.2	Flow
	150.0	11.92	2236	300.4	Pressure
	149.6	11.94	2230	301.7	Temperature
B6	155.1	11.55	2621	288.1	Power
	155.3	12.03	2574	288.8	Flow
	151.6	12.02	2556	288.2	Pressure
	154.2	11.92	2603	288.8	Temperature
B7	155.1	12.02	2500	291.9	Power
	155.0	12.04	2405	292.0	Flow
	152.0	11.99	2577	291.8	Pressure
	155.7	11.99	2496	290.2	Temperature

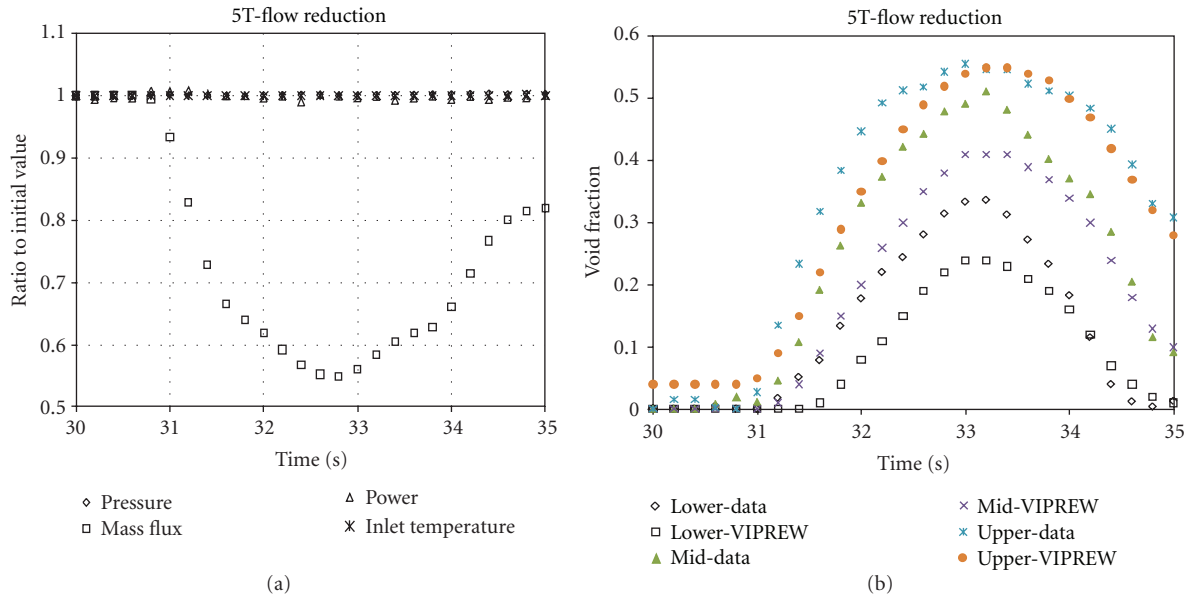


FIGURE 5: (a) B5T flow reduction (FR) transient. (b) B5T FR void comparison.

subcooled and bulk boiling model developed by Lellouche and Zolotar [4] and the associated friction multiplier also referred to as the EPRI void model [5]. It predicts the point of bubble departure from the heated surface under subcooled boiling and accounts for phase drift under bulk boiling. The EPRI void model was first selected for comparison with the PSBT data. Model sensitivity studies indicated that void predictions from other two-phase flow models in VIPRE-W were in better agreement with the test data.

The turbulent mixing in subchannels was modeled using the following empirical correlation:

$$\Delta Q = -w' \times \Delta h \times \Delta X, \quad (1)$$

where ΔQ = energy exchange due turbulent mixing (W or Btu/hr), w' = lateral turbulent flow per unit length (kg/s/m or lbm/hr-ft), Δh = enthalpy difference between two

subchannels (J/kg or Btu/lbm), ΔX = axial nodal length (m or ft)

$$w' = ABETA \times G_{AVG} \times S, \quad (2)$$

where ABETA = empirical coefficient, G_{AVG} = average axial mass flow in the connected channels (kg/s/m² or lbm/s/ft²), S = rod-to-rod gap width (m or ft).

ABETA is also referred to as thermal diffusion coefficient (TDC) derived from mixing test data. Previous rod-bundle mixing tests similar to the PSBT test indicated that turbulent mixing is sensitive to spacing between two MV grids [6], while effect of simple support grids could be neglected. Since turbulent mixing increases with reduced grid spacing, in the VIPRE-W model ABETA was varied axially to account for the nonuniform MV grid spacings of the rod bundle. The axially varied ABETA values were input through multipliers to a reference ABETA value as a function of the grid spacing.

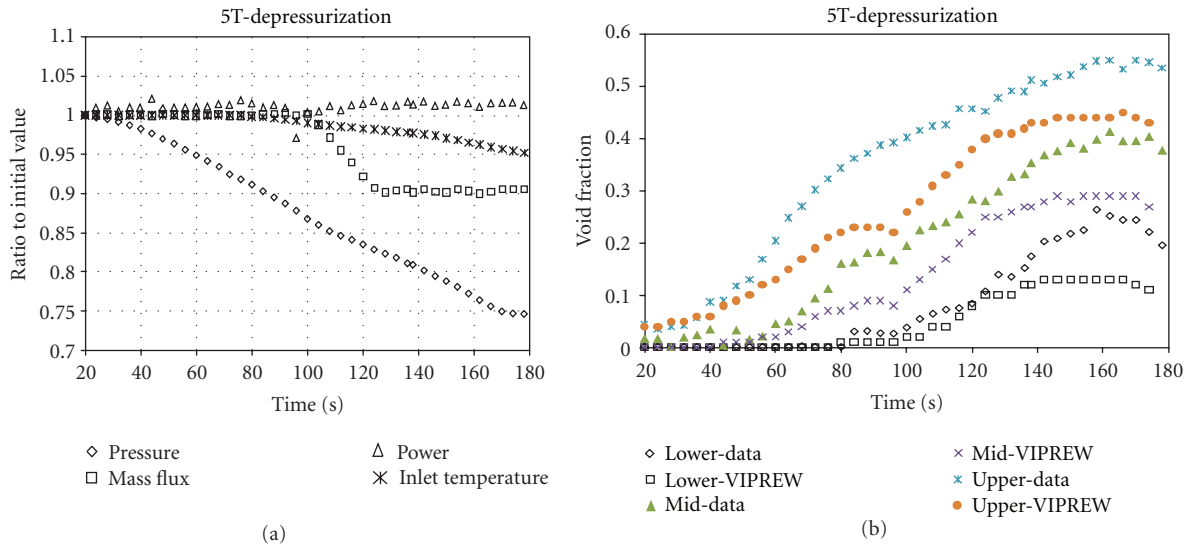


FIGURE 6: (a) B5T depressurization (DP) transient. (b) B5T DP void comparison.

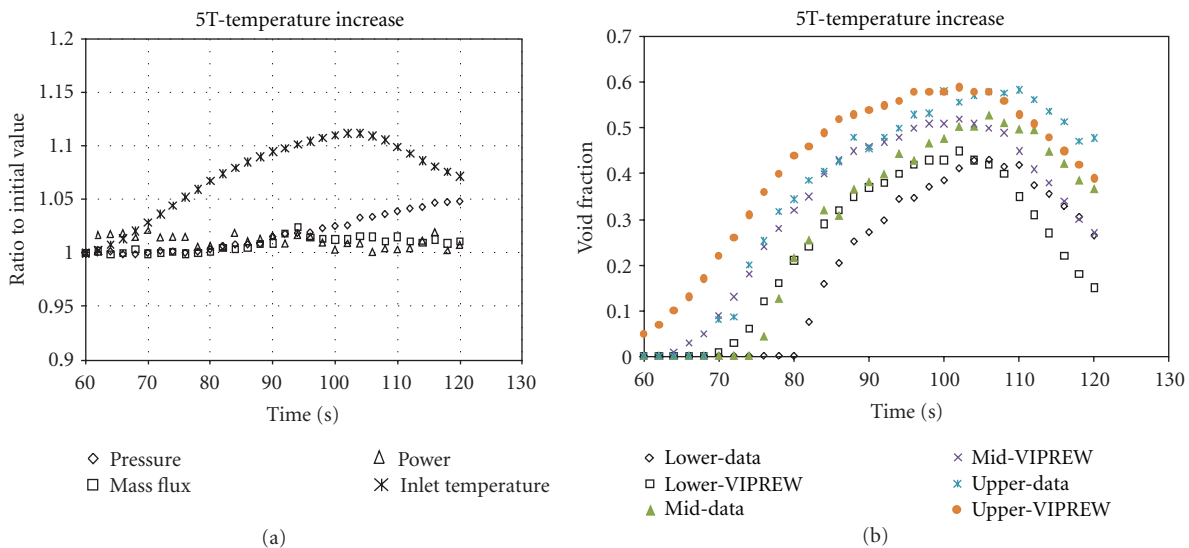


FIGURE 7: (a) B5T temperature increase (TI). (b) B5T TI void comparison.

4. Exit Temperature Comparison

Each datum of the mixing test (A1) contains fluid temperature measurements at the top of the heated length or the channel exit. A VIPRE-W sensitivity study was performed with different values of ABETA in (2). For each ABETA value, all test conditions are simulated yielding a set of subchannel exit temperature predictions. The predicted channel exit temperatures were then compared with the experimental data, in order to determine the best estimate reference ABETA value that yielded the smallest temperature differences. The multipliers to the reference ABETA value that varied ABETA axially as a function of the grid spacing remained unchanged during the study. A figure of merit is defined to obtain the ABETA value which gives the best

overall predictions: the squared difference between measured and predicted temperature in each subchannel is averaged for each test and for each ABETA value selected in the study. The smaller the value, the better the agreement between simulation and test data. Figure 3(a) shows that the temperature differences were relatively insensitive to ABETA varied in the range from 0.055 to 0.09. The best estimate reference ABETA value was found to be about 0.07, corresponding to a grid spacing of 453 mm (17.8 inches), based on the test data from the heated rod and the grid spacer arrangements in the test bundle. As shown in Figure 3(a), the estimated ABETA values remain unchanged if only the exit temperatures of the interior channels of the test bundle were taken into consideration, excluding the peripheral channels.

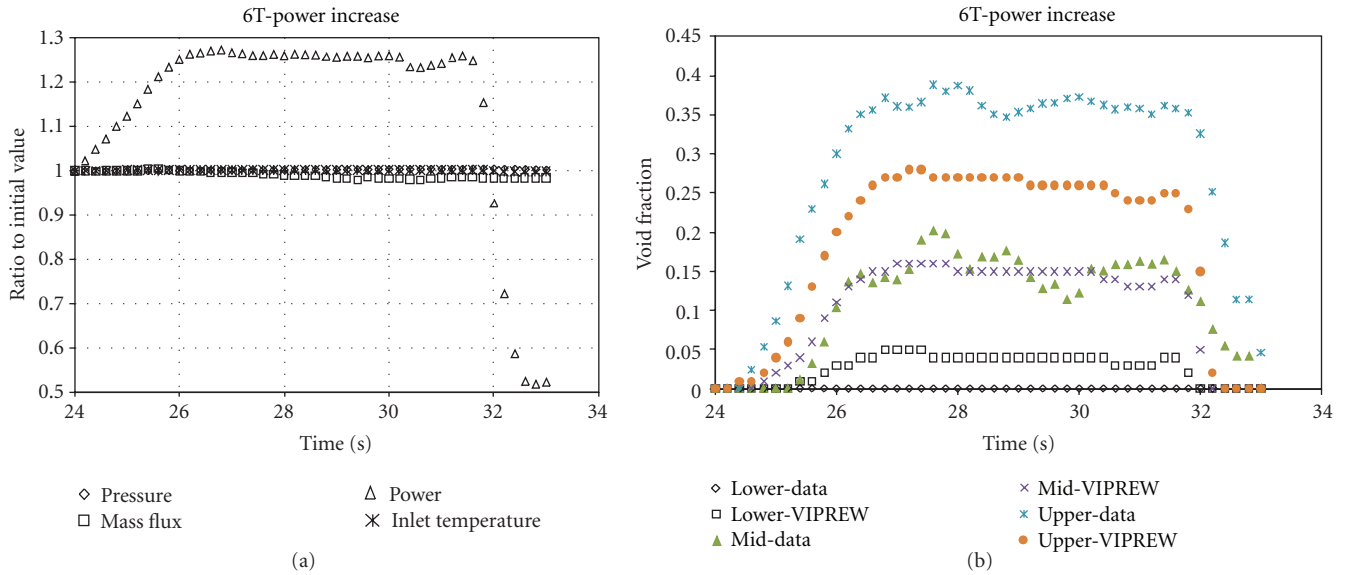


FIGURE 8: (a) B6T power increase (PI) transient. (b) B6T PI void comparison.

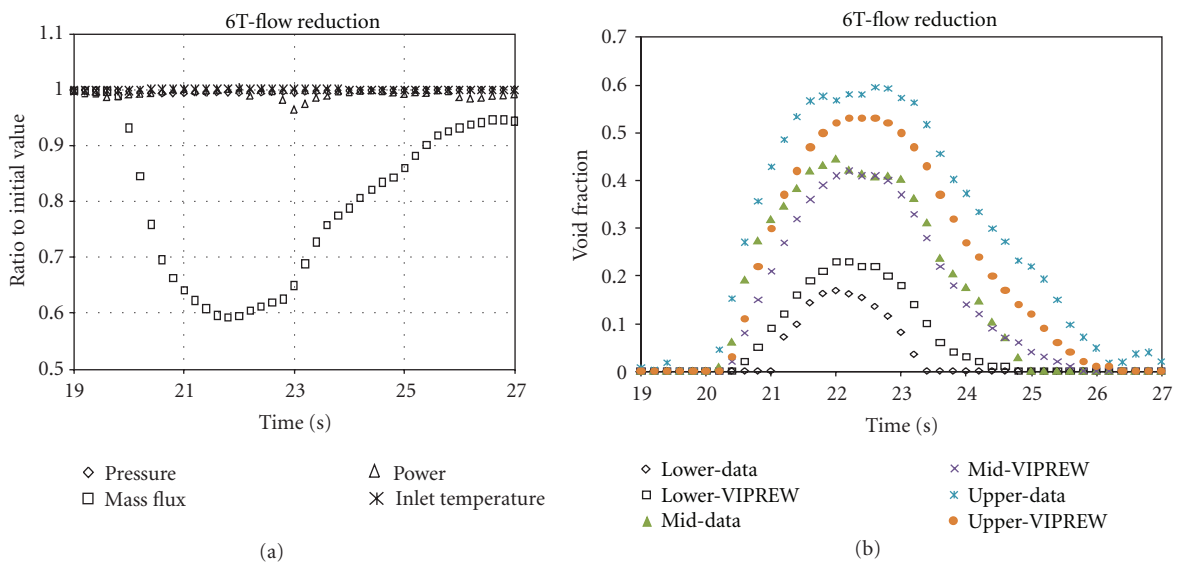


FIGURE 9: (a) B6T flow reduction (FR) transient. (b) B6T FR void comparison.

Figure 3(b) shows the average temperature differences in each channel. The temperature differences in the rod bundle appeared to be unevenly distributed. The hot rods of the mixing test were Rod no. 1, 2, 12–18, and 22–24 in Figure 2. The measured-to-predicted temperature differences were larger in the top half of the bundle (Channels 1 through 18 in Figure 2). Despite the uncertainty in the temperature differences, the reference thermal mixing coefficient (ABETA) of 0.07 from the PSBT mixing test is consistent with those values obtained from previous mixing tests of similar configurations [6]. The ABETA values in the VIPRE-W model varied with axial spacings between two MV grids in the test bundle based on the predetermined function of ABETA multiplier versus grid spacing.

5. Steady-State Void Comparison

The predicted void fractions from the central channels of the VIPRE-W model (Channels 15, 16, 21, and 22) in Figure 2 at the three elevations, 2216 mm (Lower), 2669 mm (Middle), and 3658 mm (Upper), were compared with the void measurements from the three tests, B5, B6, and B7. The comparisons based on the EPRI void model are summarized in Table 6.

There is no significant trend in the void differences with respect to the test conditions. However, the EPRI-void model tends to underpredict the void under bulk boiling at the upper elevation in comparison to the measurements. The EPRI model was modified by combining the Lellouche and

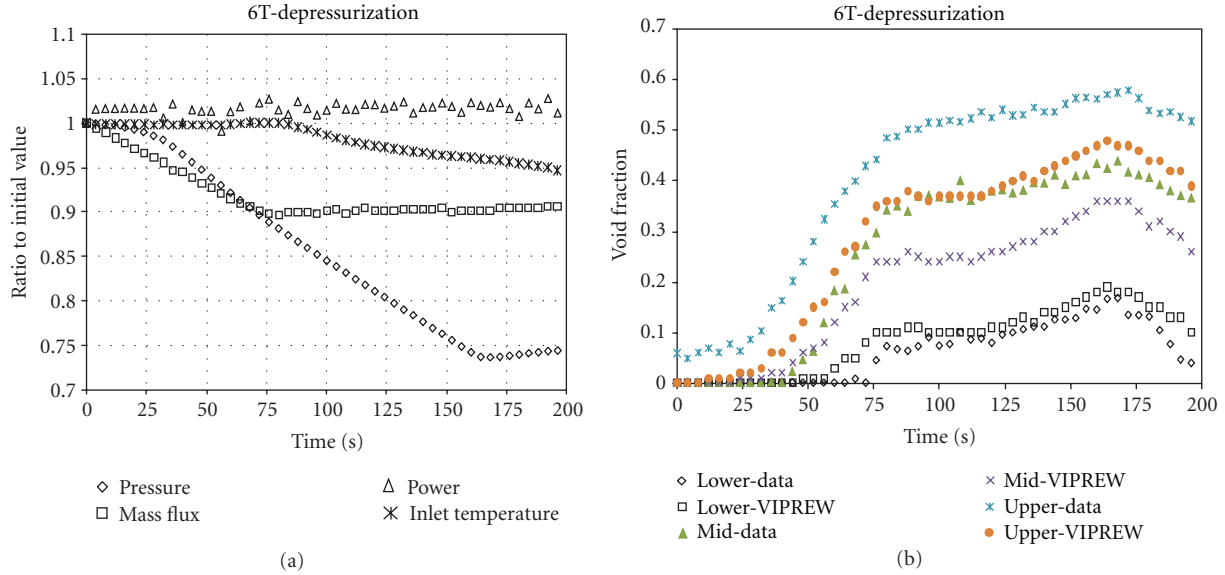


FIGURE 10: (a) B6T depressurization (DP) transient. (b) B6T DP void comparison.

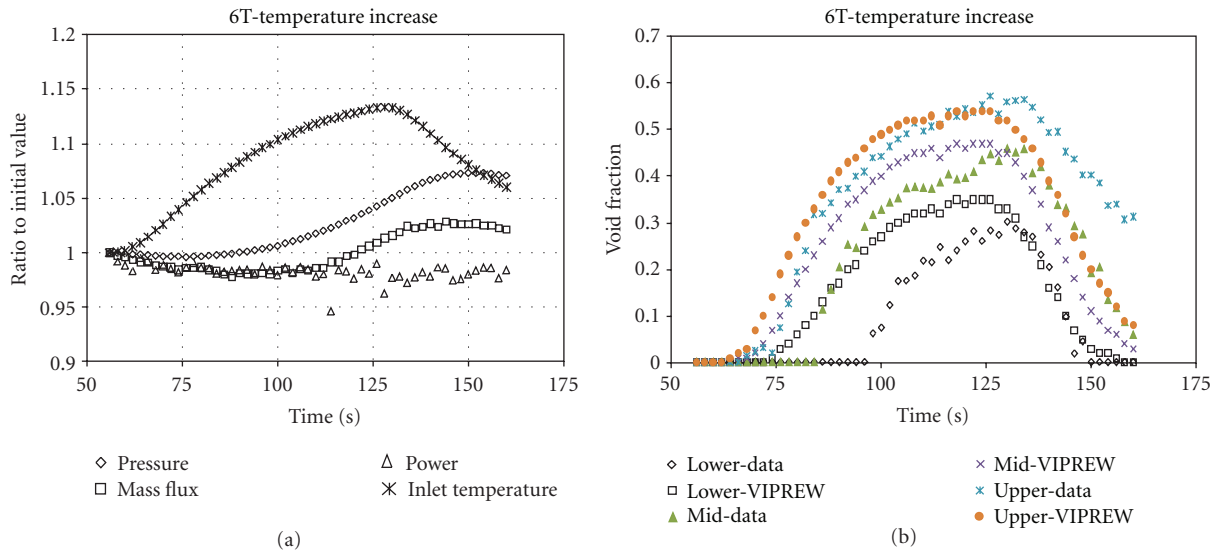


FIGURE 11: (a) B6T temperature increase (TI). (b) B6T TI void comparison.

Zolotar subcooled void correlation with the homogeneous bulk boiling and two-phase flow friction multiplier. Table 7 indicates that the void predictions from the modified EPRI model are in better agreement with the data at the upper elevation.

6. Transient Void Comparison

The VIPRE-W time-dependent calculations were performed using the modified EPRI void model (the Lellouche and Zolotar subcooled correlation combined with the homogeneous bulk boiling and two-phase flow friction multiplier) for the power increase, flow reduction, depressurization, and temperature increase transients of the three test bundles.

The predicted void fractions from the central channels of the VIPRE-W model at the three elevations were compared with the void measurements. The comparisons are shown in Figures 4, 5, 6, 7, 8, 9, 10, 11, 12, 13, 14, and 15 for the four transients of the three test bundles, B5T, B6T, and B7T. The initial condition of each transient is listed in Table 5.

The predicted time-dependent void profiles are similar to the measured values. The predicted void values are in closer agreement with the measured values from the power increase, temperature increase, and flow reduction transients than the depressurization transient. For the depressurization increase transients, the predicted values were generally lower at the upper elevation, although the magnitudes of the differences vary with the test bundles.

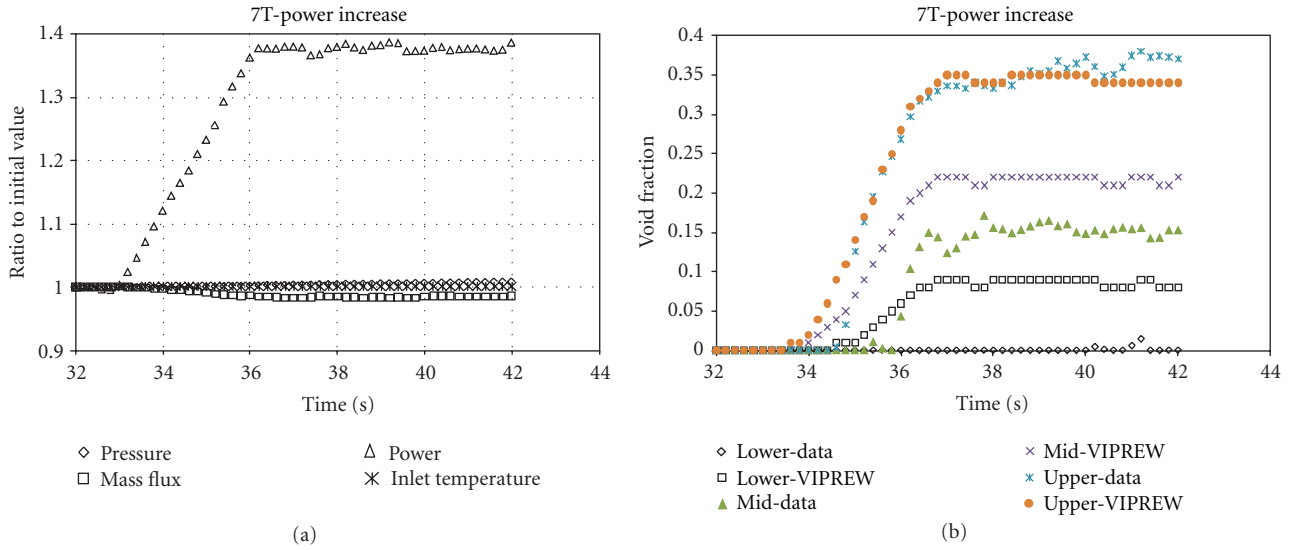


FIGURE 12: (a) B7T power increase (PI) transient. (b) B7T PI void comparison.

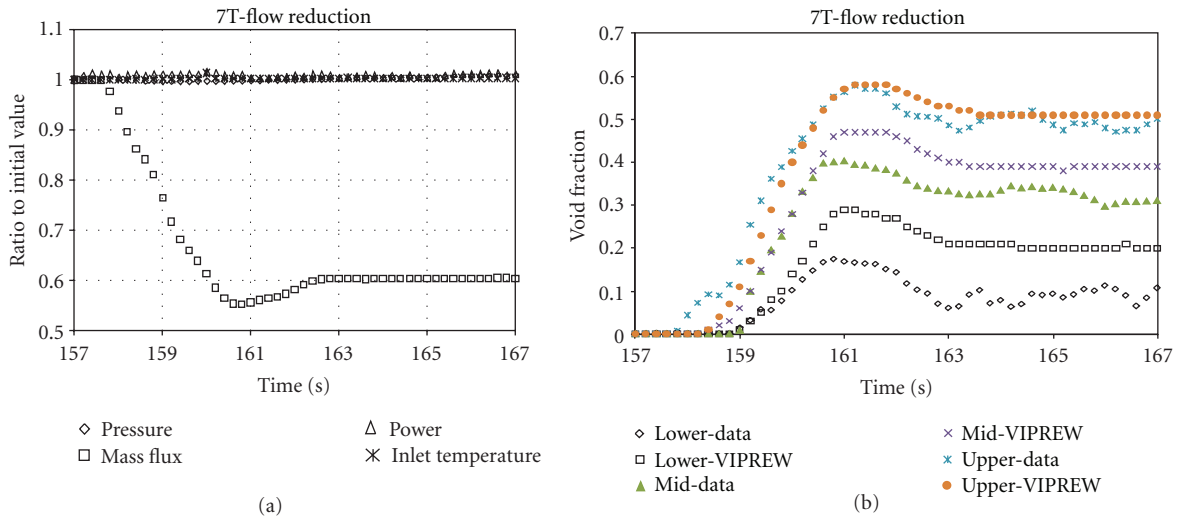


FIGURE 13: (a) B7T flow reduction (FR) transient. (b) B7T FR void comparison.

TABLE 6: Summary of steady-state void comparison based on EPRI void model.

Bundle test	Number of points	Measured-predicted void fraction					
		Lower	Mean Middle	Upper	Lower	Middle	Upper
B5	74	-0.023	-0.022	0.031	0.029	0.046	0.039
B6	74	0.026	0.051	0.072	0.049	0.038	0.044
B7	74	-0.074	-0.043	0.019	0.035	0.044	0.028

TABLE 7: Summary of steady-state void comparison based on modified EPRI void model.

Bundle test	Number of points	Measured-predicted void fraction					
		Lower	Mean Middle	Upper	Lower	Middle	Upper
B5	74	-0.025	-0.051	-0.018	0.032	0.058	0.054
B6	74	-0.029	-0.011	0.021	0.030	0.038	0.063
B7	74	-0.081	-0.080	-0.032	0.051	0.040	0.033

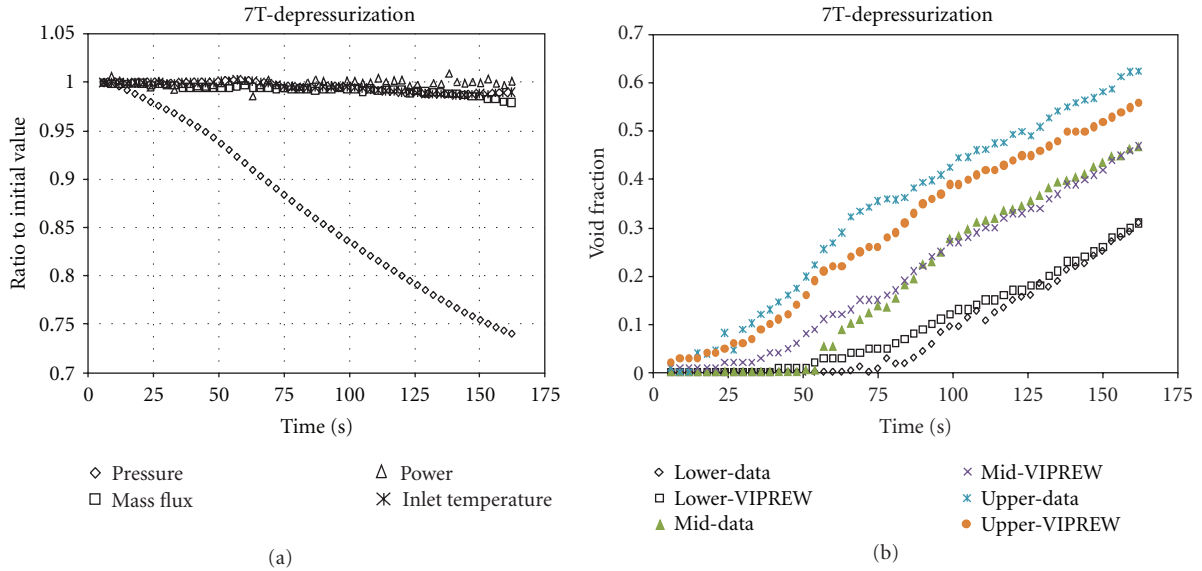


FIGURE 14: (a) B7T depressurization (DP) transient. (b) B7T DP void comparison.

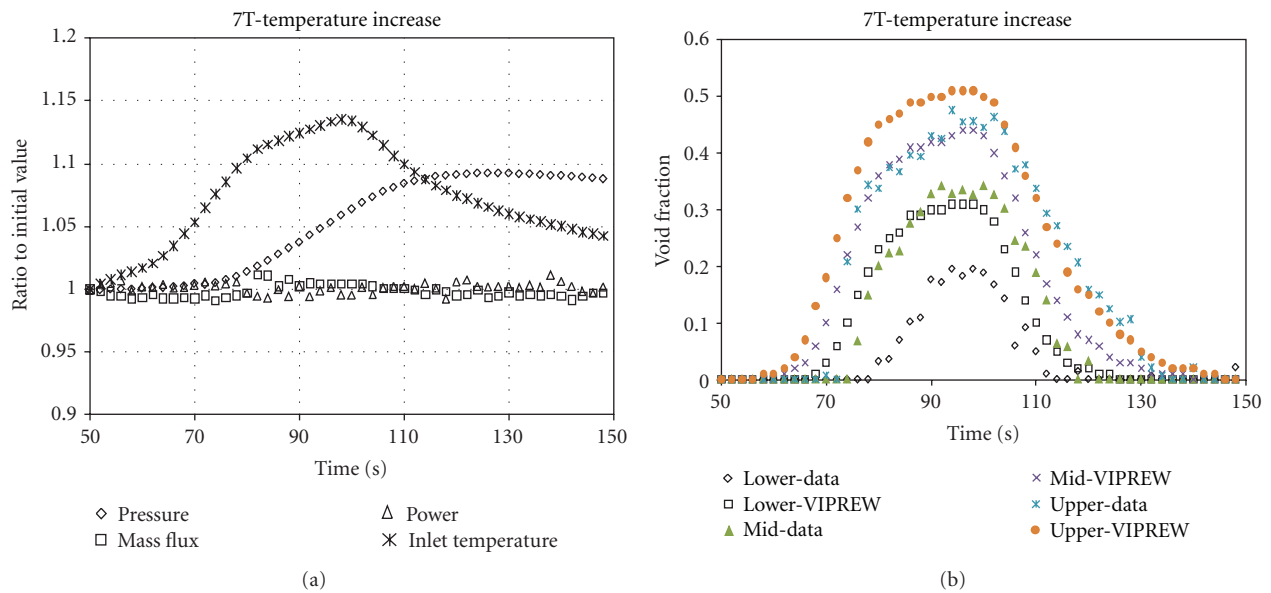


FIGURE 15: (a) B7T temperature increase (TI). (b) B7T TI void comparison.

7. Model Sensitivity Studies

In order to better understand the test data and to explore any improvement on code predictions, additional VIPRE-W model sensitivity studies were performed on the mixing test and the steady-state void and the transient void bundle tests.

7.1. Sensitivity Study on Mixing Test. Figure 3(b) showed that the measured-to-predicted temperature differences were larger in the top half of the rod bundle. Based on the input of the symmetric radial power distribution, VIPRE-W predicted channel exit temperatures were also symmetric with respect to each quarter of the test bundle.

In order to understand the differences in the measured channel exit temperatures, VIPRE-W calculations were performed by varying the rod-to-wall widths up to 50%, simulating a postulated symmetric loading of the test bundle in the housing. Although the changes in the bundle configuration affected the temperature distributions, there was no improvement on the comparisons between the predicted and measured temperatures at the bundle exit.

7.2. Sensitivity Studies on Void Tests. Tables 6 and 7 showed effect of different modeling options on the code predictions and the comparisons between the measured and predicted

void fractions. Additional VIPRE-W calculations were performed by varying the turbulent momentum factor that affected momentum mixing, thermal mixing coefficient, single-phase heat transfer coefficient, local hydraulic loss coefficients, and two-phase flow models. The results of the sensitivity studies showed no significant improvement over the steady-state results in Table 7 and the transient results in Figures 4 through 15.

8. Conclusion

The mixing and void data from the PSBT benchmark exercises were evaluated using the VIPRE-W code. The turbulent mixing coefficient derived from code predictions in comparison to the mixing data is similar to those from previous mixing tests of similar bundle configurations. The predicted void fractions using the modified EPRI void model generally agree well with the steady-state and transient void measurements, considering uncertainties in measurements and test repeatability. The results of the sensitivity studies of different modeling options in the VIPRE-W code showed no significant improvements in the code predictions as compared to the bundle mixing and void test data.

References

- [1] A. Rubin, M. Avramova, and H. Utsuno, "OECD/NRC benchmark based on NUPEC PWR subchannel and bundle tests (PSBT) volume I: experimental database and final problem specifications," Tech. Rep. NEA/NSC/DOC(2010)1, US NRC/OECD Nuclear Energy Agency.
- [2] C. F. Fighetti and D. G. Reddy, "Parametric study of CHF data," Tech. Rep. NP-2609, Electric Power Research Institute, Palo Alto, Calif, USA, 1982.
- [3] Y. Sung et al., "Westinghouse VIPRE-01 applications for PWR core analyses," in *Proceedings of the 9th International Topical Meeting on Nuclear Reactor Thermal Hydraulics (NURETH-9)*, pp. 3–8, San Francisco, Calif, USA, October 1999.
- [4] G. S. Lellouche and B. A. Zolotar, "Mechanistic model for predicting two-phase void fraction for water in vertical tubes, channels and rod bundles," Tech. Rep. NP-2246-SR, Electric Power Research Institute, Palo Alto, Calif, USA, 1982.
- [5] C. W. Stewart et al., "VIPRE-01: a thermal-hydraulic code for reactor cores," vol. 1–3 (Revision 3, August 1989) and vol. 4 (April 1987), NP-2511-CCM-A, Electric Power Research Institute, Palo Alto, Calif, USA.
- [6] F. F. Cadek, F. F. Dominicis, and D. P. Motley, "Effect of axial spacing on interchannel thermal mixing with the R mixing vane grid," Tech. Rep. WCAP-7959-A, Westinghouse Electric, 1975.

Research Article

CFD Modeling of Boiling Flow in PSBT 5×5 Bundle

Simon Lo and Joseph Osman

CD-adapco, Trident House, Basil Hill Road, Didcot OX11 7HJ, UK

Correspondence should be addressed to Simon Lo, simon.lo@cd-adapco.com

Received 17 January 2012; Accepted 8 May 2012

Academic Editor: Annalisa Manera

Copyright © 2012 S. Lo and J. Osman. This is an open access article distributed under the Creative Commons Attribution License, which permits unrestricted use, distribution, and reproduction in any medium, provided the original work is properly cited.

Three-dimensional computational fluid dynamics (CFD) method was used to model the boiling two-phase flow in one of the PSBT 5-by-5 rod bundle tests. The rod bundle with all the spacers was modeled explicitly using unstructured computational grids. The six-equation, two-fluid model with the wall boiling model was used to model the boiling two-phase flows in the bundle. The computed void fractions compare well with the measured data at the measuring plane. In addition to the averaged void data, the CFD results give a very detailed picture of the flow and void distributions in the bundle and how they are affected by solid structures in the flow paths such as the spacer grids and mixing vanes.

1. Introduction

In the NUPEC PWR Subchannel and Bundle Test (PSBT) International Benchmark exercise [1], valuable measured data were made available to test and check the accuracy of numerical simulations of boiling two-phase flows in PWR subchannels and rod bundles. The measured data released by Japan Nuclear Energy Safety (JNES) organization [2] were obtained by the Nuclear Power Engineering Corporation (NUPEC) in Japan who in the period between 1987 and 1995 performed a series of void measurement tests using full-size mock-up tests for both BWRs and PWRs. The PWR tests were considered in PSBT. This paper describes the use of three-dimensional computational fluid dynamics (CFD) to model the boiling two-phase flows in one of the 5-by-5 rod bundle tests.

The commercial CFD software STAR-CCM+ v6.06 [3] was used in this study. The rod bundle with all the spacers was modeled explicitly using unstructured computational grids. A brief description of the computational grid is given in Section 2 of the paper. The six-equation, two-fluid model with the wall boiling model was used to model the boiling two-phase flows in the bundle. Full details of the mathematical model are provided in Section 3. The steady-state bundle test B5 Run 5.1121 was analysed, and the results are presented in Section 4. The computed averaged void fraction compares well with the measured data at the upper

measuring plane. In addition to the averaged void data, the CFD results give a very detailed picture of the flow and void distributions in the bundle and how they are affected by solid structures in the flow paths such as the spacer grids and mixing vanes.

2. Computational Grid

The computational grid was generated by recreating the rod bundle and the spacers using the 3D CAD package in STAR-CCM+. The geometries of the rod bundle and the 3 different spacers were taken from the problem specification report by Rubin et al. [1]. CAD models of the 3 spacers were created separately using the CAD package Autodesk Inventor and imported into STAR-CCM+ via parasolid files. A short section of rods going through each spacer was added. An unstructured polyhedral computational grid was then created for each of the combined rod-spacer sections see Figures 1, 2, and 3. The thickness of the spacer grids is represented by 2 layers of computational grids. The springs and dimples in the spacers were included in the model. The contacts between the springs and dimples with the rods were modeled and shown in Figure 4.

The completed rod bundle assembly was created by connecting together the rod-spacer sections according to the specification given in [1]. The connections between

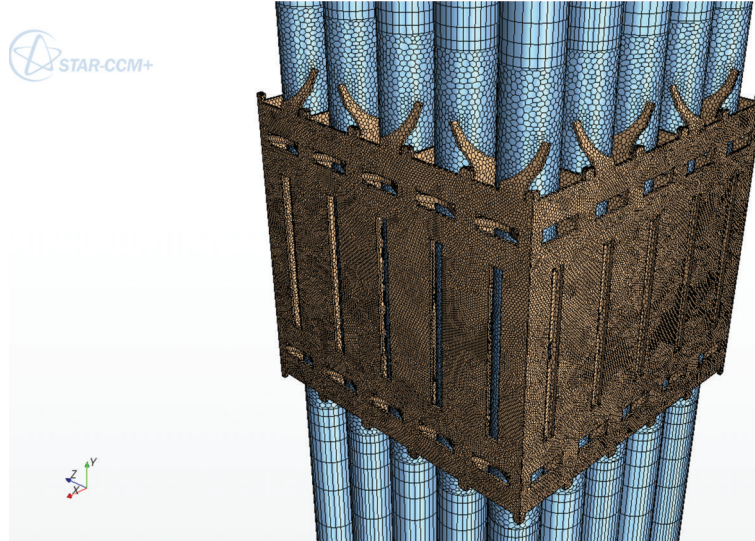


FIGURE 1: CFD grid of spacer with mixing vanes.

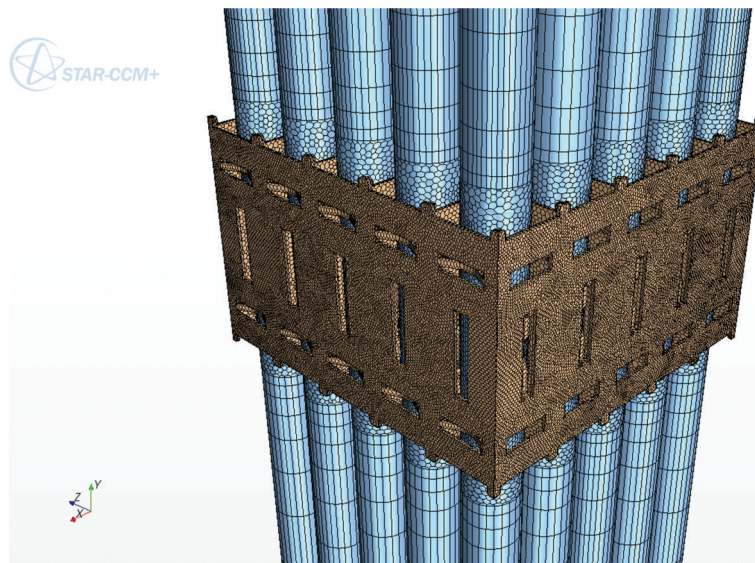


FIGURE 2: CFD grid of spacer without mixing vanes.

the sections were made by extruding the computational cells at the ends of the sections to create horizontal layers of polyhedral cells. These horizontal cell layers start with a smaller height and expand to larger height to economize on the number of computational cells used. The model includes 7 mixing vane spacers (MV), 2 nonmixing vane spacers (NMV), and 8 simple spacers (SS); see Figure 5. In total the CFD model contains 17,950,126 computational cells.

3. Mathematical Model

3.1. Two-Fluid Model. The standard six-equation, two-fluid model was used in modeling the boiling two-phase flows considered in this paper. In this model the conservation

equations for mass, momentum, and energy are solved for both phases.

The conservation of mass for phase k is

$$\frac{\partial}{\partial t} (\alpha_k \rho_k) + \nabla \cdot (\alpha_k \rho_k u_k) = \sum_{i=1}^N (\dot{m}_{ki} - \dot{m}_{ik}), \quad (1)$$

where α_k is volume fraction of phase k , ρ_k is phase density, u_k is phase velocity, \dot{m}_{ki} and \dot{m}_{ik} are mass transfer rates to and from the phase, and N is the total number of phases. The sum of the volume fractions is clearly equal to unity:

$$\sum_k \alpha_k = 1. \quad (2)$$

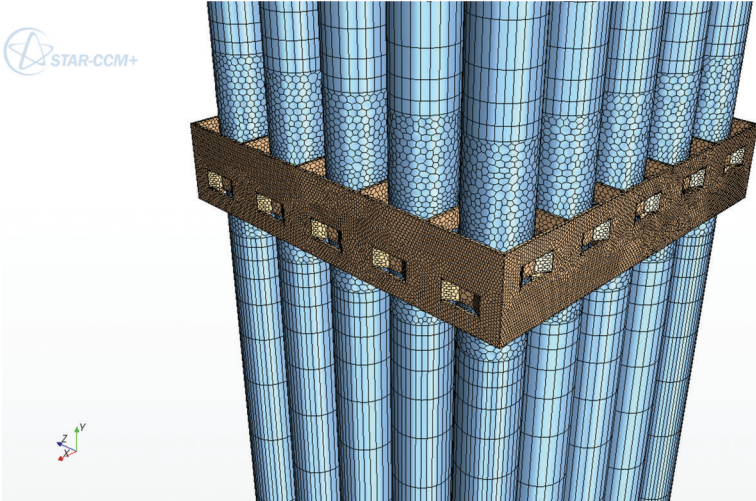


FIGURE 3: CFD grid of simple spacer.



FIGURE 4: Contacts between rods and spacers.

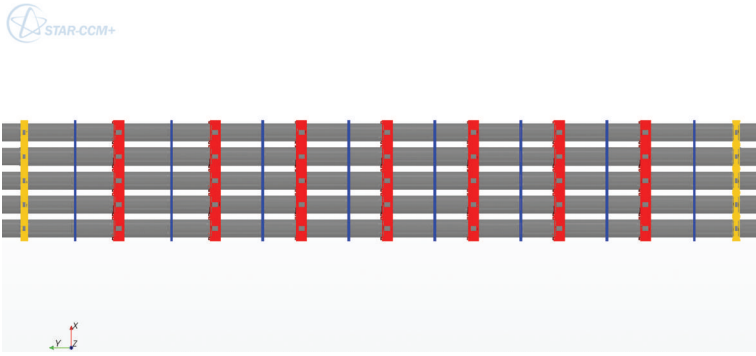


FIGURE 5: Rods and spacers (red = MV, yellow = NMV, blue = SS).

The conservation of momentum for phase k is

$$\begin{aligned} \frac{\partial}{\partial t} (\alpha_k \rho_k u_k) + \nabla \cdot (\alpha_k \rho_k u_k u_k) - \nabla \cdot (\alpha_k (\tau_k + \tau_k^t)) \\ = -\alpha_k \nabla p + \alpha_k \rho_k g + M, \end{aligned} \quad (3)$$

where τ_k and τ_k^t are laminar and turbulence shear stresses, p is pressure, and M is the sum of the interfacial forces that include drag and turbulent dispersion forces in this analysis.

The conservation of energy for phase k is:

$$\begin{aligned} \frac{\partial}{\partial t} (\alpha_k \rho_k h_k) + \nabla \cdot (\alpha_k \rho_k u_k h_k) \\ - \nabla \cdot \left(\alpha_k \left(\lambda_k \nabla T_k + \frac{\mu_t}{\sigma_h} \nabla h_k \right) \right) = Q, \end{aligned} \quad (4)$$

where h_k is phase enthalpy, λ_k is thermal conductivity, T is temperature, μ_t is turbulent viscosity, σ_h is turbulent Prandtl number, and Q is the interfacial heat transfer and other heat sources.

The standard k - ε turbulence model is solved for both phases to represent the flow turbulence and to provide the turbulent viscosities required in the model. Turbulence modeling in multiphase flows is clearly a highly complex area and not well developed or fully understood yet. Interactions between turbulent eddies and steam bubbles need to be taken into consideration. Turbulent eddies will disperse the bubbles. This effect is modeled by the turbulent dispersion force described below. Bubble motions could induce turbulence as well as dissipating turbulence. Bubble-induced turbulence models are available in the literature but not yet considered in this study. It is believed that the turbulence in the flow considered is generated mainly by the geometry and in particular around the spacer regions. The geometry-generated turbulence effects should be captured reasonably well by the grid and the k - ε model. The additional effects of bubble-induced turbulence will be investigated in the planned follow-on study in which the more advanced multiphase turbulence models will be considered.

3.2. Interfacial Forces. The drag force between the two phases includes a mean and a fluctuation component. The mean drag force is given by

$$F_D = \frac{3}{4} \frac{\alpha_d \rho_c C_D}{d} \alpha_c^n |u_r| u_r = A_D u_r, \quad (5)$$

where C_D is the drag coefficient, $u_r = (u_c - u_d)$ is the relative velocity between the two phases and d is the bubble diameter. Subscript c stands for continuous phase and d for dispersed phase. The exponent $n = 4$ is used to model the effects of high bubble concentration, sometimes called the bubble swarm effects.

The fluctuating component of the drag force accounts for the additional drag due to interaction between the dispersed phase and the surrounding turbulent eddies. This force is the turbulent dispersion force or the turbulent drag force:

$$F_T = -A_D \frac{\nu_c^t}{\alpha_d \alpha_c \sigma_\alpha} \nabla \alpha_d, \quad (6)$$

where ν_c^t is the continuous phase turbulent kinematic viscosity and σ_α is the turbulent Prandtl number; value of 1 is used.

The drag coefficient in (5) is computed according to Tomiyama [4] for a contaminated fluid system:

$$C_D = \max \left[\frac{24}{\text{Re}} (1 + 0.15 \text{Re}^{0.687}), \frac{8 \text{Eo}}{3(\text{Eo} + 4)} \right]. \quad (7)$$

The Reynolds and Eotvos numbers in (7) are defined as:

$$\begin{aligned} \text{Re} &= \frac{\rho_c u_r d}{\mu_c}, \\ \text{Eo} &= \frac{|\rho_c - \rho_d| g d^2}{\sigma}, \end{aligned} \quad (8)$$

where g is gravitational acceleration and σ is the surface tension coefficient.

The interfacial forces would generally include the lift and wall lubrication forces also. The effects of lift and wall lubrication forces are to move the steam bubbles radially away or towards the rod surfaces. Since in this exercise the computed void distributions are to be averaged across the channel, any information on radial void distribution will be lost in the comparison exercise; hence the inclusion of lift and wall lubrication forces is not important and was left out for simplicity.

3.3. Wall Boiling Model. At the heated wall, boiling occurs when the wall temperature exceeds the saturation temperature. The steam generation rate is determined by the wall heat partitioning model as follows,

$$q_w = q_l + q_Q + q_e, \quad (9)$$

where, q_w is the total heat flux from the wall, q_l is the single phase convection heat flux that takes place outside the influence area of nucleation bubbles, q_Q is the quenching heat flux within the bubble influence area, and q_e is the evaporation heat flux.

The bubble influence area A_e is defined by

$$A_e = F_A \frac{\pi d_d^2}{4} N'', \quad (10)$$

where, F_A , d_d , N'' are model constant, bubble departure size, and active nucleation site density, respectively. $F_A = 2$ is used in this study.

The evaporation heat flux can be expressed as

$$q_e = \frac{\pi d_d^3}{6} \rho_g h_{fg} f N'', \quad (11)$$

where, ρ_g is the steam density, h_{fg} is the latent heat and f is the bubble departure frequency.

The nucleation site density is obtained from Lemmert and Chawla [5]:

$$N'' = \left(m \Delta T_{\text{sup}} \right)^p, \quad (12)$$

where $\Delta T_{\text{sup}} = T_{\text{wall}} - T_{\text{sat}}$ is the wall superheat and $m = 185$ and $p = 1.805$. T_{wall} is the wall temperature and T_{sat} is the saturation temperature.

The bubble departure diameter is obtained from Toluinsky and Kostanchuk [6]:

$$d_d = d_0 \exp\left[-\frac{\Delta T_{\text{sub}}}{\Delta T_0}\right], \quad (13)$$

where $d_0 = 0.6$ mm and $\Delta T_0 = 45$ are model constants. $\Delta T_{\text{sub}} = T_{\text{sat}} - T_l$ is the liquid subcooling.

The bubble departure frequency is obtained from Cole [7]:

$$f = \sqrt{\frac{4g(\rho_l - \rho_g)}{3d_d\rho_l}}. \quad (14)$$

As the bubble detaches from the wall, the space it occupied is filled by cooler water. Part of the wall heat flux is used in heating the replacement water. This heat flux is the quenching heat flux. Del Valle and Kenning [8] modeled this heat transfer as transient heat conduction in a semi-infinite slab:

$$q_Q = h_q A_e (T_{\text{wall}} - T_l), \quad (15)$$

$$h_q = 2f \sqrt{\frac{t_w \rho_l C_{pl} \lambda_l}{\pi}},$$

where C_{pl} is the liquid heat capacity and t_w is the waiting time between the bubble departure and the activation of the next bubble:

$$t_w = \frac{0.8}{f}. \quad (16)$$

Convective heating of the liquid occurs over the area not covered by nucleation sites. The convective heat flux can be modeled as

$$q_l = h_c A_c (T_{\text{wall}} - T_l), \quad (17)$$

where the wall heat transfer coefficient h_c is obtained from the CFD wall function model and the area factor A_c is obtained from

$$A_c = 1 - A_e. \quad (18)$$

It is important to recognize that the nucleation site density, (12), and the bubble departure diameter, (13), are used together to form the effective boiling area. Correlations for these the two parameters were tuned as one model against available measured data by many investigators for a wide range of conditions. The authors have recently investigated more advanced models for these two parameters that include measured data from low pressure (1 bar) to high pressure (150 bar); see Lo et al [9]. In the Bartolomei test cases studied by Lo et al. [9] the pressure was 147 bar, close to the present study. It was found that calculating the effective boiling area using the more advanced models and the correlations given in (12) and (13) gave practically the same results. Hence the authors believe the models described are suitable for this study.

3.4. Bubble Size Distribution. A large range of bubble diameters can be expected in the flow. Since bubbles are generated by boiling and removed by condensation, the bubble diameter is expected to be function of the liquid temperature. Kurul and Podowski [10] defined the local bubble diameter using linear function between measured bubble diameters at two specified values of liquid subcooling:

$$d = \frac{d_1(\Delta T_{\text{sub}} - \Delta T_0) + d_0(\Delta T_1 - \Delta T_{\text{sub}})}{\Delta T_1 - \Delta T_0}, \quad (19)$$

$$\Delta T_0 \geq \Delta T_{\text{sub}} \geq \Delta T_1,$$

$$d = d_0, \quad \Delta T_{\text{sub}} \geq \Delta T_0,$$

$$d = d_1, \quad \Delta T_{\text{sub}} \geq \Delta T_1.$$

The following values were used in the model:

$$d_0 = 1.5 \times 10^{-4} \quad \text{at } \Delta T_0 = 13.5, \quad (20)$$

$$d_1 = 2 \times 10^{-3} \quad \text{at } \Delta T_1 = -5.$$

4. Results

The steady-state bundle test B5 Run 5.1121 was analysed. The flow conditions were given as pressure $P = 167.39$ (kg/cm²a), mass flux $G = 14.96$ (10⁶ kg/m²hr), power $Q = 2990$ (kW), and inlet temperature $T_{\text{in}} = 316.9$ (°C). The axial power distribution was uniform, and the radial distribution was Type A in which the central pins have the full power and the pins adjacent to the can walls were at 85% power. The measured void fraction averaged over the central 4 subchannels in the upper measuring plane at $z = 3.177$ m was 0.1791.

The computed results from the CFD model are shown in Figures 6 to 9. Figures 6, 7, and 8 show the nonuniformity of void distribution and flow vectors created by the mixing vanes. Figure 9 shows the computed void distributions at the 3 measuring planes. The computed averaged void over the central 4 subchannels in the upper measuring plane is 0.1576 as compared with the measured value of 0.1791. The computed void is therefore 12% lower than the measured value.

A major advantage of the 3-dimensional CFD method is the level of details it can provide about the flow pattern, void and temperature distributions, and so forth across the whole bundle as shown in Figures 6 to 9 or around individual rod as in Figures 10 and 11. Figure 10 shows the effects of the mixing vanes on void distribution. A higher void region is found in the convex side of the vane and a lower void region in the concave side. Detailed flow distribution around the mixing vane can be studied from vector plots like Figure 11.

5. Conclusions

A 3-dimensional CFD model of the PSBT 5-by-5 rod bundle was constructed using the STAR-CCM+ software. Unstructured polyhedral computational cells were used to model the rod bundle and all the spacer grids explicitly. The six-equation two-fluid model together with the wall boiling

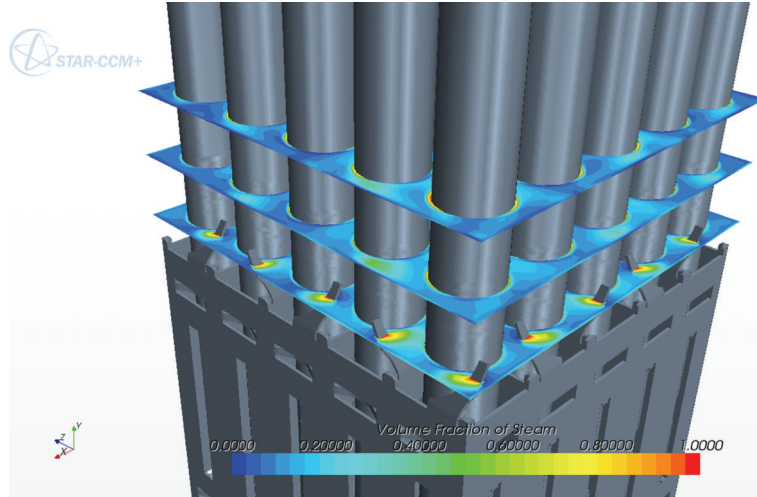


FIGURE 6: Void fraction.

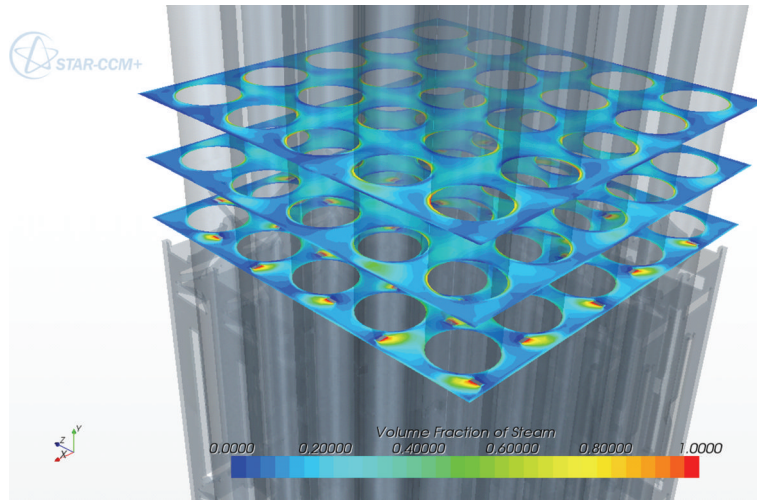


FIGURE 7: Void fraction downstream of spacer with mixing vanes.

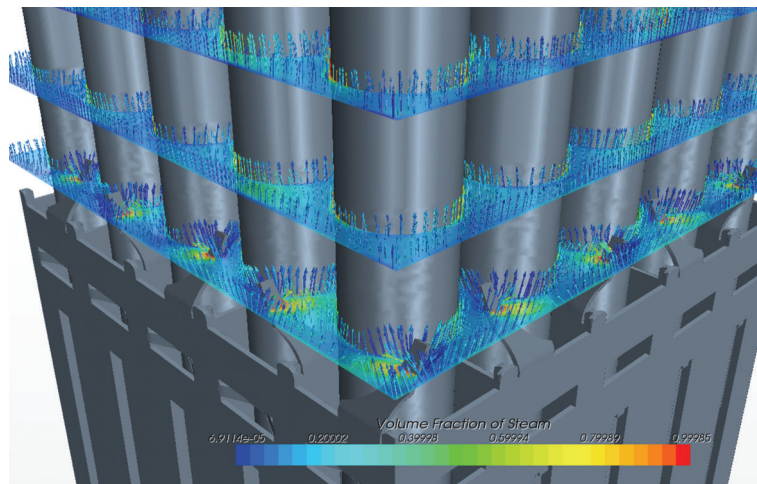


FIGURE 8: Effects of vanes on flow.

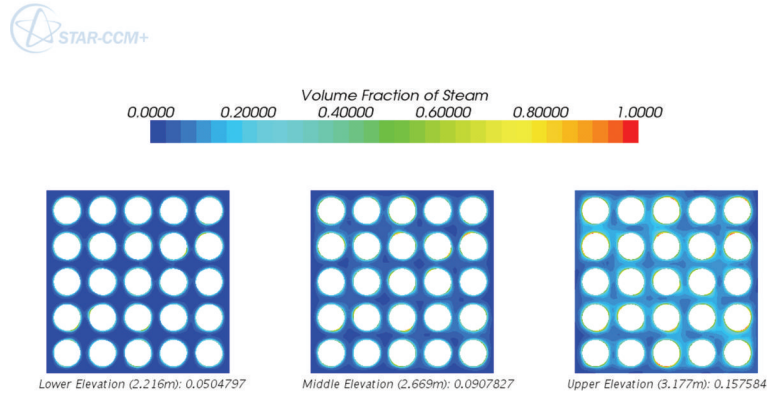


FIGURE 9: Void distributions in the 3 measuring planes.

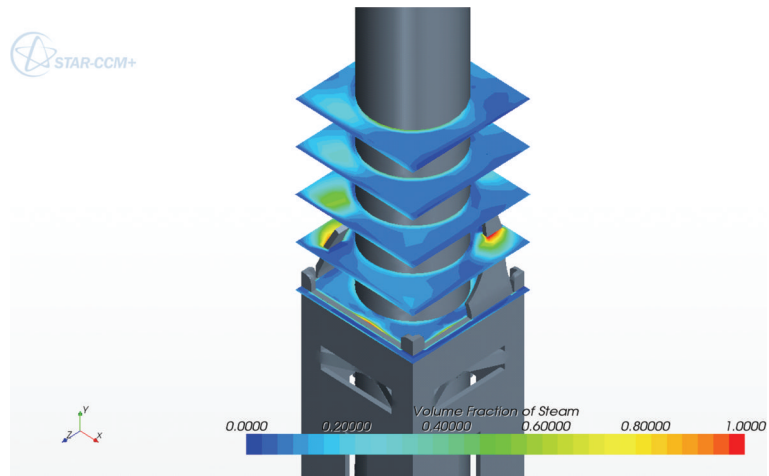


FIGURE 10: Void distribution above mixing vane spacer around one rod.

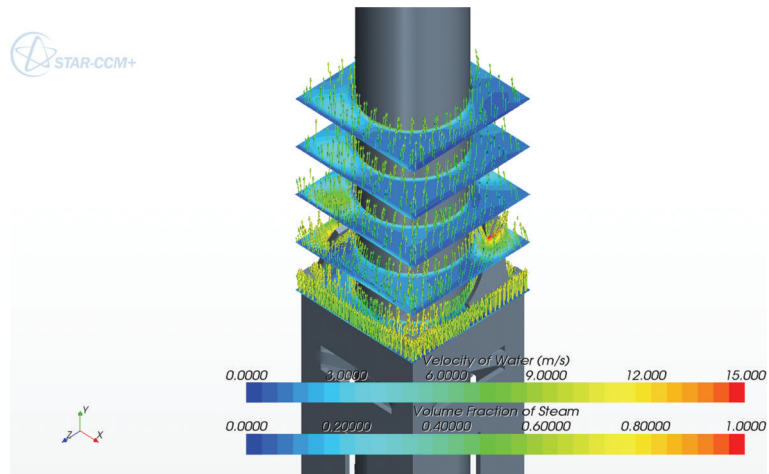


FIGURE 11: Velocity distribution above mixing vane spacer around one rod.

model was used to model the boiling two-phase flows in the bundle. The steady-state test B5 Run 5.1121 was studied. The computed void fraction averaged over the 4 central subchannels at the upper measuring plane was 0.1576 which is 12% lower than the measured value of 0.1791. This level of agreement between the results is encouraging given the

complexity of the geometry and the boiling two-phase flow physics.

A major advantage of 3-dimensional CFD is the level of details it can provide about the flow making it possible to perform detailed design analyses for spacer grid and investigating the effect of mixing vanes. However, before this

modelling technology will be accepted for design analysis much more rigorous verification and validation of the models are required. In addition to the comparison of channel-averaged results, comparison against detailed spatial distributions of void, velocity, temperature, and so forth, across the whole bundle is required. Hopefully such detailed measured data will become available soon.

References

- [1] A. Rubin, A. Schoedel, M. Avramova, H. Utsuno, S. Bajorek, and A. Velazquez-Lozada, "OECD/NRC Benchmark based on NUPEC PWR subchannel and bundle tests (PSBT), Volume I: Experimental Database and Final Problem Specifications," Report NES/NSC/DOC(2010)1, US NRC, OECD Nuclear Energy Agency, 2010.
- [2] "OECD/NEA Benchmark based on NUPEC PWR Subchannel and Bundle Tests (PSBT), Assembly Specifications and Benchmark database, Volume I," Report JNES/SAE-TH09-0019, Incorporated Administrative Agency, Nuclear Energy Safety Organization (JNES), Tokyo, Japan, 2009.
- [3] STAR-CCM+ v6.06, User Manual, CD-adapco, 2011.
- [4] A. Tomiyama, I. Kataoka, I. Zun, and T. Sakaguchi, "Drag coefficients of single bubbles under normal and micro gravity conditions," *JSMI International Journal, Series B*, vol. 41, no. 2, pp. 472–479, 1998.
- [5] M. Lemmert and J. M. Chawla, "Influence of flow velocity on surface boiling heat transfer coefficient," in *Heat Transfer in Boiling*, E. Hahne and U. Griggull, Eds., pp. 237–247, Academic Press and Hemisphere, 1977.
- [6] V. I. Tolubinsky and D. M. Kostanchuk, "Vapour bubbles growth rate and heat transfer intensity at subcooled water boiling heat transfer," in *Proceedings of the 4th International Heat Transfer Conference*, vol. 5, Paris, France, 1970, Paper no. B-2.8.
- [7] R. Cole, "A photographic study of pool boiling in the region of the critical heat flux," *AIChE Journal*, vol. 6, no. 4, pp. 533–538, 1960.
- [8] M. V. H. Del Valle and D. B. R. Kenning, "Subcooled flow boiling at high heat flux," *International Journal of Heat and Mass Transfer*, vol. 28, no. 10, pp. 1907–1920, 1985.
- [9] S. Lo, A. Splawski, and B. J. Yun, "The importance of correct modeling of bubble size and condensation in prediction of sub-cooled boiling flows," in *Proceedings of the 14th International Topical Meeting on Nuclear Reactor Thermal Hydraulics (NURETH-14)*, Toronto, Canada, September 2011.
- [10] N. Kurul and M. Z. Podowski, "Multidimensional effects in sub-cooled boiling," in *Proceedings of the 9th Heat Transfer Conference*, Jerusalem, Israel, 1990.